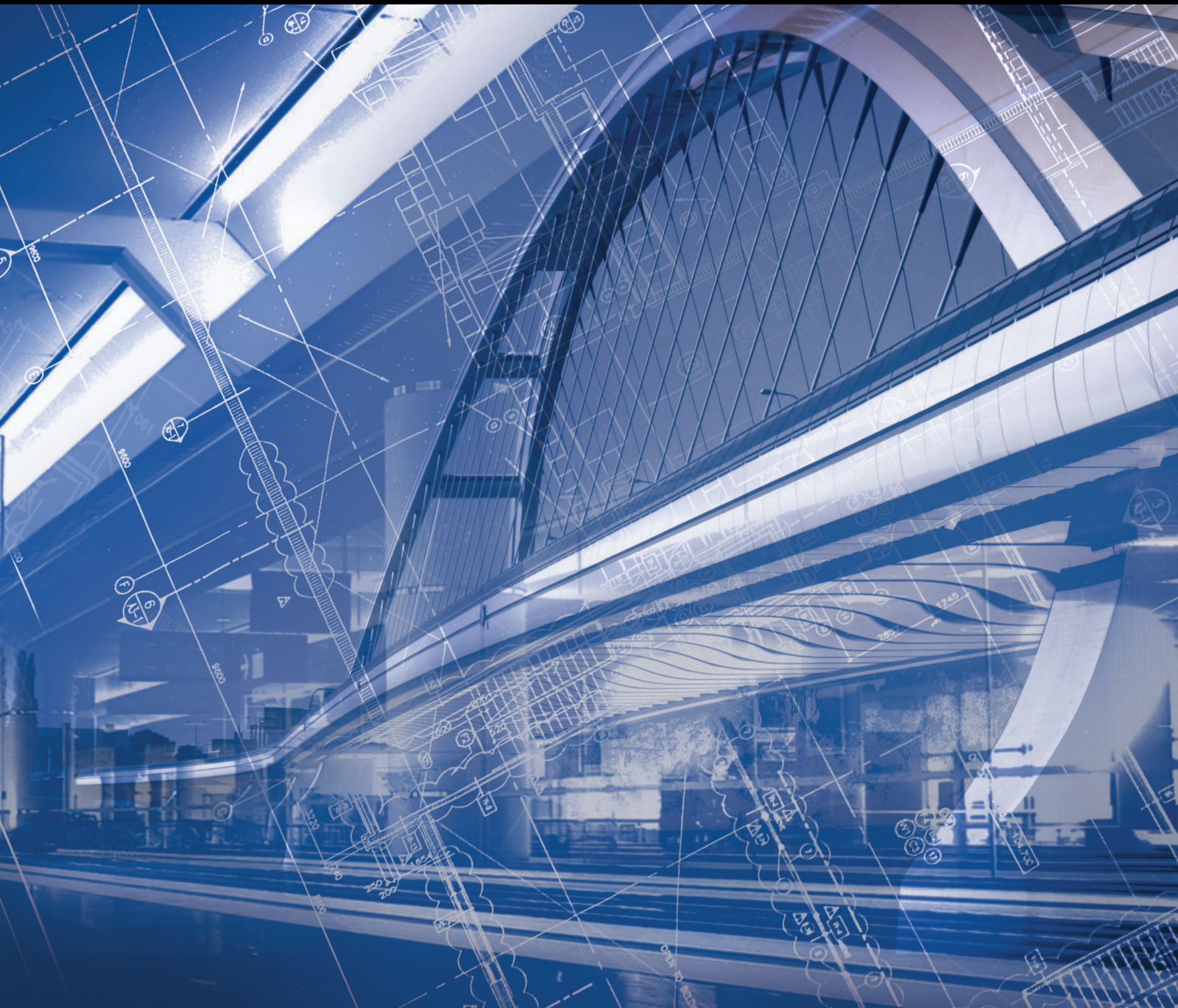


Advances in Civil Engineering

Fracture Behaviour of Rock in Complex Geological Environments

Lead Guest Editor: Rihong Cao

Guest Editors: Yunteng Wang, Jingjing Meng, and Chunyang Zhang





Fracture Behaviour of Rock in Complex Geological Environments

Advances in Civil Engineering

Fracture Behaviour of Rock in Complex Geological Environments

Lead Guest Editor: Rihong Cao

Guest Editors: Yunteng Wang, Jingjing Meng, and
Chunyang Zhang



Copyright © 2021 Hindawi Limited. All rights reserved.

This is a special issue published in "Advances in Civil Engineering." All articles are open access articles distributed under the Creative Commons Attribution License, which permits unrestricted use, distribution, and reproduction in any medium, provided the original work is properly cited.






Chief Editor

Cumaraswamy Vipulanandan, USA













Associate Editors

Chiara Bedon , Italy
Constantin Chalioris , Greece
Ghassan Chehab , Lebanon
Ottavia Corbi, Italy
Mohamed ElGawady , USA
Husnain Haider , Saudi Arabia
Jian Ji , China
Jiang Jin , China
Shazim A. Memon , Kazakhstan
Hossein Moayedi , Vietnam
Sanjay Nimbalkar, Australia
Giuseppe Oliveto , Italy
Alessandro Palmeri , United Kingdom
Arnaud Perrot , France
Hugo Rodrigues , Portugal
Victor Yepes , Spain
Xianbo Zhao , Australia

Academic Editors

José A.F.O. Correia, Portugal
Glenda Abate, Italy
Khalid Abdel-Rahman , Germany
Ali Mardani Aghabaglou, Turkey
José Aguiar , Portugal
Afaq Ahmad , Pakistan
Muhammad Riaz Ahmad , Hong Kong
Hashim M.N. Al-Madani , Bahrain
Luigi Aldieri , Italy
Angelo Aloisio , Italy
Maria Cruz Alonso, Spain
Filipe Amarante dos Santos , Portugal
Serji N. Amirkhania, USA
Eleftherios K. Anastasiou , Greece
Panagiotis Ch. Anastasopoulos , USA
Mohamed Moafak Arbili , Iraq
Farhad Aslani , Australia
Siva Avudaiappan , Chile
Ozgur BASKAN , Turkey
Adewumi Babafemi, Nigeria
Morteza Bagherpour, Turkey
Qingsheng Bai , Germany
Nicola Baldo , Italy
Daniele Baraldi , Italy

Eva Barreira , Portugal
Emilio Bastidas-Arteaga , France
Rita Bento, Portugal
Rafael Bergillos , Spain
Han-bing Bian , China
Xia Bian , China
Huseyin Bilgin , Albania
Giovanni Biondi , Italy
Hugo C. Biscaia , Portugal
Rahul Biswas , India
Edén Bojórquez , Mexico
Giosuè Boscato , Italy
Melina Bosco , Italy
Jorge Branco , Portugal
Bruno Briseghella , China
Brian M. Broderick, Ireland
Emanuele Brunesi , Italy
Quoc-Bao Bui , Vietnam
Tan-Trung Bui , France
Nicola Buratti, Italy
Gaochuang Cai, France
Gladis Camarini , Brazil
Alberto Campisano , Italy
Qi Cao, China
Qixin Cao, China
Iacopo Carnacina , Italy
Alessio Cascardi, Italy
Paolo Castaldo , Italy
Nicola Cavalagli , Italy
Liborio Cavaleri , Italy
Anush Chandrappa , United Kingdom
Wen-Shao Chang , United Kingdom
Muhammad Tariq Amin Chaudhary, Kuwait
Po-Han Chen , Taiwan
Qian Chen , China
Wei Tong Chen , Taiwan
Qixiu Cheng, Hong Kong
Zhanbo Cheng, United Kingdom
Nicholas Chileshe, Australia
Prinya Chindaprasirt , Thailand
Corrado Chisari , United Kingdom
Se Jin Choi , Republic of Korea
Heap-Yih Chong , Australia
S.H. Chu , USA
Ting-Xiang Chu , China


Zhaofei Chu , China
Wonseok Chung , Republic of Korea
Donato Ciampa , Italy
Gian Paolo Cimellaro, Italy
Francesco Colangelo, Italy
Romulus Costache , Romania
Liviu-Adrian Cotfas , Romania
Antonio Maria D'Altri, Italy
Bruno Dal Lago , Italy
Amos Darko , Hong Kong
Arka Jyoti Das , India
Dario De Domenico , Italy
Gianmarco De Felice , Italy
Stefano De Miranda , Italy
Maria T. De Risi , Italy
Tayfun Dede, Turkey
Sadik O. Degertekin , Turkey
Camelia Delcea , Romania
Cristoforo Demartino, China
Giuseppe Di Filippo , Italy
Luigi Di Sarno, Italy
Fabio Di Trapani , Italy
Aboelkasim Diab , Egypt
Thi My Dung Do, Vietnam
Giulio Dondi , Italy
Jiangfeng Dong , China
Chao Dou , China
Mario D'Aniello , Italy
Jingtao Du , China
Ahmed Elghazouli, United Kingdom
Francesco Fabbrocino , Italy
Flora Faleschini , Italy
Dingqiang Fan, Hong Kong
Xueping Fan, China
Qian Fang , China
Salar Farahmand-Tabar , Iran
Ilenia Farina, Italy
Roberto Fedele, Italy
Guang-Liang Feng , China
Luigi Fenu , Italy
Tiago Ferreira , Portugal
Marco Filippo Ferrotto, Italy
Antonio Formisano , Italy
Guoyang Fu, Australia
Stefano Galassi , Italy

Junfeng Gao , China
Meng Gao , China
Giovanni Garcea , Italy
Enrique García-Macías, Spain
Emilio García-Taengua , United Kingdom
DongDong Ge , USA
Khaled Ghaedi, Malaysia
Khaled Ghaedi , Malaysia
Gian Felice Giaccu, Italy
Agathoklis Giaralis , United Kingdom
Ravindran Gobinath, India
Rodrigo Gonçalves, Portugal
Peilin Gong , China
Belén González-Fonteboa , Spain
Salvatore Grasso , Italy
Fan Gu, USA
Erhan Güneyisi , Turkey
Esra Mete Güneyisi, Turkey
Pingye Guo , China
Ankit Gupta , India
Federico Gusella , Italy
Kemal Hacıfendioglu, Turkey
Jianyong Han , China
Song Han , China
Asad Hanif , Macau
Hadi Hasanzadehshooiili , Canada
Mostafa Fahmi Hassanein, Egypt
Amir Ahmad Hedayat , Iran
Khandaker Hossain , Canada
Zahid Hossain , USA
Chao Hou, China
Biao Hu, China
Jiang Hu , China
Xiaodong Hu, China
Lei Huang , China
Cun Hui , China
Bon-Gang Hwang, Singapore
Jijo James , India
Abbas Fadhil Jasim , Iraq
Ahad Javanmardi , China
Krishnan Prabhakan Jaya, India
Dong-Sheng Jeng , Australia
Han-Yong Jeon, Republic of Korea
Pengjiao Jia, China
Shaohua Jiang , China

MOUSTAFA KASSEM , Malaysia
Mosbeh Kaloop , Egypt
Shankar Karuppanan , Ethiopia
John Kechagias , Greece
Mohammad Khajehzadeh , Iran
Afzal Husain Khan , Saudi Arabia
Mehran Khan , Hong Kong
Manoj Khandelwal, Australia
Jin Kook Kim , Republic of Korea
Woosuk Kim , Republic of Korea
Vaclav Koci , Czech Republic
Loke Kok Foong, Vietnam
Hailing Kong , China
Leonidas Alexandros Kouris , Greece
Kyriakos Kourousis , Ireland
Moacir Kripka , Brazil
Anupam Kumar, The Netherlands
Emma La Malfa Ribolla, Czech Republic
Ali Lakirouhani , Iran
Angus C. C. Lam, China
Thanh Quang Khai Lam , Vietnam
Luciano Lamberti, Italy
Andreas Lampropoulos , United Kingdom
Raffaele Landolfo, Italy
Massimo Latour , Italy
Bang Yeon Lee , Republic of Korea
Eul-Bum Lee , Republic of Korea
Zhen Lei , Canada
Leonardo Leonetti , Italy
Chun-Qing Li , Australia
Dongsheng Li , China
Gen Li, China
Jiale Li , China
Minghui Li, China
Qingchao Li , China
Shuang Yang Li , China
Sunwei Li , Hong Kong
Yajun Li , China
Shun Liang , China
Francesco Liguori , Italy
Jae-Han Lim , Republic of Korea
Jia-Rui Lin , China
Kun Lin , China
Shibin Lin, China

Tzu-Kang Lin , Taiwan
Yu-Cheng Lin , Taiwan
Hexu Liu, USA
Jian Lin Liu , China
Xiaoli Liu , China
Xuemei Liu , Australia
Zaobao Liu , China
Zhuang-Zhuang Liu, China
Diego Lopez-Garcia , Chile
Cristiano Loss , Canada
Lyan-Ywan Lu , Taiwan
Jin Luo , USA
Yanbin Luo , China
Jianjun Ma , China
Junwei Ma , China
Tian-Shou Ma, China
Zhongguo John Ma , USA
Maria Macchiaroli, Italy
Domenico Magisano, Italy
Reza Mahinroosta, Australia
Yann Malecot , France
Prabhat Kumar Mandal , India
John Mander, USA
Iman Mansouri, Iran
André Dias Martins, Portugal
Domagoj Matesan , Croatia
Jose Matos, Portugal
Vasant Matsagar , India
Claudio Mazzotti , Italy
Ahmed Mebarki , France
Gang Mei , China
Kasim Mermerdas, Turkey
Giovanni Minafò , Italy
Masoomah Mirrashid , Iran
Abbas Mohajerani , Australia
Fadzli Mohamed Nazri , Malaysia
Fabrizio Mollaioli , Italy
Rosario Montuori , Italy
H. Naderpour , Iran
Hassan Nasir , Pakistan
Hossein Nassiraei , Iran
Satheeskumar Navaratnam , Australia
Ignacio J. Navarro , Spain
Ashish Kumar Nayak , India
Behzad Nematollahi , Australia

Chayut Ngamkhanong , Thailand
Trung Ngo, Australia
Tengfei Nian, China
Mehdi Nikoo , Canada
Youjun Ning , China
Olugbenga Timo Oladinrin , United Kingdom
Oladimeji Benedict Olalusi, South Africa
Timothy O. Olawumi , Hong Kong
Alejandro Orfila , Spain
Maurizio Orlando , Italy
Siti Aminah Osman, Malaysia
Walid Oueslati , Tunisia
SUVASH PAUL , Bangladesh
John-Paris Pantouvakis , Greece
Fabrizio Paolacci , Italy
Giuseppina Pappalardo , Italy
Fulvio Parisi , Italy
Dimitrios G. Pavlou , Norway
Daniele Pellegrini , Italy
Gatheeshgar Perampalam , United Kingdom
Daniele Perrone , Italy
Giuseppe Piccardo , Italy
Vagelis Plevris , Qatar
Andrea Pranno , Italy
Adolfo Preciado , Mexico
Chongchong Qi , China
Yu Qian, USA
Ying Qin , China
Giuseppe Quaranta , Italy
Krishanu ROY , New Zealand
Vlastimir Radonjanin, Serbia
Carlo Rainieri , Italy
Rahul V. Ralegaonkar, India
Raizal Saifulnaz Muhammad Rashid, Malaysia
Alessandro Rasulo , Italy
Chonghong Ren , China
Qing-Xin Ren, China
Dimitris Rizos , USA
Geoffrey W. Rodgers , New Zealand
Pier Paolo Rossi, Italy
Nicola Ruggieri , Italy
JUNLONG SHANG, Singapore



Nikhil Saboo, India
Anna Saetta, Italy
Juan Sagaseta , United Kingdom
Timo Saksala, Finland
Mostafa Salari, Canada
Ginevra Salerno , Italy
Evangelos J. Sapountzakis , Greece
Vassilis Sarhosis , United Kingdom
Navaratnarajah Sathiparan , Sri Lanka
Fabrizio Scozzese , Italy
Halil Sezen , USA
Payam Shafigh , Malaysia
M. Shahria Alam, Canada
Yi Shan, China
Hussein Sharaf, Iraq
Mostafa Sharifzadeh, Australia
Sanjay Kumar Shukla, Australia
Amir Si Larbi , France
Okan Sirin , Qatar
Piotr Smarzewski , Poland
Francesca Sollecito , Italy
Rui Song , China
Tian-Yi Song, Australia
Flavio Stochino , Italy
Mayank Sukhija , USA
Piti Sukontasukkul , Thailand
Jianping Sun, Singapore
Xiao Sun , China
T. Tafsirojjaman , Australia
Fujiao Tang , China
Patrick W.C. Tang , Australia
Zhi Cheng Tang , China
Weerachart Tangchirapat , Thailand
Xiixin Tao, China
Piergiorgio Tataranni , Italy
Elisabete Teixeira , Portugal
Jorge Iván Tobón , Colombia
Jing-Zhong Tong, China
Francesco Trentadue , Italy
Antonello Troncone, Italy
Majbah Uddin , USA
Tariq Umar , United Kingdom
Muahmmad Usman, United Kingdom
Muhammad Usman , Pakistan
Mucteba Uysal , Turkey

Ilaria Venanzi , Italy
Castorina S. Vieira , Portugal
Valeria Vignali , Italy
Claudia Vitone , Italy
Liwei WEN , China
Chunfeng Wan , China
Hua-Ping Wan, China
Roman Wan-Wendner , Austria
Chaohui Wang , China
Hao Wang , USA
Shiming Wang , China
Wayne Yu Wang , United Kingdom
Wen-Da Wang, China
Xing Wang , China
Xiuling Wang , China
Zhenjun Wang , China
Xin-Jiang Wei , China
Tao Wen , China
Weiping Wen , China
Lei Weng , China
Chao Wu , United Kingdom
Jiangyu Wu, China
Wangjie Wu , China
Wenbing Wu , China
Zhixing Xiao, China
Gang Xu, China
Jian Xu , China
Panpan , China
Rongchao Xu , China
HE YONGLIANG, China
Michael Yam, Hong Kong
Hailu Yang , China
Xu-Xu Yang , China
Hui Yao , China
Xinyu Ye , China
Zhoujing Ye, China
Gürol Yildirim , Turkey
Dawei Yin , China
Doo-Yeol Yoo , Republic of Korea
Zhanping You , USA
Afshar A. Yousefi , Iran
Xinbao Yu , USA
Dongdong Yuan , China
Geun Y. Yun , Republic of Korea



Hyun-Do Yun , Republic of Korea
Cemal YİĞİT , Turkey
Paolo Zampieri, Italy
Giulio Zani , Italy
Mariano Angelo Zanini , Italy
Zhixiong Zeng , Hong Kong
Mustafa Zeybek, Turkey
Henglong Zhang , China
Jiupeng Zhang, China
Tingting Zhang , China
Zengping Zhang, China
Zetian Zhang , China
Zhigang Zhang , China
Zhipeng Zhao , Japan
Jun Zhao , China
Annan Zhou , Australia
Jia-wen Zhou , China
Hai-Tao Zhu , China
Peng Zhu , China
QuanJie Zhu , China
Wenjun Zhu , China
Marco Zucca, Italy
Haoran Zuo, Australia
Junqing Zuo , China
Robert Černý , Czech Republic
Süleyman İpek , Turkey

Contents

A Case Study of Thaumassite Sulfate Attack in Tunnel Engineering

Chongbang Xu, Xingyu Zhou , Hualao Wang, Xiaojing Gao , and Xuefeng Li
Research Article (14 pages), Article ID 8787757, Volume 2021 (2021)


Research on the Strength Characteristics and Crack Propagation Law of Noncoplanar Nonthrough Jointed Rock Mass by PFC2D

Qingzhi Chen , Yuanming Liu , Shilong Mei, Kai Cao, Bin Du, and Wei Wang
Research Article (28 pages), Article ID 6935414, Volume 2021 (2021)




Seepage and Dynamic Characteristics of Carbonaceous Mudstone Coarse-Grained Soil Embankment with Different Gradations

Zhong-ming He, Xiao-qu Liu , Ke Huang, and Jian-ping Xiong
Research Article (14 pages), Article ID 4436942, Volume 2021 (2021)


Study of the Failure Mode of a Jointed Rock Mass due to a Stress Wave

Xi Kun Qian  and Cong Cong Li
Research Article (12 pages), Article ID 1342691, Volume 2021 (2021)



Flexural Fatigue Behaviors of Silicon Carbide Recycled Concrete in Corrosive Environments

Jinzhi Zhou , Tiantian Fu , Chuheng Zhong , Kun Peng, and Ziyang Shuang
Research Article (10 pages), Article ID 7459777, Volume 2021 (2021)

Experimental Study on Influence of Joint Surface Morphology on Strength and Deformation of Nonthrough Jointed Rock Masses under Direct Shear

Yuanming Liu , Qingzhi Chen, Huiyu Chen, Xun Ou, Dafu Wu, and Xingchao Tian
Research Article (17 pages), Article ID 2581382, Volume 2021 (2021)



Experimental Investigation on Effects of Bacterial Concentration, Crack Inclination Angle, Crack Roughness, and Crack Opening on the Fracture Permeability Using Microbially Induced Carbonate Precipitation

Yulin Zou, Hao Bai , Fan Shen, Hong Xu, and Yundong Shou 
Research Article (15 pages), Article ID 4959229, Volume 2021 (2021)

A Damage Constitutive Model of Rock Subjected to Freeze-Thaw Cycles Based on Lognormal Distribution

Hang Lin , Linyuan Liang, Yifan Chen , and Rihong Cao
Research Article (8 pages), Article ID 6658915, Volume 2021 (2021)

Experimental Analysis of Bending Stiffness Characteristics of Grouted Double Mortise-Tenon Joint for Prefabricated Metro Station Structure


Xiuren Yang , Fang Lin , and Meiqun Huang
Research Article (13 pages), Article ID 9958436, Volume 2021 (2021)

Numerical Analysis for the Caving Characteristics of Rock Mass with Inclined Joints in Caving Mining

Jinbo Sui, Fengyu Ren , Jianli Cao, and Huan Liu 



Research Article (12 pages), Article ID 9917744, Volume 2021 (2021)

Displacement Monitoring during the Excavation and Support of Deep Foundation Pit in Complex Environment

Zhouqiang Li 

Research Article (7 pages), Article ID 5715306, Volume 2021 (2021)

Volume Changes and Mechanical Properties of Expansive Mudstone below Canals under Wet-Dry/Wet-Dry-Freeze-Thaw Cycles

Rui Zhu , Ying-hao Huang, Zhu Song, and Feng Zhou 


Research Article (11 pages), Article ID 3791692, Volume 2021 (2021)

Experimental Study on Physical-Mechanical Properties of Expansive Soil Improved by Multiple Admixtures

Binhui Ma , Kai Cai, Xing Zeng, Zhuo Li, Zhiyong Hu, Qiunan Chen, Chengbin He, Bingchu Chen, and Xiaocheng Huang




Research Article (15 pages), Article ID 5567753, Volume 2021 (2021)

Research on the Failure and Fracture Evolution of Mylonite with a Prefabricated Circular Opening by Discrete Element Method

Kunmeng Li, Yuanhui Li , Shuai Xu, Zhipeng Xiong, and Long An


Research Article (10 pages), Article ID 5510150, Volume 2021 (2021)

The Analysis of Anchoring Mechanism of Rock Slope in Two Layers Based on the Nonlinear Twin-Shear Strength Criterion

X. B. Gu , Y. H. Wang, X. J. Ji , and Y. H. Zhu 


Research Article (8 pages), Article ID 5565320, Volume 2021 (2021)

Similar Physical Modeling of Roof Stress and Subsidence in Room and Pillar Mining of a Gently Inclined Medium-Thick Phosphate Rock

Xiaoshuang Li, Zhifang Liu, and Shun Yang 


Research Article (17 pages), Article ID 6686981, Volume 2021 (2021)

Numerical Study on Failure Mechanisms of Shaft Wall Consisting of Steel Plate and Concrete under the Effects of Explosion

YanJun Qi, Linming Dou, Zhaoxing Dong , and Bo Meng

Research Article (16 pages), Article ID 9919660, Volume 2021 (2021)

A Three-Section-Settlement Calculation Method for Composite Foundation Reinforced by Geogrid-Encased Stone Columns

Binhui Ma , Zhiyong Hu, Zhuo Li, Kai Cai, Minghua Zhao, Chengbin He, Qiunan Chen, Bingchu Chen, and Xiaocheng Huang

Research Article (10 pages), Article ID 5576713, Volume 2021 (2021)





Contents

Unloading Mechanics and Energy Characteristics of Sandstone under Different Intermediate Principal Stress Conditions

Yingjie Zhang , Jiangteng Li , Gang Ma, and Shuangfei Liu




Research Article (9 pages), Article ID 5577321, Volume 2021 (2021)

Research on Bearing Characteristics of Open-Ended Pipe Piles under Static Load

Haibao Feng , Xingke Dai , Shuiyue Chen , and Jianwei Chen 

Research Article (8 pages), Article ID 5572898, Volume 2021 (2021)

Chloride Ion Corrosion Pattern and Mathematical Model for C60 High-Strength Concrete after Freeze-Thawing Cycles

Yan Li, Bing Li , Lian-ying Zhang , Chao Ma , Jiong Zhu , Ming Li , and Hai Pu 

Research Article (11 pages), Article ID 5523499, Volume 2021 (2021)

Experimental Research on Bending Bearing Capability of Grouted Double Mortise-Tenon Joint for Prefabricated Metro Station Structure

Xiuren Yang , Fang Lin , and Meiqun Huang

Research Article (14 pages), Article ID 6635409, Volume 2021 (2021)

Research Article

A Case Study of Thaumaside Sulfate Attack in Tunnel Engineering

Chongbang Xu, Xingyu Zhou , Hualao Wang, Xiaojing Gao , and Xuefeng Li

Research Institute of Highway Ministry of Transport, Bridge & Tunnel Research Center, Beijing 100088, China

Correspondence should be addressed to Xingyu Zhou; z19980131@gmail.com

Received 27 April 2021; Accepted 9 November 2021; Published 6 December 2021

Academic Editor: Chunyang Zhang

Copyright © 2021 Chongbang Xu et al. This is an open access article distributed under the Creative Commons Attribution License, which permits unrestricted use, distribution, and reproduction in any medium, provided the original work is properly cited.

There existed ever-increasing structural diseases in the Dugongling tunnel after the completion of the construction. Systematic research was carried out based on the information of tunnel engineering geology, disease development, mineral composition of surrounding rock and concrete, and laboratory tests. Results showed that (1) the concrete structure from the Dugongling tunnel suffered from a typical thaumasite sulfate attack (TSA); (2) tunnel diseases developed under the influence of multiple geological factors such as groundwater, karst, gypsum bearing stratum, and geological tectonics. Groundwater aggravated the appearance of engineering defects of various geological factors and accelerated the softening and swelling of surrounding rock. Moreover, the additional load of supporting structure increased, and the concrete structure was prone to sulfate attack; (3) the development of tunnel diseases showed long-cycle and large-scale characteristics, and the types of diseases are heterogeneous. The tunnel diseases develop rapidly in the third year after the construction. The structure collapse disease, one of the most serious diseases of tunnel lining, occurred in the fifth year after construction; and (4) according to the conditions of TSA, technical treatment measures were proposed. These measures included blocking the flow of CO_3^{2-} , improving the impermeability of concrete structures, and decreasing the diffusion of external ions and groundwater. This work provides a solution for the treatment of similar tunnel disease and mechanism analysis.

1. Introduction

The gypsum rock in the carbonate rock area has multiple influences on the stability of the tunnel. The gypsum rock can not only cause dissolution combined with the co-deposited carbonate minerals [1], but also soften and swell under the action of groundwater [2–4]. Moreover, gypsum rock can lead to sulfate attacks in the lining concrete structures [5–9], whereas the thaumasite sulfate attack (TSA), elusive, is relatively late understood by researchers. The formation mechanism of TSA is unclear yet [10, 11]. TSAs in tunnels have occurred in Switzerland, Germany, Norway, and Australia [12–15], while these attacks are more common in water conservancy dam projects [16–18] in China. The reports on TSA in Chinese tunnel projects are extremely rare. TSA may dissolve the main hydration products of Portland cement, CSH gel, in concrete tunnel lining. The decomposition of CSH gel leads to the decrease in the bearing capacity of the tunnel lining structure and the reduction in structural safety and reliability [19, 20], which is one of the most harmful types of tunnel diseases.

Hazardous engineering conditions caused extremely serious diseases and TSAs in the tunnel supporting and lining structure after construction. Based on the analyses of sulfate erosion conditions and softening and swelling characteristics of surrounding rock, comprehensive tests of the mineral composition of surrounding rock and lining concrete and systematic analyses of the types and development rules of tunnel diseases were carried out to figure out the formation process of diseases in the Dugongling tunnel. Finally, a targeted engineering treatment plan was put forward to effectively treat the diseases. In addition, this kind of treatment provides a reference plan for the tunnel with TSAs.

2. Project Overview

The Dugongling tunnel [21] is a separated two-way four-lane highway tunnel. The starting and ending pile number of left line is from ZK33+226 to ZK35+700 with a length of 2474 m and that of right line is from YK33+227 to YK35+742 with a length of 2515 m; the overall direction of

tunnel axis is 264° , and the maximum depth of tunnel is 231 m. The construction clearance of the tunnel has a net width of 10.25 m and a height limit of 5 m (see Figure 1).

The Dugongling tunnel was completed in November 2012. Tunnel disease was first detected in the later stage of its construction. As of 2016, the total length of the tunnel structure that needed to be demolished and replaced due to diseases is 1,515 m. The main range of tunnel diseases occurred in sections from K34 + 500 to K34 + 800. Diseases in the Dugongling tunnel were mostly lining concrete cracking, and deformation at early stage of the diseases, no corrosion, and argillization phenomena of concrete were found. The concrete argillization phenomenon had not been discovered until the firebox was removed, as shown in Figure 2. Concrete argillization showed a feature of integrity in the dry environment, while seemed sludge-like under grasping in the wet.

In the supplementary survey of tunnel diseases in 2016, 223 samples from 119 cross-sectional primary support concrete were picked. The mineral compositions of the concrete were mainly calcite, dolomite, quartz, potash feldspar, plagioclase, ettringite, gypsum, and thaumasite. 60 sections of the 119 sections were detected with TSA, accounting for 50.4% of total samples; 84 of 223 samples of primary supporting concrete were detected with thaumasite (Figure 3), accounting for 37.7% of total samples. It can be seen that the disease in the Dugongling tunnel was a typical case of TSA [22].

3. Tunnel Disease Characteristics and Sulfate Attacks

3.1. Scale and Extent of Diseases

3.1.1. Main Types of Tunnel Diseases. The types of diseases in the Dugongling tunnel, listed in Table 1, show an increasing trend in previous years. In 2012, the main kinds of tunnel diseases were lining cracking, pavement uplifting, and cracking. In 2013, the overturning of the cable trench was detected; in 2014, the staff found partial cracks at arch footing and intrusion of the clearance in some sections, as shown in Figure 4; and in 2016 and 2017, the diseases of the Dugongling tunnel deteriorated, leading to the collapse and fall of the secondary lining concrete (Figure 5) and the extrusion and damage of the inner wall of the cable trench (Figure 6).

3.1.2. Scales in Previous Years. The disease scales over the years are shown in Figure 7. The disease scale of the tunnel reached 2321 m at the beginning of 2017, which accounted for 47% of the length of the tunnel. It can be seen from Figure 7 that the fastest development period of tunnel diseases took place in 2013 and 2014, 1765 m, which accounted for 76% of total length of diseases; there was a gradual increase in new diseases from 2015 to 2017. The length of new diseases was only 8 m and 58 m in 2016 and 2017, respectively. Thus, the scale of tunnel disease developed rapidly in the early stage of development of

disease, and the growth rate of the total diseases slowed down in the later stage.

3.1.3. Degree of Disease Development. According to the classification of disease levels from *technical specification of maintenance for highway tunnel* (JTG H12-2015), the variations of disease scales over the years at all levels are shown in Figure 8.

- (i) The number of Level 1 (i.e., the tunnel structure is in serviceability and safety) and Level 2 (i.e., no negative effect on the traffic safety of tunnel vehicles, and further observation is needed) diseases in the tunnel decreased from 2014 to 2017, and the reductions in Level 1 and Level 2 were 66 m and 70 m, respectively.
- (ii) The number of Level 3 and Level 4 diseases fluctuated from 2014 to 2017, indicating that tunnel diseases were developing dynamically during this period.
- (iii) The number of tunnel sections with Level 5 diseases has gradually increased in the 3 years, with an increasing rate of 86% and a length of 215 m, of which the fastest development occurred in 2014 to 2015 and 2015 to 2016. There was an increase in more than 80 m per year in 2014 to 2015 and 2015 to 2016, respectively.
- (iv) By the year when diseases began to be resolved, 2017, the total scale of Level 3, Level 4, and Level 5 diseases in need of treatment reached 1515 m.

3.1.4. Typical Cross-Sectional Cases. The design basis of YK34 + 482 ~ YK34 + 524 section is grade IV surrounding rock. The primary supporting of the tunnel is I16 I steel with a spacing of 1.0 m and C20 concrete with a thickness of 20 cm, and the secondary lining of the tunnel is C25 plain concrete with a thickness of 40 cm; a fire chamber is set on the right side of YK34 + 500 section. The development process of disease is as follows:

- (1) The process of collapse. During the construction safety inspection in March 2017, cracks around the fire chamber were discovered; the monitoring data in April showed that the length and width of the diagonal cracks on the upper left side of the fire chamber increased, extending upward from the spandrel; cracks continued to develop in May and June, and a small area of concrete surface peeling occurred; in July, the concrete collapsed suddenly (Figure 9).
- (2) Description of the surrounding rock. The concrete in the internal side of the fire chamber showed that the internal (secondary lining and primary supporting) concrete expanded and deformed outwards about 5 cm–10 cm, showing a “belly bulging” shape (Figure 10); the expansion of the waterproof board, after the collapse of concrete, was particularly obvious,

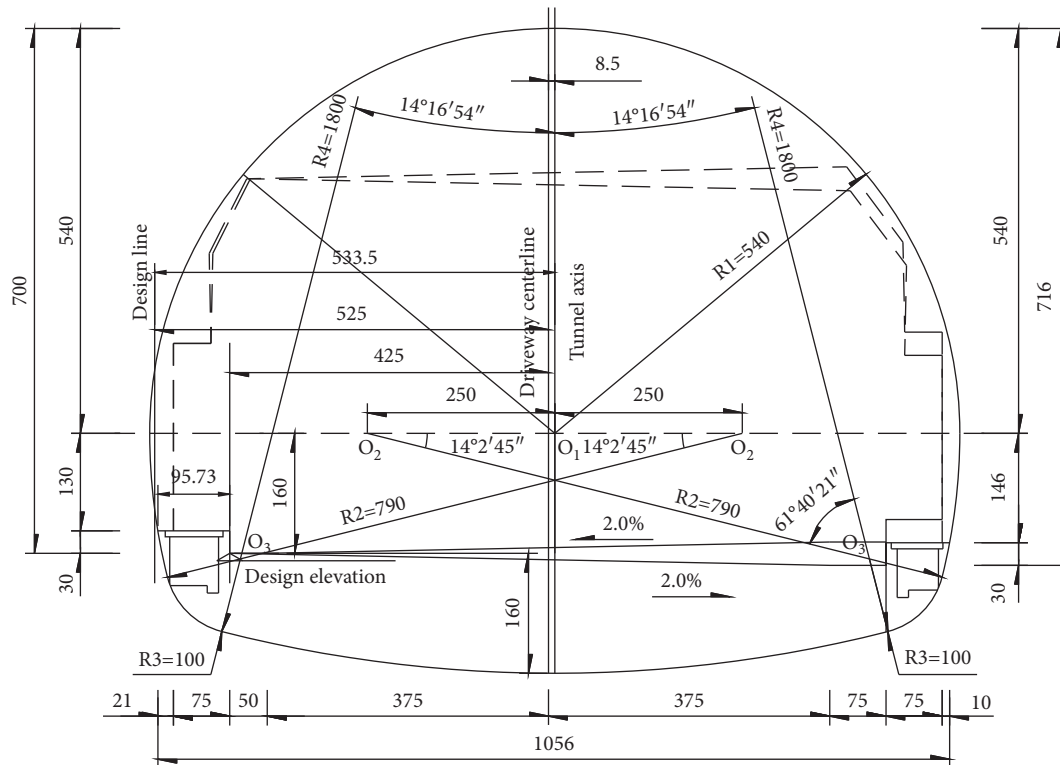


FIGURE 1: Interior outline design of the Dugongling tunnel (unit: cm).



FIGURE 2: Photographs of the corroded tunnel lining concrete.

and the primary supporting concrete behind it showed damp and sandy features.

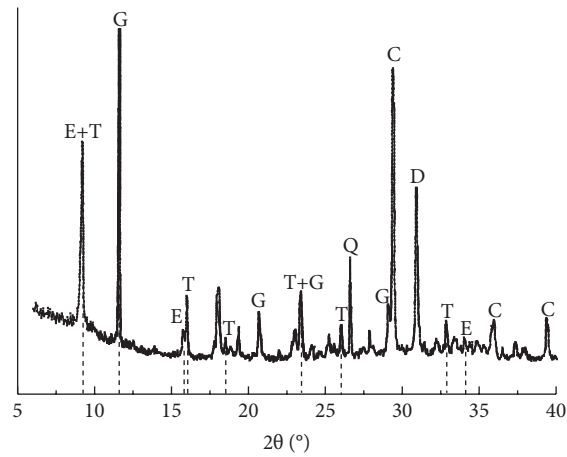
- (3) Indoor testing. The surrounding rock and concrete there were sampled and sent for compositional analysis. The results showed that the surrounding rock was gypsum rock with gypsum content of 97%–98% (Figure 11 and Table 2); the thaumasite content in the primary supporting concrete was 19.3%, and the contents of gypsum and ettringite were 17.1% and 3.8%, respectively.

4. Geological Cause Analysis of Tunnel Diseases

Thaumasite sulfate attack is a special type of sulfate attack. The formation of TSA needs slow temperature (below 15°C),

water, SO_4^{2-} , CO_3^{2-} , Si^{4+} , SiO_3^{2-} , Ca^{2+} , etc. The following analyses of the causes of the diseases in the Dugongling tunnel are based on the formation conditions of thaumasite sulfate attack.

4.1. Low Temperature. The tunnel sites in a temperate semiarid continental climate area. The temperature of this area is between -5.9°C and 23°C , and the average temperature of this area is 9.2°C . The temperature in the five months from November to March of the following year is below 10°C ; the temperature inside the tunnel ranges from -5°C to 20°C throughout the year, with an average temperature of 8.8°C . Therefore, the environment of the tunnel lining concrete structure provides low-temperature conditions for TSA.



T: Thaumasite
 E: Ettringite
 Q: Quartz
 C: Calcite
 G: Gypsum
 D: Dolomite

FIGURE 3: XRD pattern of tunnel lining concrete sample [22].

TABLE 1: Tunnel disease types over the years [23].

Years	Cracking of the lining	Uplift of the pavement	Cracking of the pavement	Overturning of the cable trench	Local bursting crack	Deformation invading limit	Cracking of the secondary lining	Extrusion of the inner wall of the cable trench
2012	✓	✓	✓					
2013	✓	✓	✓	✓				
2014	✓	✓	✓	✓	✓	✓		
2015	✓	✓	✓	✓	✓	✓		
2016	✓	✓	✓	✓	✓	✓	✓	✓
2017	✓	✓	✓	✓	✓	✓	✓	✓



FIGURE 4: Photograph of early-stage tunnel disease.



FIGURE 5: Sudden collapse of the secondary tunnel lining.



FIGURE 6: Inner wall extrusion of the cable trench.

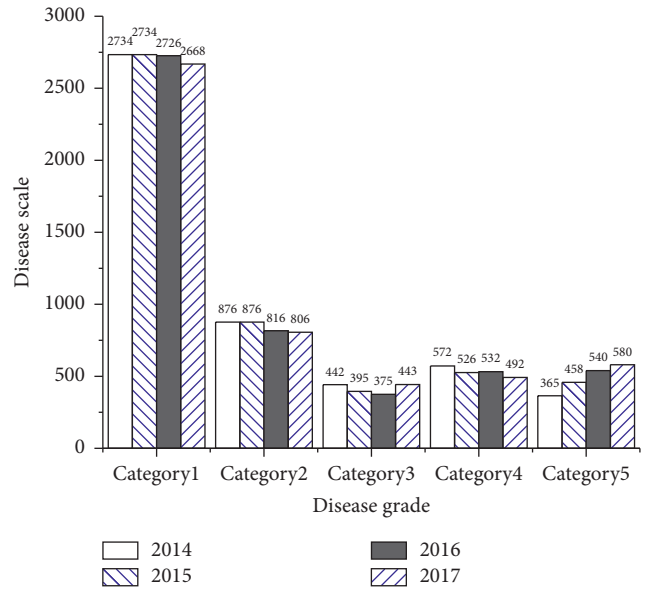


FIGURE 8: Annual variations of disease scale of different levels [23].

4.2. Groundwater

4.2.1. Type of Groundwater. The types of groundwater in the tunnel site area are carbonate fissure karst water and perched water, of which the water level of carbonate fissure karst water is lower than the design elevation of the tunnel. Therefore, this type of groundwater has little effect on the diseases of the Dugongling tunnel. The perched water, mainly replenished by atmospheric precipitation, has a large seasonal variation.

4.2.2. Supplement of Groundwater. The annual average precipitation in the tunnel site area is 592.33 mm and its main precipitation period is from July to September, which accounts for 56% to 70% of the annual precipitation. Affected by topography, surface precipitation collects and infiltrates along the mountain to low-lying places. In section K34 + 500~K34 + 800 of the tunnel, more than 100 iron ore pits distribute on the surface and its cross sections of the pits vary in size, and the shapes are mostly bands and ellipses (Figure 12) according to the surface survey. The group of surface mine pits provides conditions for surface water collection and irrigation. It is estimated that the surface water infiltration within the mine pits reaches 31 m³/d.

After the surface water infiltrates, it circulates along the internal cracks and pores in the rock mass. The dissolution and development conditions of the tunnel rock mass provide a path for this circulation. According to engineering survey data and tunnel construction information, there are many joints, cracks, and dissolution in the surrounding rock of the tunnel, and the dissolution of the tunnel site shows a typical characteristic of combined carbonate and sulfate erosions [24, 25]. Most of the dissolution is dissolution pores, channels (Figure 13), and small karst caves (Table 3). Moreover, due to the

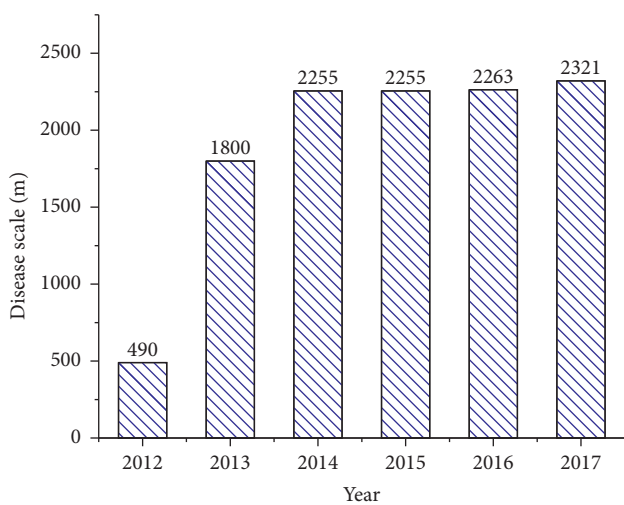


FIGURE 7: Disease statistics in previous years of the Dugongling tunnel [23].

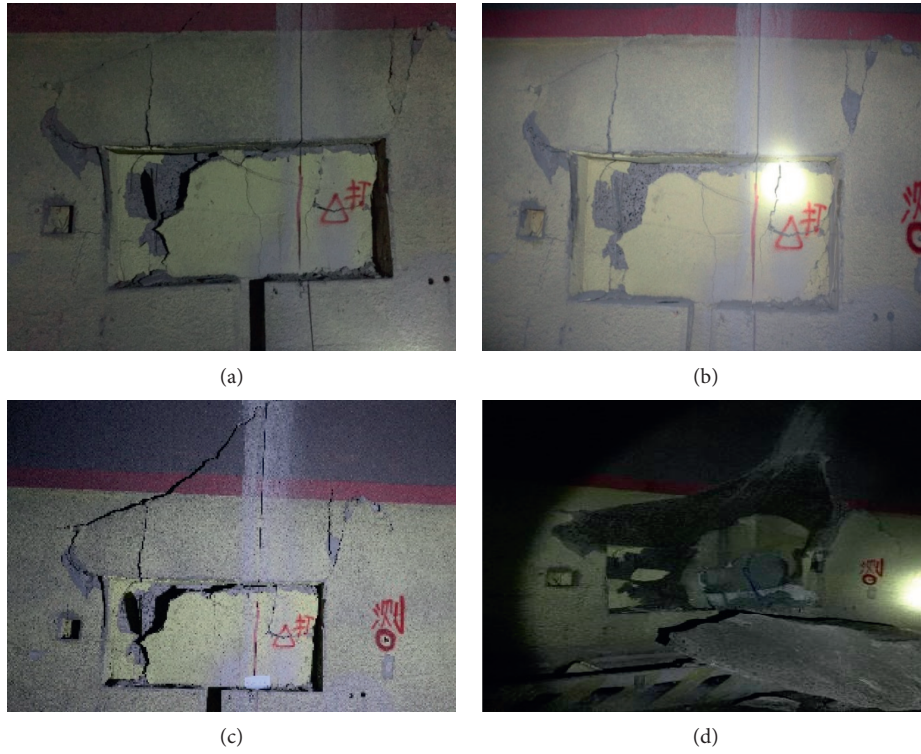


FIGURE 9: Disease development process of the fire chamber in YK34 + 500. (a) 2017.03. (b) 2017.04. (c) 2017.05. (d) 2017.07.

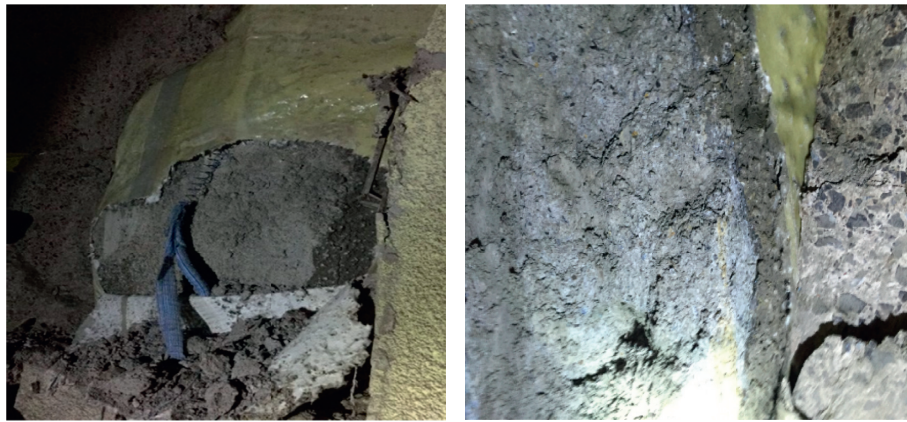


FIGURE 10: Photographs of concrete in the field of YK34 + 500.



FIGURE 11: Surrounding rock exposure and rock sample photographs in YK34 + 500.

TABLE 2: Identification results of surrounding rock samples in section YK34 + 500.

No.	Test items	Test results/descriptions
1	Name of rock sample	Gypsum rock
2	Naked-eye observation on color	Grey-white
3	Sample preparation	Thin slice
4	Structure	Granular structure
5	Tectonics	Lump
6	Identification basis	GB/T17412.1
7	Essential mineral	97%-98% gypsum
8	Secondary minerals	2-3% dolomite
9	Accessory mineral	Apatite
10	Microscopic observation	<p>The rock has lump tectonics and a granular structure.</p> <p>Gypsum is tabular and colorless with a particle size distribution of 0.01–2.0 mm and has a negative protrusion. The highest interference color is first-order yellow and white, and cleavage in one direction is observed.</p> <p>Dolomite has a semi-automorphic rhombohedral shape with a particle size distribution of 0.01–0.03 mm and is unevenly distributed. It has a prominent flash protrusion and high-order white interference color.</p>



FIGURE 12: Photographs of the corroded tunnel lining concrete.

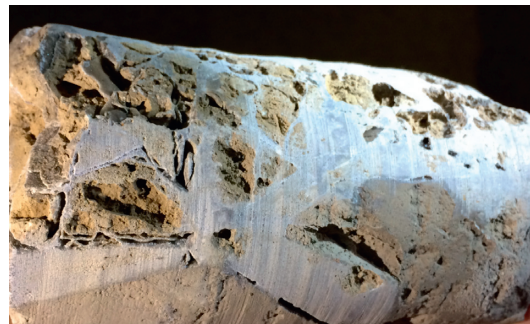


FIGURE 13: Dissolution of rock core sample in the field.

interconnection between the dissolution pores the air blow in the tunnel drilling is observed (Figure 14).

4.2.3. *The Collection of Groundwater around the Tunnel.*
 In the process of groundwater circulation in the rock mass, the groundwater accumulates in some sections due to the influence of the geological structure. The compound folded structure is in the K34 + 900-K35 + 200 section of the cave body, consisting of two synclines (S1, S3) and one anticline

(S2) and striking nearly the north-south direction: the S1 syncline crosses the tunnel at an angle of 84°, the east wing occurrence is 200°∠5°, and the west wing occurrence is 122°∠25°; S2 syncline crosses the tunnel at 88° obliquely, the east wing occurrence is 122°∠25°, and the west wing occurrence is 280°∠20°; and S3 syncline crosses the tunnel at 72°, the east wing occurrence is 280°∠20°, and the west wing occurrence is 80°∠4°. In the composite fold structure section of the tunnel, the surrounding rock below the sidewall is mainly marl, which has a strong water barrier effect. The

TABLE 3: Information of partial caves in the Dugongling tunnel.




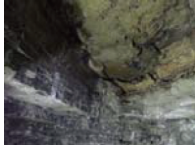

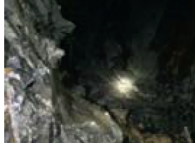
No.	Pile no.	Location	Scale	Photograph	No.	Pile no.	Location	Scale	Photograph
1	YK34+796	Arch crown	The length, width, and height are 10 m, 3.5 m, and 4 m, respectively		4	ZK35+060	Arch crown	The length, width, and height are 6 m, 6 m, and 1.7 m, respectively	
2	ZK34+308	Left spandrel	5 m long, 1 m width, 1 m height The length, width, and height are 5 m, 1 m, and 1 m, respectively		5	ZK35+302	Right spandrel	The length, width, and height are 4.8 m, 7.2 m, and 3.2 m, respectively	
3	ZK34+703	Arch crown	The length, width, and height are 4 m, 5 m, and 1.5 m, respectively		6	ZK35+248	Arch crown	The length, width, and height are 3 m, 2 m, and 3 m, respectively	



FIGURE 14: Air blow in the drilling.

coexistence of the two causes the concentration and occurrence of groundwater around the tunnel of the S1 and S3 syncline structure.

Based on the above analyses, surface precipitation flows along the surface and forms a pool at the mine pit, and flows down into the rock mass. Meanwhile, dissolved pores, caves, and small caves are the main paths for groundwater to circulate in the rock mass; groundwater converges around the tunnel under the influence of compound folded structure and marl, which provides the water for the formation of thaumasite sulfate attack.

4.3. Source of SO_4^{2-} , CO_3^{2-} , and SiO_3^{2-} . The tunnel concrete is ordinary Portland cement. The calcium and silicon substances in this type of cement provide a large amount of SiO_3^{2-} and Ca^{2+} during the hydration reaction.

Therefore, the SiO_3^{2-} and Ca^{2+} come from concrete the tunnel used.

The tunnel line mainly locates in the interbedded formation of limestone and marlstone of the upper Majiagou Formation in the Middle Ordovician. The roof of the tunnel is a formation of limestone, and the bottom is an interbedded formation of marlstone and limestone. The geological lithology of the tunnel site provides SO_4^{2-} and CO_3^{2-} . 30% of the 225 rock samples contain anhydrite or gypsum; 34% of the 121 sections contain anhydrite or gypsum. In the surrounding rock, gypsum rock is sandwiched in marlstone and is produced in layered and lenticular forms (Figure 15). The color of gypsum rock, similar to that of marlstone, is grey-white in general and grey-brown in parts (Figure 16), and the maximum content of gypsum rock in some rock samples is more than 90% (Table 2).

4.4. Other Reasons. In addition to the TSA, the softening and swelling characteristics of the surrounding rock contributed to the terrible disease in the Dugongling tunnel. The formation of marl has the properties of softening and swelling, and marl mechanical test report is listed in Table 4. Identification results of core samples of the surrounding rock are shown in Table 5. The softening coefficient of marlstone is 0.72~0.818, the free expansion rate is 0.001~0.094, the expansion force P_p varies from 0.99 to 20.6 kPa, and the saturated water absorption rate is 2.9~6.0%. It shows that the marlstone from the Dugongling tunnel has the characteristics of water absorption softening and water loss disintegration.

The irregular distribution of gypsum in the limestone formation aggravated the softening and swelling features of gypsum. According to the indoor expansion tests of lateral confinement on anhydrite in the Dugongling tunnel [21], the expansion forces of the specimens with anhydrite content are greater than 90% reaching 1.94~3.1 MPa, as shown in Figure 17. The existence of anhydrite made the swelling characteristics of the surrounding rock more significant.



FIGURE 15: Core samples from the surrounding rock and concrete.



FIGURE 16: Gypsum rocks in the abandoned dreg site of the tunnel.

TABLE 4: Test results of marlstone [26].

No.	Drilling number	Locations	Free expansion rate F_s (%)	Expansion force P_p (kPa)	Saturated water absorption rate ω_{sr} (%)	Natural compressive strength (MPa)	Saturated compressive strength (MPa)	Softening coefficient, δ
1	ZK5	K34 + 953	—	1.5	5.2	26.9	22.0	0.818
2	ZK19	K35 + 370	0.001	4.13	6.00	20.4	16.2	0.794
3	ZK4	K34 + 822	0.006	0.99	4.60	12.0	9.0	0.75
4	ZK15	K35 + 155	0.094	20.6	2.90	29.6	21.5	0.726

Marlstone and gypsum rock softened and swelled under the action of groundwater. On the one hand, the softening of the surrounding rock of the tunnel reduced the bearing capacity of the surrounding rock. On the other hand, the swelling of the surrounding rock produced lateral expansion forces, both of which deteriorated the stress condition and load of supporting and lining structures. The variations of marlstone and gypsum rock along the longitudinal direction of the tunnel were superimposed on the unfavorable conditions of surrounding rock fragmentation, crack development, and karst, which caused the inhomogeneous distribution of loads on the supporting and lining structures longitudinally and laterally, resulting in the longitudinal cracking of the tunnel sidewall, the overturning of cable trenches, and uplifting of pavement.

4.5. Results of the Analysis of Tunnel Disease Causes. Surface pits provided favorable objective conditions for groundwater replenishment. Joint fissures and karst bodies (dissolved pores, caverns, and caves) developed in the rock mass and then provided paths for the circulation of

groundwater. The composite fold structure and the water barrier formed by marl made the groundwater converge behind the tunnel section lining and kept accumulation. It dissolved and carried a large amount of sulfate ions and carbonate ions when the water flowed through, which was prone to thaumasite sulfate attack in the low temperature. In summary of various factors, the formation of tunnel diseases can be described in Figure 18 as follows.

5. Engineering Treatment Plan

According to the causes of tunnel diseases, the treatment of tunnel diseases can be done in the following aspects: groundwater treatment, surrounding rock reinforcement, and lining structure optimization.

5.1. Groundwater Treatment. According to the geological and hydrogeological conditions of the engineering project and the influence of groundwater in tunnel diseases, the treatment of groundwater mainly included programs as follows:

TABLE 5: Identification results of core samples of the surrounding rock.

No.	Test items	Test results/descriptions
1	Name of rock sample	Anhydrite rock
2	Naked-eye observation on color	Grey-white
3	Sample preparation	Thin slice
4	Structure	Fibrous structure, metasomatic residual structure
5	Tectonics	Bedded
6	Identification basis	GB/T17412.1
7	Essential mineral	90% gypsum
8	Secondary minerals	4–6% dolomite and 4–6% anhydrite
9	Accessory mineral	Zircon
10	Microscopic observation	The rock has a bedded tectonics, a fibrous structure, and a metasomatic residual structure. Gypsum is fibrous. The protrusion is low and negative, and the highest interference color is first-order yellow and white, and is arranged in a directional arrangement. Anhydrite is columnar, and most of it is converted into gypsum, and a small amount of residue can be seen in the center of the crystal. The protrusion is middle and positive, the highest interference color reaches third-order green, and it exhibits parallel extinction and polysynthetic twin development with a directional arrangement. Dolomite has an allotriomorphic granular structure with a particle size distribution of 0.005–0.02 mm, and it has a prominent twinkling and high-order white interference color.

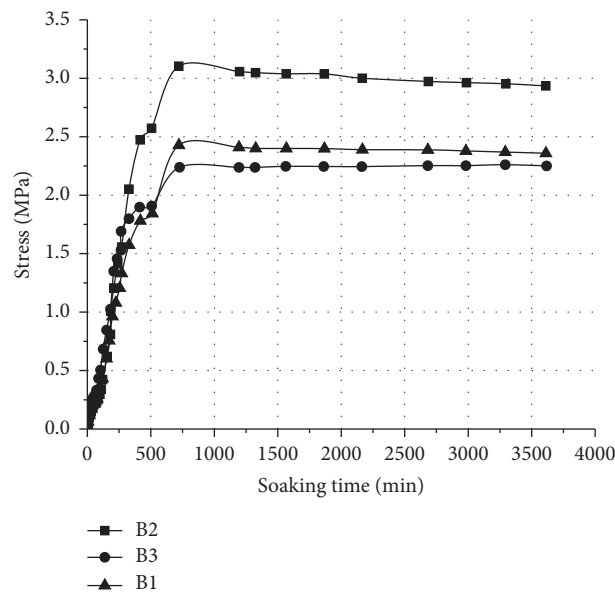


FIGURE 17: Expansive force test results of gypsum rock [21].

- (1) Surface mine pits were backfilled and sealed to prevent the surface water collection and irrigation through the pits
- (2) Grouting in the surrounding rock was adopted in the fracture zone and section of the tunnel to block the collection of groundwater behind the tunnel lining structure
- (3) The section with all-inclusive waterproofing secondary lining where tunnel lining was replaced cut off the contact between the secondary lining of the tunnel and the groundwater
- (4) The tunnel waterproof and drainage systems were improved and restored to avoid long-term collection and retention of groundwater in the tunnel

5.2. *Surrounding Rock Reinforcement in the Tunnel.* According to the softening and swelling characteristics of the surrounding rock of the tunnel and the development of karst, the reinforcement design of the tunnel surrounding rock was carried out, including the following:

- (1) Long and short anchor rods were conducted in the tunnel to enhance the self-bearing capacity of the tunnel and control the expansion and deformation of the surrounding rock
- (2) The karst development sections were filled and compacted by backfilling and grouting methods to enhance the bearing capacity and stability of the surrounding rock of the tunnel

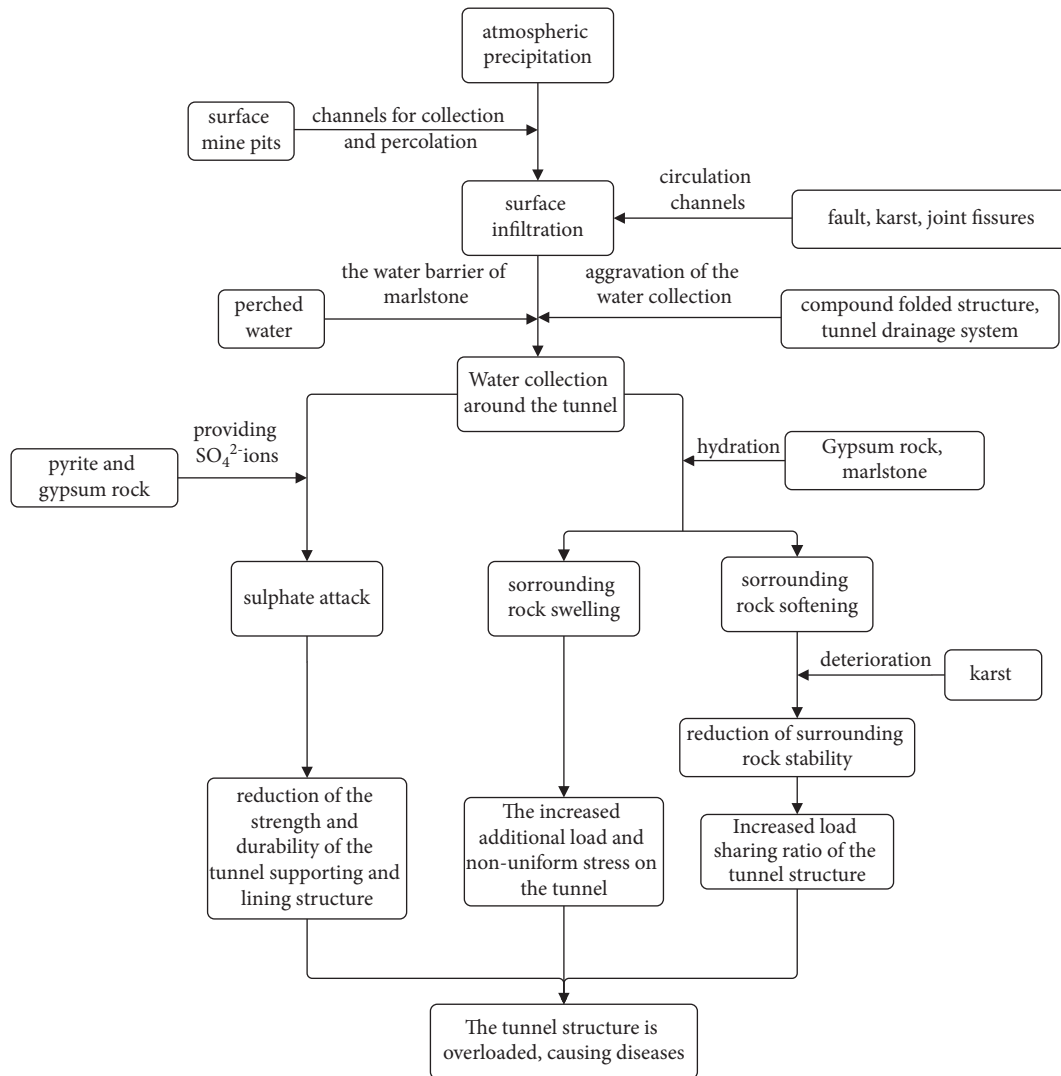


FIGURE 18: Mechanism of engineering harmfulness in the Dugongling tunnel.

5.3. *Treatment of the Tunnel Lining Structure.* According to the characteristics of the tunnel lining structure disease and the swelling and softening of the surrounding rock, the lining structure of the diseased section of the tunnel was treated as follows:

- (1) The primary supporting and secondary lining replacement programs were adopted for the tunnel concrete under sulfate attacks. To improve the strength and load-bearing capacity of the tunnel, the supporting and lining structures were enclosed into a ring, of which the initial supporting was reinforced by I20 steel framework with a spacing of 60 cm and C30 shotcrete with a thickness of 28 cm, and the secondary lining adopted a C35 reinforced concrete structure with a thickness of 50 cm (Figure 19).
- (2) Design for sulfate attack resistance of the lining structure concrete: the occurrence of TSA needs many factors and complex mechanisms [27–30]. From the perspective of engineering applications, measures including waterproofing and reducing the source of

sulfate ions were taken to prevent this disease. The measures can be summarized as “blocking the flow of CO_3^{2-} , improving the impermeability of concrete structures, and decreasing the diffusion of external ions and groundwater.” The detailed programs are as follows:

- (i) The cement, coarse and fine aggregates, and external additives in the primary supporting concrete of the tunnel contained no limestone materials. The basalt was used as gravel by replacing limestone.
- (ii) Admixtures in concrete (including preservatives, water-reducing agents and other additives, fly ash, and other admixtures) contained or produced no carbonate ions and sulfate ions.
- (iii) The impermeability grade of the initial supporting concrete was greater than P6, preferably greater than P8, and the impermeability grade of the secondary lining concrete was greater than P8.

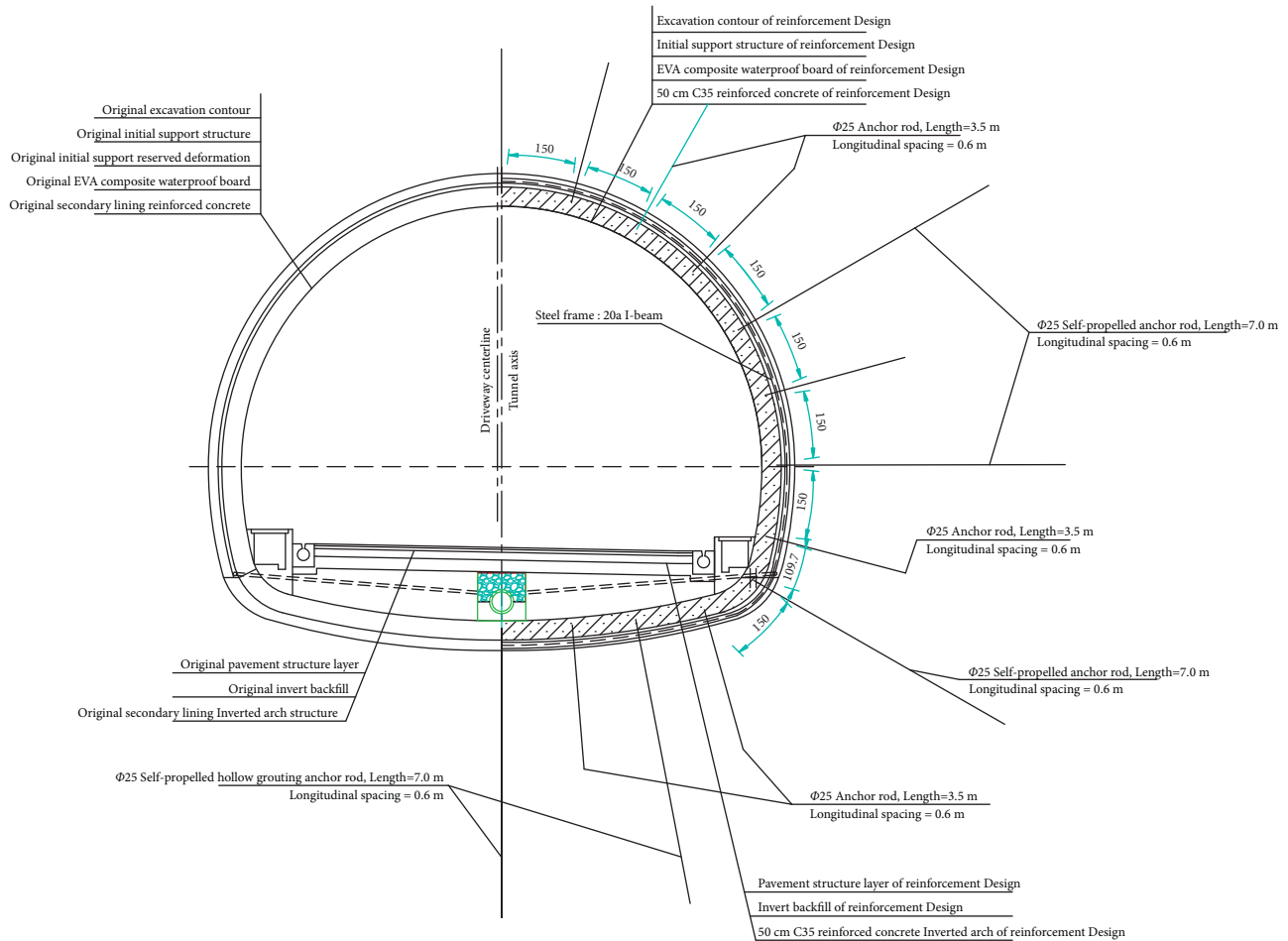


FIGURE 19: Schematic diagram of the treatment design of tunnel diseases.



FIGURE 20: Photographs of the operation site of the Dugongling tunnel.

- (iv) The sulfate-resistant concrete was used as the primary supporting and secondary lining concrete.

At present, the Dugongling tunnel has been opened to traffic for three years after the disease treatment, and the tunnel lining structure is in good technical condition (Figure 20).

6. Conclusions

- (1) The disease of the Dugongling tunnel, mainly thaumasite sulfate attack, was a long cycle with multiple types and large scale. It took 6 years from the first discovery of the disease to the treatment of tunnel diseases. During this period, the diseases continued to develop, the number of disease types increased from the first 3 to 8, and the outbreak of diseases occurred in the third year after construction (i.e., in 2014). The most serious disease, the lining structure collapse, took place in the fifth year after construction (i.e., in 2016).
- (2) The formation process of the diseases: surface water was collected from surface mine pits and infiltrated underground, and then, it circulated to marlstone formation via karst caves, dissolution cavities, and joint fissures to form the perched water; under the influence of compound folded structure and the drainage system of the tunnel, groundwater was collected and infiltrated around the tunnel; the low-temperature environment of the groundwater and the sulfate ions and carbonate ions in it caused TSAs to the tunnel lining structure, which deteriorated the

strength and induced structural diseases of the tunnel lining structure; under the influence of groundwater, the surrounding rock of the tunnel softened and expanded, the load of the tunnel lining structure increased, and finally the lining cracked.

- (3) Considering the formation conditions of TSA and the characteristics of the surrounding rock of the tunnel, the treatment measures of the tunnel diseases can [31–33] be proposed as “blocking the flow of CO_3^{2-} , improving the impermeability of concrete structures, and decreasing the diffusion of external ions and groundwater.”

Data Availability

The data used to support the findings of this study are available from the corresponding author upon request.

Conflicts of Interest

The authors declare no conflicts of interest.

Acknowledgments

This work was financially supported by the Central Public-Interest Scientific Institution Basal Research Fund (Grant no. 2020-9032) and the Science and Technology Project of Department of Transportation of Shanxi Province (Grant no. 2017-1-6).

References

- [1] Y. R. Lu, F. E. Zhang, B. R. Yan, S. Zhang, and M. Yin, “Mechanism of karst development in sulphate rocks and its main geo-environmental impacts,” *Acta Geoscientia Sinica*, vol. 23, no. 1, pp. 1–6, 2002.
- [2] Y. M. Liu, H. M. Yu, and C. Wang, “Research on mechanism of damage of anhydrock in dolomite layer to tunnel structure,” *Rock and Soil Mechanics*, vol. 32, no. 9, pp. 2704–2709, 2011.
- [3] Z. R. Jia, Z. W. Li, and J. G. Dong, “Analysis and treatment measures of expansive surrounding rock of Liangshuijing tunnel,” *Highways*, vol. 10, pp. 211–213, 2011.
- [4] Y. B. Zhu, Y. L. Wu, and H. M. Yu, “Strength behavior of tunnel’s gypsiferous surrounding rock,” *Journal of Yangtze River Scientific Research Institute*, vol. 30, no. 9, pp. 53–58, 2013.
- [5] X. K. Li, C. H. Shi, and M. F. Lei, “Defect classification of tunnel structures in sulfate environments,” *Modern Tunneling Technology*, vol. 4, pp. 19–24, 2011.
- [6] M. Wu, *Sulfate Resistance of Cement Based Materials in Low Temperature Environment*, China University of Mining and Technology, Beijing, China, 2016.
- [7] J. Y. Liu, *Study on New Type of Antihigh Concentration Sulfate Corrosion Agent and its concrete Performance*, Beijing University of Civil Engineering and Architecture, Beijing, China, 2016.
- [8] F. Y. Peng, *Study on Resistance of Alkali-Activated Slag Concrete to Sulfate Attack*, Chongqing University, Chongqing, China, 2008.
- [9] Z. Q. Liu, *Study of the Basic Mechanisms of Sulfate Attack on Cementitious Materials*, Central South University, Changsha, China, 2009.
- [10] B. Erlin and D. C. Stark, *Identification and Occurrence of Thaumasite in Concrete a Discussion for the 1965 HRB Symposium on Aggressive Fluids*, Highway Research Record, Washington, DC, USA, 1966.
- [11] D. Macphee and S. Diamond, “Thaumasite in cementitious materials,” *Cement and Concrete Composites*, vol. 25, no. 8, pp. 805–807, 2003.
- [12] M. Romer, L. Holzer, and M. Pfiffner, “Swiss tunnel structures: concrete damage by formation of thaumasite,” *Cement and Concrete Composites*, vol. 25, no. 8, pp. 1111–1117, 2003.
- [13] E. Freyburg and A. M. Berninger, “Field experiences in concrete deterioration by thaumasite formation: possibilities and problems in thaumasite analysis,” *Cement and Concrete Composites*, vol. 25, no. 8, pp. 1105–1110, 2003.
- [14] P. Hagelia, R. G. Sibbick, N. J. Crammond, and C. K. Larsen, “Thaumasite and secondary calcite in some Norwegian concretes,” *Cement and Concrete Composites*, vol. 25, no. 8, pp. 1131–1140, 2003.
- [15] F. Mittermayr, A. Baldermann, C. Kurta et al., “Evaporation - a key mechanism for the thaumasite form of sulfate attack,” *Cement and Concrete Research*, vol. 49, pp. 55–64, 2013.
- [16] M. Y. Hu, M. S. Tang, and F. M. Long, “Thaumasite sulfate attack in concrete of Yonggan Dam,” *Concrete*, vol. 11, pp. 5–7, 2004.
- [17] B. Ma, X. Gao, E. A. Byars, and Q. Zhou, “Thaumasite Formation in a tunnel of bapanxia dam in Western China,” *Cement and Concrete Research*, vol. 36, no. 4, pp. 716–722, 2006.
- [18] M. Y. Hu, F. M. Long, and M. S. Tang, “The thaumasite form of sulfate attack in concrete of Yonggan Dam,” *Cement and Concrete Research*, vol. 36, no. 10, pp. 2006–2008, 2006.
- [19] A. Neville, “The confused world of sulfate attack on concrete,” *Cement and Concrete Research*, vol. 34, no. 8, pp. 1275–1296, 2004.
- [20] P. Fredrik, F. D. Glasser, and J. Marchand, “Durability of concrete-degradation phenomena involving detrimental chemical reactions,” *Cement and Concrete Research*, vol. 38, no. 2, pp. 226–246, 2008.
- [21] C. B. Xu and H. L. Wang, “Analysis on geological characteristics of gypsiferous marl strata in tunnel,” *Chinese Journal of Underground Space and Engineering*, vol. 16, no. 1, pp. 227–233, 2020.
- [22] C. Xu, X. Gao, K. Zhang, Z. Liu, and F. Zhao, “Constitutive model of swelling gypsum rock,” *Advances in Civil Engineering*, vol. 2020, p. 1, Article ID 8878005, 2020.
- [23] X. Y. Hao, P. L. Wang, and C. B. Xu, “Study on sulfate attack and treatment technology in tunnel,” *Modern Tunneling Technology*, vol. 56, no. S2, pp. 706–711, 2019.
- [24] D. C. Wang, R. Q. Zhang, Y. H. Shi, S. Z. Xu, Q. C. Yu, and X. Liang, *General Hydrogeology*, Geological Publishing House, Beijing, China, 1997.
- [25] H. B. Bai and X.-X. Miao, “Research on main controlling factors of ordovician karst development in Lu’ an Coal Field,” *Journal of Mining & Safety Engineering*, vol. 25, no. 1, pp. 17–21, 2008.
- [26] N.-N. Lang, *Experimental Study and Application of Physical and Mechanical Properties of gypsum-containing Marl in Dugongling Tunnel*, Research Institute of Highway Ministry of Transport, Beijing, China, 2018.
- [27] X. J. Gao, B. G. Ma, and H. W. Deng, “Influence of binder composition on the thaumasite form of sulfate attack of

- concrete,” *Journal of Harbin Institute of Technology*, vol. 39, no. 10, pp. 1554–1558, 2007.
- [28] C. Wang, C. Yu, Y. L. Luo, and J. Liu, “Comparison of thaumasite sulfate attack formation speed under different erosion condition,” *Journal of Tongji University*, vol. 43, no. 5, pp. 748–753, 2015.
- [29] M. Wu, Y. S. Ji, X. F. Chen et al., “Effects of Superfine fly ash on thaumasite form of sulfate attack,” *Journal of Zhejiang University*, vol. 50, no. 8, pp. 1479–1485, 2016.
- [30] B. G. Ma, Z. T. Luo, X. J. Gao, and X. Li, “Thaumasite form of sulfate attack on different variety of cement,” *Journal of the Chinese Ceramic Society*, vol. 34, no. 5, pp. 622–625, 2006.
- [31] J. B. Wang, “The chemical action of karst water compositions of the Ordovician in Lu’an mine area,” *Coal Geology & Exploration*, vol. 27, no. 2, pp. 39–42, 1999.
- [32] Y. L. Wu, *The Engineering Geological Characteristics of gypsum Rock and the Damage Mechanism on Tunnel concrete Structure*, China University of Geosciences, Wuhan, China, 2013.
- [33] C. B. Xu and H. L. Wang, “Analysis on geological characteristics and its engineering harmfulness of dugongling tunnel,” *Journal of Highway and Transportation Research and Development*, vol. 36, no. 8, pp. 93–100, 2019.

Research Article

Research on the Strength Characteristics and Crack Propagation Law of Noncoplanar Nonthrough Jointed Rock Mass by PFC2D

Qingzhi Chen ¹, Yuanming Liu ¹, Shilong Mei,² Kai Cao,³ Bin Du,⁴ and Wei Wang⁵

¹College of Civil Engineering, Guizhou University, Guiyang 550025, Guizhou, China

²College of Architecture and Urban Planning, Guizhou University, Guiyang 550025, Guizhou, China

³Guiyang Vocational and Technical College, Guiyang 550000, Guizhou, China

⁴Guizhou Transportation Planning Survey Design & Research Institute Co., Ltd., Guiyang 550000, Guizhou, China

⁵General Construction Co. of CCTEB Group Co., Ltd., Wuhan 430064, Hubei, China

Correspondence should be addressed to Qingzhi Chen; 1064174907@qq.com and Yuanming Liu; 845612605@qq.com

Received 2 May 2021; Revised 8 June 2021; Accepted 22 July 2021; Published 3 August 2021

Academic Editor: Chunyang Zhang

Copyright © 2021 Qingzhi Chen et al. This is an open access article distributed under the Creative Commons Attribution License, which permits unrestricted use, distribution, and reproduction in any medium, provided the original work is properly cited.

In this study, five groups of numerical models with different conditions were established by using PFC2D (particle flow code) to simulate the direct shear tests of noncoplanar nonthrough jointed rock mass. It is proved that normal stress and shear rate, as well as the connectivity rate, relief angle, and inclination angle of joints, have significant influence on the strength characteristics, number of cracks, and the stress of the rock mass according to measurement taken at five different measurement circles in the rock mass. Moreover, it is determined that in the process of shearing, no matter which group of tests are conducted, the number of cracks in the rock mass caused by tension is far more than that caused by the shear action. In other words, the failure of rock mass with different planes and discontinuous joints is mainly caused by the tension in the process of the direct shear test.

1. Introduction

A rock mass is a complex geological body with obvious nonlinearity, discontinuity, heterogeneity, and anisotropy. Within a rock mass, there can be joints, cracks, bedding, schistosity, faults, folds, and other structural planes [1–4]. All these different types of structures are collectively referred to as joints, and a rock mass containing various joints is termed as the jointed rock mass. The existence of joints makes the mechanical properties of a jointed rock mass to differ greatly from those of an intact rock [5–9]. The jointed rock mass is the most common complex engineering medium in construction engineering, water conservancy and hydropower engineering, underground space engineering, mineral resource exploration and development engineering, transportation engineering, bridge and tunnel engineering, oil port engineering, and other projects. Its strength and extended through characteristics play a vital role in construction in civil engineering. The mechanical properties of the jointed rock mass are important factors that must be

considered in the analysis, evaluation, and design of rock engineering. The existence of joints makes the stability and safety of the built underground engineering projects to have great hidden dangers [10–12]. In addition, with the development of large engineering projects in recent years, the number, scale, difficulty, and complexity of rock mass engineering during the construction period have increased significantly, and the problems in rock mechanics in the construction process have become more complex. These mechanical problems of jointed rock mass will directly increase the technical difficulty of construction and affect the quality and cost of the project [13–15]. If the problems cannot be handled well, it will even cause casualties and serious losses due to the destruction of the complex rock mass. In order to facilitate the study, and based on whether the internal joint plane of the rock mass is through and the degree of joint opening or closing, a jointed rock mass is divided into two types: a through jointed rock mass and a nonthrough jointed rock mass [16–20]. On the basis of the spatial arrangement of rock masses and joints, or whether

the joint surface and shear plane are on the same plane, the nonthrough jointed rock mass can be further divided into coplanar nonthrough jointed rock mass (CNJRM) and noncoplanar nonthrough jointed rock mass (NNJRM) [21]. The schematics of CNJRM and NNJRM are shown in Figures 1 and 2, respectively. In this study, numerical simulation experiments are carried out to study the law of crack propagation and the strength characteristics of rock mass in the process of the direct shear test.

The physical model test or numerical simulation test is widely used in the study of nonthrough jointed rock mass. This is because it can be quite difficult and costly to conduct the test in the field or by using natural rock specimens. In addition, the test repeatability will be poor, and the difference between individual and overall measurements would be greater, and so would the error of the test result. However, since the physical model test is greatly affected by the machinery used in the test and the operation mode of the operator in the experimental process, the accuracy of the experimental results has certain discreteness. Moreover, the cost of the physical model test is higher than that of the numerical simulation test. Therefore, if the parameters of the simulated material can be determined, many experts and scholars tend to use the numerical simulation test to study the mechanical properties of the incoherent jointed rock mass [22–29].

There are a variety of simulation programs for performing numerical simulation tests, among which the PFC2D (particle flow code) for particle discrete element analysis developed by ITASCA has been widely used [30–34]. This program studies the mechanical properties of the medium from the perspective of microstructure, which is very suitable for the in-depth study of high-level topics such as the expansion, fracture, failure, failure impact, and microseismic response of meso- or macrojoints in solid materials. At present, many experts and scholars have shown that the simulation test results of the PFC program are stable and reliable. For example, Zhou et al. [35] simulated the direct shear test of nontransfixion jointed rock mass based on the particle discrete element theory and the PFC2D program, and also analyzed the mechanical properties and breaking mechanism of joints in experiments from both the macro- and microaspects. The results of the simulation test were compared with the results of the indoor model test, and it was found that the new particle flow calculation method is very suitable for the simulation test of nonthrough jointed rock mass. This method has high reliability and thus can provide good reference for direct shear test of jointed rock mass in the laboratory and also for parameter selection when using PFC to simulate the joint model. Zhou et al. [36, 37] also took the natural slope as the research background and used the granular model and smooth joint model to simulate a rock block and joint, respectively, based on the particle discrete element theory and by using the PFC2D numerical simulation program. By repeatedly comparing and debugging the test results of the uniaxial compression test, direct shear test, and numerical test, the micromechanical parameters of the granular model and smooth joint model were determined. In

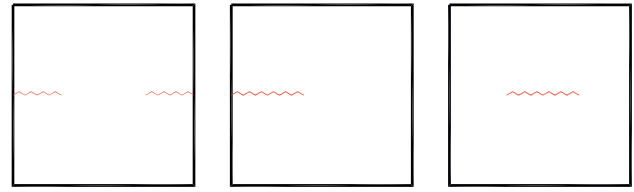


FIGURE 1: The schematic diagram of CNJRM.

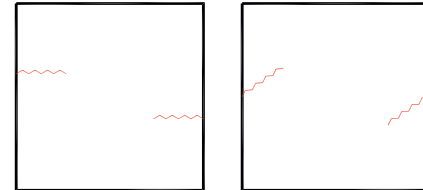


FIGURE 2: The schematic diagram of NNJRM.

addition, the mesoanalysis model of the intermittent jointed rock slope was established successfully. From the mesoscopic point of view, they successfully studied the mechanical properties of the rock mass model with two discontinuous joints and the bedding rock slope model with discontinuous joints in the failure process. Yang et al. [38] used the PFC3D program to study the effect of joint direction on the strength, deformation, and failure mode of joint blocks. Wang et al. [39] used the PFC3D program to establish the experimental model of coal gangue with different particle sizes, and simulated the triaxial compression test based on the model. By comparing the stress-strain curve, volume strain curve, and microcrack development curve under different confining pressures, he studied the strength characteristics and deformation law of coal gangue with different particle sizes. Hu et al. [40] used the PFC program to establish a rock slope model containing nonpenetrating jointed rock mass, and calculated the relevant mechanical parameters of the rock mass through simulated direct shear test, biaxial test, Brazil split test, and other conventional mechanical tests, so as to study various failure modes of the rock slope and its internal mesoscopic mechanism during the failure of the rock slope. In addition, many experts, including Huan et al. [41], Jiang et al. [42], Regassa et al. [43], Liu et al. [44], Cao et al. [45], Ghazvinian et al. [46], and Tao et al. [47], have used the PFC program or DEM (discrete element method) program to study various properties of rock masses.

Therefore, the PFC2D program was also used in this study to simulate the direct shear test, so as to investigate the influence of the undulating angle, inclination angle, joint connectivity rate, normal stress, and shear rate on the transfixion mechanism, strength, and deformation characteristics of NNJRM. By studying the stress-strain development state of the specimen as a whole based on the data collected from five measurement points inside the specimen (as shown in Figure 3) during the test, and the change in the number of cracks in the specimen during the test process, the mechanical properties of the nonpenetrating jointed rock mass under different working conditions were investigated.

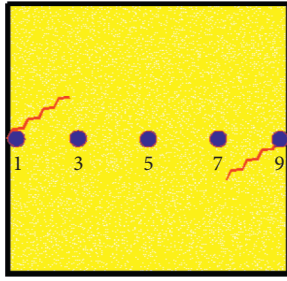


FIGURE 3: The positions of the five measurement circles.

It needs to be explained that the joint relief angle of the noncoplanar nonthrough jointed rock mass, represented by i , refers to the unevenness of a single structural plane in the joint relative to the whole joint, as shown in Figure 4. The joint inclination angle, represented by ϕ , refers to the inclined angle between the joint tendency and the stress direction of the rock mass [21], as shown in Figure 5. The joint connectivity of the noncoplanar nonthrough jointed rock mass, represented by j , is defined as the ratio of the sum of the projection lengths of each joint segment in the direction of the shear plane to the length of the survey line. Its calculation formula is $j = 2S/L$. The numerical model established in this study adopts L as a fixed value, $L = 200$ mm. The joint connectivity of the rock mass with different plane joints is shown in Figure 6.

2. Numerical Simulation Test Scheme for NNJRM

2.1. Establishment of Model. In the numerical simulation part of this study, PFC2D was used to investigate and analyze the NNJRM. The establishment process of the test model is as follows: (1) six walls were defined to form a rectangular range of $200 \text{ mm} \times 200 \text{ mm}$, (2) relevant mesomechanical parameters were calibrated, and the particles were randomly generated and the suspended ones were eliminated (a total of 9356 effective spherical particles were generated inside the wall), (3) joints with connectivity, undulation, and inclination were introduced into the model to form the NNJRM, (4) direct shear test was conducted through FISH language simulation, and (5) five measuring circles were introduced to measure the level of stress (the five measuring circles are shown in Figure 3). The entire modeling process is illustrated in Figure 7.

2.2. Selection of Microscopic Mechanical Parameters. It should be noted that the calibration of mesomechanical parameters is the core of the model establishment process. It is only when these parameters are set accurately can the test results obtained by the numerical simulation test be true and reliable and can the numerical model be applied to the study of the mechanical properties of NNJRM. The specific method of parameter calibration is as follows: a group of parameters, which can make the numerical simulation test results to match with the experimental results of the physical model test, was obtained through multiple preassignment of



FIGURE 4: The schematic diagram of the joint relief angle.

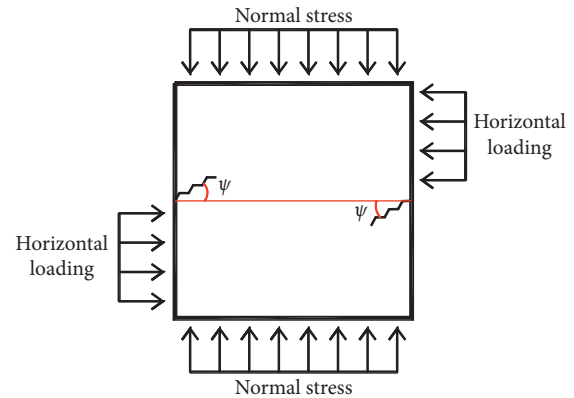


FIGURE 5: The loading mode and the joint inclination angle of NNJRM.

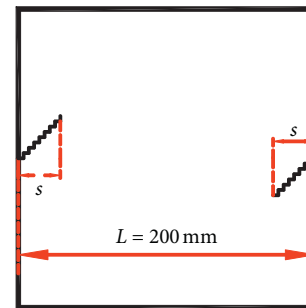


FIGURE 6: The joint connectivity of NNJRM.

micromechanical parameters such as the adhesion stiffness, bond strength, particle density, particle radius, elastic modulus of particles, and Poisson's ratio between particles and walls. Since a set of parameters that meet the requirements were already determined in previous studies [27, 28], the calibration process of the parameters was not repeated here. The set of parameters used in this model is shown in Table 1.

2.3. Description of the Test Conditions. The numerical simulation tests of a rock mass with different discontinuity joints under different working conditions are divided into five groups, as shown in Table 2.

2.3.1. Group 1: Simulation Test of NNJRM under Different Normal Stresses. When the shear rate is 0.06 mm/s , the numerical simulation tests with normal stresses of 0.5 mpa , 1.0 MPa , 1.5 mpa , 2.0 mpa , and 3.0 mpa were carried out for the NNJRM with a joint relief angle of 15° , inclination angle of 15° , and connectivity rate of 0.5 .

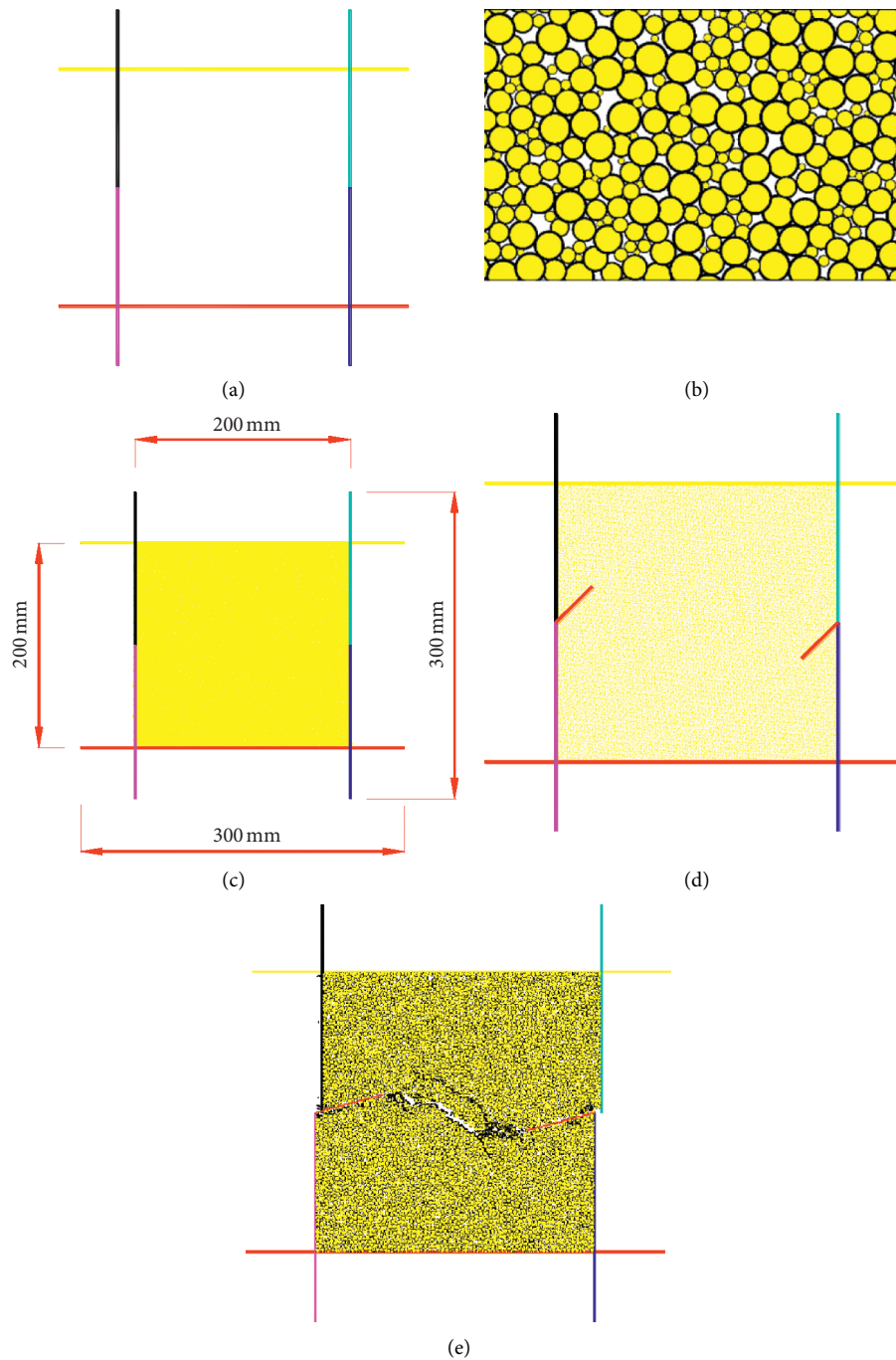


FIGURE 7: The model establishment process. (a) The range of 6-wall forming models. (b) Spherical particles formed in the wall. (c) The sample model after sphere stabilization. (d) The model after importing the different joints. (e) The model after the direct shear test.

2.3.2. Group 2: Simulation Test of NNJRM with Different Connectivity Rates. When the shear rate is 0.06 mm/s, the numerical simulation tests with a normal stress of 1.0 MPa were carried out for the NNJRM with a joint relief angle of 15° , inclination angle of 15° , and connectivity rates of 0.1, 0.2, 0.3, 0.4, and 0.5, successively.

2.3.3. Group 3: Simulation Test of NNJRM at Different Shear Rate States. When the normal stress is 1.0 MPa, the

numerical simulation tests with horizontal shear rates of 0.02 mm/s, 0.04 mm/s, 0.06 mm/s, 0.08 mm/s, and 0.10 mm/s were carried out for the NNJRM with a joint relief angle of 15° , inclination angle of 15° , and connectivity rate of 0.5.

2.3.4. Group 4: Simulation Test of NNJRM with Different Joint Relief Angles. When the shear rate is 0.06 mm/s and the normal stress is 1.0 MPa, the numerical simulation tests were carried out for the NNJRM with joint inclination angle of

TABLE 1: Some relevant parameters of numerical simulation.

Porosity distribution	Partial parameters of spherical particles					Partial parameters of the wall			Partial parameters of the bond			
	Radius (mm)	Attribute density ($\text{kg}\cdot\text{m}^{-3}$)	Damping coefficient	Normal stiffness ($\text{N}\cdot\text{m}^{-1}$)	Tangential stiffness ($\text{N}\cdot\text{m}^{-1}$)	Friction factor	Normal stiffness ($\text{N}\cdot\text{m}^{-1}$)	Tangential stiffness ($\text{N}\cdot\text{m}^{-1}$)	Radius coefficient	Normal stiffness ($\text{N}\cdot\text{m}^{-1}$)	Tangential stiffness ($\text{N}\cdot\text{m}^{-1}$)	Friction angle ($^\circ$)
0.02	0.03~0.18	2750	0.7	3×10^8	1×10^8	0.3	1×10^{10}	1×10^8	1	1×10^{10}	1×10^{10}	55

TABLE 2: Grouping of numerical simulation tests.

Group	Connectivity rate	Normal stress (MPa)	Horizontal displacement rate (mm/s)	The joint relief angle	The joint inclination angle	
1	0.5	0.5	0.06	15°	15°	
		1.0				
		1.5				
		2.0				
		3.0				
2	0.1	1.0	0.06	15°	15°	
						0.2
						0.3
						0.4
						0.5
3	0.5	1.0	0.02	15°	15°	
			0.04			
			0.06			
			0.08			
			0.10			
4	0.5	1.0	0.06	0°	15°	
				15°		
				30°		
				45°		
				60°		
5	0.5	1.0	0.06	15°	0°	
					15°	
					30°	
					45°	
					60°	

15°, connectivity rate of 0.5, and joint relief angles of 0°, 15°, 30°, 45°, and 60°, successively.

2.3.5. Group 5: Simulation Test of NNJRM with Different Joint Inclination Angles. When the shear rate is 0.06 mm/s and the normal stress is 1.0 MPa, the numerical simulation tests were carried out for the NNJRM with a joint relief angle of 15°, connectivity rate of 0.5, and joint inclination angles of 0°, 15°, 30°, 45°, and 60°, successively.

3. Results and Discussion

In this study, five groups of numerical models of rock mass with different conditions were simulated. The peak stress of the specimens, the total number of cracks in the rock mass (expressed by DFN), the number of cracks produced by tension (expressed by DFN-t), the number of cracks produced by shear (expressed by DFN-s), and the stress-strain relationship of five measuring points in the specimens were all studied to analyze the law of crack propagation and the mechanical properties of the rock mass.

3.1. Results of the First Experiment. The stress-strain curves and peak shear stress of NNJRM under different normal stresses of the first group of specimens are shown in Figure 8 and Table 3.

According to the data in Figure 8 and Table 3, it can be observed that when the normal stress increases from 0.5 MPa to 3.0 MPa, the peak stress of NNJRM increases from 3.76 MPa to 4.98 MPa, and the residual stress increases

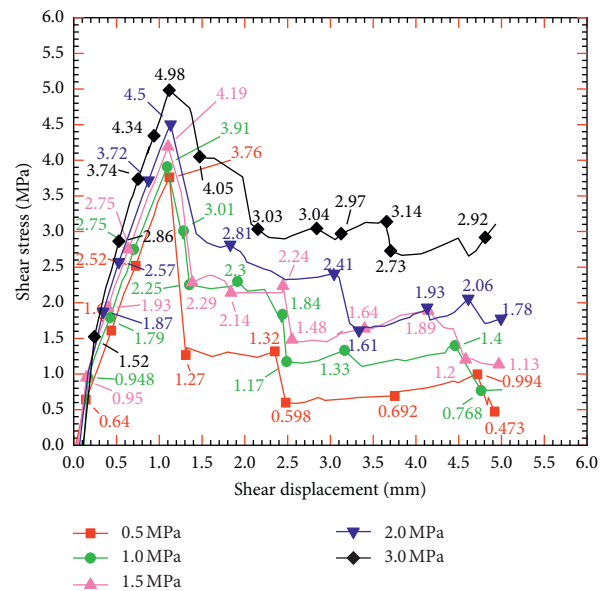


FIGURE 8: Stress-strain curves obtained from tests under different normal stresses.

TABLE 3: Peak shear stress of NNJRM under different normal stresses.

Normal stress (MPa)	0.5	1.0	1.5	2.0	3.0
Peak stress (MPa)	3.76	3.91	4.19	4.50	4.98

from 0.47 MPa to 3.15 MPa. It can be seen that with the increase in the normal stress in the test, both the shear strength and peak stress of NNJRM increase.

The number of DFN, DFN-t, and DFN-s produced in the first group of specimens under different normal stresses are shown in Figure 9 and Table 4.

It can be seen from Figure 9 and the data in Table 4 that the number of cracks generated in the rock mass increased continuously in the course of the experiment until the end of the test. When the normal stress is gradually increased from 0.5 MPa to 3.0 MPa, the total number of cracks in the rock mass increases from 293 to 515. With the gradual increase in the normal stress from 0.5 MPa to 3.0 MPa, the number of DFN-t in the rock mass increases from 198 to 409, showing an obvious trend of increase. The number of DFN-s also changes with the change in normal stress, increasing from 95 to 106, but the increase trend is not obvious. In addition, by comparing the number of DFN-t and DFN-s in Table 4, it is obvious that no matter how the normal stress changes, the number of cracks in each rock mass caused by tensile action is more than those caused by shear action. Therefore, during the direct shear test, the damage caused by the tensile action of the rock mass is more obvious. Thus, it can be said that the failure of rock mass in the test is mainly caused by tension.

In addition, the experiment under different normal stresses, the stress-strain curves, and the peak strength of each measuring circle are shown in Figure 10 and Table 5, respectively. After sorting out the data of the experiment under different normal stresses, the obtained curves of peak stress of each measured circle are shown in Figure 11.

It can be seen from the data in Figures 10 and 11 and Table 5 that with the change in the normal stress, the stress curve of each measured point in the rock mass changes significantly. On the one hand, for the same measurement point under different normal stresses: the peak stress of the rock mass will change with the increase in normal stress. The change in the peak stresses of measurement circles 1 and 5 is the most obvious. Here, the measurement circle 1 is taken as an example for analysis. When the normal stress is gradually increased from 0.5 MPa to 3.0 MPa, the measured peak stresses are 6.27 MPa, 6.32 MPa, 10.25 MPa, 10.2 MPa, and 7.43 MPa, respectively. The difference between the maximum peak stress and the minimum peak stress is 3.98 MPa. For the three other measurement circles, i.e. 3, 7, and 9, although their peak stress also changes with the increase in normal stress, the range of change is not obvious and is relatively stable. On the other hand, for the experiment with different measurement points under the same normal stress, by observing the stress curves of the five measurement points, it can be observed that no matter how much normal stress is applied during the direct shear test, the peak stress of the measurement point 5 is almost always the largest among the five measurement points. In addition, for this experiment, there is a big difference in the peak stress of measurement point 5 and that of the other measurement circles. When the normal stress is 3.0 MPa, the peak stress at the measurement point 5 is 7.43 MPa, and although this is not the maximum value, the difference between this peak stress and the maximum peak stress of 8.44 MPa is still small. It can be seen that during the shear test, the stress of the rock mass is more concentrated at the middle part of the rock mass, that is, around the measuring circle 5, which bears the main shear stress.

3.2. Results of the Second Experiment. The stress-strain curves obtained by the direct shear test of the rock mass under different shear rates are shown in Figure 12. The peak stresses of the rock mass shown in Figure 12 are statistically analyzed, and the results are shown in Table 6.

According to the data in Figure 12 and Table 6, it can be found that the shear strength of the rock mass changes according to the change in the shear rate in the direct shear test. When the shear rate is 0.02 mm/s and 0.06 mm/s, the peak shear stress of the rock mass is 3.85 MPa and 4.03 MPa, respectively. Furthermore, when the shear rate is gradually increased to 0.10 mm/s, the peak shear stress of the rock mass increases to 4.3 MPa. Therefore, the peak stress of the rock mass increases with the increase in the shear rate, and the shear strength of the rock mass is also enhanced.

In addition, the number of DFN, DFN-t, and DFN-s produced in the second group of specimens for the experiment under different shear rates are shown in Figure 13 and Table 7.

According to the data in Figure 13 and Table 7, the shear rate has significant influence on the number of cracks in the rock mass during the direct shear test. First, the total number of cracks (DFN) is analyzed. It can be seen that when the shear rate is 0.02 mm/s and 0.04 mm/s, the total number of cracks in the rock mass is 344 and 449, respectively. However, when the shear rate continues to increase, the total number of cracks tends to decrease. For instance, when the shear rate is increased to 0.10 mm/s, the total number of cracks in the rock mass decreases to 371. Therefore, it can be said that with the increase in the shear rate, the total number of cracks in the rock mass increases first and then decreases. Second, the quantity of DFN-t is analyzed, and it is found that the variation law of DFN-t is similar to that of DFN; the total number of cracks in the rock mass first increases and then decreases with the increase in the shear rate. For DFN-s, although the number of cracks also increases first and then decreases, the change is not obvious. Finally, by comparing the number of DFN-t and DFN-s, it is found that the number of DFN-t is much higher than that of DFN-s, the change of shear rate notwithstanding. Therefore, it can be concluded that, for the experiment under different shear rates, the number of cracks in the rock mass caused by tension is far higher than that caused by shear action. This means that the ultimate failure of a rock mass in the direct shear test is mainly caused by tension, rather than shear.

The stress-strain curves of each measurement circle under different shear rates are shown in Figure 14. The peak stress of each measurement circle is determined and presented in Table 8. The change curve of the peak stress of each measurement point under the condition of different shear rates is shown in Figure 15.

It can be seen from the data in Figures 14 and 15 and Table 8 that the shear rate has significant influence on rock mass stress.

- (1) On the one hand, for the stress at the same measuring point under different shear rates: there is little change in peak stress of the four measurement circles 1 (except at 0.02 mm/s, the peak stress of the

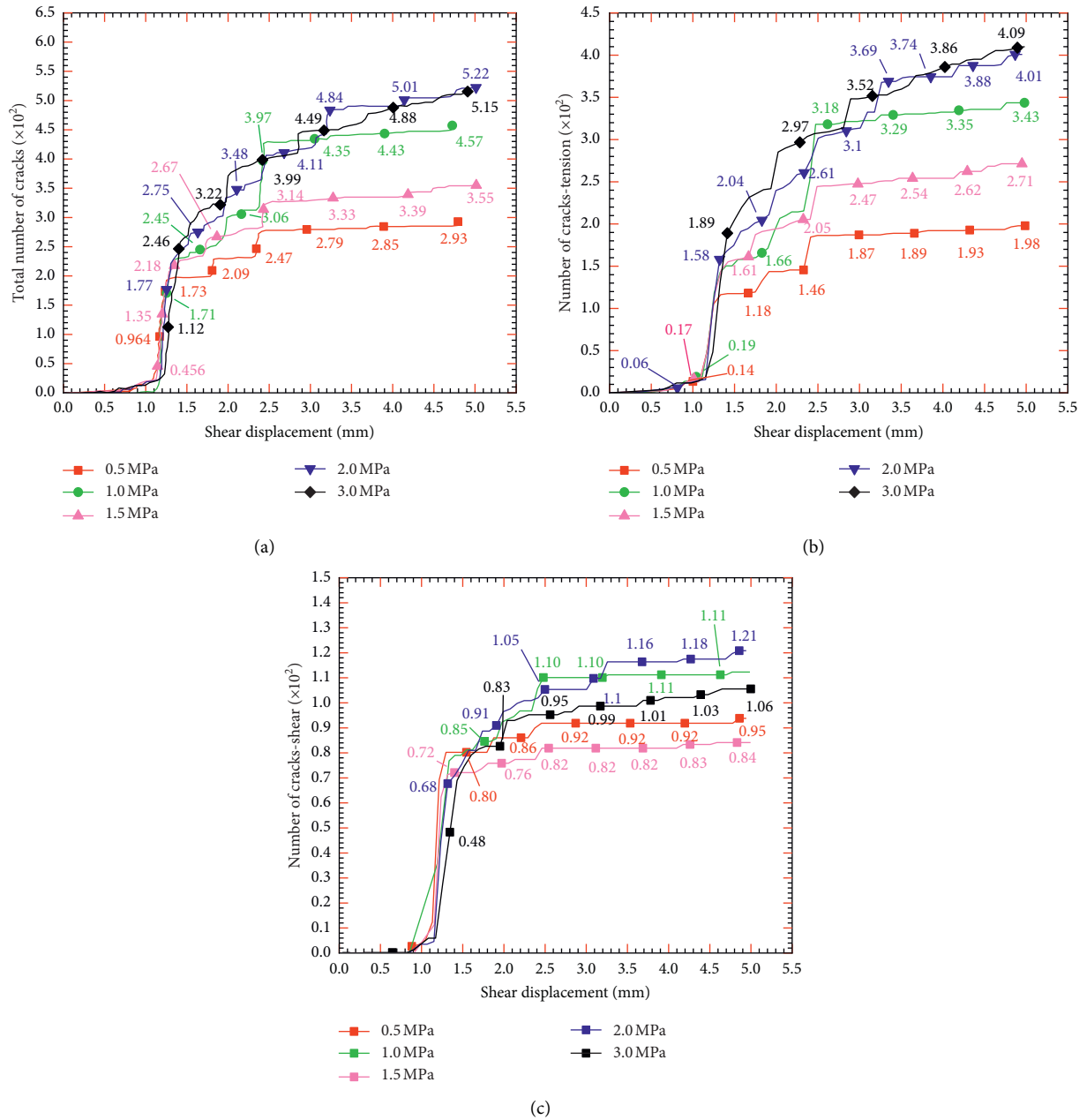


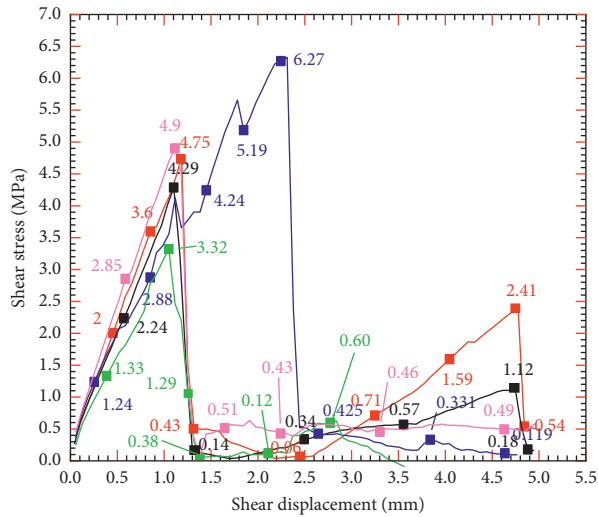
FIGURE 9: The number of cracks in the first group of specimens. (a) Total number of cracks. (b) The number of cracks caused by tension. (c) The number of cracks caused by shear action.

TABLE 4: The number of cracks generated under different normal stresses.

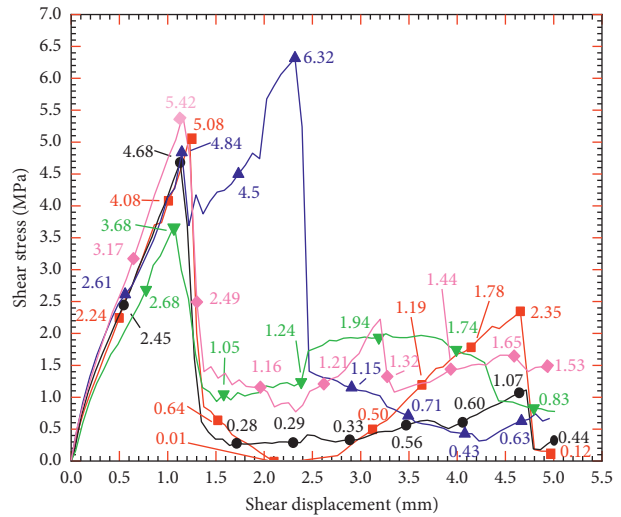
Normal stress (MPa)	0.5	1.0	1.5	2.0	3.0
DFN (strip)	293	457	355	522	515
DFN-t (strip)	198	343	271	401	409
DFN-s (strip)	95	114	84	121	106

measurement circle 1 is discrete), 3, 7, and 9, when the shear rate is adjusted. However, for the measurement circle 5, there is obvious change in the peak stress when the shear rate is adjusted. When the shear rate is increased from 0.02 mm/s to 0.10 mm/s,

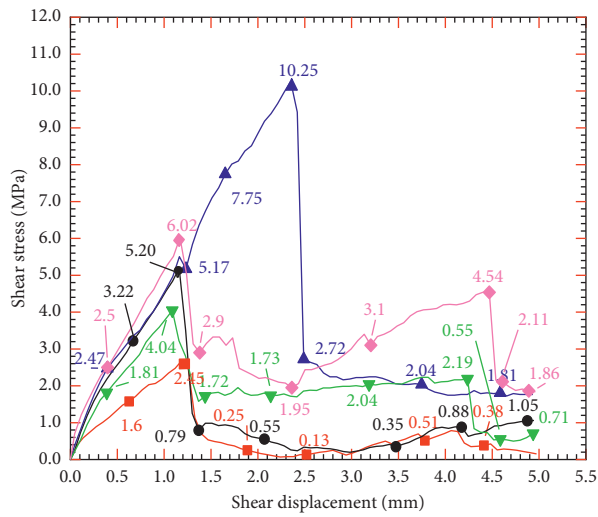
the peak stress of measurement circle 5 decreases from 9.99 MPa to 4.91 MPa. This means that the peak stress of the measurement circle 5 gradually decreases with the increase in the shear rate. Therefore, with the increase in the shear rate, both the shear



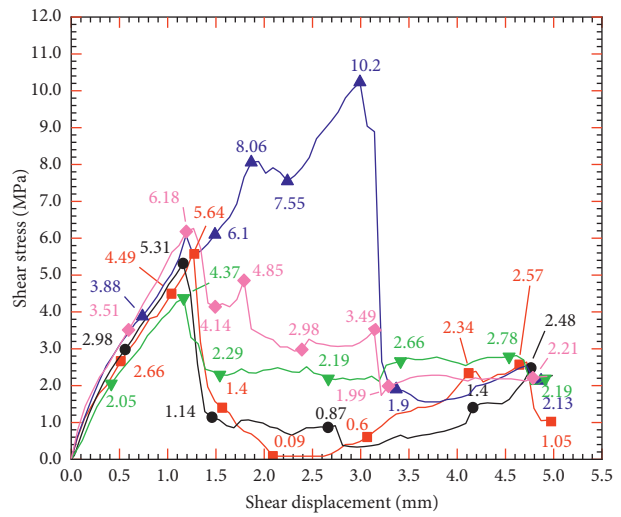
(a)



(b)



(c)



(d)

FIGURE 10: Continued.

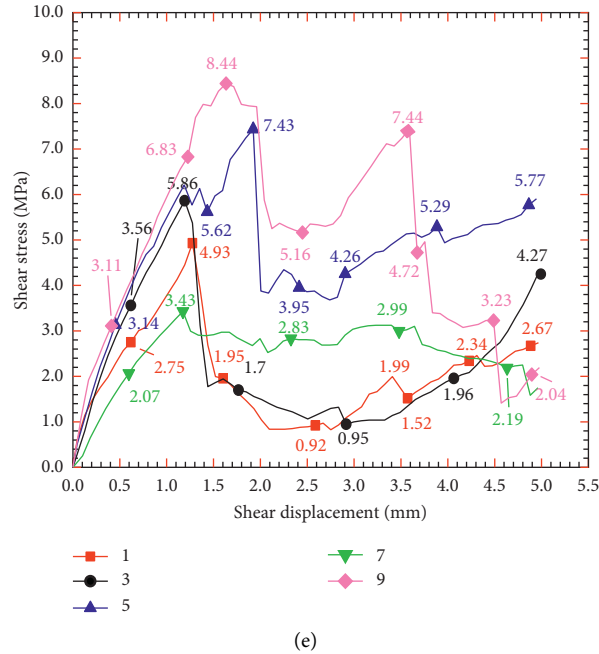


FIGURE 10: The stress-strain curves of the five measured circles in the first group of specimens when the normal stress is (a) 0.5 MPa, (b) 1.0 MPa, (c) 1.5 MPa, (d) 2.0 MPa, and (e) 3.0 MPa.

TABLE 5: The peak stress of each measurement circle in the first group of specimens (MPa).

Number of measuring circles	Normal stress (MPa)				
	0.5	1.0	1.5	2.0	3.0
1	4.75	5.08	2.45	5.64	4.93
3	4.29	4.68	5.20	5.31	5.86
5	6.27	6.32	10.25	10.2	7.43
7	3.32	3.68	4.04	4.37	3.43
9	4.9	5.42	6.02	6.18	8.44

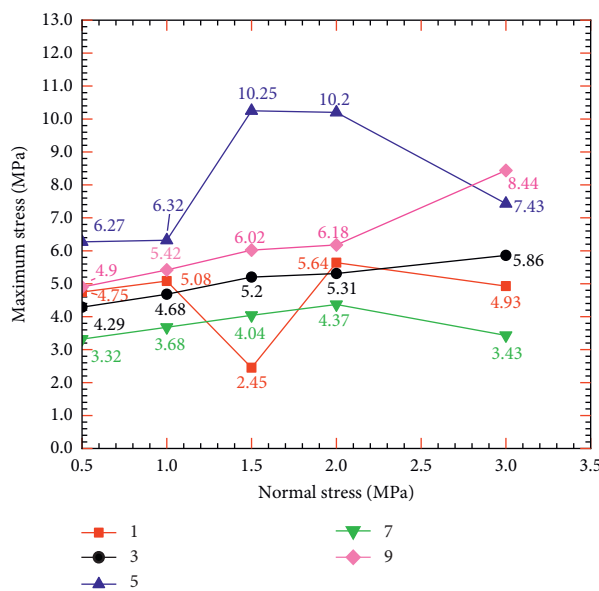


FIGURE 11: Curves of the peak stress of each measured circle in the first group of specimens.

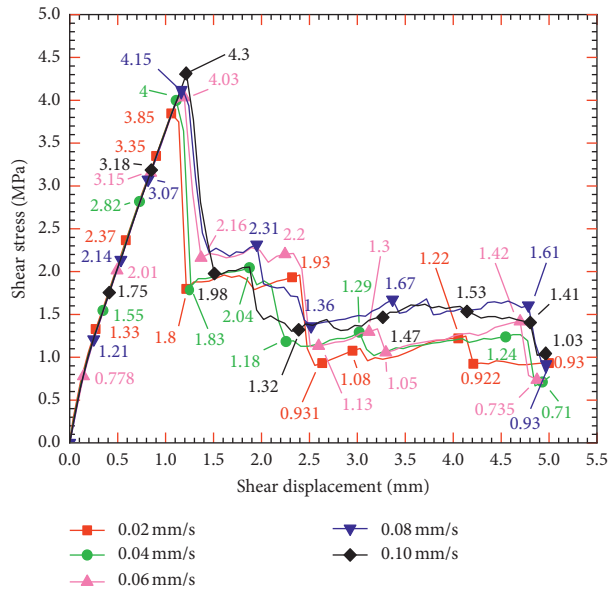


FIGURE 12: The stress-strain curves obtained from experiments under different shear rates.

TABLE 6: The peak shear stress of NNJRM under different shear rates.

Shear rate (mm/s)	0.02	0.04	0.06	0.08	0.10
Peak stress (MPa)	3.85	4.00	4.03	4.15	4.30

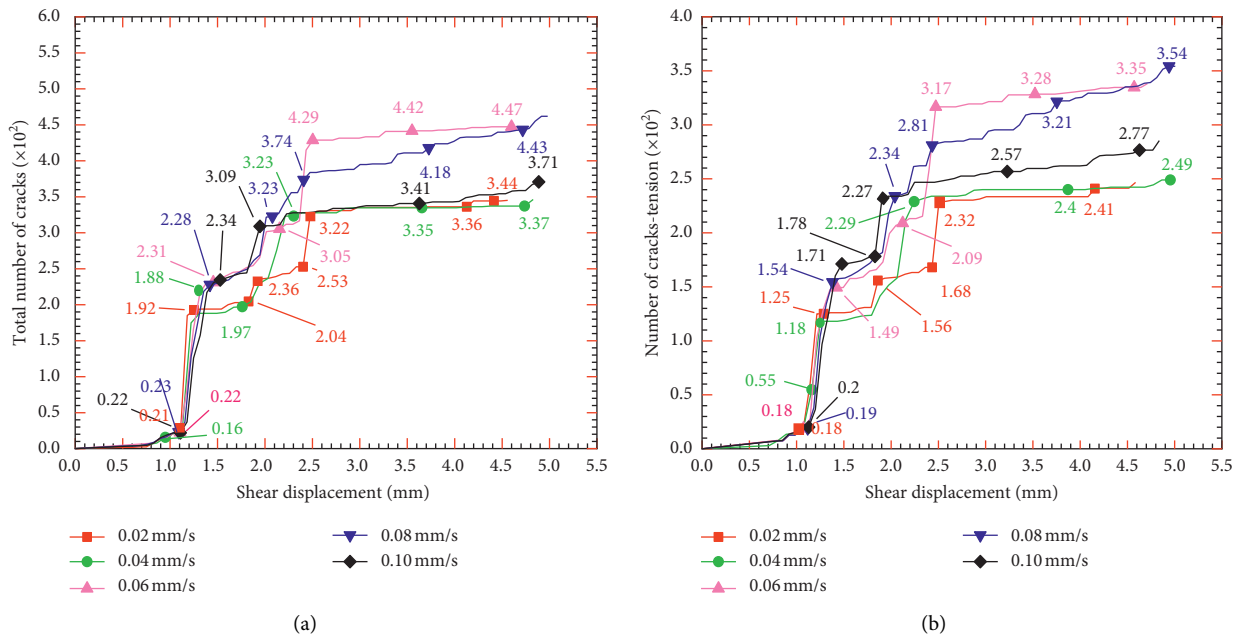


FIGURE 13: Continued.

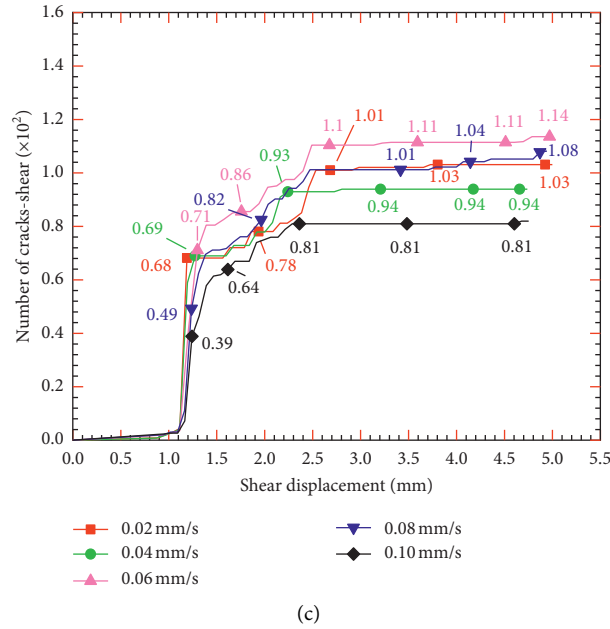


FIGURE 13: The number of cracks in the second group of specimens. (a) Total number of cracks. (b) The number of cracks caused by tension. (c) The number of cracks caused by shear action.

TABLE 7: The number of cracks generated under different shear rates.

Shear rate (mm/s)	0.02	0.04	0.06	0.08	0.10
DFN (strip)	344	343	449	462	371
DFN-t (strip)	241	249	335	354	289
DFN-s (strip)	103	94	114	108	82

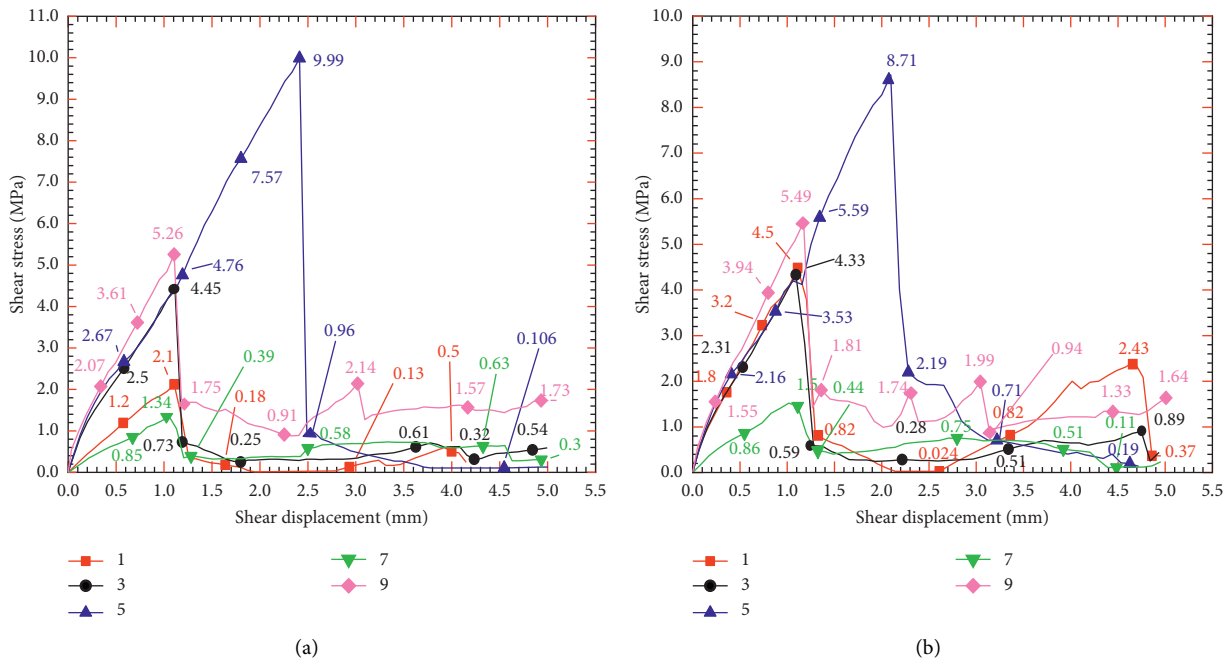


FIGURE 14: Continued.

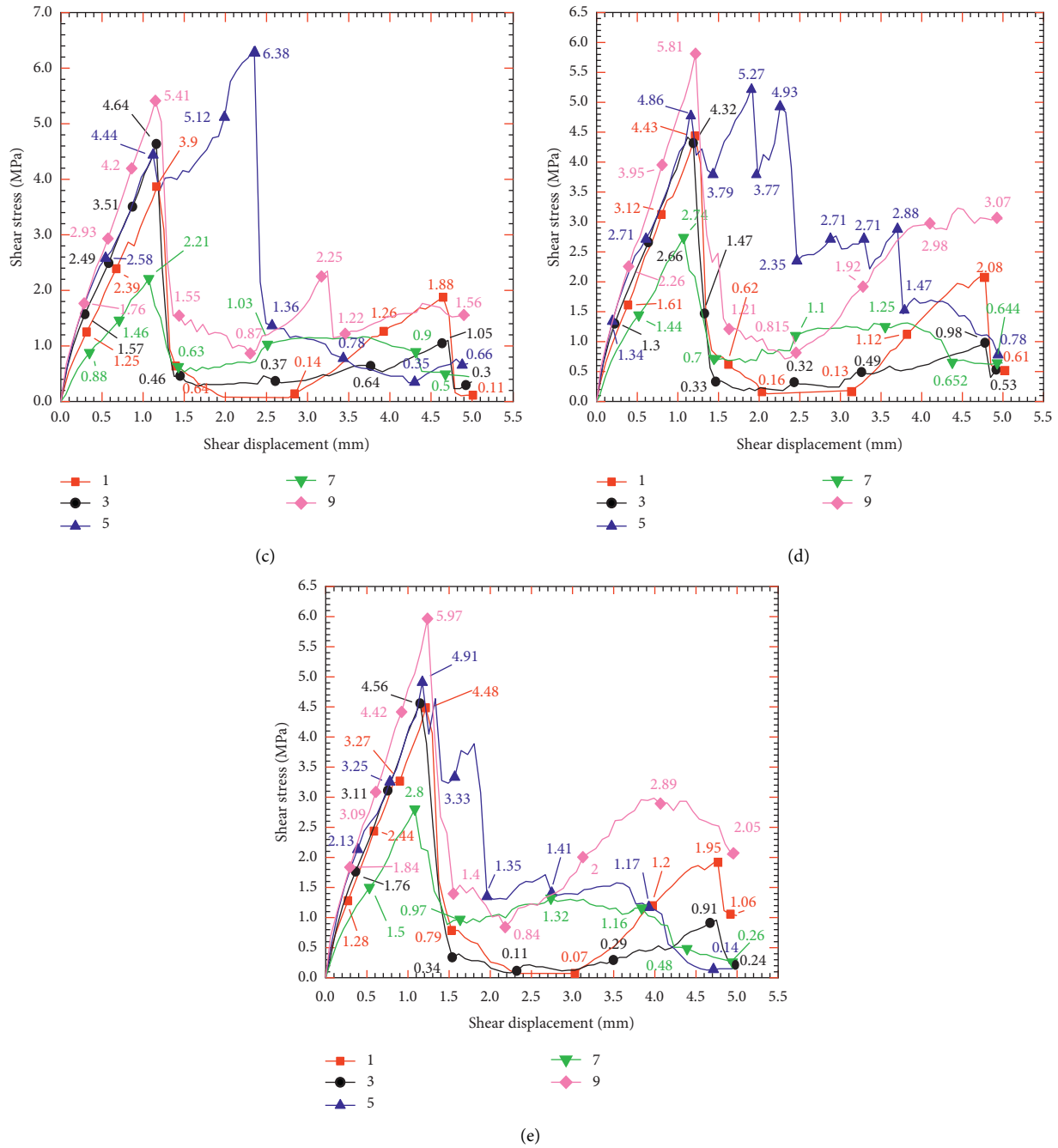


FIGURE 14: Stress-strain curves of each measurement circle in the second group of specimens when the shear rate is (a) 0.02 mm/s, (b) 0.04 mm/s, (c) 0.06 mm/s, (d) 0.08 mm/s, and (e) 0.10 mm/s.

TABLE 8: The peak stress of each measurement circle in the second group of specimens.

Number of measuring circles	Shear rate (mm/s)				
	0.02	0.04	0.06	0.08	0.10
1	2.10	4.50	3.9	4.43	4.48
3	4.45	4.33	4.64	4.32	4.56
5	9.99	8.71	6.38	5.27	4.91
7	1.34	1.51	2.21	2.74	2.80
9	5.26	5.49	5.41	5.81	5.97

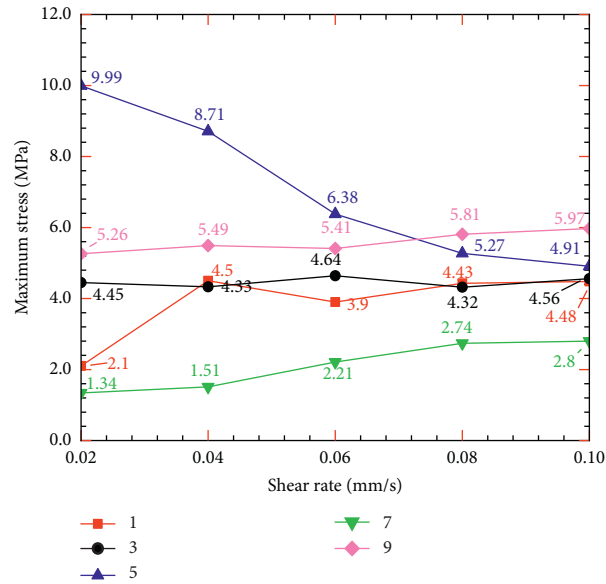


FIGURE 15: Curves of peak stress of each measured circle in the second group of specimens.

capacity and shear stress at the center point of the rock mass decrease. In addition, as can be seen from the data in Figure 12 and Table 6, the peak stress and the shear strength of the whole rock mass increase with the increase in the shear rate during the test. In summary, as the shear rate increases, the shear stress borne by the center of the rock mass decreases, and the force borne by the interior of the rock mass gradually balances.

- (2) On the other hand, for the stress of different measurement circles under the same shear rate condition: the peak stresses of the measurement circle 5 at the shear rates of 0.02 mm/s, 0.04 mm/s, and 0.06 mm/s are 9.99 MPa, 8.71 MPa, and 6.38 MPa, respectively, and these are the maximum values of the peak stress of the five measurement circles. In addition, when the shear rates are 0.08 mm/s and 0.10 mm/s, the peak stresses at the measurement circle 5 are 5.27 MPa and 4.91 MPa, respectively. Although these values differ slightly with the maximum value, they are still relatively large compared with those of other measurement circles. Therefore, in general, under different shear rates, the central position of a rock mass specimen is subjected to greater shear action and the stress variation is more obvious.

3.3. Results of the Third Experiment. The stress-strain curve obtained after the direct shear test of the rock mass with different joint connectivity rates is shown in Figure 16. The peak stress of the rock mass in Figure 16 is sorted out, and the results are presented in Table 9.

According to the data in Figure 16 and Table 9, it can be found that the test results of NNJRM with different joint connectivity rates have obvious consistency. When the connectivity of joints within the rock mass is 0.1, the peak

shear stress of the rock mass is 5.90 MPa, and the residual stress is 1.34 MPa. When the joint connectivity rate increases gradually, the peak stress and residual stress of the rock mass tend to decrease. When the joint connectivity rate increases to 0.5, the peak shear stress and residual stress decrease to 4.03 MPa and 0.75 MPa, respectively. Therefore, the smaller the joint connectivity, the greater the peak stress and residual stress of the rock mass. Furthermore, the stronger the shear capacity of a rock mass, the stronger the ability to resist external forces.

In addition, the number of DFN, DFN-t, and DFN-s produced in the third group of specimens with different joint connectivity rates are shown in Figure 17 and Table 10.

By summarizing and sorting out the data in Figure 17 and Table 10, it can be found that no matter the value of the joint connectivity rate, the number of cracks generated in the rock mass gradually increases with the progress of the test process. However, different joint connectivity rates generate different increment rates of cracks. When the connectivity of joints was 0.1, the number of DFN, DFN-s, and DFN-t increased to 829, 189, and 640, respectively. When the joint connectivity rate gradually increased to 0.5, the final total number of cracks in the experimental rock mass decreased to 457, among which 114 are DFN-s and 343 are DFN-t.

According to these data, the number of these two kinds of cracks, DFN-s, and DFN-t, which are caused by different forms of forces, decreases with the increase in joint connectivity, leading to a decrease in the total amount of cracks in the rock mass. Therefore, it can be concluded that the smaller the connectivity of joints within the rock mass, the better the integrity of the rock mass and the stronger the shear resistance capability of the rock mass. This is consistent with practical experiences in engineering practice.

The stress-strain curves of each measuring circle in the specimens with different joint connectivity rates are shown in Figure 18. The peak stress of each measuring circle is sorted out as shown in Table 11, and the change curve of

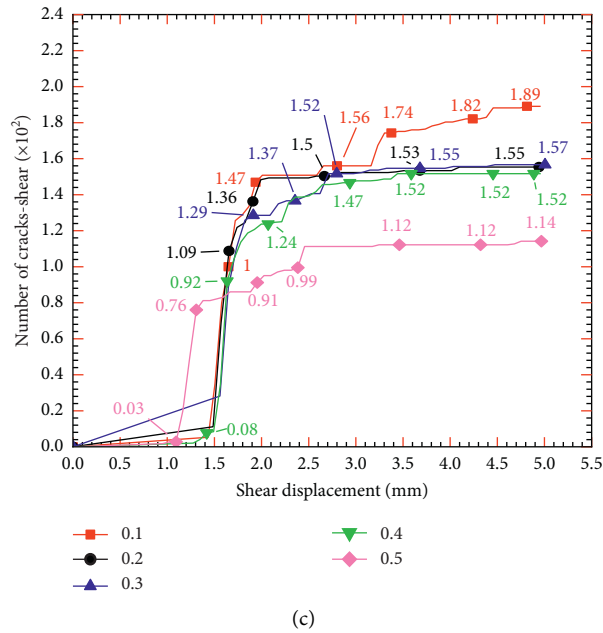


FIGURE 17: The number of cracks in the third group of specimens. (a) Total number of cracks. (b) The number of cracks caused by tension. (c) The number of cracks caused by shear action.

TABLE 10: The number of cracks generated at different connectivity rates.

Connectivity rate	0.1	0.2	0.3	0.4	0.5
DFN (strip)	829	681	720	654	457
DFN-t (strip)	640	526	563	502	343
DFN-s (strip)	189	155	157	152	114

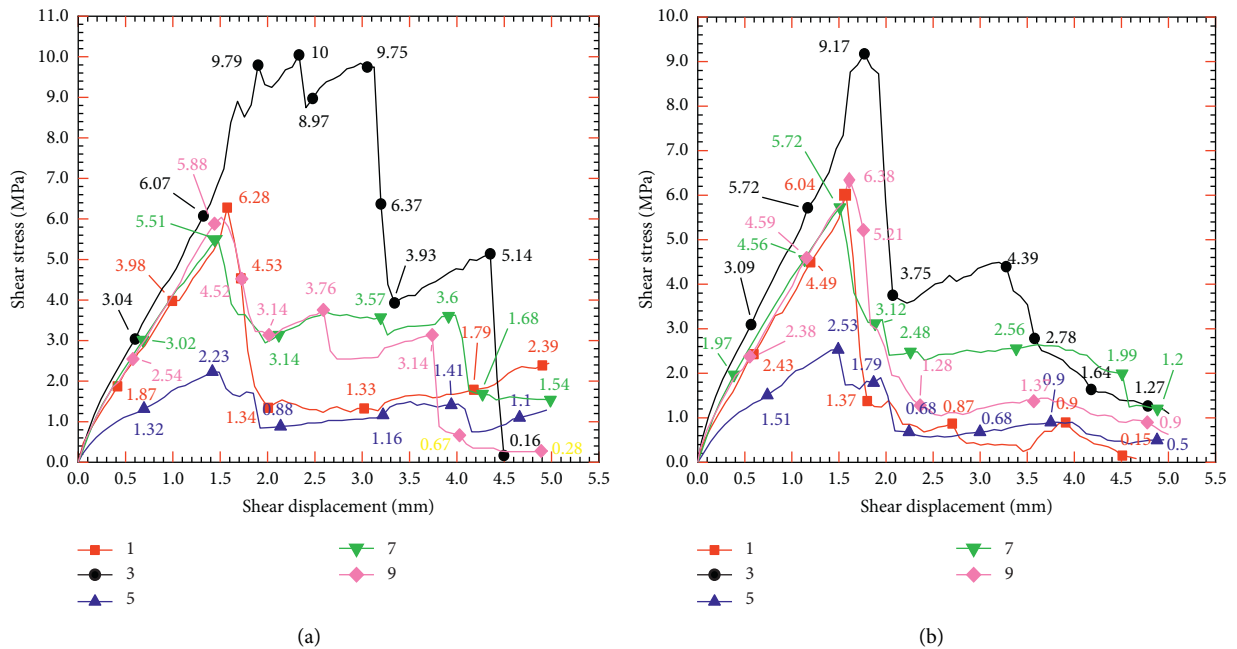


FIGURE 18: Continued.

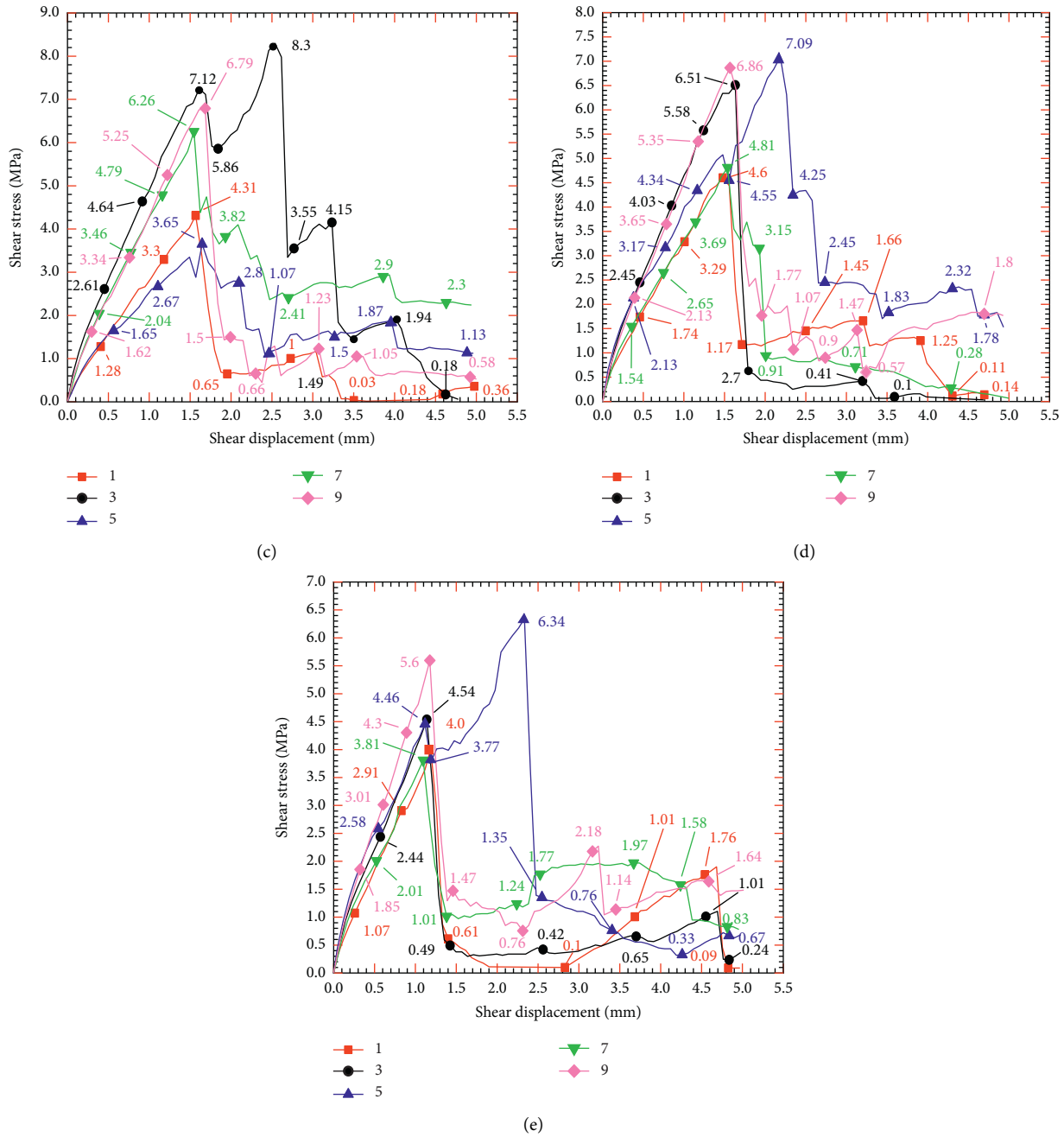


FIGURE 18: Stress-strain curves of each measurement circle in the third group of specimens when the connectivity rate is (a) 0.1, (b) 0.2, (c) 0.3, (d) 0.4, and (e) 0.5.

TABLE 11: The peak stress of each measurement circle in the third group of specimens.

Number of measuring circles	Connectivity rate				
	0.1	0.2	0.3	0.4	0.5
1	6.28	6.05	4.31	4.6	4.00
3	10.0	9.17	8.30	6.51	4.54
5	2.23	2.53	3.65	7.09	6.34
7	5.51	5.72	6.26	4.81	3.81
9	5.91	6.38	6.79	6.86	5.60

peak stress of each measurement point under the condition of different joint connectivity rates is obtained, as shown in Figure 19.

Based on the data shown in Figures 18 and 19 and Table 11, we find that, unlike direct shear tests conducted under the above controlled conditions, the maximum peak shear stress is not always at the measurement circle 5 located at the center of the specimen when the test is carried out at different joint connectivity rates. When the connectivity of the joints in the rock mass ranges from 0.1 to 0.3, the peak shear stress of the measurement circle 3 in the rock mass is the largest among the five measuring points. The peak stresses of measurement circles 1, 7, and 9 near both sides of the rock mass are large, while that of measuring circle 5 in the middle of the specimen is the smallest. Therefore, when the connection rate of joints is 0.1 to 0.3, the rock mass close to both sides of the rock mass bears more stress. However, when the connectivity of joints increases to 0.4 or 0.5, the measurement circle 5 experiences the highest peak stress among the five measuring points, and the peak stress of the five measurement circles is more uniform.

3.4. Results of the Fourth Experiment. The curves of stress-strain and peak shear stress of NNJRM with different joint relief angles of the fourth group specimens are shown in Figure 20 and Table 12.

According to the data in Figure 20 and Table 12, it can be found that the relief angle of joints has an influence on the stress-strain curve of NNJRM. If the joint relief angle changes, the peak shear stress and residual stress of the rock mass show obvious changes. However, there is no obvious regularity to this change.

The number of DFN, DFN-t, and DFN-s produced in the fourth group of specimens with different relief angles are shown in Figure 21 and Table 13.

By comparing the number of DFN, DFN-s, and DFN-t in the rock mass with five kinds of joint relief angles, it can be found that the change of joint relief angle has obvious influence on the direct shear test of a jointed rock mass. The difference between the maximum value (634) and the minimum value (342) of the total number of cracks produced by the direct shear test on the rock mass with different joint relief angles is 292. Similarly, the difference between the maximum value (504) and the minimum value (263) of the number of DFN-t is 241. Furthermore, under the same joint relief angle, the number of DFN-s generated in the specimen is significantly less than that of DFN-t. Therefore, the following conclusions can be drawn: in the direct shear tests of a rock mass with different joint relief angles, the main reason for its failure is the action of tension rather than the shear action.

The stress-strain curves of each measurement circle in the fourth group of specimens with different joint relief angles are shown in Figure 22. The peak stress of each measurement circle of the specimens under each joint relief angle is sorted out as shown in Table 14, and the change curve of the peak stress of each measured point with different joint relief angles is obtained, as shown in Figure 23.

According to the data in Figures 22 and 23 and Table 14, when conducting direct shear test on the rock mass with joints with different undulating angles, the measurement circle 5 of the rock mass experiences the largest peak stress among the five measurement circles. It is proved that the central part of the rock mass with discontinuous joints bears more forces during the direct shear test. In addition, according to the curve in Figure 23, when the joint relief angle is 0° or 60° , the peak stress of each measurement circle in the rock mass varies greatly and the stress distribution is not uniform.

3.5. Results of the Fifth Experiment. The curve of stress-strain and peak shear stress of NNJRM with different inclination angles of the fifth group of specimens are shown in Figure 24 and Table 15.

We can see from the data in Figure 24 and Table 15 that when the joint inclination angle is 0° and 15° , the peak stress of the rock mass is 3.95 MPa and 4.01 MPa, respectively. If the angle is increased to 60° , the peak shear stress increases to 6.00 MPa. It can be seen that the peak stress of the rock mass increases with the increase in the joint inclination angle. Therefore, when the inclined angle of the joints is increased, the shear strength of the rock mass with different plane joints is enhanced.

The number of cracks generated by the fifth group of specimens during the experiment is shown in Figure 25 and Table 16.

From the chart and table above, it can be found that the dip angle of the joints has a significant effect on the crack propagation of the incoherent jointed rock mass. When the inclination angle of joints is changed, the number of cracks generated in the rock mass shows a very obvious change. However, there is no specific rule for the change in the number of cracks. Although the variation law of DFN, DFN-t, and DFN-s is not obvious, the number of DFN-t is always more than that of DFN-s. It is proved that the final failure of the NNJRM with different inclination angles in the direct shear test is also caused by tension.

The stress-strain curves of each measurement circle in the specimens with different joint inclination angles are shown in Figure 26. The peak stress of each measuring circle is sorted out as shown in Table 17, and the change curve of peak stress of each measured point under the condition of different joint inclination angles is obtained, as shown in Figure 27.

Based on the data obtained through the above simulation experiment, it can be seen that the joint inclination angle has significant influence on the strength characteristics of the rock mass. Although it is not possible to establish a specific law that reflects the influence of the joint inclination angle on the peak stress at each position in the rock mass, it is certain that the peak stress of the five measurement circles in the rock mass varies with the change in the joint inclination angle. Moreover, when the joint inclination angle is 15° , the peak stresses of the five measurement circles in the rock mass are not significantly different, and the stress distribution in the model specimen is more uniform.

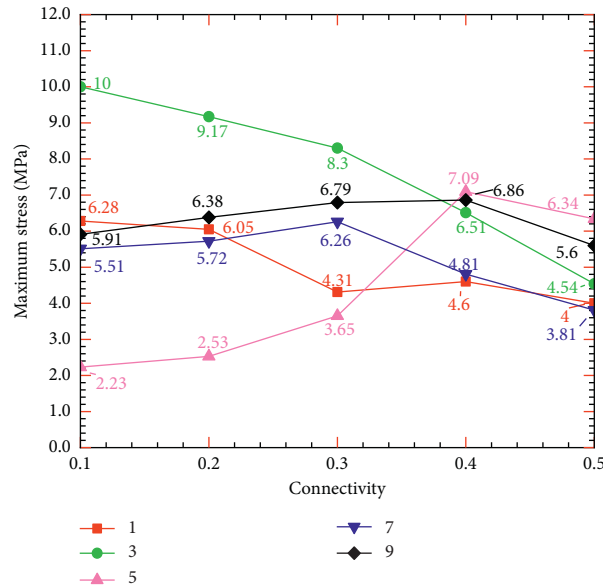


FIGURE 19: Curves of peak stress of each measurement circle in the third group of specimens.

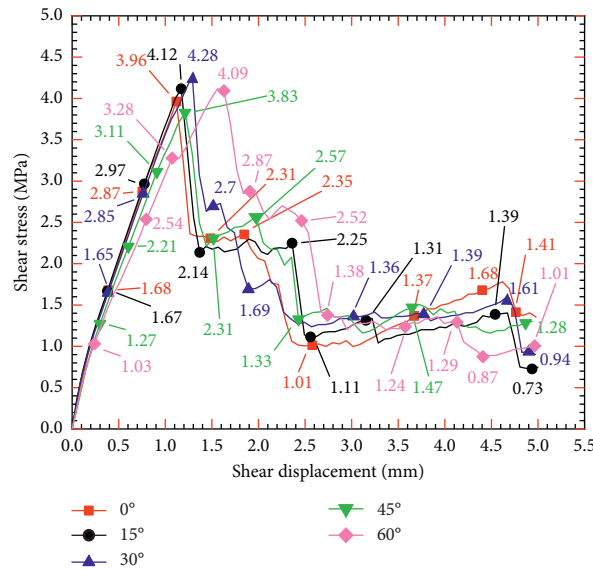


FIGURE 20: The stress-strain curves of NNJRM with different relief angles.

TABLE 12: The peak shear stress of NNJRM with different relief angles.

Relief angle	0°	15°	30°	45°	60°
Peak shear stress (MPa)	3.96	4.12	4.28	3.83	4.09

4. Summary

In this section, the results of each of the above five tests are summarized separately, and these results of this study are generally consistent with the research conclusions in relevant articles [30, 31, 45–51]. It indicates that the results are reliable. In addition, the influence of the normal stress, shear

rate, connectivity of joints, relief angle, and inclination angle of joints on the strength characteristics, crack development state, and the peak shear stress of the five measurement circles in the rock specimens is discussed below:

- (1) After the first group of tests, it has been found that normal stress has significant influence on the characteristics of a rock mass. Specifically, the greater the normal stress, the greater the peak stress and residual stress of noncoplanar nonthrough jointed rock mass, and the stronger the shear capacity of the rock mass. Similarly, the larger the normal stress, the more the cracks produced by shear and tension in the rock mass. The peak shear stresses of measurement

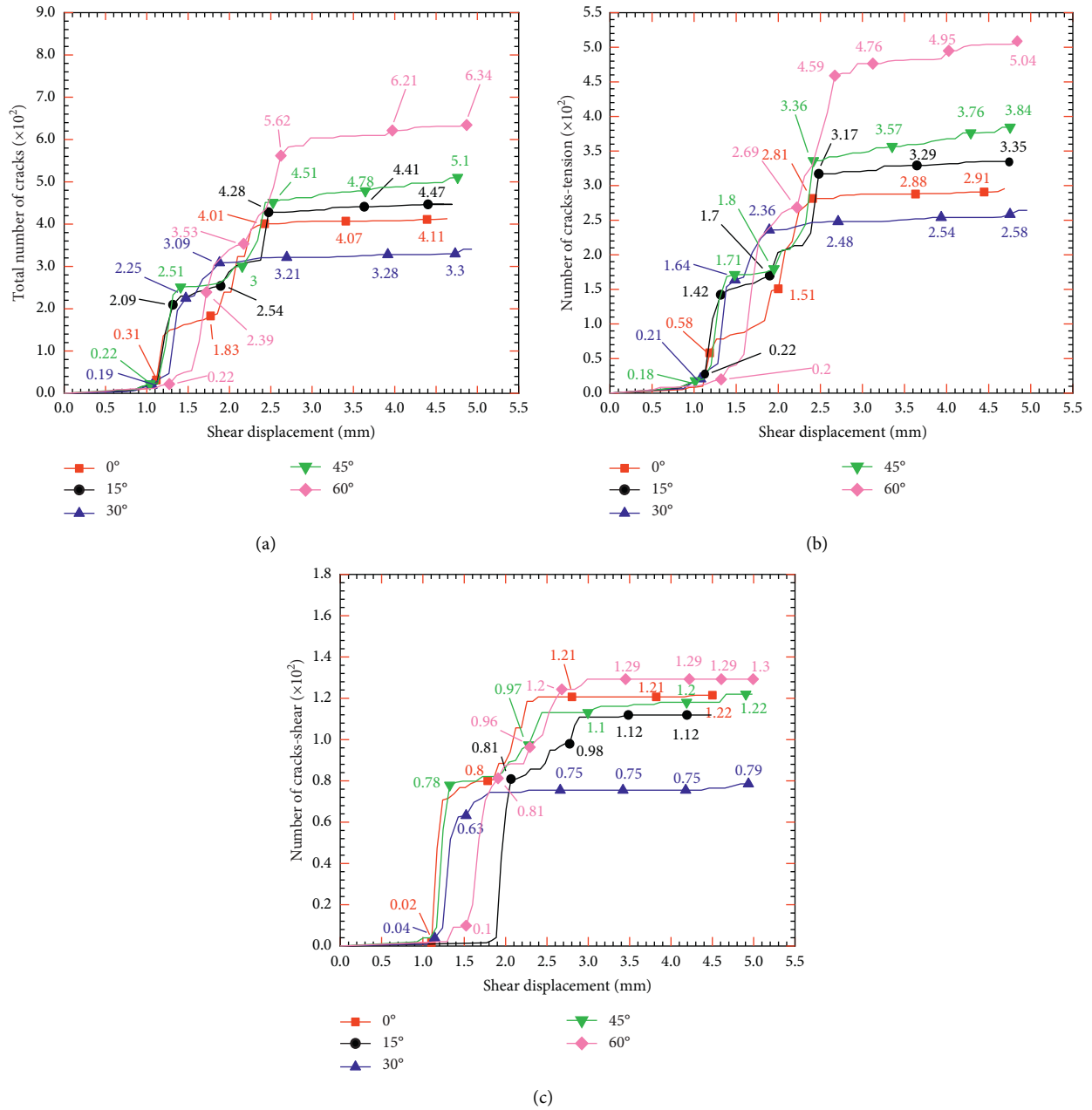


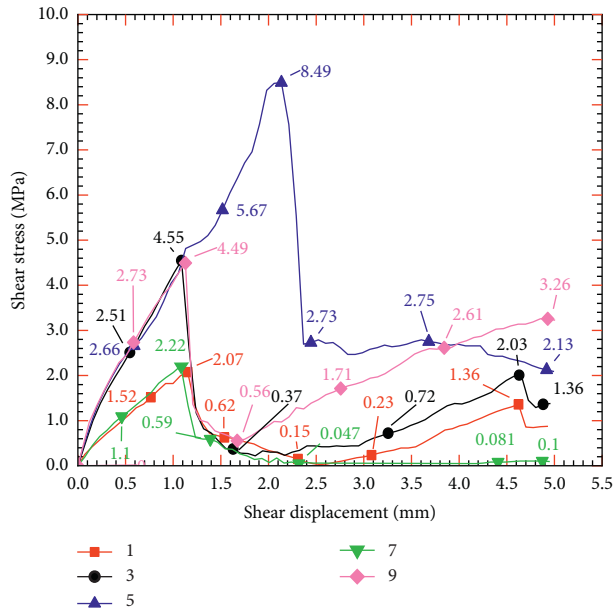
FIGURE 21: The number of cracks in the fourth group of specimens. (a) Total number of cracks. (b) The number of cracks caused by tension. (c) The number of cracks caused by shear action.

TABLE 13: The number of cracks generated with different relief angles.

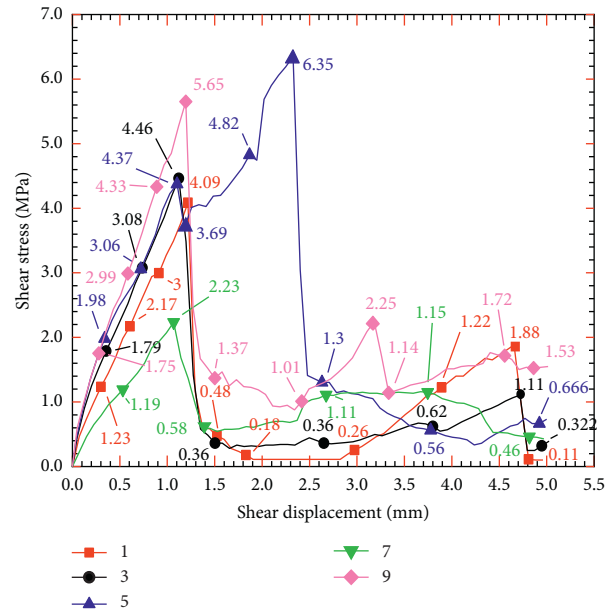
Relief angle	0°	15°	30°	45°	60°
DFN (strip)	414	447	342	510	634
DFN-t (strip)	292	335	263	386	504
DFN-s (strip)	122	112	79	124	130

circles 1 and 5 in the rock mass are hugely affected by the normal stress, whereas the peak shear stresses of measurement circles 3, 7, and 9 are not significantly affected by the normal stress. In the first group of

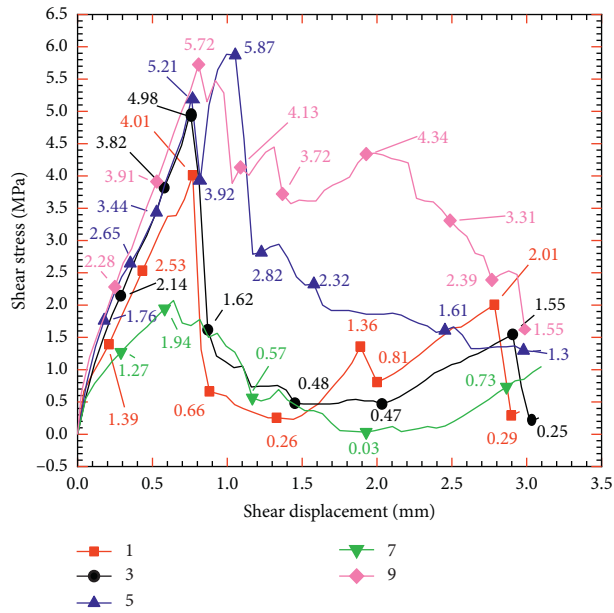
tests, the rock mass near the center experiences more concentrated stress, especially at the position of the measurement circle 5, which bears the main shear stress.



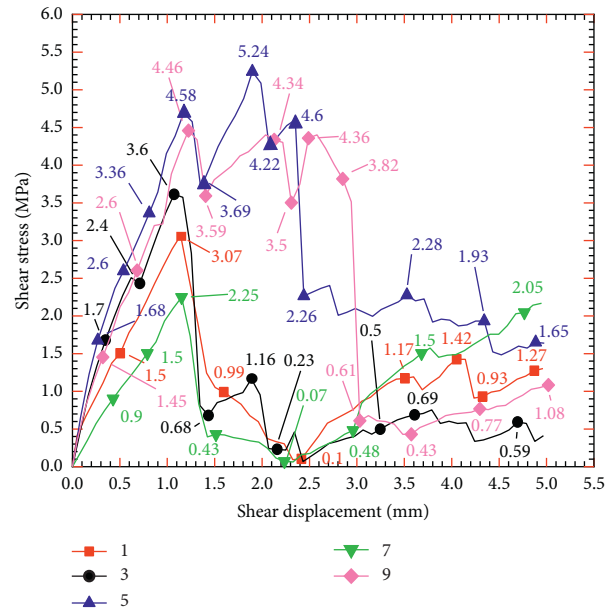
(a)



(b)



(c)



(d)

FIGURE 22: Continued.

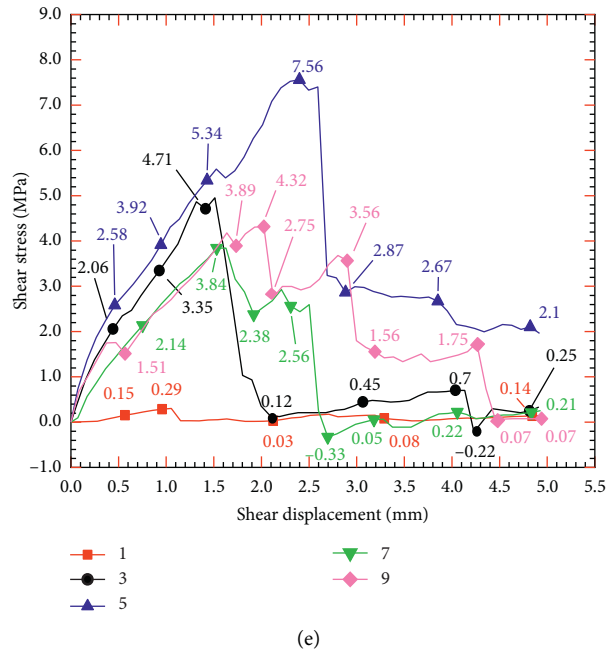


FIGURE 22: The stress-strain curves of each measurement circle in the fourth group of specimens when the relief angle is (a) 0°, (b) 15°, (c) 30°, (d) 45°, and (e) 60°.

TABLE 14: The peak stress of each measurement circle in the fourth group of specimens.

Number of measuring circles	Relief angle				
	0°	15°	30°	45°	60°
1	2.07	4.09	4.01	3.07	0.29
3	2.55	4.46	4.98	3.6	4.71
5	8.49	6.35	5.87	5.24	7.56
7	2.22	4.37	2.04	2.25	3.84
9	4.49	5.65	5.72	4.46	4.32

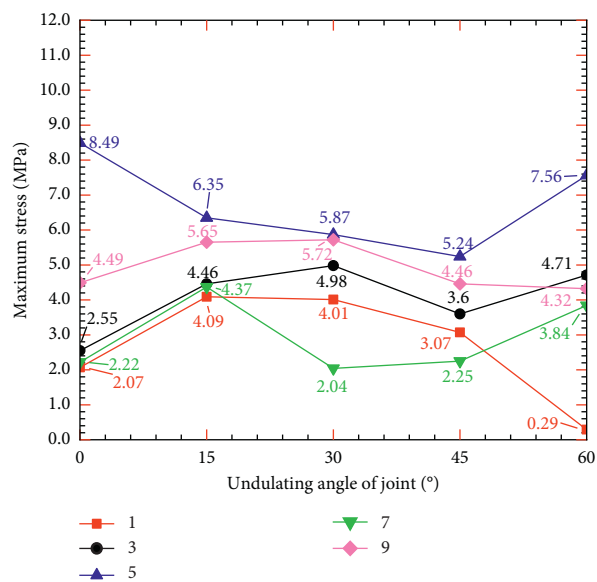


FIGURE 23: Curves of peak stress of each measurement circle in the fourth group of specimens.

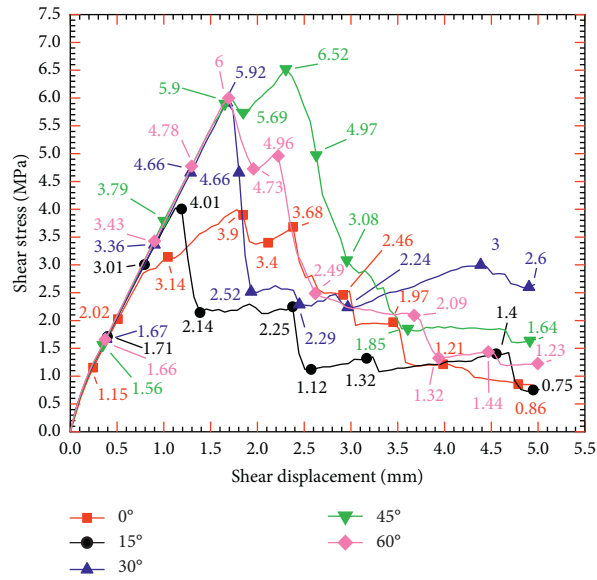


FIGURE 24: The stress-strain curves of NNJRM with different joint inclination angles.

TABLE 15: The peak shear stress of NNJRM with different joint inclination angles.

Joint inclination angle	0°	15°	30°	45°	60°
Peak shear stress (MPa)	3.95	4.01	5.92	6.52	6.00

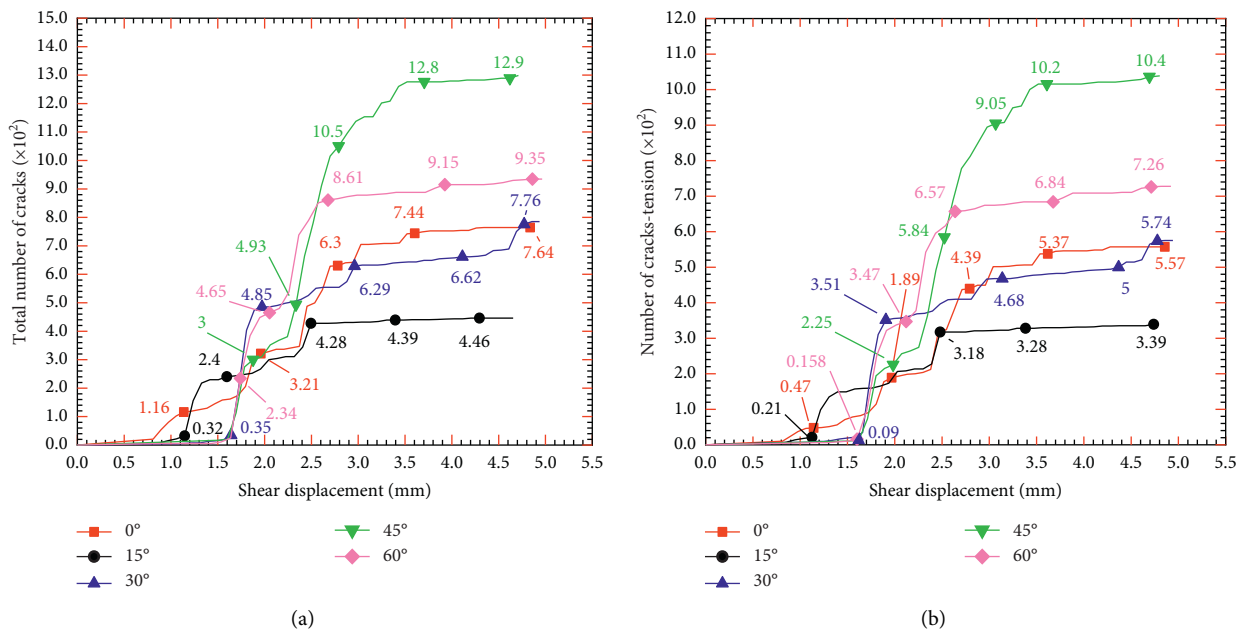


FIGURE 25: Continued.

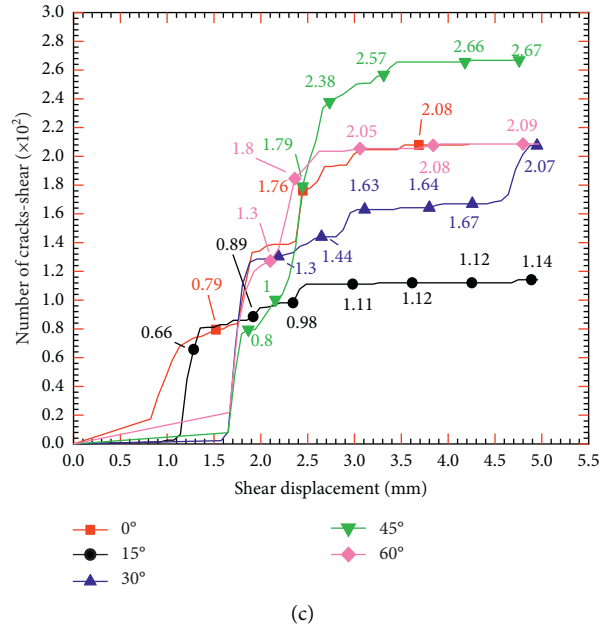


FIGURE 25: The number of cracks in the fifth group of specimens. (a) Total number of cracks. (b) The number of cracks caused by tension. (c) The number of cracks caused by shear action.

TABLE 16: The number of cracks generated with different joint inclination angles.

Joint inclination angles	0°	15°	30°	45°	60°
DFN (strip)	765	453	781	1307	935
DFN-t (strip)	557	340	574	1040	726
DFN-s (strip)	208	114	207	267	209

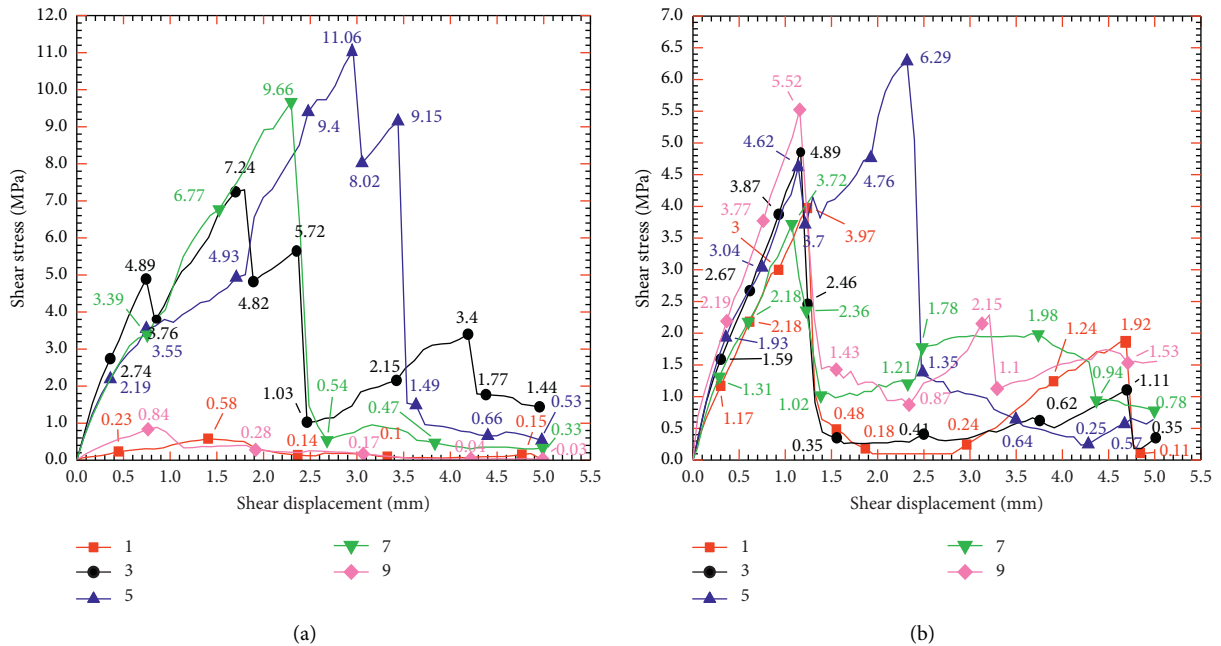


FIGURE 26: Continued.

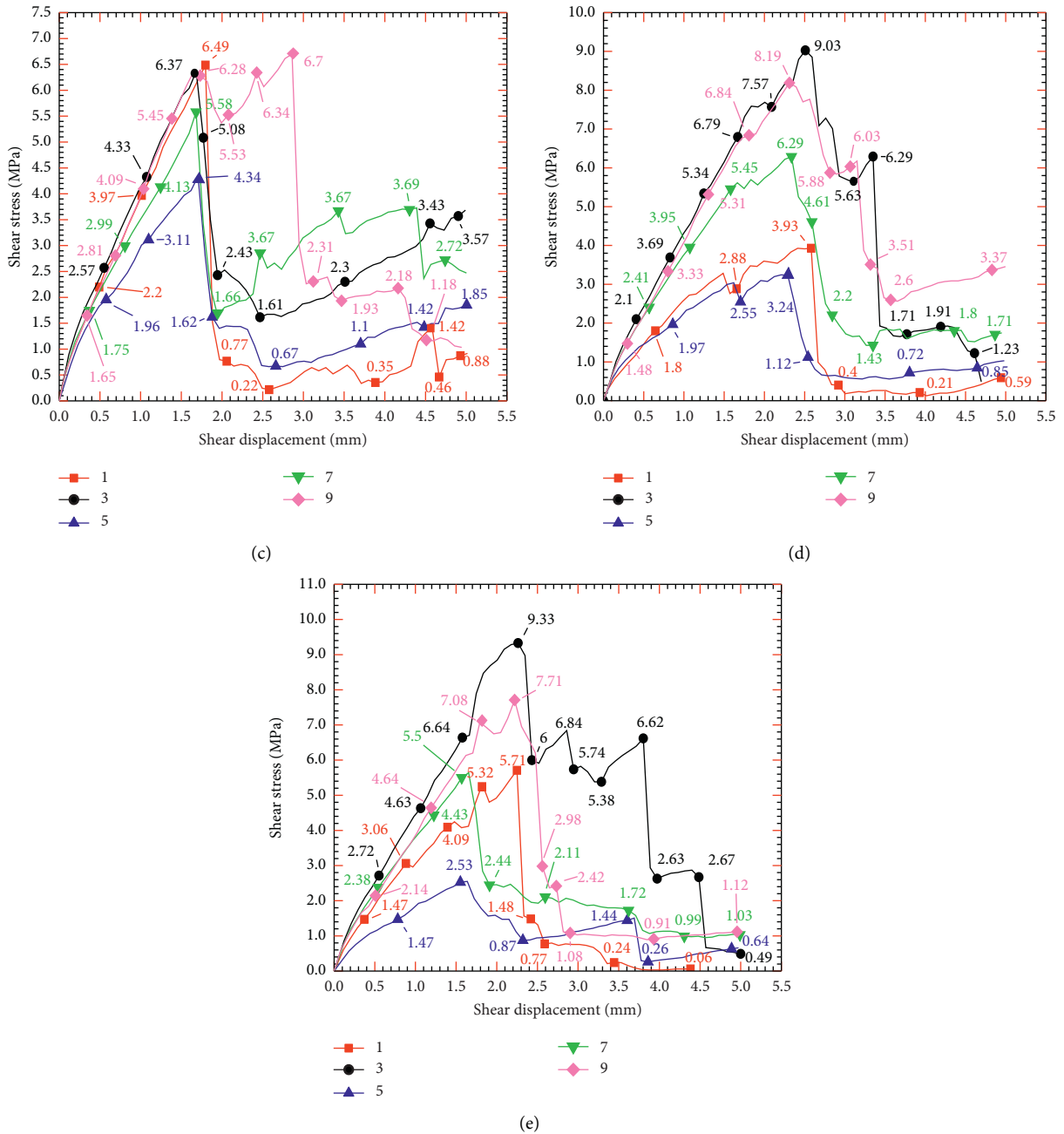


FIGURE 26: The stress-strain curves of each measurement circle in the fifth group of specimens when the joint inclination angle is (a) 0°, (b) 15°, (c) 30°, (d) 45°, and (e) 60°.

TABLE 17: The peak stress of each circle in the fifth group of specimens.

Number of measuring circles	Joint inclination angle				
	0°	15°	30°	45°	60°
1	0.58	3.97	6.49	3.93	5.71
3	7.26	4.89	6.37	9.03	9.33
5	11.06	4.62	4.34	3.24	2.53
7	9.66	3.72	5.58	6.27	5.53
9	0.84	5.52	6.70	8.19	7.71

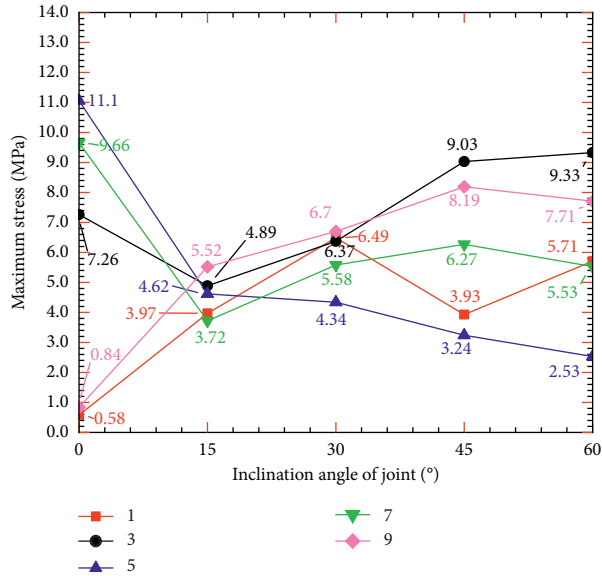


FIGURE 27: Curves of peak stress of each measurement circle in the fifth group of specimens.

- (2) After the second group of tests, it has been determined that both the peak shear stress and shear strength of the rock mass increase with the increase in the shear rate. In addition, with the increase in the shear rate, the number of total cracks, the cracks produced by shear and tension in the rock mass, increases first and then decreases. Moreover, with the increase in the shear rate, the peak shear stress of measurement circle 5 (the measurement circle with the highest peak stress in the rock mass) decreases, the shear stress borne by the central position of rock mass decreases, and so does the shear strength of the central position of the rock specimen. However, since the peak stress of the whole rock mass increases with the increase in the shear rate, the overall shear strength of the rock mass increases. Therefore, it is obvious that the forces within in the rock mass gradually balance with the increase in the shear rate.
- (3) After the third group of tests, it has been noted that with the gradual increase in joint connectivity, the peak stress and residual stress of the rock mass decrease and the rock mass resistance to external forces weakens. In addition, the smaller the connection rate of the joints contained in the rock mass, the fewer the cracks generated in the rock mass, the better the integrity of the rock mass, and the stronger the shear resistance of the rock mass. This is consistent with the on-field experience in engineering practice. When the connectivity of joints contained in the rock mass ranges between 0.1 and 0.3, among the five measurement points, the largest peak shear stress is experienced at measurement circle 3, while the smallest is experienced at measurement circle 5. Therefore, when the joint connectivity is between 0.1 and 0.3, the internal stress of the rock mass is distributed close to both

sides of the rock mass. When the connectivity of the joints increases to 0.4 or 0.5, among the five measurement points, the maximum peak stress is experienced at measurement circle 5 in the rock mass, and the peak stresses of the five measured circles are also relatively uniform.

- (4) After the fourth group of tests, it has been determined that the peak shear stress, residual stress, the number of total cracks in the rock mass, and the cracks produced by shear and tension in the rock mass show obvious changes with the increase in the joint undulation angle. The peak stress of each measurement circle in the rock mass varies greatly with the change in the joint relief angle. However, a very obvious rule in these changes has not been observed.
- (5) After the fifth group of tests, it has been noted that the peak stress of the rock mass increases with the increase in the joint inclination angle. In addition, with the increase in the joint inclination angle, the shear capacity of the noncoplanar nonthrough jointed rock mass increases. Furthermore, the joint inclination angle has significant influence on the generation of the number of cracks in the rock mass. However, the results of this simulation test cannot clearly reveal the precise variation law of the number of cracks. In addition, the peak stresses of the five measurement circles in the rock mass vary significantly with different joint inclination angles. The smallest difference in the peak stresses of the five measuring circles is obtained when the inclination angle is 15°, meaning the stress distribution in the specimen is more uniform.
- (6) According to the quantitative relationship between the cracks produced by shear and tension in the rock mass under all the different conditions discussed above, it is proved that the failure of a rock mass in the direct shear test is mainly caused by tension rather than shear action.

Data Availability

The data used to support the findings of this study are available within this article.

Conflicts of Interest

The authors declare that they have no conflicts of interest.

Acknowledgments

This work was supported by the National Natural Science Foundation Project (11562005), the First Class Discipline Construction Project of Civil Engineering in Guizhou Province (QYNYL [2017] 0013), the Natural Science Foundation of Guizhou Province (qkeheji [2019] No. 1057), and Major Scientific and Technological Projects of Guizhou Province (Qiankehe major special project [2018] 3011).

References

- [1] Y. M. Liu and C. C. Xia, "Weakening mechanism of mechanical behaviors and failure models of rock mass containing discontinuous joints under direct shear condition," *Rock and Soil Mechanics*, vol. 31, no. 3, pp. 695–701, 2010.
- [2] W. Z. Ren, H. Chen, Y. G. Wang, and F. Chen, "Failure mechanism and mechanical characteristics of rockmass containing close intermittent joints under plane stress condition," *Key Engineering Materials*, vol. 9, pp. 353–358, 2007.
- [3] J.-y. Lin, Y.-j. Zuo, J. Wang et al., "Stability analysis of underground surrounding rock mass based on block theory," *Journal of Central South University*, vol. 27, no. 10, pp. 3040–3052, 2020.
- [4] K. Peng, H. Lv, F. Z. Yan, Q. L. Zou, X. Song, and Z. P. Liu, "Effects of temperature on mechanical properties of granite under different fracture modes," *Engineering Fracture Mechanics*, vol. 226, Article ID 106838, 2020.
- [5] K. Peng, J. Zhou, Q. Zou, Y. Zhang, and G. Tan, "Deformation characteristics and failure modes of sandstones under discontinuous multi-level cyclic loads," *Powder Technology*, vol. 373, pp. 599–613, 2020.
- [6] L. X. Xiong, H. J. Chen, T. B. Li, and Y. Zhang, "Uniaxial compressive study on mechanical properties of rock mass considering joint spacing and connectivity rate," *Arabian Journal of Geosciences*, vol. 12, no. 21, p. 642, 2019.
- [7] Z. H. Wang and L. X. Xiong, "Uniaxial compression test of single-joint fractured rock mass considering the influence of thickness and length of joint surface and numerical simulation," *Geological Hazards and Environmental Protection*, vol. 30, no. 2, pp. 81–85, 2019.
- [8] Y. Liu, F. Dai, P. Fan, N. Xu, and L. Dong, "Experimental investigation of the influence of joint geometric configurations on the mechanical properties of intermittent jointed rock models under cyclic uniaxial compression," *Rock Mechanics and Rock Engineering*, vol. 50, no. 6, pp. 1453–1471, 2017.
- [9] M. Liu and E. Liu, "Dynamic mechanical properties of artificial jointed rock samples subjected to cyclic triaxial loading," *International Journal of Rock Mechanics and Mining Sciences*, vol. 98, pp. 54–66, 2017.
- [10] C. Zhang, C. Pu, R. Cao, T. Jiang, and G. Huang, "The stability and roof-support optimization of roadways passing through unfavorable geological bodies using advanced detection and monitoring methods, among others, in the Sanmenxia Bauxite Mine in China's Henan Province," *Bulletin of Engineering Geology and the Environment*, vol. 78, no. 7, pp. 5087–5099, 2019.
- [11] C. Y. Zhang, Y. X. Wang, H. Ruan, B. Ke, and H. Lin, "The strain characteristics and corresponding model of rock materials under uniaxial cyclic load/unload compression and their deformation and fatigue damage analysis," *Archive of Applied Mechanics*, vol. 91, pp. 1–16, 2021.
- [12] X. S. Li, Z. F. Liu, and S. Yang, "Similar physical modeling of roof stress and subsidence in room and pillar mining of a gently inclined medium-thick phosphate rock," *Advances in Civil Engineering*, vol. 2021, Article ID 6686981, 17 pages, 2021.
- [13] X. S. Li, K. Peng, J. Peng, and D. Hou, "Effect of thermal damage on mechanical behavior of a fine-grained sandstone," *Arabian Journal of Geosciences*, vol. 14, Article ID 1212, 2021.
- [14] X. S. Li, S. Yang, Y. M. Wang et al., "Macro-micro response characteristics of surrounding rock and overlying strata towards the transition from open-pit to underground mining," *Geofluids*, vol. 2021, Article ID 5582218, 18 pages, 2021.
- [15] C. Y. Zhang, Y. X. Wang, and T. T. Jiang, "The propagation mechanism of an oblique straight crack in a rock sample and the effect of osmotic pressure under in-plane biaxial compression," *Arabian Journal of Geosciences*, vol. 13, no. 15, Article ID 736, 2020.
- [16] Y. M. Liu, J. Liu, and C. C. Xia, "Research on strength behavior of rock mass containing discontinuous joints by direct shear test under different joint surface morphologies," *Rock and Soil Mechanics*, vol. 5, pp. 1269–1274, 2014.
- [17] Y. Q. Zhao, J. W. Liu, A. B. Jin, H. Sun, B. X. Wang, and Y. D. Wei, "Study on failure characteristics of intermittent jointed rock mass under loading and unloading condition," *Journal of Central South University*, vol. 51, no. 7, pp. 1893–1901, 2020.
- [18] M. Bahaaddini, "Effect of boundary condition on the shear behaviour of rock joints in the direct shear test," *Rock Mechanics and Rock Engineering*, vol. 50, no. 5, pp. 1141–1155, 2017.
- [19] M. Bahaaddini, P. C. Hagan, R. Mitra, and B. K. Hebblewhite, "Parametric study of smooth joint parameters on the shear behaviour of rock joints," *Rock Mechanics and Rock Engineering*, vol. 48, no. 3, pp. 923–940, 2014.
- [20] S. Chen and C. Qiao, "Composite damage constitutive model of jointed rock mass considering crack propagation length and joint friction effect," *Arabian Journal of Geosciences*, vol. 11, no. 11, p. 283, 2018.
- [21] Y. M. Liu, *Study on Failure Models and Strength of Rockmass Containing Discontinuous Joints in Direct Shear*, Tongji University, Shanghai, China, 2007.
- [22] M. Bahaaddini, G. Sharrock, and B. K. Hebblewhite, "Numerical investigation of the effect of joint geometrical parameters on the mechanical properties of a non-persistent jointed rock mass under uniaxial compression," *Computers and Geotechnics*, vol. 49, pp. 206–225, 2013.
- [23] B. Wang, Q. H. Jiang, C. Yao, and T. Xie, "Numerical analysis on failure mechanism of intermittent joints," *Advanced Materials Research*, vol. 255–260, pp. 113–117, 2011.
- [24] K. Bian, J. Liu, X. J. Hu, P. C. Li, L. Z. Chen, and Z. P. Liu, "Study on failure mode and dynamic response of rock slope with non-persistent joint under earthquake," *Yantu Lixue/Rock & Soil Mechanics*, vol. 39, no. 8, pp. 3029–3037, 2018.
- [25] C. Zhou, M. Karakus, C. Xu, and J. Shen, "A new damage model accounting the effect of joint orientation for the jointed rock mass," *Arabian Journal of Geosciences*, vol. 13, no. 7, p. 295, 2020.
- [26] S. Niu, H. Jing, K. Hu, and D. Yang, "Numerical investigation on the sensitivity of jointed rock mass strength to various factors," *Mining Science and Technology*, vol. 20, no. 4, pp. 530–534, 2010.
- [27] W. G. Cao, X. Tan, C. Zhang, and M. He, "A constitutive model to simulate the full deformation and failure process for rocks considering initial compression and residual strength behaviors," *Canadian Geotechnical Journal*, vol. 56, no. 5, 2018.
- [28] P. Wang, T. Yang, T. Xu, M. Cai, and C. Li, "Numerical analysis on scale effect of elasticity, strength and failure patterns of jointed rock masses," *Geosciences Journal*, vol. 20, no. 4, pp. 539–549, 2016.
- [29] P. Wang, F. Ren, and M. Cai, "Influence of joint geometry and roughness on the multiscale shear behaviour of fractured rock mass using particle flow code," *Arabian Journal of Geosciences*, vol. 13, no. 4, p. 165, 2020.

- [30] Y. T. Wang and J. Cui, "Direct shear strength characteristics and energy evolution mechanism of discontinuous rock bridge based on PFC2D," *Journal of Water Conservancy and Building Engineering*, vol. 17, no. 5, pp. 234–238, 2019.
- [31] Z. H. Wu, L. An, Z. J. Qi, Y. P. Kou, and B. S. Li, "The numerical simulation method of rock mass blasting based on PFC combined with LS-DYNA," *Journal of Mining and Safety Engineering*, vol. 38, no. 3, pp. 609–614, 2020.
- [32] D. Huang, Y. Li, D. F. Cen, and Q. H. Jiang, "Effect of microscopic crystal grains on strength and fracture behavior of marble under compressive-tensile stress state," *Rock and Soil Mechanics*, vol. S2, pp. 1–12, 2020.
- [33] Q. Z. Chen, Y. M. Liu, A. J. Zhu, and W. Wang, "PFC2D-based simulative study on influence from non-penetrative heterogeneous joint under various working conditions on mechanical properties of rock mass," *Water Resources and Hydropower Engineering*, vol. 50, no. 4, pp. 190–199, 2019.
- [34] Q. Z. Chen, Y. S. Zhang, Y. M. Liu, W. Wang, and K. Cao, "Influence of joint undulation angle on mechanical properties of non-penetrated joint rock mass," *Journal of Underground Space and Engineering*, vol. 16, no. 2, pp. 351–358+365, 2020.
- [35] Y. Zhou, A. Misra, S. C. Wu, and X. P. Zhang, "Macro- and meso-analyses of rock joint direct shear test using particle flow theory," *Journal of Rock Mechanics and Engineering*, vol. 31, no. 6, pp. 1245–1256, 2012.
- [36] Y. Zhou, G. Han, S. C. Wu, and N. L. Hu, "Meso failure mechanism of rock mass and slope with intermittent joints," *Journal of Rock Mechanics and Engineering*, vol. 35, no. S2, pp. 3878–3889, 2016.
- [37] Y. Zhou, J. F. Chai, and G. Han, "Meso numerical study on the failure mechanism of rock slope with bedding intermittent joints," *Engineering Review: Međunarodni Časopis Namijenjen Publiciranju Originalnih Istraživanja S Aspekta Analize Konstrukcija, Materijala I Novih Tehnologija U Području Strojarsva, Brodogradnje, Temeljnih Tehničkih Znanosti, Elektrotehnike, Računarstva I Građevinarstva*, University of Rijeka, Rijeka, Croatia, 2017.
- [38] X. X. Yang and P. Kulatilake, "PFC3D modeling of a jointed rock block behavior near an underground excavation and comparison with physical model test results," in *Proceedings of the 4th Itasca Symposium on Applied Numerical Modeling*, Lima, Perú, March 2016.
- [39] M. L. Wang, "Simulation of compression test on gangue by PFC-(3D)," *Chinese Journal of Rock Mechanics and Engineering*, vol. 32, no. 7, pp. 1350–1357, 2013.
- [40] X. J. Hu, K. Bian, Y. F. Ge, P. C. Li, and L. Z. Chen, "Failure mode of rock slope with non-persistent joint under static loading based on PFC," *Safety and Environmental Engineering*, vol. 24, no. 3, pp. 34–42, 2017.
- [41] J. Y. Huan, M. M. He, Z. Q. Zhang, and N. Li, "Parametric study of integrity on the mechanical properties of transversely isotropic rock mass using DEM," *Bulletin of Engineering Geology and the Environment*, vol. 79, 2019.
- [42] M. J. Jiang, Y. Sun, H. Chen, J. Y. Yuan, and S. G. Zhang, "DEM numerical simulation of rock masses containing non-coplanar intermittent joints in direct shear test," *Journal of Rock Mechanics and Engineering*, vol. 34, no. S2, pp. 3667–3675, 2015.
- [43] B. Regassa, N. Xu, and G. Mei, "An equivalent discontinuous modeling method of jointed rock masses for DEM simulation of mining-induced rock movements," *International Journal of Rock Mechanics and Mining Sciences*, vol. 108, pp. 1–14, 2018.
- [44] X. R. Liu, Z. Y. Deng, Y. Q. Liu, Y. M. Lu, S. L. Liu, and Y. F. Han, "Macroscopic and microscopic analysis of particle flow in pre-peak cyclic direct shear test of rock joint," *Journal of Coal*, vol. 44, no. 7, pp. 2103–2115, 2019.
- [45] R. Cao, P. Cao, H. Lin, and X. Fan, "Experimental and numerical study of the failure process and energy mechanisms of rock-like materials containing cross un-persistent joints under uniaxial compression," *PLoS One*, vol. 12, no. 12, Article ID e0188646, 2017.
- [46] A. Ghazvinian, V. Sarfarazi, W. Schubert, and M. Blumel, "A study of the failure mechanism of planar non-persistent open joints using PFC2D," *Rock Mechanics and Rock Engineering*, vol. 45, no. 5, pp. 677–693, 2012.
- [47] L. J. Tao, H. C. Dong, T. Meng, L. Liu, and J. D. Li, "Simulation study of blasting of jointed rock mass using PFC," *Blasting*, vol. 30, no. 4, pp. 14–19, 2013.
- [48] X. Fan, K. Li, H. Lai, Y. Xie, R. Cao, and J. Zheng, "Internal stress distribution and cracking around flaws and openings of rock block under uniaxial compression: a particle mechanics approach," *Computers and Geotechnics*, vol. 102, pp. 28–38, 2018.
- [49] Z. F. Zhang, W. M. Tang, and H. B. Jia, "Particle flow simulation of direct shear test on rock mass containing discontinuous joints with different roughness coefficients," *Journal of Changjiang River Scientific Research Institute*, vol. 37, no. 266, pp. 130–136, 2020.
- [50] Q. Z. Chen, *Research on the Extended Penetration Mechanism and Strength of Non-hole-through Jointed Rock Mass*, Guizhou University, Guiyang, China, 2019.
- [51] F. S. Liu, Y. F. Xue, and J. Yang, "Simulation of particle flow for direct shear test on infilled joint," *Water Resources and Hydropower Engineering*, vol. 51, no. 557, pp. 163–174, 2020.

Research Article

Seepage and Dynamic Characteristics of Carbonaceous Mudstone Coarse-Grained Soil Embankment with Different Gradations

Zhong-ming He,^{1,2} Xiao-qu Liu ,² Ke Huang,² and Jian-ping Xiong¹

¹Guangxi Transportation Science & Technology Group, Nanning 530000, China

²School of Traffic & Transportation Engineering, Changsha University of Science & Technology, Changsha 410114, China

Correspondence should be addressed to Xiao-qu Liu; 19101030063@stu.csust.edu.cn

Received 28 April 2021; Accepted 22 July 2021; Published 31 July 2021

Academic Editor: Rihong Cao

Copyright © 2021 Zhong-ming He et al. This is an open access article distributed under the Creative Commons Attribution License, which permits unrestricted use, distribution, and reproduction in any medium, provided the original work is properly cited.

This study investigates the seepage and deformation characteristics of carbonaceous mudstone coarse-grained soil embankment with different gradations under the action of dynamic load and rainfall. An indoor geotechnical test is conducted, and the mechanical parameters of carbonaceous mudstone coarse-grained soil with different gradations are analyzed. A numerical calculation model of seepage and dynamic characteristics of carbonaceous mudstone coarse-grained soil embankment is established on the basis of the test data. The different effects of rainfall infiltration and vehicle load are evaluated. The seepage, settlement, and slope stability evolution characteristics of graded carbonaceous mudstone coarse-grained soil embankment slope are studied. Results show that under the condition of the same rainfall time, the greater the nonuniformity coefficient, the faster the decrease in pore water pressure of the coarse-grained soil embankment at the same monitoring point. The seepage velocity vector in the embankment is concentrated below the soil shoulder. The smaller the saturated permeability coefficient and saturated water content, the larger the seepage velocity vector. The greater the nonuniformity coefficient, the larger the coarse-grained soil embankment under vehicle load. The smaller the embankment settlement, the lower the safety factor of embankment. The safety factor decreases slowly at first and then decreases rapidly in the whole study period under the effect of dynamic wetting. The research results provide a theoretical reference for the practical engineering application of carbonaceous mudstone coarse-grained soil embankment in rainy areas.

1. Introduction

Carbonaceous mudstone is widely distributed in southwest China [1, 2]. It was often discarded as bad filling material in highway construction in the past due to its strong water resistance, easy weathering, low strength, and large deformation. However, with the rapid development of highway construction in China, suitable filling materials are extremely scarce in many areas. Considering the economy and environmental protection, the use of carbonaceous mudstone for embankment filling is imperative. However, the rheological phenomenon of coarse-grained soil filler often occurs during the operation period under long-term vehicle dynamic load and rainwater infiltration. This condition leads to the gradual weakening of the service performance (water stability, strength, and stability) of high embankment with

coarse-grained soil and then causes the local or overall instability of high embankment [3, 4]. Considering this problem, scholars at home and abroad have conducted numerous research and considered that the influence of seepage and dynamic load on embankment is mainly reflected in the following aspects: (1) the change in matric suction of unsaturated soil is mainly caused by gradation [5]; (2) the seepage flow along the embankment slope direction during rainfall infiltration increases the overall sliding force of the slope [6, 7]; (3) the rainfall infiltration reduces the matric suction of unsaturated soil, and mass suction leads to the decrease in soil shear strength [8].

In the aspect of the influence of gradation on the hydraulic characteristics of coarse-grained soil, Wang et al. [9] investigated the influence of gradation on the hydraulic characteristics of coarse-grained soil. On the basis of Van Genuchten

(VG) water retention model, two pedotransfer functions are proposed by using semiphysical and semistatistical methods to estimate the water retention curve of sand. Feng et al. [10] studied the influence of porosity and fractal dimension of particles on the seepage characteristics of sandstone. Chiu et al. [11] presented a method to estimate the soil-water characteristic curve by using particle size distribution. Meng et al. [12] explored the deformation characteristics of coarse-grained soil with different gradations.

The particle size distribution of soil sample affects its hydraulic and mechanical parameters in different degrees. Therefore, the hydraulic and physical properties of carbonaceous mudstone coarse-grained soil embankment filling with different gradations are compared to investigate the deformation characteristics of carbonaceous mudstone filling with different gradations. This process can verify the feasibility of carbonaceous mudstone coarse-grained soil filling road and determine the feasibility of the project. The best graded carbonaceous mudstone coarse-grained soil embankment is determined in the project. However, the above studies only consider the influence of soil particle gradation and disregard the influence of soil load in the analysis of the hydraulic characteristics of soil.

In the aspect of saturated-unsaturated seepage of embankment slope, Wang et al. [8], Liu et al. [13], Kim et al. [14], and Kim et al. [15] studied the influence of water volume content and pore water pressure of unsaturated soil on slope stability under rainfall conditions. Wu et al. [16] conducted numerical analysis on unsaturated seepage of loess slope caused by rainfall infiltration and quantitatively evaluated the relationship between rainfall infiltration and slope stability by monitoring the water content, pore water pressure, and slope deformation of loess slope. Liu et al. [17], Volz et al. [18], and Kim et al. [19] conducted numerical simulation on the rainfall damage of unsaturated soil embankment slope and analyzed the influence of rainfall intensity, rainfall duration, and soil long-term intensity on the instability characteristics of unsaturated soil embankment slope under rainfall. Cho [20] and Nguyen and Likitlersuang [21] used numerical models to analyze the slope stability under heavy rainfall and predict the probability of slope instability. The above research results reveal the seepage characteristics of rainfall infiltration in the embankment and show that the numerical software can better simulate the gradual process of real embankment slope instability. In practical engineering, many factors affect the embankment deformation, and indoor model test is difficult to restore the real environment and vehicle load of the embankment. Therefore, the help of numerical analysis software to simulate the real situation of embankment deformation characteristics can maximize the simulation of the actual project, so as to lay a good theoretical foundation for practical engineering application. Relevant scholars have conducted many studies on the mechanical properties of carbonaceous mudstone. However, they only consider the influence of rainfall or static load. Few studies have been performed on the mechanical properties of carbonaceous mudstone coarse-grained soil embankment under the combined action of rainfall infiltration and dynamic load.

Research on the migration characteristics of seepage water in embankment under the combined action of vehicle load and rainfall infiltration is lacking at home and abroad. The aim of this study is thus to study the influence of rainfall infiltration and vehicle load on the seepage field and dynamic characteristics of carbonaceous mudstone coarse-grained soil slope with different gradations using the GeoStudio and FLAC 3D software. The influence of displacement field and stability evolution can provide theoretical guidance for engineering practice.

1.1. Analysis of Particle Size Distribution. According to engineering experience, disintegrated carbonaceous mudstone is generally used as embankment filler instead of bulk carbonaceous mudstone [22]. In this study, carbonaceous mudstone was placed outdoors for disintegration and was sprayed with appropriate amount of water every day until it was naturally dried. After 30 days, the carbonaceous mudstone coarse-grained soil was mixed with a shovel to mix it evenly [23]. The coarse granular soil of carbonaceous mudstone was screened. The gradation used in this study is based on the design data of the project, as shown in Table 1, and the gradation curve is shown in Figure 1. In this study, soil samples with three different gradations are called gradation 1, gradation 2, and gradation 3, respectively.

Existing research shows that when the fractal dimension is greater than 2.3, carbonaceous mudstone coarse-grained soil can be used as embankment [24] filler in accordance with the calculation formula of passing percentage and fractal dimension of carbonaceous mudstone coarse-grained soil [25]. The fractal dimension of carbonaceous mudstone coarse-grained soil used in this study after disintegration is shown in Table 2. The fractal dimension of each soil sample is greater than 2.3, which meets the requirements of road use.

1.2. Physical and Mechanical Parameters. The test data through the indoor geotechnical test of the soil sample prepared on the basis of the proposed gradation in the project are shown in Table 3. These data provide accurate physical and mechanical parameters for the subsequent numerical simulation.

2. Analysis of the Seepage Characteristics of Embankment

2.1. Seepage Numerical Model. This study establishes a seepage calculation model based on a highway carbonaceous mudstone coarse-grained soil embankment project in Guangxi to explore the seepage change law of carbonaceous mudstone coarse-grained soil embankment under different rainfall conditions. The embankment height is 8 m, and the slope is 1:1.5. The specific geometric size is shown in Figure 2. GeoStudio numerical analysis software is used to establish the seepage numerical model, as shown in Figure 3. The mesh is divided in accordance with the four-node method [26], with a total of 2698 nodes and 2588 elements. Eleven monitoring points are set in the embankment slope model to analyze the variation of volume moisture content

TABLE 1: Grading statistics of carbonaceous mudstone coarse-grained soil.

Soil sample	d_{10}	d_{30}	d_{60}	C_u	C_c	Fractal dimension
Gradation 1	1.14	8.43	26.55	23.29	2.35	2.46
Gradation 2	0.40	2.90	9.80	24.50	2.15	2.55
Gradation 3	0.60	3.30	10.40	17.33	1.75	2.50

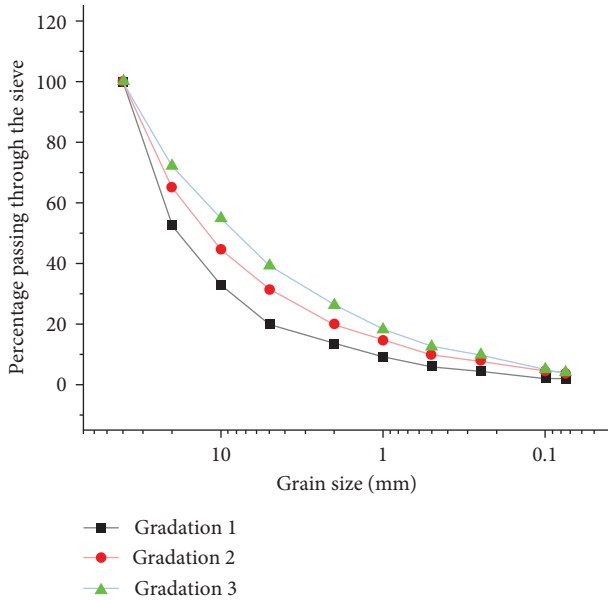


FIGURE 1: Particle size distribution curve.

in the process of rainwater seepage. The monitoring points 1–5 are buried at the depth of 0.5 m below the slope, and the spacing of each monitoring point is 3.2 m. The monitoring points 6, 8, 9, and 3 are in the same horizontal position, and the spacing of each monitoring point is 0.7 m. The monitoring points 7, 10, and 11 are below monitoring point 3, and their spacing is 0.7 m, as shown in Figure 3.

In this model, the soil shoulder, embankment slope surface, and subgrade surface on the right side of the slope toe are taken as rainfall infiltration boundary, and the pavement is taken as impermeable boundary. The left groundwater level is set at the depth of 10 m below the carbonaceous mudstone coarse-grained soil embankment. The right groundwater level is set at the depth of 11 m below the carbonaceous mudstone coarse-grained soil embankment.

The influence of heavy rainfall on the slope seepage characteristics is evaluated on the basis of the local rainfall data. The rainfall intensity is determined to be 1.16×10^{-6} m/s, and the rainfall duration is 72 h. The seepage parameters of soil with different gradations are shown in Table 2. The VG model is used to fit the soil-water characteristic curve of coarse-grained carbonaceous mudstone soil with different gradations, as shown in Figure 4.

2.2. Variation Law of the Negative Pore Water Pressure and Volume Moisture Content of Embankment. In the process of water level rise and fall, the pore water pressure in the embankment changes with the moisture migration. This

study only lists the distribution of pore water pressure in the embankment of carbonaceous mudstone coarse-grained soil with different gradations at 24 and 72 h, as shown in Figure 5.

As shown in Figure 5, the variation trend of the pore water pressure of coarse-grained carbonaceous mudstone soil with different gradations is similar during rainfall infiltration. The continuous rainfall causes the groundwater level to rise, and the carbonaceous mudstone coarse-grained soil embankment forms a transient saturation zone at the bottom of the slope. Soil sample 2 has the largest rainfall infiltration depth compared with soil samples 1 and 3.

Figures 6 and 7 show the variation curves of negative pore water pressure and volumetric water content with time at different depths of monitoring points under the effect of rainfall infiltration.

As shown in Figure 6, the negative pore water pressure of embankment slope gradually decreases with the increase in rainfall duration after the beginning of rainfall. The negative pore water pressure on the slope surface decreases fast, and the negative pore water pressure inside the slope decreases slowly. Within 35 h of rainfall, the negative pore water pressure of three grading soil samples at monitoring points 1–5 decreases to 0. The order of decreasing rate is monitoring point 1 > monitoring point 2 > monitoring point 3 > monitoring point 4 > monitoring point 5. The change law can be summarized in three stages: rapid decrease in 0–20 h, slow decrease in 20–35 h, and basically stable in 35–72 h. After 10 h of rainfall, soil sample 2 has a more obvious downward trend than soil samples 1 and 3.

The hydraulic characteristics of soil sample 2 are better than that of soil samples 1 and 3 through comparative analysis. For soil sample 2, monitoring points 6 and 7 in the slope are reduced to 0 kPa within 55 h, and the reduction rate is monitoring point 6 > monitoring point 7. For monitoring points 3, 6, 8, and 9, the matric suction decreases from the slope surface to the slope interior. For monitoring point 11 of soil sample 2, the negative pore water pressure of soil sample 2 decreases rapidly from 120 kPa to 40 kPa within 35–72 h of rainfall, which decreases by 66%.

As shown in Figure 7, the water content of the embankment slopes of three carbonaceous mudstone coarse-grained soil samples increases under the effect of rainfall. The water content of the points close to the slope surface increases rapidly. The transient saturation area gradually expands to the inside of the slope after forming at the surface of the embankment slope. The saturated water content of the soil at monitoring point 5 first reaches the top of the slope, and that of the soil at monitoring point 1 at the foot of the slope increases rapidly. The growth rate of negative pore water pressure is the slowest. For soil sample 2, the volumetric moisture content in monitoring points 1–5 located on the slope reaches saturation within 55 h of rainfall, and the order of increasing rate is monitoring point 1 > monitoring point 2 > monitoring point 3 > monitoring point 4 > monitoring point 5. The monitoring point 6 located in the slope reaches the saturated water content after 72 h of rainfall. For monitoring points 3, 7, 10, and 11, the increase rate of volumetric moisture content decreases from top to bottom in the vertical

TABLE 2: Calculation parameters of road bed and pavement materials.

Material parameters	Thickness (m)	Volume weight (kN/m ³)	Elastic modulus (MPa)	Poisson's ratio	Damping ratio (%)
Pavement surface	0.15	25.0	1200.0	0.25	0.12
Pavement base	0.36	24.0	1100.0	0.27	0.10
Embankment 1	8.00	22.4	300.0	0.28	0.15
Embankment 2	8.00	22.2	401.5	0.28	0.15
Embankment 3	8.00	22.1	340.0	0.28	0.15
Subgrade	15.00	19.0	200.0	0.33	0.22

TABLE 3: Physical and mechanical parameters.

	Optimum moisture content (%)	Maximum dry density (g/cm ³)	Saturated water content (%)	Cohesion (kPa)	Internal friction angle (°)	Elastic modulus (MPa)	Saturated permeability coefficient (m/s)	Unit weight (kN/m ³)
Gradation 1	6.6	2.24	38.33	30.0	21.9	300.0	5.88×10^{-7}	22.4
Gradation 2	6.0	2.22	36.56	37.6	20.2	401.5	3.45×10^{-7}	22.2
Gradation 3	6.0	2.21	37.44	30.8	20.5	340.0	4.09×10^{-7}	22.1

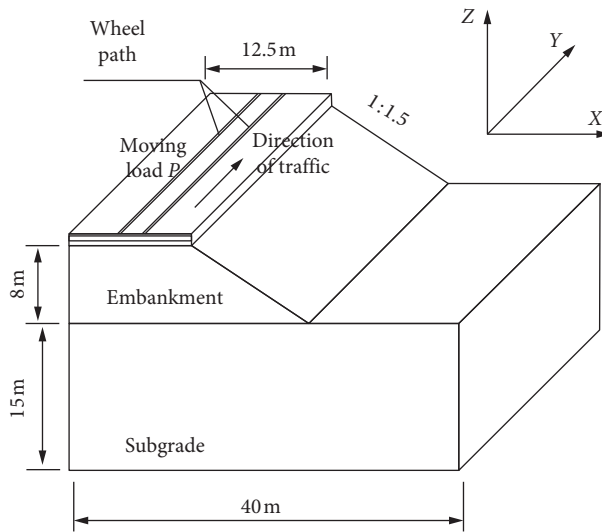


FIGURE 2: Moving dead load model.

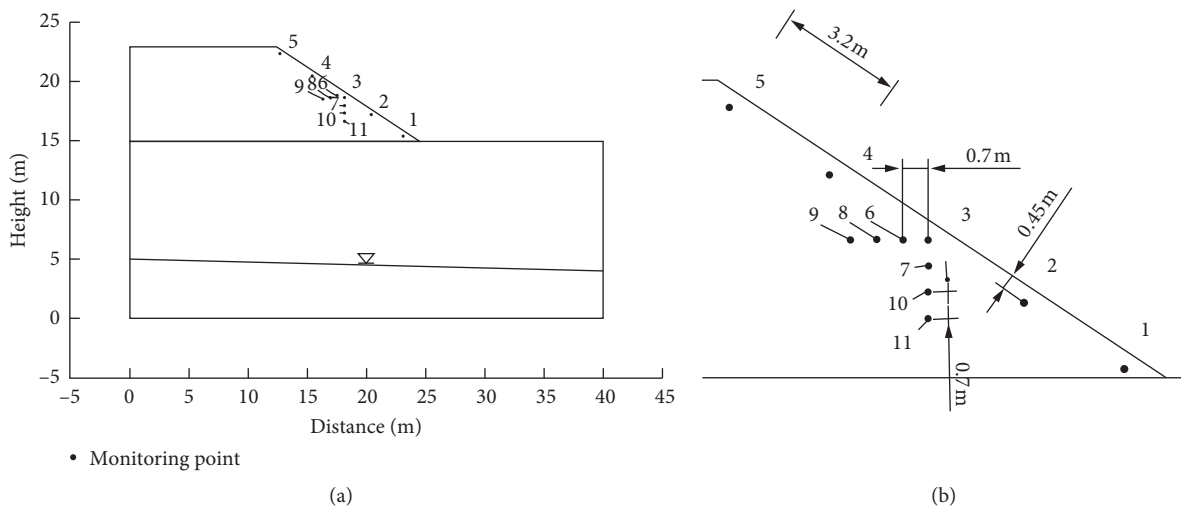
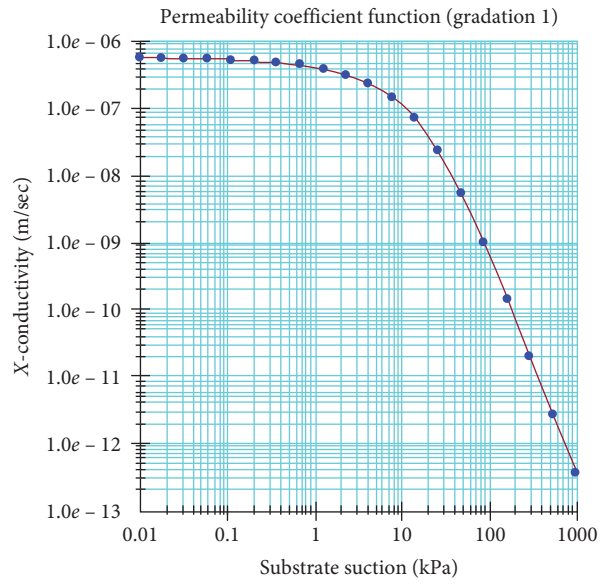
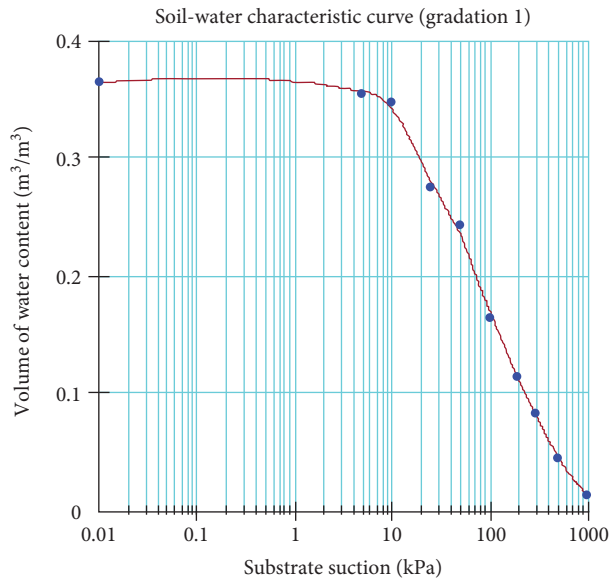
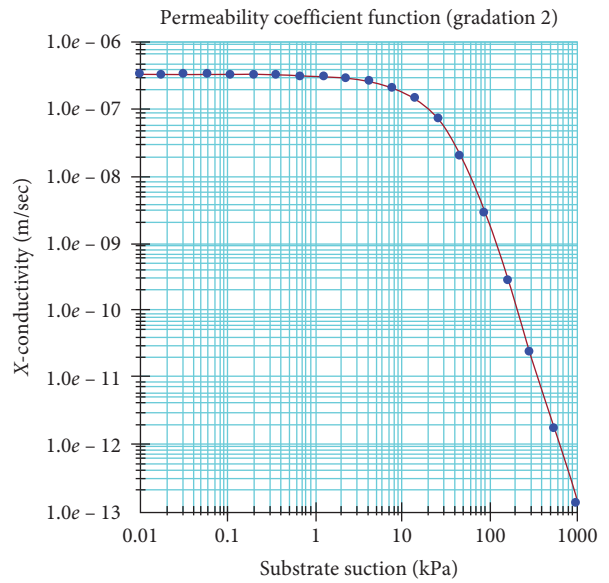
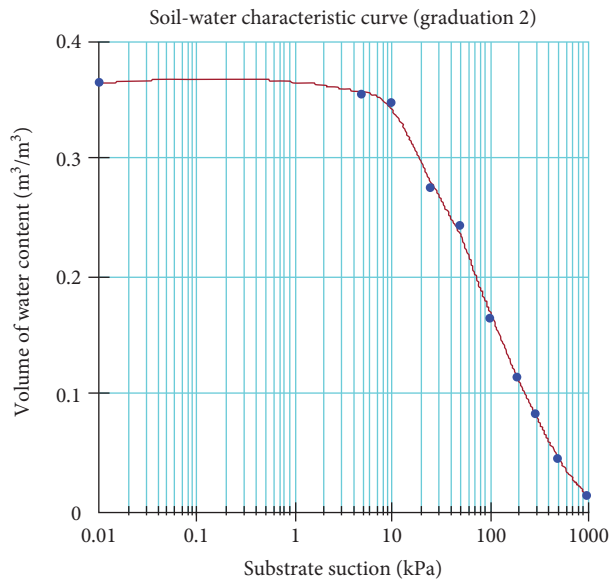


FIGURE 3: Numerical analysis model of embankment seepage. (a) Overall model diagram. (b) Specific location of monitoring points.



(a)



(b)

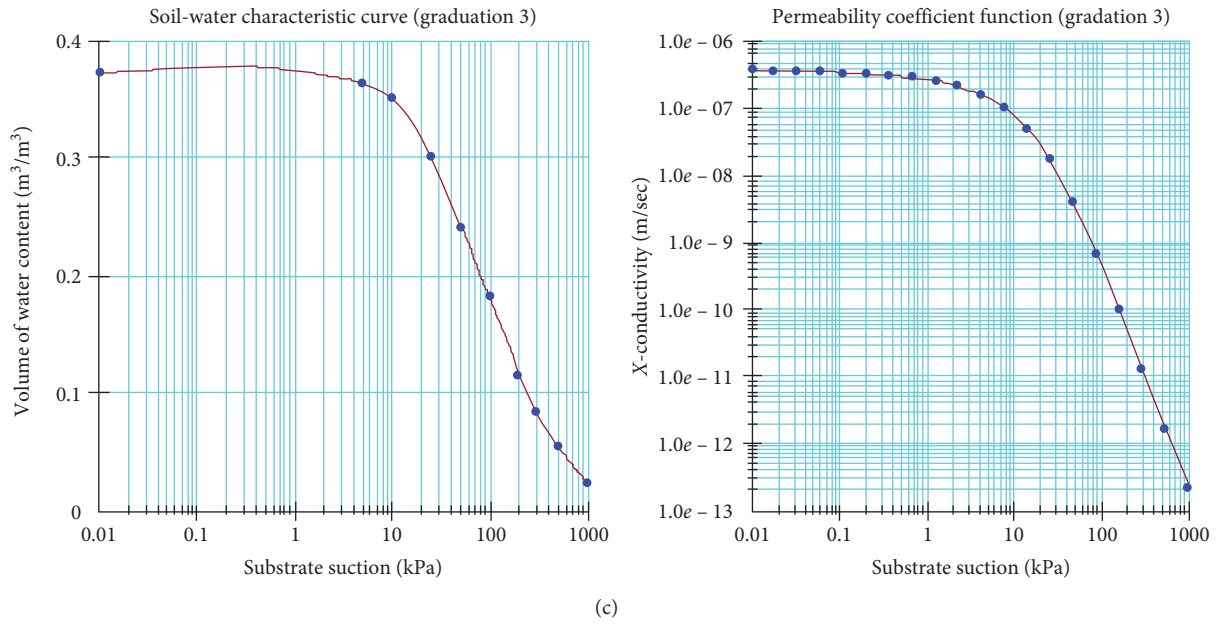
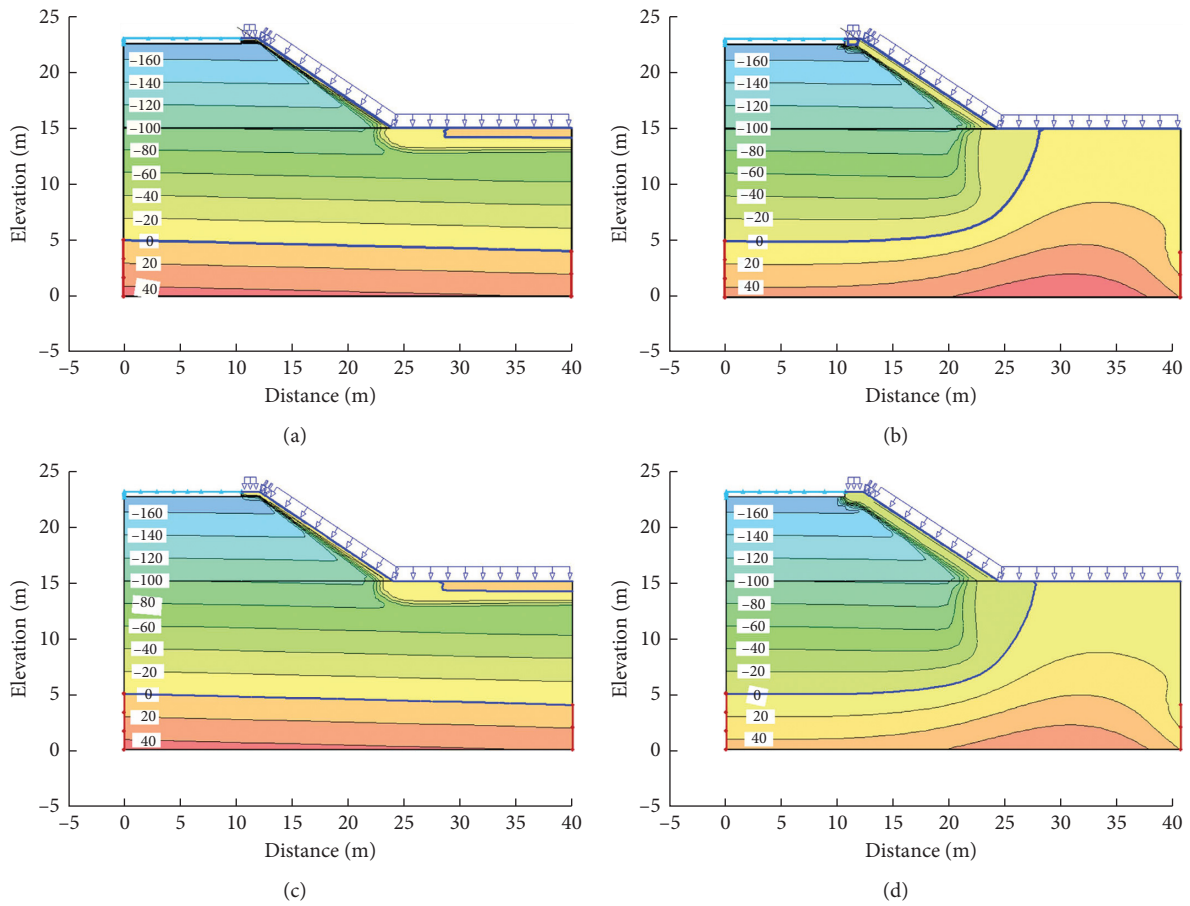


FIGURE 4: Fitting soil-water characteristic curve and permeability coefficient curve of carbonaceous mudstone coarse-grained soil. (a) Gradation 1. (b) Gradation 2. (c) Gradation 3.



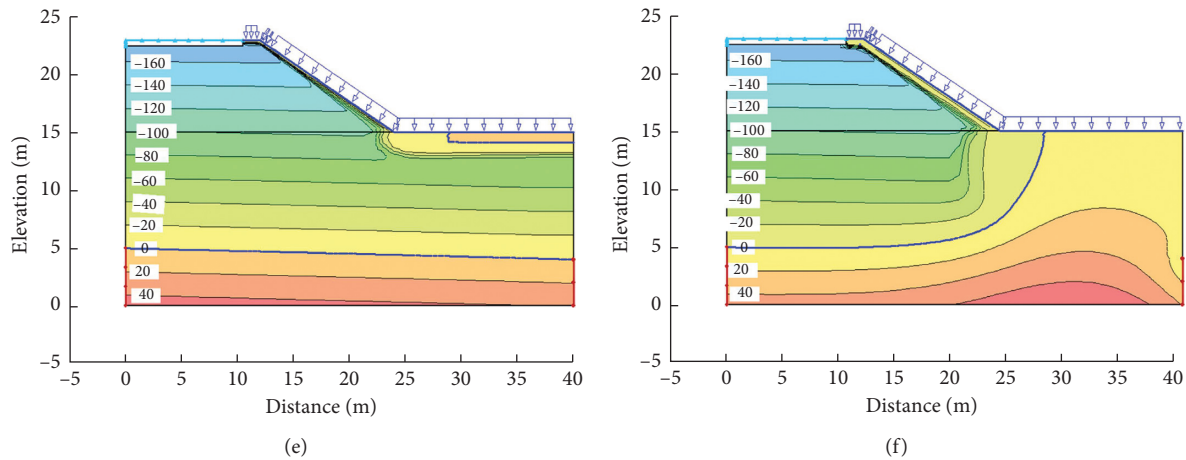


FIGURE 5: Cloud chart of the pore water pressure of carbonaceous mudstone coarse-grained soil embankment. (a) Gradation 1 (24 h rainfall). (b) Gradation 1 (72 h rainfall). (c) Gradation 2 (24 h rainfall). (d) Gradation 2 (72 h rainfall). (e) Gradation 3 (24 h rainfall). (f) Gradation 3 (72 h rainfall).

direction of embankment slope. For monitoring points 3, 6, 8, and 9, the volumetric moisture content decreases from the slope surface to the slope interior in the horizontal direction of the embankment slope. Specifically, the wetting front expands from the slope surface to the slope interior.

In conclusion, the negative pore water pressure of soil embankment decreases under the effect of rainfall, and the water volume content of the area affected by rainfall infiltration increases or reaches the saturated water content. The changes in the above physical quantities can be summarized in the following two points: (1) the water content of carbonaceous mudstone coarse-grained soil increases, and the surface tension of soil decreases gradually after rainwater infiltration in the embankment. This condition results in the rapid decrease in the negative pore water pressure of soil until it reaches 0 kPa. However, the monitoring points located in the embankment far from the slope surface are less affected by rainwater infiltration. Thus, the change in pore water pressure is unremarkable. (2) The influence degree of rock and soil slopes affected by rainfall is related to the rainfall time. The longer the rainfall time, the greater the rainfall infiltration depth. Under the action of gravity and head difference, the rainwater infiltrating in the slope moves to the lower and front of the carbonaceous mudstone coarse-grained soil embankment. With the increase in rainfall duration, the range and depth of transient saturation zone expand along the slope direction.

2.3. Variation Law of the Seepage Velocity Vector. The rainwater migrates inside and forms a seepage field after it infiltrates into the surface of the carbonaceous mudstone coarse-grained soil embankment. During seepage, the rainwater fills the pores of the coarse-grained soil particles and exerts a drag force on the coarse-grained soil particles, forming a seepage force. The size and direction of this force can be expressed with the seepage velocity vector generated by the embankment. The seepage velocity vector calculation results of different soil samples are shown in Figure 7.

As shown in Figure 8, the variation trend of the seepage velocity vector of three soil samples is similar. The smaller the saturated permeability coefficient and saturated water content of embankment, the larger the seepage velocity vector. Under the action of atmospheric rainfall, the seepage field first forms on the surface of carbonaceous mudstone coarse-grained soil embankment slope. When the rainfall is 24 h, the seepage velocity vector is mainly concentrated below the soil shoulder, and the arrow length is large, forming a dense area of seepage velocity vector. When the rainfall reaches 72 h, the seepage velocity vector at the toe of the embankment slope gradually turns upward at the groundwater level, forming a return flow zone. This phenomenon may be due to the following reasons. In the initial stage of rainfall, part of the rainwater collects and infiltrates at the soil shoulder of the embankment because it is relatively flat. This condition results in a large amount of rainwater infiltration under the soil shoulder and a rapid seepage speed, forming a dense seepage area. With the continuous rainfall, the rainwater infiltrating in the slope gradually collects at the foot of the slope. When the rainwater expands to the groundwater level, the groundwater level gradually climbs up along the foot of the slope, forming a return flow zone.

3. Analysis of the Stress and Deformation Characteristics of Embankment

3.1. Dynamic Simulation Scheme. The data of embankment pore water pressure under different rainfall conditions are imported into FLAC 3D software to investigate the influence of dynamic humidification on embankment deformation. The seepage results are combined with a dynamic model. A strength reduction method is used to calculate the stability of embankment slope with different grades of carbonaceous mudstone coarse-grained soil under dynamic humidification.

The moving dead load model adopted in this study is shown in Figure 3. The vehicle load before the dynamic loading of the carbonaceous mudstone coarse-grained soil embankment model is based on the calculation method of

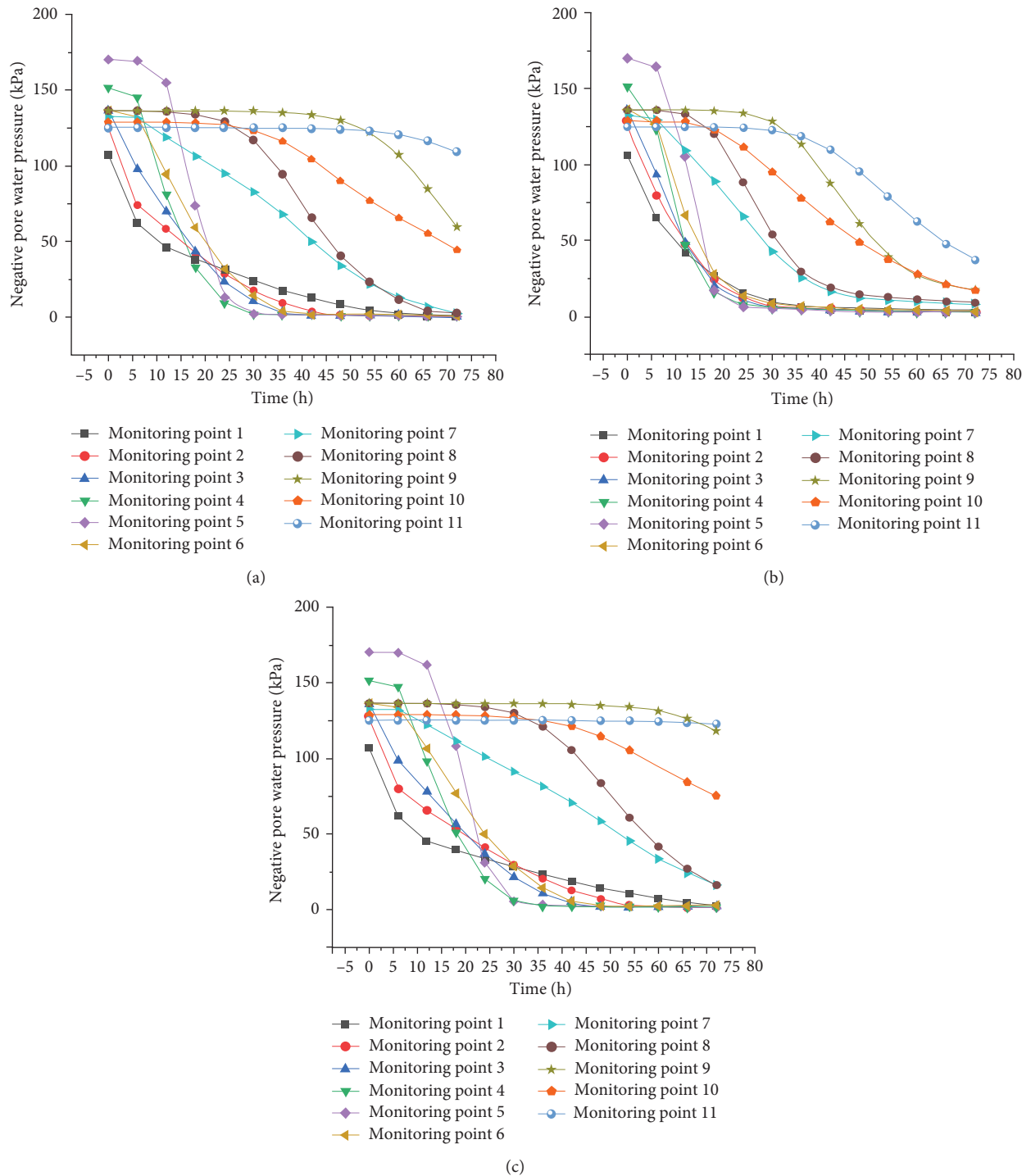


FIGURE 6: Pore water pressure variation of the monitoring points of carbonaceous mudstone coarse-grained soil embankment. (a) Gradation 1. (b) Gradation 2. (c) Gradation 3.

unit load. The equivalent circular load is simplified to $0.37 \text{ m} \times 0.25 \text{ m}$ rectangular load, and the vehicle load is converted into uniformly distributed load [27, 28]. The load track is set along the vehicle driving direction, and the track width and uniform load are calculated. At this time, the vehicle load is equivalent to the uniformly distributed load acting on the road, and the load size remains unchanged. The action position gradually moves along the driving direction

with the movement time, and the vehicle speed can be realized by controlling the action time of the vehicle load at a certain point. The load running from the starting point to the end point of the track is regarded as one loading. This loading is imported into the seepage model of carbonaceous mudstone coarse-grained soil embankment after 24 and 72 h of rainfall. The model is loaded 7000 times under the standard axle load of 100 kN.

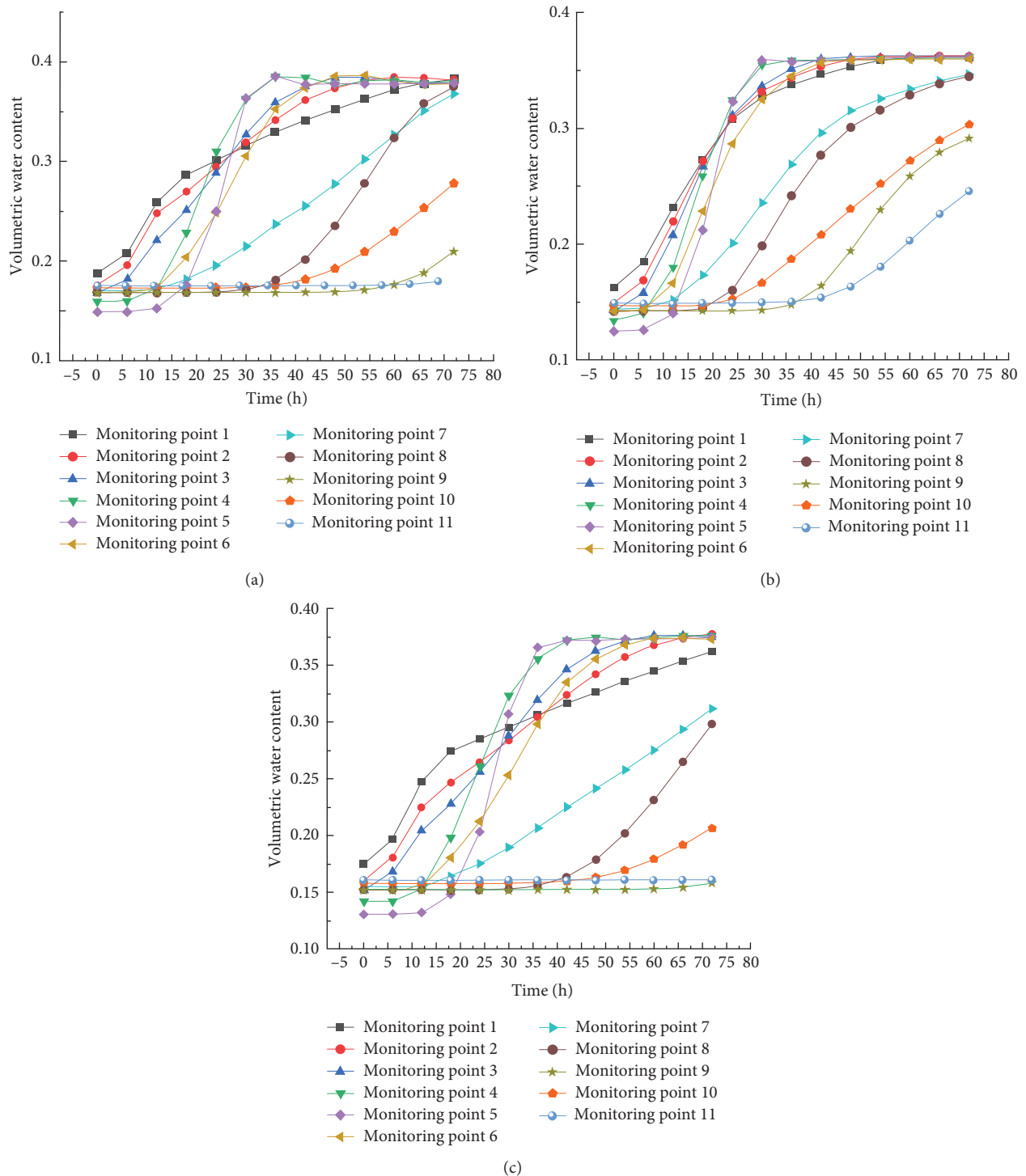


FIGURE 7: Water volume content of the monitoring points of carbonaceous mudstone coarse-grained soil embankment.

Selection of calculation parameters: the calculation parameters of road bed and pavement materials in accordance with the indoor experimental results and design data are shown in Table 2.

As shown in Table 2, the rigidity of the surface and basic structure is large. An elastic model is adopted for surface and base courses to ensure the accuracy of numerical simulation. The Mohr–Coulomb constitutive model is adopted for

embankment and soil foundation. The material dissimulation of surface and basic structure is disregarded in the model calculation.

The 3D equivalent model of FLAC3D established in this study is shown in Figure 9. The shape, quantity, and size of the embankment cross section mesh are consistent with the seepage model. In the setting of boundary conditions, Y constraints are applied along the boundary of vehicle driving

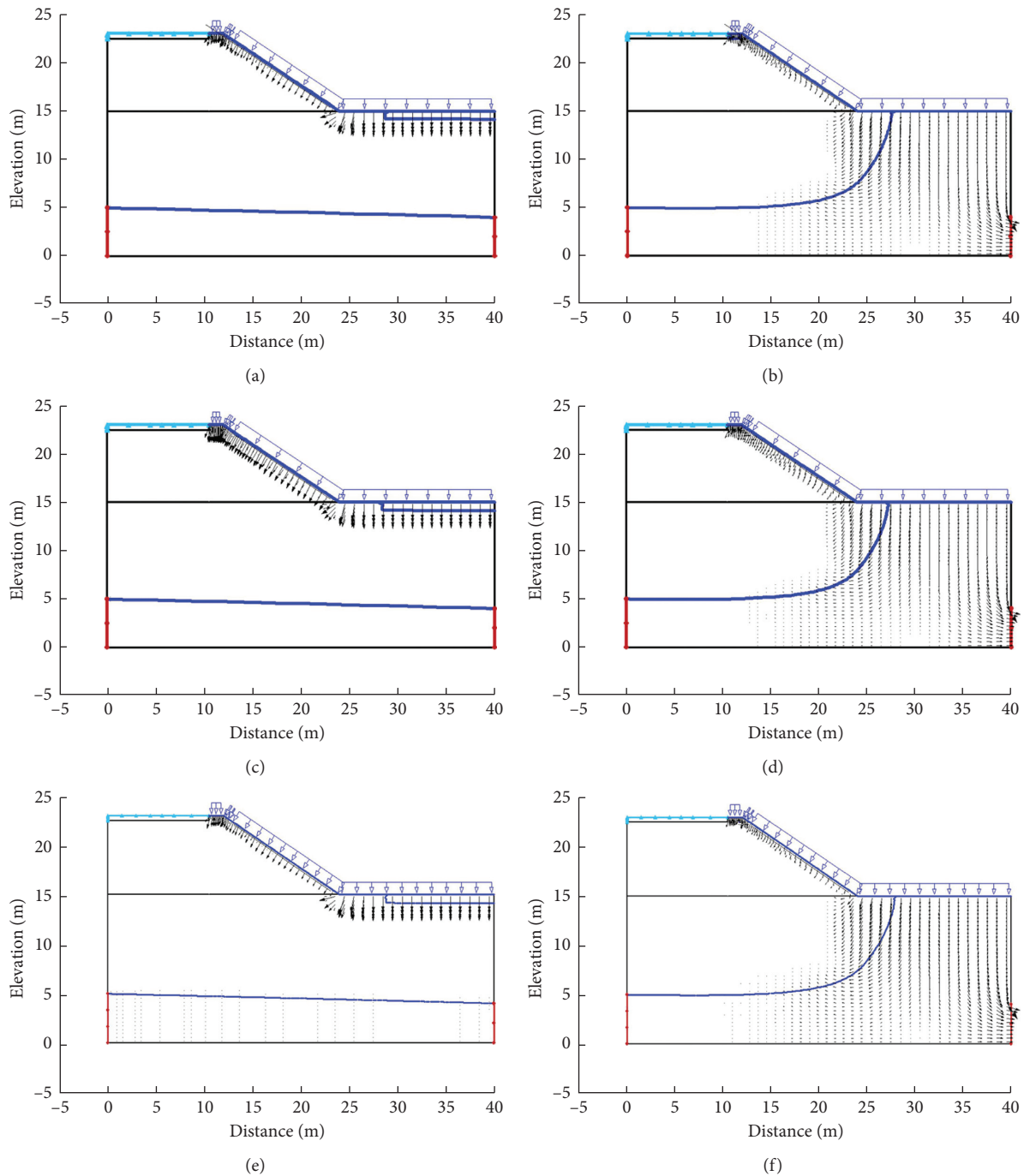


FIGURE 8: Variation law of velocity vector. (a) Gradation 1 (24 h rainfall). (b) Gradation 1 (72 h rainfall). (c) Gradation 2 (24 h rainfall). (d) Gradation 2 (72 h rainfall). (e) Gradation 3 (24 h rainfall). (f) Gradation 3 (72 h rainfall).

direction to ensure the accuracy of the model calculation results. X and Y constraints are applied perpendicular to the boundary of vehicle driving direction, and X , Y , and Z constraints are applied at the bottom of the model. The model is loaded under the condition of 100 kN standard axle load and 80 km/h vehicle speed.

In this study, the vehicle load is equivalent to the uniformly distributed load on the road, which has a wide range of influence on the dynamic response of the subgrade and pavement. Selecting typical monitoring points is necessary

to monitor the dynamic stress change law under the action of vehicle load. This process is performed to study the dynamic response characteristics of the subgrade within the lateral effective range. Therefore, 13 monitoring points are set on the top of the subgrade to explore the dynamic response of the same depth. On the basis on these monitoring points, the dynamic stress at different depths is analyzed. The layout of monitoring points is shown in Figure 10.

In this calculation, three types of graded carbonaceous mudstone coarse-grained soil are selected, the depth of

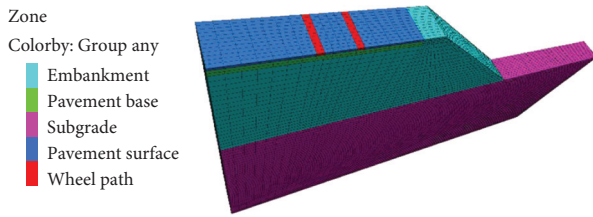


FIGURE 9: Pavement structure of numerical analysis.

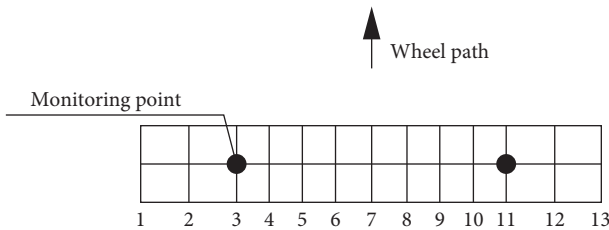


FIGURE 10: Layout of transverse monitoring points on subgrade.

subgrade working area is 1.77 m, and unfavorable conditions are considered. Monitoring point 3 is taken as the research object, starting from the subgrade surface, every 0 m to study the dynamic response of carbonaceous mudstone coarse-grained soil subgrade in the vertical direction. The peak value of vertical dynamic stress at different subgrade depths is calculated at 25 m.

3.2. Dynamic Response Characteristics of Embankment

3.2.1. Dynamic Response of the Lateral Monitoring Points of Embankment. Gradation 2 is selected as the research object in this study because the dynamic stress curves of the three soil samples are the same. In accordance with the peak stress of each monitoring point in the carbonaceous mudstone coarse-grained soil embankment, the vertical stress peak curve of the monitoring point is drawn, as shown in Figure 11.

As shown in Figure 11, the three curves all take monitoring point 7 as the center, showing an axisymmetric trend. On the subgrade surface, the peak value of vertical stress of the three soil samples at monitoring points 3 and 11 directly below the wheel reaches the maximum value, and the peak value of vertical stress at monitoring point 7 in the center of two wheels is the minimum. Therefore, when the vehicle load moves to a certain point on the subgrade surface, the vertical dynamic stress response at that point is the most obvious. With the increase in the distance from the point, the degree of vertical dynamic stress response gradually decreases.

3.2.2. Dynamic Stress Response of Embankment at Different Depths. The vertical dynamic stress peak values at different subgrade depths are calculated every 0.25 m from the subgrade surface to study the dynamic response of carbonaceous mudstone coarse-grained soil subgrade in the vertical direction. The calculation results are shown in Figure 12.

As shown in Figure 12, when the vehicle load is 100 kN and the vehicle speed is 80 km/h, the vertical dynamic stress of

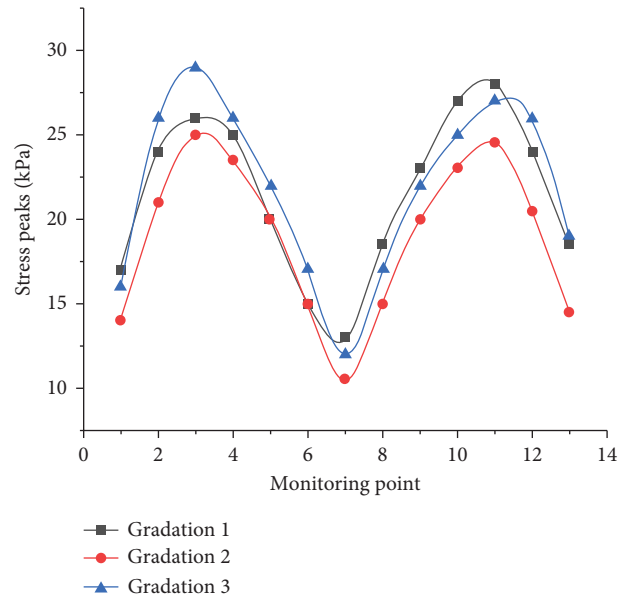


FIGURE 11: Peak stress curve of transverse monitoring points on subgrade surface.

three soil samples at the monitoring point gradually decreases with the increase of subgrade depth. The peak vertical dynamic stress of subgrade surface of soil sample gradation 1 is 24 kPa. When the depth of monitoring point reaches 2 m, the peak value of vertical dynamic stress is only 3 kPa, which decreases by 87.5%. The peak value of vertical dynamic stress of soil gradation 2 decreases from 25 kPa to 4 kPa, which decreases by 84%. Soil sample of gradation 3 decreased by 89.1%.

3.3. Variation Law of the Embankment Settlement Displacement. Figure 13 shows the settlement displacement curve of embankment with different gradations of carbonaceous mudstone coarse-grained soil.

As shown in Figure 13, the settlement displacement of the three graded carbonaceous mudstone coarse-grained soil subgrades is extremely small, and the cumulative rate of plastic strain is low when the number of vehicle loads acting on the carbonaceous mudstone coarse-grained soil embankment with rainfall duration of 24 and 72 h is less than 2000 times. When the number of vehicle loads acting on the carbonaceous mudstone coarse-grained soil embankment reaches 5000 times, the settlement displacement of the three graded carbonaceous mudstone coarse-grained soil embankments increases greatly. The settlement displacement of the embankment increases to 16, 14, and 13 mm after 24 h of rainfall (plus quantity). The settlement displacement of the embankment increases to 20, 19, and 16 mm after 72 h of rainfall. The plastic deformation of carbonaceous mudstone coarse-grained soil subgrade accumulates rapidly. When the vehicle load acts on the carbonaceous mudstone coarse-grained soil embankment for 7000 times, the settlement displacement of carbonaceous mudstone coarse-grained soil subgrade with different gradations tends to be stable.

The data show that the subgrade soil is mainly elastic strain at the initial loading stage. The subgrade soil can

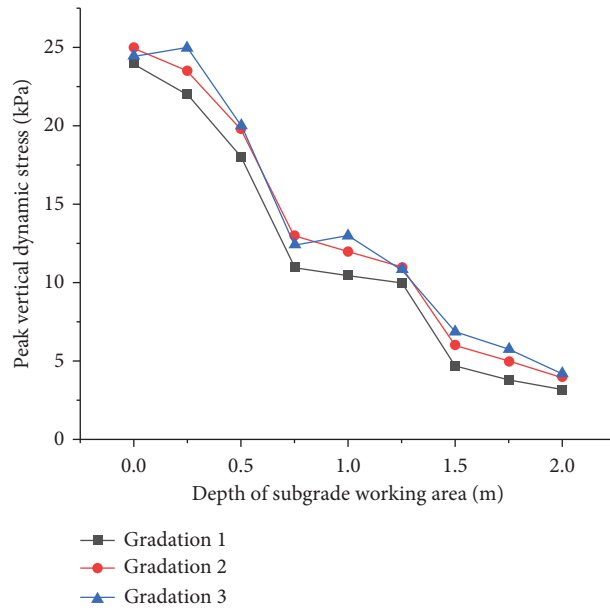


FIGURE 12: Vertical dynamic stress peak curve at different subgrade depths.

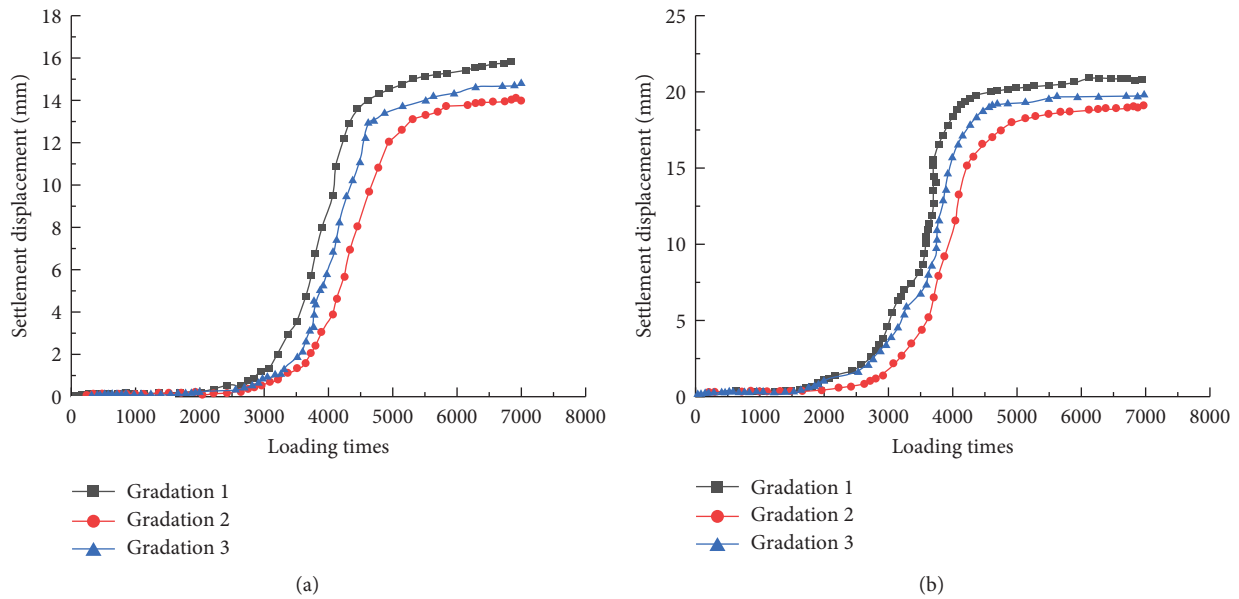


FIGURE 13: Displacement curve of embankment with different gradations. (a) Displacement curve of embankment (24 h). (b) Displacement curve of embankment (72 h).

restore to its original state in time after each loading. However, a small plastic strain still remains in the subgrade soil. With the increase in loading times, the residual plastic strain gradually accumulates, and the subgrade soil cannot restore to its original state immediately. When the loading times reach a certain degree, the subgrade soil gradually compacts, and the soil particles become close to each other. Each loading leads to the decrease in the plastic strain of the subgrade soil and gradually tends to be stable.

3.4. Variation Law of the Embankment Safety Factor. The stability of carbonaceous mudstone coarse-grained soil

embankment is measured in terms of safety factor. According to the rules of the safety coefficient of The Highway Roadbed Design Specification (JTG d30-2015), the stability state of the carbonaceous mudstone coarse-grained soil embankment slope used in this study can be divided into three states: stable, unstable, and unstable, as shown in Table 4. The variation law of the safety factor of embankment slope with different grades of carbonaceous mudstone coarse-grained soil under dynamic humidification is shown in Figure 14.

As shown in Figure 14, the safety factors of three graded carbonaceous mudstone coarse-grained soil embankments decrease with the increase in time. During 0–24 h, the embankment safety factor of soil samples 1, 2, and 3

TABLE 4: Classification standard for the safety factor of embankment slope.

Slope condition	Safety factor standard
Steady state	$1.35 \leq F_S$
Unsteady state	$1.00 < F_S < 1.35$
Stability failure	$F_S \leq 1.00$

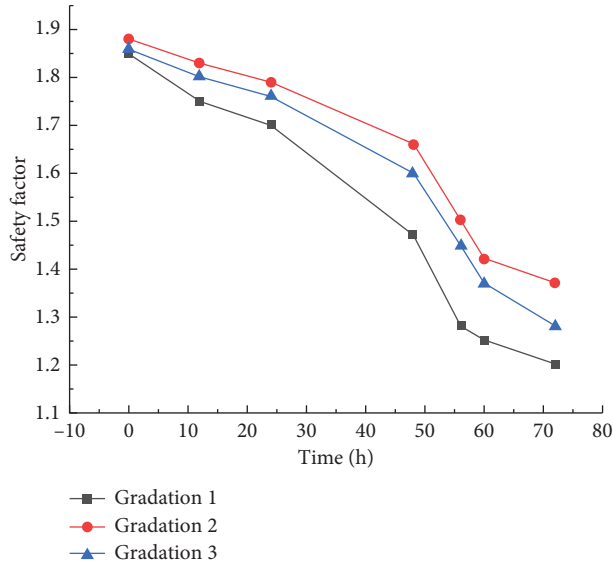


FIGURE 14: Variation law of safety factor.

decreases from 1.88, 1.87, and 1.85 to 1.80, 1.77, and 1.70, respectively. The average decrease in the three soil samples is 0.003, 0.004, and 0.006 per hour, respectively. The embankment safety factor shows a small decline. When the study lasted for 24–72 h, the embankment safety factor of soil samples 1, 2, and 3 decreases to 1.38, 1.28, and 1.20, respectively. The average decrease rate of the three soil samples is 0.01 per hour, and the decrease rate of safety factor increases considerably. When the rainfall lasted for 72 h, the safety factor reaches the lowest value. The safety factor of soil sample 2 is greater than that of other soil samples at the same time, and the safety factor of soil sample 1 is the lowest. In accordance with the above data, the variation law of embankment safety factor shows a trend of slow decrease at first and then rapid decrease during the whole study period.

Slow decreasing stage: in the initial stage of rainfall, the infiltration depth of rainwater on the surface of embankment slope is limited. The effect on the embankment slope of carbonaceous mudstone coarse-grained soil is relatively small, and the number of vehicle loads is minimal. Thus, the safety factor of the embankment slope of carbonaceous mudstone coarse-grained soil has a small downward trend. **Rapid reduction stage:** with the continuous influence of dynamic humidification, the seepage velocity vector of embankment slope gradually increases. The contribution of seepage force to slope stability is gradually obvious, resulting in the rapid decline rate of embankment safety factor.

4. Conclusion

- (1) After the beginning of rainfall, the matric suction near the embankment slope decreases rapidly, the volume moisture content of soil increases rapidly. The wetting front expands from the slope surface to the slope interior, and the negative pore water pressure of gradation 2 decreases rapidly from 120 kPa to 40 kPa within 35–72 h of rainfall, which decreases by 66%. Under the condition of the same rainfall time, the greater the nonuniformity coefficient, the faster the decrease in the pore water pressure of the soil sample at the same monitoring point.
- (2) The smaller the saturated permeability coefficient and saturated water content are, the larger the seepage velocity vector is.
- (3) At the initial loading stage, the carbonaceous mudstone coarse-grained soil subgrade mainly produces recoverable elastic strain that can be recovered after driving. However, a small irrecoverable plastic deformation is still found under the elastic deformation. This deformation gradually accumulates and develops into settlement displacement under the cyclic action of vehicle load. When the settlement displacement reaches a certain position, the gap between the soil particles decreases gradually, causing the subgrade soil to be dense, and the settlement displacement tends to be stable. In the stable stage, the larger the nonuniformity coefficient, the smaller the settlement displacement.
- (4) Under the effect of dynamic humidification, the variation of embankment safety factor in the whole study period shows a trend of slow reduction at first and then rapid reduction. In the slow reduction stage, gradations 1, 2, and 3 decrease by 0.003, 0.004, and 0.006 per hour on average, respectively. In the rapid reduction stage, all the three soil samples decrease by 0.01 per hour on average. On the whole, the safety factor of the soil sample with large nonuniformity coefficient is better than that of the two other graded carbonaceous mudstone coarse-grained soil samples.

Data Availability

The data used to support the finding of this study are available from the corresponding author upon request.

Conflicts of Interest

The authors declare that there are no conflicts of interest regarding the publication of this paper.

Acknowledgments

This research was financially supported by the Open Fund of Guangxi Key Laboratory of Road Structure and Materials

(2020gxjgclkf002) and the National Natural Science Foundation of China (Grant no. 51978084).

References

- [1] T. Guo, "Evaluation of highly thermally mature shale-gas reservoirs in complex structural parts of the Sichuan basin," *Journal of Earth Science*, vol. 24, no. 6, pp. 863–873, 2013.
- [2] L. Zeng, X. Yao, J. Zhang, Q.-F. Gao, J. Chen, and Y. Gui, "Ponded infiltration and spatial-temporal prediction of the water content of silty mudstone," *Bulletin of Engineering Geology and the Environment*, vol. 79, no. 10, pp. 5371–5383, 2020.
- [3] Z. He, Y. Liu, H. Tang, Y. Xing, and H. Bian, "Experimental study on cumulative plastic deformation of coarse-grained soil high-grade roadbed under long-term vehicle load," *Advances in Civil Engineering*, vol. 2018, Article ID 8167205, 8 pages, 2018.
- [4] Z. He and B. Wang, "Instability process model test for bedding rock slope with weak interlayer under different rainfall conditions," *Advances in Civil Engineering*, vol. 2018, Article ID 8201031, 8 pages, 2018.
- [5] X. Q. Wang, W. L. Zou, Y. D. Luo, W.-D. Deng, and Z. Wang, "Influence of compaction degree and gradation on SWCC of compacted clay soil," *Rock and Soil Mechanics*, vol. 32, no. 4, pp. 181–184, 2011.
- [6] H. Rahardjo, T. H. Ong, R. B. Rezaur, and E. C. Leong, "Factors controlling instability of homogeneous soil slopes under rainfall," *Journal of Geotechnical and Geoenvironmental Engineering*, vol. 133, no. 12, pp. 1532–1543, 2007.
- [7] S. Cuomo and M. Della Sala, "Rainfall-induced infiltration, runoff and failure in steep unsaturated shallow soil deposits," *Engineering Geology*, vol. 162, pp. 118–127, 2013.
- [8] Y. Wang, J. Chai, J. Cao, Y. Qin, Z. Xu, and X. Zhang, "Effects of seepage on a three-layered slope and its stability analysis under rainfall conditions," *Natural Hazards*, vol. 102, no. 3, pp. 1269–1278, 2020.
- [9] J.-P. Wang, N. Hu, B. François, and P. Lambert, "Estimating water retention curves and strength properties of unsaturated sandy soils from basic soil gradation parameters," *Water Resources Research*, vol. 53, no. 7, pp. 6069–6088, 2017.
- [10] M. Feng, J. Wu, D. Ma, X. Ni, B. Yu, and Z. Chen, "Experimental investigation on the seepage property of saturated broken red sandstone of continuous gradation," *Bulletin of Engineering Geology and the Environment*, vol. 77, no. 3, pp. 1167–1178, 2018.
- [11] C. F. Chiu, W. M. Yan, and K.-V. Yuen, "Estimation of water retention curve of granular soils from particle-size distribution—a Bayesian probabilistic approach," *Canadian Geotechnical Journal*, vol. 49, no. 9, pp. 1024–1035, 2012.
- [12] F. Meng, J.-s. Zhang, X.-b. Chen, and Q.-y. Wang, "Deformation characteristics of coarse-grained soil with various gradations," *Journal of Central South University*, vol. 21, no. 6, pp. 2469–2476, 2014.
- [13] K. Liu, P. J. Vardon, M. A. Hicks, and P. Arnold, "Combined effect of hysteresis and heterogeneity on the stability of an embankment under transient seepage," *Engineering Geology*, vol. 219, pp. 140–150, 2017.
- [14] M. S. Kim, Y. Onda, T. Uchida, J. K. Kim, and Y. S. Song, "Effect of seepage on shallow landslides in consideration of changes in topography: case study including an experimental sandy slope with artificial rainfall," *Catena*, vol. 161, pp. 50–62, 2018.
- [15] J. Kim, W. Hwang, and Y. Kim, "Effects of hysteresis on hydro-mechanical behavior of unsaturated soil," *Engineering Geology*, vol. 245, pp. 1–9, 2018.
- [16] L. Z. Wu, Y. Zhou, P. Sun, J. S. Shi, G. G. Liu, and L. Y. Bai, "Laboratory characterization of rainfall-induced loess slope failure," *Catena*, vol. 150, pp. 1–8, 2017.
- [17] J. Liu, C. Yang, J. Gan, Y. Liu, L. Wei, and Q. Xie, "Stability analysis of road embankment slope subjected to rainfall considering runoff-unsaturated seepage and unsaturated fluid-solid coupling," *International Journal of Civil Engineering*, vol. 15, no. 6A, pp. 865–876, 2017.
- [18] C. Volz, P.-J. Frank, D. F. Vetsch, W. H. Hager, and R. M. Boes, "Numerical embankment breach modelling including seepage flow effects," *Journal of Hydraulic Research*, vol. 55, no. 4, pp. 480–490, 2017.
- [19] J. Kim, S. Jeong, and R. A. Regueiro, "Instability of partially saturated soil slopes due to alteration of rainfall pattern," *Engineering Geology*, vol. 147–148, pp. 28–36, 2012.
- [20] S. E. Cho, "Probabilistic stability analysis of rainfall-induced landslides considering spatial variability of permeability," *Engineering Geology*, vol. 171, pp. 11–20, 2014.
- [21] T. S. Nguyen and S. Likitlersuang, "Reliability analysis of unsaturated soil slope stability under infiltration considering hydraulic and shear strength parameters," *Bulletin of Engineering Geology and the Environment*, vol. 78, no. 8, pp. 5727–5743, 2019.
- [22] H. Fu, J. Liu, and H. Zha, "Study of the strength of disintegrated carbonaceous mudstone modified with nano- Al_2O_3 and cement," *Journal of Nanoscience and Nanotechnology*, vol. 20, no. 8, pp. 4839–4845, 2020.
- [23] Z.-M. He, D. Xiang, Y.-X. Liu, Q.-F. Gao, and H.-B. Bian, "Deformation behavior of coarse-grained soil as an embankment filler under cyclic loading," *Advances in Civil Engineering*, vol. 2020, Article ID 4629105, 13 pages, 2020.
- [24] M. Kai, Research on hydraulic characteristics of carbon mudstone and postconstruction dynamic deformation properties of embankment, Master's dissertation, vol. 2013, Changsha University of Science and Technology, Changsha, China, 2013.
- [25] Z. A. Erguler and R. Ulusay, "Assessment of physical disintegration characteristics of clay-bearing rocks: disintegration index test and a new durability classification chart," *Engineering Geology*, vol. 105, no. 1–2, pp. 11–19, 2009.
- [26] J. Zhang, F. Li, L. Zeng, J. Peng, and J. Li, "Numerical simulation of the moisture migration of unsaturated clay embankments in southern China considering stress state," *Bulletin of Engineering Geology and the Environment*, vol. 80, no. 1, pp. 11–24, 2021.
- [27] R. Blab and J. T. Harvey, "Modeling measured 3D tire contact stresses in a viscoelastic FE pavement model," *International Journal of Geomechanics*, vol. 2, no. 3, pp. 271–290, 2002.
- [28] L. Sun and T. W. Kennedy, "Spectral analysis and parametric study of stochastic pavement loads," *Journal of Engineering Mechanics*, vol. 128, no. 3, pp. 318–327, 2002.

Research Article

Study of the Failure Mode of a Jointed Rock Mass due to a Stress Wave

Xi Kun Qian ¹ and Cong Cong Li²

¹Investment Project Management Institute of Dongbei University of Finance and Economics, Dalian 116024, China

²Jinan Urban Construction Group, Jinan 250000, China

Correspondence should be addressed to Xi Kun Qian; 451867306@qq.com

Received 28 April 2021; Accepted 6 July 2021; Published 16 July 2021

Academic Editor: Chunyang Zhang

Copyright © 2021 Xi Kun Qian and Cong Cong Li. This is an open access article distributed under the Creative Commons Attribution License, which permits unrestricted use, distribution, and reproduction in any medium, provided the original work is properly cited.

The mechanical response and failure process of a jointed rock mass subjected to dynamic loading is very important for the safety and stability of rock engineering projects. In this study, we use RFPA2D-Dynamic, a rock dynamic failure process analysis platform, to establish a two-dimensional impact model of a jointed rock mass to analyze the mechanism of crack propagation in a jointed rock mass with preexisting cracks under dynamic loading. We discuss the influence of the stress wavelength and precrack inclination on the dynamic failure process and mode of the rock mass and compare this failure process with the failure model under static loading. The results show that the dynamic failure process and crack initiation type of a jointed rock mass are closely related to the stress wavelength. For a given peak, as the stress wavelength increases, the failure mode changes from local cracking that occurs above the precracks to a global instability caused by wing cracks. Meanwhile, as the wavelength increases, the shear cracks and mixed tensile-shear cracks generated at the two ends of the precracks are replaced by tensile cracks. The precrack inclination on a jointed rock mass mainly affects the strength of the jointed rock mass and the final failure mode. Specifically, when the joint inclination is small, the rock mass is severely damaged in the region above the precracks because the stress wave forms a region of cracks with a concentrated distribution. As the joint inclination increases, the damaged region becomes larger while the rock mass is less prone to failure; the strength of the rock mass gradually increases, and the wing cracks produced at the two ends of precracks propagate toward the upper and lower ends of the rock mass. However, when the stress wavelength is small, the precracks of different inclinations form cracks in the region above the precracks with a length similar to the precracks. For this condition, the propagation of the cracks is mainly controlled by the stress wavelength, while the influence of the inclination of the precracks is not significant. There is a significant difference between the failure modes of a rock specimen under dynamic loading or static loading because the stress wave produces a reflected tension wave in the direction parallel to the wave attack of the joint plane, which leads to spalling, while the wing cracks are more likely to occur under static loading.

1. Introduction

Because the jointed rock mass is a type of nonhomogeneous material, its failure process not only relies on the stress wavelength but is also related to the distribution of its internal joints [1, 2]. Therefore, studying the patterns of crack propagation of a jointed rock mass with different wavelengths and precrack inclinations has both theoretical significance and engineering value.

Rock masses are generally characterized by discontinuities such as fractures, joints, pores, and other original

defects that influence their mechanical properties and fracture behavior of rocks in the stability assessments of rock engineering. The failure of rock masses is usually associated with fractures propagation along preexisting flaw, because it often induces the initiation of cracking [3–8]. Moreover, it is well known that the loading rate also plays a crucial important role in the mechanical properties during the dynamic failure processes [9–12]. Therefore, a systematic study of the mechanisms of crack initiation and propagation processes in rock masses under dynamic loading condition promises benefit in many areas from

rock mechanics to mining engineering and earth quake prediction.

In recent decades, many laboratory experimental and numerical investigations have been well conducted to study crack initiation, propagation, and coalescence in rock and rock-like materials under static loading. For instance, papers [13–15] investigated the strength and cracking behaviors of rock and rock-like material containing single or multiple preexisting flaws under static loading condition. With regard to the dynamic investigations, they are extensively researched to study the dynamic mechanical properties of intact rock specimens under dynamic loading [16–23]. However, not so well understood is the dynamic failure process, which is closely related to crack behavior in terms of initiation, propagation and coalescence of cracks when the rock specimen is undertook different loading conditions. There have been few studies researching dynamic crack behaviors in rock specimen under different loading ratios [24–27]. For instance, Yang et al. [26] studied the mechanism of crack branching and curving in rock-like material under dynamic biaxial. They found that the loading ratio, crack dip angle, and material heterogeneity play a significant role in crack curving and branching. The loading ration, which is the load in horizontal and vertical direction, controls the crack curving. The crack dip angle and heterogeneity of the material are the decisive factor on the tensile properties and failure patterns of heterogeneity material with internal defects. Li and Wong [28] researched the crack initiation and propagation from preexisting flaw specimens under different loading conditions. The results indicate that different loading condition would produce different resultant crack types, crack initiation sequences, and crack pattern. Tensile cracks would tend to initiate prior to shear cracks under a relatively low loading rate. Meanwhile, the effect of flaw dip angle on the dynamic failure processes is also investigated by some researchers. Several researchers hold the view that the flaw dip angle has a limited influence on the crack propagation modes [29–33]. For instance, Li et al. [32] conducted dynamic loading tests using a modified split-Hopkinson pressure bar device to study the effects of preexisting flaws with different flaw angles and lengths on the dynamic failure processes. They have found that the geometry of the flaws appears to have a slight effect on failure patterns of flawed specimens. Zou et al. [30] revealed the effect of the flaw dip angle on crack trajectories during the dynamic failure processes by the SHPB. According to the experimental results, the effect of the flaw dip angle on the development of macrocracks is very limited under impact loadings. However, other researchers thought that there are significant influences of the flaw dip angle on the crack behaviors [27, 34–36]. Li et al. [37] numerically investigated the failure process of intermittent jointed rock mass subjected to dynamic loading. The failure characteristics of intermittent jointed rock mass with different flaw dip angles are simulated. The numerical results imply that the failure process is closely related to the dip angle of flaw. With the increase of the flaw dip angle, the damage range expands and the rock mass is more difficult to initiate new cracks. Besides, the fracture effect of rock mass with a flaw

dip angle of 45° – 60° is the best. In view of these arguments, further study of the effect of the flaw dip angle on the dynamic process in flawed specimen under a wide range of loading rates is essential to illuminate the relationship of these two factors. In addition, the similarities and differences of the crack propagation patterns on the specimen containing a preexisting flaw subjected to static and dynamic loading conditions have been summarized by several researchers [29, 31, 37, 38], whereas difference of the crack propagation patterns under static and dynamic loading conditions still needs more detailed research.

In this study, we select the dynamic analysis system of RFPA dynamic to conduct numerical experiments on the dynamic characteristics of a jointed rock mass and investigate the influence of the stress wavelength and joint inclination on the dynamic failure of a rock mass as well as the difference in the failure modes of a jointed rock mass with different preset inclinations under dynamic loading and static loading. We also discuss in depth the relationship between the influence of the stress wavelength on the type of initiation cracks and the influence of the wavelength and inclination on the mode of crack propagation, thus providing a reference for the design of relevant rock mass engineering projects.

2. Verification of the Numerical Method and Model Setup

2.1. Verification of the Numerical Method. The RFPA-dynamic analytical system used in this study can simulate the cracking process of a brittle nonhomogeneous material such as rock under dynamic loading. Details about the RFPA-dynamic software can be found in the literature [26, 39].

To ensure the accuracy and comparability of simulation results, we first verify the accuracy of numerical simulation results comparing them with results from a physical experiment in the literature [31]. The experiment utilized a horizontal impact test platform with a split Hopkinson pressure bar (SHPB) with a diameter of 50 mm to evaluate a brittle, rock-like material. The macroscopic modulus of elasticity, uniaxial compressive strength, and Poisson's ratio of the specimen were 4.5 GPa, 25.5 MPa, and 0.2, respectively. Figure 1 compares the results from the numerical simulation and physical experiment of the precracked specimen with the SHPB. We can see that the numerical simulation satisfactorily reproduces the crack propagation mode of the rock specimen under an impact load and reveals an "X"-type final failure mode, which is consistent with the experimental result.

To validate the feasibility of the numerical method on simulating the stress wave propagation characteristics, the SHPB test on limestone by Frew et al. [40] is selected. The geometric and material parameters of the SHPB model are consistent with those in the literature. The length of impact bar, incident bar, transmission bar, and rock sample is 152 mm, 2130 mm, 915 mm, and 12.5 mm, respectively, and the diameter is 12.5 mm. The schematic diagram of the model is shown in Figure 2. To maximize computational efficiency based on guaranteed accuracy, the element size is

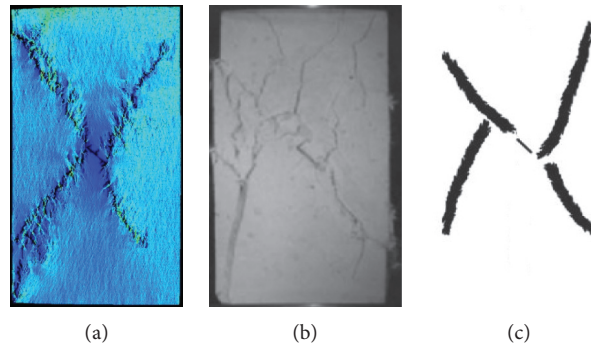


FIGURE 1: Comparison of numerical and experimental rock failure modes for SHPB.

selected as 0.5 mm according to the findings by Liao et al. [41]. Meanwhile, the impact bar, incident bar, and transmission bar are homogeneous materials, and the rock homogeneity coefficient is 4. In addition, the right boundary of the transmission bar is set with artificial absorption boundary to eliminate the influence of the reflected stress wave on the monitoring results. The monitoring points are located on the incident bar and the transmission bar, respectively, which is consistent with the literature. The mechanical parameters of rock and bar are shown in Table 1.

Through comparison between the reflected wave histories measured by Frew and the simulation results, as shown in Figure 3, good agreement can be found. It is found that the waveforms of incident wave, reflected wave, and transmitted wave obtained by numerical simulation and experiment are in good agreement. However, the stress waves in the simulated test are slightly greater than that in the laboratory experiment. This is because the impact process is ideal in the simulation, which ignores the roughness at the impact interface between the rock specimen and bars. The results indicate that the RFPA can simulate the stress wave propagation in dynamic loading process. Therefore, in the present study, this numerical code, which is able to simulate the responses of rock subjected to dynamic loading, is used.

2.2. Model Setup. The computational model employed in this study is shown in Figure 4. The size of the model is 50×100 mm, and the number of elements is $200 \times 400 = 80,000$. The computational model does not consider the influence of damping for the time being. A plane stress condition is assumed in the model, and all boundaries of the numerical rock samples are set as the free boundary, except the bottom one, which is set as viscoelastic absorption boundary. The specimen is fixed at the lower surface and subjected to a triangular compressive stress wave σ at the upper surface.

According to the modulus of elasticity and density of rock materials, we can calculate the propagation velocity of a one-dimensional longitudinal wave as 3,798 m/s. To study the influence of different stress wavelengths and peaks on the failure mode of the specimen, we apply the stress waves shown in Figure 5 to the numerical model. In Figure 5, the peaks of the stress waves I to IV are all 20 MPa, and the

wavelengths λ of the applied compressive stress waves I to IV are 7.6, 37.98, 75.96, and 189.9 mm, respectively. The time step size Δt is set to be $0.1 \mu\text{s}$ in the calculation. To fully consider the propagation and action time of the stress wave inside the rock mass, the time t needed for a specimen to end its dynamic response is $70 \mu\text{s}$ in the calculation.

To study the influence of the precrack inclination on the failure mode of the specimen, we set the precrack to be an unfilled pore element, which is located in the middle of a specimen. To reduce the influence of the precrack size, we set the precrack to be 15 mm long and 0.5 mm wide. The crack inclination α is 0° , 15° , 30° , 45° , 60° , 75° , or 90° .

The matrix elements in the model of this study have an average compressive strength of 205 MPa, average modulus of elasticity of 37.5 GPa, degree of homogeneity of 3, density of $2,600 \text{ kg/m}^3$, friction angle of 50° , Poisson's ratio of 0.25, compression-tension strength ratio of 10, damping factor of 0 (i.e., the influence of damping is not considered), and time step of $0.1 \mu\text{s}$. The model has a free boundary, and a plane stress analysis is adopted.

3. Analysis of the Calculated Results

3.1. Influence of the Stress Wavelength on the Failure Process of a Rock Mass. Herein we use the example of $\alpha = 45^\circ$ and the peak of the stress wave is 20 MPa to discuss in detail the influence of the stress wavelength on the pattern of precrack propagation.

Figure 6(a) shows the distribution of the maximum shear stresses during the failure process of the rock mass specimen with precracks under stress wave I ($\lambda = 7.6$ mm). We can see from the simulation plot the whole process of the stress wave propagating at a certain velocity from the upper end to the lower end of the specimen. The color brightness of the elements in the figure reflects the relative magnitude of the elemental shear stress; a brighter position means a larger maximum shear stress at that location. The influence of the reflection on the two side boundaries of the rock specimen is considered. As the stress wave propagates downward, the stress waves are reflected and superposed on the side boundaries and act jointly with the applied compressive stress wave on the rock specimen. The propagation of the stress wave is accompanied by the failure of elements, which also changes the distribution of the stress field. When the

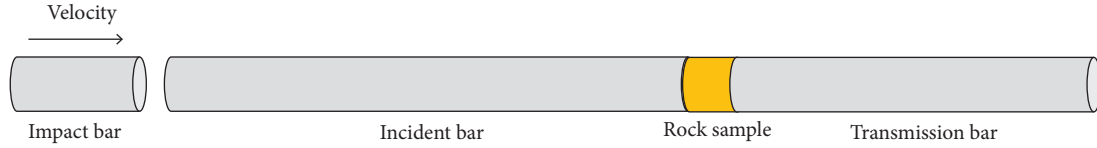


FIGURE 2: Schematic diagram of SHPB numerical model.

TABLE 1: The material properties of SHPB tests.

	E (GPa)	ν	σ (MPa)	ρ (kg/m ³)
Rock sample	24	0.23	67	2650
SHPB bar	200	0.28	2500	8100

stress wave propagates to the crack tip, a stress concentration occurs in the local zone, which causes a damaged and failing element to appear. As the stress wave continues to propagate, the number of damaged elements at the crack tip gradually increases, and the damaged elements coalesce to form wing cracks that are perpendicular to the precrack. In addition, the presence of joints changes the propagation path of the stress wave, and the stress wave is reflected at the crack, which causes the compressive stress wave to become a tensile stress wave and leads to a spalling failure above the precrack plane. Meanwhile, the cracks undergo close contact under a compressive stress wave when the stress wave transmission occurs at the crack. As the stress wave continues to propagate downward, the tension-damaged elements gradually appear in the region parallel to and above the precrack. They develop into fine cracks and finally coalesce to form a macroscopic crack, which is parallel to and has a similar length of the precrack, indicating that the failure mode of a rock mass is closely related to the existing joint cracks inside the rock mass.

From the diagram of the maximum shear stress distribution shown in Figure 6(b), we can clearly see the failure process and stress distribution of the rock specimen when its upper surface is subjected to stress wave II ($\lambda = 37.98$ mm). Due to the difference of the stress wavelength, the initiation and propagation of cracks in the rock specimen are different from those of the specimen under stress wave I ($\lambda = 7.6$ mm):

- (1) The stress waves reflected on the two sides of the specimen are superposed in the middle of the upper end of the specimen, causing a failure in the middle of the specimen top end. As the stress wave propagates downward, the superposition position of the stress waves continuously moves downward, and the damaged elements gradually coalesce to form a macroscopic crack, which appears almost simultaneously as the wing crack perpendicular to the tip of the precrack, as shown in Figure 6(b). As the energy of the stress wave continuously attenuates during the propagation process, the intensity of the tensile stress wave that is reflected and superposed on the two sides gradually decreases, and the crack at the upper end of specimen develops to a certain extent and then stops.

- (2) The wing crack perpendicular to the precrack tip appears; the densely distributed short and small cracks appear in the region parallel to and above the precrack, and they gradually coalesce to form a local fractured region.
- (3) A macroscopic wing crack perpendicular to the lower end of the precrack is formed at the lower end of the crack. When a wing crack develops to a certain length, its direction gradually aligns itself with the direction of the external loading. When the stress wave propagates to the lower end of the specimen, it is reflected and refracted, which leads to failure of the new elements at the lower end of the specimen gradually developing into fine cracks. As the reflected stress wave propagates upward, the cracks at the lower end of specimen develop upward, and, therefore, a concentrated failure zone appears at the lower end of the specimen.

When stress wave III ($\lambda = 75.96$ mm) is applied to the upper surface of the rock specimen, the distribution of the maximum shear stress, as shown in Figure 6(c), shows that the crack propagation of the rock mass is similar but different than that under stress wave II ($\lambda = 37.98$ mm). The crack in the upper end of the specimen produced by the tensile stress wave reflected by the two sides of the specimen is longer, as shown in Figure 6(c). The wing crack perpendicular to the tip of the precrack continuously develops and propagates with the stress wave in the rock specimen and gradually connects with the crack in the upper end of the specimen. Meanwhile, the wing crack generated at the lower end of the precrack continuously develops downward, with its direction gradually aligning with the direction of the external loading, and it gradually connects to the fractured region produced by the tensile stress wave reflected at the lower end of the specimen. The wing crack eventually coalesces to form two macroscopic cracks through the upper and lower ends of the specimen.

When the stress wavelength continues to increase to a certain level ($\lambda = 189.9$ mm), as shown in Figure 6(d), the final failure mode of the specimen is similar to that under static loading. A wing crack perpendicular to the precrack is gradually produced at the upper and lower ends of the precrack, and it gradually propagates to the upper and lower

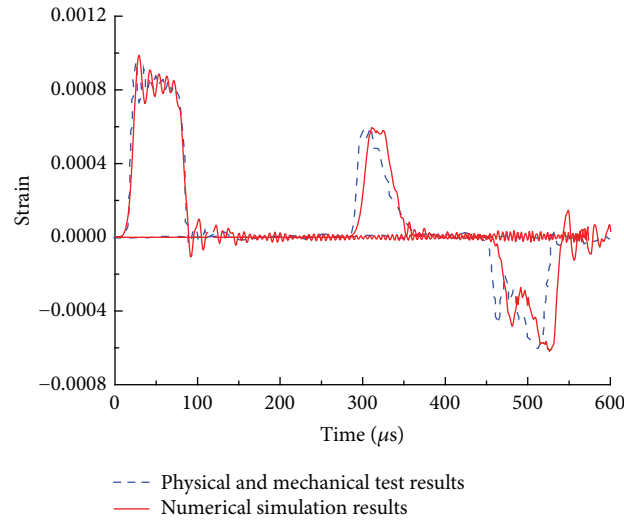


FIGURE 3: Comparison of numerical and experimental stress wave waveforms for SHPB impact test.

ends of the specimen. The development direction of the wing crack gradually aligns itself with the direction of the external loading and eventually forms two macroscopic cracks.

The maximum shear stress diagram in Figure 6 clearly shows the influence of the stress wavelength on the crack propagation and failure mode of the rock mass. As shown in Figure 6(a), when the stress wavelength is short ($\lambda = 7.6$ mm), a new crack is initiated parallel to and above the precrack, and its length is similar to that of the precrack. As the stress wavelength continues to increase, the wing cracks perpendicular to the precrack appear at the upper and lower ends of the precrack, and they expand and coalesce toward the upper and lower ends of the rock specimen. When the stress wavelength increases to a certain length, the final failure mode of the specimen is similar to that under static loading.

3.2. Failure Process of the Rock Mass with Different Precrack Inclinations. To study the influence of different inclinations of the precrack on the crack propagation and failure process of rock mass, we apply stress wave II to the upper surface of the fractured rock mass with precrack inclinations α of 0° , 15° , 30° , 45° , 60° , 75° , and 90° .

We use three failure mode types corresponding to 0° , 30° , and 75° for a detailed discussion. Different inclinations of the precrack change the propagation direction of the stress wave, thus leading to different crack propagation modes. The diagram of the maximum shear stress for the failure process of the rock specimen with a precrack inclination $\alpha = 0^\circ$ is shown in Figure 7. As the stress wave propagates inside the rock mass, the tensile stress wave and the subsequent stress wave reflected by the precrack plane are superposed in the upper part of the precrack plane, forming a tensile failure zone, and the damaged elements gradually increase to form macroscopic cracks. The newly generated macroscopic cracks are approximately parallel to the precrack plane and distributed in layers from near to far relative to the precrack plane and their lengths are similar to that of the precrack. In

particular, the two ends of the new cracks closest to the precrack plane gradually connect to the two ends of the precrack and form a closed failure zone. Meanwhile, the failure of the rock mass below the precrack plane is initiated by gradual generation of a macroscopic crack nearly perpendicular to the surface of the precrack and from the middle of the precrack, which extends downward as the stress wave propagates in the rock mass. When α is 30° , the new cracks above the precrack are parallel to the precrack and approximately distributed in layers. The initiation direction of the new cracks under the precrack plane is perpendicular to the precrack, and the initiation position of the cracks gradually moves from the middle to the bottom of the precrack. As the inclination of the precrack continues to increase, the wing cracks perpendicular to the precrack are generated at the two tips of the precrack, and they gradually propagate toward the upper and lower ends of the rock specimen with the propagation of the stress wave. When the inclination of the precrack is 75° , the development of new cracks at the upper tip of the precrack is not significant, while the direction of new cracks at the lower tip of the precrack is nearly aligned with the direction of the external loading, as shown in Figure 7(c).

In this study, we also conduct a numerical simulation on the rock specimen with the precrack inclination of 15° , 45° , 60° , and 90° . The propagation mode of cracks with $\alpha = 15^\circ$ is similar to that with $\alpha = 0^\circ$ (Figure 7(a)). When the inclination of the precrack is 45° or 60° , the propagation of the wing crack at the lower end of the precrack initially exhibits a step-like zigzag, and then it tends to develop downward in the loading direction. Wing cracks perpendicular to the precrack are generated at the precrack tip and, as the precrack inclination gradually increases, the propagation direction of the wing cracks gradually inclines toward the top of the rock mass. When the precrack inclination α is 90° , the incident direction of the stress wave is parallel to the precrack, and the new cracks in the lower end of the precrack propagate along the existing precrack, while there is no obvious crack generated above the precrack. Figure 8 shows a diagram of

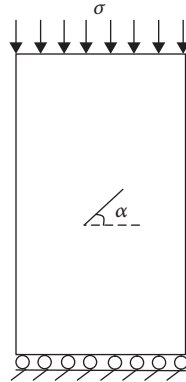


FIGURE 4: Geometrical parameters and loading conditions of rock specimen.

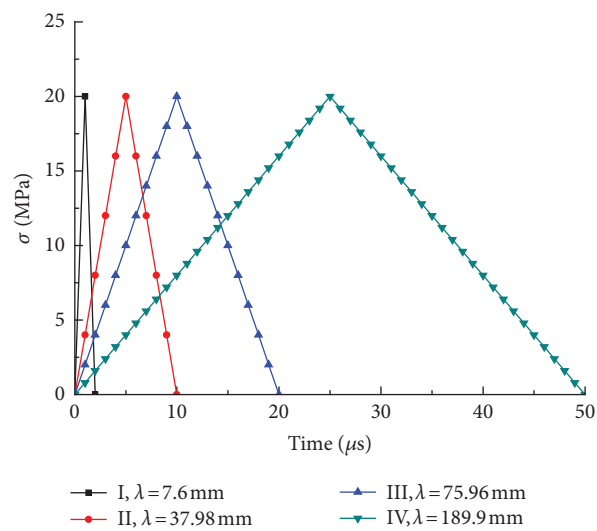


FIGURE 5: Stress waves applied on the rock specimen.

the final failure shear stress at $t = 30 \mu\text{s}$ for different inclinations. When $\alpha = 0^\circ$, cracks in the rock mass develop most significantly, which leads to the most severe failure. As the precrack inclination gradually increases, the degree of the rock mass failure also decreases, which indicates that the precrack inclination has an important influence on the response of the rock mass to dynamic loading.

3.3. Comparative Analysis of Failure Modes under Dynamic Loading and Static Loading. To compare the initiation, propagation, and coalescence process of cracks under both dynamic loading and static loading and to reveal the corresponding differences in failure modes of the specimens with precracks, we obtain through simulation the failure modes of rock specimens with different precrack inclinations under static loading, as shown in Figure 9. A displacement-controlled static loading rate of 0.003 mm/step is adopted.

We can see from Figure 9 that, under static loading, the cracks are initially closed under pressure, and the stress concentration occurs simultaneously at the two ends of the

crack. When the precrack inclination $\alpha = 0^\circ$, as the load increases, the failure occurs in the middle of the precrack and gradually develops upward and downward, eventually forming two macroscopic cracks aligned with the direction of the loading. As the precrack inclination gradually increases, new cracks are always initiated at the precrack tip and eventually form two macroscopic cracks through the upper and lower ends of the specimen. Through a comprehensive comparison, we obtain the following patterns:

- (1) The propagation mode of cracks under a relatively long stress wavelength is close to that under static loading.
- (2) The stress wave generates a reflected tension wave in the direction parallel to the wave attack of the joint plane, which leads to spalling, while wing cracks are more likely to occur under static loading.
- (3) The morphology of crack propagation under static loading has a symmetric distribution. Unlike static loading, the stress wave generates an asymmetric failure at the upper and lower ends of the specimen as well as above and below the cracks. Due to the

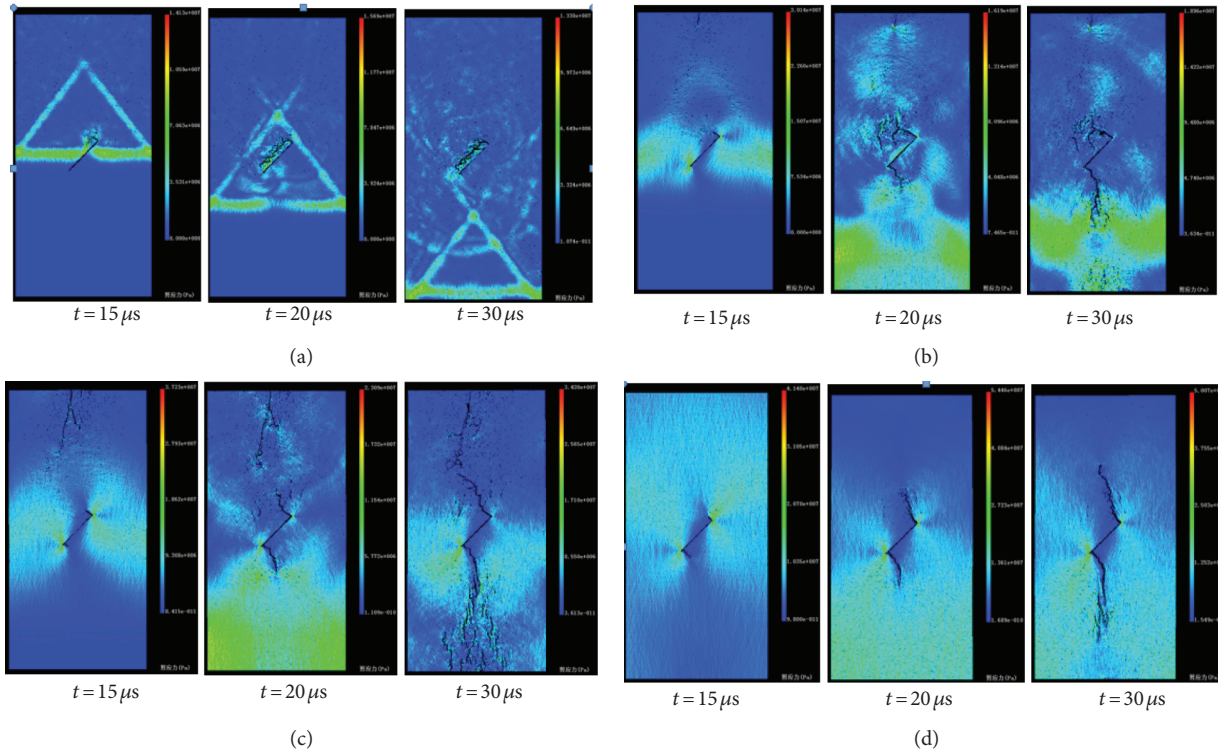


FIGURE 6: Failure process of flawed rock specimen with $\alpha = 45^\circ$ when subjected to stress wave from I to IV. (a) Failure process of flawed rock specimen with $\alpha = 45^\circ$ when subjected to stress wave I. (b) Failure process of flawed rock specimen with $\alpha = 45^\circ$ when subjected to stress wave II. (c) Failure process of flawed rock specimen with $\alpha = 45^\circ$ when subjected to stress wave III. (d) Failure process of flawed rock specimen with $\alpha = 45^\circ$ when subjected to stress wave IV.

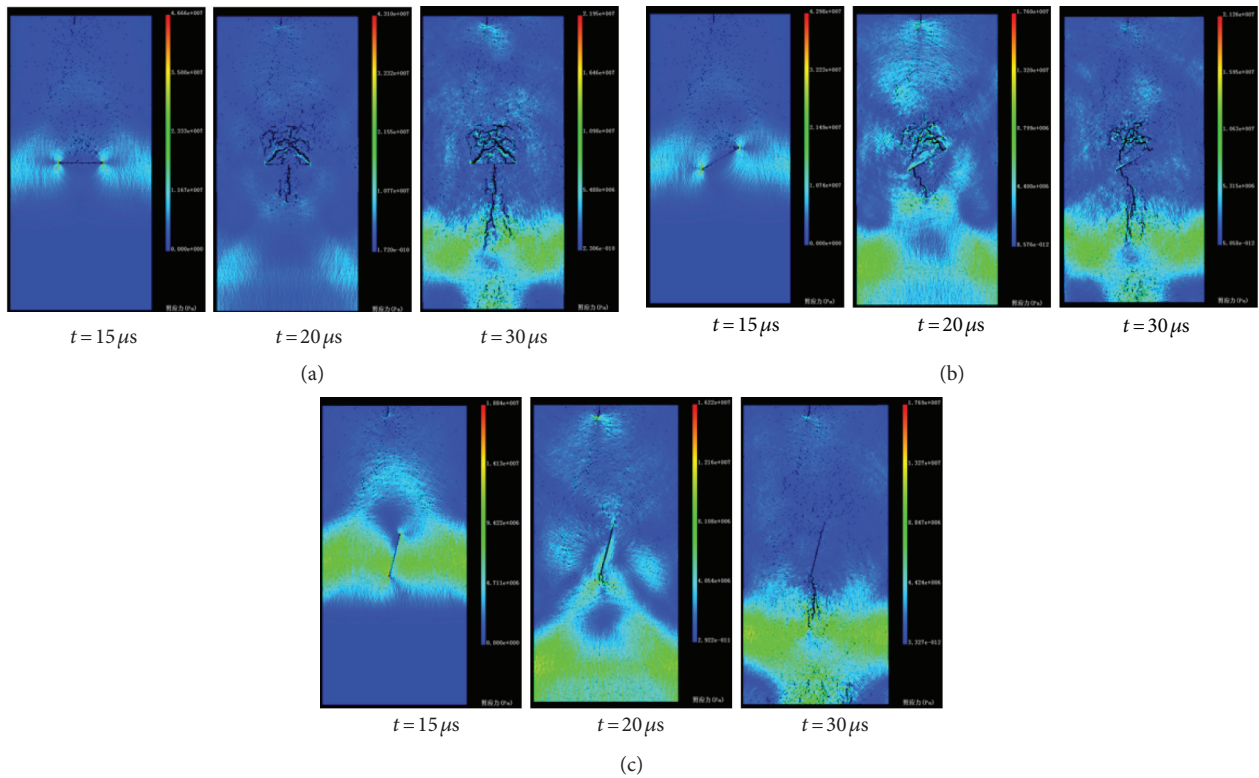


FIGURE 7: Failure process of rock specimen with different angle preexisting crack. (a) Failure process of flawed rock specimen with $\alpha = 0^\circ$ when subjected to stress wave II. (b) Failure process of flawed rock specimen with $\alpha = 30^\circ$ when subjected to stress wave II. (c) Failure process of flawed rock specimen with $\alpha = 75^\circ$ when subjected to stress wave II.

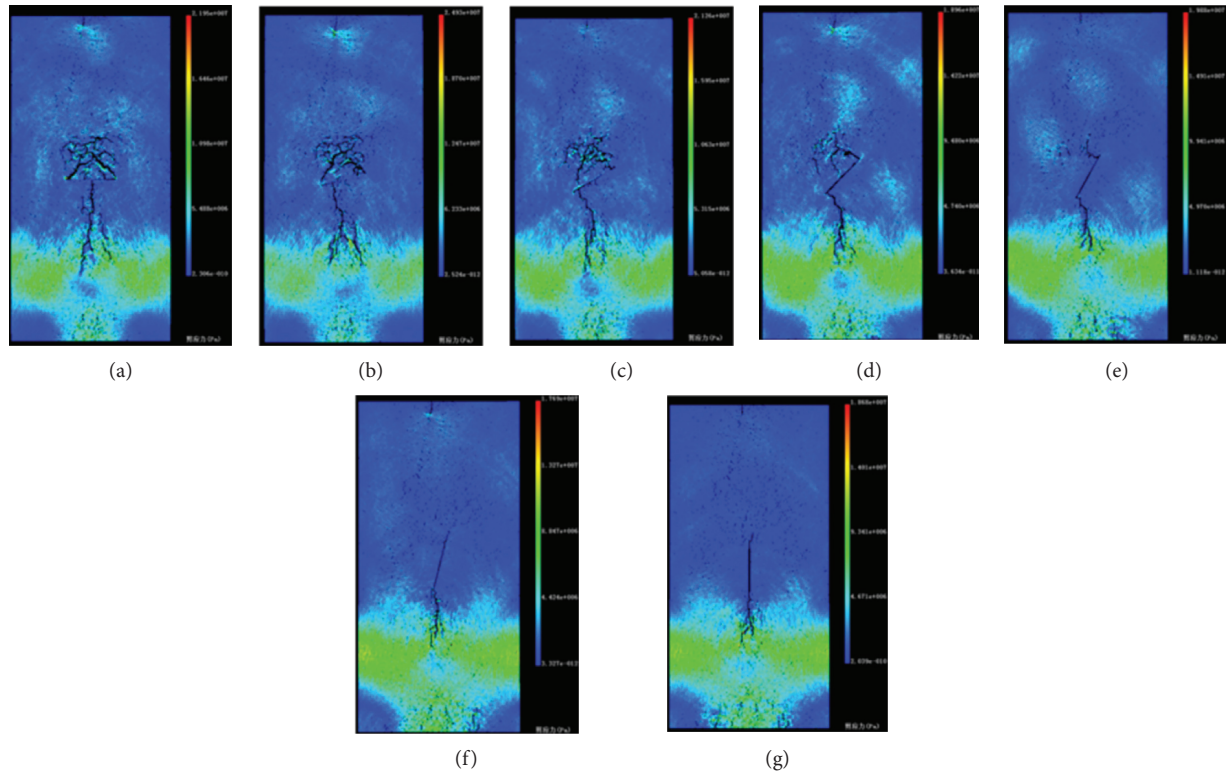


FIGURE 8: Failure patterns of rock specimens with different inclination angles of preexisting cracks when subjected to stress wave II. (a) $\alpha = 0^\circ$. (b) $\alpha = 15^\circ$. (c) $\alpha = 30^\circ$. (d) $\alpha = 45^\circ$. (e) $\alpha = 60^\circ$. (f) $\alpha = 75^\circ$. (g) $\alpha = 90^\circ$.

shielding effect of cracks, the stress wave is attenuated after passing through the cracks, which leads to changes in the propagation mode above and below the precrack.

- (4) Relative to static loading, the cracked rock mass under dynamic loading exhibits a stress field with a complicated distribution. Due to the shielding effect of cracks and the reflection effect of the boundaries, the stress waves inside the specimen under a dynamic loading undergo complicated interactions and thus exhibit a complicated distribution of the stress field.
- (5) The influence of the crack inclination on the dynamic and static strengths of a rock mass is also different. When the crack inclination varies in the range of 0° – 90° , the static strength of the specimen exhibits a U-shaped decrease-increase distribution curve. Under dynamic loading, as the inclination increases, the contact area between the stress wave and the crack inclination decreases and more energy is applied to the specimen, and, therefore, the rock mass strength monotonically increases.

4. Discussion

4.1. Influence of the Stress Wavelength on the Type of Cracks. The cracks produced around the precrack in the rock specimen under dynamic loading have different types of generated cracks for different wavelengths. Figure 10 shows the propagation modes of cracks in the rock

specimen under four different stress wavelengths. In reference to the crack type definition in Figure 11, we discuss the influence of different wavelengths on the type of generated cracks. When the rock mass is subjected to stress wave I, a large number of damaged elements appear parallel to and above the precrack plane in the region above the precrack, and the elements gradually coalesce to cause a spalling failure with a length similar to that of the precrack. When stress wave II acts on the cracked specimen, significant shear cracks are generated in the upper end of the precrack. As the wavelength increases, the crack type in the upper end of the precrack gradually evolves from a shear crack to a mixed tension-shear crack, and when stress wave IV is applied, the crack type completely evolves to a tensile crack. In the lower end of the precrack, different types of cracks also appear as the wavelength varies. Due to the reflection and attenuation of the stress wave, when only subjected to the stress wave II, a tensile crack occurs in the upper end of the precrack. Numerical simulation results reveal that, in combination with a long wavelength, the tensile crack is the main type of crack that appears around the precrack; as the wavelength decreases, the type of cracks gradually changes from tensile cracks to mixed tensile-shear cracks and then to shear cracks, which eventually leads to fracturing of the local region. Meanwhile, even if subjected to the same stress wave, due to the difference in positions, different types of cracks appear at the two ends of the precrack. Therefore, the stress wavelength and the relative position of the precrack

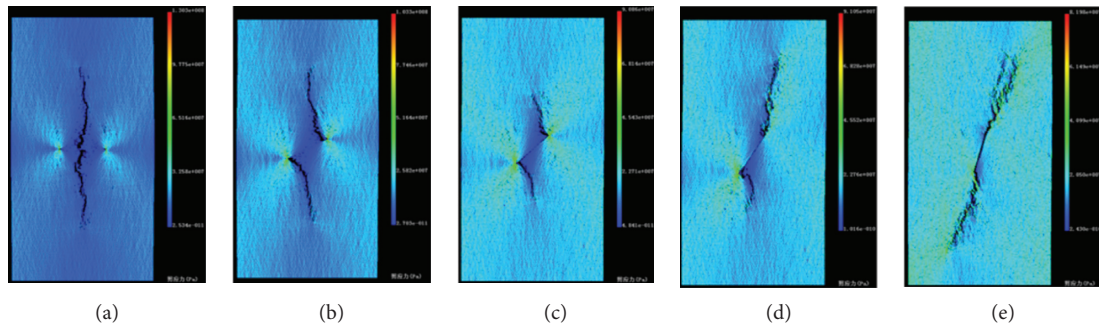


FIGURE 9: Failure patterns of rock specimens with different inclination angles of preexisting cracks under static loading. (a) $\alpha = 0^\circ$. (b) $\alpha = 30^\circ$. (c) $\alpha = 45^\circ$. (d) $\alpha = 60^\circ$. (e) $\alpha = 75^\circ$.

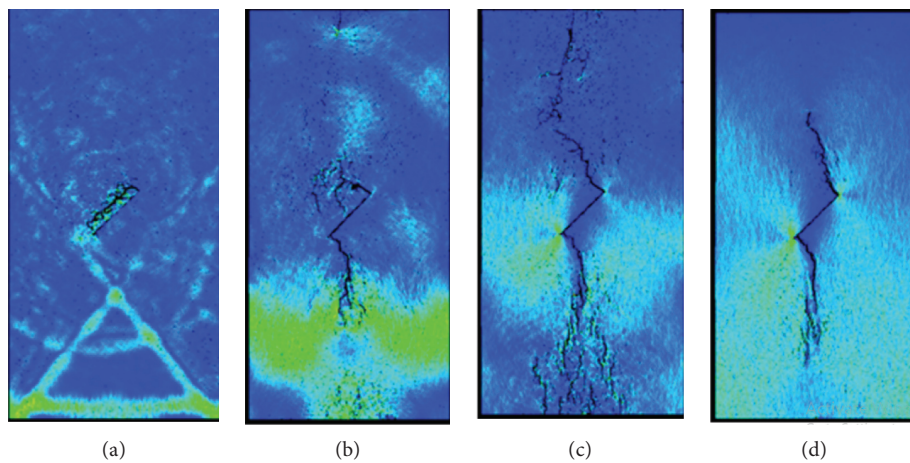


FIGURE 10: Failure patterns of rock specimen crack when subjected to stress wave from I to IV. (a) $\lambda = 7.6$ mm. (b) $\lambda = 37.98$ mm. (c) $\lambda = 75.96$ mm. (d) $\lambda = 189.9$ mm.

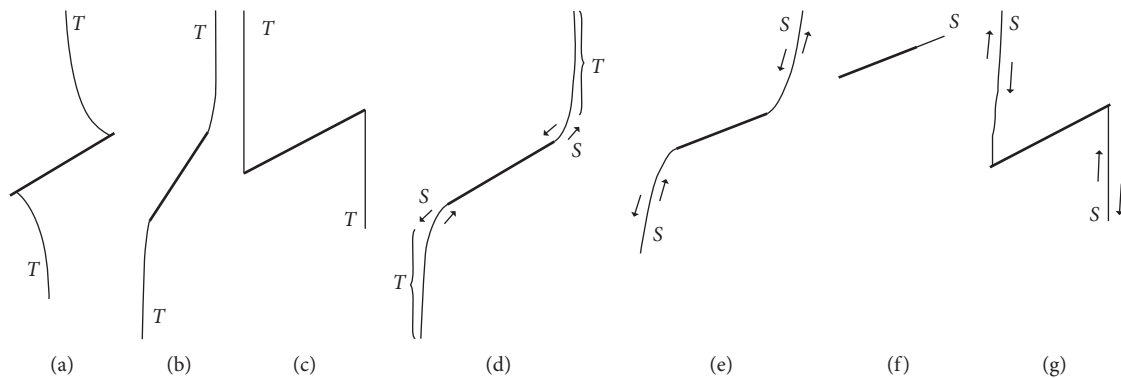


FIGURE 11: Various crack types initiated from the preexisting flaws identified [42]. *T*—tensile cracks. *S*—shear cracks. (a) Type 1 tensile crack (tensile wing crack). (b) Type 2 tensile crack. (c) Type 3 tensile crack. (d) Mixed tensile-shear crack. (e) Type 1 shear crack. (f) Type 2 shear crack. (g) Type 3 shear crack.

jointly determine the type of cracks that dominate specimen failure.

4.2. Influence of the Stress Wavelength and Pre-crack Inclination on the Propagation of Cracks in a Rock Mass. On the basis of previous studies, to illustrate the influence of the

stress wavelength and pre-crack inclination on the crack propagation mode of a rock mass, we simulate the failure process of rock specimens with pre-cracks for different inclinations under stress wave I as a supplemental study. Figure 12 shows a diagram of the shear stress at time $t = 20 \mu\text{s}$ for the rock specimen with pre-crack inclinations of 0° , 30° , and 60° under stress wave I. Although different from those

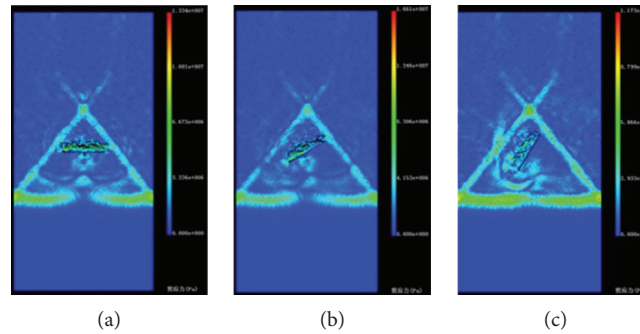


FIGURE 12: Failure process of rock specimen with different preexisting crack inclination angle when subjected to stress wave I. (a) $\alpha = 0^\circ$. (b) $\alpha = 30^\circ$. (c) $\alpha = 60^\circ$.

under stress wave II, the propagation modes of cracks in a rock mass under stress wave I are almost identical for the different precrack inclinations. As the stress wave propagates in the rock mass, the damaged elements appear parallel to and above the precrack plane and gradually coalesce to form a spalling failure with a length similar to that of the precrack. The failure mode of rocks is not significantly affected by the precrack inclination, and the level of failure gradually decreases as the precrack inclination increases. That is, when the stress wave applied above the rock specimen has a relatively short wavelength, the propagation of cracks is mainly controlled by the stress wavelength and is not significantly influenced by the precrack inclination.

5. Conclusions

- (1) The stress wavelength has a relatively large influence on the crack propagation and failure mode of a rock specimen. When the stress wavelength is short, the length of new cracks initiated parallel to and above the precrack is similar to that of the precrack. As the stress wavelength gradually increases, the wing cracks produced at the two ends of the precrack change from shear cracks to mixed tensile-shear cracks to tensile cracks. The failure mode changes from local failure to global instability. When the stress wavelength increases to a certain level, the failure mode of the rock specimen is rather close to that under static loading.
- (2) The morphology of the spatial distribution of joints has an important influence on the failure mode of a rock mass. The smaller the precrack inclination is, the larger the failure zone that occurs in the upper part of the cracks because the stress wave is reflected by the precrack and wing cracks appear at the lower end of the cracks. As the precrack inclination increases, the wing cracks perpendicular to the precrack are formed at the upper and lower tips of the precrack, and the propagation of cracks at the lower tip is more significant. As the inclination increases and the propagation of the stress wave is parallel to the crack surface, the rock mass is less vulnerable to failure. Otherwise, when the direction of the stress

wave is perpendicular to the crack plane, the rock mass is more vulnerable to failure.

- (3) Under dynamic loading and static loading, there is a significant difference in the failure modes of a rock specimen. The stress wave produces a reflected tension wave in the direction parallel to the wave attack of the joint plane, which leads to spalling, while the wing cracks are more likely to occur under static loading. The morphology of crack propagation under static loading is symmetrically distributed, while the stress wave leads to asymmetric failure at the upper and lower ends of the specimen as well as above and below the cracks.
- (4) Under a certain peak condition, when the shear wavelength is relatively short, the propagation of cracks is mainly controlled by the wavelength, and the precrack inclination has a relatively small influence on the propagation of cracks.

Data Availability

The data used to support the findings of this study are available from the corresponding author upon request.

Conflicts of Interest

The authors declare that they have no conflicts of interest regarding this paper.

Acknowledgments

This work was supported by the National Natural Science Foundation of China (grant nos. 51779031 and 51678170).

References

- [1] C. Y. Zhang, Y. X. Wang, and T. T. Jiang, "The propagation mechanism of an oblique straight crack in a rock sample and the effect of osmotic pressure under in-plane biaxial compression," *Arabian Journal of Geosciences*, vol. 13, no. 15, pp. 1–16, 2020.
- [2] X. S. Li, Z. F. Liu, and S. Yang, "Similar physical modeling of roof stress and subsidence in room and pillar mining of a gently inclined medium-thick phosphate rock," *Advances in Civil Engineering*, vol. 2021, pp. 1–17, 2021.

- [3] R. H. C. Wong, C. A. Tang, K. T. Chau, and P. Lin, "Splitting failure in brittle rocks containing pre-existing flaws under uniaxial compression," *Engineering Fracture Mechanics*, vol. 69, no. 17, pp. 1853–1871, 2002.
- [4] L. N. Y. Wong and H. Q. Li, "Numerical study on coalescence of two pre-existing coplanar flaws in rock," *International Journal of Solids & Structures*, vol. 50, no. 22-23, pp. 3685–3706, 2013.
- [5] X. P. Zhou, J. Bi, and Q. H. Qian, "Numerical simulation of crack growth and coalescence in rock-like materials containing multiple pre-existing flaws," *Rock Mechanics and Rock Engineering*, vol. 48, no. 3, pp. 1097–1114, 2015.
- [6] C. Y. Zhang, C. Z. Pu, R. H. Cao, T. Jiang, and G. Huang, "The stability and roof-support optimization of roadways passing through unfavorable geological bodies using advanced detection and monitoring methods, among others, in the Sanmenxia Bauxite Mine in China's Henan Province," *Bulletin of Engineering Geology and the Environment*, vol. 78, no. 7, pp. 5087–5099, 2019.
- [7] X. K. Qian, Z. Z. Liang, Z. Y. Liao, and K. Wang, "Numerical investigation of dynamic fracture in rock specimens containing a pre-existing surface flaw with different dip angles," *Engineering Fracture Mechanics*, vol. 223, Article ID 106675, 2019.
- [8] X. S. Li, S. Yang, Y. M. Wang, W. Nie, and Z. F. Liu, "Macro-micro response characteristics of surrounding rock and overlying strata towards the transition from open-pit to underground mining," *Geofluids*, vol. 2021, pp. 1–18, 2021.
- [9] S. H. Cho, Y. Ogata, and K. Kaneko, "Strain-rate dependency of the dynamic tensile strength of rock," *International Journal of Rock Mechanics and Mining Sciences*, vol. 40, no. 5, pp. 763–777, 2003.
- [10] F. Dai, R. Chen, and K. Xia, "A semi-circular bend technique for determining dynamic fracture toughness," *Experimental Mechanics*, vol. 50, no. 6, pp. 783–791, 2010.
- [11] F. Dai, K. Xia, H. Zheng, and Y. X. Wang, "Determination of dynamic rock Mode-I fracture parameters using cracked chevron notched semi-circular bend specimen," *Engineering Fracture Mechanics*, vol. 78, no. 15, pp. 2633–2644, 2011.
- [12] C. Y. Zhang, Y. X. Wang, H. Ruan, B. Ke, and H. Lin, "The strain characteristics and corresponding model of rock materials under uniaxial cyclic load/unload compression and their deformation and fatigue damage analysis," *Archive of Applied Mechanics*, vol. 91, no. 6, pp. 2481–2496, 2021.
- [13] R. H. C. Wong, M. L. Huang, M. R. Jiao, C. A. Tang, and W. S. Zhu, "The mechanisms of crack propagation from surface 3-D fracture under uniaxial compression," *Key Engineering Materials*, vol. 261-263, pp. 219–224, 2004.
- [14] H. Lee and S. Jeon, "An experimental and numerical study of fracture coalescence in pre-cracked specimens under uniaxial compression," *International Journal of Solids and Structures*, vol. 48, no. 6, pp. 979–999, 2011.
- [15] S. Y. Wang, S. W. Sloan, D. C. Sheng, and C. A. Tang, "Numerical analysis of the failure process around a circular opening in rock," *Computers and Geotechnics*, vol. 39, pp. 8–16, 2012.
- [16] X. B. Li, T. S. Lok, and J. Zhao, "Dynamic characteristics of granite subjected to intermediate loading rate," *Rock Mechanics and Rock Engineering*, vol. 38, no. 1, pp. 21–39, 2005.
- [17] S. Y. Wang, S. W. Sloan, H. Y. Liu, and C. A. Tang, "Numerical simulation of the rock fragmentation process induced by two drill bits subjected to static and dynamic (impact) loading," *Rock Mechanics and Rock Engineering*, vol. 44, no. 3, pp. 317–332, 2010.
- [18] F. Dai, S. Huang, K. Xia, and Z. Tan, "Some fundamental issues in dynamic compression and tension tests of rocks using split Hopkinson pressure bar," *Rock Mechanics and Rock Engineering*, vol. 43, no. 6, pp. 657–666, 2010.
- [19] S. Huang, K. Xia, and F. Dai, "Establishment of a dynamic mohr-coulomb failure criterion for rocks," *International Journal of Nonlinear Sciences and Numerical Simulation*, vol. 13, no. 1, pp. 55–60, 2012.
- [20] T. Kazerani, G. F. Zhao, and J. Zhao, "Dynamic fracturing simulation of brittle material using the distinct lattice spring method with a full rate-dependent cohesive law," *Rock Mechanics and Rock Engineering*, vol. 43, no. 6, pp. 717–726, 2010.
- [21] W. C. Zhu, Y. Bai, X. B. Li, and L. L. Niu, "Numerical simulation on rock failure under combined static and dynamic loading during SHPB tests," *International Journal of Impact Engineering*, vol. 49, pp. 142–157, 2012.
- [22] W. C. Zhu, L. L. Niu, S. H. Li, and Z. H. Xu, "Dynamic Brazilian test of rock under intermediate strain rate: pendulum hammer-driven SHPB test and numerical simulation," *Rock Mechanics and Rock Engineering*, vol. 48, no. 5, pp. 1867–1881, 2015.
- [23] J. Zhao, "Modelling of Rock Materials Subjected to Dynamic Loading Using a Particle-Based Numerical Manifold Method (PNMM)," in *International Conference on Analysis of Discontinuous Deformation*, Wuhan, China, October 2015.
- [24] W. C. Zhu and C. A. Tang, "Numerical simulation of Brazilian disk rock failure under static and dynamic loading," *International Journal of Rock Mechanics and Mining Sciences*, vol. 43, no. 2, pp. 236–252, 2006.
- [25] S. Y. Wang, L. Sun, C. Yang, S. Q. Yang, and C. A. Tang, "Numerical study on static and dynamic fracture evolution around rock cavities," *Journal of Rock Mechanics and Geotechnical Engineering*, vol. 5, no. 4, pp. 262–276, 2013.
- [26] Y. F. Yang, C. A. Tang, and K. W. Xia, "Study on crack curving and branching mechanism in quasi-brittle materials under dynamic biaxial loading," *International Journal of Fracture*, vol. 177, no. 1, pp. 53–72, 2012.
- [27] X. Li, M. Tao, F. Gong et al., "Theoretical and experimental study of hard rock spalling fracture under impact dynamic loading," *Chinese Journal of Rock Mechanics & Engineering*, vol. 30, no. 6, pp. 1081–1088, 2011.
- [28] H. Li and L. N. Y. Wong, "Influence of flaw inclination angle and loading condition on crack initiation and propagation," *International Journal of Solids and Structures*, vol. 49, no. 18, pp. 2482–2499, 2012.
- [29] C. Zou and L. N. Y. Wong, "Experimental studies on cracking processes and failure in marble under dynamic loading," *Engineering Geology*, vol. 173, pp. 19–31, 2014.
- [30] C. J. Zou, L. N. Y. Wong, and Y. Cheng, "The Strength and Crack Behavior of the Rock-like gypsum under High Strain Rate," in *ARMA, 46th US Rock Mechanics/Geomechanics Symposium*, pp. 1–15, Chicago, IL, USA, 2012.
- [31] C. Zou, L. N. Y. Wong, J. J. Loo, and B. S. Gan, "Different mechanical and cracking behaviors of single-flawed brittle gypsum specimens under dynamic and quasi-static loadings," *Engineering Geology*, vol. 201, pp. 71–84, 2016.
- [32] X. Li, Z. Tao, and D. Li, "Dynamic strength and fracturing behavior of single-flawed prismatic marble specimens under impact loading with a split-hopkinson pressure bar," *Rock Mechanics & Rock Engineering*, vol. 50, no. 1, pp. 1–16, 2017.
- [33] N. P. Daphalapurkar, K. T. Ramesh, L. Graham-Brady, and J.-F. Molinari, "Predicting variability in the dynamic failure strength of brittle materials considering pre-existing flaws,"

- Journal of the Mechanics and Physics of Solids*, vol. 59, no. 2, pp. 297–319, 2011.
- [34] X.-P. Zhang and L. N. Y. Wong, “Loading rate effects on cracking behavior of flaw-contained specimens under uniaxial compression,” *International Journal of Fracture*, vol. 180, no. 1, pp. 93–110, 2013.
- [35] C. Jiang, G. Zhao, J. Zhu et al., “Investigation of dynamic crack coalescence using a gypsum-like 3D printing material,” *Rock Mechanics and Rock Engineering*, vol. 49, no. 10, pp. 3983–3998, 2016.
- [36] C. Jiang, G. F. Zhao, and N. Khalili, “On crack propagation in brittle material using the Distinct Lattice Spring Model,” *International Journal of Solids and Structures*, vol. 118–119, pp. 41–57, Article ID S0020768317301750, 2017.
- [37] D.-Y. Li, T. Wang, T.-J. Cheng, and X.-L. Sun, “Static and dynamic tensile failure characteristics of rock based on splitting test of circular ring,” *Transactions of Nonferrous Metals Society of China*, vol. 26, no. 7, pp. 1912–1918, 2016.
- [38] Q. B. Zhang and J. Zhao, “Quasi-static and dynamic fracture behaviour of rock materials: phenomena and mechanisms,” *International Journal of Fracture*, vol. 189, no. 1, pp. 1–32, 2014.
- [39] C.-A. Tang and Y.-F. Yang, “Crack branching mechanism of rock-like quasi-brittle materials under dynamic stress,” *Journal of Central South University*, vol. 19, no. 11, pp. 3273–3284, 2012.
- [40] D. J. Frew, M. J. Forrestal, and W. Chen, “A split Hopkinson pressure bar technique to determine compressive stress-strain data for rock materials,” *Experimental Mechanics*, vol. 41, no. 1, pp. 40–46, 2001.
- [41] Z. Y. Liao, J. B. Zhu, K. W. Xia et al., “Determination of dynamic compressive and tensile behavior of rocks from numerical tests of split Hopkinson pressure and tension bars,” *Rock Mechanics & Rock Engineering*, vol. 49, no. 10, pp. 1–18, 2016.
- [42] L. N. Y. Wong and H. H. Einstein, “Crack coalescence in molded gypsum and carrara marble: Part 1. Macroscopic observations and interpretation,” *Rock Mechanics and Rock Engineering*, vol. 42, no. 3, pp. 475–511, 2009.

Research Article

Flexural Fatigue Behaviors of Silicon Carbide Recycled Concrete in Corrosive Environments

Jinzi Zhou ¹, Tiantian Fu ¹, Chuheng Zhong ¹, Kun Peng,² and Ziyang Shuang³

¹College of Civil Engineering Architecture and Environment, Hubei University of Technology, Wuhan 430068, China

²The Third Construction Co., Ltd. of China Construction Third Engineering Bureau, Wuhan 430068, China

³The First Company of China Eighth Engineering Bureau Ltd., Guangzhou 510700, China

Correspondence should be addressed to Chuheng Zhong; chuheng.zhong@hbut.edu.cn

Received 11 April 2021; Accepted 29 June 2021; Published 9 July 2021

Academic Editor: Rihong Cao

Copyright © 2021 Jinzi Zhou et al. This is an open access article distributed under the Creative Commons Attribution License, which permits unrestricted use, distribution, and reproduction in any medium, provided the original work is properly cited.

An experimental study on the flexural fatigue behaviors of recycled concrete (RC) and silicon carbide recycled concrete (SiCRC) was conducted. The immersion time was 0 d, 30 d, 60 d, and 90 d in 5% NaCl solution for these two kinds of recycled concrete specimens, respectively, and then, four-point flexural fatigue tests were performed by MTS fatigue testing machine. The fatigue life for varying stress levels ranging from 0.9 to 0.6 was obtained. The fatigue life was given considering the failure probability according to the fatigue life and stress level of the specimen via the logarithmic normal distribution and Weibull distribution, respectively. The relationship between fatigue life and failure probability was also obtained. The fatigue life with failure probability of 1% and 50% was further predicted. The results showed that the fatigue life of RC and SiCRC increased in corrosive environments. The fatigue life of SiCRC is higher than that of RC, and the incorporation of SiCRC can improve the fatigue life of recycled concrete.

1. Introduction

With the development of the city, construction waste is growing. It is conservatively estimated that, over the next 10 years, China will produce more than 1.5 billion tons of construction waste per year, reaching 7.3 billion tons in 2030 [1]. At present, the construction waste are mainly brick and concrete, which are treated as recycled aggregate and prepared as inorganic mixture for road pavement base. Considering environment and economy, replacing nonrenewable natural aggregate with renewable construction waste, construction waste recycling can not only reduce carbon emissions but also lower costs [2, 3].

Many scholars at home and abroad have studied the mechanics and durability of recycled concrete [4–10]. Ramesh et al. [11] found that the split-tensile strength, the compressive strength, and the elastic modulus of recycled concrete with substitution rate of 30%, 50%, 70%, and 100% were lower than that of natural concrete, and the splitting tensile strength can be increased by 0.7% after incorporation

of steel fiber. Aref et al. [12] showed that it was feasible to build self-compacting concrete with a 100% replacement rate of recycled aggregate. Rahal [13] found that the compressive strength and indirect shear strength of 28-day cube and cylinder of recycled aggregate concrete were 90% of natural aggregate concrete under the same mix proportions. Thomas et al. [14] discussed the effect of recycled aggregate on concrete under the same w/c ratio by partially and completely replacing natural aggregate. The durability of recycled aggregate concrete was poor due to the porosity of recycled aggregate itself. Subsequently, Pinghua Zhu et al. [15] reported the durability of recycled concrete with different substitution rates under the coupling of freeze-thaw cycle and chloride erosion.

However, many engineering structures such as bridge decks, piers, offshore structures, highway pavements, and railway sleepers are more vulnerable to fatigue loading [16]. Therefore, scholars have also carried out studies on the fatigue properties of recycled concrete. Singh and Kaushik [17] found that steel fiber recycled concrete statistical

distribution of equivalent fatigue life at a given stress level S , approximately, submitted to the two-parameter Weibull distribution. Cusson et al. [18] mentioned that because of the increase of traffic load and the change of environmental conditions, deterioration will affect the service life of the bridge; the use of deicing salt on the road in winter will lead to more serious corrosion deterioration and reduce its durability. The test under the coupled action of freezing-thawing cycles and chloride attack was completed by Hao et al. [19] The results showed that the bending stress had significant negative effect on the frost resistance of RATIC. Wang et al. [20] found that silicon carbide concrete had better working performance on compressive and flexural strength than that of ordinary concrete. Silicon carbide can be used as wear-resistant floor in logistics workshop and distribution workshop to enhance the wear resistance of pavement [21].

In conclusion, the flexural fatigue performance of common recycled concrete and silicon carbide recycled concrete in corrosion environment will be studied by experiments in this paper in order to obtain useful conclusions.

2. Experimental Program

2.1. Materials. In this experiment, constituents of silicon carbide recycled concrete (SiCRC) are Ordinary Portland Cement, coarse aggregates, river sand, manufactured sand, silicon carbide, and admixtures. Ordinary Portland Cement has been obtained from the local supplier. Coarse aggregates have NA and RA two types. Particle size of NA and RA of is 5–30 mm, whose physical properties are given in Table 1. The RA used in this study was completely wetted by spraying water. Fine aggregate was river sand and silicon carbide. The fineness modulus of river sand is 2.8, which belongs to medium sand in II area, with mud content of 0.7%. The size of silicon carbide is $1190\ \mu\text{m}$. Admixtures are polycarboxylic acid. The water-reduction rate of that is 30%, and the gas and solid content is about 4.7% and 8.8%. Fly ash and slag as materials were mingled to improve the performance of specimens. Chloride containing environment is 5% NaCl solution.

2.2. Specimen. The experiment carries on the mix proportion design of the reference concrete C30 according to the JCJ55-2011 (Specification for Mix Proportion Design of Ordinary Concrete). The substitution rate of recycled aggregate is 20% in RC. Further, based on RC, 10% fine aggregate can be replaced with an equal volume of silicon carbide, which made SiCRC.

There are two kinds of concrete specimens, the mineral powder is $100\ \text{kg}/\text{m}^3$, the cement is $210\ \text{kg}/\text{m}^3$, the fly ash is $60\ \text{kg}/\text{m}^3$, and the water and water reducer are $160\ \text{kg}/\text{m}^3$ and $7.4\ \text{kg}/\text{m}^3$, respectively. The amount of other materials is given in Table 2. The flexural fatigue test was carried out with $150\ \text{mm} \times 150\ \text{mm} \times 550\ \text{mm}$ standard trabecular specimens. It has 2 mix proportion and 8 groups of specimens. The flexural fatigue specimens of each group were 9. The specimens were standard cured for 28 d. Then, specimens' soaking time periods were 0, 30, 60, and 90 d in 5% NaCl solution.

3. Test Methods

Fatigue test was carried out on the MTS in the structure hall of Hubei University of Technology, as shown in Figure 1. Loading mode selected load control, four-point bending method, and sine wave cycle loading mode; loading frequency is 10 Hz; the stress level is 0.6, 0.7, and 0.9; the test flow is shown in Figure 2.

4. Test Results and Analysis

4.1. Experimental Phenomena. The results show that white spots and concave-convex pits are produced on the surface of RC and SiCRC specimens after chlorine salt soaking. With loading, crack gradually appears in the middle of the tension side of the specimen and extends to the compression zone. Due to the weak bond between coarse aggregate and cement gel, when loaded to the ultimate load, the specimen produced brittle fractures, accompanied by the sound of bang. The destroyed image is shown in Figure 3.

4.2. Fatigue Test Data. The results of the fatigue tests as obtained in this investigation are given in Tables 3 and 4. In bending fatigue tests, even with the same batch of raw materials, the produced samples are differences. Because silicon carbide recycled concrete is a composite, it has been treated with chlorine salt soaking. Fatigue failure is more complicated than static load failure. The results of fatigue test are very discrete. S - N relation graph is a widely accepted method to evaluate the fatigue life of practical engineering. When considering the effect of minimum stress, constant life fatigue diagram can be used such as Haigh or Smith diagrams to represent. The recycled concrete has a different fatigue life under different bending fatigue stress levels. The relationship between stress level S and fatigue life N can be described by the rectangular Cartesian coordinate system. The S - N curve can clearly and intuitively describe the fatigue characteristics of materials [4]. Figure 4 shows the S - N curves of recycled concrete of different types and different immersion ages showing the relationship between fatigue life (N) and stress level (S), respectively.

It can be seen from Figure 4 that the fatigue life of each group of recycled concrete specimens decreases with the increase of stress level. When the stress level is certain, with the increase of soaking age, the fatigue life of recycled concrete and silicon carbide recycled concrete increases. When the stress level is certain and the soaking age is the same, the fatigue life of silicon carbide recycled concrete under chlorine salt immersion is higher than that of recycled concrete.

Without the chlorine, due to the higher porosity and lower strength of RC, the size of silicon carbide is small and can be filled between other aggregate gaps, which improves the density of concrete. The addition of silicon carbide and coal fly ash improves the inner capillary structure of concrete and improves the bonding ability of concrete as a whole. Meanwhile, the hydroxyl of concrete admixture and silicon carbide, main components' SiC on the surface, and oxygen

TABLE 1: Physical properties of coarse aggregate.

Category	Particle size (mm)	Water absorption (%)	Apparent density (kg/m ³)	Crushing value (%)
Recycled coarse aggregate	5~30	9.5	2520	14.9
Natural coarse aggregate	5~30	0.9	2650	9

TABLE 2: Mixture proportion (kg/m³).

Concrete type	Cement	NA	RA	Silicon carbide	Manufactured sand	River sand	Water
RC	210	824	206	—	380	455	160
SiCRC	210	824	206	83.5	342	409	160

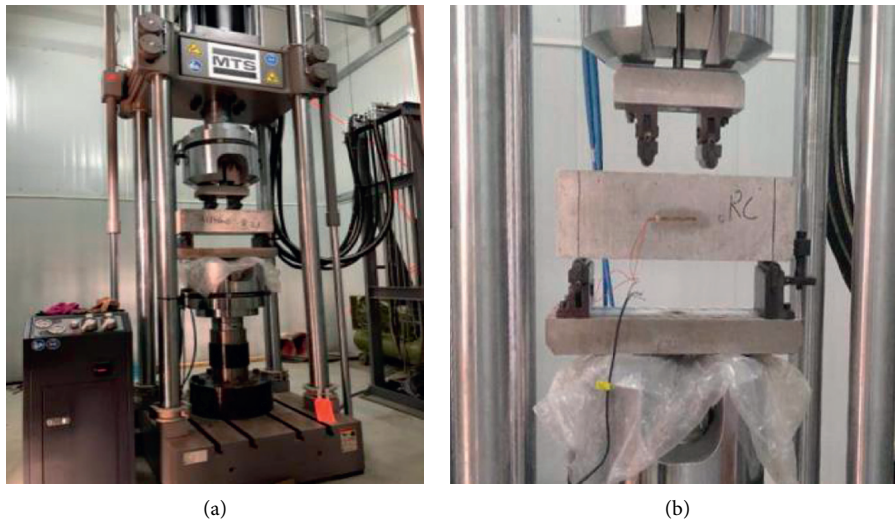


FIGURE 1: Fatigue test equipment.

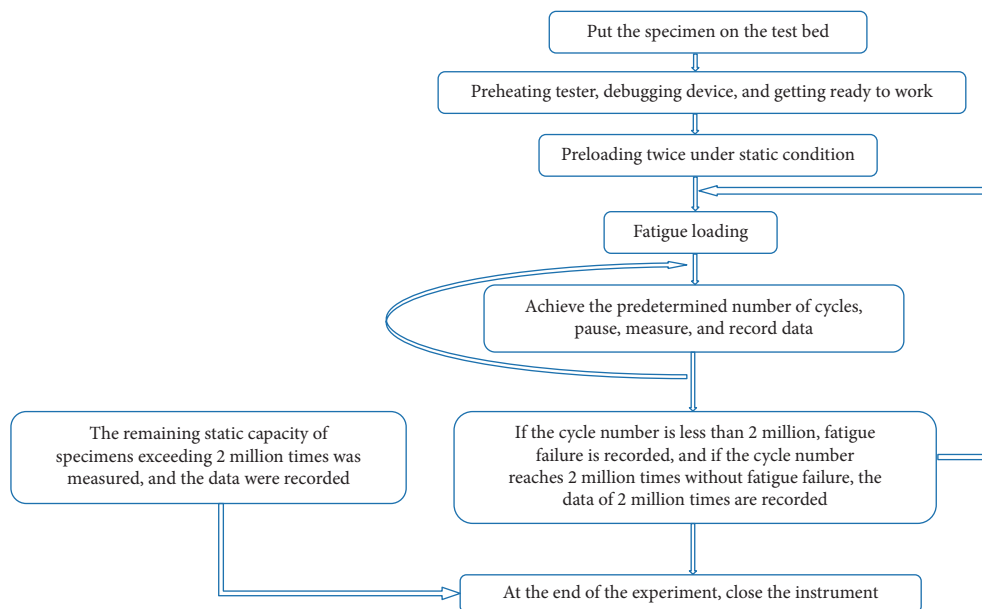


FIGURE 2: Test procedure for fatigue test.



FIGURE 3: Failure morphology of specimens.

TABLE 3: Fatigue life (N) for RC.

Specimen no.	Stress level	Fatigue life data (N)		
RC (0 d)	0.9	113	211	319
	0.7	14647	31841	45239
	0.6	57981	106042	148596
RC (30 d)	0.9	125	223	332
	0.7	16135	33855	48271
	0.6	60458	108267	151029
RC (60 d)	0.9	136	236	346
	0.7	17737	35324	50736
	0.6	62549	110749	153773
RC (90 d)	0.9	145	247	357
	0.7	19319	36973	52632
	0.6	64597	112823	156175

TABLE 4: Fatigue life (N) for SiCRC.

Specimen no.	Stress level	Fatigue life data (N)		
SiCRC (0 d)	0.9	255	404	612
	0.7	22716	61953	93326
	0.6	70463	135524	196022
SiCRC (30 d)	0.9	262	408	619
	0.7	23941	63117	94565
	0.6	71926	137033	197576
SiCRC (60 d)	0.9	266	413	623
	0.7	24851	64028	95447
	0.6	73942	139031	199527
SiCRC (90 d)	0.9	272	419	631
	0.7	26044	65238	96646
	0.6	76186	141231	201767

atom with strong negative charge in cement clinker molecules generate a hydrogen bond, which further improves the strength of concrete.

After soaking in chloride, the fatigue life of SiCRC increases as follows. In the long-term immersion of NaCl solution, chlorine salt diffuses into the concrete with the increase of soaking age. Because a large number of chloride ions exist, the crystals of salt are formed in concrete. It is mainly that tricalcium aluminate combines with chloride ion to form "Fessler salt." At the same time, the cement hydration will continue to produce calcium hydroxide and other substances, which will make the interior of concrete more dense. The connection between

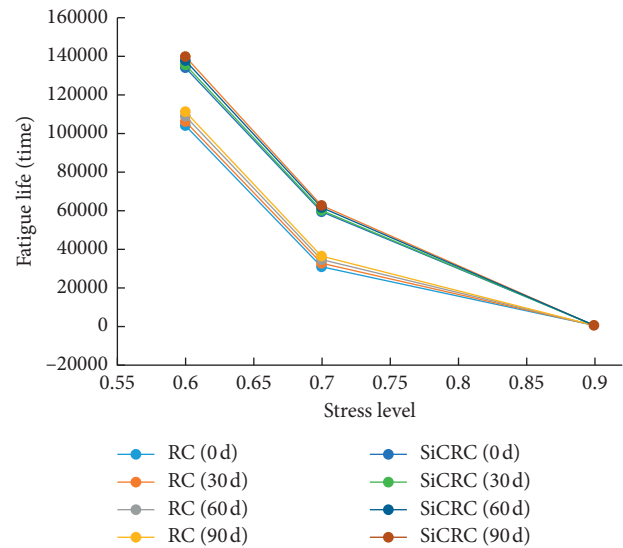


FIGURE 4: S-N curves.

the aggregate inside the concrete closer and strength of the concrete increases. Silicon carbide is a kind of aggregate with high toughness and hardness, and the SiCRC is a kind of material with good uniformity. The addition of silicon improves toughness and crack resistance of concrete as a whole. The performance of RC under the condition of chlorine salt soaking and the mechanism of chlorine salt erosion are similar to SiCRC, but the fatigue life performance is not as good as that of SiCRC because of the lack of the addition of silicon improves.

5. Numerical Distribution Analysis

On the strength and fatigue life of concrete materials, scholars mostly use the lognormal distribution model and the Weibull distribution model [22–25]. In this section, lognormal distribution and two-parameter Weibull distribution model will be used to analyze the fatigue performance of recycled concrete in chloride immersion.

5.1. Lognormal Distribution. The logarithm of specimens' fatigue life ($S = \lg N$) obeys normal distribution; then, the probability density function is as follows:

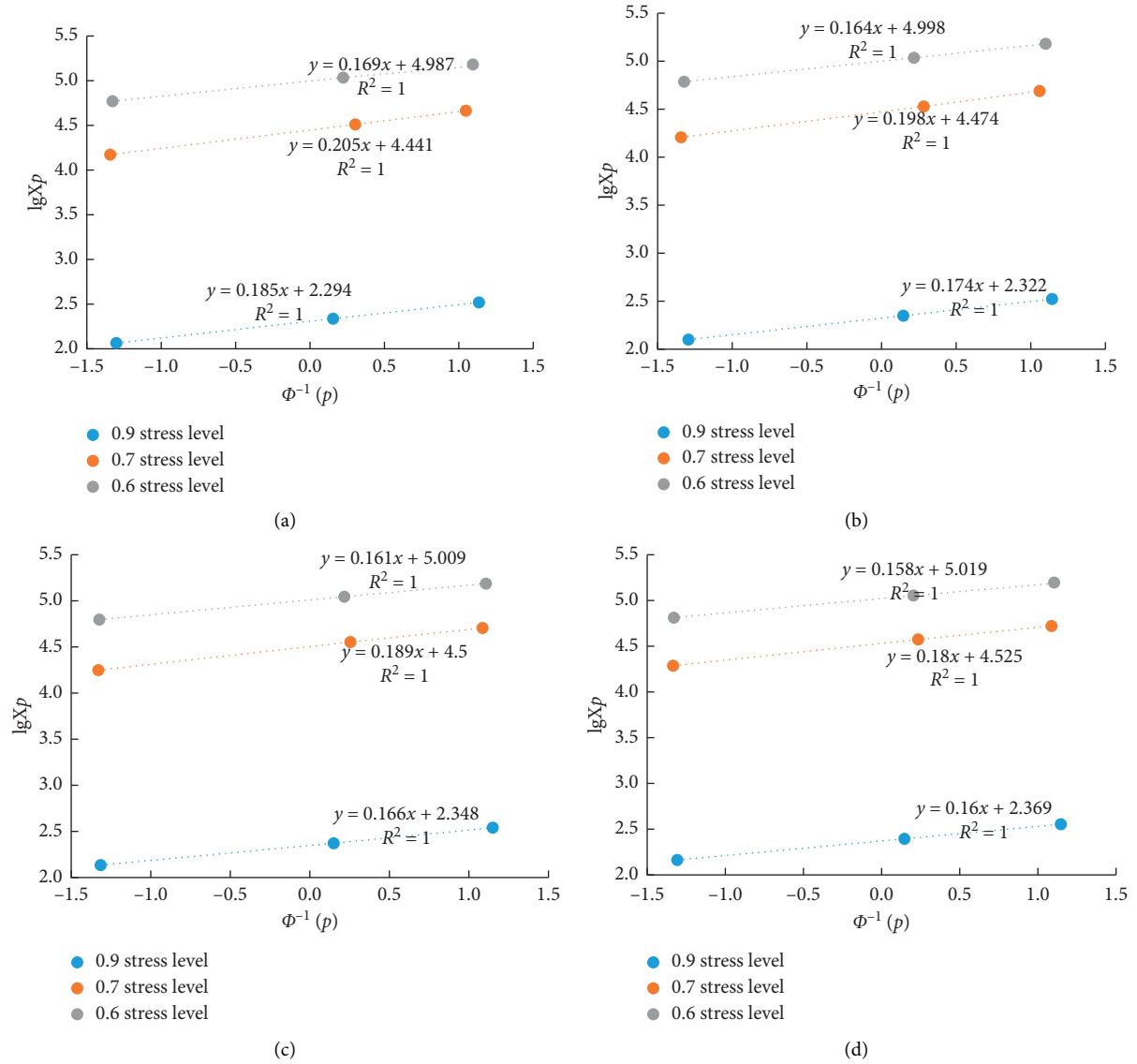


FIGURE 5: RC linear regression. (a) RC (0 d). (b) RC (30 d). (c) RC (60 d). (d) RC (90 d).

$$f_N(n) = \frac{1}{\sqrt{2\pi} \ln 10 \sigma_0 n} \exp\left[-\frac{(\lg n - \mu_0)^2}{2\sigma_0^2}\right], \quad (1)$$

where μ_0 and σ_0 of $\lg N$ are average value and standard deviation and distribution parameters N is the random variable:

$$F_N(n) = P(N \leq n) = \varphi\left(\frac{\lg n - \mu_0}{\sigma_0}\right). \quad (2)$$

The function values to the cumulative distribution function is called cumulative failure probability or unreliable. Then, the reliability function is as follows:

$$R_N(n) = 1 - F_X(x) = 1 - \varphi\left(\frac{\lg n - \mu_0}{\sigma_0}\right). \quad (3)$$

In order to regress the model distribution parameters, the cumulative failure probability is known to be p . Taking $\varphi^{-1}(\cdot)$ on both sides at the same time, reliability life of $(1 - p)$ is as follows:

$$\lg n_p = \mu_0 + \varphi^{-1}(p)\sigma_0, \quad (4)$$

When $Y = \lg x_p$, $Z = \varphi^{-1}(p)$, $a = \mu_0$, and $b = \sigma_0$, equation (4) can be transformed into the following primary linear equation:

$$\begin{aligned} Y &= a + bN, \\ \hat{\mu}_0 &= \hat{a}, \\ \hat{\sigma}_0 &= \hat{b}. \end{aligned} \quad (5)$$

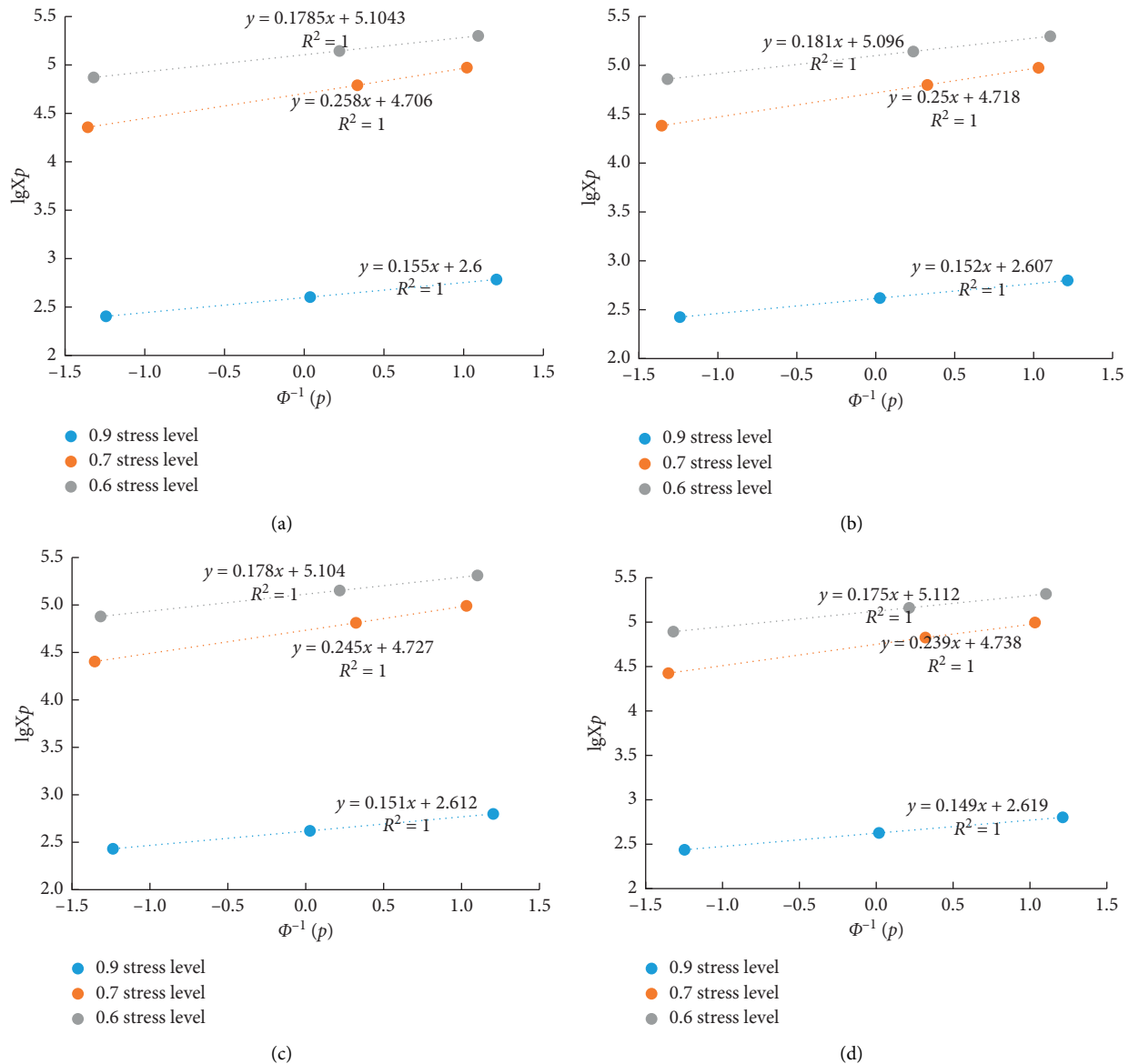


FIGURE 6: SiCRC linear regression. (a) SiCRC (0 d). (b) SiCRC (30 d). (c) SiCRC (60 d). (d) SiCRC (90 d).

a and b can be obtained by regression of test data with formula (5) to determine the distribution parameters μ_0 and σ_0 .

Fatigue life of RC and SiCRC in corrosive environments was analyzed by using lognormal distribution theory. The fitting results are shown in Figures 5 and 6.

5.2. Weibull Distribution. According to Weibull distribution theory, the distribution law of fatigue life N of each specimen can be expressed by Weibull function under the same stress level:

$$Y = bX - a, \quad (6)$$

where $Y = \ln[\ln(1/p)]$, $X = \ln N$, and $a = b \ln N_a$.

The data of fatigue life are brought into Y and X , and the data are regressed analysis. The data show a clear linear relationship; then, the results show that the data of four-

point bending fatigue test accord with the two-parameter Weibull distribution. On the contrary, the assumption is not tenable.

Fatigue life of RC and SiCRC in corrosive environments was analyzed by using Weibull distribution theory. The fitting results are shown in Figures 7 and 8.

From Figures 5–8 and Table 5, all the correlation coefficient R^2 is 1.0 by using lognormal distribution and R^2 is above 0.95 by using Weibull distribution. The results show that the fatigue life of the two kinds of concrete under the condition of chlorine salt soaking is better from lognormal distribution and Weibull distribution at different ages. Both the lognormal distribution and the two-parameter Weibull distribution, the fatigue life of chloride attack increased to varying degrees compared with that before chloride attack.

For the normal distribution theory, the correlation coefficient R^2 is 1.0, which indicates that it is completely

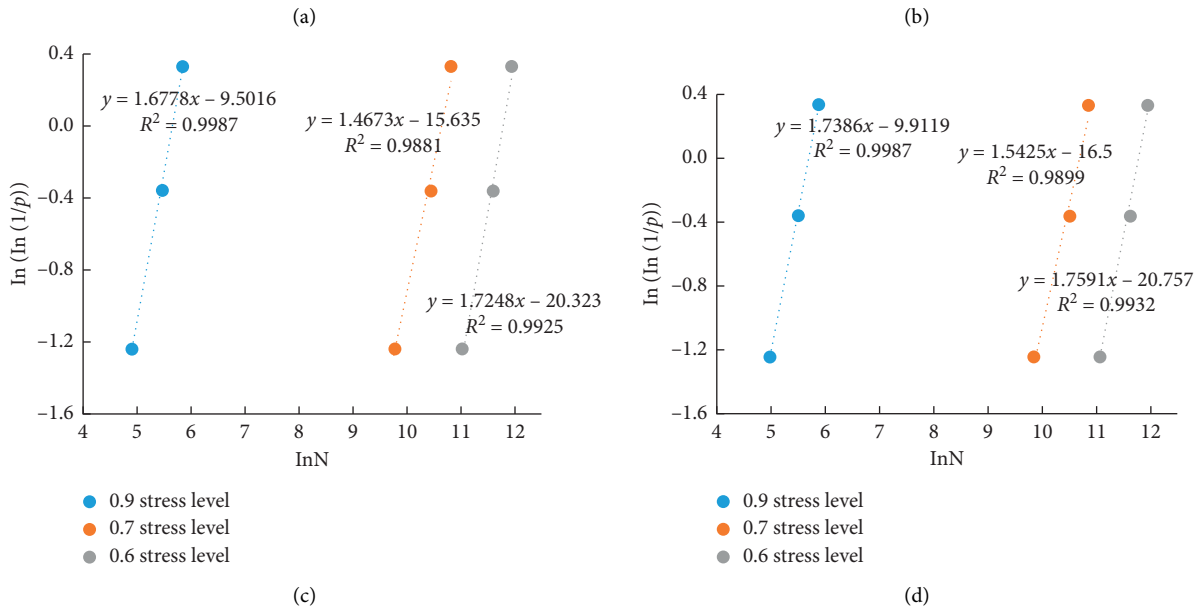
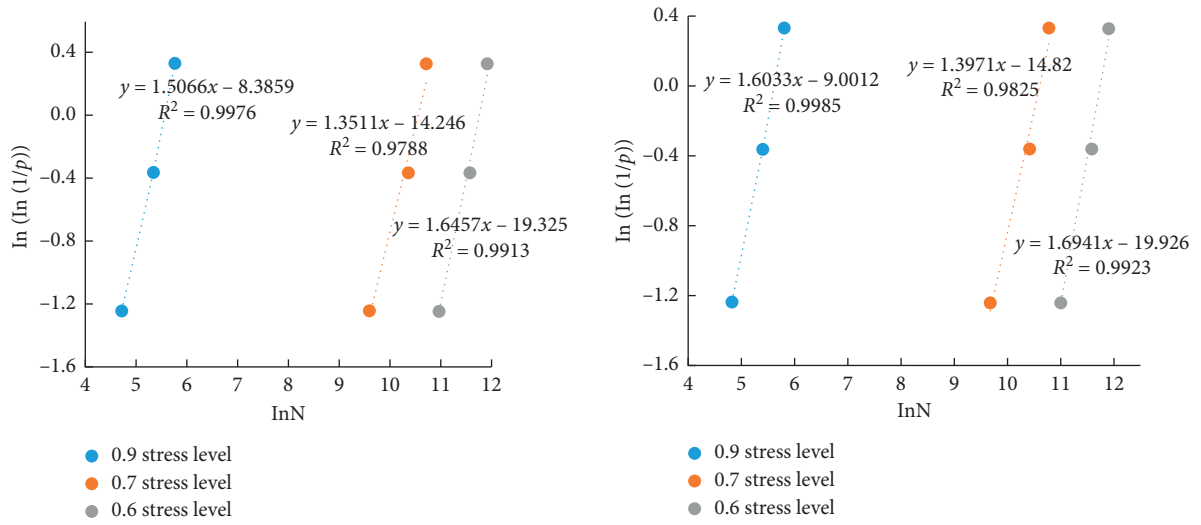


FIGURE 7: RC linear regression. (a) RC (0 d). (b) RC (30 d). (c) RC (60 d). (d) RC (90 d).

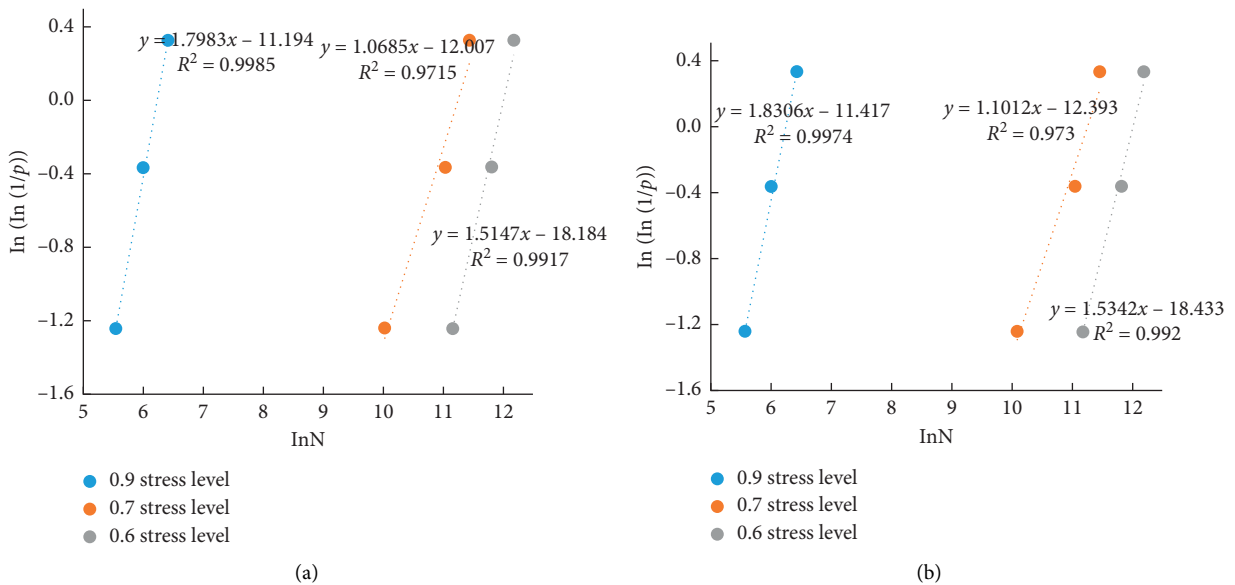


FIGURE 8: Continued.

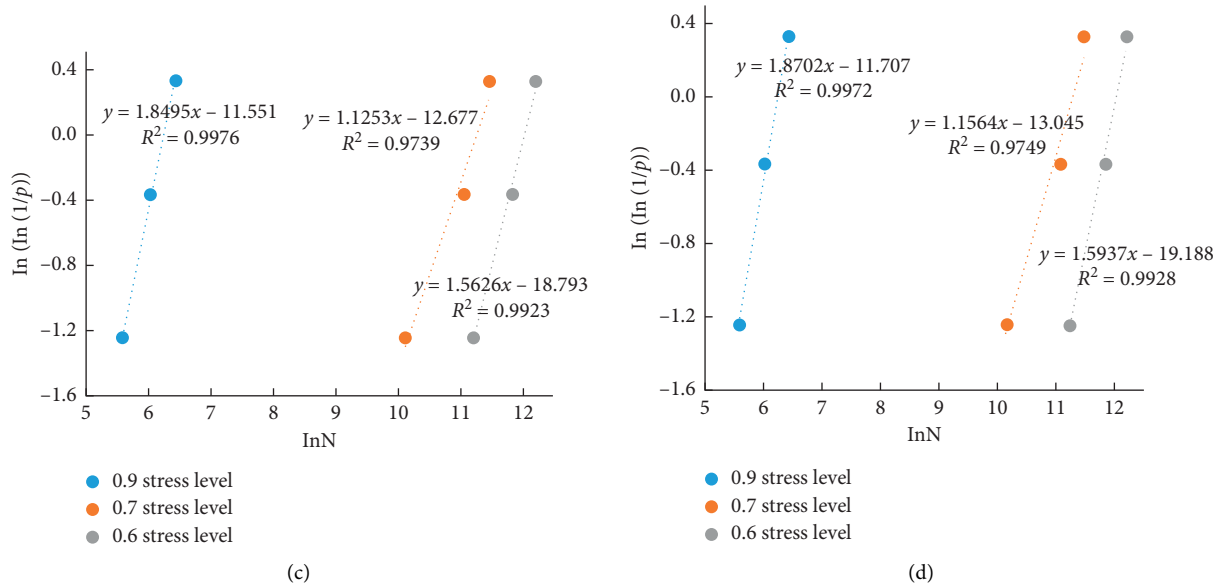


FIGURE 8: SiCRC linear regression. (a) SiCRC (0 d). (b) SiCRC (30 d). (c) SiCRC (60 d). (d) SiCRC (90 d).

TABLE 5: Fitting results of lognormal distribution and Weibull distribution.

Group number	Max stress level	Lognormal distribution					Weibull distribution				
		<i>a</i>	<i>b</i>	R^2	Failure probability		<i>a</i>	<i>b</i>	R^2	Failure probability	
					1%	50%				1%	50%
RC (0 d)	0.9	2.294	0.185	1.0	73	197	1.5066	8.3859	0.9976	59	205
	0.7	4.41	0.205	1.0	8572	25704	1.3511	14.246	0.9788	7175	28933
	0.6	4.987	0.169	1.0	39250	97051	1.6457	19.325	0.9913	32058	100711
RC (30 d)	0.9	R^2	0.174	1.0	83	210	1.6033	9.001	0.9985	67	218
	0.7	4.474	0.198	1.0	10312	29785	1.3971	14.82	0.9825	8078	31112
	0.6	4.998	0.164	1.0	41350	99541	1.6941	19.926	0.9923	33984	103327
RC (60 d)	0.9	2.348	0.166	1.0	92	223	1.6778	9.502	0.9987	75	232
	0.7	4.5	0.189	1.0	11490	31623	1.4673	15.635	0.9881	9154	33052
	0.6	5.009	0.161	1.0	43098	102094	1.7248	20.323	0.9925	35529	105907
RC (90 d)	0.9	2.369	0.16	1.0	99	234	1.7386	9.9119	0.9987	82	242
	0.7	4.525	0.18	1.0	12771	33497	1.5425	16.5	0.9899	10281	34868
	0.6	5.019	0.158	1.0	44816	104472	1.7591	20.757	0.9932	37068	108167
SiCRC (0 d)	0.9	2.6	0.155	1.0	173	398	1.7983	11.194	0.9985	145	412
	0.7	4.706	0.258	1.0	12758	50816	1.0685	12.007	0.9715	9239	53865
	0.6	5.104	0.178	1.0	48875	127151	1.5147	18.184	0.9917	37024	128418
SiCRC (30 d)	0.9	2.607	0.152	1.0	179	405	1.8306	11.417	0.9974	149	418
	0.7	4.718	0.25	1.0	13690	52240	1.1012	12.393	0.9731	10002	55340
	0.6	5.096	0.181	1.0	47308	124738	1.5342	18.433	0.992	38072	129971
SiCRC (60 d)	0.9	2.612	0.151	1.0	182	409	1.8496	11.551	0.9976	153	423
	0.7	4.727	0.245	1.0	13456	53333	1.1253	12.677	0.9739	10569	56373
	0.6	5.104	0.178	1.0	48968	127057	1.5626	18.793	0.9923	39601	132217
SiCRC (90 d)	0.9	2.619	0.149	1.0	187	416	1.8702	11.707	0.9972	157	430
	0.7	4.738	0.239	1.0	15206	54702	1.1564	13.045	0.9749	11324	57743
	0.6	5.112	0.175	1.0	50686	129420	1.5937	19.188	0.9928	41269	134582

correlated. It does not match the actual situation, and there is a little error.

For the Weibull distribution theory, when the stress level is the same, the correlation coefficient R^2 increases gradually

with the increase of soaking age, which shows that the linear relationship is enhanced. When the soaking age is the same, the correlation coefficient of the same type concrete is higher at the stress level 0.9. When the stress level and soaking age

are the same, the SiCRC's correlation coefficient R^2 is higher than RC, which indicates that the straight line fitting effect is better. In addition, at the high stress level, the fitting discreteness of fatigue life is large, the fatigue life is 0 when the failure probability is 0, which is wrong with the actual existence.

6. Conclusions

- (1) The fatigue life of each concrete specimens decreases with the increase of the stress level, and the fatigue life of both types of concrete increases with the increase of soaking age when the stress level is fixed.
- (2) The fatigue life of RC and SiCRC increased in corrosive environments. The fatigue life of SiCRC is higher than that of RC, and the incorporation of SiCRC can improve the fatigue life of recycled concrete.
- (3) By both the lognormal distribution and two-parameter Weibull distribution, the fatigue life for chlorine salt erosion increased in varying degrees under the corresponding failure probability.

Data Availability

The data used to support the findings of this study are included within the article.

Conflicts of Interest

The authors declare no conflicts of Interest.

Acknowledgments

This research was financially supported by the State Key Laboratory for Health and Safety of Bridge Structures (Grant no. BHSKL19-04-KF) and Teaching Research Project of Higher Educational Institutions of Hubei Province (2017314). The authors would like to express their appreciation to these financial assistances.

References

- [1] "Rule of law daily," http://www.ce.cn/cysc/stwm/gd/202009/24/t20200924_35806871.shtml.
- [2] H. Liu, Z. Wang, H. Zhen, P. Zhu, X. Wang, and C. Chen, "Effect of recycled coarse aggregate quality on corrosion resistance of concrete," *Journal of Civil & Environmental Engineering*, pp. 1–7, 2021.
- [3] W. Zhou, Z. Zhang, and Y. Xu, "Mechanics and frost resistance of recycled aggregate inorganic mixture for construction waste," *Guide to Materials*, vol. 34, no. S1, pp. 234–236, 2020.
- [4] M. Kou, X. Liu, S. Tang, and Y. Wang, "3-D X-ray computed tomography on failure characteristics of rock-like materials under coupled hydro-mechanical loading," *Theoretical and Applied Fracture Mechanics*, vol. 104, no. 7, Article ID 102396, 2019.
- [5] R. S. Ravindraraj, M. Steward, and D. Greco, "Variability of recycled concrete aggregate and its effect on concrete properties—a case study in Australia," in *Proceedings of the International Workshop on Recycled Concrete*, Tokyo, Japan, September 2000.
- [6] Y. T. Wang, X. P. Zhou, and M. M. Kou, "Three-dimensional numerical study on the failure characteristics of intermittent fissures under compressive-shear loads," *Acta Geotechnica*, vol. 14, no. 4, pp. 1161–1193, 2018.
- [7] R. K. Dhir, M. R. Jones, H. E. H. Ahmed, and A. M. G. Seneviratne, "Rapid estimation of chloride diffusion coefficient in concrete," *Magazine of Concrete Research*, vol. 42, no. 152, pp. 177–185, 1990.
- [8] M. M. Kou, Y. J. Lian, and Y. T. Wang, "Numerical investigations on crack propagation and crack branching in brittle solids under dynamic loading using bond-particle model," *Engineering Fracture Mechanics*, vol. 212, pp. 41–56, 2019.
- [9] G. De Schutter, "Quantification of the influence of cracks in concrete structures on carbonation and chloride penetration," *Magazine of Concrete Research*, vol. 51, no. 6, pp. 427–435, 1999.
- [10] K. Kapoor, S. P. Singh, and B. Singh, "Durability of self-compacting concrete made with recycled concrete aggregates and mineral admixtures," *Construction and Building Materials*, vol. 128, pp. 67–76, 2016.
- [11] R. B. Ramesh, O. Mirza, and W. H. Kang, "Mechanical properties of steel fiber reinforced recycled aggregate concrete," *Structural Concrete*, vol. 20, no. 2, pp. 745–755, 2019.
- [12] S.-N. Aref, B. Javad, A. Sahar, L.-O. Omid, S.-N. Adel, and M. Karimaei, "The effect of recycled concrete aggregates and meta kaolin on the mechanical properties of self-compacting concrete containing nanoparticles," *Iranian Journal of Science and Technology, Transactions of Civil Engineering*, vol. 43, no. 1, pp. 503–515, 2019.
- [13] K. Rahal, "Mechanical properties of concrete with recycled coarse aggregate," *Building and Environment*, vol. 42, no. 1, pp. 407–415, 2007.
- [14] C. Thomasa, J. Setiéna, J.A. Polanco, P. Alaejosb, and M. Sánchez de Juan, "Durability of recycled aggregate concrete," *Construction and Building Materials*, vol. 40, pp. 1054–1065, 2013.
- [15] P. Zhu, Y. Hao, H. Liu, X. Wang, and L. Gu, "Durability evaluation of recycled aggregate concrete in a complex environment," *Journal of Cleaner Production*, vol. 273, Article ID 122569, 2020.
- [16] B. S. Saini and S. P. Singh, "Flexural fatigue strength prediction of self compacting concrete made with recycled concrete aggregates and blended cements," *Construction and Building Materials*, vol. 264, Article ID 120233, 2020.
- [17] S. P. Singh and S. K. Kaushik, "Fatigue strength of steel fibre reinforced concrete in flexure," *Cement and Concrete Composites*, vol. 25, no. 7, pp. 779–786, 2003.
- [18] D. Cusson, Z. Lounis, and L. Daigle, "Durability monitoring for improved service life predictions of concrete bridge decks in corrosive environments," *Computer-Aided Civil and Infrastructure Engineering*, vol. 26, pp. 524–541, 2011.
- [19] L. Hao, Y. Liu, and J. Xiao, "Durability of recycled aggregate thermal insulation concrete under combined flexural loading and freeze-thaw cycles," *Construction and Building Materials*, vol. 272, no. 2, Article ID 121652, 2020.
- [20] R. Wang, G. Wu, and C. Han, "A study on mix proportion design and mechanical properties of silicon carbide concrete," *Road*, no. 7, pp. 145–149, 2004.
- [21] R. Zhang, "Construction technology of carborundum floor," *Industrial Buildings*, vol. 43, no. S1, pp. 817–818, 2013.
- [22] L. Darren Graham, S. D. Smith, and P. Dunlop, "Lognormal distribution provides an optimum representation of the

- concrete delivery and placement process,” *Journal of Construction Engineering and Management*, vol. 131, no. 2, pp. 230–238, 2005.
- [23] D. Graham, S. Smith, and P. Dunlop, “The lognormal distribution provides the optimal representation of the concrete placement process,” *Journal of Construction Engineering and Management*, vol. 131, no. 2, 2005.
- [24] B. W. Jo, S. Chakraborty, and H. Kim, “Prediction of the curing time to achieve maturity of the nano cement based concrete using the Weibull distribution model,” *Construction and Building Materials*, vol. 84, pp. 307–314, 2015.
- [25] X. X. He and Z. H. Xie, “Experimental study on statistical parameters of concrete strength based on Weibull probability distribution,” *Key Engineering Materials*, vol. 477, pp. 224–232, 2011.

Research Article

Experimental Study on Influence of Joint Surface Morphology on Strength and Deformation of Nonthrough Jointed Rock Masses under Direct Shear

Yuanming Liu , Qingzhi Chen, Huiyu Chen, Xun Ou, Dafu Wu, and Xingchao Tian

School of Civil Engineering, Guizhou University, Guiyang 550003, Guizhou, China

Correspondence should be addressed to Yuanming Liu; 845612605@qq.com

Received 19 April 2021; Revised 18 June 2021; Accepted 30 June 2021; Published 9 July 2021

Academic Editor: Rihong Cao

Copyright © 2021 Yuanming Liu et al. This is an open access article distributed under the Creative Commons Attribution License, which permits unrestricted use, distribution, and reproduction in any medium, provided the original work is properly cited.

Direct shear tests were carried out on nonthrough jointed rock masses (NTJRM) with three types of joints under five normal stresses. The strength characteristics of shear strength, initial crack strength, and residual strength and the deformation characteristics of tangential displacement and dilatancy displacement as well as the transformation of failure mode and the variation of shear parameters of rock mass with different joint morphology are studied. Under the same normal stress, with the increase of joint undulation, the shear strength of NTJRM increases, and the corresponding tangential displacement of NTJRM increases. Two typical failure modes are observed: TTTS mode and TSSS mode. TTTS model indicates that the initial failure, extension failure, and final failure of rock mass are caused by tensile action, while the failure mode of through plane is formed by shear action. The initial failure of TSSS mode rock mass is caused by tensile action, while the expansion and final failure are caused by shear action, and the failure mode of through plane is formed under shear action. When the joint undulation is small and the normal stress is small, NTJRM will fail in TTTS mode; when the joint undulation is large and the normal stress is large, NTJRM will fail in TSSS mode. The results show that the shear parameters of NTJRM are related to the joint morphology, the bond force increases with the increase of joint undulation, and the internal friction angle increases with the increase of joint undulation. The research results of direct shear test of nonthrough jointed rock mass can provide reference for related research.

1. Introduction

Jointed rock mass is a familiar complex engineering-geological body in nature [1], in which the joint plays an essential role in reducing the rock mass strength [2–4]. The close association between internal joints coalescence and failure in rock engineering has been proven by various studies [5–8]. Generally, the jointed rock mass can be classified into nonthrough jointed rock mass (NTJRM) and through jointed rock mass (TJRM) according to the connectivity of joint. And, the failure mechanism of NTJRM is different from TJRM. Therefore, it is of great significance to investigate the shear strength and failure characteristics of NTJRM. A number of researches have been carried out to understand the influence of different joint geometry

parameters on the mechanical behavior of NTJRM. For instance, Bobet and Einstein [9] investigated the failure modes of specimens with two different types of joints under uniaxial loading. Wong and Chau [10] performed uniaxial loading tests on rock-like specimens containing double joints and summarized the relationship between failure modes and joint angles and rock bridges.

Recently, more attention has been drawn to study crack propagation. Morgan and Einstein [11] used shale containing natural bedding plane to fabricate specimens and found that the cracks at the joint tips usually grow along the bedding plane. Alneasan et al. [12] theoretically analyzed the propagation of inclined interface cracks in two different rock layers under both compression and tension. Wang et al. [13] utilized artificial layered rock mass with a single joint using

cement mortar material to analyze the influences of the bedding plane and joint on the mechanical characteristics. Cao et al. [14, 15] conducted experimental and numerical compression-shear tests on double-notched specimens to investigate the fracturing characteristics of transversely isotropic rock under planar shear fracture loading. Zhang et al. [16] studied the propagation mechanism of an oblique straight crack and revealed its mechanical characteristics under in-plane biaxial compression. Lin et al. [17, 18] performed uniaxial compression tests on jointed rock-like specimens with two dissimilar layers. Fan et al. [19] used the PFC program to establish numerical models containing one open flaw and two circular openings. The digital image correlation (DIC) techniques are employed to study the crack coalescence process of specimens with two dissimilar layers under uniaxial loading [20, 21].

Direct shear test is one of the effective methods to study the effect of shear stress on jointed rock mass, which can simulate the shear stress state of jointed rock mass. Lajtai [22, 23] studied the failure mode of jointed plaster by direct shear test, in which the failure modes of jointed plaster are sorted into three types: tensile failure, shear failure, and crushing failure. Chen et al. [24], Qin et al. [25], and Heng et al. [26] have studied the failure characteristics of rock mass with nonthrough joints under different connectivity and normal stress. Zhao et al. [27] used PFC software to study the deformation and failure mode of jointed rock mass. Wang et al. [28] carried out numerical analysis on the scale effect of elasticity, strength, and failure mode of jointed rock mass. Chen et al. [29] conducted direct shear tests on NTJRM with different connection rates to study their shear failure process and strength characteristics. Numerical methods are another effective method to study the strength and deformation characteristics of NTJRM under shear test.

It is generally known that joint morphology has an important influence on the strength and deformation characteristics of jointed rock mass. But the influence of joint morphology on the strength and deformation of NTJRM is not considered in the above studies. Only several scholars have considered the influence of joint morphology and conducted direct shear tests. Wang et al. [30] and Ma et al. [31] studied the effect of joint morphology on shear behavior of joints. Liu and Xia [32] proposed the failure mode of NTJRM. Liu et al. [33] and Chen et al. [34] studied the influence of joint morphology on the shear strength of NTJRM.

In this study, the influence of joint surface morphology on the strength and deformation characteristics of NTJRM is studied by direct shear test, and the variation of shear parameters with joint morphology is studied. The relationship between failure mode and joint surface morphology of NTJRM is investigated. The failure mode of NTJRM in direct shear test can provide experimental verification for numerical simulation.

2. Material and Method

2.1. Preparation of Specimens. Rock-like materials are used to prepare rock mass specimens with discontinuous joints. The rock-like material used in this experiment is cement

mortar with a mixing ratio of sand : cement : water = 3 : 2 : 1 (the sand is dug from a river in Shanghai area). The length \times width \times thickness of the NTJRM specimens is 300 mm \times 300 mm \times 150 mm. The joints had serrated morphology, a connection rate of 0.53, and undulation angles of 0°, 15°, and 30°. The size of the specimens is shown in Figure 1.

As shown in Figure 2, a self-made wooden mold was used to prepare the specimens. Serrated joints with undulation angles of 0°, 15°, and 30° were prepared by inserting thin steel sheets of 0.3 mm thickness into the poured specimens. The steel sheets were drawn out before the initial setting of the specimens.

2.2. Physical and Mechanical Properties of the Specimens. The physical and mechanical property parameters of the rock bridge section of the NTJRM are listed in Table 1. The shear parameters of the serrated joints are summarized in Table 2. All the mechanical property is obtained in the compressive and tensile strength test. The corresponding specimens after the compressive and the tensile test are demonstrated in Figures 3 and 4, respectively.

2.3. The Instruments Used in This Test. As shown in Figure 5, the specimen was installed in the rock mass direct shear apparatus, which is composed of the main engine, a hydraulic system, a servocontrol system, and a computerized control and treatment system. The main technical parameters of this rock mass direct shear apparatus are given as follows: (1) the maximum normal load is 500 kN, with a measurement accuracy of $\pm 1\%$; (2) the maximum tangential load is 1000 kN, with a measurement accuracy of $\pm 1\%$; (3) the measurement range of normal deformation is 0~20 mm, and the measurement accuracy of normal load deformation is $\pm 0.5\%$ F.S; (4) the measurement range of tangential deformation is 0~50 mm, and the measurement accuracy of tangential load deformation is $\pm 0.5\%$ F.S; (5) output pressure of hydraulic station is ≤ 21 MPa; (6) deformation rate is 0.05~50.0 mm/min.

2.4. The Testing Procedure. The specimens were divided into three groups for serrated joints with undulation angles of 0°, 15°, and 30°. In each group, the direct shear tests were carried out under five different normal stress levels (0.5 MPa, 1.0 MPa, 1.5 MPa, 2.0 MPa, and 3.0 MPa). During the direct shear test, the normal load was controlled by load, while the tangential load is controlled by displacement. Under the normal stress test mode, the normal stress was first loaded to the set value and then the shear stress is applied. After the normal load servo was stable, the horizontal load was then applied at a rate of 0.01 mm/s. The relevant data, including normal load, normal displacement, tangential load, and tangential displacement, were collected automatically by the computer.

In addition, an external monitoring system containing a camera was installed beside the testing machine to monitor

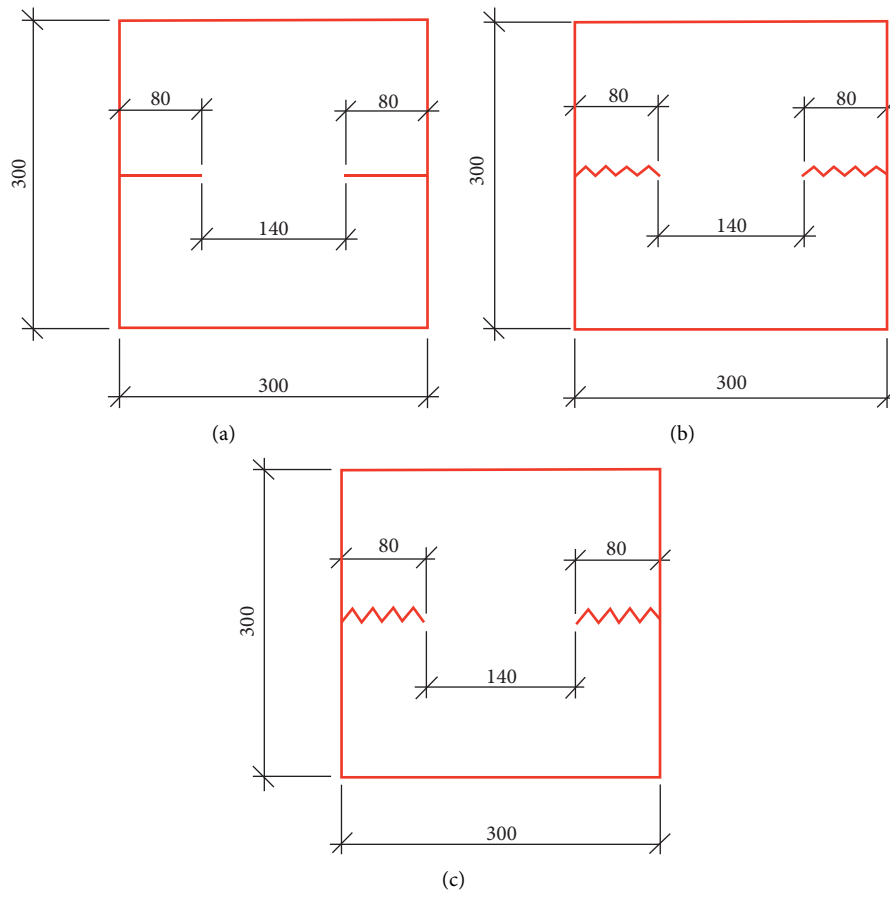


FIGURE 1: Specimens of rock mass with discontinuous joints. (a) $\alpha = 0^\circ$. (b) $\alpha = 15^\circ$. (c) $\alpha = 30^\circ$.

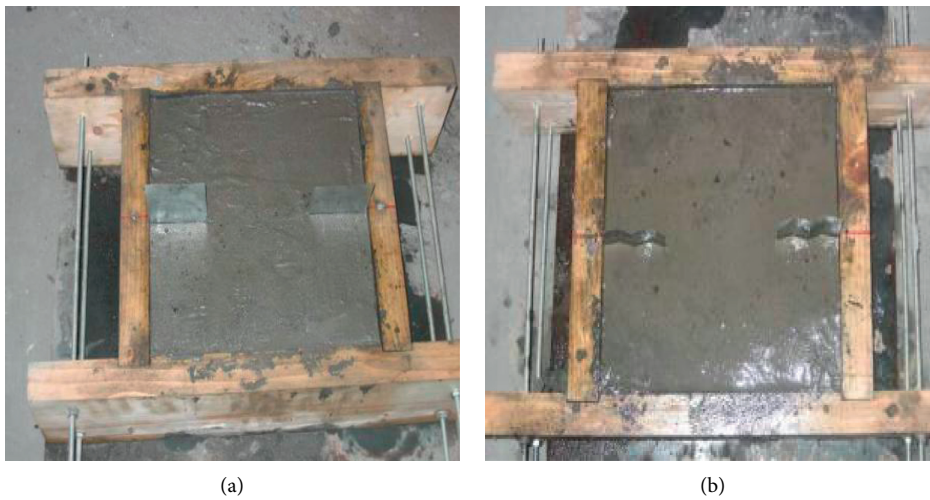


FIGURE 2: Continued.



(c)

FIGURE 2: Preparation process of specimens with different undulation angles. (a) Specimen with undulation angle of 0° . (b) Specimen with undulation angle of 15° . (c) Specimen with undulation angle of 30° .

TABLE 1: Physical and mechanical property parameters of the rock bridges.

Density (g/cm^3)	Compressive strength (MPa)	Tensile strength (MPa)	Modulus of elasticity (GPa)	Poisson's ratio	Cohesion (MPa)	Angle of internal friction ($^\circ$)
2.10	18.0	1.71	3.70	0.16	3.93	41.6

TABLE 2: Shear parameters of serrated joints.

The undulation angle ($^\circ$)	Cohesion (MPa)	Angle of internal friction ($^\circ$)
0	0.56	32.3
15	0.56	47.3
30	0.56	62.3



FIGURE 3: Specimens after the compressive strength test.



FIGURE 4: Specimens after the tensile strength test.

the initiation and propagation of the crack at the end of the joint and record the time when the initial crack appeared.

3. Results and Discussions

3.1. Deformation Characteristics of Rock Specimens during the Test

3.1.1. *Normal Deformation of Rock Specimens.* It can be seen from Figure 6 [33] that the normal deformation curve of

NTJRM is similar to the normal deformation curve of joints, and both of them are approximately double-curving. This indicates that, under normal stress, the joints of NTJRM also undergo closed deformation. The closed deformation makes the upper and lower joint surfaces contact closely. When the tangential force is applied, friction will be generated, so that joints and rock bridges share the tangential load.

Under five levels of normal stress, the normal displacements of the specimens are shown in Table 3 and Figure 7. Obviously, the normal stress and joint surface



FIGURE 5: The main engine of the rock mass direct shear apparatus.

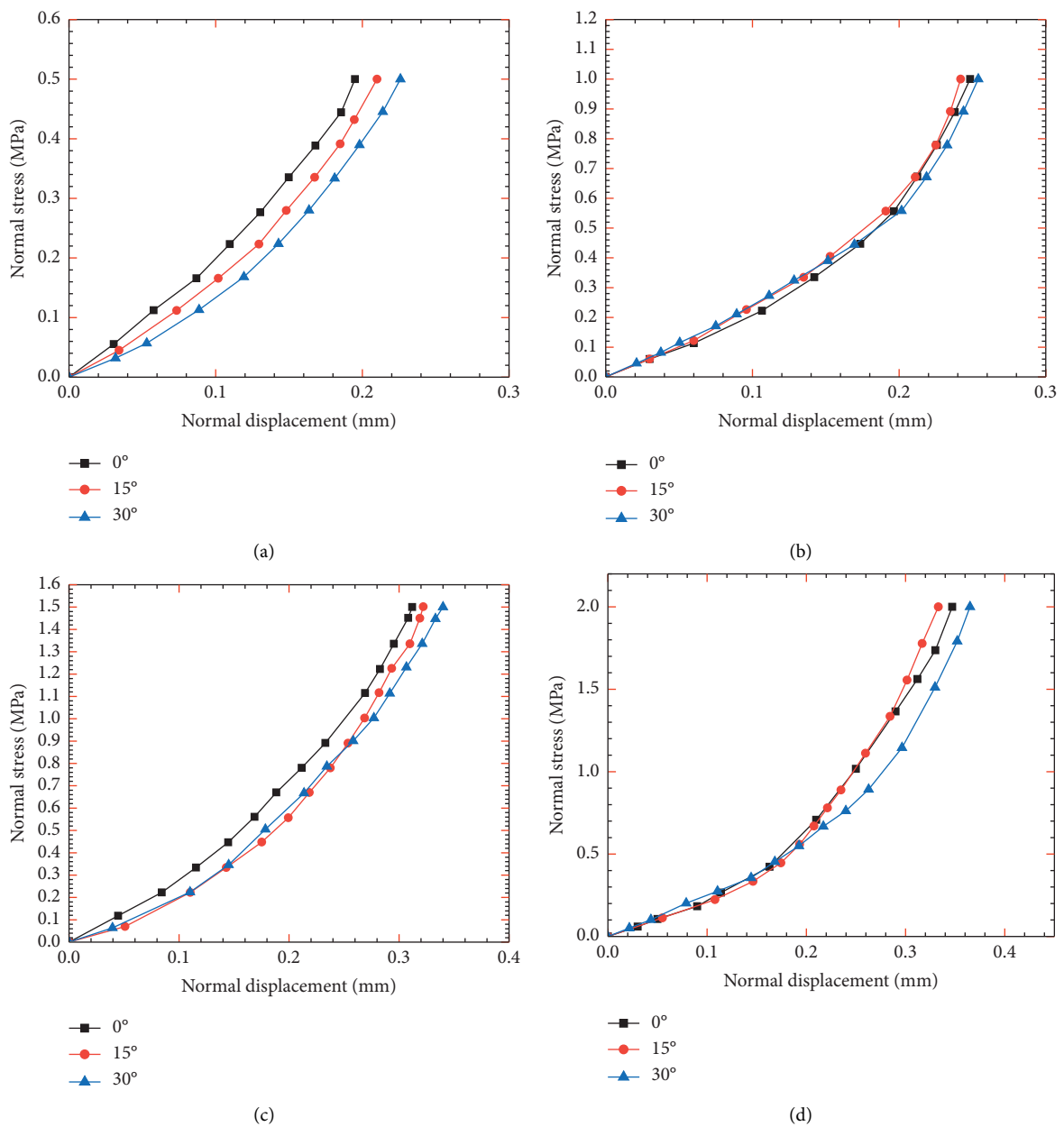


FIGURE 6: Continued.

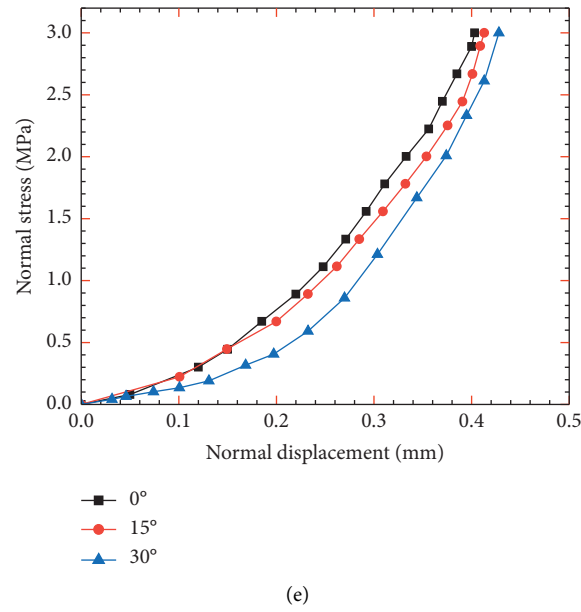


FIGURE 6: Normal deformation curve of the rock specimens (a) when the normal stress is 0.5 MPa, (b) when the normal stress is 1.0 MPa, (c) when the normal stress is 1.5 MPa, (d) when the normal stress is 2.0 MPa, and (e) when the normal stress is 3.0 MPa.

TABLE 3: Peak normal displacements of specimens, unit: mm.

Undulation angle	Normal stress (MPa)				
	0.5	1.0	1.5	2.0	3.0
0°	0.20	0.24	0.31	0.35	0.41
15°	0.21	0.25	0.32	0.36	0.43
30°	0.23	0.26	0.34	0.37	0.44

morphology have significant influence on the normal deformation of rock mass with discontinuous joints. Firstly, the normal deformation increases with the increase of normal stress. Secondly, under the same normal stress condition, the normal deformation of the joint changes with the surface morphology of the joint. The larger the undulation angle, the greater the normal displacement.

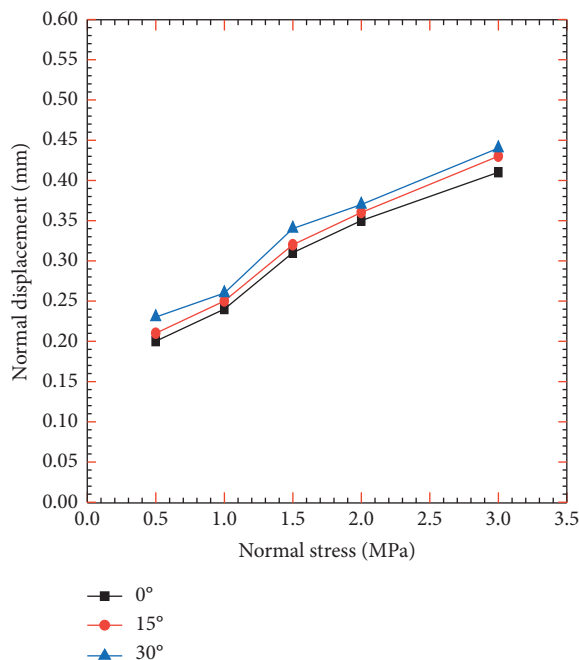


FIGURE 7: Normal displacement of the rock specimens.

3.1.2. Tangential Deformation of the Rock Specimens. Under five different levels of normal stress, the curves of the tangential displacement of the specimens are shown in Figure 8. The peak tangential displacements of these rock specimens are shown in Table 4.

As shown in Figure 8(a) and Table 4, when the undulation angle of the joints is 0°, the peak tangential displacement is 1.95 mm under a normal stress of 0.5 MPa and 2.86 mm under a normal stress of 3.0 MPa. As shown in Figure 8(b) and Table 4, when the undulation angle of the joints is 15°, the peak tangential displacement is 1.89 mm under a normal stress of 0.5 MPa and 2.56 mm under a normal stress of 3.0 MPa. As shown in Figure 8(c) and Table 4, when the undulation angle of the joints is 30°, the peak tangential displacement is 1.84 mm under a normal stress of 0.5 MPa and 2.48 mm under a normal stress of 3.0 MPa. To sum up, it can be seen from the data shown in Table 4 and the curve shown in Figure 8 that, for the NTJRM with the same joint surface morphology, the larger the normal stress applied during the test, the larger the peak tangential displacement of the rock mass. Under the same normal stress, the larger the undulation angle of the serrated joints, the smaller the peak tangential displacement. It can be

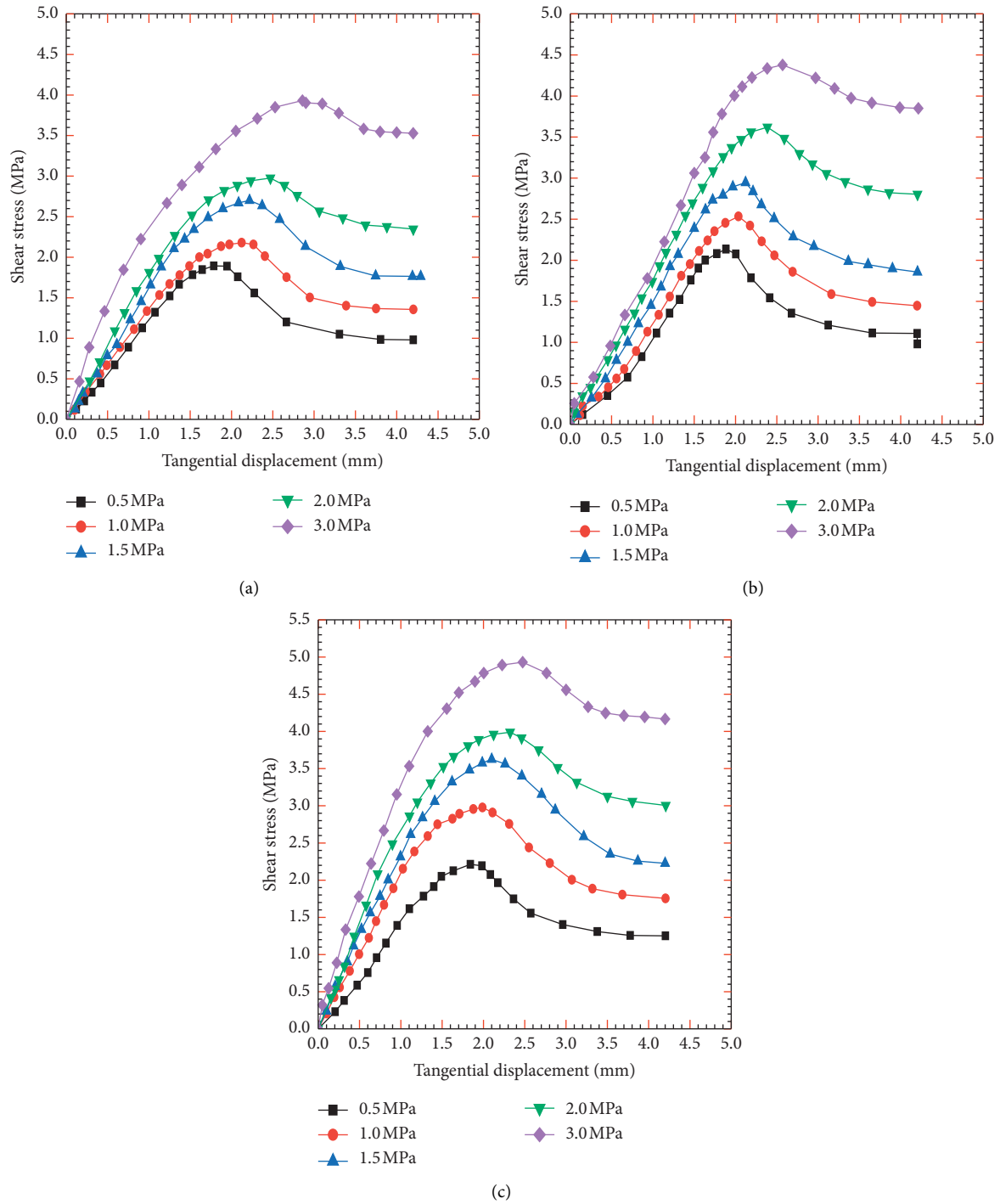


FIGURE 8: The curves of tangential deformation of the rock specimens (a) when the undulation angle is 0°, (b) when the undulation angle is 15°, (c) and when the undulation angle is 30°.

TABLE 4: The peak tangential displacement of rock specimens, unit: mm.

Undulation angle	Normal stress (MPa)				
	0.5	1.0	1.5	2.0	3.0
0°	1.95	2.12	2.22	2.47	2.86
15°	1.89	2.05	2.12	2.39	2.57
30°	1.84	1.99	2.01	2.32	2.48

seen that the peak tangential displacement increases with the increase of normal stress level. In addition, it can be seen from Figure 8 that the curves of tangential deformation of an NTJRM can be divided into four stages. In the first stage, the curve is slightly convex downward and the tangential stress increases rapidly with the increase of tangential displacement. In this stage, the surface of the joints appears gradually, and the folds begin to appear. In the second stage, the curve is approximately a straight line, and the tangential stress increases rapidly with the increase of tangential displacement. In the third stage, the curve is convex upward, and the tangential stress increases with the increase of tangential displacement, but the rate of increase of tangential stress is obviously lower than that of the two preceding stages. This stage exhibits the unstable extension of the new joint surface, which lasts until the rock bridge breaks. In the fourth stage, the curve is also convex downward, and the tangential stress first decreases with the increase of tangential displacement and finally tends to maintain residual strength.

3.1.3. Shear Dilatancy Deformation of the Rock Specimens.

The shear dilatancy curve of the discontinuous jointed rock mass with the undulation angles of 0° , 15° , and 30° under the five levels of normal stress is shown in Figure 9. Under a normal stress of 0.5 MPa or 1.0 MPa, the curve of shear expansion of NTJRM decreases with the increase of tangential displacement. This indicates that, under the action of tangential stress, the nonthrough jointed rock can overcome the suppression of normal stress and make the normal displacement decrease gradually. When the curve of shear expansion is below the abscissa, i.e., when the normal displacement is less than zero, under the action of shear force the NTJRM completely overcomes the action of normal stress.

When the normal stress is 1.5 MPa, 2.0 MPa, and 3.0 MPa, the curve of shear expansion of the NTJRM decreases gradually with the increase of tangential displacement. This also indicates that, under the action of tangential stress, the NTJRM overcomes the inhibition of normal stress and makes the normal displacement of the rock mass decrease gradually. However, the curves of shear expansion are all above the abscissa; that is, the normal displacement is greater than zero, which indicates that under the action of shear force the NTJRM cannot overcome the normal stress completely. By observing the curves of normal displacement and tangential displacement under various normal stress tests, it is found that the cracks formed in NTJRM are larger when normal stress is 0.5 MPa or 1.0 MPa, but are smaller when normal stress is 1.5 MPa, 2.0 MPa, or 3.0 MPa.

3.2. Strength Characteristics of the Rock Specimens during the Test. During the direct shear test of the NTJRM, the failure modes of the joint ends and rock bridges are observed, and the shear forces and corresponding tangential displacements during the failure are recorded. The internal system of the rock testing machine automatically recorded the curve of shear stress and shear displacement over time. And the

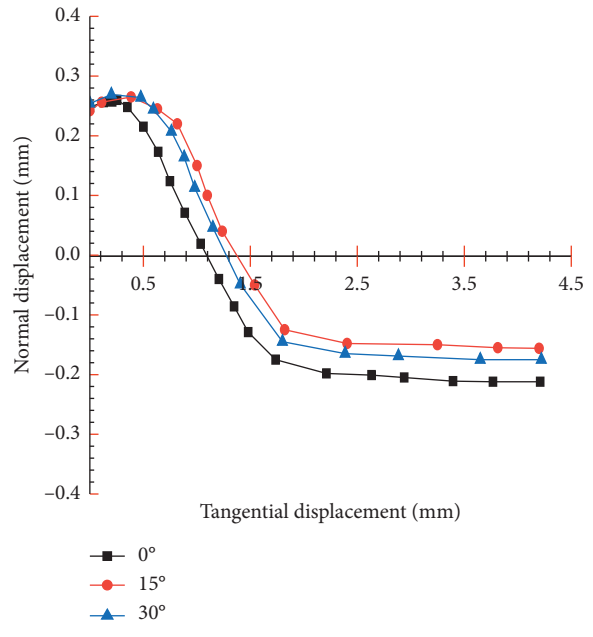
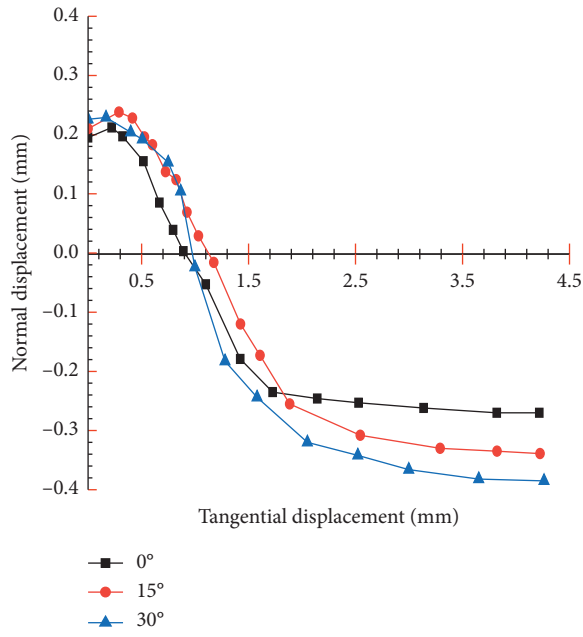
external monitoring system recorded the time when the initial crack occurs. After the shear test, the shear stress and shear displacement recorded by the internal test system were found according to the time of initial crack generation provided by the external monitoring system. Then the initial crack strength of NTJRM can be determined according to the form of the tangential deformation curve. The initial fracture strength, peak strength, and residual strength of the NTJRM with three different relief angles of joints are presented in Tables 5–7.

3.2.1. The Peak Strength of the Rock Specimens. The peak strength of the NTJRM with serrated joints with undulation angles of 0° , 15° , and 30° is shown in Table 8 and Figure 10. It can be observed that the shear strength of the rock mass containing noncontinuous joints with the same joint surface morphology (the same undulation angle of joints) increases with the increase of normal stress. In addition, under the same normal stress, the shear strength of the NTJRM increases with the increase of the undulation angle of the serrated joints.

3.2.2. Initial Fracture Strength of the Rock Specimens. The data of the initial fracture strength of the rock mass under different normal stresses are sorted out to obtain the curve shown in Figure 11.

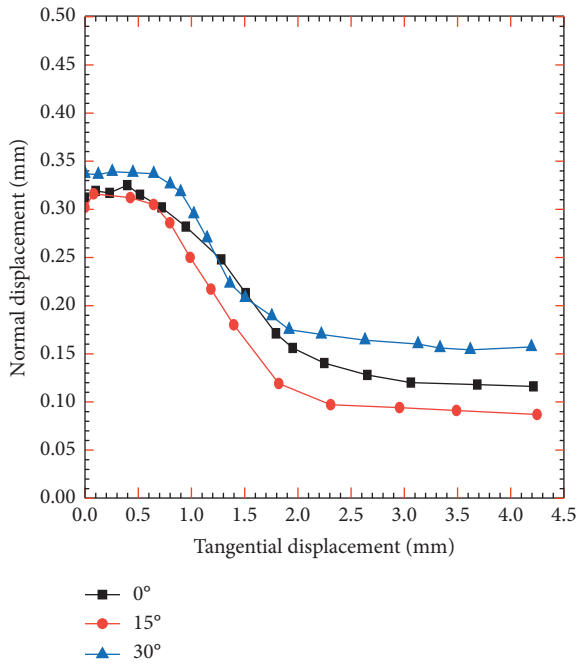
From Figures 10 and 11, it can be seen that the change trend of the initial fracture strength of the NTJRM with three different surface morphologies under different normal stresses is the same as that of the peak strength. When the joint surface morphology of all rock specimens was set to be the same in the test, the initial fracture strength increased with the increase of normal stress. When the normal stress was controlled to be consistent in the test, the initial fracture strength increased with the increase of the undulation angle of the serrated joints. According to Tables 5–7 and Figure 11, it can be observed that, under different normal stresses, the percentage of initial fracture strength and peak strength of the NTJRM is between 67.92% and 70.03% when the undulation angle is 0° . Additionally, the percentage ranges from 69.91% to 70.30% when the undulation angle is 15° and from 71.49% to 72.85% when the undulation angle is 30° . From the above it can be seen that the ratio of the initial fracture strength to peak strength of the NTJRM with the three kinds of serrated joint surfaces is between 65%–75%.

3.2.3. Residual Strength of the Rock Specimens. The residual strengths of NTJRM containing serrated joints with relief angles of 0° , 15° , and 30° are shown in Tables 5–7. They are then sorted out and plotted in Figure 12. By comparing Figures 11 and 12, it can be seen that in this test the variation trend of the residual strength of the NTJRM with three kinds of surface morphologies under different normal stresses is the same as that of the peak strength. By comparing the experimental data, it can be found that, for the NTJRM with the same joint surface morphology, the residual strength increases with the increase of normal stress. Additionally,

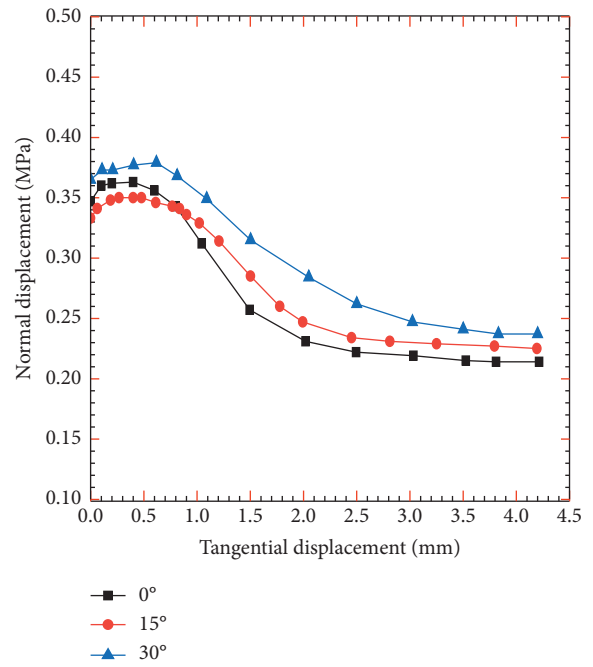


(a)

(b)

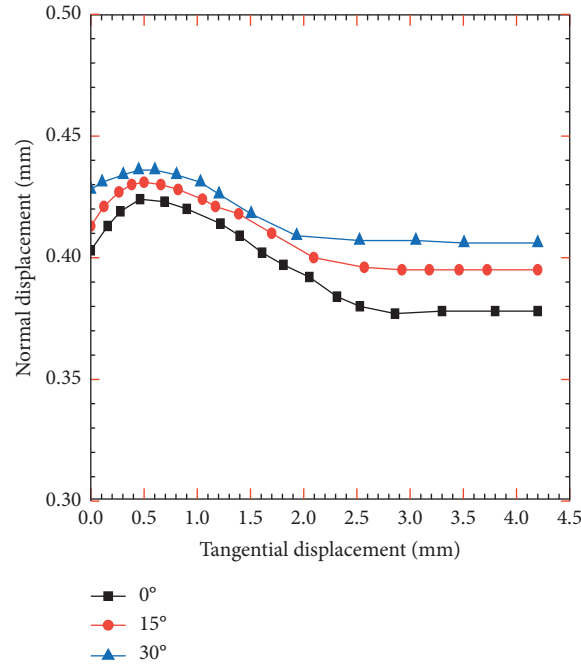


(c)



(d)

FIGURE 9: Continued.



(e)

FIGURE 9: The shear dilatancy curve of the rock mass specimens (a) when the normal stress is 0.5 MPa, (b) when the normal stress is 1.0 MPa, (c) when the normal stress is 1.5 MPa, (d) when the normal stress is 2.0 MPa, and (e) when the normal stress is 3.0 MPa.

TABLE 5: Strength of some rock specimens ($\alpha = 0^\circ$).

Normal stress (MPa)	Peak strength τ_m (MPa)	Initial fracture strength		Residual strength	
		τ_0 (MPa)	Ratio to peak strength (%)	τ_r (MPa)	Ratio to peak strength (%)
0.5	1.89	1.32	69.88	0.98	51.88
1.0	2.18	1.53	70.03	1.36	62.23
1.5	2.70	1.88	69.63	1.76	65.26
2.0	2.98	2.03	68.24	2.35	78.86
3.0	3.93	2.67	67.92	3.53	89.75

TABLE 6: Strength of some rock specimens ($\alpha = 15^\circ$).

Normal stress (MPa)	Peak strength τ_m (MPa)	Initial fracture strength		Residual strength	
		τ_0 (MPa)	Ratio to peak intensity (%)	τ_r (MPa)	Ratio to peak intensity (%)
0.5	2.13	1.52	71.23	1.11	52.01
1.0	2.53	1.81	71.30	1.45	57.05
1.5	2.95	2.07	70.29	1.86	63.02
2.0	3.62	2.54	70.22	2.80	77.43
3.0	4.38	3.06	69.91	3.85	87.94

TABLE 7: Strength of some of the specimens ($\alpha = 30^\circ$).

Normal stress (MPa)	Peak strength τ_m (MPa)	Initial fracture strength		Residual strength	
		τ_0 (MPa)	Ratio to peak intensity (%)	τ_r (MPa)	Ratio to peak intensity (%)
0.5	2.21	1.61	72.85	1.25	56.56
1.0	2.98	2.15	72.25	1.75	58.92
1.5	3.63	2.61	72.06	2.23	61.38
2.0	3.99	2.86	71.72	3.00	75.31
3.0	4.93	3.53	71.49	4.17	84.49

TABLE 8: The peak strength of all rock mass specimens, unit: MPa.

Normal stress (MPa)	Undulation angle		
	0°	15°	30°
0.5	1.89	2.13	2.19
1.0	2.18	2.53	2.98
1.5	2.70	2.95	3.63
2.0	2.98	3.62	3.99
3.0	3.93	4.38	4.93

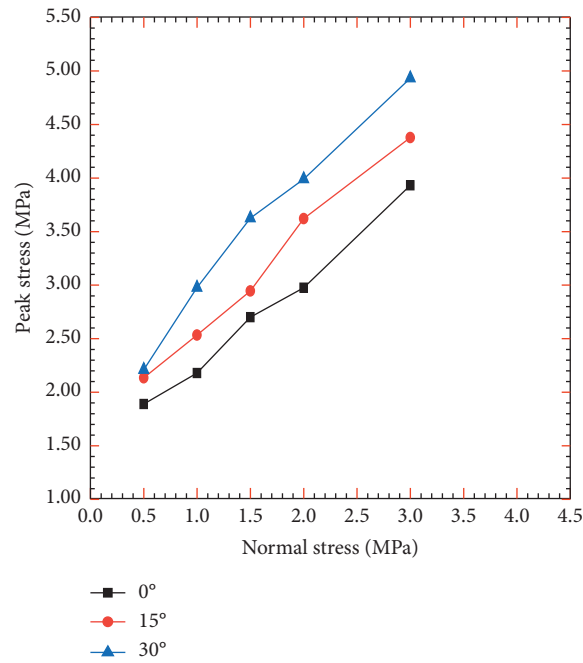


FIGURE 10: The peak strength of all rock mass specimens.

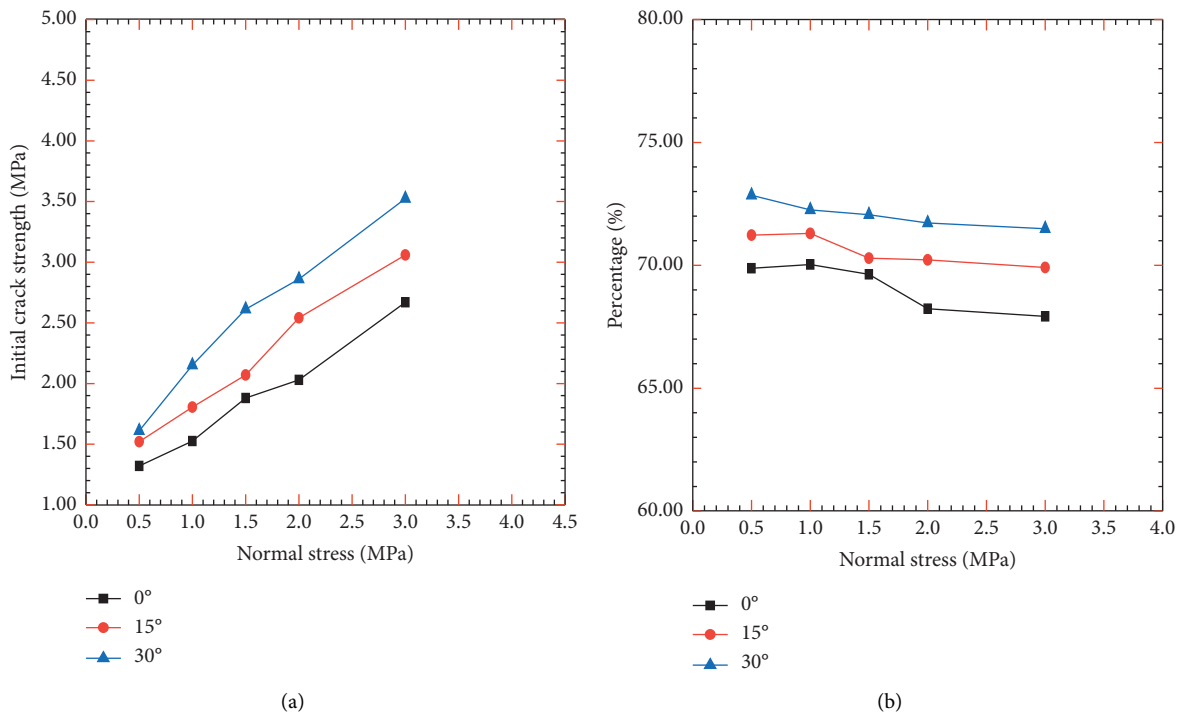


FIGURE 11: The initial crack strength of the specimens. (a) Initial fracture strength of specimens. (b) Ratio of the initial crack strength to peak strength.

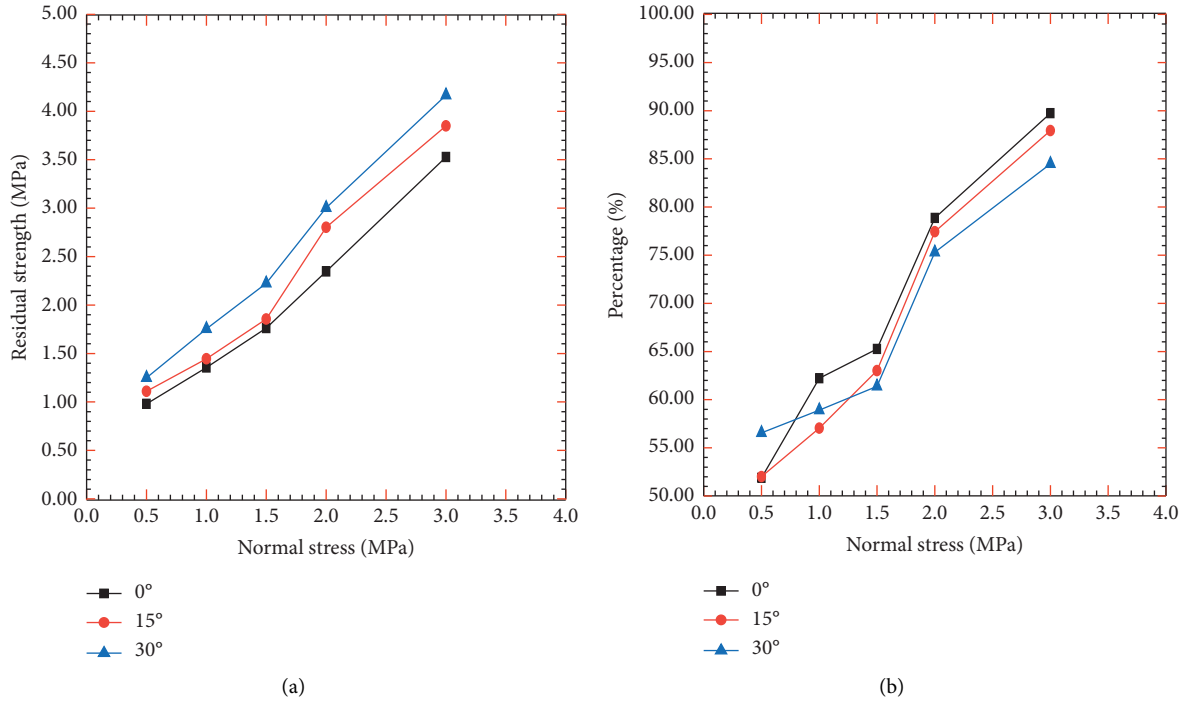


FIGURE 12: The residual strength of the NTJRM specimens. (a) Residual strength of specimens. (b) Ratio of the residual strength to peak strength.

under the same normal stress, the residual strength increases with the increase of the relief angle of the serrated joint. According to Tables 5–7 and Figure 12, under different normal stresses, the percentage of residual strength and peak strength of NTJRM is between 51.88% and 89.75% when the relief angle is 0°. Additionally, the percentage ranges from 52.01% to 87.94% when the undulation angle is 15° and from 56.56% to 84.49% when the undulation angle is 30°. Therefore, the ratio of residual strength to peak strength of discontinuous jointed rock mass specimens with three kinds of serrated joint surfaces is between 50% and 90%.

3.3. The Failure Modes of the Rock Bridges. The failure modes of rock mass with discontinuous joints can be divided into four types: TTTS, TSSS, TTTN, and SSSS [32]. Two failure modes, TTTS and TSSS, were observed in the tests. The failure mode is called TTTS mode in which the initial failure, expansion, and coalescence failure of the rock mass are all caused by the tensile action and the final coalescence surface is formed due to the shear action. The failure mode is called TSSS mode in which the initial failure of rock mass is caused by tensile action, while the expansion and final failure are caused by shear action, and the final coalescence surface is formed due to the shear action [32]. It can be found in the direct shear test under the normal stress of 1.0 MPa, the failure mode of rock specimens with joint undulation angle of 0° is TTTS mode, as shown in Figure 13. In the direct shear test under the normal stress of 1.0 MPa, the failure mode of rock specimens with joint undulation angle of 30° is TSSS mode, as

shown in Figure 14, and when the normal stress is 1.5 MPa, the failure mode is also TSSS, as shown in Figure 15.

All the failure modes of rock specimens with different joint morphologies under different normal stresses are shown in Table 9. It can be seen from Table 9 that the failure modes of rock specimens with nonthrough joints in this test are TTTS and TSSS. The details are as follows:

- (1) Under five levels of normal stress, the failure mode of rock mass specimens with undulation angle of 0° is TTTS mode.
- (2) The failure mode of rock mass specimens with undulation angle of 15° is TTTS mode when the normal stress is less than 2.0 MPa, but it is TSSS mode when the normal stress is greater than or equal to 2.0 MPa.
- (3) The failure mode of rock mass specimens with undulation angle of 30° is TTTS mode when the normal stress is less than 1.0 MPa, but it is TSSS mode when the normal stress is greater than or equal to 1.0 MPa.

3.4. Analysis of Shear Strength Parameters. The peak shear strength of the three kinds of NTJRM specimens presented in Table 5 is plotted in Figure 16. According to Figure 16, the shear strength parameters of the rock mass specimens can be obtained by fitting, as shown in Table 10. It can be seen from Table 10 that the shear parameters cohesion and internal friction angle of rock mass with nonthrough joints increase with the increase of undulation angle of serrated joints.

In addition, the shear strength parameters of the specimens calculated according to Jennings' method [35] are given by

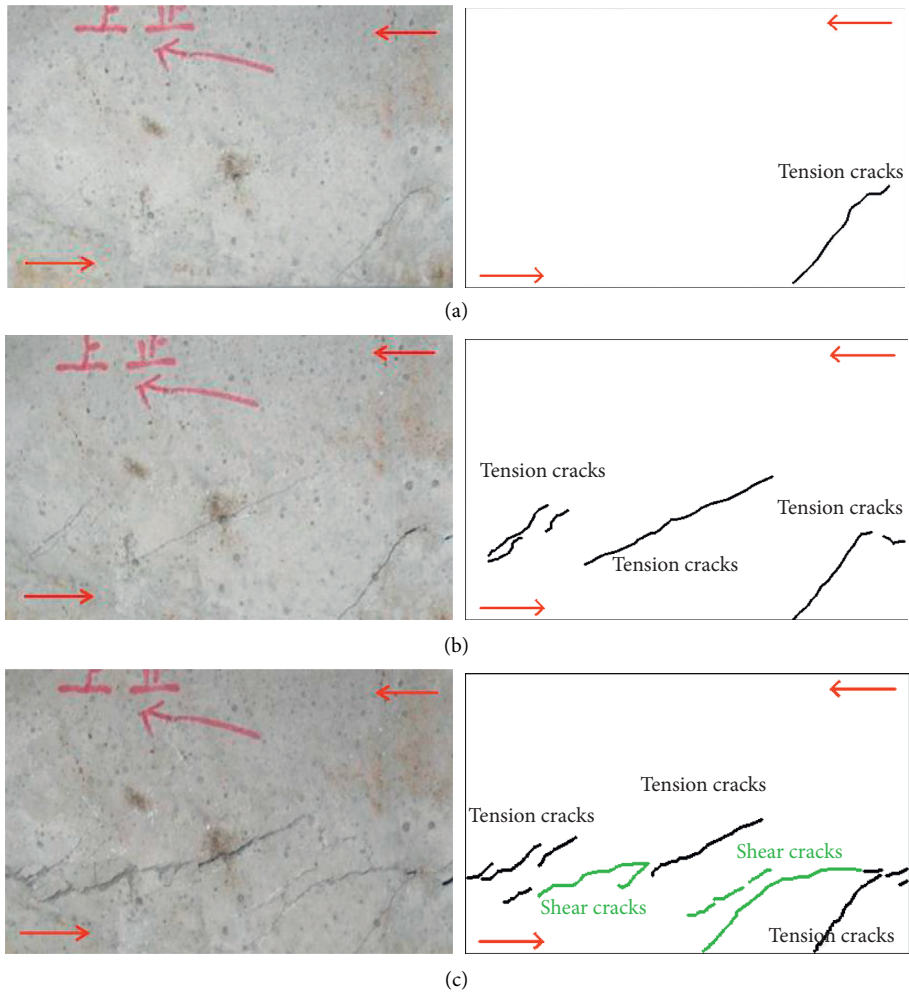


FIGURE 13: The failure modes of some of the rock specimens ($\sigma = 1.0 \text{ MPa}$, $\alpha = 0^\circ$). (a) Initial failure. (b) Extended destruction. (c) Transfixion failure.

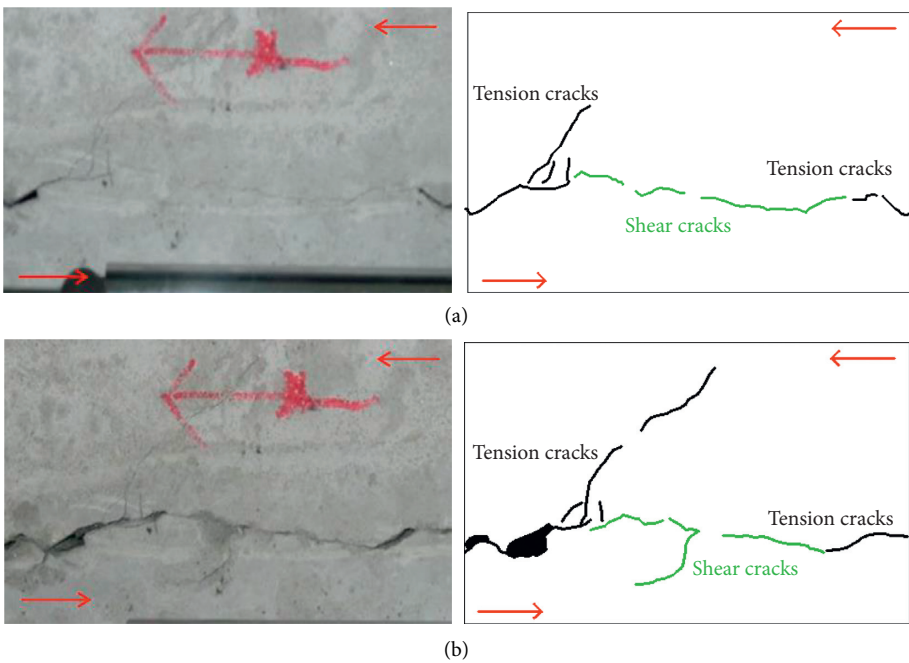


FIGURE 14: Continued.

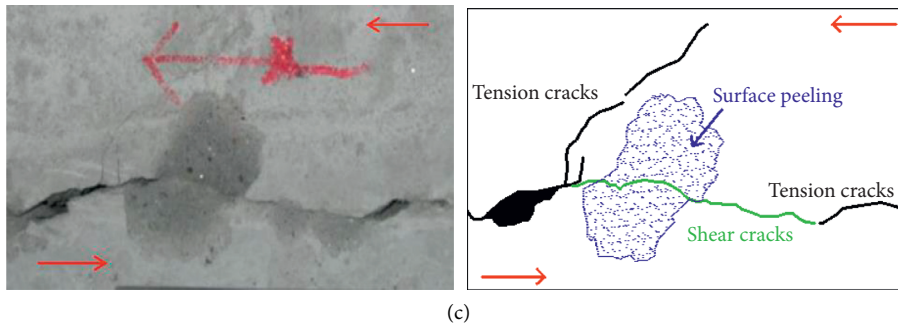


FIGURE 14: The failure modes of some of the rock specimens ($\sigma=1.0$ MPa, $\alpha=30^\circ$). (a) Initial damage. (b) Extended destruction. (c) Transfixion failure.

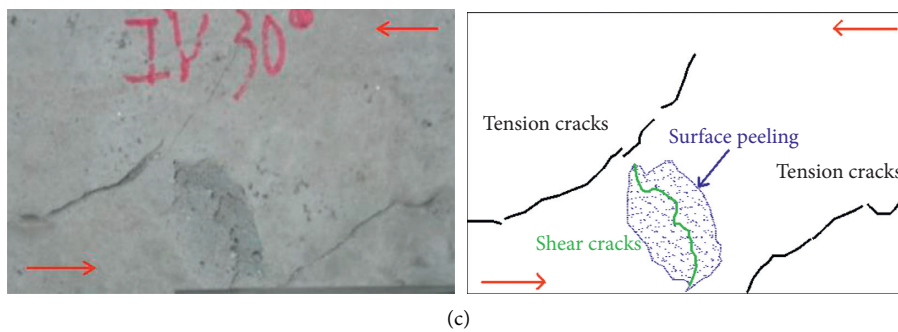
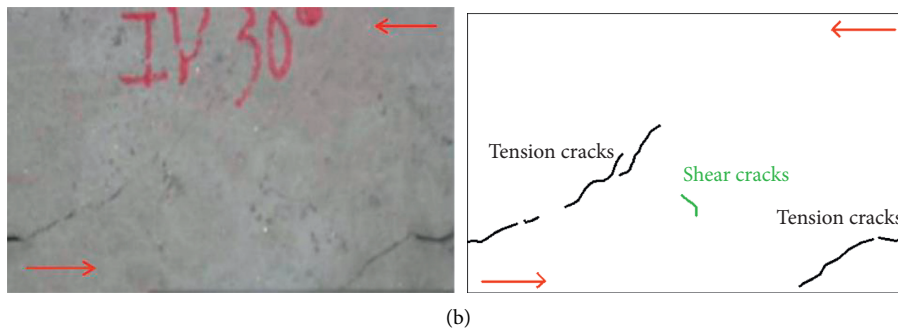
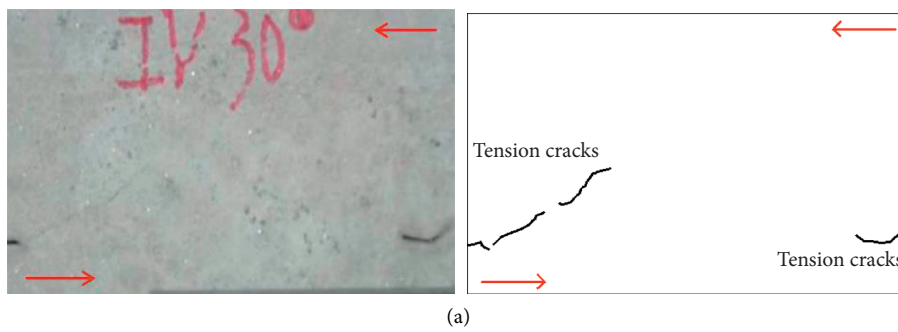


FIGURE 15: The failure modes of some of the rock specimens ($\sigma=1.5$ MPa, $\alpha=30^\circ$). (a) Initial failure. (b) Extended destruction. (c) Transfixion failure.

TABLE 9: The failure modes of all the rock mass specimens.

Undulation angle of joints	Normal stress (MPa)				
	0.5	1.0	1.5	2.0	3.0
0°	TTTS	TTTS	TTTS	TTTS	TTTS
15°	TTTS	TTTS	TTTS	TSSS	TSSS
30°	TTTS	TSSS	TSSS	TSSS	TSSS

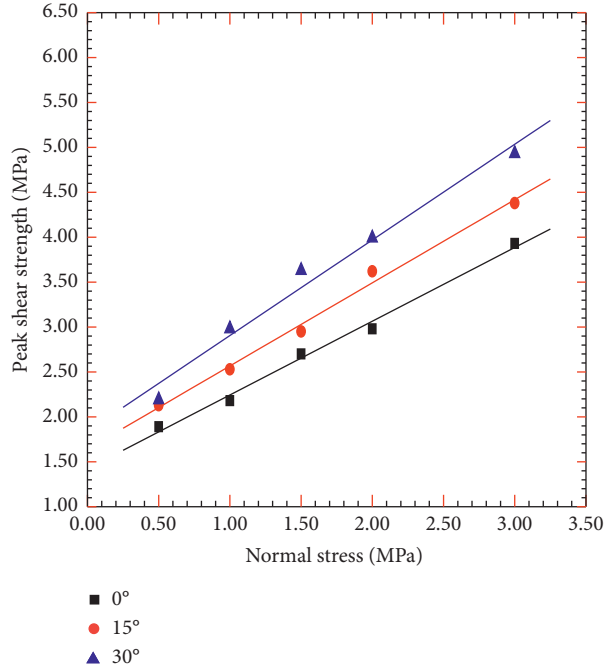


FIGURE 16: Peak shear strength of the rock mass specimens.

TABLE 10: Shear parameters results obtained through tests and calculations.

The angle of joint relief	The fitted value of the test results	
	Cohesion (MPa)	Angle of internal friction (°)
0°	1.42	39.4
15°	1.64	42.8
30°	1.84	46.8

TABLE 11: Shear parameters results obtained through Jennings.

The angle of joint relief	The fitted value of the test results	
	Cohesion (MPa)	Angle of internal friction (°)
0°	2.14	37.0
15°	2.14	44.8
30°	2.14	54.8

$$\begin{aligned}
 c &= kc_j + (1 - k)c_b, \\
 \tan \phi &= k \tan \phi_j + (1 - k)\tan \phi_b, \\
 \varphi &= \arctan \varphi,
 \end{aligned}
 \tag{1}$$

where c is cohesion of rock mass with discontinuous joints, φ_j is internal friction angle, k is joint connectivity, c_j is joint

cohesion of rock mass with discontinuous joints, φ_j is internal friction angle of joint, c_b is cohesion of rock bridge, and φ_b is internal friction angle of rock bridge.

The parameters of shear strength of the NTJRM specimens calculated by Jennings' method are listed in Table 11.

It can be seen from Tables 10 and 11 that the cohesion calculated by Jennings' method is greater than by test fitting.

Except the fluctuation angle 0° , the internal friction angle calculated by Jennings' method is larger than that fitted by experiment. In a word, the shear strength of the rock mass with discontinuous joints calculated by Jennings' method will be greater than the actual experimental results.

4. Conclusions

Direct shear tests of nonthrough jointed rock masses with three kinds of morphologies joints are carried out under five levels of normal stress. The main conclusions are as follows:

- (1) Under the same normal stress, the normal displacement and the peak tangential displacement increase with the increase of undulation angle.
- (2) The joint morphology has influence on the strength characteristics of rock mass with discontinuous joints. Under the same normal stress, the shear strength, initial crack strength, and residual strength of rock mass with nonthrough joints increase with the increase of undulation angle.
- (3) The failure mode of rock mass with discontinuous joints is related to the joint morphology and normal stress. Under the same normal stress, the rock mass with low undulation angle is prone to failure in TTTS mode, and the rock mass with high undulation angle is prone to failure in TSSS mode.
- (4) The shear parameters calculated by Jennings' method are larger than those fitted by experiments. The shear strength of the rock mass with discontinuous joints calculated by Jennings' method will be greater than the actual experimental results.

Data Availability

The data which support the findings of this study are available within this article.

Conflicts of Interest

The authors declare that they do not have any commercial or associative interest that represents conflicts of interest in connection with this work.

Acknowledgments

This work was supported by the National Natural Science Foundation Project (11562005), the First Class Discipline Construction Project of Civil Engineering in Guizhou Province (QYNYL [2017] 0013), the Natural Science Foundation of Guizhou Province (qkeheji [2019] No. 1057), and Major Scientific and Technological Projects of Guizhou Province (Qiankehe major special project [2018] 3011).


References

- [1] H. K. Singh and A. Basu, "A comparison between the shear behavior of "real" natural rock discontinuities and their replicas," *Rock Mechanics and Rock Engineering*, vol. 51, no. 1, pp. 329–340, 2018.
- [2] J. B. Zhu, H. Li, and J. H. Deng, "A one-dimensional elastoplastic model for capturing the nonlinear shear behaviour of joints with triangular asperities based on direct shear tests," *Rock Mechanics and Rock Engineering*, vol. 52, no. 6, pp. 1671–1687, 2018.
- [3] K. Zhang, Y. Chen, W. Fan, X. Liu, H. Luan, and J. Xie, "Influence of intermittent artificial crack density on shear fracturing and fractal behavior of rock bridges: experimental and numerical studies," *Rock Mechanics and Rock Engineering*, vol. 53, no. 2, pp. 553–568, 2019.
- [4] Y. T. Wang, X. P. Zhou, and Y. D. Shou, "The modeling of crack propagation and coalescence in rocks under uniaxial compression using the novel conjugated bond-based peridynamics," *International Journal of Rock Mechanical and Sciences*, vol. 128, 2017.
- [5] Z. B. Guo, J. Y. Fan, F. N. Wang, H. B. Zhou, and W. Li, "Geomechanical model experiment study on deformation and failure mechanism of the mountain tunnel in layered jointed rock mass," *Advances in Civil Engineering*, vol. 2021, Article ID 6645124, 2021.
- [6] Q. B. Lin, P. Cao, J. J. Meng, R. H. Cao, and Z. Y. Zhao, "Strength and failure characteristics of jointed rock mass with double circular holes under uniaxial compression: insights from discrete element method modelling," *Theoretical and Applied Fracture Mechanics*, vol. 109, Article ID 102692, 2020.
- [7] Q. B. Lin, P. Cao, Y. Z. Liu, R. H. Cao, and J. T. Lia, "Mechanical behaviour of a jointed rock mass with a circular hole under compression-shear loading: experimental and numerical studies," *Theoretical and Applied Fracture Mechanics*, vol. 114, Article ID 102998, 2021.
- [8] F. Xiang, Z. J. Yang, and K. Li, "Effects of the lining structure on mechanical and fracturing behaviors of four-arc shaped tunnels in a jointed rock mass under uniaxial compression," *Theoretical and Applied Fracture Mechanics*, vol. 112, Article ID 102887, 2021.
- [9] A. Bobet and H. H. Einstein, "Fracture coalescence in rock-type materials under uniaxial and biaxial compression," *International Journal of Rock Mechanics and Mining Sciences*, vol. 35, no. 7, pp. 863–888, 1998.
- [10] R. H. C. Wong and K. T. Chau, "Crack coalescence in a rock-like material containing two cracks," *International Journal of Rock Mechanics and Mining Sciences*, vol. 35, no. 2, pp. 147–164, 1998.
- [11] S. P. Morgan and H. H. Einstein, "Cracking processes affected by bedding planes in opalinus shale with flaw pairs," *Engineering Fracture Mechanics*, vol. 176, pp. 213–234, 2017.
- [12] M. Alneasan, M. Behnia, and R. Bagherpour, "Analytical investigations of interface crack growth between two dissimilar rock layers under compression and tension," *Engineering Geology*, vol. 259, Article ID 105188, 2019.
- [13] D.-J. Wang, H. Tang, D. Elsworth, and C. Wang, "Fracture evolution in artificial bedded rocks containing a structural flaw under uniaxial compression," *Engineering Geology*, vol. 250, pp. 130–141, 2019.
- [14] R. H. Cao, H. Lin, Q. B. Lin, and J. Meng, "Failure mechanism of non-persistent jointed rock-like specimens under uniaxial loading: laboratory testing," *International Journal of Rock Mechanics and Mining Sciences*, vol. 132, pp. 147–164, Article ID 104341, 2020.
- [15] R. H. Cao, R. B. Yao, T. Hu, C. S. Wang, H. Li, and J. J. Meng, "Failure and mechanical behavior of transversely isotropic rock under compression-shear tests: laboratory testing and numerical simulation," *Engineering Fracture Mechanics*, vol. 2020, Article ID 107389, 2020.

- [16] C. Y. Zhang, Y. X. Wang, and T. T. Jiang, "The propagation mechanism of an oblique straight crack in a rock sample and the effect of osmotic pressure under in-plane biaxial compression," *Arabian Journal of Geosciences*, vol. 13, no. 15, Article ID 736, 2020.
- [17] Q. B. Lin, P. Cao, G. P. Wen, J. J. Meng, R. H. Cao, and Z. Y. Zhao, "Crack coalescence in rock-like specimens with two dissimilar layers and pre-existing double parallel joints under uniaxial compression," *International Journal of Rock Mechanics and Mining Sciences*, vol. 139, Article ID 104621, 2021.
- [18] Q. B. Lin, P. Cao, R. H. Cao, H. Lin, and J. J. Meng, "Mechanical behavior around double circular openings in a jointed rock mass under uniaxial compression," *Archives of Civil and Mechanical Engineering*, vol. 20, 2020.
- [19] X. Fan, X. Jiang, Y. Liu, H. Lin, and Z. He, "Local stress distribution and evolution surrounding flaw and opening within rock block under uniaxial compression," *Theoretical and Applied Fracture Mechanics*, vol. 112, Article ID 102941, 2021.
- [20] G. Wang, Y. Zhang, Y. Jiang, S. Wang, and W. Jing, "Macromicro failure mechanisms and damage modeling of a bolted rock joint," *Advances in Materials Science and Engineering*, vol. 2017, Article ID 1627103, 2017.
- [21] C. Zhao, Y. M. Zhou, C. F. Zhao, and C. Bao, "Cracking processes and coalescence modes in rock-like specimens with two parallel pre-existing cracks," *Rock Mechanics and Rock Engineering*, vol. 51, no. 11, pp. 3377–3393, 2018.
- [22] E. Z. Lajtai, "Strength of discontinuous rocks in direct shear," *Géotechnique*, vol. 19, no. 2, pp. 218–233, 1969.
- [23] E. Z. Lajtai, "Shear strength of weakness planes in rock," *International Journal of rock mechanics and mining sciences abstract*, vol. 6, no. 7, pp. 499–515, 1969.
- [24] G. Q. Chen, J. C. Wang, W. Wang, F. Y. Luo, and Z. B. Li, "Failure characteristics of rock mass with intermittent joints of different connecting rates under direct shear test," *Journal of Engineering Geology*, vol. 25, no. 2, pp. 322–329, 2017.
- [25] C. A. Qin, G. Q. Chen, H. J. Zheng, and P. Tang, "Failure of rock bridge at the end and fracture condition under direct shear tests," *Rock and Soil Mechanics*, vol. 25, no. 2, pp. 642–652, 2019.
- [26] S. Heng, X. Z. Li, X. Liu, and X. D. Zhang, "Study on the propagation mechanisms of shale fractures under direct shear conditions," *Journal of rock mechanics and engineering*, vol. 25, no. 2, pp. 2438–2450, 2019.
- [27] W. Zhao, R. Huang, and M. Yan, "Study on the deformation and failure modes of rock mass containing concentrated parallel joints with different spacing and number based on smooth joint model in PFC," *Arabian Journal of Geosciences*, vol. 8, no. 10, pp. 7887–7897, 2015.
- [28] P. Wang, T. Yang, T. Xu, M. Cai, and C. Li, "Numerical analysis on scale effect of elasticity, strength and failure patterns of jointed rock masses," *Geosciences Journal*, vol. 20, no. 4, pp. 539–549, 2016.
- [29] Q. Z. Chen, Y. S. Zhang, Y. M. Liu, W. Wang, and K. Cao, "Influence of joint undulation angle on mechanical properties of non-penetrated joint rock mass," *Journal of Underground Space and Engineering*, vol. 16, no. 2, pp. 351–358, 2020.
- [30] P. Wang, F. Ren, and M. Cai, "Influence of joint geometry and roughness on the multiscale shear behaviour of fractured rock mass using particle flow code," *Arabian Journal of Geosciences*, vol. 13, no. 4, p. 165, 2020.
- [31] M. H. Ma, F. H. Ren, and W. S. Liu, "Experimental investigation on shear failure mechanism of rock mass with intermittent joints," *Advances in Civil Engineering*, vol. 2021, Article ID 6623148, 10 pages, 2021.
- [32] Y. M. Liu and C. C. Xia, "Weakening mechanism of mechanical behaviors and failure model of rock mass containing discontinuous joints under direct shear condition," *Rock and Soil Mechanics*, vol. 31, no. 3, pp. 695–701, 2010.
- [33] Y. M. Liu, J. Liu, and C. C. Xia, "Research on strength behavior of rock mass containing discontinuous joints by direct shear test under different joint surface morphologies," *Rock and Soil Mechanics*, vol. 35, no. 5, Article ID 12691274, 2014.
- [34] Q. Z. Chen, Y. M. Liu, and S. Y. Pu, "Strength characteristics of nonpenetrating joint rock mass under different shear conditions," *Advances in Civil Engineering*, vol. 2020, Article ID 3579725, 13 pages, 2020.
- [35] H. H. Einstein, D. Veneziano, G. B. Baecher, and K. J. O'Reilly, "The effect of discontinuity persistence on rock slope stability," *International Journal of Rock Mechanics and Mining Science & Geomechanics Abstracts*, vol. 20, no. 5, pp. 227–236, 1983.

Research Article

Experimental Investigation on Effects of Bacterial Concentration, Crack Inclination Angle, Crack Roughness, and Crack Opening on the Fracture Permeability Using Microbially Induced Carbonate Precipitation

Yulin Zou,^{1,2} Hao Bai ,³ Fan Shen,⁴ Hong Xu,⁵ and Yundong Shou ^{5,6}

¹Sichuan Railway Investment Group Co., Ltd., Chengdu 100036, China

²Sichuan Yanjiang Panning Expressway Co., Ltd., Panzhihua 617000, China

³Sichuan Expressway Construction & Development Group Co., Ltd., Chengdu, China

⁴School of Civil Engineering, Wuhan University, Wuhan 430072, China

⁵National Breeding Base of Technology and Innovation Platform for Automatic-Monitoring of Geologic Hazards (Chongqing Engineering Research Center of Automatic Monitoring for Geological Hazards), Chongqing 400042, China

⁶Guizhou Provincial Key Laboratory of Rock and Soil Mechanics and Engineering Safety, Guiyang 550025, China

Correspondence should be addressed to Hao Bai; secdbh@126.com and Yundong Shou; syd6188@163.com

Received 25 April 2021; Accepted 23 June 2021; Published 7 July 2021

Academic Editor: Yunteng Wang

Copyright © 2021 Yulin Zou et al. This is an open access article distributed under the Creative Commons Attribution License, which permits unrestricted use, distribution, and reproduction in any medium, provided the original work is properly cited.

Uncontrollable leakage has significant effects on the safety of fractured rock mass, and microbially induced carbonate precipitation (MICP) is an effective way to control the seepage. In this study, four sets of seepage experiments are conducted on transparent rock-like specimens containing MICP filled single cracks to investigate the effects of bacterial concentration, crack inclination angle, crack roughness, and crack opening on fracture permeability. The experimental results show that calcium carbonate precipitation is produced when *Sporosarcina pasteurii* and cementing fluid are injected into the cracks, which can seal the cracks and reduce the permeability of the cracks. Moreover, the calcium carbonate produced by *Sporosarcina pasteurii* increases with increasing bacterial concentration. Furthermore, the fracture permeability of the MICP filled crack increases first and then decreases with increasing inclination, roughness, and opening of cracks. The experimental results provide a better understanding of the influence of different construction conditions on fracture permeability when the MICP technology is applied in rock engineering.

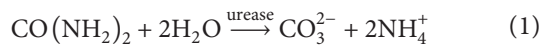
1. Introduction

As an important part of engineering rock mass, cracks affect not only the integrity and stability of rock mass, but also cause the seepage disaster in rock engineering [1–12]. Cracks in rock mass provide the flow channels for groundwater in rock engineering, which lead to water disasters, and cause huge casualties and property losses [13], such as dam collapse of Malpasset Reservoir in France [14], bank collapse of Vajont Reservoir in Italy [15], instability of Libby abutment in the United States [16], and water inrush from various roadways [17]. Therefore, it is

necessary to strengthen the surrounding rock with fissures in rock engineering.

Cementitious and chemical grouts are commonly employed to improve the permeability strength by sealing the cracks in fractured rock mass [18]. However, those grout materials may contribute risk to environmental or human health by poisoning the groundwater in functional aquifers [19]. In addition, the viscosity of cement grout is high so that the cement grout cannot be injected to intact rock, which has restricted its limitation of application. Moreover, the expensive cost and low life of chemical grouts seriously restrict extension and utilization of the technology [20]. To

overcome those limitations of cementitious and chemical grouts, a new grouting method, microbially induced carbonate precipitation (MICP), has been developed based on microorganisms [21]. The MICP is a novel grouting technology with the advantages of low viscosity, low pressure, and environmental friendliness [22]. *Sporosarcina pasteurii*, which is a common non-pathogenic and aerobic bacterium, is adopted to generate the cementing agent of CaCO_3 to plug the flow paths in fractured rock mass. The MICP process involves a sequence of biochemical reactions that can be divided into two stages. First, *Sporosarcina pasteurii* secretes urease during its growth, and the urea in fissure water is broken down to bicarbonate ions by urease. Second, calcium carbonate precipitation is obtained by the chemical reaction between bicarbonate ions and calcium ions from the calcium salts. Then, the biochemical reaction in the MICP process can be written as follows [23, 24]:



Since the product of the MICP process, CaCO_3 , is a kind of high-strength calcium salts, which is durable in alkaline environments, MICP can be employed in strengthening soil mass. Many scholars have carried out extensive research on MICP strengthening soil mass [24–30], and the results showed that MICP can increase uniaxial compressive strength of soils and can significantly decrease the water permeability of soils. Furthermore, a series of laboratory and field tests on the effect of fractures sealed in rock mass have been conducted using the MICP technology. Ferris et al. [31] applied the MICP technology in porous media, and they found that calcium carbonate can be used as a plugging agent and binder to control the flow of water in rock mass. Cuthbert et al. [32] applied the MICP technology to fractured rock mass through a model experiment and theoretical deduction. The results showed that the permeability of fractured rock mass can be reduced very well, which provide a new idea for crack seepage resistance. Moreover, Phillips et al. [33] used the MICP technology to treat fractured sandstone, and they found that the permeability of the treated samples is decreased by 2 to 4 orders of magnitude, which can be used to mitigate the potential of CO_2 leakage. The experimental results obtained by Bucci et al. [34] showed that the permeability of the cracks in an artificially fractured sandstone specimen is decreased by 80% after the MICP method is used, especially at the top and bottom of the cracks. Mountassir et al. [35] studied the effect of crack width and opening on the filling process of MICP, and the results showed that the treated crack size decreased and the crack permeability is decreased after the MICP method is used. Tobler et al. [36] studied the effect of MICP on sandstone and fractured media, and they found that the permeability of samples treated by MICP is greatly reduced, and the shear resistance of filled cracks is increased. Wu et al. [37, 38] investigated the distribution and filled state of MICP in fissures by means of model experiments, and they

analyzed the permeability of cracks after filling using a numerical simulation. The results showed that calcium carbonate was mainly concentrated near the injection port, and a semiempirical formula was proposed to evaluate the decrease of fissure permeability. Minto et al. [20] investigated the influence of fluid velocity on the distribution of calcium carbonate. They found that calcium carbonate can precipitate in large quantities and the precipitation amount and location can be controlled by the flow rate.

Experimental results showed that microbially induced carbonate precipitation can be successfully applied in grouted cracks to seal the flow paths. However, many external factors, such as bacterial concentration, fracture inclination angle, crack roughness, and fracture aperture, are involved in practical engineering, which have not been studied. Therefore, this experiment studies these factors through the design of grouting device and processing of prefabricated crack samples, aiming to provide some reference for practical engineering.

2. *Sporosarcina pasteurii*

2.1. Bacterial Culture. In this paper, *Sporosarcina pasteurii* purchased from American Type Culture Collection (No. ATCC 11859) are selected as the bacteria to secrete urease. They are aerobic Gram-positive bacteria which grow in alkaline environment and show optimal growth at $25^\circ\text{C}\sim 37^\circ\text{C}$. Bacteria are cultured on CASO + urea medium; the component and dosage of the culture medium are shown in Table 1. The culture medium is sterilized at 121.3°C for 20 minutes in a pressure pot, and then after cooling, urea is added to the culture medium by filtration sterilization. In addition, the pH (pondus hydrogenii) value of the culture medium is adjusted to 7.3 with 1 mol/L NaOH solution during culturing. Finally, the culture medium is incubated at 30°C on an orbital shaker at 200 rpm for approximately 48 h, and then the bacteria can be clearly observed in the medium as shown in Figure 1.

Bacteria absorb or scatter at a specific wavelength, and the concentration of bacteria is proportional to the amount of light absorbed. Therefore, bacterial concentration can be measured through the absorbance (turbidimetry) method. The optical density of bacteria at 600 nm wavelength determined by ultraviolet-visible spectrophotometer is used to measure the concentration of bacteria in present experiment. Figure 2 shows growth curve of bacteria. It can be found from Figure 2 that the optical density of bacteria at 600 nm wavelength grows slowly in 0–3 hours because bacteria need to adapt to the new environment, which leads to the decrease of reproduce. As the bacteria adapt to the new culture medium environment, OD grows rapidly in 3–24 hours and enters logarithmic growth period. Finally, the concentration of bacteria gradually stabilizes in 24–48 hours, and the OD value of bacterial solution gradually stabilizes to 2.25.

The rate of urea hydrolysis caused by urease is termed as the urease activity which can be determined by measuring the change rate of solution electroconductivity [26]. To determine the urease activity of bacterial suspension, 2 ml

TABLE 1: CASO medium components.

Reagent name	Peptone from soymeal (g)	Peptone from casein (g)	Urea (g)	NaCl (g)	Agar (g)	Deionized water (L)
Liquid medium	5	15	20	5	—	1
Solid medium	5	15	20	5	20	1

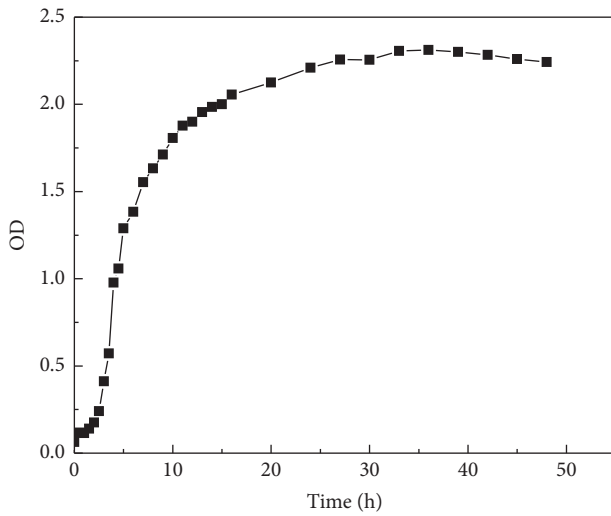
FIGURE 1: The appearance of *Sporosarcina pasteurii* in (a) liquid medium and (b) solid medium.

FIGURE 2: Variations in bacterial concentration with time.

bacterial solution is added to 18 ml 1 mol/L urea solution and the change in electroconductivity is monitored over 5 min as nonionic urea is hydrolyzed producing ionic ammonia. Then, the urease activity can be expressed as

$$k_{\text{urease}} = \frac{10c\Delta E}{\Delta t}, \quad (3)$$

where k_{urease} is the urease activity, ΔE is the change in electroconductivity between measurements, Δt is the time interval between measurements, 10 is dilution factor, and c is the coefficient between the change of electroconductivity and the amount of urea hydrolysis [25].

Figure 3 shows the variations in the bacterial urease activity in solution. It is found from Figures 2 and 3 that the changes of bacterial concentration and urease activity are

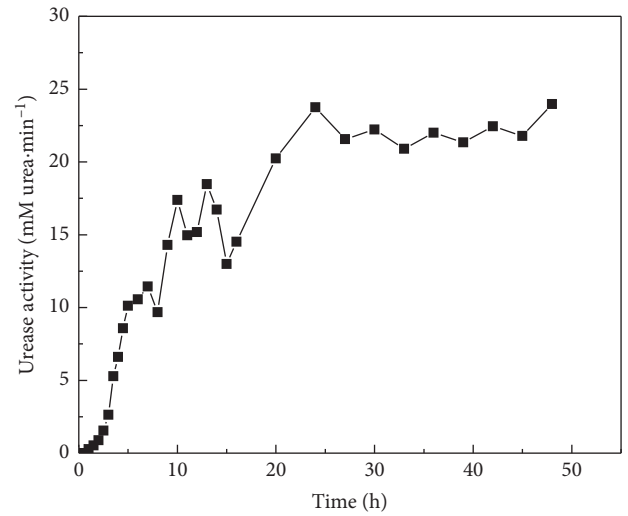


FIGURE 3: Variations in bacterial urease activity with time.

consistent in the process of bacterial culture, showing a slow growth within 0–3 h and a rapid growth within 3–24 h. The urease activity reaches the maximum value after 24 hours of culture. In the present experiment, bacteria solution cultured for 24 h is selected for the experiment to ensure the consistency of bacterial concentration and urease activity.

2.2. Specimen Preparation. In order to prefabricate cracks with different roughness, polymethyl methacrylate (PMMA) material is applied to make rock-like specimens. Based on Barton's theory [39] of crack roughness, four cylindrical rock-like specimens containing prefabricated cracks with different joint roughness coefficients (JRCs) are manufactured using numerically controlled (NC) machine

tools, as shown in Figure 4. The cylindrical specimens are 50 mm in diameter and 100 mm in height. A small pad with a certain width is used to splice the specimens between the crack surfaces to form a crack with a required width. A groove with width of 3 mm and depth of 3 mm is made at the top of the crack on each specimen to place burette tubes, as shown in Figure 4(a). Furthermore, glass glue is used to seal the two sides of the pre-existing crack, and a single layer of gauze is placed at the bottom of the pre-existing crack to simulate the crack tip.

2.3. Experimental Setup. As shown in Figures 5(a) and 5(b), a bracket for placing samples during the titration process was designed and manufactured. The bracket was composed of two plastic plates which were joined together. The connecting part was designed to be rotatable so that the effects of inclination angle on fracture permeability can be investigated. A bracket was set behind the plate to adjust the angle between the two plates. A groove for collecting waste liquid was installed under the bracket and a catheter was inserted to facilitate the discharge of waste liquid.

The permeability coefficient of fractures is tested using the variable head method [30]. As shown in Figure 5(c), the bacteria-filled specimens were put into the Buchner funnel and sealed with glass glue and waterproof tape. A vertical and scaled glass tube was used to connect closely with the bottom of the funnel through a rubber tube, and water was added to the rubber hose to a specified height to maintain the water column. When the upper surface of the fracture overflows, the initial head height h_1 was recorded, and the time when the head dropped to a certain height h_2 was recorded. The initial head height was changed, and repeated measurements were made.

2.4. Injection Strategy. The filling fluid is composed of bacterial solution and CaCl_2 solution. According to Harkes's work [26], the concentration of CaCl_2 solution is 0.8 mol/L in this study. The two solutions are packed in two containers, respectively. The titrator tubes are placed in the groove above the fracture. Then, bacteria solution and urea + CaCl_2 solution are added into the pre-existing crack in the specimen through two titrator tubes at the same time and same injection rate. The biogrowth flows under the action of gravity with the rate of 0.003 ml/s. Each specimen is treated three times using the above method, 50 ml of bacterial solution is added each round, and the specimens are placed for 12 hours after each treatment.

In the present experiment, the effects of bacterial concentration, crack inclination angle, crack roughness, and crack width on the filling effect of MICP are studied. The optical density (OD) is 0.5, 1.0, 1.5, and 2.0. The JRC of the pre-existing cracks for each specimen is set to 6.7, 10.8, 14.5, and 18.7, respectively. The crack opening is 0.5 mm, 1 mm, 1.5 mm, and 2 mm, respectively. The inclination angle of cracks is set to 30°, 45°, 60°, and 75°, respectively. The experimental design is shown in Table 2.

2.5. Calcium Carbonate Content Test. The effluent from each filling process is collected, and the content of calcium ion in the effluent is measured by the titration method. The total amount of calcium ion in the solution is subtracted from the amount of calcium ion in the effluent to obtain the content of calcium carbonate in the cracks. Then, the content of calcium carbonate can be written as

$$M_c = M_t - M_s, \quad (4)$$

in which M_c is the content of calcium carbonate, M_t represents the total amount of calcium ion in the solution, and M_s denotes the amount of calcium ion in the effluent.

2.6. Permeability Analysis. According to the research of Mountassir et al. [35], calcium carbonate produced by the MICP process is granular and it can fill the fracture, so the relevant formula of the variable head test is used to calculate the fracture permeability in this study. Then, the permeability coefficient of the crack can be obtained as

$$k = 2.3 \frac{aL}{A\Delta t} \lg\left(\frac{H_1}{H_2}\right), \quad (5)$$

where a is the cross-sectional area of rubber hose, L represents the seepage diameter, i.e., the height of the sample, t denotes the time interval, H_1 and H_2 are the initial head height and the termination head height, and A is the cross-sectional area of fracture.

3. Result and Discussion

After several MICP filling processes, it can be observed that the pre-existing cracks of the rock-like specimens are gradually filled with white calcium carbonate. However, with the change of external factors, the filling mode of calcium carbonate in the filling process and the final filling effect are different. The following sections are the analysis of the filling mode and filling effect of calcium carbonate under different factors, and the mechanism of its action is elaborated.

3.1. Effect of Bacterial Concentration on Reduction Infiltration.

Figure 6(a) shows the filling process of calcium carbonate under different bacterial concentrations. It can be observed from the Figure 6(a) that the filling process of calcium carbonate changes significantly with the increase of bacterial concentration. During the filling process, the liquid was injected by the injection port and flows under the action of gravity, producing obvious white calcium carbonate precipitation on the flow path. With the increase of bacterial concentration, the precipitation diffusion rate of calcium carbonate increased, and the overall performance was that the filling mode of calcium carbonate gradually changed from the upward filling mode at the bottom of the fracture to the filling mode around the injection inlet, and the calcium carbonate distribution in the fracture was more even.

The variations of calcium carbonate content with different ODs and treatment times are plotted in Figure 6(b). According to Figures 6(a) and 6(b), with the increase of

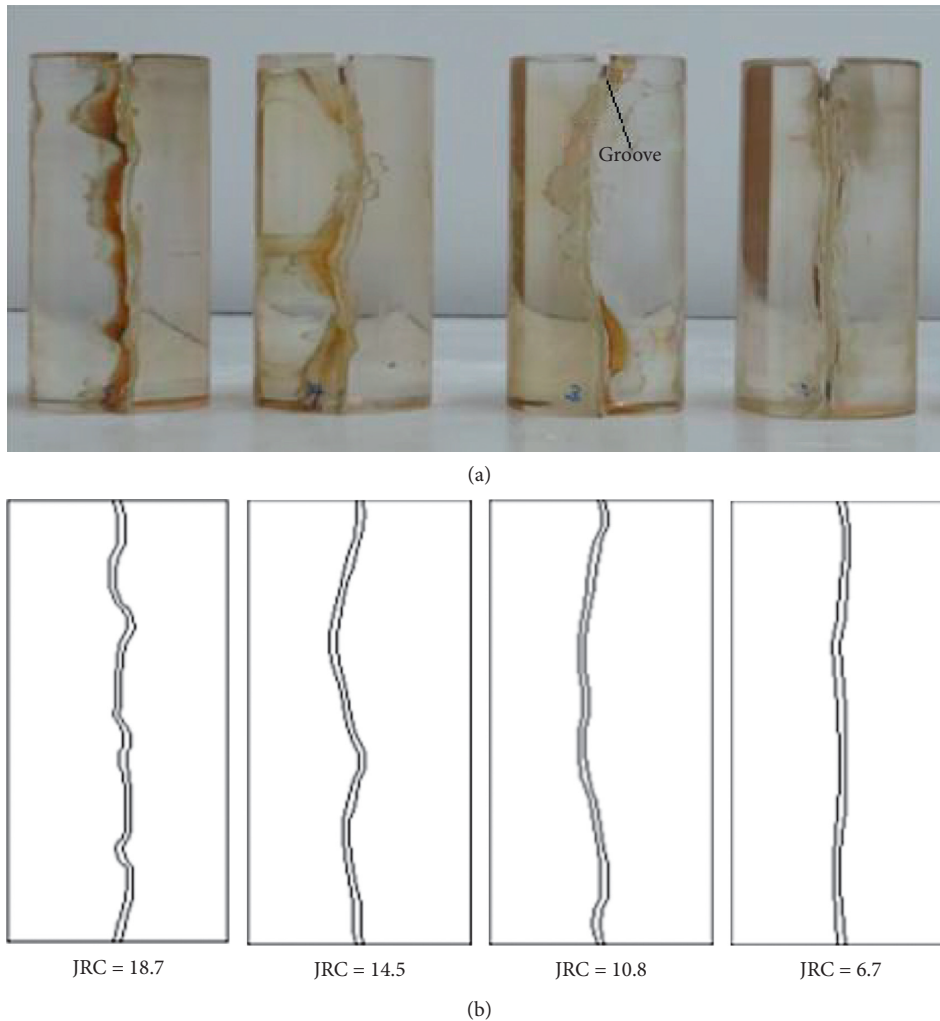


FIGURE 4: Specimens with prefabricated cracks. (a) Rock-like specimens containing prefabricated cracks with different joint roughness coefficients. (b) Sketch of prefabricated cracks with different joint roughness coefficients.

filling times, the precipitation range of calcium carbonate generated near the injection port and in the flow path increases, and the yield of calcium carbonate increases during each filling process. This is because the continuous filling of calcium carbonate affects the subsequent slurry flow and increases the filling efficiency of calcium carbonate [32]. As shown Figure 6(b), in the first filling process, the yield of calcium carbonate increases from 35% to 65% with the increase of bacterial concentration. In the second filling round, the yield of calcium carbonate increases from 42% to 81%. In the third filling round, the yield of calcium carbonate increased from 51% to 79%. It can be observed from Figure 6(c) that the content of calcium carbonate in fractures increases from 42% to 75% with the increase of bacterial concentration after the filling process, which indicated that bacterial concentration had a great influence on the yield of calcium carbonate in the filling process. The fracture permeability decreases with the increase of bacterial concentration, from 1.475×10^{-2} cm/s to 3.1×10^{-3} cm/s, which is caused by the increase of

calcium carbonate content in the fracture and the more uniform distribution.

According to the second part of the study, the variation trend of bacterial concentration and urease activity with culturing is consistent, which affects the decomposition rate of urea in solution. Under the same flow conditions, the increase of bacterial concentration leads to the acceleration of urea decomposition and increases the precipitation rate of calcium carbonate, making it easier to precipitate in the injection port and flow path. Figures 6(b) and 6(c) also show that the increase of bacterial concentration will enhance the precipitation rate of calcium carbonate. In addition, it can be noted that no matter how the concentration of bacteria changes, white calcium carbonate will be produced at the bottom of the fracture, which is different from the results of study in sand [23]. However, MICP grouting slurry has low flow viscosity and fast filling speed. When it is applied to sandy soil, excessive bacterial concentration will make a large amount of calcium carbonate rapidly produced near the injection port and lead to the failure of subsequent grout

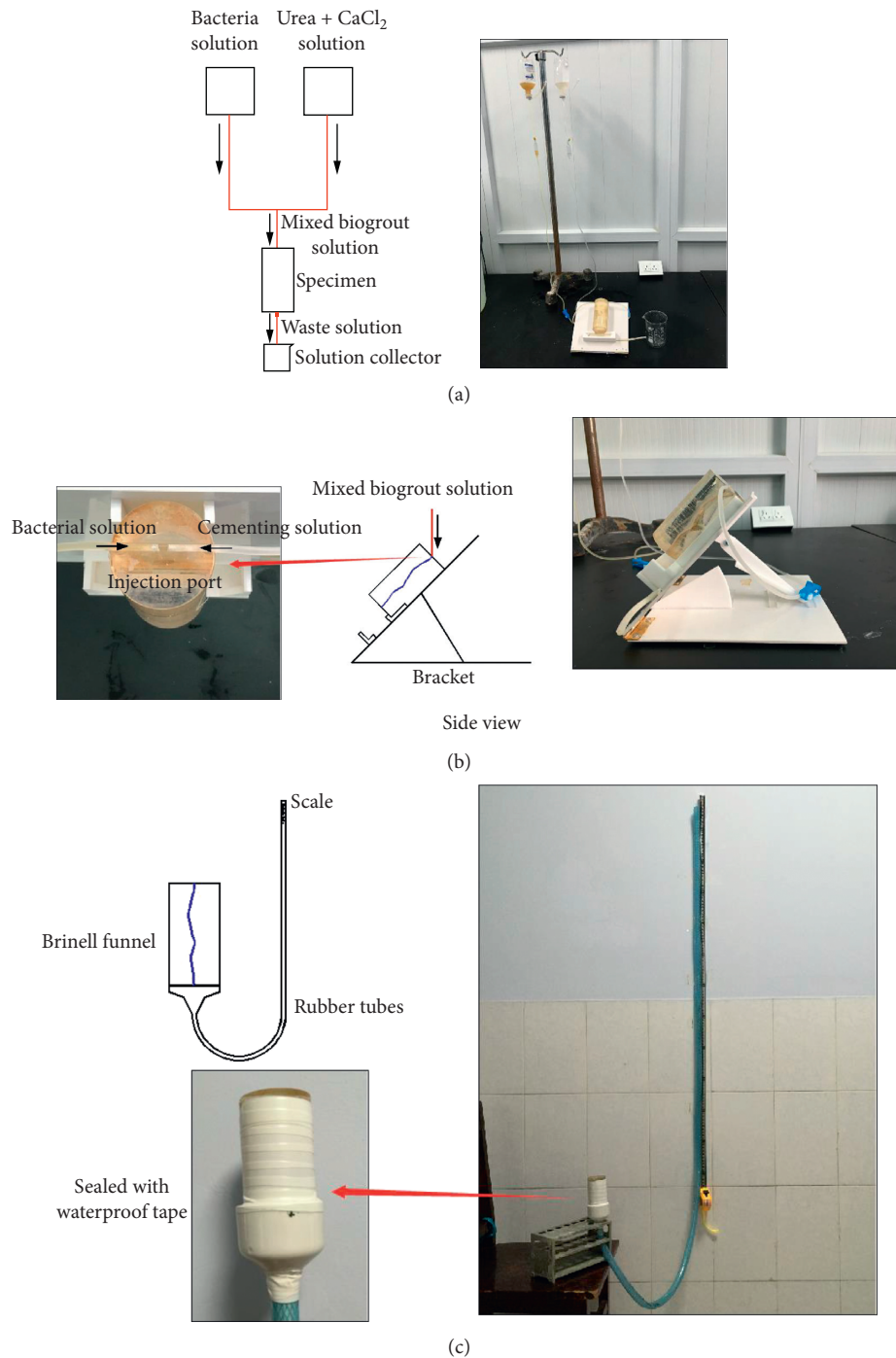


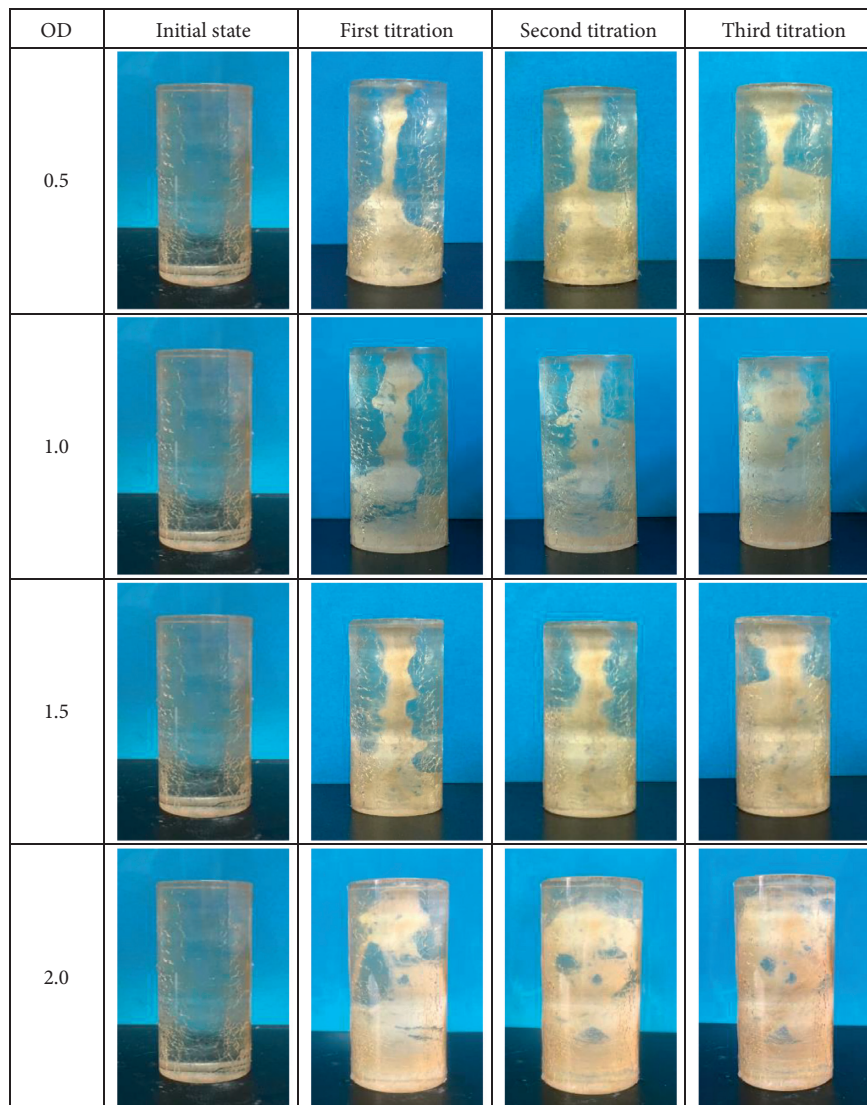
FIGURE 5: Experimental setup. (a) Schematic of biogrouting solution flow arrangement. (b) Side view of experimental bracket. (c) The measuring equipment of permeability coefficient.

to enter. The fracture farther away from the injection port tended to decrease the calcium carbonate content. However, it can be obtained from Figure 6 that under certain fracture conditions, the increase of bacterial concentration has a promoting effect on the filling effect. This situation is caused by the slurry retention ability of the fracture, and it also proves that the application of MICP technology to fracture rock mass has practical engineering significance.

3.2. Effect of Crack Inclination Angle on Reduction Infiltration. In the present experiment, the biogrouting solution was produced under the action of 1g gravity, and the slurry flow velocity also changed when the crack inclination angle changed. Figure 7(a) shows the filling process of calcium carbonate under different crack inclination angles. It can be observed from Figure 7(a) that the filling mode of calcium carbonate changes with the increase of fracture inclination

TABLE 2: Experimental design.

Number	JRC	Crack inclination angle (°)	OD	Crack opening (mm)
3	14.5	45	0.5	1.5
3	14.5	45	1	1.5
3	14.5	45	1.5	1.5
3	14.5	45	2	1.5
3	14.5	30	2	1.5
3	14.5	60	2	1.5
3	14.5	75	2	1.5
1	6.7	45	2	1.5
2	10.8	45	2	1.5
4	18.7	45	2	1.5
3	14.5	45	2	0.5
3	14.5	45	2	1
3	14.5	45	2	2



(a)

FIGURE 6: Continued.

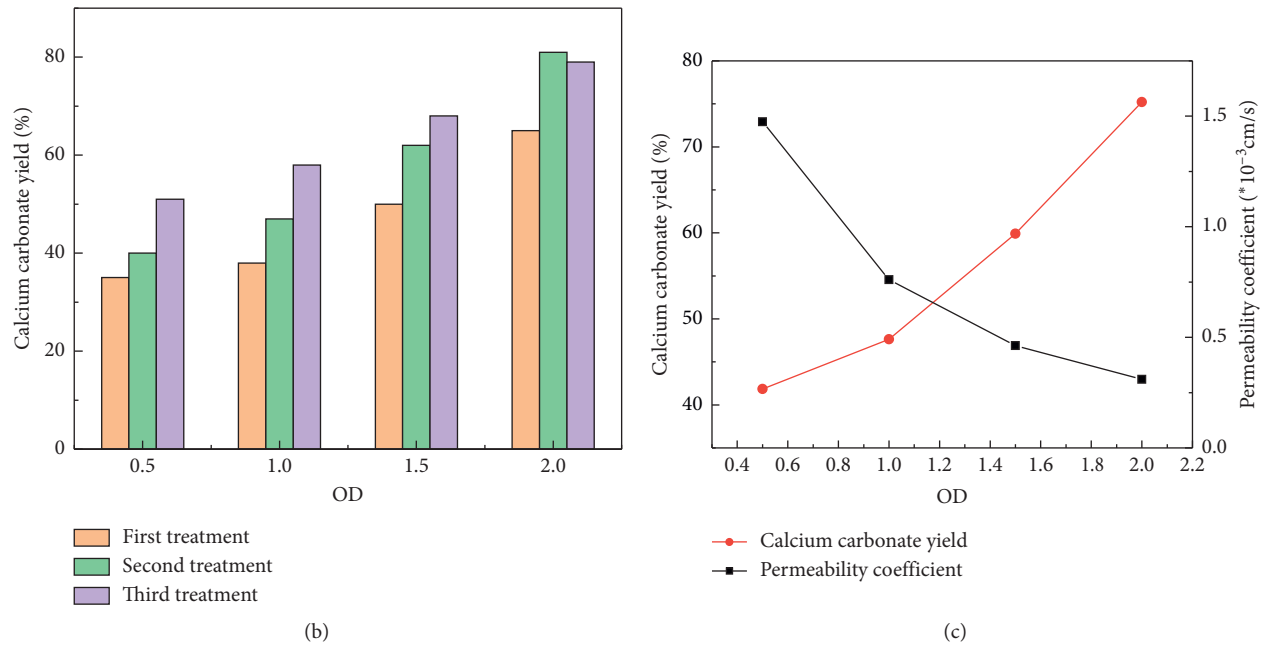


FIGURE 6: Filling effects of calcium carbonate with different bacterial concentrations. (a) Calcium carbonate filling process. (b) Change of calcium carbonate content. (c) Change of fracture permeability.

angle. When the crack inclination angle is 30°, a large amount of calcium carbonate is produced near the injection port and on the flow path during the first filling process. With the increase of the crack dip angle, it is found that the calcium carbonate produced in the injection port and the flow path is significantly reduced after the first filling process. This indicates that the liquid flow rate has an effect on the precipitation of calcium carbonate [35]. When the slurry flow speed is slow, the deposition rate of calcium carbonate increases, and it is easy to precipitate near the injection port and on the flow path. At the end of the three filling processes, the filling effect of calcium carbonate is different in the fractures. When the inclination angle is 30°, the middle part of the fractures is not filled; when the inclination angles are 45° and 60°, the distribution of calcium carbonate is uniform; when the inclination angle is 75°, the upper part of the fractures is not filled.

It can be obtained from Figure 7(b) that during the first filling process, the yield of calcium carbonate decreases with the increase of fracture inclination angle, from 71.7% to 50.2%. During the second filling process, the change trend of calcium carbonate yield changes, and the yield of calcium carbonate increases first and then decreases. The yield of calcium carbonate reaches its maximum value (81%) when the fracture inclination angle is set to 45°. During the third filling process, the yield of calcium carbonate increases first and then decreases. When the dip angle is 30°, the minimum yield of calcium carbonate is about 36%, and the maximum yield of fracture is 79% when the dip angles are 45° and 60°. The reason is that too small fracture dip will cause calcium carbonate to deposit around the injection port, which will affect the entrance of the subsequent slurry and lead to a decrease in the yield of calcium carbonate. It can also be

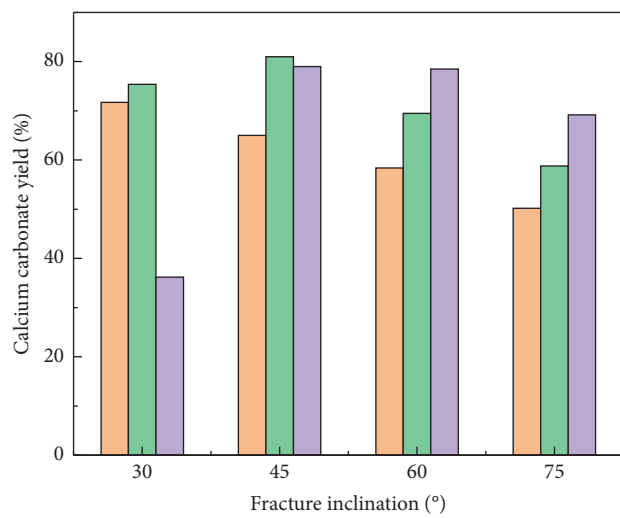
found from Figure 7(c) that after the completion of the three filling processes, with the increase of the fracture inclination angle, the total yield of calcium carbonate first increases and then decreases. As shown in Figure 7(c), with the increase of fracture inclination angle, the permeability of the fracture increases from 2.106×10^{-3} cm/s to 8.66×10^{-3} cm/s. The overall performance is that the more the calcium carbonate content in the fracture, the lower the permeability coefficient. It is worth noting that when the dip angle of the fracture is 30°, although the content of calcium carbonate in the fracture is very low, the permeability of the fracture is the lowest. According to the experimental phenomenon and the research results of Wu et al. [37], it can be concluded that when the inclination angle is small, the slurry flow velocity slows down and a dense calcium carbonate layer is generated around the injection port, which greatly reduces the permeability of the fracture. It can be seen from the above analysis that when the MICP technology is used to prevent seepage in fractures, it greatly depends on the content of calcium carbonate in the fractures. Therefore, the key of the MICP technology is whether the calcium carbonate in the fractures can form a dense water barrier.

3.3. Effect of Crack Roughness on Reduction Infiltration.

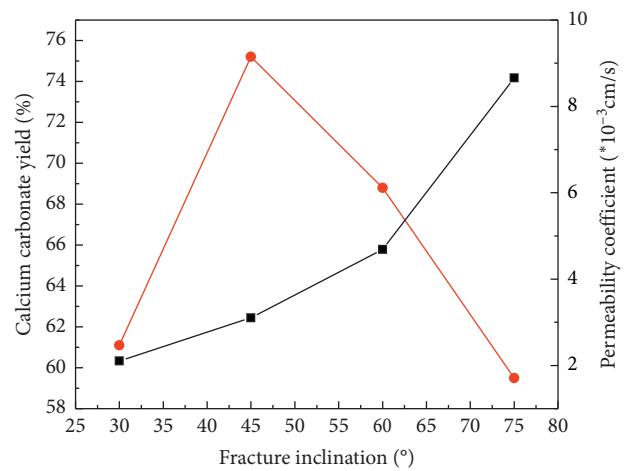
Figure 8(a) shows the change of filling mode of calcium carbonate in pre-existing cracks with different crack roughness. It is found from Figure 8(a) that with the increase of crack roughness, the filling range of calcium carbonate increases in the flow path. The filling mode of calcium carbonate generally changes from filling upward from the bottom of the fracture to diffusing around the injection port and the flow path. After the grouting process, it can be



(a)



(b)

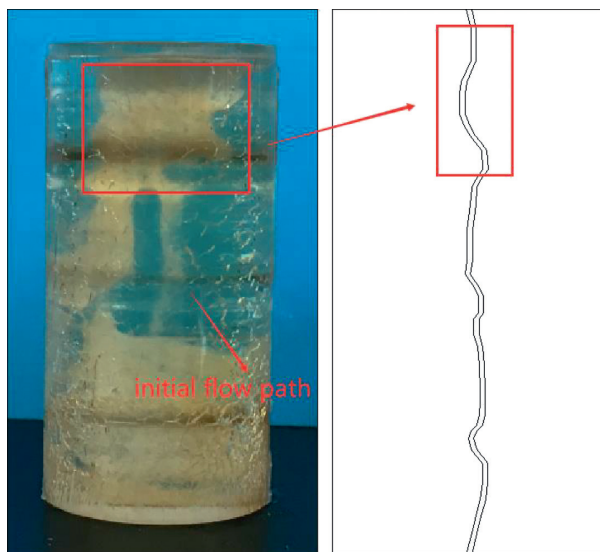


(c)

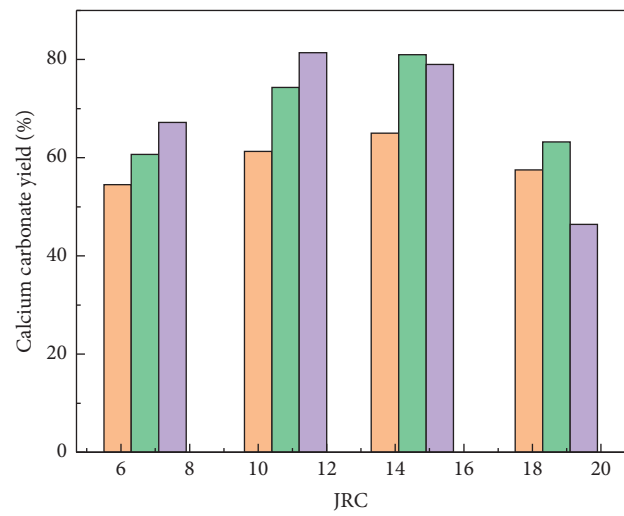
FIGURE 7: Filling effect of calcium carbonate with different fracture inclination angles. (a) Calcium carbonate filling process. (b) Change of calcium carbonate content. (c) Change of fracture permeability.



(a)



(b)



■ First treatment
■ Second treatment
■ Third treatment

(c)

FIGURE 8: Continued.

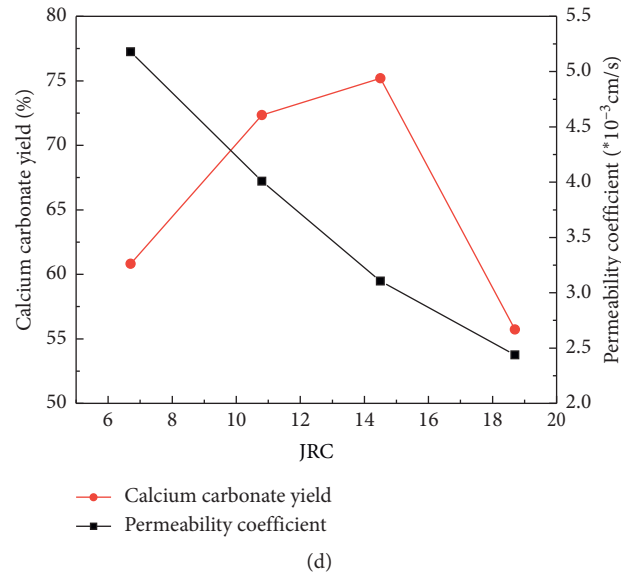


FIGURE 8: Filling effect of calcium carbonate with different fracture roughness. (a) Calcium carbonate filling process. (b) Specimen after first filling process (JRC = 18.7). (c) Change of calcium carbonate content. (d) Change of fracture permeability.

obtained that when the fracture roughness is small (JRC = 6.7, JRC = 10.8), a small part of the injection port is not filled, while when JRC = 18.7, a large part of the middle part of the fracture is not filled.

According to the research of Cuthbert et al. [32] and Minto et al. [20], calcium carbonate is more easily able to precipitate in the parts with large crevice fluctuations. Figure 8(b) shows the specimen with the JRC = 18.7 after the first filling process, and it can be seen from Figure 8(b) that calcium carbonate deposits the most in the fracture where the fracture fluctuation is the largest. Due to the precipitation of calcium carbonate, the subsequent slurry flow is restricted, and the slurry flow path is changed. Figure 8(c) shows the content of calcium carbonate in the fracture during the filling process. In the first filling process, the yield of calcium carbonate is the lowest (54.5%) when the JRC value of the fracture is 6.7, and it is the highest (65%) when the JRC value of the fracture surface is 14.5. During the second filling process, the yield of calcium carbonate is the smallest (60.7%) when the JRC value of the fracture surface is 6.7, and the yield of calcium carbonate reaches largest (81%) when the JRC value of the fracture surface is 14.5. In the third filling process, the yield of calcium carbonate is the smallest (46.4%) when the fracture JRC value is 18.7, and it is the largest (81.4%) when the fracture JRC value is 10.8. This indicates that the increase of crack roughness is conducive to the precipitation of calcium carbonate, but when the fracture roughness is too large, the precipitation of calcium carbonate in the early stage will restrict the subsequent slurry injection and lead to the decrease of the yield of calcium carbonate.

Figure 8(d) shows the change of permeability of the fracture with different JRCs. The permeability coefficient of the fracture decreases with the increase of the roughness of the fracture, which is negatively correlated with the content

of calcium carbonate in the fracture. However, in the fracture with JRC = 18.7, the content of calcium carbonate is the lowest and the permeability coefficient is the lowest. It means that calcium carbonate forms dense calcium carbonate precipitation in the part with the biggest fluctuation of the fracture, which reduces the permeability of the fracture.

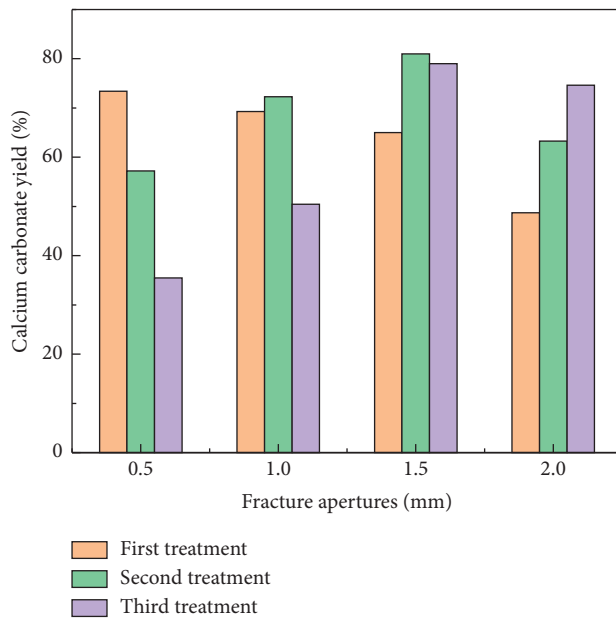
3.4. Effect of Crack Opening on Reduction Infiltration.

Figure 9(a) shows the filling process of calcium carbonate in the pre-existing cracks under different aperture conditions. It can be seen from Figure 9(a) that with the increase of aperture, the precipitation of calcium carbonate around the injection port decreases, while the distribution of calcium carbonate at the bottom of the fractures increases. During the first filling process, the filling velocity of calcium carbonate decreases with the increase of crack opening. According to the cubic law, the reduction of crack opening will reduce the water passing capacity of the fracture and accelerate the precipitation of calcium carbonate. At the same time, small crack opening can be filled with calcium carbonate more quickly, which will restrict the subsequent grouting process and accelerate the precipitation of calcium carbonate. After the grouting process, the middle part of the fracture with an aperture of 0.5 mm is not filled. With the increase of the crack opening, the filling effect is improved. When the crack opening is 2 mm, the upper part of the fracture cannot be filled.

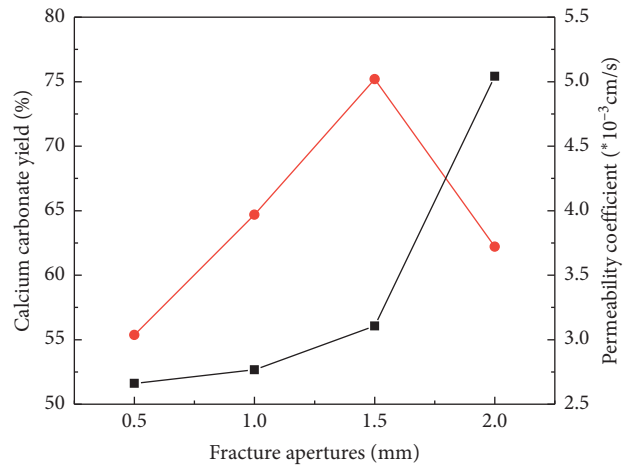
The changes of calcium carbonate content in fractures with different fracture aperture in the filling processes are illustrated in Figure 9(b). During the first filling process, the yield of calcium carbonate in the fracture decreases from 73.4% to 48.7% as the aperture of the fracture increases. In the second filling process, the yield of calcium carbonate



(a)



(b)



(c)

FIGURE 9: Filling effect of calcium carbonate with different fracture apertures. (a) Calcium carbonate filling process. (b) Change of calcium carbonate content. (c) Change of fracture permeability.

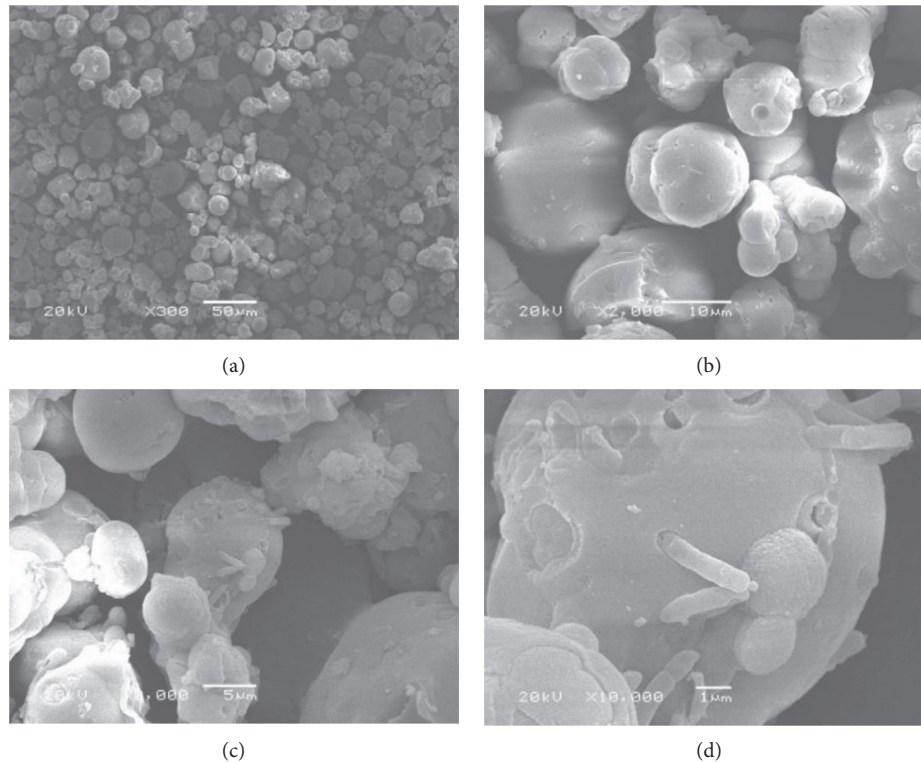


FIGURE 10: Microscopic morphology of calcium carbonate produced by MICP.

increases first and then decreases. The yield of calcium carbonate reaches the smallest (57.2%) when the crack opening is 0.5 mm, and it is the largest (81%) when the crack opening is 1.5 mm. During the third filling process, the yield of calcium carbonate is the smallest (35.5%) when the crack opening is set to 0.5 mm, and the yield of calcium carbonate reaches the largest (79%) when the crack opening is 1.5 mm. This indicates that small crack opening (0.5 mm, 1.0 mm) is conducive to the precipitation of calcium carbonate, but the precipitation of calcium carbonate near the injection port will hinder the subsequent grouting process and reduce the subsequent grouting efficiency. The large crack opening (1.5 mm, 2 mm) is not conducive to the precipitation of calcium carbonate in the early stage of filling, but in the subsequent grouting process, the precipitation of calcium carbonate at the bottom of the fracture will reduce the flow of slurry and improve the precipitation efficiency of calcium carbonate. Moreover, it can be found from Figure 9(c) that with the increase of crack opening, the permeability coefficient of the fracture increases after filling processes. On the one hand, the smaller crack opening leads to the smaller water passing capacity. On the other hand, the smaller crack opening is more easily blocked by calcium carbonate.

3.5. The Microscopic Morphology of Calcium Carbonate.

Figure 10 shows the microstructure of calcium carbonate with different observation scales produced by MICP. It can be obtained from Figures 10(a)–10(d) that calcium carbonate generated by the MICP process is granular, with a diameter of about 20 μm . The particles are formed in the

form of accumulation and bonding. As shown in Figures 10(c) and 10(d), it is found that the bacteria are wrapped inside the calcium carbonate particles, which are consistent with the existing research conclusion [24, 40].

According to Kohnhauser's work [41], the MICP process is the production of urease by *Sporosarcina pasteurii* in the metabolic process, and the urease acts as a catalyst promoting the decomposition of urea in the environment (the decomposition rate is increased by 104 times). Since bacteria have negative charges themselves, calcium ions in the solution will adhere to the surface of bacteria, and bacteria provide crystal nuclei for the formation of calcium carbonate, which is conducive to the formation of precipitation [24]. In the MICP process, bacteria are mainly used to produce urease and to provide crystal nuclei for calcium carbonate precipitation. Therefore, *Sporosarcina pasteurii* has two main roles in the process of MICP: one is to provide urease and accelerate the decomposition of urea and the other is to provide the crystal nucleus for the formation of calcium carbonate and accelerate the precipitation of calcium carbonate.

4. Conclusion

In this study, the process of filling cracks with MICP is investigated. The effects of four external factors such as bacterial concentration, fracture inclination angle, crack roughness, and fracture aperture on the filling effect are studied. The results showed that calcium carbonate precipitation can be formed when bacteria and cementing fluid are injected into the cracks, which can seal the cracks and

reduce the permeability of the cracks. The conclusions are drawn as follows:

- (1) The content of calcium carbonate in cracks increases with the increase of bacterial concentration, and it increases first and then decreases with the increase of inclination angle, roughness, and opening of cracks, respectively.
- (2) The filled crack permeability increases with the increase of bacterial concentration and crack roughness, and it decreases with the increase of crack inclination angle and crack opening, respectively.
- (3) The concentration of bacteria is mainly reflected in the hydrolysis rate of urea in the slurry. And the fracture morphology will affect the filling mode of calcium carbonate. Therefore, it is necessary to make appropriate plans according to the actual situation of the engineering site when the MICP technology is applied to practical engineering.
- (4) It can be concluded that the MICP technology can reduce the permeability of fractured rock mass and has the potential to be applied in waterproofing measures of fractured rock engineering. In order to get better practicability of the technology in engineering, it is necessary to conduct in-depth research including large-scale cracks and different injection methods in the future.

Data Availability

The data used to support the findings of this study are included within the article.

Conflicts of Interest

The authors confirm that the received funding that has been mentioned did not lead to any conflicts of interest regarding the publication of this manuscript.

Acknowledgments

This study was supported by National Breeding Base of Technology and Innovation Platform for Automatic Monitoring of Geologic Hazards and Chongqing Engineering Research Center of Automatic Monitoring for Geological Hazards.

References

- [1] X. P. Zhou, J. Bi, and Q. H. Qian, "Numerical simulation of crack growth and coalescence in rock-like materials containing multiple pre-existing flaws," *Rock Mechanics and Rock Engineering*, vol. 48, no. 3, pp. 1097–1114, 2015.
- [2] X. P. Zhou, Y. X. Zhang, Q. L. Ha, and K. S. Zhu, "Micro-mechanical modelling of the complete stress-strain relationship for crack weakened rock subjected to compressive loading," *Rock Mechanics and Rock Engineering*, vol. 41, no. 5, pp. 747–769, 2008.
- [3] J. Bi, X. P. Zhou, and Q. H. Qian, "The 3D numerical simulation for the propagation process of multiple pre-existing flaws in rock-like materials subjected to biaxial compressive loads," *Rock Mechanics and Rock Engineering*, vol. 49, no. 5, pp. 1611–1627, 2016.
- [4] X. P. Zhou, J. Z. Zhang, and L. N. Y. Wong, "Experimental study on the growth, coalescence and wrapping behaviors of 3D cross-embedded flaws under uniaxial compression," *Rock Mechanics and Rock Engineering*, vol. 51, no. 5, pp. 1379–1400, 2018.
- [5] Y. Wang, X. Zhou, X. Xu, and X. Xu, "Numerical simulation of propagation and coalescence of flaws in rock materials under compressive loads using the extended non-ordinary state-based peridynamics," *Engineering Fracture Mechanics*, vol. 163, pp. 248–273, 2016.
- [6] J. Z. Zhang and X. P. Zhou, "Forecasting catastrophic rupture in brittle rocks using precursory AE time series," *Journal of Geophysical Research: Solid Earth*, vol. 125, no. 8, Article ID e2019JB019276, 2020.
- [7] Z. Zhao and X. P. Zhou, "An integrated method for 3D reconstruction model of porous geomaterials through 2D CT images," *Computers & Geosciences*, vol. 123, pp. 83–94, 2019.
- [8] Z. Zhao and X.-P. Zhou, "Establishment of numerical cracking constitutive models using 3D reconstruction and X-ray CT images of geomaterials," *International Journal of Mechanical Sciences*, vol. 183, Article ID 105814, 2020.
- [9] X. C. Huang and X. P. Zhou, "Probabilistic assessment for slope using the generalized Chebyshev inequalities," *International Journal of Geomechanics*, vol. 20, no. 4, Article ID 06020003, 2020.
- [10] X. P. Zhou, X. C. Huang, P. F. Liu, and T. F. Li, "A probabilistic method to analyze collapse failure of shallow rectangular tunnels," *Tunnelling and Underground Space Technology*, vol. 82, pp. 9–19, 2018.
- [11] X. P. Zhou, X. C. Huang, and X. F. Zhao, "Optimization of the critical slip surface of three-dimensional slope by using an improved genetic algorithm," *International Journal of Geomechanics*, vol. 20, no. 8, Article ID 04020120, 2020.
- [12] X. P. Zhou, X. C. Huang, and J. X. Li, "Reliability assessment of tunnel based on P -wave seismic velocity," *International Journal of Geomechanics*, vol. 18, no. 11, Article ID 06018030, 2018.
- [13] Y. Shou and X. Zhou, "A coupled hydro-mechanical non-ordinary state-based peridynamics for the fissured porous rocks," *Engineering Analysis with Boundary Elements*, vol. 123, pp. 133–146, 2021.
- [14] P. Duffaut, "The traps behind the failure of Malpasset arch dam, France, in 1959," *Journal of Rock Mechanics and Geotechnical Engineering*, vol. 5, no. 5, pp. 335–341, 2013.
- [15] C. R. J. Kilburn and D. N. Petley, "Forecasting giant, catastrophic slope collapse: lessons from Vajont, Northern Italy," *Geomorphology*, vol. 54, no. 1, pp. 21–32, 2003.
- [16] N. D. Rose and O. Hungr, "Forecasting potential rock slope failure in open pit mines using the inverse-velocity method," *International Journal of Rock Mechanics and Mining Sciences*, vol. 44, no. 2, pp. 308–320, 2007.
- [17] K. Q. He, W. C. Yu, and W. F. Jiang, "Analysis of groundwater inrush conditions and critical inspection parameters at the baixiangshan iron mine, China," *Mine Water and the Environment*, vol. 30, pp. 274–283, 2011.
- [18] J. Chu, V. Ivanov, J. He, and M. Naeimi, "Development of microbial geotechnology in Singapore," in *Proceedings of the Geo-Frontiers Congress 2011*, pp. 070–4078, ASCE, Dallas, TX, USA, March 2011.

- [19] M. B. Ali, R. Saidur, and M. S. Hossain, "A review on emission analysis in cement industries," *Renewable and Sustainable Energy Reviews*, vol. 15, no. 5, pp. 2252–2261, 2011.
- [20] J. M. Minto, E. MacLachlan, G. El Mountassir, and R. J. Lunn, "Rock fracture grouting with microbially induced carbonate precipitation," *Water Resources Research*, vol. 52, no. 11, pp. 8827–8844, 2016.
- [21] V. Ivanov and J. Chu, "Applications of microorganisms to geotechnical engineering for bioclogging and biocementation of soil in situ," *Reviews in Environmental Science and Biotechnology*, vol. 7, no. 2, pp. 139–153, 2008.
- [22] J. K. Mitchell and J. C. Santamarina, "Biological considerations in geotechnical engineering," *Journal of Geotechnical and Geoenvironmental Engineering*, vol. 131, no. 10, pp. 1222–1233, 2005.
- [23] Q. Zhao, L. Li, C. Li, M. Li, F. Amini, and H. Zhang, "Factors affecting improvement of engineering properties of MICP-treated soil catalyzed by bacteria and urease," *Journal of Materials in Civil Engineering*, vol. 26, no. 12, Article ID 04014094, 2014.
- [24] J. T. DeJong, M. B. Fritzges, and K. Nüsslein, "Microbially induced cementation to control sand response to undrained shear," *Journal of Geotechnical and Geoenvironmental Engineering*, vol. 132, no. 11, pp. 1381–1392, 2006.
- [25] V. S. Whiffin, L. A. van Paassen, and M. P. Harkes, "Microbial carbonate precipitation as a soil improvement technique," *Geomicrobiology Journal*, vol. 24, no. 5, pp. 417–423, 2007.
- [26] M. P. Harkes, L. A. van Paassen, J. L. Booster, V. S. Whiffin, and M. C. M. van Loosdrecht, "Fixation and distribution of bacterial activity in sand to induce carbonate precipitation for ground reinforcement," *Ecological Engineering*, vol. 36, no. 2, pp. 112–117, 2010.
- [27] H. Yasuhara, K. Hayashi, and M. Okamura, "Evolution in mechanical and hydraulic properties of calcite-cemented sand mediated by biocatalyst," in *Proceedings of the Geo-Frontiers Congress 2011*, Dallas, TX, USA, March 2011.
- [28] M. Burbank, T. Weaver, R. Lewis, T. Williams, B. Williams, and R. Crawford, "Geotechnical tests of sands following bio-induced calcite precipitation catalyzed by indigenous bacteria," *Journal of Geotechnical and Geoenvironmental Engineering*, vol. 139, no. 6, pp. 928–936, 2012.
- [29] L. A. V. Paassen, R. Ghose, T. J. M. V. D. Linden, W. R. L. V. D. Star, and M. C. M. V. Loosdrecht, "Quantifying biomediated ground improvement by ureolysis: large-scale biogROUT experiment," *Journal of Geotechnical and Geoenvironmental Engineering*, vol. 136, no. 12, pp. 1721–1728, 2010.
- [30] D. Li, K. L. Tian, H. L. Zhang, Y. Y. Wu, K. Y. Nie, and S. C. Zhang, "Experimental investigation of solidifying desert aeolian sand using microbially induced calcite precipitation," *Construction and Building Materials*, vol. 172, pp. 251–262, 2018.
- [31] F. G. Ferris, L. G. Stehmeier, A. Kantzas, and F. M. Mourits, "Bacteriogenic mineral plugging," *Journal of Canadian Petroleum Technology*, vol. 35, no. 8, pp. 56–61, 1996.
- [32] M. O. Cuthbert, L. A. McMillan, S. Handley-Sidhu, M. S. Riley, D. J. Tobler, and V. R. Phoenix, "A field and modeling study of fractured rock permeability reduction using microbially induced calcite precipitation," *Environmental Science and Technology*, vol. 47, no. 23, pp. 13637–13643, 2013.
- [33] A. J. Phillips, E. Lauchnor, J. Eldring et al., "Potential CO₂ leakage reduction through biofilm-induced calcium carbonate precipitation," *Environmental Science and Technology*, vol. 47, no. 1, pp. 142–149, 2013.
- [34] N. A. Bucci, E. Ghazanfari, and H. J. Lu, "Microbially-induced calcite precipitation for sealing rock fractures," in *Proceedings of the Geo-Chicago 2016*, Chicago, IL, USA, August 2016.
- [35] G. E. Mountassir, R. J. Lunn, H. Moir, and E. MacLachlan, "Hydrodynamic coupling in microbially mediated fracture mineralisation: formation of self-organised flow channels," *Water Resources Research*, vol. 50, no. 1, pp. 1–16, 2013.
- [36] D. J. Tobler, J. M. Minto, G. E. Mountassir, R. J. Lunn, and V. R. Phoenix, "Microscale Analysis of fractured rock sealed with microbially induced CaCO₃ precipitation: influence on hydraulic and mechanical performance," *Water Resources Research*, vol. 54, no. 10, pp. 8295–8308, 2018.
- [37] C. Wu, J. Chu, S. Wu, and W. Guo, "Quantifying the permeability reduction of biogROUTED rock fracture," *Rock Mechanics and Rock Engineering*, vol. 52, no. 3, pp. 947–954, 2018.
- [38] C. Wu, J. Chu, S. Wu, and Y. Hong, "3D characterization of microbially induced carbonate precipitation in rock fracture and the resulted permeability reduction," *Engineering Geology*, vol. 249, pp. 23–30, 2019.
- [39] N. Barton and V. Choubey, "The shear strength of rock joints in theory and practice," *Rock Mechanics*, vol. 10, no. 1-2, pp. 1–54, 1977.
- [40] V. Achal, A. Mukherjee, and M. S. Reddy, "Microbial concrete: way to enhance the durability of building structures," *Journal of Materials in Civil Engineering*, vol. 23, no. 6, pp. 730–734, 2011.
- [41] K. O. Kohnhauser, *Introduction to Geomicrobiology*, Blackwell Publishing, Malden, MA, USA, 2007.

Research Article

A Damage Constitutive Model of Rock Subjected to Freeze-Thaw Cycles Based on Lognormal Distribution

Hang Lin , Linyuan Liang, Yifan Chen , and Rihong Cao

School of Resources & Safety Engineering, Central South University, Changsha 410083, China

Correspondence should be addressed to Yifan Chen; 1051361824@qq.com

Received 18 April 2021; Revised 16 June 2021; Accepted 22 June 2021; Published 28 June 2021

Academic Editor: Wei-yao Guo

Copyright © 2021 Hang Lin et al. This is an open access article distributed under the Creative Commons Attribution License, which permits unrestricted use, distribution, and reproduction in any medium, provided the original work is properly cited.

The constitutive model of rock is closely connected with the mechanical properties of rock. To achieve a more accurate quantitative analysis of the mechanical properties of rock after the action of freeze-thaw cycles, it is necessary to establish the constitutive models of rock subjected to freeze-thaw cycles from the view of rock damage. Based on the assumption of rock couple damage, this study established a statistical damage constitutive model of rock subjected to freeze-thaw cycles by combining the lognormal distribution, which is commonly used in engineering reliability analysis, and the strain strength theory. Then, the coordinates and derivative at the peak of the stress-strain curve of the rock after the action of freeze-thaw cycles were obtained through experiments to solve the statistical distribution parameters μ_ε and S of the model, whereafter, the theoretical curves by the established model were compared with the experimental curves to verify the validity of it, which shows a great agreement. Finally, the sensitivity analysis of the statistical distribution parameters was implemented. The results indicate that μ_ε reflects the strength of the rock, which shows a positive relation, and S stands for the brittleness of the rock, which shows a negative relation.

1. Introduction

Freeze and thaw effect is widely encountered in cold areas, which shows significant influences on the rock mass when constructing geotechnical engineering. In order to ensure the stability of the projects, in addition to considering the inherent mechanical properties of rock mass, it is also necessary to consider the deterioration of the rock mechanical properties under the low-temperature environment and the repeated freezing and thawing action, which has been a research focus in the field of rock mechanics. Extensive research studies have been carried out on the degradation of rock mechanical properties caused by freeze-thaw cycles. Typically, the changes in the compressive mechanical properties [1–5], shear mechanical properties [6–10], tensile mechanical properties [11–13], and dynamic compressive mechanical properties [14–16] of rocks were studied under the influence of freeze-thaw cycles. Despite these studies providing crucial conclusions about the degradation effect of freeze-thaw cycles on the mechanical properties of rocks, the majority of them still

remain in the qualitative stage, which may not be used for accurately predicting the mechanical behaviors of rocks subjected to freeze-thaw cycles. As a result, it is necessary to establish a constitutive model of rock subjected to freeze-thaw cycles to reflect the mechanical behaviors more precisely.

Since the concept of rock statistical damage constitutive was put forward by combining continuous damage theory and statistical strength theory, it has become an efficient method to studying the rock stress-strain relationships [17–19]. Current damage constitutive models mainly adopt the Weibull distribution to describe the statistical characteristics of rock microunits [20–23], while research evidence indicates that Weibull statistical theory may not apply to quasi-brittle materials such as rock. Comparing with the Weibull distribution, the lognormal distribution, as a classic distribution commonly used in engineering reliability analysis, has a wider applicability. Therefore, on the basis of the previous statistical models, this paper established a statistical damage constitutive model of rock subjected to freeze-thaw cycles based on lognormal distribution, which

was verified by the comparison between the theoretical curves and experimental curves.

2. Derivation of the Damage Constitutive Model of the Rock after Freezing and Thawing Action

2.1. Freeze-Thaw Damage Variable D_n . There exist multitudinous microdefects (cracks, pores, etc.) inside the rock. The water in these microdefects freezes into ice when the temperature around the rock decreases below 0°C, causing volume expansion, while it melts into water when the temperature rises above 0°C, in which progress part of the water will migrate [24, 25]. Under the repeated action of freeze and thaw, the water in the rock continuously goes through phase transitions and migrates, resulting in the expansion, connection, and destruction of these microdefects in the rock, which ultimately manifests as the deterioration of the macromechanical properties of rock [26, 27]. Therefore, the degradation of the rock macroscopic mechanical properties can be used to characterize the freeze-thaw damage variable. Because the elastic modulus of the rock after freeze-thaw cycles is easy to measure and analyze, so this study used the following formula to define the rock freeze-thaw damage variable:

$$D_n = 1 - \frac{E_n}{E_0}, \quad (1)$$

where E_n is the elastic modulus of the rock after different freeze-thaw cycles and E_0 is the initial elastic modulus of the rock.

2.2. Damage Variable under Loading D_p . For a quasi-brittle material such as rock, the strain caused by loading is often used to analyze the rock damage. Due to the rock discontinuity and the random distribution of load-bearing particles, it can be assumed that the strain limit of the rock microunits after the action of freeze-thaw cycles obeys a certain statistical distribution, and the failure occurs when the strain of the microunit exceeds the limit. In order to calculate the damage variable D_p of the rock at a certain strain level after the action of freeze-thaw cycle, the initial number of rock microunits after the action of freeze-thaw cycles was denoted as N_0 , and the failure number of rock microunits under a certain strain level is N_p . Definition:

$$D_p = \frac{N_p}{N_0}. \quad (2)$$

For the statistical distribution that the strain limit of rock microunits after the action of freeze-thaw cycles obeys, the previous research studies mainly employed the Weibull distribution. However, rock is a kind of quasi-brittle material; due to the obvious characteristic length, the problem of size effect in Weibull statistical theory does not apply to quasi-brittle material [28]. Therefore, this paper intended to select the normal distribution to describe the distribution of

the strain limit of the microunits. In general, the strain limit of the rock microunits is greater than 0. If the normal distribution is directly applied, the negative value is definitely unreasonable. In the structural reliability theory, the lognormal distribution is generally used as the structural resistance probability distribution, so this article finally adopted the lognormal distribution as the statistical distribution of the strain limit. Suppose $\ln \varepsilon \sim N(\mu_\varepsilon, S^2)$; then, its probability density function is

$$f(\varepsilon) = \frac{1}{\varepsilon S \sqrt{2\pi}} \exp\left[-\frac{(\ln \varepsilon - \mu_\varepsilon)^2}{2S^2}\right], \varepsilon \geq 0, \quad (3)$$

where μ_ε and S are the statistical parameters of the lognormal distribution.

In the process of the rock microunits, strain increases from 0 to ε_1 , and the number of the damaged rock microunits is

$$\begin{aligned} N_p &= N_0 \int_0^{\varepsilon_1} f(\varepsilon) d\varepsilon \\ &= N_0 \int_0^{\varepsilon_1} \frac{1}{\varepsilon S \sqrt{2\pi}} \exp\left[-\frac{(\ln \varepsilon - \mu_\varepsilon)^2}{2S^2}\right] d\varepsilon \\ &= N_0 \Phi\left(\frac{\ln \varepsilon_1 - \mu_\varepsilon}{S}\right), \end{aligned} \quad (4)$$

where Φ refers to the distribution function of the standard normal distribution.

From formulas (2) and (4), the following formulas can be obtained:

$$D_p = 1 - \Phi\left(\frac{\mu_\varepsilon - \ln \varepsilon_1}{S}\right). \quad (5)$$

2.3. Damage Constitutive Model of Rock Subjected to Freeze-Thaw Cycles Based on Lognormal Distribution. The damage variables of the rock subjected to the freeze-thaw cycles and the loading separately were deduced above. According to the generalized equivalent strain principle proposed in [29], taking the damage state of the rock after the action of freeze-thaw cycles as the reference state and the state of the rock after being loaded as the damaged state, the coupling damage can be gained:

$$\begin{aligned} D &= 1 - (1 - D_n)(1 - D_p) \\ &= D_n + D_p - D_n D_p, \end{aligned} \quad (6)$$

where D is the total damage variable of the rock under the coupling effect of freeze-thaw cycles and loading.

From formulas (1), (5), and (6), the following formula can be obtained:

$$D = 1 - \frac{E_n}{E_0} \Phi\left(\frac{\mu_\varepsilon - \ln \varepsilon_1}{S}\right). \quad (7)$$

When the rock is not subject to freeze-thaw cycles ($E_n = E_0$),

$$D = 1 - \Phi\left(\frac{\mu_\varepsilon - \ln \varepsilon_1}{S}\right) = D_p. \quad (8)$$

When the rock is unloaded ($\varepsilon_1 = 0$),

$$\Phi\left(\frac{\mu_\varepsilon - \ln \varepsilon_1}{S}\right) = 1, \quad (9)$$

$$D = 1 - \frac{E_n}{E_0} = D_n.$$

According to the Lemaitre equivalent strain principle [30] and the generalized Hooke's law, the constitutive equation of the rock under conventional triaxial compression can be obtained:

$$\sigma_1 = E_0 \varepsilon_1 (1 - D) + 2\nu_n \sigma_3. \quad (10)$$

From formulas (7) and (8), the constitutive equation of freeze-thaw damage of rock based on lognormal distribution is

$$\sigma_1 = E_n \varepsilon_1 \Phi\left(\frac{\mu_\varepsilon - \ln \varepsilon_1}{S}\right) + 2\nu_n \sigma_3, \quad (11)$$

where ν_n is Poisson's ratio of the rock after different freeze-thaw cycles.

2.4. Determination of Model Parameters μ_ε and S . As shown in Figure 1, the general compression stress-strain curve of rock after the action of freeze-thaw cycles also includes five stages (the compaction stage of the OP section, the elastic stage of the PA section, the stable expansion section of the AB section, the unstable and unstable expansion section of the BC section, and the postpeak stage of the CD section).

It can be seen from Figure 1 that the stress-strain curve passes the peak point and the derivative at the peak point is equal to zero: ① $\varepsilon_1 = \varepsilon_c$, $\sigma_1 = \sigma_c$; ② $d\sigma_1/d\varepsilon_1|_{\varepsilon_1=\varepsilon_c} = 0$.

Then, the following formulas can be obtained:

$$\sigma_c = E_n \varepsilon_c \Phi\left(\frac{\mu_\varepsilon - \ln \varepsilon_c}{S}\right) + 2\nu_n \sigma_3, \quad (12)$$

$$\frac{\Phi\left(\frac{\mu_\varepsilon - \ln \varepsilon_c}{S}\right) - \phi\left(\frac{\mu_\varepsilon - \ln \varepsilon_c}{S}\right)}{S} = 0, \quad (13)$$

where ϕ is the probability density function of the standard normal distribution:

$$\phi(x) = \frac{1}{\sqrt{2\pi}} \exp\left(-\frac{x^2}{2}\right), x \in R. \quad (14)$$

Assuming $X = (\mu_\varepsilon - \ln \varepsilon_c)/S$, it can be obtained that $(\sigma_c - 2\nu_n \sigma_3)/E_n \varepsilon_c = \Phi(X)$ from formula (12). Substituting the peak point $(\varepsilon_c, \sigma_c)$ of the rock stress-strain curve after different freeze-thaw cycles and different confining pressures, the values of $\Phi(X)$ can be obtained; then, the values of X can be obtained by checking the standard normal distribution function table.

From formulas (12)–(14), the following formula can be obtained:

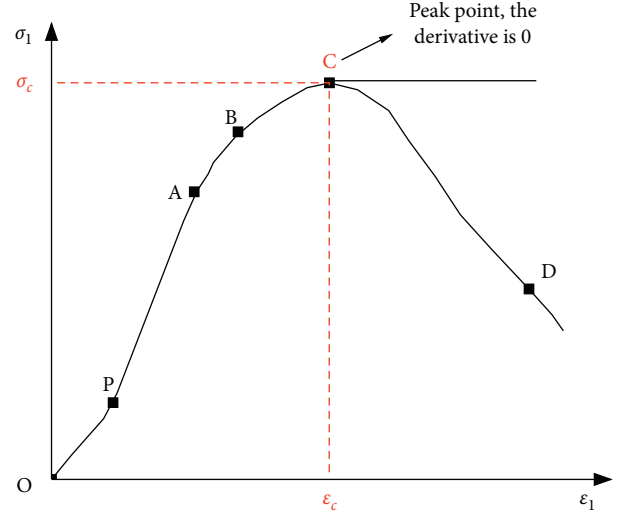


FIGURE 1: The general compression stress-strain curve of rock after the action of freeze-thaw cycles.

$$\sqrt{2\pi} \frac{\sigma_c - 2\nu_n \sigma_3}{E_n \varepsilon_c} S = \exp\left(-\frac{X^2}{2}\right). \quad (15)$$

Taking the logarithm of both sides of formula (1), we obtain

$$\ln\left[\sqrt{2\pi} \frac{\sigma_c - 2\nu_n \sigma_3}{E_n \varepsilon_c}\right] + \ln S = -\frac{X^2}{2}. \quad (16)$$

From formula (14), the following formulas can be obtained:

$$S = \exp\left\{-\frac{X^2}{2} - \ln\left[\sqrt{2\pi} \frac{\sigma_c - 2\nu_n \sigma_3}{E_n \varepsilon_c}\right]\right\}, \quad (17)$$

$$\mu_\varepsilon = XS + \ln \varepsilon_c. \quad (18)$$

3. Model Verification

The test results of red sandstone triaxial compression after different freeze-thaw cycles conducted in [31] were used to verify the rationality and applicability of the damage constitutive model of the rock subjected to freeze-thaw cycles based on lognormal distribution proposed in this paper.

According to the test results of [31], the model parameters established in this paper were shown in Table 1. The lognormal distribution parameters under the different freeze-thaw cycles and the different confining pressure were calculated by formulas (17) and (18).

For example, when the number of freeze-thaw cycles $n = 5$, $\sigma_3 = 2$ MPa. From Table 1, it can be obtained that

$$\begin{aligned} E_n &= 1.295 \text{ GPa}, \\ \nu_n &= 0.259, \\ \sigma_c &= 13.101 \text{ MPa}, \\ \varepsilon_c &= 10.6. \end{aligned} \quad (19)$$

TABLE 1: Parameter values of the rock damage constitutive model under different freeze-thaw cycles.

F-T cycles	σ_3 (MPa)	ϕ_n (°)	E_n (GPa)	ν_n	σ_c (MPa)	$\varepsilon_c/10^{-3}$	$S/10^{-3}$	$\mu_\varepsilon/10^{-3}$
0	2	38.4	1.387	0.258	14.572	11.0	0.2144	2.6588
	4		1.628	0.255	19.652	13.0	0.3018	2.8553
	6		1.649	0.254	24.866	16.0	0.3078	3.0644
5	2	35.8	1.295	0.259	13.101	10.6	0.2295	2.6289
	4		1.452	0.257	19.132	13.2	0.2099	2.8386
	6		1.565	0.255	24.347	17.0	0.3499	3.1278
10	2	33.6	1.156	0.262	12.701	11.3	0.2078	2.6821
	4		1.289	0.260	18.910	14.5	0.1950	2.9239
	6		1.325	0.259	23.519	19.2	0.3465	3.2494
20	2	30.9	0.890	0.268	11.356	12.1	0.0985	2.6606
	4		1.066	0.264	18.100	18.0	0.2996	3.1804
	6		1.240	0.260	22.903	21.1	0.4157	3.3369
40	2	29.2	0.710	0.277	10.570	15.2	0.2325	2.9907
	4		0.917	0.273	17.121	19.0	0.2627	3.2253
	6		0.932	0.269	21.274	24.9	0.3832	3.5076

Then, $\Phi(X) = (\sigma_c - 2\nu_n\sigma_3) / E_n\varepsilon_c = 13.101 - (2 * 0.259 * 2) / 1.295 * 10.6 = 0.8789$. By checking the normal distribution table, $X = 1.168$.

Substituting it into formula (17), we obtain

$$S = \exp \left\{ -\frac{1.168^2}{2} - \ln \left[\sqrt{2\pi} \frac{13.101 - (2 * 0.259 * 2)}{1.295 * 10.6} \right] \right\}$$

$$= 0.2295. \quad (20)$$

Finally, substituting $S = 0.2295$ into formula (18), we obtain

$$\mu_\varepsilon = XS + \ln \varepsilon_c = 1.168 * 0.2295 + \ln 10.6 = 2.6289. \quad (21)$$

Then, according to formula (11), the theoretical stress-strain curves of the rock under different freeze-thaw cycles and confining pressure were calculated, which were then compared with the experimental curves. The results were shown in Figure 2, wherein Figures 2(a)–2(e), respectively, represent the comparisons corresponding to the 0, 5, 10, 20, and 40 cycles of freeze-thaw.

It can be seen from Figure 2 that the theoretical values and the experimental values are relatively close, and the error is within a reasonable range, indicating that the statistical damage constitutive model is reasonable. The proposed model can accurately reflect the elasticity and yield stage of the rock. However, it must be pointed out that the theoretical curve cannot describe the compaction stage of the rock well. This is because the statistical constitutive model assumes that the loaded material are the rock microunits while the pores of the rock are not considered. Therefore, the effect of gas pressure in the pores of the rock during the compaction stage is ignored. In addition, the theoretical curve cannot describe the postpeak stage of the rock. This is because the statistical constitutive model believes that once the strain of rock microunits reaches the strain limit, it is completely

damaged and no longer bears any load. In fact, due to the friction between microunits, they still bear a certain residual stress after failure. Thus, this statistical constitutive model is not suitable for the postpeak stage of the rock.

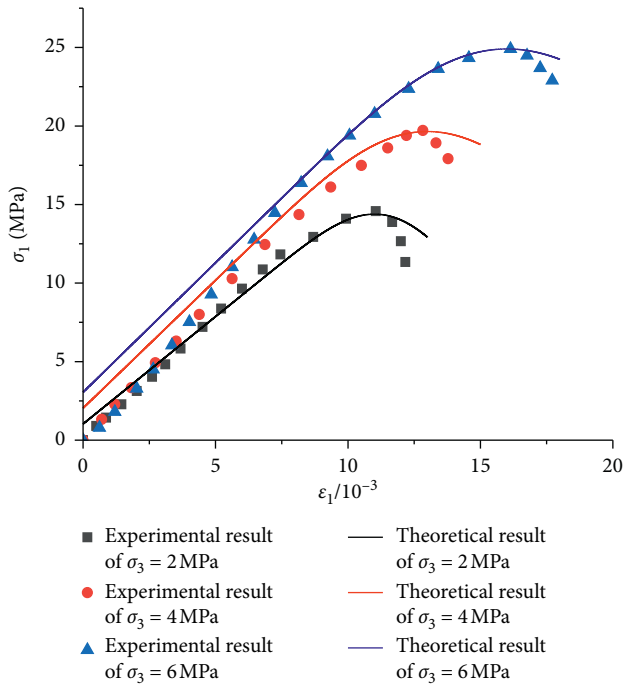
4. The Physical Meaning of Model Parameters μ_ε and S

Through carrying out sensitivity analysis of parameters μ_ε and S , respectively, the physical meanings they represent were discussed.

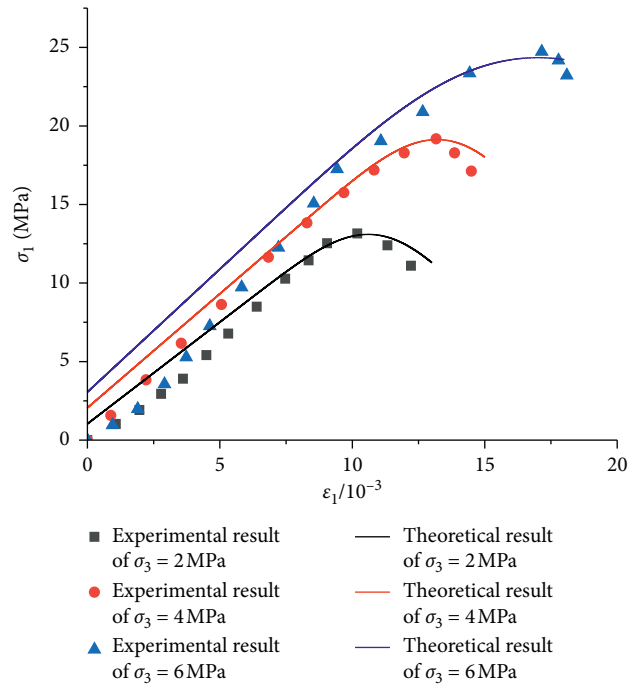
By fixing $E_n = 2$ GPa, $S = 1$, and $\sigma_3 = 0$ MPa and supposing $\mu_\varepsilon = 0.8, 0.9, 1.0, 1.1, \text{ and } 1.2$, respectively, the different stress-strain curves were shown in Figure 3. It can be seen from Figure 3 that when other parameters remain unchanged, as the parameter μ_ε increases, the elastic segments of the stress-strain curve basically overlap, the peak strength of the rock increases significantly, and the postpeak curves are roughly parallel. So, it can be considered that μ_ε reflects the strength of the rock, which is positively related with the strength of the rock.

Similarly, keeping $E_n = 2$ GPa, $\mu_\varepsilon = 1$, and $\sigma_3 = 0$ MPa and supposing $S = 0.8, 0.9, 1.0, 1.1, \text{ and } 1.2$, respectively, the different stress-strain curves were shown in Figure 4. It can be seen from Figure 4 that when other parameters are fixed, with the continuous increase of the parameter S , the elastic segments of the stress-strain curve basically coincide, the peak strength of the rock increases, and the curve after the peak becomes more and more gentle, indicating that the ductility of the rock is enhancing. So, it can be considered that the parameter S represents the brittleness of the rock. As S increases, the ductility of the rock increases while the brittleness of the rock decreases.

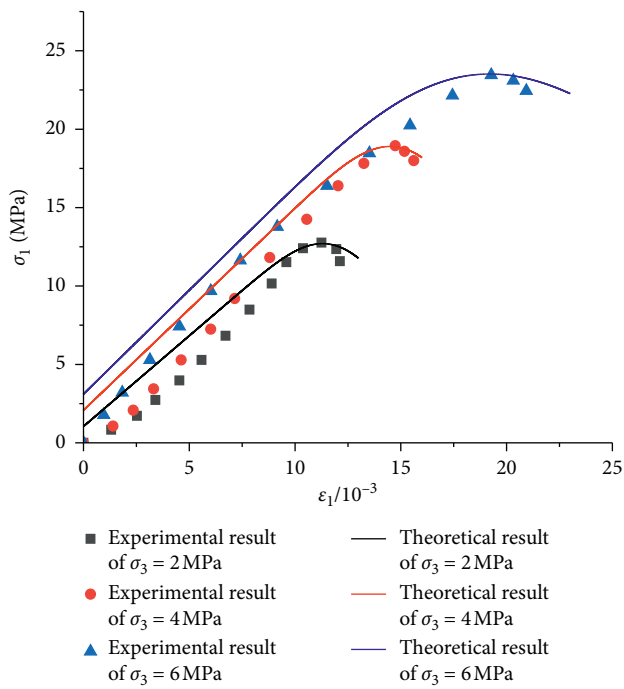
In the lognormal distribution, S represents the variance, which means the dispersion degree of the variable. When the value of S is small, the dispersion of the rock strain limit is also small, and the rock is more likely to undergo



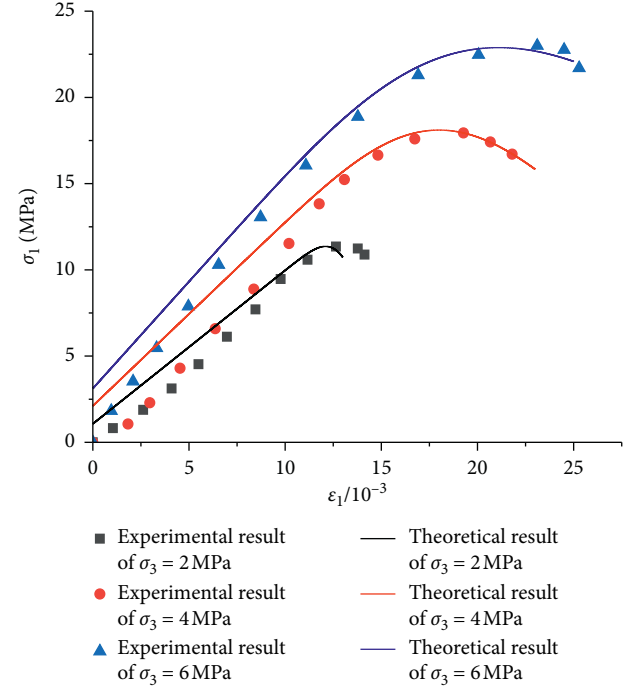
(a)



(b)



(c)



(d)

FIGURE 2: Continued.

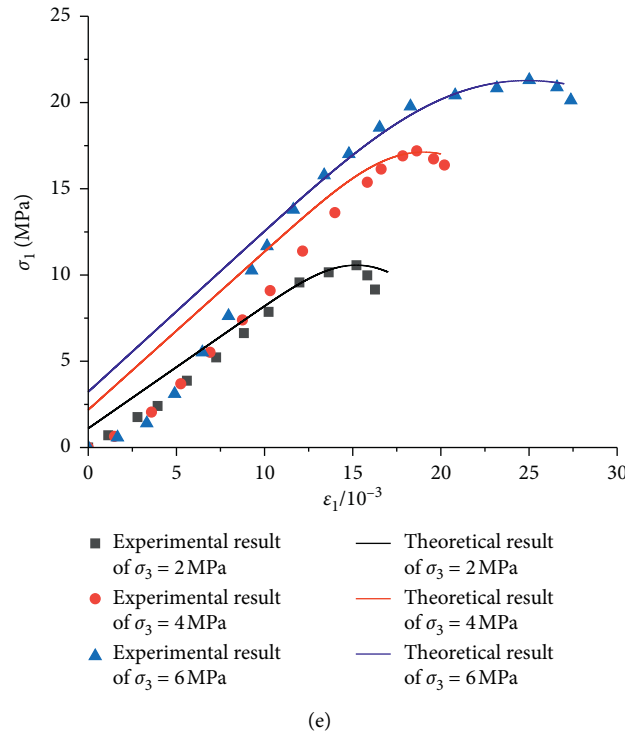


FIGURE 2: The stress-strain curves of rock subjected to different freeze-thaw cycles. (a) $n = 0$, (b) $n = 5$, (c) $n = 10$, (d) $n = 20$, and (e) $n = 40$.

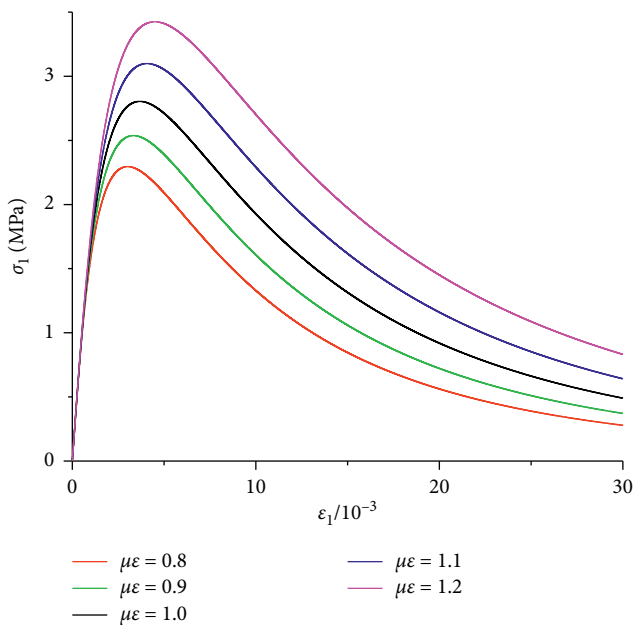


FIGURE 3: The sensitivity analysis of parameters μ_ϵ .

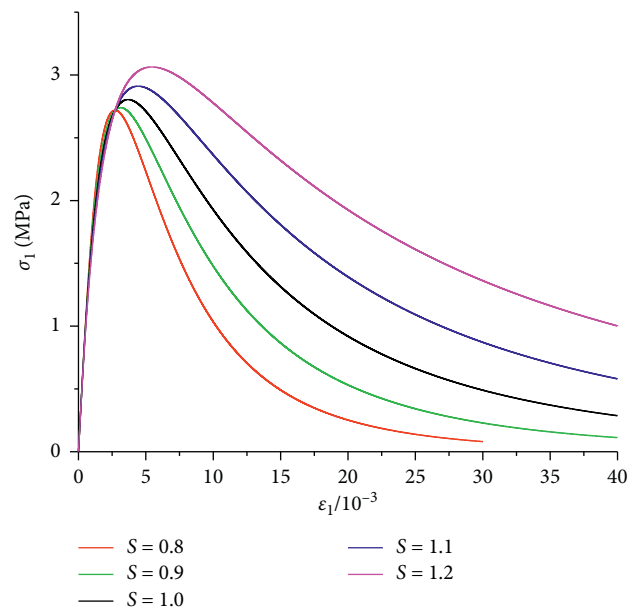


FIGURE 4: The sensitivity analysis of parameters S .

concentrated failure once the strain reaches the average value of the rock strain limit, causing brittle failure. In the case of large value of S , there is still a large part of the rock that has not failed when the strain value reaches the average strain limit, which results in the ductile failure of rock. This is consistent with the previous conclusion drawn by Figure 4.

5. Conclusion

- (1) Through theoretical derivation, this paper established a new statistical damage constitutive model of rock subjected to freeze-thaw cycles based on the lognormal distribution. The model is simple in expression, the parameters are easy to solve, and the stress-strain curve of the rock after the action of

different freeze-thaw cycles can be obtained, which has strong applicability.

- (2) The calculated theoretical curves by established model were compared with the experimental curves, which have similar trends and show a great coincidence, indicating that the statistical damage constitutive model is reasonable and valid. However, it cannot describe the compaction stage and the postpeak stage of the rock very well.
- (3) The sensitivity analysis of two lognormal distribution statistical parameters μ_ε and S have been carried out. The results show that μ_ε reflects the strength of the rock, which shows a positive relation. S represents the brittleness of the rock. When other parameters remain unchanged, the rock ductility increases while the rock brittleness decreases, as S increases.

Data Availability

Some or all data, models, or code that support the findings of this study are available from the corresponding author upon request.

Conflicts of Interest

The authors declare that they have no conflicts of interest.

Acknowledgments

This work was funded by the project (51774322) supported by National Natural Science Foundation of China and the project (2018JJ2500) supported by Hunan Provincial Natural Science Foundation of China.

References

- [1] X. Fan, X. Jiang, Y. Liu, H. Lin, K. Li, and Z. He, "Local stress distribution and evolution surrounding flaw and opening within rock block under uniaxial compression," *Theoretical and Applied Fracture Mechanics*, vol. 112, p. 102914, 2021.
- [2] S. Huang, Y. Liu, Y. Guo, Z. Zhang, and Y. Cai, "Strength and failure characteristics of rock-like material containing single crack under freeze-thaw and uniaxial compression," *Cold Regions Science and Technology*, vol. 162, pp. 1–10, 2019.
- [3] Y. Lu, X. Li, Y. Han, and J. Wu, "Mechanical properties of rock samples with a single natural weak plane after freeze-thaw action," *Cold Regions Science and Technology*, vol. 181, Article ID 103179, 2021.
- [4] S. Xie, H. Lin, Y. Wang et al., "Nonlinear shear constitutive model for peak shear-type joints based on improved Harris damage function," *Archives of Civil and Mechanical Engineering*, vol. 20, p. 95, 2020.
- [5] Y. Zhao, L. Zhang, W. Wang, W. Wan, and W. Ma, "Separation of elastoviscoplastic strains of rock and a nonlinear creep model," *International Journal of Geomechanics*, vol. 18, Article ID 4017129, 2018.
- [6] J. Mu, X. Pei, R. Huang, N. Rengers, and X. Zou, "Degradation characteristics of shear strength of joints in three rock types due to cyclic freezing and thawing," *Cold Regions Science and Technology*, vol. 138, pp. 91–97, 2017.
- [7] Y. Chen, H. Lin, X. Ding, and S. Xie, "Scale effect of shear mechanical properties of non-penetrating horizontal rock-like joints," *Environmental Earth Sciences*, vol. 80, p. 192, 2021.
- [8] H. Lin, X. Zhang, Y. X. Wang et al., "Improved nonlinear Nishihara shear creep model with variable parameters for rock-like materials," *Advances in Civil Engineering*, vol. 2020, Article ID 7302141, 15 pages, 2020.
- [9] Y. Zhao, L. Zhang, J. Liao, W. Wang, Q. Liu, and L. Tang, "Experimental study of fracture toughness and subcritical crack growth of three rocks under different environments," *International Journal of Geomechanics*, vol. 20, Article ID 4020128, 2020.
- [10] Y. Mo, S. Zuo, Z. Wu, Y. Zhang, and Y. Huang, "Experiment study on in-situ shearing characteristics and crack propagation of shale structural plane," *Water Resources and Hydropower Engineering*, vol. 52, pp. 134–143, 2021.
- [11] T. C. Chen, M. R. Yeung, and N. Mori, "Effect of water saturation on deterioration of welded tuff due to freeze-thaw action," *Cold Regions Science and Technology*, vol. 38, pp. 127–136, 2004.
- [12] C. Liu, D. Wang, Z. Wang, B. Ke, P. Li, and S. Yu, "Dynamic splitting tensile test of granite under freeze-thaw weathering," *Soil Dynamics and Earthquake Engineering*, vol. 140, Article ID 106411, 2021.
- [13] Y. Xu and F. Dai, "Dynamic response and failure mechanism of brittle rocks under combined compression-shear loading experiments," *Rock Mechanics and Rock Engineering*, vol. 51, pp. 747–764, 2018.
- [14] Q. Ma, D. Ma, and Z. Yao, "Influence of freeze-thaw cycles on dynamic compressive strength and energy distribution of soft rock specimen," *Cold Regions Science and Technology*, vol. 153, pp. 10–17, 2018.
- [15] J. Li, R. B. Kaunda, and K. Zhou, "Experimental investigations on the effects of ambient freeze-thaw cycling on dynamic properties and rock pore structure deterioration of sandstone," *Cold Regions Science and Technology*, vol. 154, pp. 133–141, 2018.
- [16] A. Li, Y. Liu, F. Dai, K. Liu, and M. Wei, "Continuum analysis of the structurally controlled displacements for large-scale underground caverns in bedded rock masses," *Tunnelling and Underground Space Technology*, vol. 97, pp. 1–15, Article ID 103288, 2020.
- [17] Y. Liu, F. Dai, L. Dong, N. Xu, and P. Feng, "Experimental investigation on the fatigue mechanical properties of intermittently jointed rock models under cyclic uniaxial compression with different loading parameters," *Rock Mechanics and Rock Engineering*, vol. 51, pp. 47–68, 2018.
- [18] X. Qu, L. Meng, and C. Hao, "Triaxial creep experiment and damage model for slate under different confining pressures and beddings," *Water Resources and Hydropower Engineering*, vol. 51, pp. 159–167, 2020.
- [19] B. Zhang, L. Wang, and S. Zhang, "Study on constitutive model for unloading damage of sandstone under effect of heat-wet cycle," *Water Resources and Hydropower Engineering*, vol. 49, pp. 162–168, 2018.
- [20] H. Zhang, X. Meng, and G. Yang, "A study on mechanical properties and damage model of rock subjected to freeze-thaw cycles and confining pressure," *Cold Regions Science and Technology*, vol. 174, Article ID 103056, 2020.
- [21] Y. Lu, X. Li, and A. Chan, "Damage constitutive model of single flaw sandstone under freeze-thaw and load," *Cold Regions Science and Technology*, vol. 159, pp. 20–28, 2019.
- [22] F. Gao, X. Xiong, C. Xu, and K. Zhou, "Mechanical property deterioration characteristics and a new constitutive model for

- rocks subjected to freeze-thaw weathering process,” *International Journal of Rock Mechanics and Mining Sciences*, vol. 140, Article ID 104642, 2021.
- [23] S. Huang, Q. Liu, A. Cheng, and Y. Liu, “A statistical damage constitutive model under freeze-thaw and loading for rock and its engineering application,” *Cold Regions Science and Technology*, vol. 145, pp. 142–150, 2018.
- [24] A. Li, F. Niu, C. Xia, C. Bao, and H. Zheng, “Water migration and deformation during freeze-thaw of crushed rock layer in Chinese high-speed railway subgrade: large scale experiments,” *Cold Regions Science and Technology*, vol. 166, Article ID 102841, 2019.
- [25] Z. Wang, Z. Zhu, and S. Zhu, “Thermo-mechanical-water migration coupled plastic constitutive model of rock subjected to freeze-thaw,” *Cold Regions Science and Technology*, vol. 161, pp. 71–80, 2019.
- [26] M. Deprez, T. De Kock, G. De Schutter, and V. Cnudde, “A review on freeze-thaw action and weathering of rocks,” *Earth-Science Reviews*, vol. 203, Article ID 103143, 2020.
- [27] X. Zhang, H. Lin, Y. Wang, R. Yong, Y. Zhao, and S. Du, “Damage evolution characteristics of saw-tooth joint under shear creep condition,” *International Journal of Damage Mechanics*, vol. 30, pp. 453–480, 2021.
- [28] Z. P. Bazant, “Size effect,” *International Journal of Solids and Structures*, vol. 37, pp. 69–80, 2000.
- [29] H. M. Zhang and G. S. Yang, “Research on rock damage model under the coupling action of freeze-thaw and load,” *Chinese Journal of Rock Mechanics and Engineering*, vol. 29, pp. 471–476, 2010.
- [30] J. Lemaitre, “How to use damage mechanics,” *Nuclear Engineering and Design*, vol. 80, pp. 233–245, 1984.
- [31] C. Peng, “Research on damage and failure characteristics of freeze-thaw loaded rock based on residual strength,” Science and Technology University of Xi’an, Xi’an, China, Master Degree, 2017.

Research Article

Experimental Analysis of Bending Stiffness Characteristics of Grouted Double Mortise-Tenon Joint for Prefabricated Metro Station Structure

Xiuren Yang ^{1,2}, Fang Lin ^{1,2} and Meiqun Huang^{1,2}

¹Beijing Urban Construction Design and Development Group Co., Ltd., Beijing 100037, China

²National Engineering Laboratory for Green & Safe Construction Technology in Urban Rail Transit, Beijing 100037, China

Correspondence should be addressed to Xiuren Yang; yangxr@bjucd.com and Fang Lin; felyo@foxmail.com

Received 5 March 2021; Revised 29 March 2021; Accepted 14 June 2021; Published 23 June 2021

Academic Editor: Rihong Cao

Copyright © 2021 Xiuren Yang et al. This is an open access article distributed under the Creative Commons Attribution License, which permits unrestricted use, distribution, and reproduction in any medium, provided the original work is properly cited.

The grouted mortise-tenon joint, invented as the connection between the large prefabricated components, is the key to the prefabricated underground structures, and the double-tenon joint is most widely used in the prefabricated metro station structure. This paper conducts characteristic analysis of bending stiffness with a 1 : 1 prototype test in key working direction of different joint types for grouted double mortise-tenon joint. The results show that the double-tenon joint is characteristic of variable stiffness under different loads. Change laws of double-tenon joint bending stiffness without and with auxiliary pretightening device in tension side and compression side are also discussed. The correlations for calculating double-tenon joint bending stiffness with various axial loads and bending moments are derived at last, which offers the theory foreshadowing of similar joints.

1. Introduction

With the rapid development of rail transit construction in China, social-environmental awareness increases continuously. Moreover, long and tight construction period, large resource consumption, decrease of young laborers of civil engineering causing shortage of skilled labor, and not guaranteed structure quality bring great challenges to traditional construction technology of metro station. The above situations are particularly prominent in the northeast of China like Changchun city, located in the northeast region, which is so cold that 4~5 months' winter break is needed for metro construction, which causes huge deadline pressure and is hard to guarantee construction quality under low temperature [1–4].

To address these problems, a new prefabricated technology has been researched, developed, and implemented by Yang et al. team for constructing metro stations [5–7]. Shuangfeng Station on Changchun Metro Line 2 was selected in 2012 as a test station to conduct systemic research and develop the prefabrication technology for designing

underground metro station structures. The prefabricated structure has significant advantages of high efficiency, high quality, and green and environmental protection. For now, 6 prefabricated metro stations have been completed.

The six cut-and-cover stations are all supported by an anchor-pile system. All those horseshoe-shaped two-storey stations are 20.5 m wide and 17.45 m high. The full prefabricated station structure is assembled by seven 2 m width prefabricated components (see Figure 1) without any concrete wet spraying. The grouted double-tenon joint is the most widely used joint connection method in the prefabricated station structure of Changchun Metro Line 2 (see Figure 1). The joint performance of a prefabricated metro station has an important impact on the mechanical properties of the whole structure [5–7]. The bending stiffness (rotational stiffness) of the joint is one of the main factors that directly affect the distribution of internal force (especially bending moment) of the structural system. Its stiffness presents a complex mechanical relationship, which changes with the load atmosphere, joint type and size, and other factors.

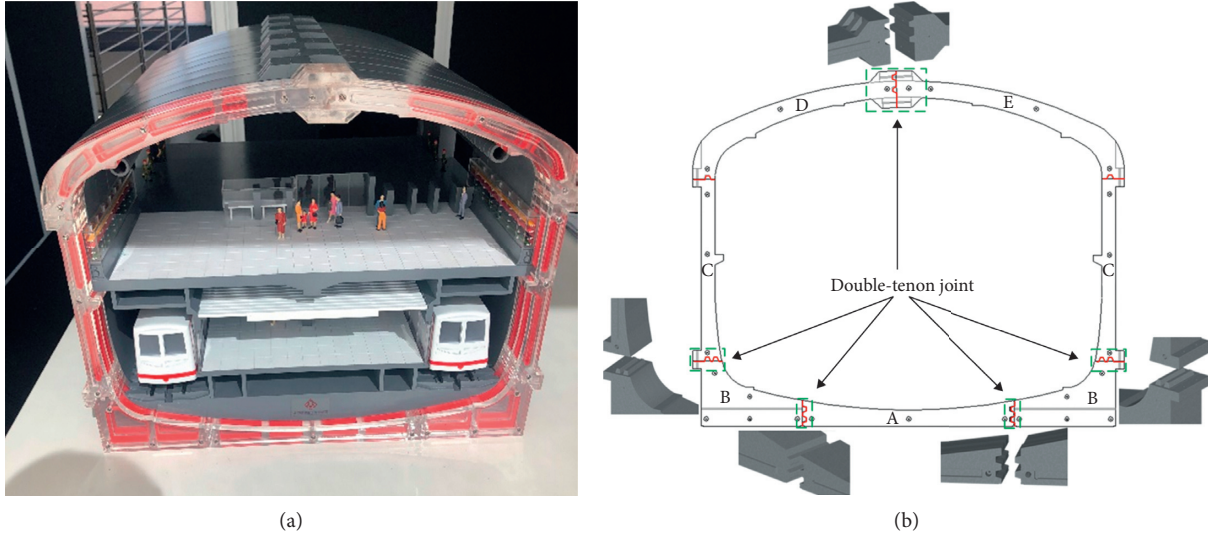


FIGURE 1: Prefabricated metro station display and arrangement of grouted double-tenon joint.

In the past, scholars have carried out a more in-depth study on the mechanical behavior of shield tunnel segment joints [8–11], but due to the great differences in the structural type, connection method, and loading process of prefabricated station, the research results of shield tunnel cannot be directly applied [12–15]. Therefore, the research team independently developed a set of comprehensive test systems which can be used for prototype or large-scale component joint test [16]. Taking the joint used in Changchun prefabricated station as the research object, the mechanical properties of grouted mortise-tenon joint were studied through prototype test. Based on the test data, this paper analyzes the bending stiffness characteristics of grouted double-tenon joint and puts forward the relevant empirical calculation formula of bending stiffness of the joint. It is the first time to study the characteristics of the newly developed joint for the new prefabricated underground structure, and it is very helpful for engineering application.

2. Test Scheme

In this study, the bending properties of three kinds of grouted double-tenon joints under various axial loads were tested, including (1) the joint without auxiliary pretightening device; (2) the joint with auxiliary pretightening device in tension side; (3) the joint with auxiliary pretightening device in compression side. The test conditions and loading mode are shown in Table 1. The auxiliary pretightening device is composed of the pretightening steel bar and a boss, as shown in the blue dotted box in Table 1. The specimen is 1:1 prototype size along the key loading direction (cross-section direction shown in Figure 1), and the actual width of 2000 mm is taken as 500 mm along the nonkey loading direction.

In the test, the edge measurement method is used to indirectly measure the joint rotation angle (as shown in Figure 2). The angle θ is calculated by the values of A and B

measured by the draw-wire displacement sensors and the carrier rod displacement sensors arranged on the top surface and two sides of the joint specimen. The calculation formula is as follows:

$$\left\{ \begin{array}{l} A \times X_2 = B \times X_1, \\ \sin \frac{\theta}{2} = \frac{B}{2X_2}, \\ X_1 + X_2 = \frac{1.02}{1.42}, \\ \left(\frac{\text{without}}{\text{with auxiliary pretightening device}} \right). \end{array} \right. \quad (1)$$

3. Analysis of Test Results

3.1. Joint Resistance Bending Moment. The main structural components of prefabricated metro station are in an eccentric compression state. For the joint interface, compression effects of axial force, the connection force of joint (such as the force of steel bar, the bond force of interface, etc.), and the embedment of long tenon are a pair of equilibria corresponding to the bending action of the joint. The bending moment formed by the axial force, the joint connection force, and the embedment effect of the long tenon in bending deformation are used to resist the bending moment of the joint. It is an important factor to keep the joint stable, which we call the “resistance” of the joint.

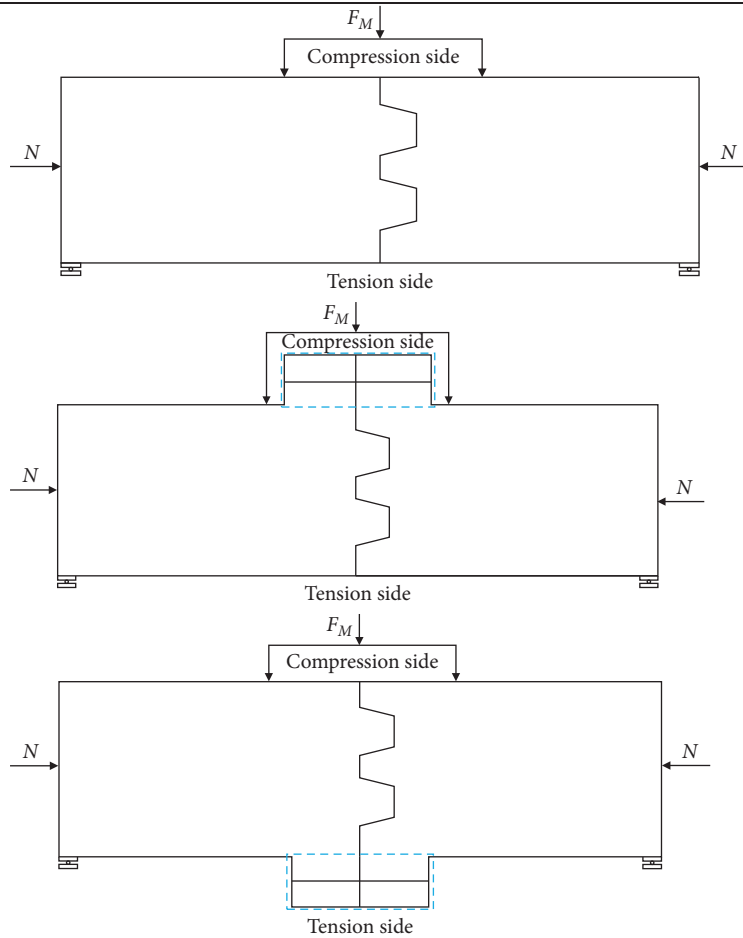
The expression of “resistance” is $M = M_R + M_{R2} + M_{R3} + M_{R4}$, including the following:

- (a) The resistance moment (resistance caused by the active force) formed by the axial force of the components changes with the axial force, and the

TABLE 1: Test cases and layout.

Cases	Axial load: 0 kN, 500 kN, 1000 kN, and 1250 kN	Without auxiliary pretightening device	
Test content	The amount of opening and compression of the joint (so as to obtain the joint rotation angle); the whole process record of crack development details of the joint		

Loading layout



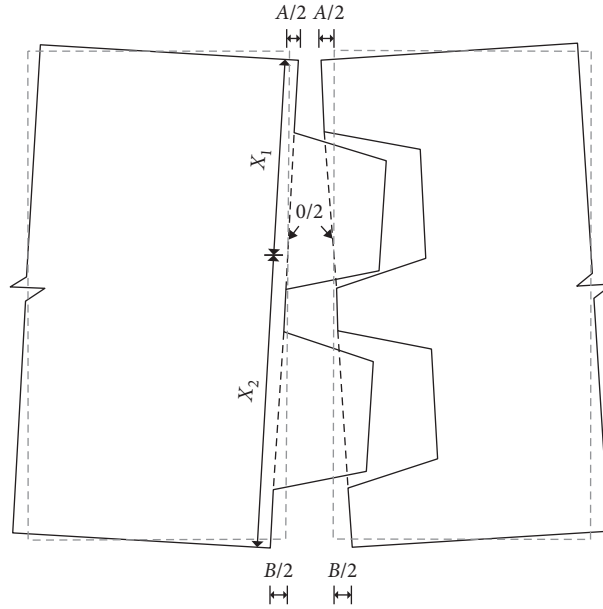


FIGURE 2: Measurement method for rotation-displacement of grouted double-tenon joint.

resistance moment M_R can be calculated according to Figure 3 with the following formula:

$$M_R = N \cdot l_R, \quad (2)$$

where M_R is the resistance moment formed by axial force; N denotes the axial force; l_R represents the resistance arm, taking $h/2$ as the length of the contact surface of the joint (i.e., grouting length).

- (b) The resistance force M_2 caused by the joint connecting steel bar includes the pretightening moment of the steel bar and the moment formed by the tensile force of the steel bar at the joint opening side caused by the opening (or compression) of the joint under loading (the pretightening force of the steel bar is relaxed for the compressed side). This part of resistance can be calculated according to the following formula in Figure 4:

When $T_0 > N$, the pretightening effect of the steel bar is not completely offset by the compressive stress generated by the axial force; here, $M_2 = T \cdot h_T$. T_0 is the initial pretightening force. T is the actual pretightening force. T is a positive value when the steel bar is located in tension side, and it is a negative value when the steel bar is located in compression side.

When $T_0 \leq N$, the steel bar is relaxed ($T = 0$), and the pretightening effect of the steel bar can be ignored.

- (c) Due to the low tensile strength of concrete, the resistance of M_{3-1} caused by bond strength of the joints can be negligible.
- (d) The mortise and tenon of the joint embedded together can also provide a certain resistance under the

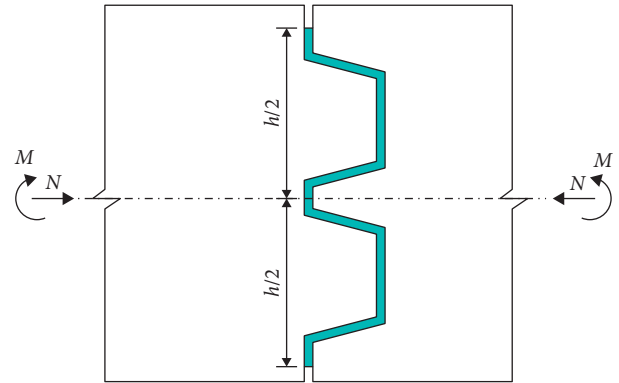


FIGURE 3: Calculation model of resistance bending moments M_R .

action of bending moment. In calculation, the moment M_4 (when there is bending effect of tenon) and (or) the moment M_{3-2} formed by the bond action between mortise and tenon can be included according to the actual stress trend. Because the two tenons of the double-tenon joint are located at the core of the tension and compression area under the bending action, the tenon bears the tension and compression effect, and the bending effect is weak, so the embedment effect between mortise and tenon cannot be considered. Considering the low bond strength between mortise and tenon, the tension and compression effect can also be ignored.

The joint resistance, especially the resistance moment, is an important index to analyze the mechanical behavior of the joints.

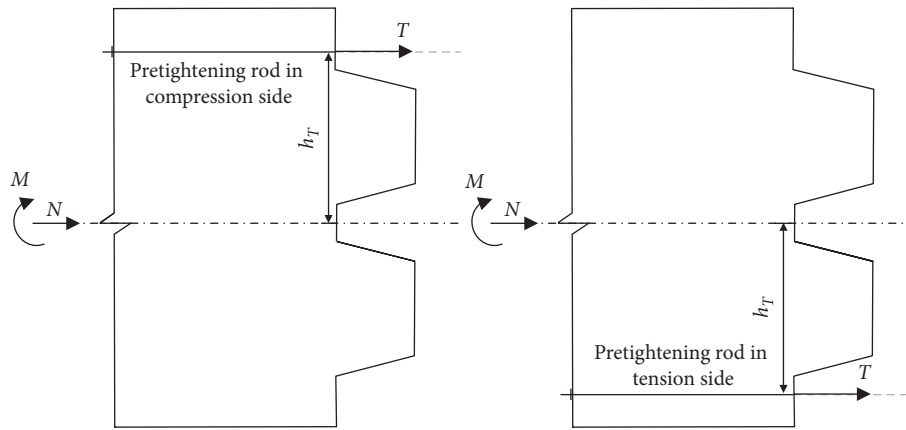


FIGURE 4: Calculation model of resistance M_R from pretightening rod.

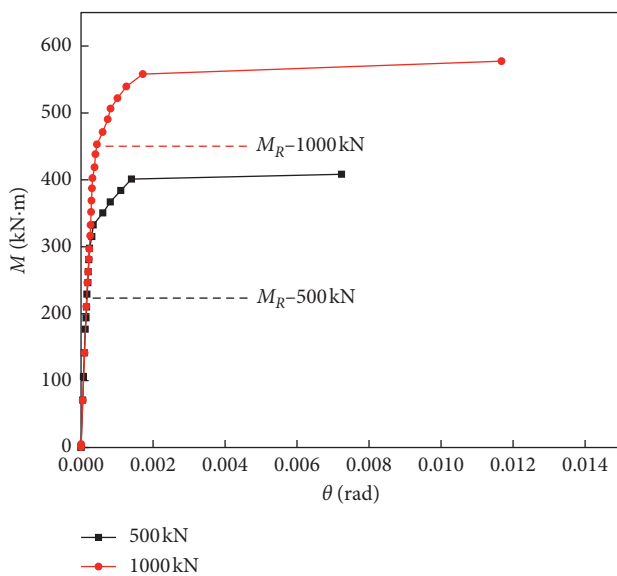


FIGURE 5: Comparison of $M-\theta$ relationship curve for double-tenon joint without auxiliary pretightening device under different axial loads.

3.2. Bending Moment: Rotation Relationship of Double-Tenon Joint under Different Working Conditions

3.2.1. Joint without the Auxiliary Pretightening Device. According to the joint rotation angle θ obtained from the test under different axial loads and bending moments, the $M-\theta$ relationship curve of the grouted double-tenon joint without auxiliary pretightening device is shown in Figure 5.

It can be found that $M-\theta$ curve is composed of linear segment and one (or more) nonlinear segment. The axial force has a great influence on the $M-\theta$ curve, and its bending capacity is proportional to the axial force.

Through in-depth analysis of $M-\theta$ curve (see Figure 6), it is found that the straight segment (linear segment) corresponds to the stage in which the joint remains intact without any damage (or very slight damage), and the bending moment loading value at this stage is basically equivalent to the joint resistance moment. When the bending moment loading value exceeds the resistance moment, the joint

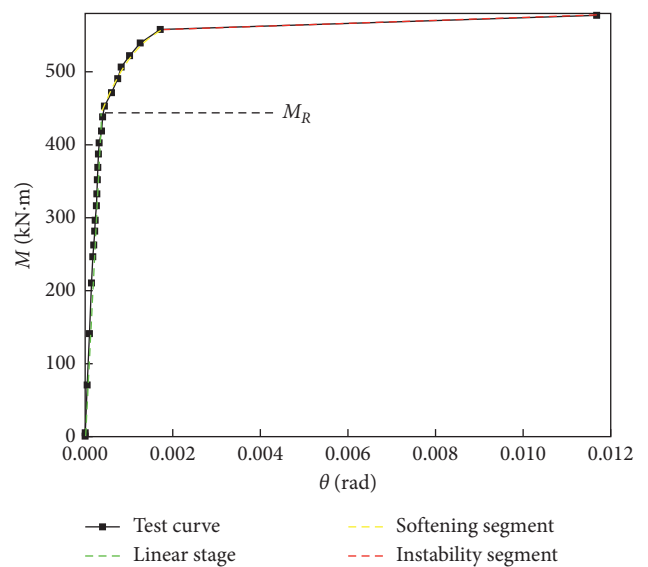


FIGURE 6: $M-\theta$ relationship curve of double-tenon joint without auxiliary pretightening device under axial load 1000 kN.

cracks appear and develop with the increase of bending moment. The integrity of the joint becomes worse, and the joint softens. The $M-\theta$ curve enters the nonlinear stage at the same time. At the end of the softening stage, the joint cracks are completely penetrated and rapidly developed, and the joints are subject to transient failure and completely lose the bearing capacity.

After clarifying the physical meaning of the above joint behavior, we can divide the $M-\theta$ curve of the joint loading process into three stages:

- (a) Linear stage: in this stage, the peak load moment does not exceed the resistance moment of the joint. The joint is not damaged at this stage, and the bending moment is basically linear with the rotation angle. Particularly in the initial stage of loading, there is almost no rotation for the joint surface, and the rotation angle comes from the rotation of the beam.
- (b) Nonlinear stage (joint softening stage): the main reason of joint softening at this stage is that the

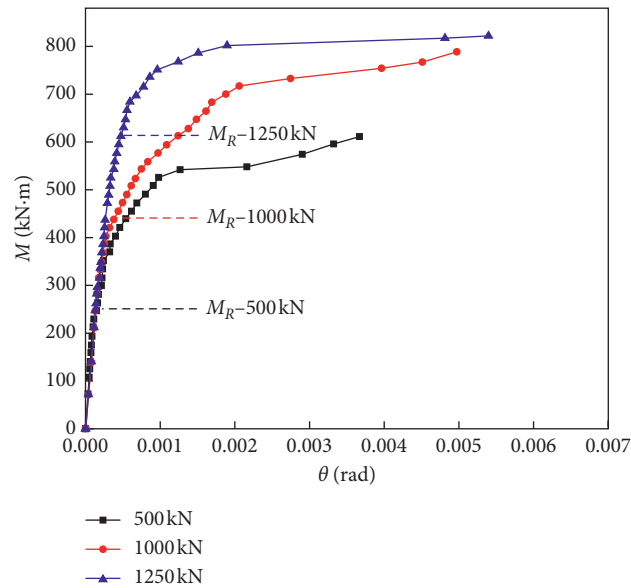


FIGURE 7: Comparison of M - θ relationship curve for double-tenon joint with auxiliary pretightening device in tension side under different axial loads.

integrity of joint becomes worse after cracks appear in the joint, and the other reason is that the concrete has entered a significant plastic stage.

- (c) Joint instability stage: at the end of the softening stage, the cracks of the joint are completely penetrated, transient failure and instability occur in the joint, and the bearing capacity is completely lost. The joint rotation angle develops rapidly. At this time, the M - θ curve is a straight line approximately horizontal. According to the rotational deformation of the joint, with the increase of axial force, the deformation of the joint at the end of the softening stage has a small increase trend, but in the linear stage, the deformation is basically the same regardless of the axial force.

3.2.2. Joint with the Auxiliary Pretightening Device in Tension Side. Figure 7 shows the M - θ curve of double-tenon joint of auxiliary pretightening device (two steel bars with diameter of 18 mm) in tension side under different axial loads. It can be seen from the curve that the axial force also has a great influence on the bearing capacity of the joint. The M - θ curve also shows a three-stage distribution similar to that of the joint without auxiliary pretightening device, that is, linear stage, nonlinear stage (joint softening section), and instability stage, but it is also different.

Figure 8 shows the comparison of M - θ curves of joints with and without auxiliary pretightening devices in tension side. The difference can be clearly seen from the figure: the overall bearing capacity of the joint with auxiliary pretightening device is improved (the linear stage is lengthened, and the nonlinear stage is extended). The lengthening of the linear stage is mainly due to the increase of the resistance moment caused by preload of pretightening steel bar. The extension of nonlinear stage is mainly due to the following reasons: (a) The

preload of pretightening steel bar provides the unbalanced additional preload on the contact surface of the joint in addition to the axial force (the distribution of the preload is uneven, mainly concentrated near the steel bar). These preloads form a change process from large to small (harmless release section) with the increase of joint bending load, which can delay the occurrence of joint damage. (b) The axial force increases with the opening of the joint, which provides additional resistance moment, delays (reduces) the deterioration process of the joint, and improves the ductility of the joint. It can be seen that the joint rotation is effectively restrained in the nonlinear stage due to the additional tension of the steel bar.

3.2.3. Joint with the Auxiliary Pretightening Device in Compression Side. Figure 9 shows the M - θ curve of double-tenon joint of auxiliary pretightening device in compression side under different axial loads. It can be seen from the curve that the axial force still has a great influence on the bearing capacity of the joint. The greater the axial force is, the higher the bearing capacity of the joint is.

There are significant differences in the form of M - θ relationship curve among the joint without auxiliary pretightening device and the joint with auxiliary pretightening device in tension side, which are mainly reflected in the following aspects: (a) the curve shape evolves from the three-stage distribution to the two-stage distribution, which is composed of linear segment and instability failure segment, and the nonlinear segment is significantly shortened or even disappeared; (b) the slope of the linear segment is significantly reduced and changes from the steep shape to the relatively gentle slope state; (c) in the early stage of instability stage, the joint rotation angle becomes smaller and the joint is more likely to be damaged.

Figure 10 shows the comparison of M - θ curves between the auxiliary pretightening device in compression side and in

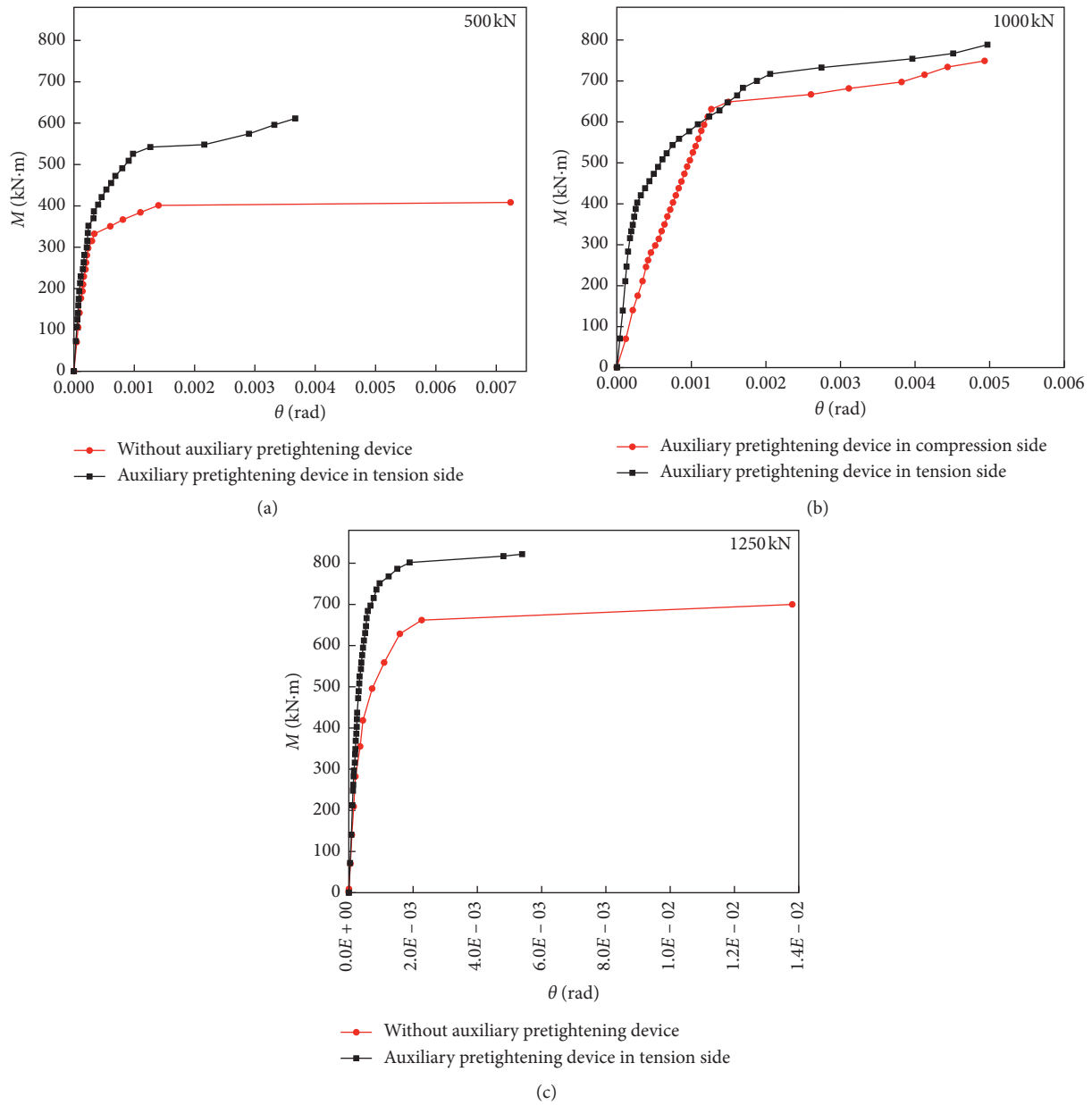


FIGURE 8: Comparison of $M-\theta$ relationship curve for double-tenon joint with and without auxiliary pretightening device under different axial loads.

tension side. It is not difficult to find that the bearing capacity of the auxiliary pretightening device in compression side is lower than that of the auxiliary pretightening device in tension side, and the slope of the linear segment is significantly reduced, which means that the stiffness of the joint is greatly reduced. The nonlinear segment of the joint is longer when the pretightening steel bar is in tension side, which means that the joint has good ductility. However, there is no ductile transition segment in the joint when the pretightening steel bar is in compression side. When the loading reaches the limit, it directly connects with the failure stage. It is found that when the pretightening steel bar is in compression side, the tensile force can form a negative resistance moment (consistent with the bending direction), which will

reduce the ability of the joint to bear bending moment. The pretightening steel bar increases the stress of the concrete in compression side, which results in the joint damage ahead of time and reaches the limit faster after loading, the allowable rotation deformation range of the joint decreases, and the overall deformation decreases. Under the same bending moment, the joint rotation is greater than that of the joint with auxiliary pretightening device in tension side.

3.3. Bending Stiffness Characteristics of Double-Tenon Joint. The bending stiffness k_θ ($k_\theta = dM/d\theta$, i.e., the loading value of bending moment forming unit rotation angle) reflects the ability of joint to resist bending moment.

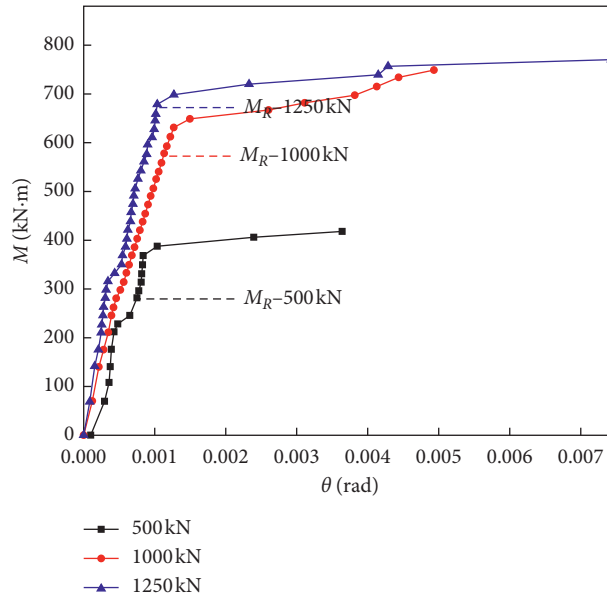


FIGURE 9: Comparison of $M-\theta$ relationship curve for double-tenon joint with auxiliary pretightening device in compression side under different axial loads.

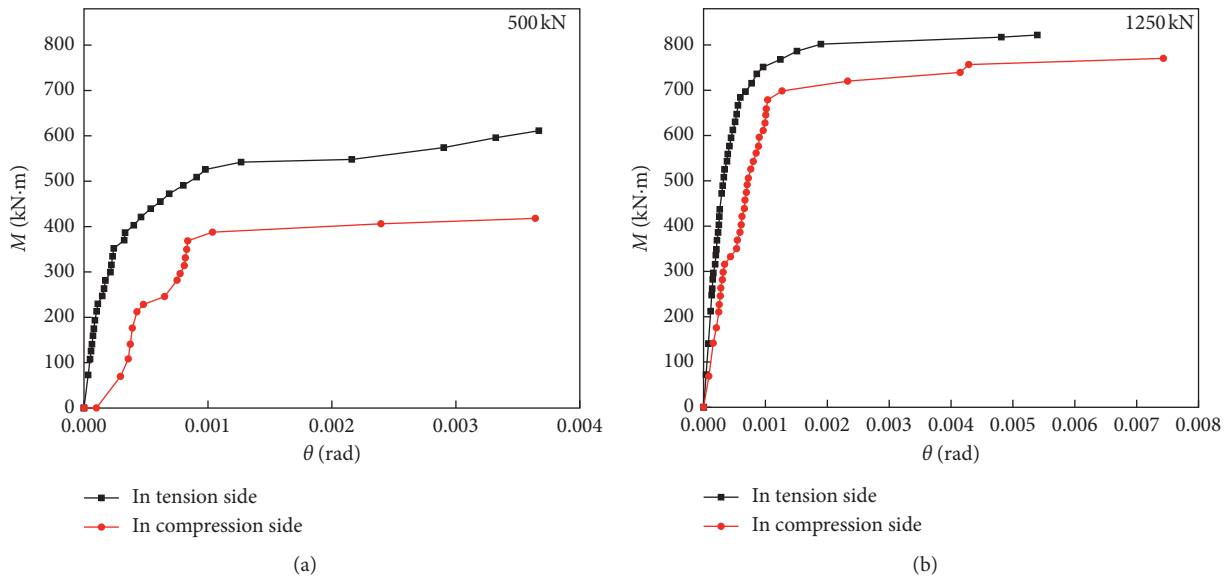


FIGURE 10: Comparison of $M-\theta$ relationship curve for double-tenon joint with auxiliary pretightening device in compression side and without auxiliary pretightening device under different axial loads.

In the past, a fixed value of joint bending stiffness is usually used for structural analysis according to experience in the structural design of shield tunnel. According to the $M-\theta$ curve obtained from the joint test under different conditions, it can be seen that the stiffness of the joint does not keep a constant value under different stress conditions, and the bending stiffness characteristics of the joint with the change of the stress environment will have an important impact on the mechanical behavior of the prefabricated

structure, so it is very important to master the bending stiffness characteristics of the joint.

In this paper, the $M-\theta$ curve obtained from the previous joint test is used to fit the empirical formulas of $M=f(\theta)$, and then according to $k_{\theta}=dM/d\theta$ relationship, the empirical formulas of bending stiffness of joints are obtained, respectively, and the stiffness characteristics of joints are analyzed. On the basis of identifying the key stress points and characteristic points of failure stage, the practical

application range of bending stiffness of different types of joints is proposed.

3.3.1. Joint without the Auxiliary Pretightening Device. Using the $M-\theta$ curve of the joint without auxiliary pretightening device, the curve type conforms to the logarithmic function type. Next, according to $k_\theta = dM/d\theta$ relationship, the joint bending stiffness curve in the whole loading process is shown in Figure 11, and the fitting stiffness expression is shown in formula (3). The position of key points on the curve, including joint resistance moment (transition point of linear segment and nonlinear segment) and end of nonlinear segment (transition point of joint softening segment and instability segment), is identified in the diagram. Under the condition of small axial load of 500 kN, the transition point of linear segment and nonlinear segment is about 325 kN·m. In addition, in the initial stage of loading ($M \leq 140$ kN·m), the rotation is very small, which is basically equal to the rotation angle of continuous beam. In order to avoid the infinite value of $dM/d\theta$, the stiffness of continuous beam is used instead. At the end of bearing, because of joint instability, it is not considered as the use stage, and the stiffness calculation formula of this part is not considered. After analysis, the stiffness curve has the following key characteristics:

- In the whole loading range, with the change of the load atmosphere, the stiffness of the joint is also in a state of constant change, and the variable stiffness characteristics of the joint are obvious. The specific change trend is as follows: under a certain axial force, the stiffness of the joint decreases with the increase of bending moment. Under the same bending moment, the stiffness of the joint increases with the increase of axial force.
- The joint stiffness of load-bearing zone and design utilization zone under different axial loads is present in Table 2.

$$k_\theta = \begin{cases} 91.15 \cdot e^{(1024.2 - M/91.15)} & (500 \text{ kN}), \\ 145.67 \cdot e^{(1498.1 - M/145.67)} & (1000 \text{ kN}), \\ 170.26 \cdot e^{(1717 - M/170.26)} & (1250 \text{ kN}). \end{cases} \quad (3)$$

3.3.2. Joint with the Auxiliary Pretightening Device. From the $M-\theta$ curve of Section 3.2.3, it can be seen that the negative resistance moment caused by the auxiliary pretightening device in compression side increases the joint rotation and reduces the joint stiffness compared with the joint without auxiliary pretightening device. In this paper, the stiffness characteristics of the joint with auxiliary pretightening device in tension side are discussed in detail.

The $M-\theta$ curve of the joint with auxiliary pretightening device in tension side also conforms to the logarithmic function type. According to $k_\theta = dM/d\theta$ relationship, the joint bending stiffness curve in the whole loading process is shown in Figure 12, and the fitting stiffness expression is shown in formula

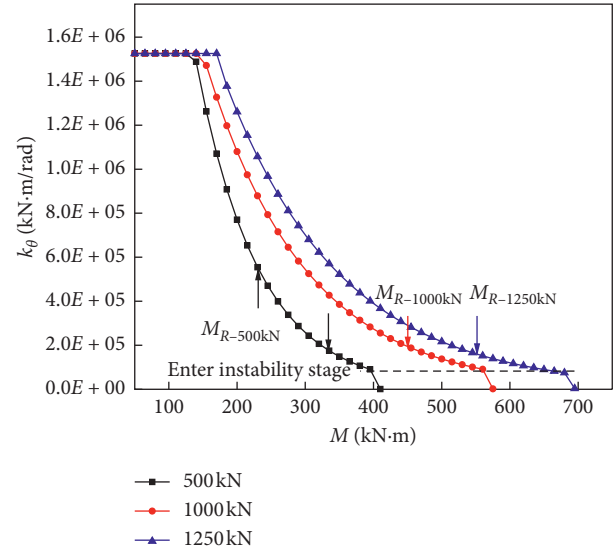


FIGURE 11: Bending stiffness curve of double-tenon joints without auxiliary pretightening device under different axial loads.

(4). The position of key points on the curve, including joint resistance moment (transition point of linear segment and nonlinear segment) and end of nonlinear segment (transition point of joint softening segment and instability segment), is identified in the diagram. Under the condition of small axial force of 500 kN, the transition point of linear section and nonlinear section is about 380 kN·m. In addition, in the initial stage of loading, the rotation is very small, which is basically equal to the rotation angle of the continuous beam. In order to avoid the infinite $dM/d\theta$, the stiffness of the continuous beam is used instead. At the end of the bearing period, because of the instability of the joint, this part of the stiffness calculation formula is not considered. After analysis, the stiffness curve has the following key characteristics:

- The characteristics of variable stiffness of the joint are basically consistent with those of the joint without auxiliary pretightening device when the auxiliary pretightening device is located in tension side. However, due to the reinforcement effect of the pretightening steel bar, the joint stiffness is in a constant change state with the change of the load atmosphere, and the variable stiffness characteristics of the joint are obvious. The specific change trend is as follows: under a certain axial force, the stiffness of the joint decreases with the increase of bending moment. Under the same bending moment, the stiffness of the joint increases with the increase of axial force.
- The joint stiffness of load-bearing zone and design utilization zone under different axial loads is present in Table 3.

$$k_\theta = \begin{cases} 136.83 \cdot e^{(1468.51 - M/136.83)} & (500 \text{ kN}), \\ 163.85 \cdot e^{(1722.23 - M/163.85)} & (1000 \text{ kN}), \\ 241.33 \cdot e^{(2429.8 - M/241.33)} & (1250 \text{ kN}). \end{cases} \quad (4)$$

TABLE 2: Design ranges and stiffness values of double-tenon joints without auxiliary pretightening device under different axial loads.

Axial load (kN)	Design bearing range (kN·m)	Design using bending stiffness (kN·m/rad)
500	0~325	$1.96E+05 \sim 1.53E+06$
1000	0~450	$1.94E+05 \sim 1.53E+06$
1250	0~562.5	$1.52E+05 \sim 1.53E+06$

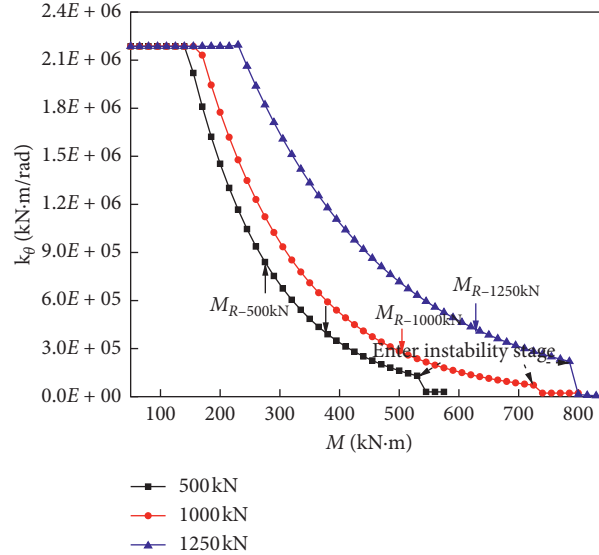


FIGURE 12: Bending stiffness curve of double-tenon joints with auxiliary pretightening device in tension side under different axial loads.

3.3.3. Variation Law and Influence Factors of Bending Stiffness

(1) Different Axial Loads and Bending Moment Combinations.

According to the empirical formula of bending stiffness fitted by the test, a three-dimensional diagram of the bending stiffness of the double-tenon joint with auxiliary pretightening device in tension side under the combined axial and bending force is drawn, as shown in Figure 13. It can be seen that the bending stiffness of double-tenon joint is affected by both axial force and bending moment and decreases with the increase of the ratio of bending moment to axial force, that is, eccentricity. Under the same axial force, the bending stiffness of double-tenon joint decreases. When the bending moment is small, the bending stiffness is very large and decreases with the increase of bending moment.

It can be seen that the joint reflects the characteristics of variable stiffness, and the bending stiffness increases with the increase of the axial force of the structure and decreases with the increase of the bending moment. In the beginning, the joint stiffness is large, with the bending moment loading exceeding the resistance moment, the joint crack appears, the joint stiffness decreases, and in the later stage of bearing, the permanent crack forms and enters the instability stage and the bending stiffness decreases rapidly.

(2) Different Types of Double-Tenon Joint. Figure 14 shows the bending stiffness curves of three types of double-tenon joints under 1000 kN axial force. It can be seen that the bending stiffness of the joint with auxiliary pretightening device in tension side is larger than that of the joint with auxiliary

pretightening device in compression side and without auxiliary pretightening device. The bending stiffness of the joint with auxiliary pretightening device in compression side is smaller than that of the joint without auxiliary pretightening device in the initial stage due to the influence of negative resistance moment, and the bending stiffness of the joint with auxiliary pretightening device is gradually greater than that of the joint without auxiliary pretightening device in the middle and late bearing stage.

The joint without auxiliary pretightening device enters the instability stage at the earliest stage (560 kN·m), followed by the joint with auxiliary pretightening device in compression side (680 kN·m), and the joint with auxiliary pretightening device in tension side enters the instability stage at the latest (717 kN·m). At this moment, the bending stiffness is reduced to the order of 4 of 10 and then rapidly decays.

From the view of resistance moment, when the load of the joint without auxiliary pretightening device exceeds the resistance moment of 450 kN·m, the bending stiffness of the joint without auxiliary pretightening device is $1.94E+05$ kN·m/rad, the bending stiffness of the joint with auxiliary pretightening device in compression side is $3.01E+05$ kN·m/rad, and the bending stiffness of the joint with auxiliary pretightening device in tension side is $3.86E+05$ kN·m/rad. It can be seen that the joint with auxiliary pretightening device can delay the stiffness attenuation when the bending moment exceeds the resistance moment; that is to say, the setting of the auxiliary pretightening device is helpful to improve the bending performance of the joint, and it is more advantageous to set the auxiliary pretightening device in tension side regardless of the early and late stages.

TABLE 3: Design ranges and stiffness values of double-tenon joints with auxiliary pretightening device in tension side under different axial loads.

Axial load (kN)	Design bearing range (kN·m)	Design using bending stiffness (kN·m/rad)
500	0~380	$3.90E+05 \sim 2.19E+06$
1000	0~490	$3.02E+05 \sim 2.19E+06$
1250	0~637.5	$4.06E+05 \sim 2.19E+06$

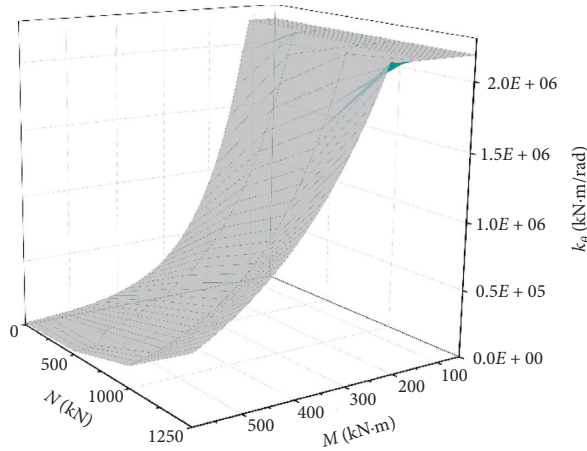


FIGURE 13: Change law of joint bending stiffness under different axial load and bending moment.

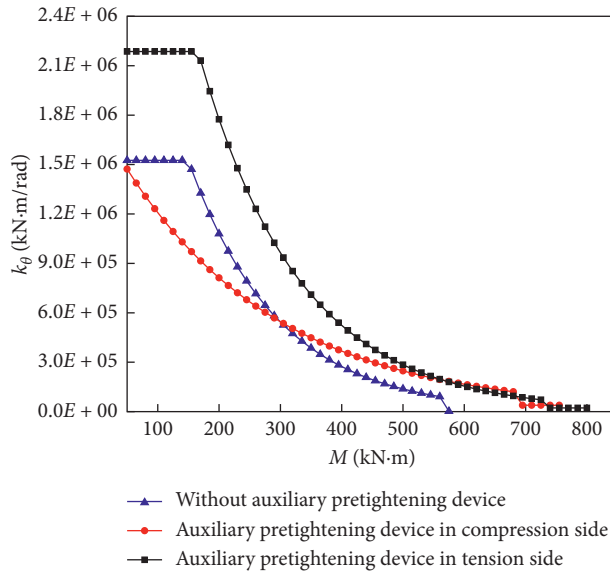


FIGURE 14: Comparison of joint bending stiffness among different double-tenon joints (1000 kN).

4. Empirical Formula of Bending Stiffness of Double-Tenon Joint

Through the analysis of $M-\theta$ curves of different types of double-tenon joints under different axial force conditions, the logarithmic function $M = A \ln(\theta) + B$ is used to fit the curves, and $k_\theta = A \cdot e^{(B-M/A)}$ is obtained.

Furthermore, the coefficient A and B are fitted and analyzed; that is, the functional relationship between axial force and parameters A and B is analyzed (as shown in Figure 15, the fitting of A and B of the joint without auxiliary pretightening device) is obtained, and the empirical formula of grouted double-tenon joint is shown in Table 4.

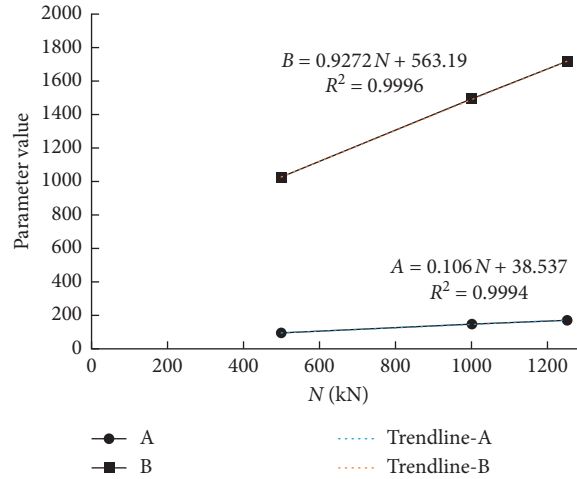


FIGURE 15: Relation curve of parameter (A) and (B) and axial force (double-tenon joint without auxiliary pretightening device).

TABLE 4: Empirical formula of bending stiffness for grouted double mortise-tenon joint.

Joint types	Empirical formulas
Without auxiliary pretightening device	$k_{\theta} = A \cdot e^{(B-M/A)}, \begin{pmatrix} A = 0.106 \cdot N + 38.537 \\ B = 0.9272 \cdot N + 563.19 \end{pmatrix}$
Auxiliary pretightening device in tension side	$k_{\theta} = A \cdot e^{(B-M/A)}, \begin{pmatrix} A = 0.1271 \cdot N + 64.117 \\ B = 1.1711 \cdot N + 800 \end{pmatrix}$

5. Conclusion

This paper analyzes the loading test data of 1:1 prototype joint under the combined action of axial force and bending moment for various types of grouted double-tenon joints and obtains the basic law of bending stiffness characteristics of grouted double-tenon joint based on the $M-\theta$ curve under different axial loads and bending moment. The main conclusions are as follows:

- The test study reveals that the double-tenon joints have variable stiffness characteristics. The joint also shows different joint stiffness properties under different load atmosphere. The stiffness changes with the change of axial force and bending moment. For the same type of joint, with the increase of axial force, the bearing capacity and bending stiffness of the joint increase.
- Under the action of constant axial force, the stiffness is closely related to the loading moment. The $M-\theta$ curve presents a three-stage development of linear stage-nonlinear stage-joint instability stage. The bending stiffness decreases with the increase of bending moment. As the load exceeds the resistance moment, the linear stage ends, cracks appear, and the cracking of joint correspondingly reduces the bearing height characteristics of the bearing section. At this time, the nonlinearity of material results in the attenuation of bending stiffness.
- On the whole, the setting of auxiliary pretightening device in tension side is helpful to improve the bending bearing capacity of the joint. However, the auxiliary pretightening device in compression side

forms a negative moment in compression side, which reduces the bending stiffness in the early stage of loading. The auxiliary pretightening device in tension side provides additional resistance moment, delays the deterioration process of the joint, and improves the ductility of the joint.

- The empirical formulas for calculating the bending stiffness of different types of double-tenon joints with different axial loads and bending moments are obtained, which is helpful for the design and calculation of similar joints in the future.

Data Availability

The data used to support the findings of this study are available from the corresponding author upon request.

Conflicts of Interest

The authors declare that they have no conflicts of interest.

Authors' Contributions

Xiuren Yang supervised the project and developed the concept and methodologies with Meiqun Huang. Fang Lin performed the experimental and theoretical studies.

Acknowledgments

This research was funded by the National Key S&T Special Projects, under Grant no. 2017YFB1201104.

References

- [1] L. Rozsa, "Precast concrete segment lining of the budapest metro," *Tunnels & Tunnelling International*, vol. 11, no. 10, 1979.
- [2] K. Beilasov, Q. H. Qian, and C. Z. Qi, *The Essence of the Construction of Russian Underground Railway*, China Railway Press, Beijing, China, 2012.
- [3] J. H. Liu and X. Y. Hou, "The history of shield tunneling," *Shield Tunneling*, pp. 4-5, China Railway Press, Beijing, China, 1991.
- [4] H. Backmann and A. Steinle, *Precast Concrete Structures*, Ernst & Sohn, Berlin, Germany, 2011.
- [5] X. R. Yang, M. Q. Huang, and F. Lin, "Research strategies on new prefabricated technology for underground metro stations," *Urban Rail Transit*, vol. 5, no. 3, pp. 1-10, 2019.
- [6] X. R. Yang, Z. H. Shi, and F. Lin, "Influence of geometrical parameters on performance of grouted mortise and tenon joints for application in prefabricated underground structures," *Advances in Civil Engineering*, vol. 2019, Article ID 3747982, 14 pages, 2019.
- [7] X. R. Yang, Z. H. Shi, and F. Lin, "Research on shear capacity and checking method of MT-G-joint for application in prefabricated underground structures," *Advances in Materials Science and Engineering*, vol. 201912 pages, Article ID 4065301, 2019.
- [8] S. T. Song, "Experimental study and theoretical analysis in bending and joint shear of high-speed railway precast segmental concrete box bridges," Doctoral Dissertation, Southeast University, Dhaka, Bangladesh, 2015.
- [9] J. S. Chen and H. O. Mo, "Three-dimensional fem analysis on flexural rigidity of segment joints in shield tunnel," *Journal of the China Railway Society*, vol. 4, pp. 87-91, 2009.
- [10] Z. G. Yan, H. H. Zhu, and S. M. Liao, "A study on performance of steel fiber reinforced concrete segment," *Chinese Journal of Rock Mechanics and Engineering*, vol. 25, no. s1, pp. 2888-2893, 2006.
- [11] L. T. Wu, "FEM analysis on mechanical behaviors of segment joints of shield tunnel," Doctoral Dissertation, Southwest Jiaotong University, Chengdu, China, 2005.
- [12] R. Gao, K. Zhou, W. Liu, and Q. Ren, "Correlation between the pore structure and water retention of cemented paste backfill using centrifugal and nuclear magnetic resonance methods," *Minerals*, vol. 10, no. 7, p. 610, 2020.
- [13] R. Gao, Y. Luo, and H. Deng, "Experimental study on repair of fractured rock mass by microbial induction technology," *Royal Society open science*, vol. 6, no. 11, Article ID 191318, 2019.
- [14] X. Luo, P. Cao, Q. Lin, and S. Li, "Mechanical behaviour of fracture-filled rock-like specimens under compression-shear loads: an experimental and numerical study," *Theoretical and Applied Fracture Mechanics*, vol. 113, Article ID 102935, 2021.
- [15] J. Hu, G. Wen, Q. Lin, P. Cao, and S. Li, "Mechanical properties and crack evolution of double-layer composite rock-like specimens with two parallel fissures under uniaxial compression," *Theoretical and Applied Fracture Mechanics*, vol. 108, Article ID 102610, 2020.
- [16] X. R. Yang and F. Lin, "Prefabrication technology for underground metro station structure," *Tunnelling and Underground Space Technology*, vol. 108, Article ID 103717, 2021.

Research Article

Numerical Analysis for the Caving Characteristics of Rock Mass with Inclined Joints in Caving Mining

Jinbo Sui, Fengyu Ren , Jianli Cao, and Huan Liu 

School of Resources and Civil Engineering, Northeastern University, Shenyang 110819, China

Correspondence should be addressed to Huan Liu; gyliuhuan@163.com

Received 4 March 2021; Accepted 24 May 2021; Published 14 June 2021

Academic Editor: Rihong Cao

Copyright © 2021 Jinbo Sui et al. This is an open access article distributed under the Creative Commons Attribution License, which permits unrestricted use, distribution, and reproduction in any medium, provided the original work is properly cited.

In caving mining, the successful initiation and propagation of caving require one low-dip joint set. However, not every mine has a low-dip joint set. The Hemushan Iron Mine in China was taken as the engineering background, and the caving characteristics of rock mass with inclined joints were analyzed based on the synthetic rock mass (SRM) model. First, the inclined joints were investigated in the Hemushan Iron Mine. Second, model parameters were determined based on the geological conditions of the mine, and seven models were established. Third, the caving process was simulated, and caving characteristics were monitored. For rock mass with inclined joints after undercutting, the research showed that the crack zone was significant, and the crack zone existed not only around the undercut area but also further away in the model. The stress concentration areas dispersed in the model except for the top of the undercut area. The caving line was not a standard arch, and the highest point of the caving line was biased towards the direction of the undercut. Under the same undercut width, with the decrease of joint length in the joint system, the number of cracks decreased, the degree of stress concentration became weaker, and the height of the caving line decreased.

1. Introduction

Caving mining is a mining method used for underground mines. It refers to all mining operations in which the orebody caves naturally after undercutting [1]. Thus, the mining costs of caving mining are smaller than those of other mining methods. This method is of growing interest to companies concerned with the exploitation of massive orebodies because of its low cost [2]. However, theoretical and practical knowledge of caving characteristics, particularly in complex jointed rock masses, is also limited. The caving characteristics affect the mining design and even affect whether caving mining is suitable for a particular mine.

According to Brown [2], any unsupported rock mass will cave if it is undercut to a sufficient extent. Caving occurs as a result of gravity and induced stresses; the induced stresses are caused by undercut engineering or caving of rock mass. The process of caving depends on the relationships between the induced stresses, the strength of the rock mass, and the geometry and strengths of discontinuities in the rock mass. Kendorski [3] contended that the successful initiation and

propagation of caving requires the presence of a well-developed, low-dip discontinuity set. The most ideal rock mass conditions for caving are at least two steep-dip discontinuity sets and one low-dip discontinuity set [2]. The steep-dip discontinuity sets provide the vertical displacement for caving. Duplancic and Brady [4] used a seismic monitoring system to study the early stages of caving and developed a conceptual model of caving. The model contains five regions: the caved zone, air gap, zone of discontinuous deformation, seismogenic zone, and surrounding rock mass. They also found that a flat-lying discontinuity set is required to act as a release mechanism for caving. Based on physical models and field observations, Cumming-Potvin et al. [5] also pointed out that the Duplancic model needs to be extended to include fracture banding. Jiang and Yang [6] performed a numerical simulation of caving characteristics and found that the stress balance arch formed in the orebody and stress concentration appeared at the arch foot. Song et al. [7] used boreholes to monitor the caving mechanism and determined that the caving height of rock strata is closely related to the rock mass quality and is seriously affected by the contact zone of rock strata. Zhang and Zhao [8] used RFPA software

to study stope roof caving and concluded that the profile of the caved rock mass under high geostress changes gradually from a parabolic shape to a stratiform shape, while that with horizontal and vertical joints changes to a saddle shape and tower shape, respectively. In summary, the caving characteristics of jointed rock mass are complex, especially for different joint conditions. One of the conditions for caving is the existence of one low-dip discontinuity set; this condition is not found in many mines. Therefore, the caving characteristics with no discontinuity set with a low dip, such as those of inclined joints, also need to be studied.

At present, there are three main methods of studying caving characteristics. The first method is field tests in mining, such as seismic monitoring [4, 5, 9, 10]. This method is not suitable for mines at the feasibility study stage or design stage, but it is suitable for monitoring the process of caving. The second method is the use of a physical model [5, 11–14] in the laboratory. This method has difficulty realizing the conditions of complex jointed rock mass, and it usually assumes that the rock mass is intact or simple (such as a coal seam). The third method is the numerical method, which is mainly based on the discrete-element method and finite-element method. Numerical methods have rapidly developed and been applied in recent years because they can ensure the consistency of mechanical properties and simulate the complex conditions of a rock mass. Hassen et al. [15] analyzed an attentive caving phenomenon incorporating main geotechnical parameters based on the discrete-element method and finite-element method. Vyazmensky et al. [16] analyzed the interaction between block cave mining and a large overlying open pit by finite-element modeling/discrete-element modeling. Vakili and Hebblewhite [17] developed a new cavability assessment criterion for top-coal, and the discrete-element method was employed as the main analytical tool. Li et al. [18] investigated strata movement during the caving process based on a finite-element technique that incorporates an elasto-brittle fracture mechanics constitutive criterion. Cao et al. [19] simulated the ground settlement process caused by mining activity by the universal distinct-element code (UDEC). Paluszny and Zimmerman [20] simulated the growth of fractures around an undercut during caving by a finite-element-based method. Rafiee et al. [21] studied the influence parameters on the cavability of rock mass in block caving mines by using PFC3D software. Ren et al. [22] analyzed the damage evolution of a rock mass during caving and the surface subsidence mechanism based on RFPA2D. Eremin et al. [23] applied the finite-difference method and the continuum damage mechanics approach to simulate the stress-strain evolution of a rock mass on the underground opening during coal extraction. Each of the methods mentioned above has its own advantages and applicable conditions. However, the caving process of a rock mass is a dynamic and continuous process after undercutting. The crack distribution, stress distribution, and caving line are important components for the study of caving characteristics. Therefore, the numerical method is a good approach for studying the caving characteristics of jointed rock mass.

In this paper, taking the Hemushan Iron Mine in China as the engineering background, the caving characteristics of rock mass with inclined joints are investigated based on synthetic rock mass (SRM) models. A series of numerical models are compared and analyzed, and the characteristics of the crack distribution, stress distribution, and caving line are determined for a rock mass with inclined joints.

2. Inclined Joints

The Hemushan Iron Mine is an underground mine in China, located in Maanshan, Anhui Province. The orebody of the Hemushan Iron Mine is located in diorite and limestone, and its shape is lenticular and layered. As shown in Figure 1(a), the dip angle of the orebody is generally 45° to 60° , the horizontal thickness is generally 10 to 85 m, and the length is 130 to 335 m along the strike. In addition, the ore is mainly magnetic ore. At the -150 m level, the strength of ore is low, and the stability of the orebody is poor. In this situation, it is difficult to form the ore drawing conditions and the bottom structure based on the original design of the sublevel open stope mining method, and this situation is suitable for caving mining.

The conditions of low ore strength and unstable orebody are advantageous for caving [1, 2, 24]. However, the occurrences of joints in the mine are investigated and analyzed. As shown in Figure 1(b), there are few low-dip joints in the mine, and the dominant joints are inclined. Therefore, it is necessary to study the caving characteristics of the inclined jointed rock mass and prevent potential safety hazards or ore loss and dilution in the mine.

3. Methodology

The initiation and propagation of caving may be caused by the following three reasons: rock blocks become free to fall under the influence of gravity, large rocks are broken and become free to fall under induced stresses and gravity, or rock blocks become free to slide on the joint under induced stresses and gravity. Therefore, the numerical method of the particle flow code was selected since it could be used to study intact rock, jointed rock mass, and large displacements of rock blocks.

The particle flow code provides an embodiment of the distinct-element method [25]. It consists of bodies (particles, clumps, and walls) and mechanical contacts (contact models). A body is composed of one or more constituent pieces that make up the body surface. The particles are rigid bodies with finite mass that move independently of one another and can both translate and rotate. The interaction between particles occurs through internal forces and moments. Contact mechanics is embodied in particle-interaction laws (referred to as contact models) that update the internal forces and moments. The time evolution of the system is computed via Newton's laws of motion. The particle flow code provides a synthetic material consisting of an assembly of rigid particles that interact at contacts, such as intact rock, jointed rock mass, and granular materials.

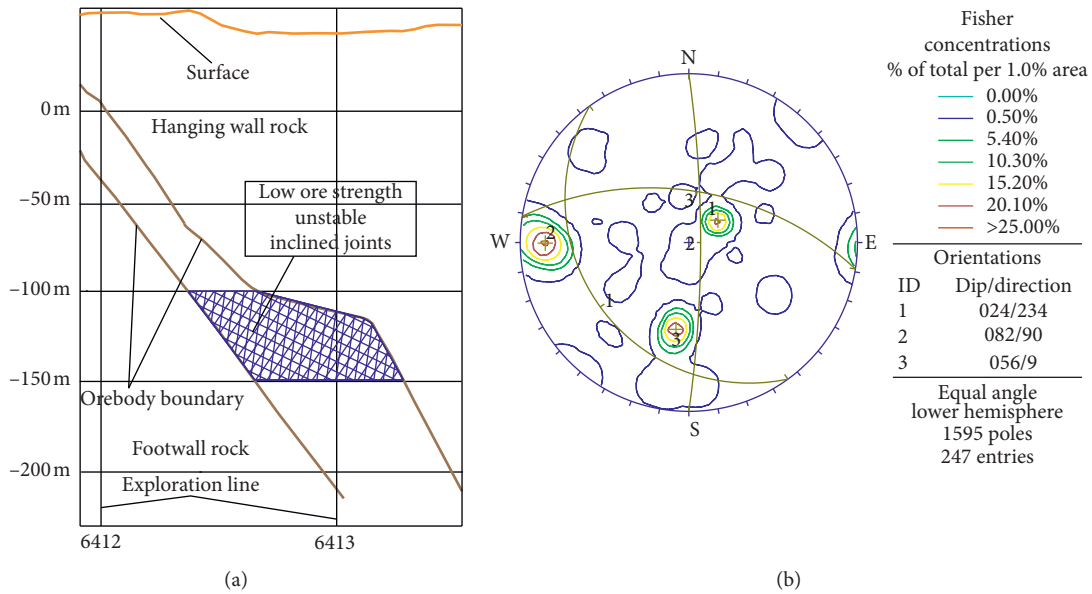


FIGURE 1: Orebody and inclined joints. (a) Orebody profile. (b) Contour plot of joints.

3.1. Synthetic Rock Mass (SRM). The particle flow code has been successfully used to study the mechanical properties or mechanical behavior of jointed rock mass [26–30] due to the development of the smooth-joint contact model [31]. The method has been termed the synthetic rock mass (SRM) methodology [25]. As shown in Figure 2, the modeling approach consists of joints (or discontinuities) information (discrete fracture network) in a bonded-particle model [32]. The bonded-particle model is used to represent the intact rock, and the mechanical behavior of the joint is introduced by modifying the contact models at the joint position.

In SRM modeling, two contact models need to be determined. One is the smooth-joint contact model used to represent the properties of joints, and the other is the bonded-particle model representing the properties of intact rock. First, the smooth-joint model simulates the behavior of a planar interface regardless of the local particle contact orientations along with the interface. As shown in Figure 2, the joint geometry consists of a planar interface separating two surfaces (surface 1 and surface 2). The behavior of a frictional or bonded joint can be modeled by assigning smooth-joint models to all contacts between particles that lie on opposite sides of the joint. Second, the flat-joint model is selected in the bonded-particle model. Because it can be applied to hard rock, and larger ratio of uniaxial compression strength to tensile strength can be obtained [33]. As shown in Figure 2, the flat-joint contact simulates the behavior of an interface between two notional surfaces (called faces), each of which is rigidly connected to a piece of a body [32]. In the flat-jointed model, the basic element is referred to as faced grains, each of which is depicted as a circular core and a number of skirted faces. Thus, faced grains can provide grain interlocking and rotational resistance even after the interface breaks [34]. An interface exists between each set of adjoining faces and is discretized into elements, with each element being either bonded or unbonded. The breakage of

each bonded element contributes partial damage to the interface, and each breakage event is denoted as a crack [32].

3.2. Parameters of the Model. The microscopic parameters of a flat-jointed model could not be directly obtained from rock properties. The parameters needed to be calibrated by numerical tests, so that the numerical simulation results were consistent with the actual results. The calibration process for flat-jointed models was systematically introduced by several researchers [25, 34, 35]. In this paper, a large number of uniaxial compression and tensile numerical tests were carried out, and the calibration objectives of ore properties included the uniaxial compressive strength, tensile strength, Young's elastic modulus, and Poisson's ratio. The numerical tests performed for calibration are shown in Figure 3, and the microscopic parameters of the flat-jointed model are listed in Table 1. The results show that rock properties are very close for those of the numerical model and those of magnetic ore. The flat-jointed model is appropriate, especially for a larger ratio of uniaxial compression strength to tensile strength.

The parameters of the joints also needed to be determined. Through field investigation in mine, the properties of joints were "FAIR" (smooth, moderately weathered, and altered surfaces) based on the chart for GSI estimates (modified by Cai et al. [36]). Under such conditions, Poulsen et al. [28] suggested that the joint friction coefficient was 0.5 and cohesive and tensile strengths were equal to 0. These parameters were also suggested by Zhang et al. [37].

3.3. Model Design. In underground mining, the rock mass was subjected to vertical compressive stress and confining pressure. Therefore, the servo control method was used to exert pressure on the model. As shown in Figure 4, the vertical compressive stress is 4.96 MPa and the confining pressure is 1.98 MPa according to the in-situ stress of the

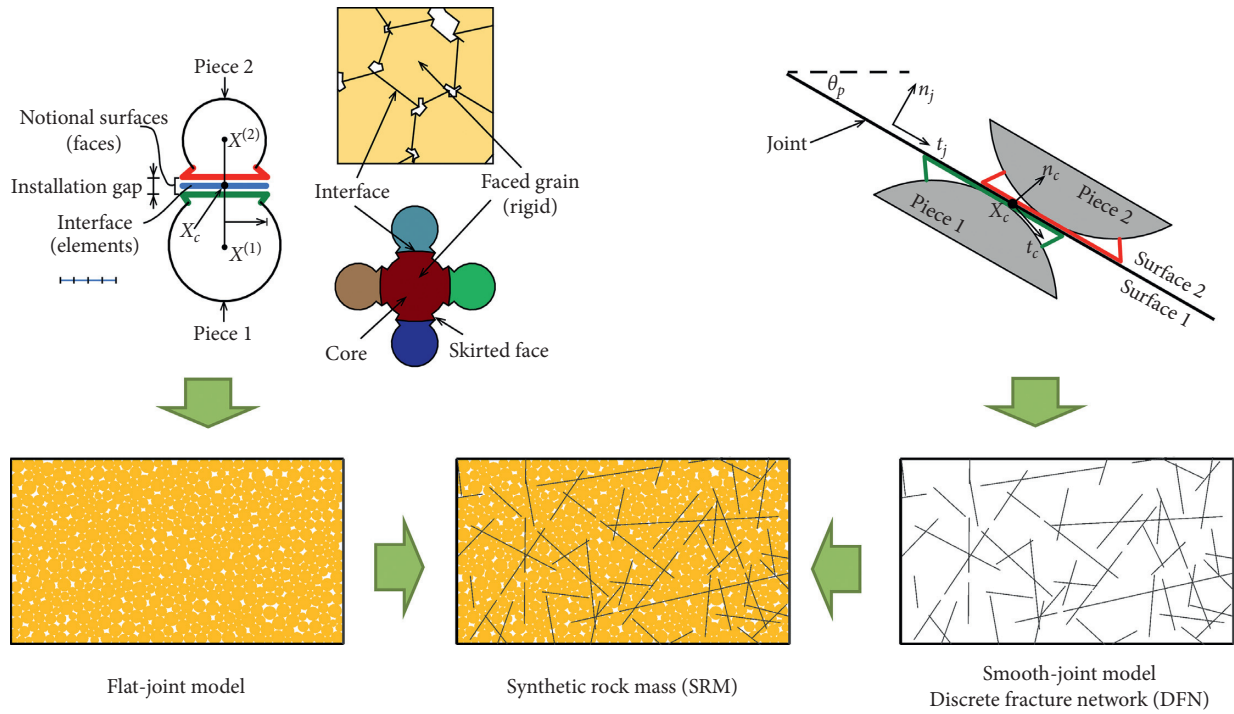


FIGURE 2: Synthetic rock mass (SRM) [25, 31, 32].

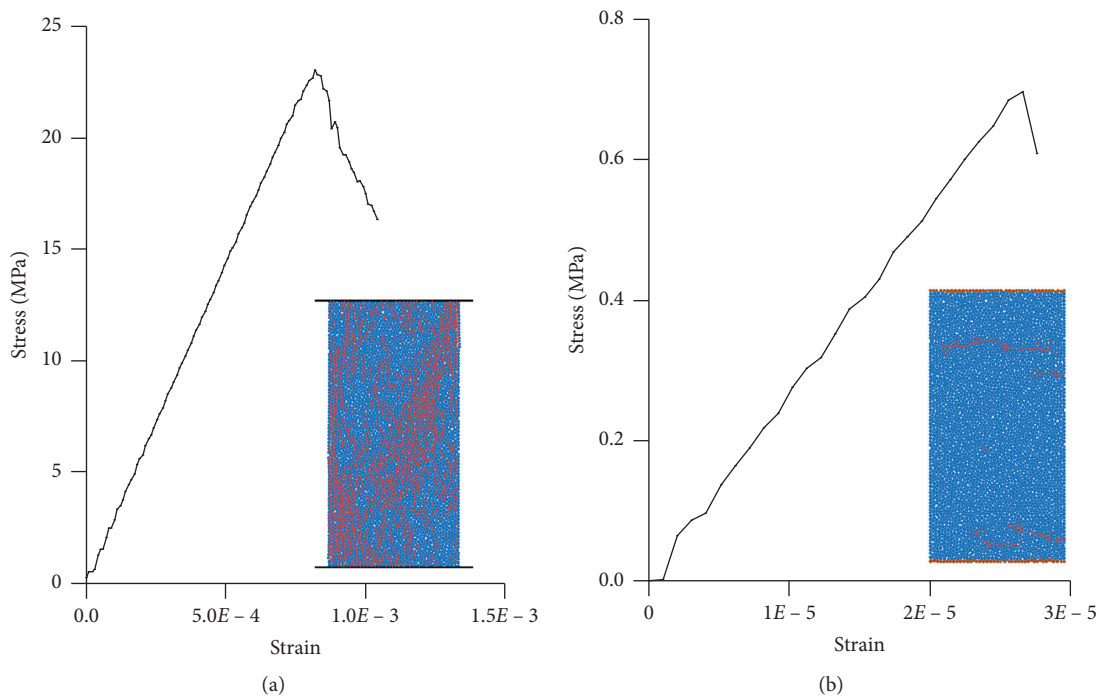


FIGURE 3: Numerical tests of the calibration parameters for the flat-jointed model. (a) Uniaxial compression test. (b) Tensile numerical test.

mine. The width of the model is 90 m, and the height is 50 m. The height of the undercut is 7 m, the width of each undercut is 2 m, and the total width of the undercut is 40 m. The process of each undercut involves deleting the particles in the specified area (2 m × 7 m) until the total undercut width reaches 40 m. For the convenience of expression, the angle of

the joint is redefined such that it refers to the angle between the undercut direction and the joint in the clockwise direction, as shown in Figure 4. It should be acknowledged that the caving particles from the model were deleted (by monitoring the velocity of the particles) to improve the calculation speed.

TABLE 1: Calibrated parameters for the numerical model.

	Description	Numerical model	Magnetic ore
<i>Particle-based properties</i>	Particle radius (cm)	10~15	
	Particle density (g/cm^3)	3.37	
<i>Flat-jointed parameters</i>	Effective modulus (GPa)	16.0	
	Normal-to-shear stiffness ratio	0.24	
	Friction angle ($^\circ$)	5.0	
	Friction coefficient	0.5	
	Tensile strength (MPa)	0.9	
	Cohesion (MPa)	16.5	
<i>Rock properties</i>	Compressive strength (MPa)	23.20	22.61
	Young's elastic modulus (GPa)	28.80	30.00
	Poisson's ratio	0.26	0.25
	Tensile strength (MPa)	0.70	0.69

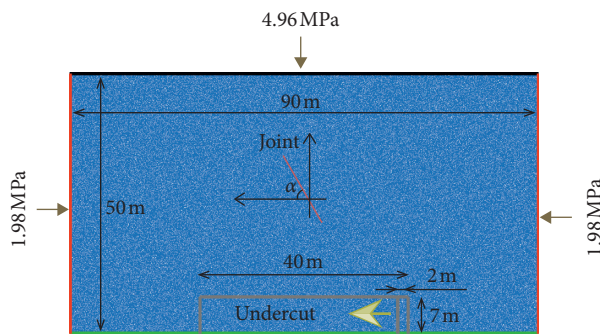


FIGURE 4: Design of the numerical model.

Another design involved adding joints in the model. According to the conditions of the Hemushan Iron Mine and the requirements for analysis and comparison, seven models were established based on the SRM model. The seven models are shown in Figure 5, and the parameters of each model are shown in Table 2. The average density of the joint system is 3 per meter in model (e). Models (b), (c), and (d) are established by deleting the joint set in model (e). Models (f) and (g) are established by shortening the length of the joints in model (e). Models (a) to (d) are used to study the caving characteristics of rock mass with no joints and joint sets, models (b) to (e) are used to study the caving characteristics of rock mass with joint sets and joint systems, and models (e) to (g) are used to study the caving characteristics of rock mass with different joint lengths in the joint system.

4. Numerical Simulation Results

To determine the caving characteristics of a rock mass with inclined joints, the crack distribution, stress distribution, and caving line were monitored during the process of numerical simulation (undercut engineering).

4.1. Crack Distribution and Propagation. The SRM model was composed of bonded particles and joints, and the caving of the rock mass occurred as a result of undercutting. During the caving process, failure occurred in selected bonded contacts, and cracks were generated in the model. Therefore, the cracks were monitored during the different widths of the

undercut, the results are shown in Figure 6, and red represents cracks.

In the model with no joints, as shown in Figure 6(a), cracks initially appear at the top of the undercut area and extend vertically. With the increase in the undercut width, the direction of crack propagation appears inclined, and then, they connect with each other and lead to the caving of the rock mass. Cracks mainly appear at the top of the undercut area.

The joint set models are shown in Figures 6(b)–6(d), and cracks initially appear around the undercut area. With the increase in the undercut width, the direction of crack propagation appears almost perpendicular or inclined to the joint direction, and then, they connect with each other or joints and lead to the caving of the rock mass. Cracks appear at the top of the undercut area, and the heights of the cracks are the highest at the top of the undercut area in the 98° joint set model, but cracks also appear at the upper inclined ends on both sides of the undercut area in the 24° and 124° joint set model. Compared with a model with no joints, the joint set is favorable for the formation of cracks, and the 124° joint set is obvious for the Hemushan Iron Mine.

Joint system models are shown in Figures 6(e)–6(g), and cracks initially appear around the undercut area. With the increase in the undercut width, the direction of crack propagation is inclined to the joint direction, and then, they connect with each other or joints and lead to the caving of the rock mass. With decreasing joint length, the number of cracks decreases under the same width of the undercut. Cracks appear at the top of the undercut area and the upper inclined ends on both sides of the undercut area.

4.2. Stress Distribution. The contact force between particles could be determined by the particle flow code, and the stress distribution and stress concentration area could be determined by the contact force. In the process of numerical simulation, the contact forces were determined during the different widths of the undercut. The results are shown in Figure 7.

The model with no joints is shown in Figure 7(a). The stress concentration areas are mainly distributed in the upper two corners of the rectangular undercut area. With the increase in the undercut width, stress concentration areas also appear on the sides of the undercut area, especially when

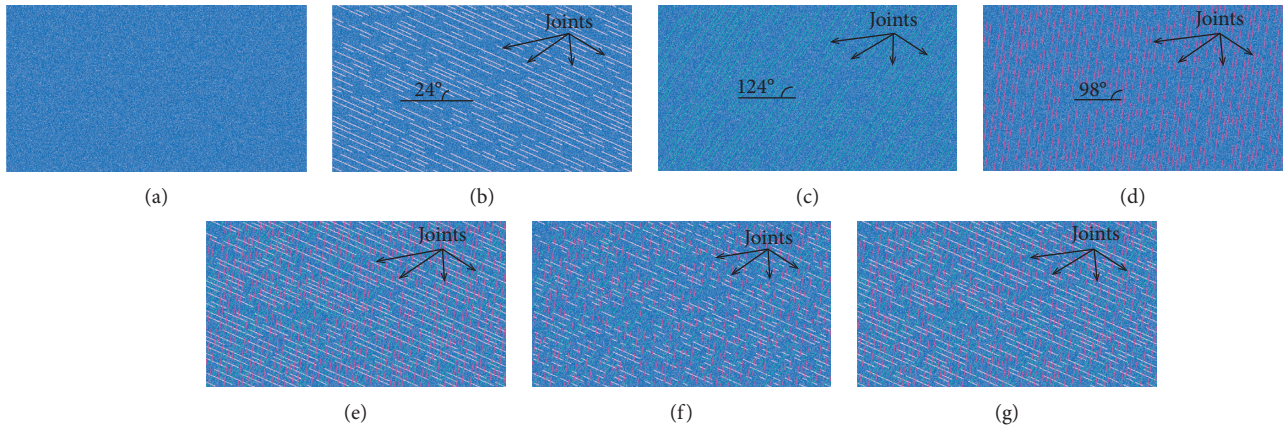


FIGURE 5: Numerical models. (a) No joints. (b) 24° joint set. (c) 124° joint set. (d) 98° joint set. (e) Joint system 1. (f) Joint system 2. (g) Joint system 3.

TABLE 2: Joint parameters of the numerical model.

Number	Model	Description	Angle	Joint	Length
a		No joints			
b		24° joint set	24°		3~25 m
c		124° joint set	124°		3~25 m
d		98° joint set	98° (steep-dip)		3~25 m
e		Joint system 1	24°, 124°, 98°		3~25 m
f		Joint system 2	24°, 124°, 98°		1.5~12.5 m
g		Joint system 3	24°, 124°, 98°		2.4~20 m

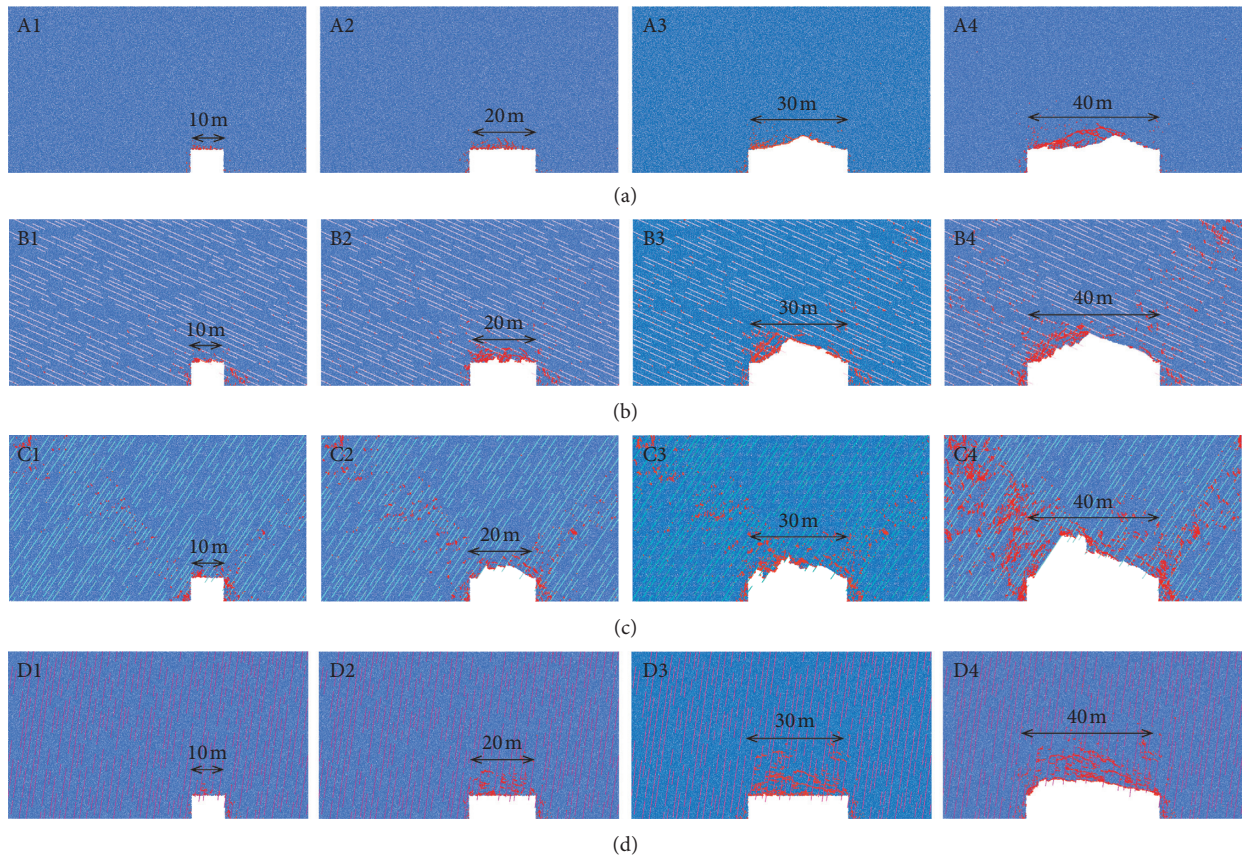


FIGURE 6: Continued.

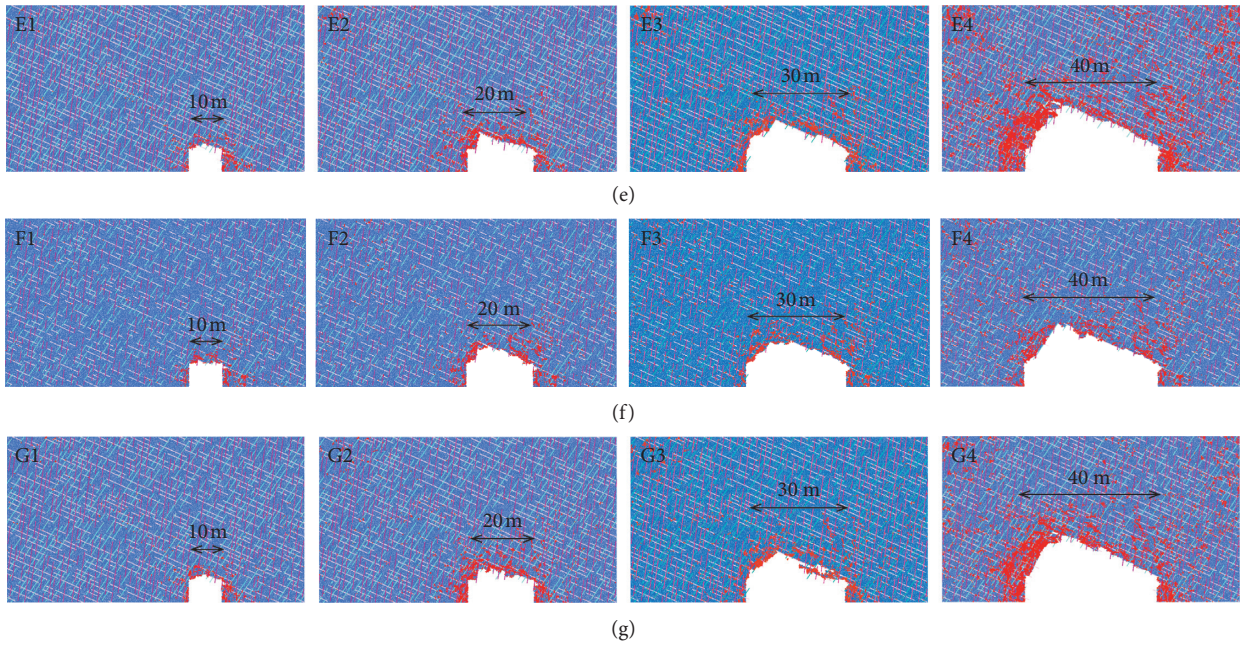


FIGURE 6: Crack propagation of the seven models. (a) No joints. (b) 24° joint set. (c) 124° joint set. (d) 98° joint set. (e) Joint system 1. (f) Joint system 2. (g) Joint system 3.

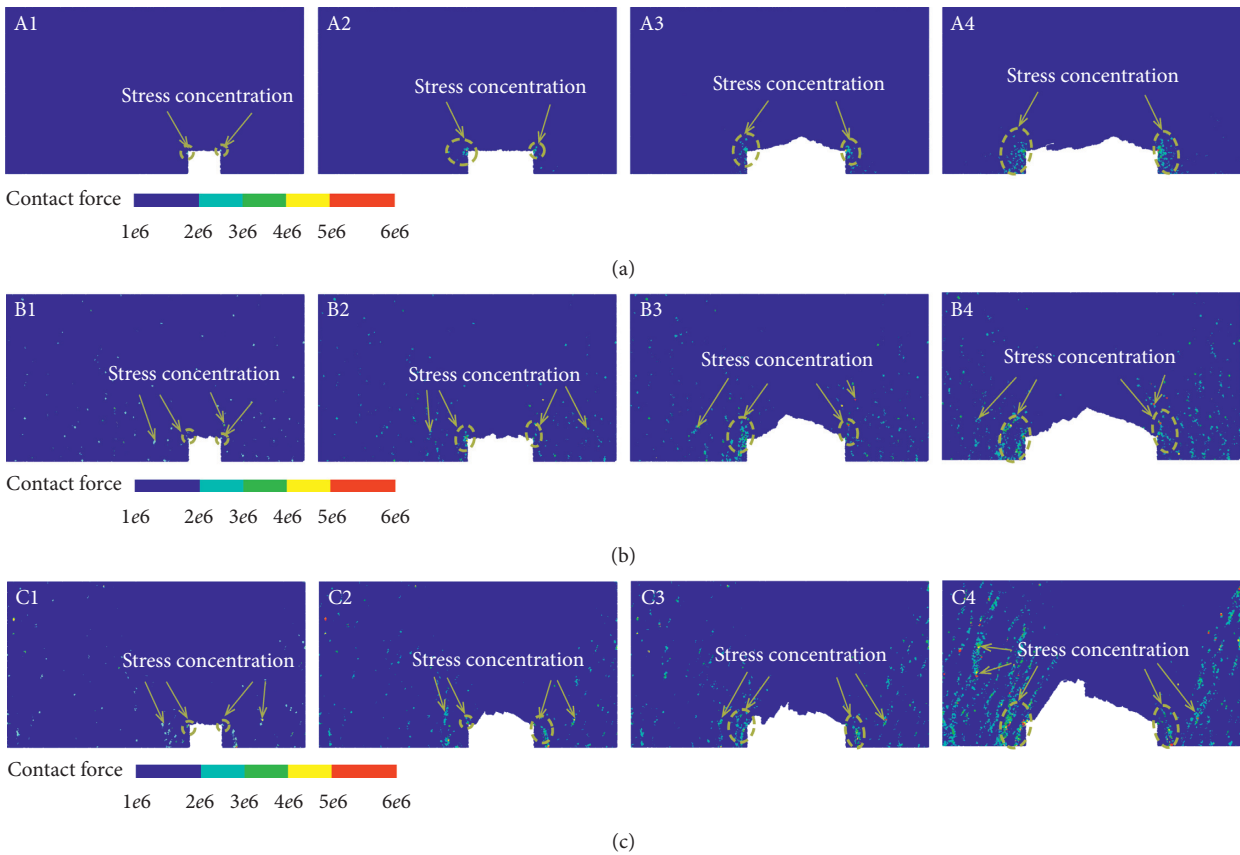


FIGURE 7: Continued.

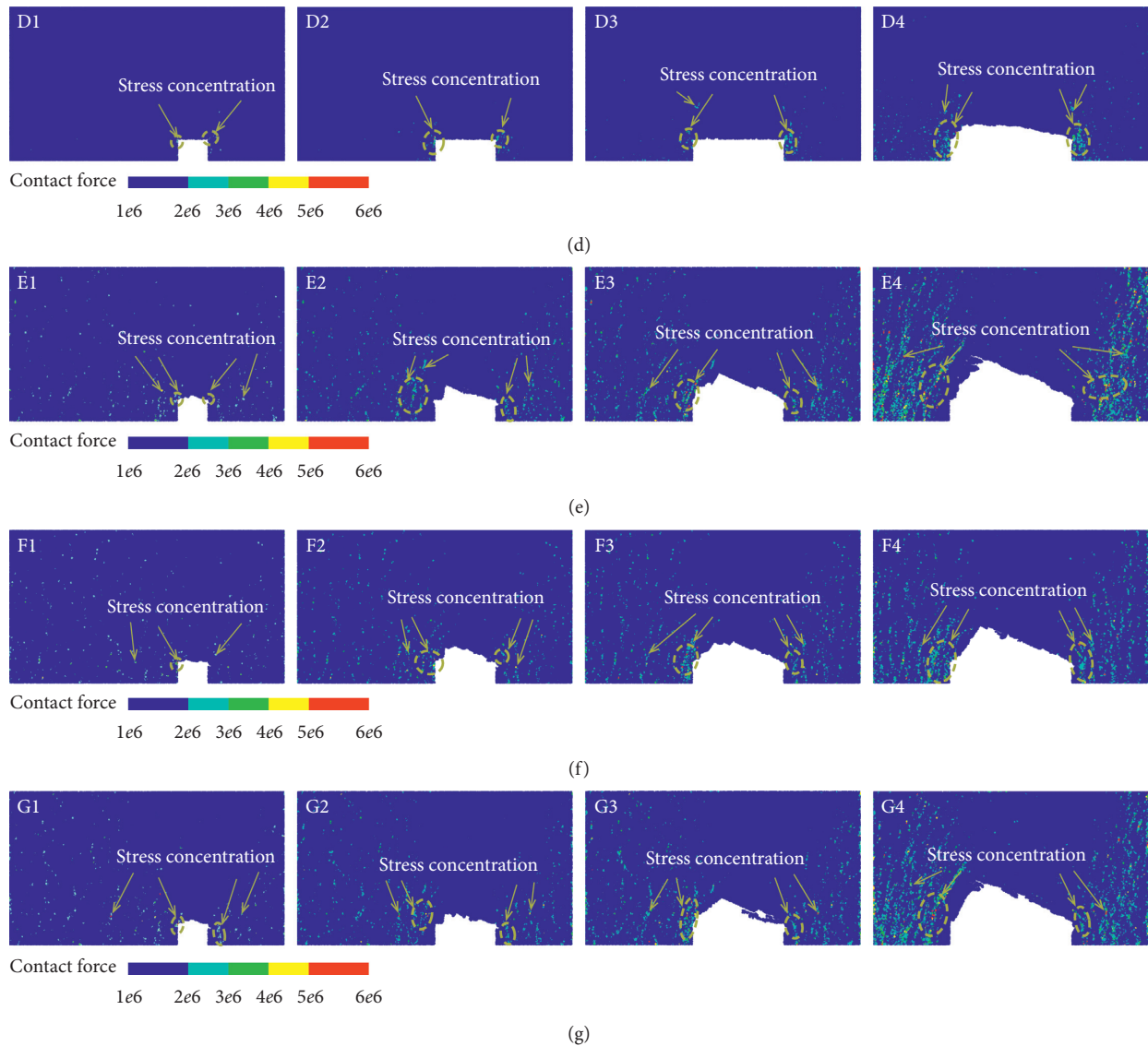


FIGURE 7: Stress distribution of the seven models. (a) No joints. (b) 24° joint set. (c) 124° joint set. (d) 98° joint set. (e) Joint system 1. (f) Joint system 2. (g) Joint system 3.

the width of the undercut is 40 m. However, the stress concentration areas are mainly distributed around the undercut area. Joint set models are shown in Figures 7(b)–7(d). The stress concentration areas are distributed in the upper two corners of the rectangular undercut area, but they also appear in other areas in the models except for the top of the undercut area. With the increase in the undercut width, the stress concentration areas on both sides of the undercut area are significant. The joint system models are shown in Figures 7(e)–7(g), and the stress concentration areas are similar to those of the joint set models. With decreasing joint length, the degree of stress concentration becomes weaker under the same width of the undercut.

4.3. Caving Line. The caving line is also known as the caving arch because the shape of the caving line is usually considered to be an arch. In the process of numerical simulation,

caving lines are drawn for the different widths of the undercut, and the results are shown in Figure 8.

In the no joints model, as shown in Figure 8(a), the highest point of the caving line is basically located in the middle of the undercut width, and the angle between the caving line and the horizontal direction is small. The joint set models are shown in Figures 8(b)–8(d). The highest point of the caving line is biased towards the direction of the undercut, and the angle between the caving line and the horizontal direction is larger than that of the model with no joints. The joint system models are shown in Figures 8(e)–8(g). The highest point of the caving line is also biased towards the direction of the undercut, and the angle between the caving line and the horizontal direction is larger than that of the model with no joints and that of the joint set models. With decreasing joint length, the height of the caving line decreases under the same width of the undercut.

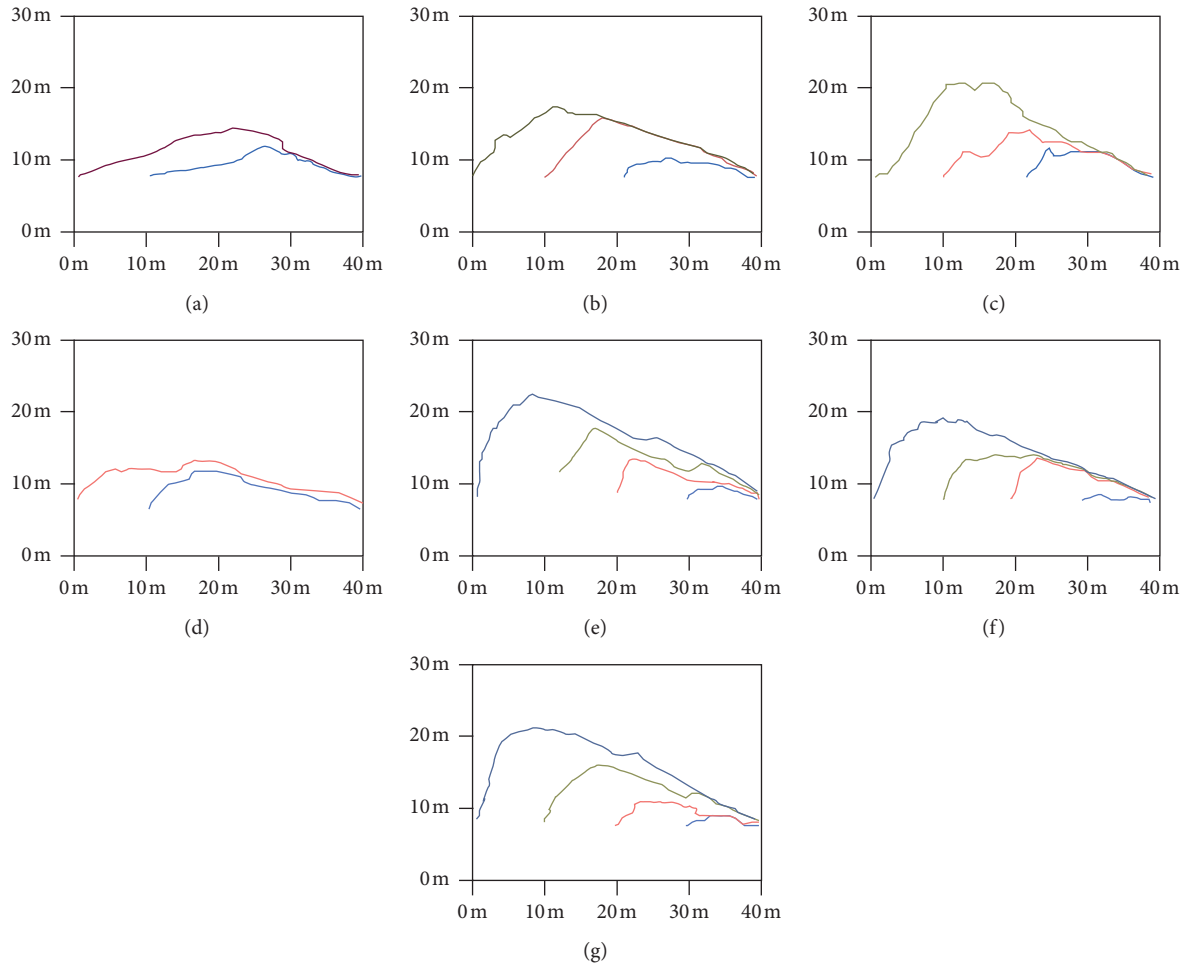


FIGURE 8: Caving line of the seven models. (a) No joints. (b) 24° joint set. (c) 124° joint set. (d) 98° joint set. (e) Joint system 1. (f) Joint system 2. (g) Joint system 3.

5. Discussion

Based on the simulation results of seven numerical models, the caving characteristics of the model with no jointed rock mass and the model with an inclined rock mass can be analyzed.

The caving characteristics of rock masses with no joints were simple, but caving mining was difficult. The crack zone mainly appeared at the top of the undercut area, the stress concentration areas were mainly distributed in the upper two corners of the rectangular undercut area, and the caving line could be simplified as an arch. It could be concluded that joints had an important influence on the caving characteristics.

The caving characteristics of rock mass with joint sets or joint systems are complicated, but they are beneficial for caving mining. The caving characteristics were as follows:

- (1) Crack zone and propagation: an obvious crack zone existed in the inclined jointed rock mass after undercutting. The distribution of the crack zone was related to the undercut width, the dip angle of the joint set, and the joint length in the joint system.

With the increase in the undercut width, the crack zone not only existed around the undercut area but also existed further away in the model (such as in the upper inclined ends on both sides of the undercut area). The direction of crack propagation was inclined to the joint direction, and then, the cracks connected with each other or the joints, which led to the caving of the rock mass. With the decrease in the joint length in the joint system, the number of cracks decreased under the same undercut width.

- (2) Stress distribution: with the increase in the undercut width in the inclined jointed rock mass, the stress concentration areas were not only distributed in the upper two corners of the rectangular undercut area but also distributed in other areas in the models except the top of the undercut area. With decreasing joint length, the degree of stress concentration became weaker under the same width of the undercut.
- (3) Caving line: the caving line in the inclined jointed rock mass was not a standard arch. With the increase in the undercut width, the highest point of the caving line was biased towards the direction of the undercut,

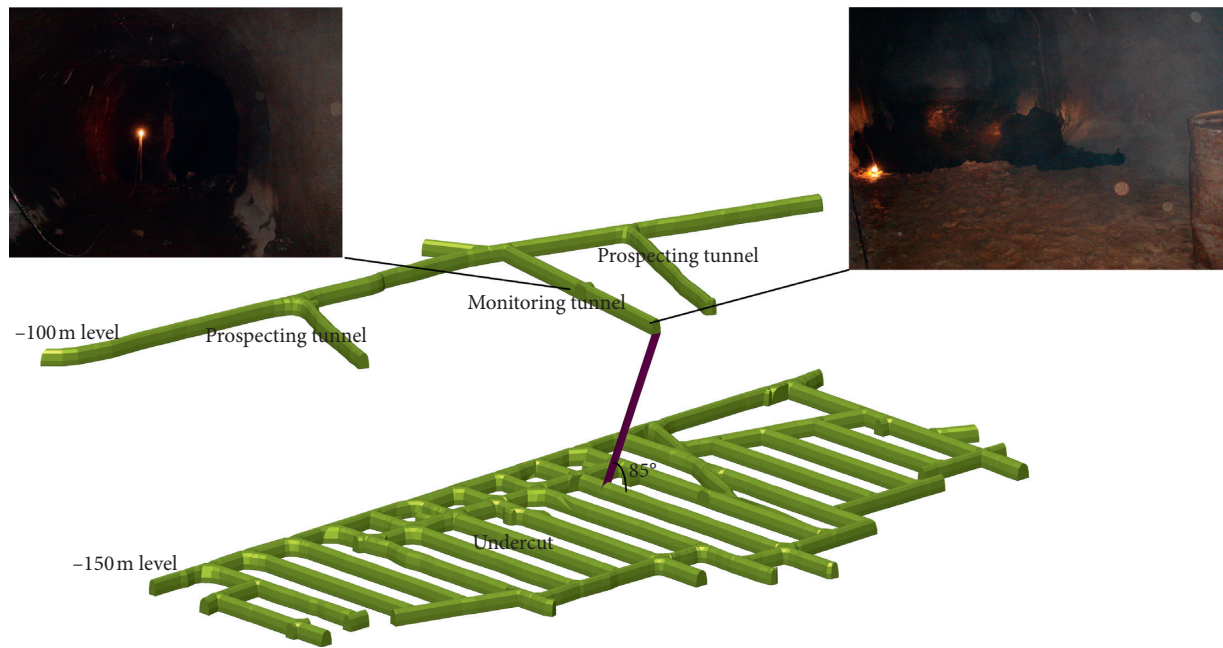


FIGURE 9: Monitoring of caving mining.

and the angle between the caving line and the horizontal direction was related to the conditions of the joint. For the rock mass of the joint system in this paper, one side of the caving line was very steep (Figures 8(e)–8(g)), and the angle between the caving line and the horizontal direction reached more than 80° . In actual mining, the monitoring tunnel was set up to monitor the caving process (Figure 9), and the results showed that the angle between the caving line and the horizontal direction reached 85° . With the decrease in joint length, the height of the caving line decreased under the same width of the undercut.

It should be noted that the caving of a rock mass with a steeply dipping joint set (such as the 98° joint set in this paper) was difficult in the early stage of mining. However, a large number of cracks existed above the undercut area (Figure 6(d)). With the continuous increase in the undercut width, the number of cracks also increased, and then, they connected with each other or joints, which led to the caving of the rock mass. In this situation, the amount of rock mass that caved was very large, which would threaten miners, mining equipment, mining facilities, etc. Protection or treatment measures, such as increasing the height of the blasted orebody during undercut engineering and using the blasting ore as the overburden or using hydraulic fracturing to promote caving of the rock mass in the early stage of mining, are necessary for the safety mining of mine.

6. Conclusions

In this study, the caving characteristics of rock mass with inclined joints in caving mining were investigated. For this purpose, seven numerical models were established based on the SRM model and the conditions of the Hemushan Iron Mine.

The crack distribution, stress distribution, and caving line were determined for rock mass with different joint conditions, and the joint conditions included no joints, joint sets, and joint systems. The main conclusions for the caving characteristics of rock mass with inclined joints were as follows:

- (1) In the caving process, the crack zone was significant, and it not only existed around the undercut area but also existed further away in the model. The distribution of the crack zone was related to the undercut width, the dip angle of the joint set, and the joint length in the joint system.
- (2) The stress concentration areas not only existed in the upper two corners of the rectangular undercut area (or arch corner) but also dispersed elsewhere in the model except for the top of the undercut area.
- (3) The caving line was not a standard arch, and the highest point of the caving line was biased towards the direction of the undercut.
- (4) The joint length had an influence on the caving characteristics of rock mass with inclined joints. Under the same undercut width, with the decrease in the joint length in the joint system, the number of cracks decreased, the degree of stress concentration became weaker, and the height of the caving line decreased.

Data Availability

The data used to support the findings of this study are included within the article.

Conflicts of Interest

The authors declare that they have no conflicts of interest.

Acknowledgments

This study was jointly supported by grants from the National Key Research and Development Program of China (Grant no. 2016YFC0801601) and the Key Program of the National Natural Science Foundation of China (Grant no. 51534003). The authors are grateful for the support.

References

- [1] D. H. Laubscher, "Cave mining—the state of the art," *The Journal of the South African Institute of Mining and Metallurgy*, vol. 94, no. 10, pp. 279–293, 1994.
- [2] E. T. Brown, *Block Caving Geomechanics*, Julius Kruttschnitt Mineral Research Center, Indooroopilly, Australia, 2003.
- [3] F. Kendorski, "The cavability of ore deposits," *Min. Engng.* vol. 30, no. 6, pp. 628–631, 1978.
- [4] P. Duplancic and B. H. Brady, "Characterisation of caving mechanisms by analysis of seismicity and rock stress," in *Proceedings of the 9th International Congress on Rock Mechanics*, G. Vouille and P. Berest, Eds., International Society for Rock Mechanics and Rock Engineering, Paris, France, pp. 1049–1453, August 1999.
- [5] D. Cumming-Potvin, J. Wesseloo, S. W. Jacobsz, and E. Kearsley, "Fracture banding in caving mines," *Journal of the Southern African Institute of Mining and Metallurgy*, vol. 116, no. 8, pp. 753–761, 2016.
- [6] Z. Jiang and B. Yang, "Numerical simulation of caving law in natural caving mining method based on deformable discrete element method," *Rock and Soil Mechanics*, vol. 26, no. 2, pp. 239–242, 2005.
- [7] W. Song, J. Du, X. Yin, and G. Tang, "Caving mechanism of hangingwall rock and rules of surface subsidence due to no-pillar sub-level caving method in an iron mine," *Journal of China Coal Society*, vol. 35, no. 7, pp. 1078–1083, 2010.
- [8] G. Zhang and X. Zhao, "Numerical simulation on induced caving of rock mass," *Journal of Northeastern University*, vol. 33, no. 8, pp. 1190–1193, 2012.
- [9] G. Cheng, T. Ma, C. Tang, H. Liu, and S. Wang, "A zoning model for coal mining—induced strata movement based on microseismic monitoring," *International Journal of Rock Mechanics and Mining Sciences*, vol. 94, pp. 123–138, 2017.
- [10] Y. Zhao, T. Yang, M. Bohnhoff et al., "Study of the rock mass failure process and mechanisms during the transformation from open-pit to underground mining based on microseismic monitoring," *Rock Mechanics and Rock Engineering*, vol. 51, no. 5, pp. 1473–1493, 2018.
- [11] M. Ju, X. Li, Q. Yao, S. Liu, S. Liang, and X. Wang, "Effect of sand grain size on simulated mining-induced overburden failure in physical model tests," *Engineering Geology*, vol. 226, pp. 93–106, 2017.
- [12] B. Ghabraie, G. Ren, and J. V. Smith, "Characterising the multi-seam subsidence due to varying mining configuration, insights from physical modelling," *International Journal of Rock Mechanics and Mining Sciences*, vol. 93, pp. 269–279, 2017.
- [13] D. Huayang, L. Xugang, L. Jiyan et al., "Model study of deformation induced by fully mechanized caving below a thick loess layer," *International Journal of Rock Mechanics and Mining Sciences*, vol. 47, no. 6, pp. 1027–1033, 2010.
- [14] J.-a. Wang, J. Tang, and S.-h. Jiao, "Seepage prevention of mining-disturbed riverbed," *International Journal of Rock Mechanics and Mining Sciences*, vol. 75, pp. 1–14, 2015.
- [15] F. H. Hassen, L. Spinnler, and J. Fine, "A new approach for rock mass cavability modeling," *International Journal of Rock Mechanics and Mining Sciences & Geomechanics Abstracts*, vol. 30, no. 7, pp. 1379–1385, 1993.
- [16] A. Vyazmensky, D. Stead, D. Elmo, and A. Moss, "Numerical analysis of block caving-induced instability in large open pit slopes: a finite element/discrete element approach," *Rock Mechanics and Rock Engineering*, vol. 43, no. 1, pp. 21–39, 2009.
- [17] A. Vakili and B. K. Hebblewhite, "A new cavability assessment criterion for longwall top coal caving," *International Journal of Rock Mechanics and Mining Sciences*, vol. 47, no. 8, pp. 1317–1329, 2010.
- [18] L. C. Li, C. A. Tang, X. D. Zhao, and M. Cai, "Block caving-induced strata movement and associated surface subsidence: a numerical study based on a demonstration model," *Bulletin of Engineering Geology and the Environment*, vol. 73, no. 4, pp. 1165–1182, 2014.
- [19] S. Cao, W. Song, D. Deng, Y. Lei, and J. Lan, "Numerical simulation of land subsidence and verification of its character for an iron mine using sublevel caving," *International Journal of Mining Science and Technology*, vol. 26, no. 2, pp. 327–332, 2016.
- [20] A. Paluszny and R. W. Zimmerman, "Modelling of primary fragmentation in block caving mines using a finite-element based fracture mechanics approach," *Geomechanics and Geophysics for Geo-Energy and Geo-Resources*, vol. 3, no. 2, pp. 121–130, 2017.
- [21] R. Rafiee, M. Ataei, R. KhalooKakaie, S. E. Jalali, F. Sereshki, and M. Noroozi, "Numerical modeling of influence parameters in cavability of rock mass in block caving mines," *International Journal of Rock Mechanics and Mining Sciences*, vol. 105, pp. 22–27, 2018.
- [22] F. Ren, D. Zhang, J. Cao, M. Yu, and S. Li, "Study on the rock mass caving and surface subsidence mechanism based on an in situ geological investigation and numerical analysis," *Mathematical Problems in Engineering*, vol. 2018, Article ID 6054145, 18 pages, 2018.
- [23] M. Eremin, G. Esterhuizen, and I. Smolin, "Numerical simulation of roof cavings in several Kuzbass mines using finite-difference continuum damage mechanics approach," *International Journal of Mining Science and Technology*, vol. 30, no. 2, pp. 157–166, 2020.
- [24] D. H. Laubscher, "A geomechanics classification system for the rating of rock mass in mine design," *Journal of the Southern African Institute of Mining and Metallurgy*, vol. 90, no. 10, pp. 257–273, 1990.
- [25] Itasca Consulting Group, *PFC Version 5.0 User's Manual*, Itasca Consulting Group, Minneapolis, MN, USA, 2017.
- [26] Y. Zhang, X. Liu, T. Yang, P. Jia, X. Liu, and F. Ren, "A 3D synthetic rock mass numerical method for characterizations of rock mass and excavation damage zone near tunnels," *Bulletin of Engineering Geology and the Environment*, vol. 70, no. 2, pp. 5615–5629, 2020.
- [27] D. Mas Ivars, M. E. Pierce, C. Darcel et al., "The synthetic rock mass approach for jointed rock mass modelling," *International Journal of Rock Mechanics and Mining Sciences*, vol. 48, no. 2, pp. 219–244, 2011.
- [28] B. A. Poulsen, D. P. Adhikary, M. K. Elmouttie, and A. Wilkins, "Convergence of synthetic rock mass modelling and the Hoek-Brown strength criterion," *International Journal of Rock Mechanics and Mining Sciences*, vol. 80, pp. 171–180, 2015.

- [29] J. A. Vallejos, K. Suzuki, A. Brzovic, and D. M. Ivars, "Application of synthetic rock mass modeling to veined core-size samples," *International Journal of Rock Mechanics and Mining Sciences*, vol. 81, pp. 47–61, 2016.
- [30] X. Yang, P. H. S. W. Kulatilake, H. Jing, and S. Yang, "Numerical simulation of a jointed rock block mechanical behavior adjacent to an underground excavation and comparison with physical model test results," *Tunnelling and Underground Space Technology*, vol. 50, pp. 129–142, 2015.
- [31] M. E. Pierce and C. Fairhurst, "Synthetic rock mass applications in mass mining," in *Harmonising Rock Engineering and the Environment*, Q. Qian and Y. Zhou, Eds., pp. 109–114, Taylor & Francis Group, London, UK, 2012.
- [32] D. O. Potyondy, "The bonded-particle model as a tool for rock mechanics research and application: current trends and future directions," *Geosystem Engineering*, vol. 18, no. 1, pp. 1–28, 2015.
- [33] F. Ren, H. Liu, R. He, G. Li, and Y. Liu, "Point load test of half-cylinder core using the numerical model and laboratory tests: size suggestion and correlation with cylinder core," *Advances in Civil Engineering*, vol. 2018, Article ID 3870583, 11 pages, 2018.
- [34] S. Wu and X. Xu, "A study of three intrinsic problems of the classic discrete element method using flat-joint model," *Rock Mechanics and Rock Engineering*, vol. 49, no. 5, pp. 1813–1830, 2015.
- [35] K. Li, Y. Cheng, and X. Fan, "Roles of model size and particle size distribution on macro-mechanical properties of Lac du Bonnet granite using flat-joint model," *Computers and Geotechnics*, vol. 103, pp. 43–60, 2018.
- [36] M. Cai, P. K. Kaiser, H. Uno, Y. Tasaka, and M. Minami, "Estimation of rock mass deformation modulus and strength of jointed hard rock masses using the GSI system," *International Journal of Rock Mechanics and Mining Sciences*, vol. 41, no. 1, pp. 3–19, 2004.
- [37] Y. Zhang, F. Y. Ren, T. H. Yang, S. Y. Wang, W. F. Zhang, and M. X. Yu, "An improved rock mass characterization method using a quantified geological strength index and synthetic rock mass model," *Rock Mechanics and Rock Engineering*, vol. 51, no. 11, pp. 3521–3536, 2018.

Research Article

Displacement Monitoring during the Excavation and Support of Deep Foundation Pit in Complex Environment

Zhouqiang Li 

402 Geological Prospecting Party, Hunan Exploration Design Institute, Changsha 410004, China

Correspondence should be addressed to Zhouqiang Li; lizhouqiang2021@126.com

Received 14 April 2021; Accepted 1 June 2021; Published 7 June 2021

Academic Editor: Rihong Cao

Copyright © 2021 Zhouqiang Li. This is an open access article distributed under the Creative Commons Attribution License, which permits unrestricted use, distribution, and reproduction in any medium, provided the original work is properly cited.

Taking a super large deep foundation pit project as an example, the horizontal displacement of crown beam and driveway, surface settlement, axial force of anchor cable, and underground water level in the construction process of the foundation pit are dynamically monitored and analyzed. The excavation deformation rule of the deep foundation pit and the influence of excavation on surrounding buildings are analyzed. The results show that, with the excavation of the foundation pit, the crown beam and driveway of the foundation pit incline towards the direction of the pit and eventually tend to be stable. The variation of axial force of the prestressed anchor cable in the first layer of the foundation pit is basically consistent with the variation of horizontal displacement time history. The variation trend of the groundwater level at each side of the foundation pit is different but tends to be stable in a short time. In the whole monitoring period, the cumulative settlement value of each area of the foundation pit is within the controllable range, but the surface settlement of the north side of the foundation pit and a surrounding building has not reached stability, so it is suggested to extend the monitoring time of settlement in the relevant area.

1. Introduction

The excavation of the foundation pit is accompanied by the stress redistribution of the surrounding soil [1–4]. Under the action of earth pressure, a certain displacement will be generated towards the pit, which will affect the stability of the foundation pit and surrounding buildings. Therefore, relevant supporting measures need to be taken [5, 6]. As a foundation pit supporting structure, the pile-anchor structure has been widely used in practical engineering [7–10]. It can make rational use of the soil's own characteristics, give full play to the mutual bonding between soil and pile-anchor structure, and have the advantages of rapid construction and low cost [11, 12]. With the continuous development of urban construction and excavation equipment, the scale of foundation pit engineering is developing towards a larger and deeper direction [13, 14]. For the construction process of super high-rise buildings and underground garages, the excavation of the deep foundation pit

has little influence on the surrounding buildings and traffic roads, so it is necessary to monitor the dynamic changes of soil indexes around the foundation pit during the excavation process [15–18]. The stability of geotechnical materials is affected by many factors [19–23]. In order to ensure the stability of the foundation pit itself and the surrounding environment as well as the pile-anchor retaining structure, dynamic monitoring is widely used as an effective means [24]. Through monitoring, the monitoring data can be compared with the design value to judge whether the previous step of construction technology and construction parameters meet the expected requirements and determine and optimize the next step of construction parameters, so as to achieve information construction [25, 26]. Zhu et al. [27] carried out physical model experiments in the laboratory based on a pit-in-pit foundation. Bennett et al. [28] present an overview of the most used nondestructive inspection (NDI) and structural health monitoring (SHM) technologies for freshwater pipes and sewers. By analyzing the

monitoring data, we can judge whether the previous construction effect meets the requirements and guide and optimize the next step of foundation pit excavation. Based on a very large pile-anchor bracing deep foundation pit engineering as an example, the foundation pit crown beam settlement and horizontal displacement, anchor axial force, the change of underground water level in the construction period for dynamic monitoring, and the analysis of deformation of soil around the foundation pit are summarized, and the influence of excavation on surrounding buildings can provide reference for the local similar deep foundation pit engineering.

2. Project Overview and Support Scheme

This project is a super large underground project, the shape of which is approximately rectangular. The safety level of the foundation pit is level 1. The excavation depth of the foundation pit is about 34 m, and the supporting length of the foundation pit is about 1330 m. The site consists of quaternary overburden, which includes artificial fill, alluvium and eluvium, and cretaceous bedrock, which includes silty sand and local coarse sandstone and conglomerate. The groundwater of the site is mainly quaternary pore water and bedrock fissure water. The quaternary pore water occurs in the pores of sand layer and silty clay. The sand layer is the main aquifer, and the depth of the groundwater level is 1.07~4.90 m. There is a small amount of water leakage in bedrock fissure water, but the overall water content of bedrock is small. Combined with the engineering characteristics and site conditions, double row triple high-pressure jet grouting piles are constructed around the foundation pit to strengthen the surrounding soil and cut off the seepage path of the peripheral groundwater into the foundation pit. The foundation pit support method is "double row jet grouting pile sealing curtain + artificial excavated pile + anchor cable," which is widely used in the foundation engineering [29, 30]. The layout of foundation pit monitoring points is shown in Figure 1, where C1–C4 represent the driveway.

3. Monitoring Results and Analysis

3.1. Horizontal Displacement of Foundation Pit Crown Beam and Foundation Pit Driveway. Three reference points are set outside the influence range of building deformation, and the buried depth is 0.5 m. The monitoring points are arranged along the perimeter of the foundation pit on the concrete roof or crown beam of the foundation pit slope. The horizontal spacing of the monitoring points is less than 20 m, and the polar coordinate measurement method is adopted for horizontal displacement monitoring. As shown in the distribution map of the foundation pit monitoring points, the positive and negative of the horizontal displacement only represent the direction. For the convenience of analysis, the absolute value of all the monitoring data is processed. The horizontal displacement monitoring data of the short side B49, B50, B51, and B52 on the west side of the foundation pit, the long side B12, B15, and B17 on the south side of the

foundation pit, and the roadway C1, C1-1, C2, C2-1, C3, and C4 of the foundation pit are taken for analysis, as shown in Figure 2. It can be seen from Figures 2(a) and 2(b) that the variation law of horizontal displacement monitoring curves of the long and short sides of the foundation pit is basically similar, and the overall trend increases with the excavation time. As shown in Figure 2(a), with the progress of soil excavation, the excavation face of the foundation pit increases continuously, and the horizontal displacement of the top of the foundation pit increases rapidly under the earth pressure outside the foundation pit. As soil excavation and prestressed anchor cable construction are carried out at the same time, the horizontal displacement of the soil around the support is limited and grows slowly. As the excavation continues, the restriction of the prestressed anchor cable on the horizontal displacement of the surrounding soil is weakened, and the pile top tends to move towards the pit. About 550 d after excavation, the change curve of the horizontal displacement of the pile top tends to be flat. Until the end of monitoring, the horizontal displacement of the pile top fluctuates within a controllable range. The maximum value of the horizontal displacement in the X direction is the monitoring point C3, with a value of 29.3 mm, and the maximum value of the horizontal displacement in the Y direction is the monitoring point B49, with a value of 27.3 mm, both of which do not exceed the alarm value. In addition, according to Figure 2(b), although the final cumulative values of horizontal displacements on the short edge of the foundation pit are similar, the horizontal displacements in the middle of the short edge of the foundation pit (B50 and B51) are greater than those on both sides of the short edge of the foundation pit (B49 and B52) during the excavation process. Combined with the distribution of monitoring points of the driveway and Figure 2(c), it can be seen that, in the whole monitoring cycle, with the increase of depth, the final cumulative value of horizontal displacement of the driveway increases continuously, and the curve rises at a faster rate.

3.2. Surface Settlement in Each Area of Foundation Pit.

For the convenience of observation, settlement displacement observation points and horizontal displacement observation points are arranged at the same point, and round trip confluence leveling is adopted for settlement monitoring. The monitoring data of B49 and B50 on the short side of the foundation pit, B15 and B17 on the long side, C2 and C3 on the driveway of the foundation pit, and F1, F2, F3, and F4 on the surrounding buildings of the foundation pit are selected for analysis. The settlement displacement curves of the crown beam and driveway of the foundation pit are shown in Figure 3, and the settlement curves of the surrounding buildings are shown in Figure 3(b). In addition, according to the occurrence of uneven settlement on the north side of the foundation pit, additional monitoring points A1, A2, A3, and A5 were selected for analysis, and the time-history variation curve of relevant settlement was shown in

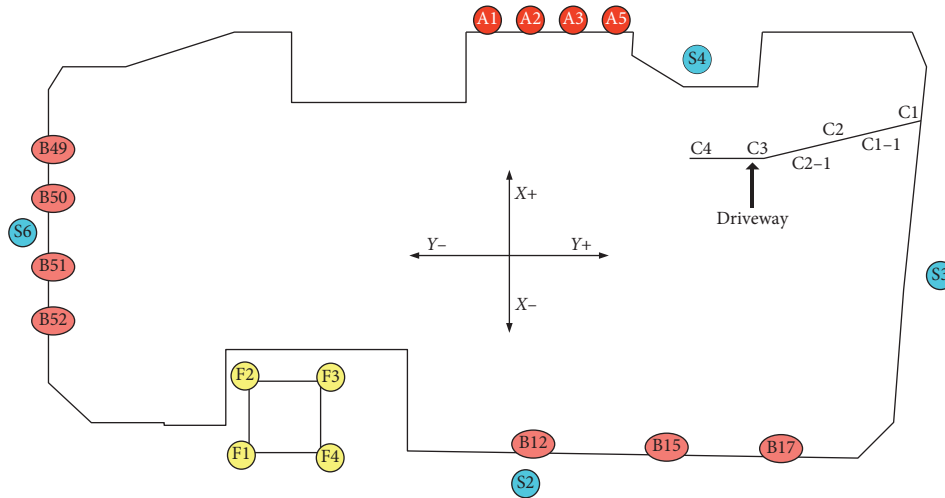


FIGURE 1: Layout of foundation pit monitoring points.

Figure 3(c). As can be seen from Figure 3(a), the settlement displacement of the crown beam and driveway in the foundation pit is roughly the same, both of which settle to a certain extent with the progress of soil excavation and eventually tend to be stable. The maximum settlement accumulation of the crown beam and driveway occurred at the monitoring point C2, which was 7.03 mm, not reaching the alarm value (± 20 mm), which proved that the supporting system adopted in the foundation pit engineering played a good role in restraining the settlement of the soil in the foundation pit. Figure 3(b) shows that the settlement displacement curve of buildings around the foundation pit continues to decline after a period of stability (600 d–1000 d) and does not reach a stable state again in the whole monitoring cycle. It can be seen from Figure 3(c) that the soil on the north side of the foundation pit has subsidence in the whole monitoring period. Although the ground subsidence observed at the monitoring points on the north side of the foundation pit (A1, A2, A3, and A5) and the surrounding buildings (F1, F2, F3, and F4) were all alarm values until the end of monitoring, the monitored settlement displacement curve could not reflect the maximum deformation value of the ground subsidence there. The same phenomenon is also mentioned in literature [1, 2]. Therefore, it is suggested to extend the monitoring time of surface subsidence in these two places.

3.3. Stress of Anchor Cable. The anchor cable stress monitoring adopts the anchor cable dynamometer installed on the anchor cable [31–34], which is installed in the middle of each edge, the sun corner, and the section with complex geological conditions. Correspondent to the horizontal displacement curve of pile head, the monitoring data (M10, M15, M33, and M45) of the first layer of the anchor cable in different areas were selected for analysis to obtain the curve

of the axial force of anchor cable in the first layer over time, as shown in Figure 4. As can be seen from Figure 4, in the whole monitoring cycle, the change rule of axial force of the first layer anchor cable with time in different areas is basically the same. With the excavation, the axial force of anchor cable decreases and finally becomes stable. The time-history evolution curve of the anchor cable axial force has a good consistency with the horizontal displacement curve of the pile top. At the beginning of excavation, the anchor cable axial force curve has a large drop and then enters the period of shock decline. Finally, the anchor cable axial force curve tends to be stable with the completion of soil excavation. It is not difficult to find that corresponding to the horizontal displacement of each side of the foundation pit is similar, and the cumulative loss of axial force of the anchor cable of the first layer in different areas is also roughly the same, which indicates that the supporting system adopted in this project has played a better role in limiting the displacement of the soil.

3.4. Groundwater Level. The water level monitoring holes are arranged along the foundation pit and around the protected object [35, 36]. The interval between the monitoring holes is 20 m–50 m, and a total of water level monitoring holes are arranged. The bottom of the water level pipe is sealed to prevent sediment from entering the pipe. The bottom of the water level pipe flows 0.5–1 m to deposit a small amount of mud and sand brought by the water filter section. No holes shall be drilled in the area 2 m below the surface to ensure the sealing quality and the pores outside the pipe shall be blocked with cohesive soil to avoid the inflow of surface water into the pipe. The water level pipe is about 300 mm above the ground, and it is covered to prevent rainwater from entering. During the water level measurement, the side head is moved slowly downward.

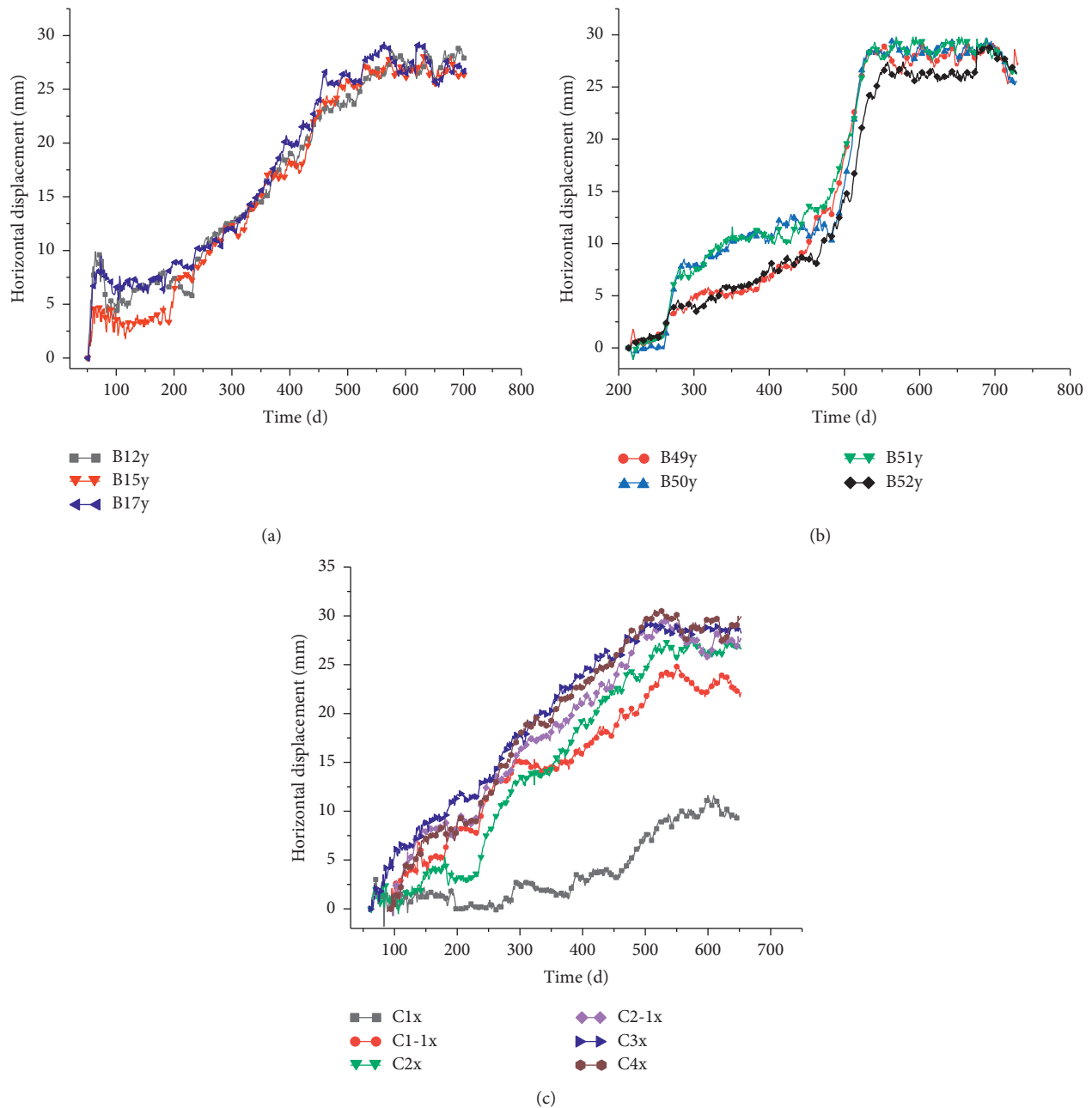


FIGURE 2: Horizontal displacement curve of crown beam and driveway in the foundation pit. (a) Horizontal displacement of the long side of the foundation pit. (b) Horizontal displacement of short edge of the foundation pit. (c) Horizontal displacement of the driveway.

When the side head touches the water surface, the receiving system sends out a signal, and the ground water level elevation can be obtained according to the reading of the steel ruler cable at the pipe opening. The groundwater level monitoring data (S2, S3, S4, and S6) at each side of the foundation pit were selected for analysis, and the time-history variation curve of the groundwater level of the

foundation pit was obtained, as shown in Figure 5. Figure 5 shows that there are great differences in the specific changes of the groundwater level at each side of the foundation pit. The water level in the south and east side of the foundation pit experienced a large drop in a short time and then quickly stabilized. The S4 data of the monitoring point on the north side of the foundation pit showed that the water

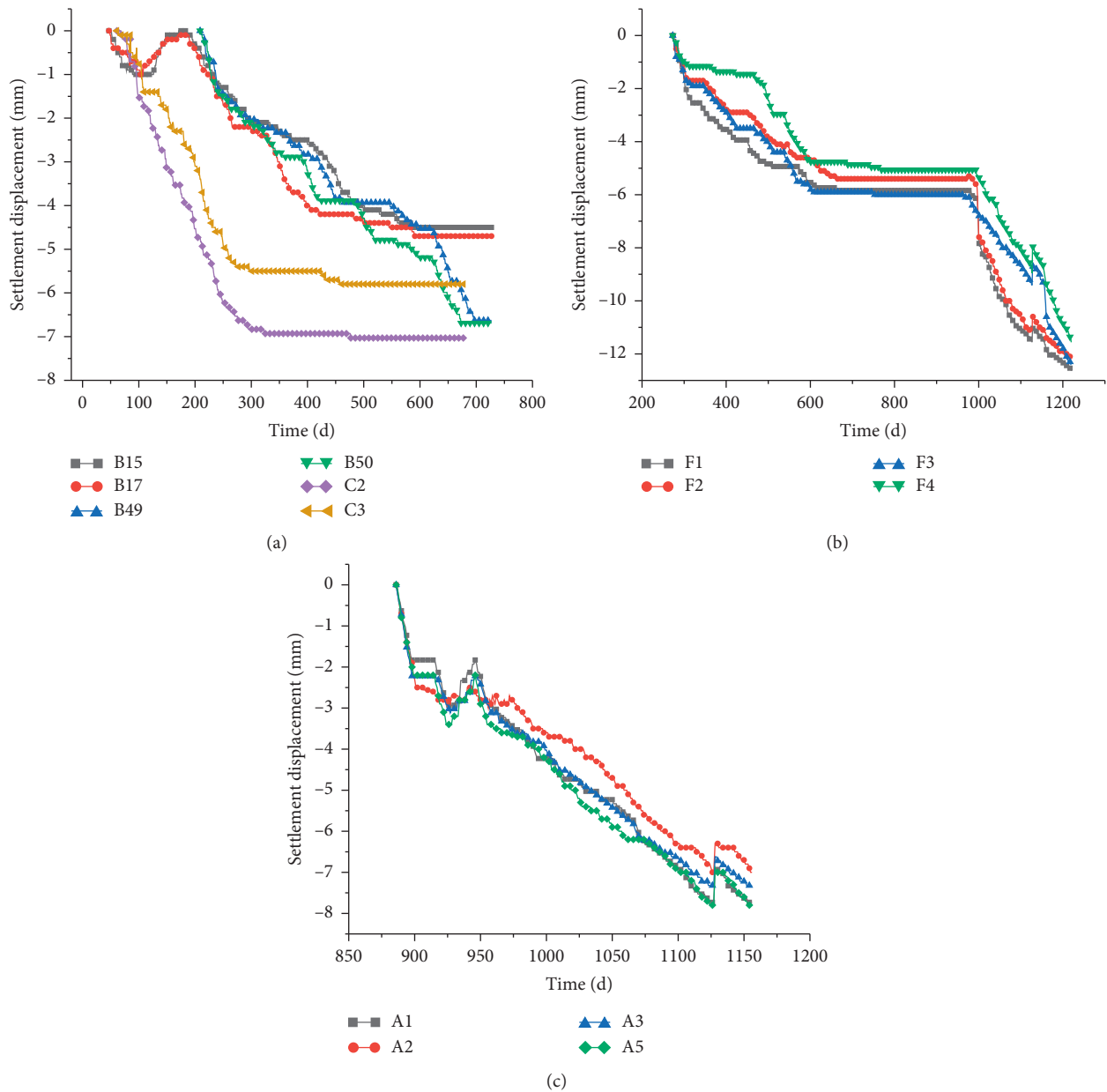


FIGURE 3: Settlement displacement curve of each area of the foundation pit. (a) Settlement displacement curve of the foundation pit crown beam and driveway. (b) Settlement displacement curve of buildings around the foundation pit. (c) Settlement displacement curve on the north side of foundation pit.

level changed little during the whole monitoring period. The groundwater level in the east of the foundation pit decreases first and then rises to the initial level and then tends to be stable. It is proved that the water stop curtain of double row jet grouting pile plays a good water retaining function in the foundation pit engineering. According to the data of four monitoring points, the groundwater level of S2 on the south side of the foundation pit fluctuates the

most, up to 5.4 m. The second is S3 on the east side of the foundation pit, and the change of the groundwater level is about 1.6 m. Yadav et al. [1] also found that the change of the groundwater level in the foundation pit reached 4.5 m within dozens of days. This is mainly because the groundwater in the deep foundation pit project in this paper is abundant and fluctuates greatly, but it does not trigger the monitoring and alarm system.

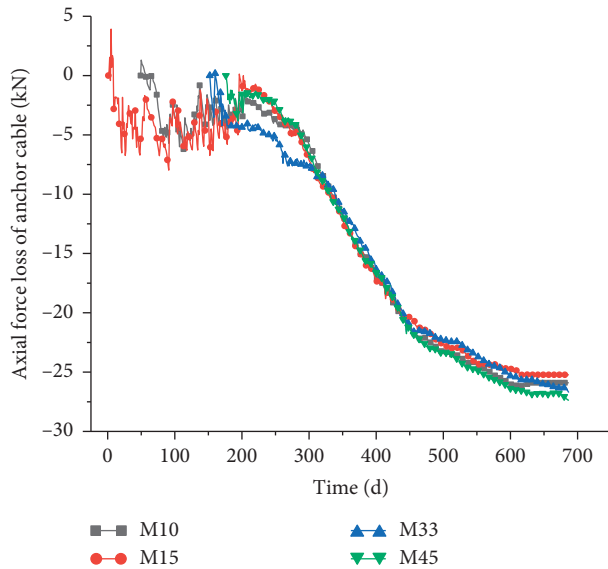


FIGURE 4: Time-history variation curve of axial force loss of the anchor cable.

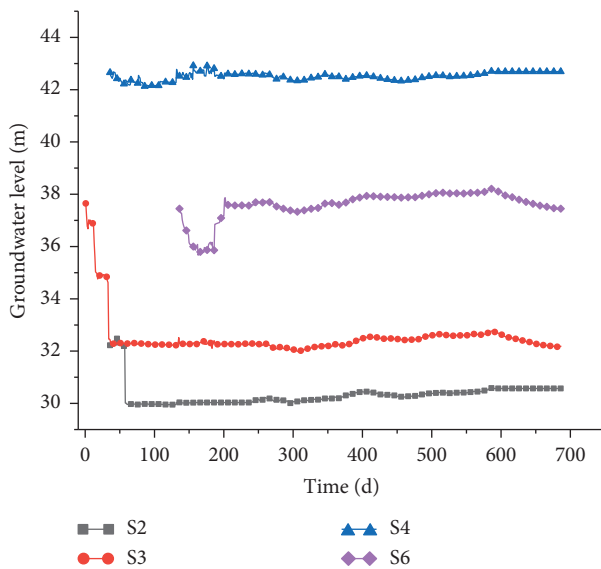


FIGURE 5: Time-history curve of the groundwater level.

4. Conclusions

- (1) For super-large deep foundation pit engineering, the support system of double row jet grouting pile water-sealing curtain + artificial hole-digging pile + prestressed anchor cable plays a good supporting role. In the whole monitoring period, the horizontal displacement of the crown beam and driveway of the foundation pit, the ground settlement in each area of the foundation pit, the axial force loss of the anchor cable, and the change of the underground water level do not reach the alarm value, which indicates that the design scheme of the pile-anchor supporting system used in the foundation pit is safe and reliable.

- (2) With the excavation of the foundation pit, the crown beam and driveway of the foundation pit will move in the direction of the pit and eventually tend to be stable. The variation curve of the prestressed anchor cable of the first layer in each area of the foundation pit is in good consistency with the variation curve of the horizontal displacement time history. The variation trend of the groundwater level at each side of the foundation pit is different but tends to be stable in a short time.
- (3) With the excavation of the soil, the settlement of the foundation pit and the surrounding area will occur to a certain extent. During the whole monitoring period, the cumulative settlement value of each area of the foundation pit is within the controllable range. However, the data of the newly added monitoring points on the north side of the foundation pit and the monitoring points of a surrounding building show that the surface settlement has not reached stability. Therefore, it is suggested to extend the monitoring time of settlement in the relevant areas.

Data Availability

The data used to support the findings of this study are available from the corresponding author upon reasonable request.

Conflicts of Interest

The authors declare that there are no conflicts of interest.



References

- [1] S. K. Yadav, U. Amjad, and P. K. Basudhar, "Reinforcement effect on the static analysis of circular footing resting over winkler elastic foundation," *Geotechnical & Geological Engineering*, vol. 38, pp. 1–17, 2018.
- [2] Y. Wang, P. Guo, F. Dai, X. Li, Y. Zhao, and Y. Liu, "Behavior and modeling of fiber-reinforced clay under triaxial compression by combining the superposition method with the energy-based homogenization technique," *International Journal of Geomechanics*, vol. 18, no. 12, Article ID 04018172, 2018.
- [3] T. Wood and M. Karstunen, "Modelling the creep of deep foundations in soft gothenburg clays," *European Journal of Environmental and Civil Engineering*, vol. 87, pp. 1–19, 2017.
- [4] C. Panganayi, H. Ogata, K. Hattori, and T. Tom, "Interaction between engineered cementitious composites lining and foundation subsurface drain," *Advances in Civil Engineering*, vol. 2011, Article ID 280717, 9 pages, 2011.
- [5] R. Yang, J. Huang, D. V. Griffiths, J. Li, and D. Sheng, "Importance of soil property sampling location in slope stability assessment," *Canadian Geotechnical Journal*, vol. 56, no. 3, pp. 335–346, 2019.
- [6] D. W. M. Chan, T. O. Olawumi, and A. M. L. Ho, "Perceived benefits of and barriers to building information modelling (BIM) implementation in construction: the case of Hong Kong," *Journal of Building Engineering*, vol. 25, Article ID 100764, 2019.

- [7] B. Yuan, M. Sun, L. Xiong, Q. Luo, S. P. Pradhan, and H. Li, "Investigation of 3D deformation of transparent soil around a laterally loaded pile based on a hydraulic gradient model test," *Journal of Building Engineering*, vol. 28, Article ID 101024, 2020.
- [8] B. Yuan, M. Sun, Y. Wang, L. Zhai, Q. Luo, and X. Zhang, "Full 3D displacement measuring system for 3D displacement field of soil around a laterally loaded pile in transparent soil," *International Journal of Geomechanics*, vol. 19, no. 5, Article ID 04019028, 2019.
- [9] B. Yuan, K. Xu, Y. Wang, R. Chen, and Q. Luo, "Investigation of deflection of a laterally loaded pile and soil deformation using the PIV technique," *International Journal of Geomechanics*, vol. 17, no. 6, 2017.
- [10] L. Luan, Y. Liu, and Y. Li, "Numerical simulation for the soil-pile-structure interaction under seismic loading," *Mathematical Problems in Engineering*, vol. 2015, Article ID 959581, 7 pages, 2015.
- [11] C. Chreties, L. Teixeira, and G. Simarro, "Pile group protection with riprap mattress," *Advances in Civil Engineering*, vol. 2012, Article ID 693506, 7 pages, 2012.
- [12] N. Letizia, C. Iodice, and A. Mandolini, "A local design method for pile foundations," *Advances in Civil Engineering*, vol. 2018, Article ID 9486945, 14 pages, 2018.
- [13] M. Mohammed, A. Sharafati, N. Al-Ansari, and Z. M. Yaseen, "Shallow foundation settlement quantification: application of hybridized adaptive neuro-fuzzy inference system model," *Advances in Civil Engineering*, vol. 2020, Article ID 7381617, 14 pages, 2020.
- [14] M. -Y. Zhang, J. -X. Ma, S. -J. Yang, Y. -H. Wang, X. -Y. Bai, and S. -X. Sun, "Experimental study on bending moment of double-row steel pipe piles in foundation excavation," *Advances in Civil Engineering*, vol. 2020, Article ID 8882713, 8 pages, 2020.
- [15] H. Lai, H. Zheng, R. Chen, Z. Kang, and Y. Liu, "Settlement behaviors of existing tunnel caused by obliquely under-crossing shield tunneling in close proximity with small intersection angle," *Tunnelling and Underground Space Technology*, vol. 97, Article ID 103258, 2020.
- [16] A. Alam, N. Wang, G. Zhao, and A. Barkat, "Implication of radon monitoring for earthquake surveillance using statistical techniques: a case study of wenchuan earthquake," *Geofluids*, vol. 2020, Article ID 2429165, 14 pages, 2020.
- [17] C. Zhang, C. Pu, R. Cao, T. Jiang, and G. Huang, "The stability and roof-support optimization of roadways passing through unfavorable geological bodies using advanced detection and monitoring methods, among others, in the Sanmenxia Bauxite Mine in China's Henan Province," *Bulletin of Engineering Geology and the Environment*, vol. 78, no. 7, pp. 5087–5099, 2019.
- [18] M. Naderloo, M. Moosavi, and M. Ahmadi, "Using acoustic emission technique to monitor damage progress around joints in brittle materials," *Theoretical and Applied Fracture Mechanics*, vol. 104, Article ID 102368, 16 pages, 2019.
- [19] Y. Chen, H. Lin, X. Ding, and S. Xie, "Scale effect of shear mechanical properties of non-penetrating horizontal rock-like joints," *Environmental Earth Sciences*, vol. 80, no. 5, p. 192, 2021.
- [20] S. Xie, H. Lin, Y. Wang et al., "Nonlinear shear constitutive model for peak shear-type joints based on improved Harris damage function," *Archives of Civil and Mechanical Engineering*, vol. 20, no. 3, p. 95, 2020.
- [21] T. Dezert, S. Palma Lopes, Y. Fargier, L. Saussaye, and P. Côte, "Data fusion of in situ geophysical and geotechnical information for levee characterization," *Bulletin of Engineering Geology and the Environment*, vol. 80, no. 6, pp. 5181–5197, 2021.
- [22] C. Gokceoglu, S. Kocaman, H. A. Nefeslioglu, and A. O. Ok, "Use of multisensor and multitemporal geospatial datasets to extract the foundation characteristics of a large building: a case study," *Bulletin of Engineering Geology and the Environment*, vol. 80, no. 4, pp. 3251–3269, 2021.
- [23] H. Lin, X. Zhang, R. Cao, and Z. Wen, "Improved nonlinear Burgers shear creep model based on the time-dependent shear strength for rock," *Environmental Earth Sciences*, vol. 79, no. 6, p. 149, 2020.
- [24] M. O. Kluger, S. Kreiter, F. T. Stähler, M. Goodarzi, T. Stanski, and T. Mörz, "Cone penetration tests in dry and saturated Ticino sand," *Bulletin of Engineering Geology and the Environment*, vol. 80, no. 5, pp. 4079–4088, 2021.
- [25] P. Rizzo, "Water and wastewater pipe nondestructive evaluation and health monitoring: a review," *Advances in Civil Engineering*, vol. 2010, Article ID 818597, 13 pages, 2010.
- [26] Y. Chen, H. Lin, R. Cao, and C. Zhang, "Slope stability analysis considering different contributions of shear strength parameters," *International Journal of Geomechanics*, vol. 21, no. 3, Article ID 04020265, 2021.
- [27] C. Zhu, K. Zhang, H. Cai et al., "Combined application of optical fibers and CRLD bolts to monitor deformation of a pit-in-pit foundation," *Advances in Civil Engineering*, vol. 2019, Article ID 2572034, 16 pages, 2019.
- [28] V. Bennett, T. Abdoun, M. Zeghal, A. Koelewijn, M. Barendse, and R. Dobry, "Real-time monitoring system and advanced characterization technique for civil infrastructure health monitoring," *Advances in Civil Engineering*, vol. 2011, Article ID 870383, 12 pages, 2011.
- [29] C. Zhang, C. Wu, and P. Wang, "Seismic fragility analysis of bridge group pile foundations considering fluid-pile-soil interaction," *Shock and Vibration*, vol. 2020, Article ID 8838813, 17 pages, 2020.
- [30] Y. Xie and S. Chi, "Optimization method of reducing the differential settlements of piled raft foundations based on pile-to-pile interaction theory," *Advances in Civil Engineering*, vol. 2020, Article ID 1521876, 14 pages, 2020.
- [31] M. Y. Koca, C. Kincal, A. T. Arslan, and H. R. Yilmaz, "Anchor application in Karatepe andesite rock slope, Izmir-Türkiye," *International Journal of Rock Mechanics and Mining Sciences*, vol. 48, no. 2, pp. 245–258, 2011.
- [32] H. Lin, P. Sun, Y. Chen, Y. Zhu, X. Fan, and Y. Zhao, "Analytical and experimental analysis of the shear strength of bolted saw-tooth joints," *European Journal of Environmental and Civil Engineering*, vol. 24, pp. 1–15, 2020.
- [33] E. Komurlu and A. Kesimal, "Experimental study on usability of friction rockbolts with plastic bodies," *International Journal of Geomechanics*, vol. 17, 2017.
- [34] M. Ranjbarnia, A. Fahimifar, and P. Oreste, "Practical method for the design of pretensioned fully grouted rockbolts in tunnels," *International Journal of Geomechanics*, vol. 16, no. 1, Article ID 04015012, 2016.
- [35] D. Kuttah and H. Arvidsson, "Effect of groundwater table rising on the performance of a Swedish-designed gravel road," *Transportation Geotechnics*, vol. 11, pp. 82–96, 2017.
- [36] M. Pirone, R. Papa, M. V. Nicotera, and G. Urciuoli, "In situ monitoring of the groundwater field in an unsaturated pyroclastic slope for slope stability evaluation," *Landslides*, vol. 12, no. 2, pp. 259–276, 2015.

Research Article

Volume Changes and Mechanical Properties of Expansive Mudstone below Canals under Wet-Dry/Wet-Dry-Freeze-Thaw Cycles

Rui Zhu ^{1,2,3}, Ying-hao Huang,³ Zhu Song,¹ and Feng Zhou ^{1,2}

¹School of Transportation Engineering, Nanjing Tech University, Nanjing 211816, China

²Key Laboratory of Ministry of Education for Geomechanics and Embankment Engineering, Hohai University, Nanjing 210098, China

³Geotechnical Engineering Department, Nanjing Hydraulic Research Institute, Nanjing 210024, China

Correspondence should be addressed to Feng Zhou; zhoufeng@njtech.edu.cn

Received 18 April 2021; Accepted 26 May 2021; Published 7 June 2021

Academic Editor: Rihong Cao

Copyright © 2021 Rui Zhu et al. This is an open access article distributed under the Creative Commons Attribution License, which permits unrestricted use, distribution, and reproduction in any medium, provided the original work is properly cited.

The complex environment in northern China is the main reason for degradation of expansive mudstone below the canals, which resulted in instability and damage of canal slopes. In this study, a serial of laboratory tests was conducted to explore the volume changes and mechanical behaviors of expansive mudstone below the canals in Xinjiang. The experimental program includes wet-dry (WD) and wet-dry-freeze-thaw (WDFT) tests, volume measurement, and unconfined compression tests. The test results show that during the WD cycles, the volume changes of expansive mudstones with a higher dry range would be more significant. The freeze-thaw process in the WDFT cycles resulted in a decrease of volume change ranges when the expansive mudstones had a relatively smaller dry range and a slight increase of volume change ranges when the expansive mudstones had a relatively larger dry range. In the meantime, the stress-strain relationships of expansive mudstones with different dry ranges all presented strain softening under the cycles of WD or WDFT. The first cycle resulted in a significant decrease of failure strength. After seven WD/WDFT cycles, the failure strength of expansive mudstones with different dry ranges decreased by 37.2%~59.1%. In addition, the freeze-thaw process in the WDFT cycles promoted the softening of the stress-strain relationships and aggravated the failure strength attenuation of expansive mudstones. Through this study, we expect to provide a preliminary basis for the construction and maintenance of expansive mudstone canals in Xinjiang.

1. Introduction

Long-distance water transfer projects are a major strategy to realize the optimal allocation of water resources, and water transfer canals are the main methods used in water transfer projects. China has approximately 4.5 million km of various water transfer canals, but the utilization coefficient of canal water is relatively low [1]. Canals in northern China are particularly susceptible to damage by the harsh natural environment, resulting in hidden dangers to the stable operation of the canals [2, 3], as shown in Figure 1.

Wet-dry cycles and freeze-thaw cycles are two typical boundaries simplified from natural environment of on-site canals. On this basis, a large number of experimental studies have been conducted on volume changes and mechanical

degradation of foundation soils below the canals under wet-dry and freeze-thaw cycles [4–8]. Lu et al. [9, 10] investigated the freeze-thaw performance of the expansive soil taken from South-to-North Water Transfer Project by UCS and SEM tests. It is found that the internal porosity of expansive soil increased and became more uniform after several freeze-thaw cycles, which is more significant among the soils with a higher moisture content. Wang et al. [11, 12] studied the mechanical characteristics of saline soil under different moisture contents, salt contents, and freeze-thaw cycles, which provide a basic reference for canal construction in Jilin. Li et al. [13–15] investigated the frost damage mechanism of foundation soil in cold regions, which is helpful to theoretical and numerical studies. Recently, some innovative instruments, such as NMR, CT, and TDR, have been used in



FIGURE 1: Typical damages of canals in northern China [2, 3].

frozen soil studies [16–18], which greatly perfect the quantitative analysis of unfrozen water content and microstructure development [19–22]. Additionally, Zhu et al. [23] investigated the relationships between surface cracks and mechanical properties of expansive soil and then analyzed the damage characteristics of canal slopes under wet-dry cycles by centrifugal model tests [24, 25].

The above studies play an important role in the mechanism investigation of foundation soil below the canals under cyclic actions of wet-dry or freeze-thaw [26–28]. However, studies related to a typical canal in Xinjiang showed that the expansive mudstone below the canals experienced a wet-dry-freeze-thaw process throughout the year [29–31], as shown in Figure 2. The volume changes and mechanical properties of expansive mudstone below the canals in Xinjiang are very scarce in the literature. Consequently, current studies cannot provide a well reference for these canals.

Accordingly, the objective of this study is to investigate the volume changes and mechanical properties of expansive mudstone below the canals in Xinjiang. Specially, a series of wet-dry (WD)/wet-dry-freeze-thaw (WDFT) tests and unconfined compressive strength tests were performed, and then, performances of deformation and strength upon the dry ranges and cycle numbers of WD/WDFT were analyzed. Through this study, we expect to provide a preliminary basis for the construction and maintenance of expansive mudstone canals in Xinjiang.

2. Materials

The samples tested in this study were prepared with a natural expansive mudstone material, which was taken from the field of a typical canal in Xinjiang [29, 30], as shown in Figure 3. Some fundamental properties of the mudstone were measured following procedures described in the specifications [32–34], as given in Table 1. In the meantime, the grain size distribution was analyzed using sieving analysis [35] and the hydrometer method in the laboratory [36], as shown in Figure 4. It is found that the percent passing #200 sieve is as high as approximately 69%.

3. Experimental Program

3.1. Sample Preparation. Before preparation, the original soil material was air-dried for about two weeks. Then, it was grinded and sieved through a 2.0 mm sieve. The sieved soil

was stored in buckets. According to the test scheme, the soil was added with water in measured quantities and mixed completely until initial moisture content reached 18.4%, which is the optimum moisture content. The mixed soil was sealed in plastic bags for approximately 24 hours for a homogeneous soil moisture distribution. Next, the soil was compacted using a stratified sample preparation device and prepared samples with 39.1 mm in diameter and 80 mm in height, as shown in Figure 5. Six samples for each condition were prepared. Among them, three samples were for the measurement of volume changes and three samples were for unconfined compression tests, which significantly reduced the disturbance of the samples for mechanical tests [9, 10, 37]. All the samples were compacted to the same dry density of 1.60 mg/m^3 , which is on the basis of the field test results [23–25]. After compaction, the samples were extracted from the mold for the WD and WDFT tests.

3.2. WD and WDFT Tests. After sample preparation, all the samples were divided into two series: half of the samples experienced the repeated WD processes while the other part underwent the WDFT cycles. Both of the WD cycles and the WDFT cycles were 0, 1, 3, and 7 cycles, which was decided because the soil properties tended towards stability after 3 WD cycles [38, 39]. The wet, dry, freeze, and thaw processes were as follows:

(1) Wet process

The wet process corresponds to the operation period of the typical canal. During this period, the foundation soil below the canals was saturated due to the water infiltration. Consequently, the wet process of the samples was simulated by the vacuum saturation method.

(2) Dry process

The drying process corresponds to the nonoperation period of the typical canal. During this period, there is no water inside the canal, resulting in that the foundation soil below the canals was air-dried continuously. Thus, the samples were air-dried in the test room with a temperature of $20 \pm 1^\circ\text{C}$ and a relative humidity of $55 \pm 5\%$. The saturation variations of samples were monitored by weight, and the dry process would be terminated until it came to the target saturation (S_t).

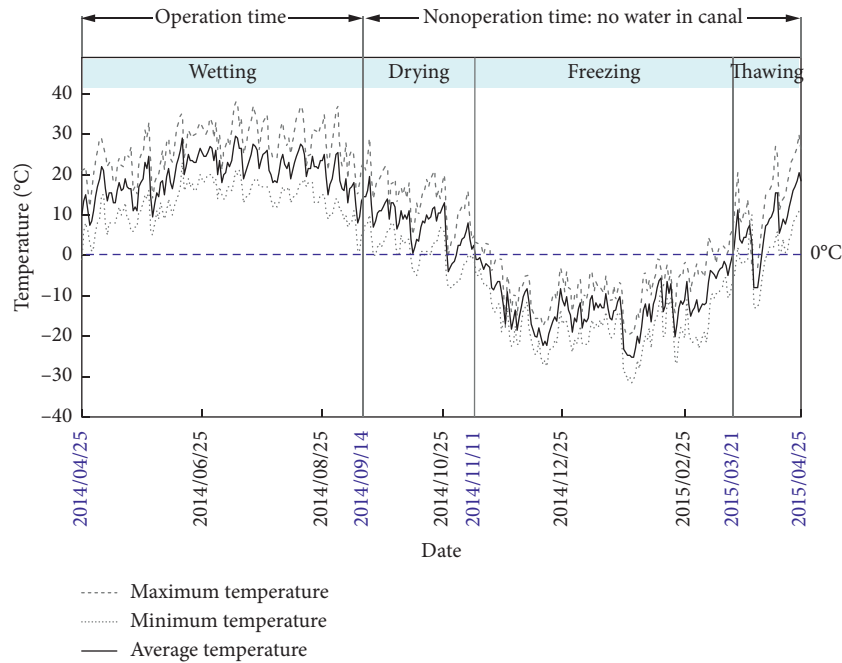


FIGURE 2: Temperature observed by a weather station along the canal in Xinjiang [29–31].

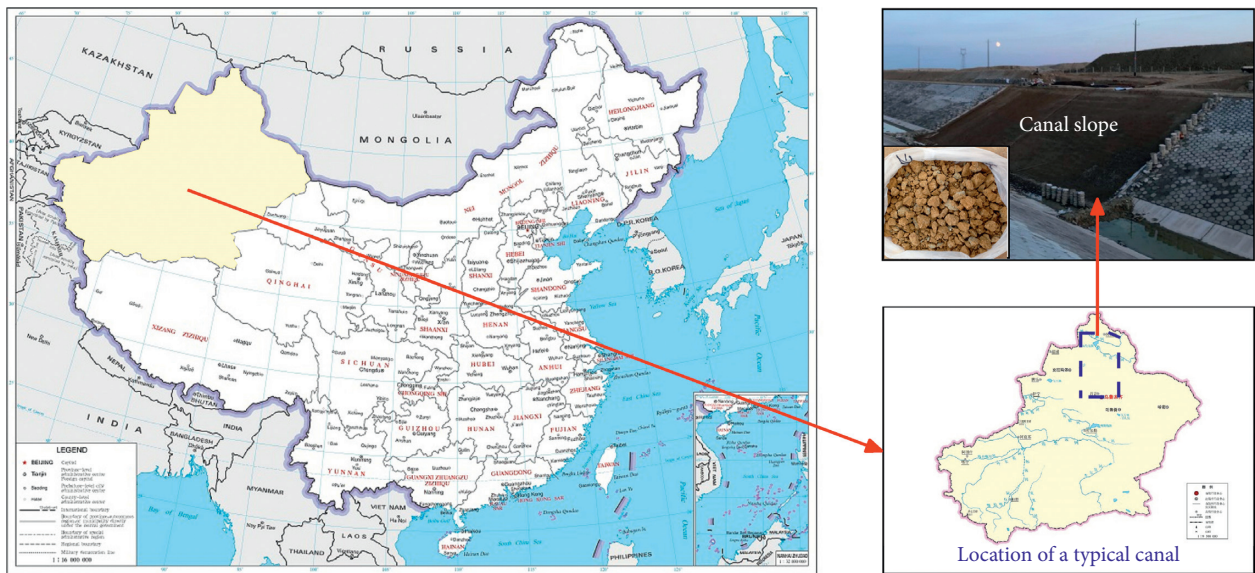


FIGURE 3: Location of the sampling area in Xinjiang, China.

(3) Freeze process

The freeze process corresponds to the time when the field temperature was lower than 0°C. Therefore, the freeze process of the samples was simulated by the low-temperature environment test chamber in Nanjing Hydraulic Research Institute, as shown in Figure 6. The samples were wrapped with plastic film first, which was effective to avoid moisture loss in the freeze process and thaw process in the previous studies [9, 10]. Then, the wrapped samples were exposed to three-dimensional closed environment with a consistent temperature of -20°C for 12 hours.

(4) Thaw process

The thaw process corresponds to the time when the field temperature was higher than 0°C. Thus, the thaw process of the samples was simulated by thawing at the room temperature of 20°C for 12 hours.

It is noted that the -20°C in the freeze process and 20°C in the thaw process were derived from the average temperature in the field during winter and the average temperature in the field during summer, respectively. The time of the freeze process and thaw process was decided because 12 hours proved that it

TABLE 1: Fundamental properties of mudstone material.

Properties	Value
Specific gravity	2.67
Potential expansion	71.0
CHCS classification	CH
Consistency limit	
Liquid limit	52.6%
Plastic limit	18.4%
Plasticity index	34.2
Compaction study	
Optimum moisture content	18.4%
Maximum dry density	1.70 mg/m ³
Mineral components	
Montmorillonite	61.5%
Quartz	31.9%
Feldspar	6.1%
Calcite and albite	0.5%

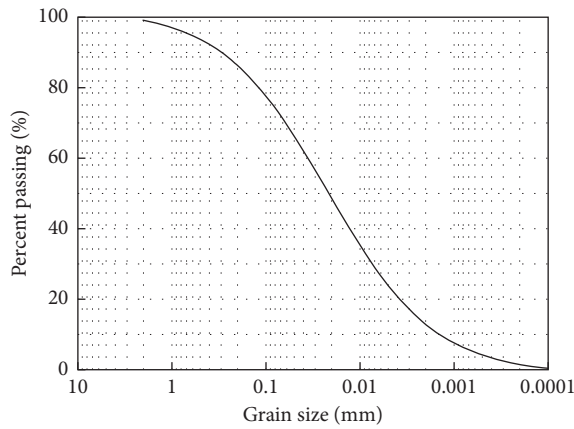


FIGURE 4: Grain size distribution.

is an adequate period after which the volume changes would become constant [9, 10]. Additionally, the target saturation (S_t) of samples was a variable in the dry process, resulting in that the sample saturation changed during the cyclic WD processes and WDFT processes, which are given in Table 2.

3.3. Measurement of Volume Changes and Unconfined Compression Strength Tests. In order to obtain the volumes changes of samples exposed to WD cycles and WDFT cycles, the diameter (D) and height (H) of samples were measured after each period of wet, dry, freeze, and thaw, since the sample deformation was basically homogeneous along the sample height. The measurement of sample dimensions using an electronic vernier caliper has a precision of 0.01 mm, as shown in Figure 7. Additionally, the measured dimensions of samples were derived from the three values along cross-section and two values along the longitudinal section. Consequently, the average values of sample volume were calculated on the basis of the above measured values of diameter and height during the cyclic WD and WDFT processes.

The strength of samples was measured by an YSH-2 unconfined compression device in Nanjing Hydraulic Research Institute (Figure 8), which can obtain a great quantity of data to describe the mechanical behaviors of samples. The maximum load capacity and maximum strain rate of this device are 5 kN and 1 mm/min, respectively. The samples were deformed under a compression load until the axial strain of samples reached 16%. During this process, the strain rate was kept at 0.8 mm/min, which is equal to 1%/min. Consequently, the stress-strain response, resilient modulus, and failure strength of samples subjected to WD cycles and WDFT cycles can be obtained. Figure 9 shows the typical failure characteristics of samples with different dry ranges.

4. Test Results

4.1. Volume Changes. In order to characterize the volume changes of samples better, a dimensionless parameter, named volumetric strain (ε_v), was proposed to indicate relative volume change of samples during the cyclic WD and WDFT processes. The volumetric strain can be calculated as

$$\begin{aligned} \varepsilon_v &= \frac{\Delta V}{V_0}, \\ &= \frac{(V_N - V_0)}{V_0}, \end{aligned} \quad (1)$$

where V_N is the sample volume after N cycles of WD or WDFT, and V_0 is the initial volume of samples after preparation. Consequently, the positive values of volumetric strain indicated volume expansion, while the negative ones represented volume contraction. Figure 10 shows the curves of volume changes variation with WD and WDFT cycles. Among the horizontal axis, 0 represents the initial state of samples, and 1, 2, 3, 4, 5, 6, and 7 refer to the completion of corresponding cycles of WD or WDFT.

As shown in Figure 10(a), the samples presented the typical characteristics of volume expansion in the wet process and volume contraction in the dry process, and the sample volumes changed alternately with the increasing WD cycles. Specifically, the volume variation trend of samples with dry range I during each WD cycle is relatively constant, especially after four WD cycles. Additionally, the volumetric strain of samples with dry range II during each WD cycle showed the similar variation characteristics to the ones with dry range I. However, the volumetric strain of samples with dry range II decreased gradually, resulting in a downward trend of sample volumes after each WD cycle. Different from the above samples with dry range I and dry range II, the volumetric strain of samples with dry range III during the wet process and dry process decreased significantly with the increasing WD cycles. Compared with the volumetric strain in the first WD cycle, the volumetric strain of samples with dry range III in the seventh cycle decreased by 65.8%. In the meantime, it is also found from Figure 10(a) that the samples with dry range I showed the largest volumetric strain in a single WD cycle, indicating that the volume changes of



FIGURE 5: Stratified sample preparation device.

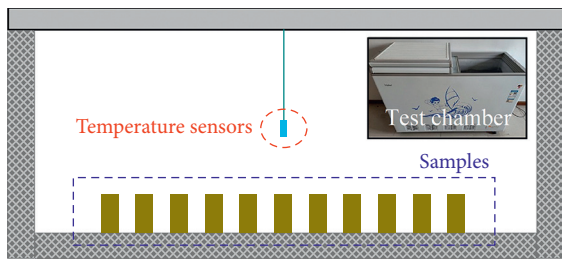


FIGURE 6: Low-temperature environment test chamber.

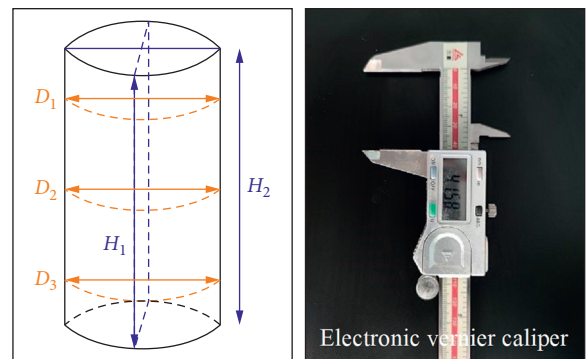


FIGURE 7: Schematic diagram of sample dimension measurement.

TABLE 2: Saturation variations of sample during the WD/WDFT processes.

Processes	Wet S_t	Dry S_t	Freeze S_t	Thaw S_t
Sample		30% (dry range I)	30%	30%
Saturation	100%	70% (dry range II) 90% (dry range III)	70% 90%	70% 90%
Remarks	In the dry process, different S_t means different dry ranges. Among them, dry range I represents that S_t is 30%; dry range II represents that S_t is 70%; dry range III represents that S_t is 90%.			

samples with a larger dry range would be more significant, which is consistent with that reported in the literature [40].

Figure 10(b) shows the volume changes of samples exposed to WDFT cycles. It is found that the volumetric strain of samples with different dry ranges all present the variation characteristics of fluctuation during the cyclic WDFT processes. Among them, the volumetric strain of samples with dry range I after each WDFT cycle is relatively stable and basically remains constant after three WDFT cycles, while the volumetric strain of samples with dry range

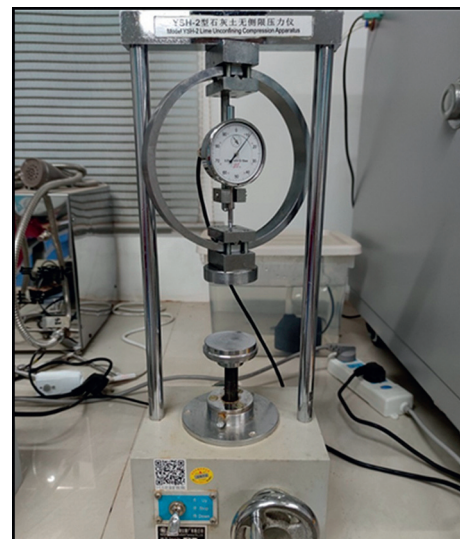


FIGURE 8: Device for unconfined compression.

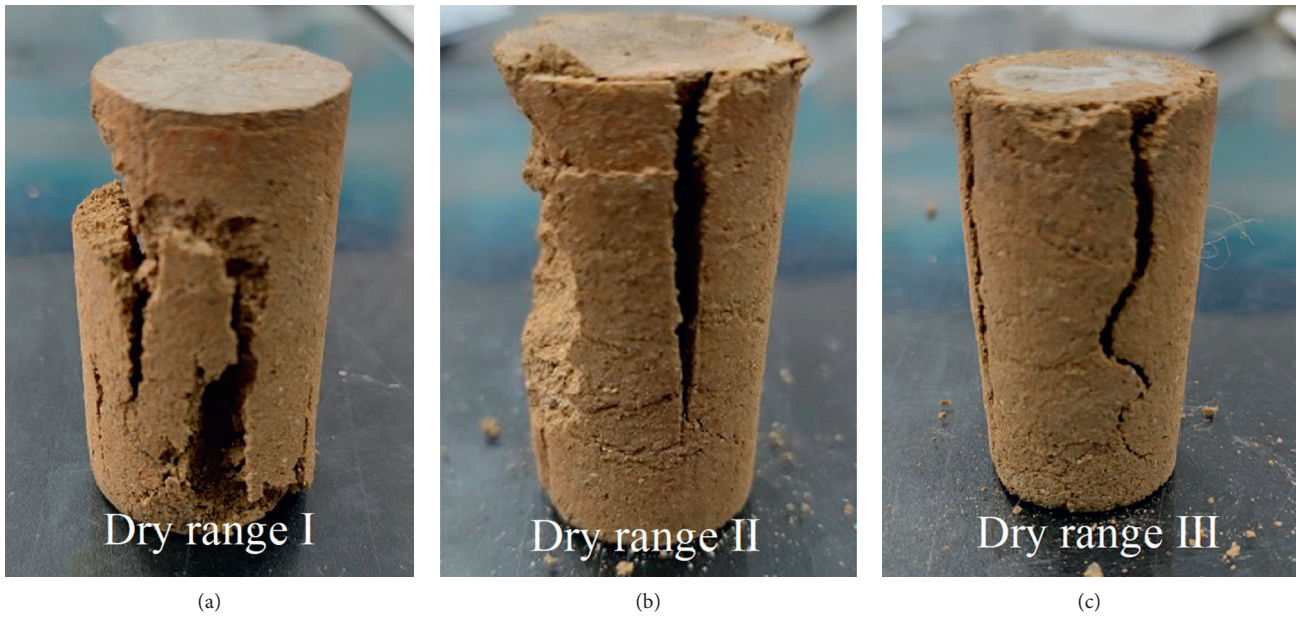


FIGURE 9: Typical failure characteristics of samples subjected to WDFT cycles.

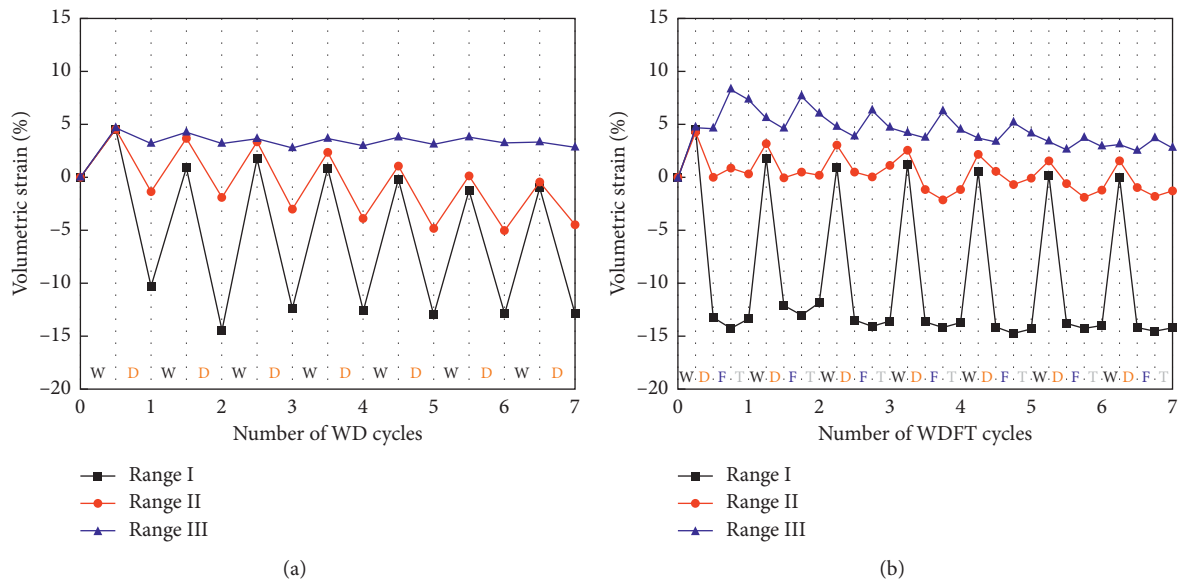


FIGURE 10: Curves of volume changes with cycles under different dry ranges. (a) Samples exposed to WD cycles. (b) Samples exposed to WDFT cycles.

II and dry range III after each WDFT cycle presented a downward trend with the increasing WDFT cycles. In addition, the samples with dry range I showed a significant wet-dry effect on the volume changes, which is reflected in a higher volume changes in the wet-dry process during the WDFT cycles than that in the freeze-thaw process during the WDFT cycles. Conversely, the samples with dry range III showed the freeze-thaw effect on the volume changes, which means that the volumes of samples with dry range III changed significantly in the freeze-thaw process during the WDFT cycles than that in the wet-dry process during the WDFT cycles. As previously mentioned, the volume changes

of samples with dry range III presented a downward trend, indicating that the freeze-thaw effect weakened gradually with the increasing WDFT cycles, which is consistent with the volume change characteristics of expansive soils under freeze-thaw cycles reported in the literature [41]. The samples with dry range II, which is between dry range I and dry range III, presented a different volume change variation under WDFT cycles. At the beginning of WDFT cycles, the samples with dry range II had larger variation ranges of volumetric strain in the wet-dry process during the WDFT cycles, indicating a more significant wet-dry effect on the volume changes in the cyclic WDFT processes. With the

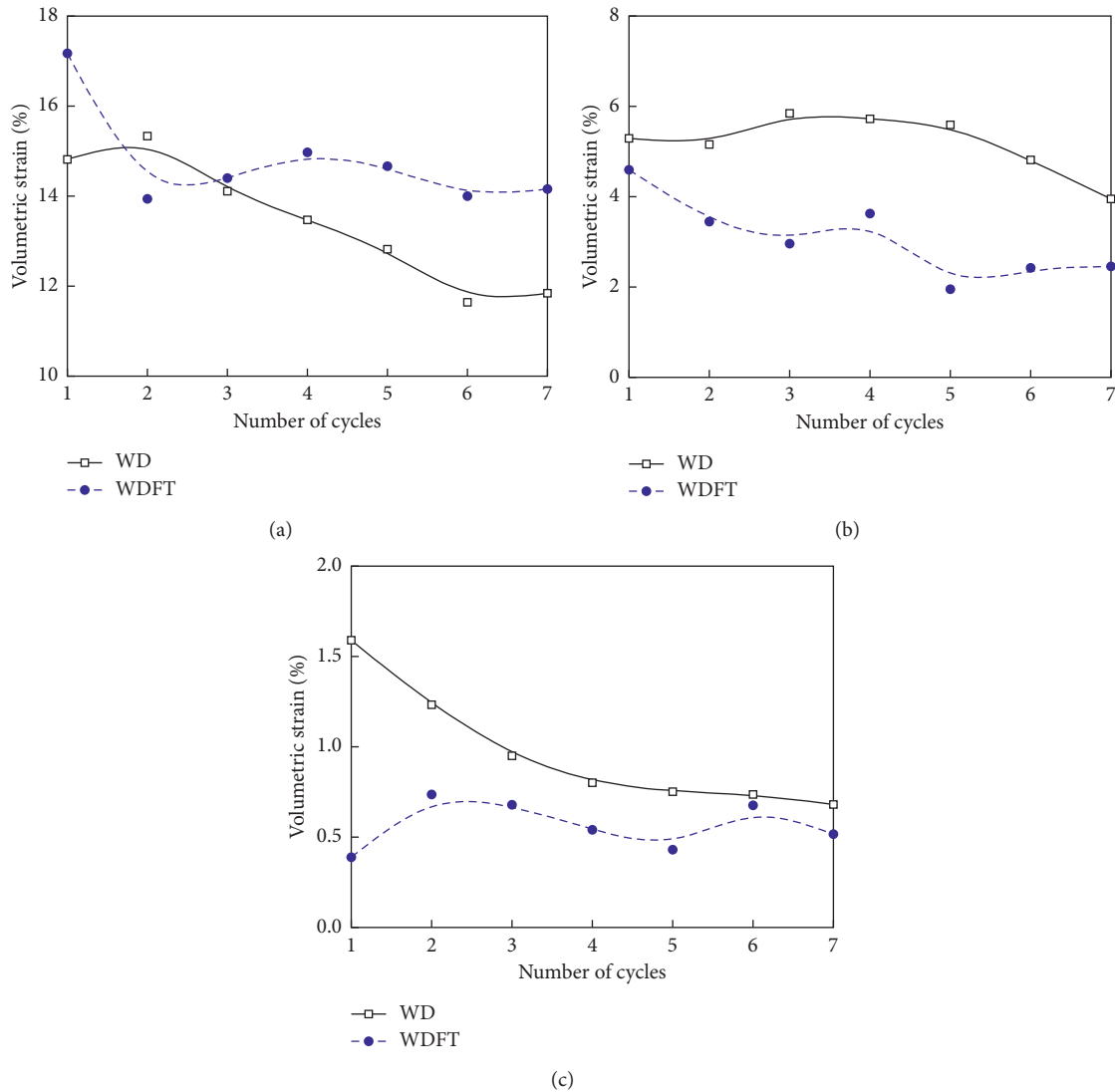


FIGURE 11: Comparison curves of volume changes under WD and WDFT cycles. (a) Dry range I. (b) Dry range II. (c) Dry range III.

increase of WDFT cycles, the volumes of samples with dry range II changed more significantly in the freeze-thaw process during the WDFT cycles, indicating that the freeze-thaw effect gradually dominated the volume changes of samples during the cyclic WDFT processes. This phenomenon indicated that there may be a coupled effect between the wet-dry process and freeze-thaw process when the samples with a medium dry range were exposed to WDFT cycles, which was never reported in the previous studies.

It was noted that the volumetric strain of samples with dry range I and dry range II showed a downward trend in the freeze process and a rising trend in the thaw process. The main reason for this phenomenon is as follows: the saturation of samples with dry range I and dry range II is relatively low after the dry process. During the freezing process, a large number of air in the pores and the water in the sample turned into ice, leading to an increase of sample volumes. In the meantime, the expansive mudstone particles lost water and shrink, and the shrinkage would be large due to the

sufficient shrinkage space, which offset the frost heave. Consequently, the macrovolume of samples decreased in the freeze process. In the thaw process, the ice in the pores thawed into water. Concurrently, the expansive mudstone particles expanded with water, and the expansion was greater than the shrinkage. Therefore, the macrovolume of samples would increase in the thaw process [9, 10].

For the purpose of quantitatively analyzing the difference of volume changes with WD cycles and WDFT cycles, the relationships between the difference of the maximum volumetric strain and the minimum volumetric strain during each cycle and the number of cycles are plotted, as shown in Figure 11. It is found that with the increasing cycles, the volume changes of samples with dry range I under WD cycles were more significant than that under WDFT cycles, while the samples with dry range II and dry range III showed the opposite phenomenon. It indicated that the freeze-thaw process in the WDFT cycles resulted in a decrease of volume change ranges when the samples had a

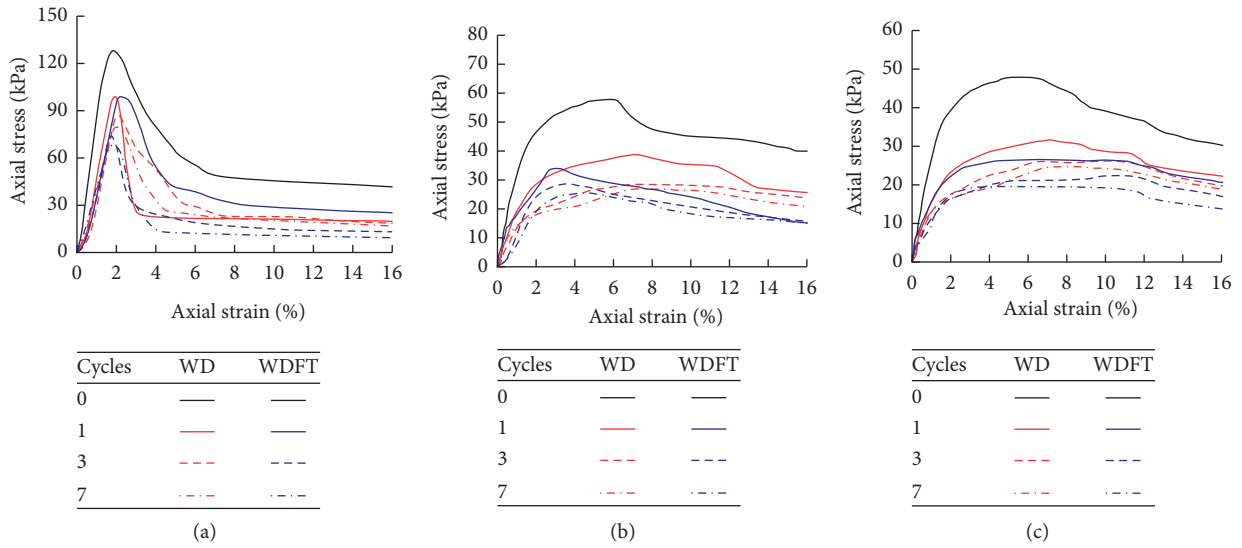


FIGURE 12: Curves of stress-strain relationships. (a) Dry range I. (b) Dry range II. (c) Dry range III.

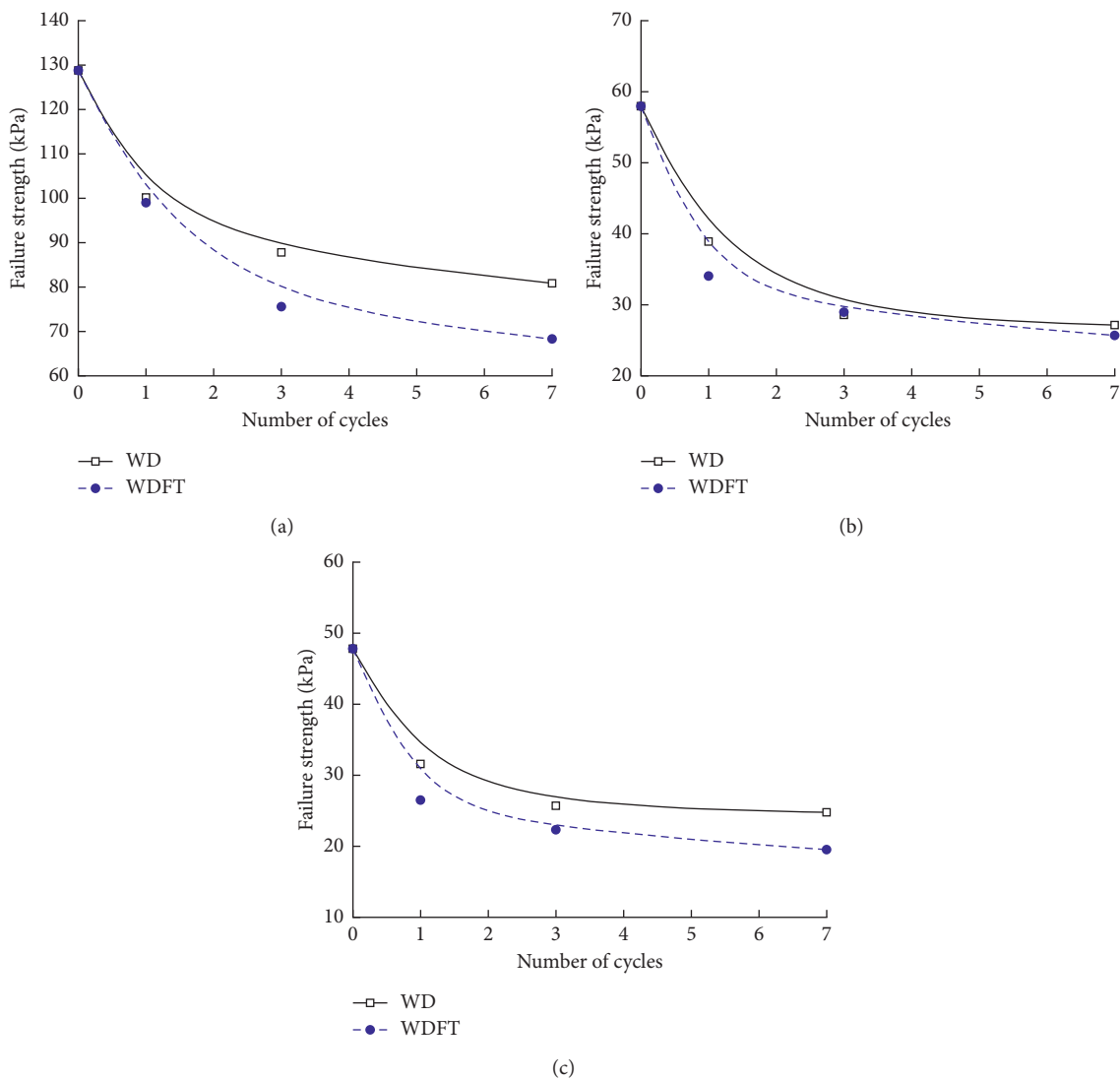


FIGURE 13: Curves of failure strength variation with cycles. (a) Dry range I. (b) Dry range II. (c) Dry range III.

relatively smaller dry range and a slight increase of volume change ranges when the samples had a relatively larger dry range. This is also consistent with the volume change characteristics of shallow foundation soils below the canal with a large dry range in Xinjiang [29, 30].

4.2. Mechanical Behaviors

4.2.1. Stress-Strain Behaviors. Unconfined strength tests were conducted on samples exposed to WD cycles and WDFT cycles. To compare the characteristics of stress-strain behaviors, the stress-strain relationships of samples subjected to 0, 1, 3, and 7 cycles of WD and WDFT are plotted as shown in Figure 12. It is found that under WD and WDFT cycles, the stress-strain relationships of samples with different dry ranges all presented strain softening. According to the previous studies [42], the stress-strain relationships of soils had six types. Consequently, the stress-strain relationships of samples in this study could be divided into strong softening type, general softening type, and weak softening type, respectively, which depended on the dry ranges of samples. Specifically, the stress-strain relationships of samples with dry range II and dry range III were general softening type and weak softening type, respectively, while the stress-strain relationships of samples with dry range I was strong softening type, indicating that the samples maintained high strength within a small strain. Additionally, compared with the stress-strain relationships under WD cycles, the stress-strain relationships of samples subjected to WDFT cycles entered the softening stage earlier, which indicated that the freeze-thaw process in the WDFT cycles promoted the softening of the stress-strain relationships.

4.2.2. Failure Strength. As previously described, all the stress-strain relationships of samples showed strain softening. Consequently, the failure strength of samples was estimated according to the peak values shown in Figure 12. Figure 13 shows the curves of failure strength variation with cycles. It is found that under the WD and WDFT cycles, the failure strength of samples with the same dry range has a similar variation trend, that is, decreased at the beginning of cycles and then tended to be stable. Among them, the first cycle resulted in a significant decrease of soil strength, which was consistent with that reported in the literature. After seven WD cycles and WDFT cycles, the failure strength of samples with dry range I decreased by 37.2% and 46.9%, while the failure strength of samples with dry range II and dry range III decreased by 53.2%, 55.7% and 48.2%, 59.1%, respectively. In addition, compared with the failure strength of samples subjected to WD cycles, the failure strength attenuation of samples subjected to WDFT cycles was more significant. It indicated that the freeze-thaw process in the WDFT cycles aggravated the failure strength attenuation of samples.

According to the previous studies [23–25], it is found that the average dry range of shallow foundation soil below the canals in the field was close to dry range II. For the purpose of accurately predicting the variation trend of the

failure strength of foundation soils below the canal with WDFT cycles, the failure strength of samples (dry range II) with WDFT cycles shown in Figure 13(b) was fitted with a COD (R^2) of 0.99. The formula was as follows:

$$f_{\text{WDFT}} = 27.1 + 30.9 \cdot e^{-1.44 \cdot N_{\text{WDFT}}}. \quad (2)$$

5. Conclusions

On the basis of the above studies, the following conclusions are drawn:

- (1) During the WD cycles, the volume changes of expansive mudstone with a higher dry range would be more significant. The freeze-thaw process in the WDFT cycles resulted in a decrease of volume change ranges when the expansive mudstone had a relatively smaller dry range and a slightly increase of volume change ranges when the expansive mudstone had a relatively larger dry range.
- (2) Under the cycles of WD or WDFT, the stress-strain relationships of samples with different dry ranges all presented strain softening. In the meantime, the freeze-thaw process in the WDFT cycles promoted the softening of the stress-strain relationships.
- (3) During the WD/WDFT cycles, the first cycle resulted in a significant decrease of failure strength. After seven WD/WDFT cycles, the failure strength of expansive mudstones with different dry ranges decreased by 37.2%~59.1%. Additionally, the freeze-thaw process in the WDFT cycles aggravated the failure strength attenuation of expansive mudstones.
- (4) Further study is encouraged on the investigation of phase change materials used to treat expansive mudstone under freeze-thaw/wet-dry-freeze-thaw cycles

Data Availability

The data used to support the findings of this study are included within the article.

Conflicts of Interest

The authors declare that they have no conflicts of interest.

Acknowledgments

This work was funded by the National Natural Science Foundation of China (51879166, 51778287, and 51708291) and the Open Research Fund Program of State Key Laboratory of Permafrost Engineering of China (SKLFSE201909).

References

- [1] J. Q. Chen and J. Xia, "Facing the challenge: barriers to sustainable water resources development in China," *Hydrological Sciences Journal*, vol. 44, no. 4, pp. 507–516, 1999.
- [2] J. Xu, Q. Z. Wang, J. L. Ding, Y. F. Li, S. H. Wang, and Y. G. Yang, "Frost heave of irrigation canals in seasonal frozen

- regions," *Advances in Civil Engineering*, vol. 2019, Article ID 2367635, 14 pages, 2019.
- [3] S. Liu, Y. Lu, L. Weng, and F. Bai, "Field study of treatment for expansive soil/rock channel slope with soilbags," *Geotextiles and Geomembranes*, vol. 43, no. 4, pp. 283–292, 2015.
 - [4] Y. Lu, S. Liu, L. Weng, L. Wang, Z. Li, and L. Xu, "Fractal analysis of cracking in a clayey soil under freeze-thaw cycles," *Engineering Geology*, vol. 208, pp. 93–99, 2016.
 - [5] P. F. He, Y. H. Mu, Z. H. Yang, W. Ma, J. H. Dong, and Y. T. Huang, "Freeze-thaw cycling impact on the shear behavior of frozen soil-concrete interface," *Cold Regions Science and Technology*, vol. 173, Article ID 103024, 2020.
 - [6] L. Tang, S. Cong, L. Geng, X. Ling, and F. Gan, "The effect of freeze-thaw cycling on the mechanical properties of expansive soils," *Cold Regions Science and Technology*, vol. 145, pp. 197–207, 2018.
 - [7] L. Tang, S. Cong, X. Ling, W. Xing, and Z. Nie, "A unified formulation of stress-strain relations considering micro-damage for expansive soils exposed to freeze-thaw cycles," *Cold Regions Science and Technology*, vol. 153, pp. 164–171, 2018.
 - [8] L. Miao, S. Liu, and Y. Lai, "Research of soil-water characteristics and shear strength features of Nanyang expansive soil," *Engineering Geology*, vol. 65, no. 4, pp. 261–267, 2002.
 - [9] Y. Lu, S. Liu, E. Alonso, L. Wang, L. Xu, and Z. Li, "Volume changes and mechanical degradation of a compacted expansive soil under freeze-thaw cycles," *Cold Regions Science and Technology*, vol. 157, pp. 206–214, 2019.
 - [10] Y. Lu, S. H. Liu, Y. G. Zhang, Z. Li, and L. Xu, "Freeze-thaw performance of a cement-treated expansive soil," *Cold Regions Science and Technology*, vol. 170, Article ID 102926, 2020.
 - [11] J. Q. Wang, Q. Wang, S. Lin, Y. Han, and N. Wang, "Relationship between the shear strength and microscopic pore parameters of saline soil with different freeze-thaw cycles and salinities," *Symmetry*, vol. 12, no. 10, p. 1709, 2020.
 - [12] Y. Liu, Q. Wang, S. Liu et al., "Experimental investigation of the geotechnical properties and microstructure of lime-stabilized saline soils under freeze-thaw cycling," *Cold Regions Science and Technology*, vol. 161, pp. 32–42, 2019.
 - [13] S. Li, Y. Lai, W. Pei, S. Zhang, and H. Zhong, "Moisture-temperature changes and freeze-thaw hazards on a canal in seasonally frozen regions," *Natural Hazards*, vol. 72, no. 2, pp. 287–308, 2014.
 - [14] Z. Li, J. Chen, and M. Sugimoto, "Pulsed NMR measurements of unfrozen water content in partially frozen soil," *Journal of Cold Regions Engineering*, vol. 34, no. 3, Article ID 04020013, 2020.
 - [15] S. Li, M. Zhang, Y. Tian, W. Pei, and H. Zhong, "Experimental and numerical investigations on frost damage mechanism of a canal in cold regions," *Cold Regions Science and Technology*, vol. 116, pp. 1–11, 2015.
 - [16] B. Kong, F. Xia, B. Yu, T. Xia, and Z. Ding, "Pore size changes in marine soft soil under various freezing conditions," *Journal of Marine Science and Engineering*, vol. 8, no. 3, p. 170, 2020.
 - [17] S. Suzuki, "Dependence of unfrozen water content in unsaturated frozen clay soil on initial soil moisture content," *Soil Science and Plant Nutrition*, vol. 50, no. 4, pp. 603–606, 2004.
 - [18] S. Wang, P. Yang, and Z. Yang, "Characterization of freeze-thaw effects within clay by 3D X-ray Computed Tomography," *Cold Regions Science and Technology*, vol. 148, pp. 13–21, 2018.
 - [19] J. K. Torrance, T. Elliot, R. Martin, and R. J. Heck, "X-ray computed tomography of frozen soil," *Cold Regions Science and Technology*, vol. 53, no. 1, pp. 75–82, 2008.
 - [20] J. Liu, P. Yang, L. Li, and T. Zhang, "Characterizing the pore size distribution of a chloride silt soil during freeze-thaw processes via nuclear magnetic resonance relaxometry," *Soil Science Society of America Journal*, vol. 84, no. 5, pp. 1577–1591, 2020.
 - [21] K. Watanabe and T. Wake, "Measurement of unfrozen water content and relative permittivity of frozen unsaturated soil using NMR and TDR," *Cold Regions Science and Technology*, vol. 59, no. 1, pp. 34–41, 2009.
 - [22] A. Liernur, A. Schomburg, P. Turberg, C. Guenat, R.-C. Le Bayon, and P. Brunner, "Coupling X-ray computed tomography and freeze-coring for the analysis of fine-grained low-cohesive soils," *Geoderma*, vol. 308, pp. 171–186, 2017.
 - [23] R. Zhu, Y. H. Huang, C. Zhang, W. L. Guo, and H. Chen, "Laboratory and centrifugal model tests on failure mechanism of canal slopes under cyclic action of wetting-drying," *European Journal of Environmental and Civil Engineering*, Article ID 1773321, 2020.
 - [24] R. Zhu, Z.-Y. Cai, Y.-H. Huang, C. Zhang, W.-L. Guo, and X. Zhu, "Centrifugal and field studies on water infiltration characteristics below canals under wetting-drying-freezing-thawing cycles," *Journal of Central South University*, 2021.
 - [25] S. Y. Li, Y. M. Lai, M. Y. Zhang, W. S. Pei, C. Zhang, and F. Yu, "Centrifuge and numerical modeling of the frost heave mechanism of a cold-region canal," *Acta Geotechnica*, vol. 14, no. 12, pp. 1113–1128, 2018.
 - [26] C. W. W. Ng, L. T. Zhan, C. G. Bao, D. G. Fredlund, and B. W. Gong, "Performance of an unsaturated expansive soil slope subjected to artificial rainfall infiltration," *Géotechnique*, vol. 53, no. 2, pp. 143–157, 2003.
 - [27] L. Miao, S. L. Houston, Y. Cui, and J. Yuan, "Relationship between soil structure and mechanical behavior for an expansive unsaturated clay," *Canadian Geotechnical Journal*, vol. 44, no. 2, pp. 126–137, 2007.
 - [28] C. Zhang, Z. Y. Cai, Y. H. Huang, and H. Chen, "Laboratory and centrifugal model tests on influence of swelling rock with drying-wetting cycles on stability of canal slope," *Advances in Civil Engineering*, vol. 2018, Article ID 4785960, 10 pages, 2018.
 - [29] Z. Y. Cai, R. Zhu, Y. H. Huang, C. Zhang, W. L. Guo, and H. Chen, "Influences of freeze-thaw process on the deterioration mode of expansive soil canal slope," *Journal of Hydraulic Engineering*, vol. 51, no. 8, pp. 915–923, 2020, in Chinese.
 - [30] Z. Y. Cai, R. Zhu, Y. H. Huang, C. Zhang, and W. L. Guo, "Centrifugal model tests on deterioration process of canal under cyclic action of coupling wetting-drying and freeze-thaw," *Chinese Journal of Geotechnical Engineering*, vol. 42, no. 10, pp. 1773–1782, 2020, in Chinese.
 - [31] Z. Zeng, L. Kong, M. Wang, and H. M. Sayem, "Assessment of engineering behaviour of an intensely weathered swelling mudstone under full range of seasonal variation and the relationships among measured parameters," *Canadian Geotechnical Journal*, vol. 55, no. 12, pp. 1837–1849, 2018.
 - [32] ASTM, *Standard Test Methods for Liquid Limit, Plastic Limit, and Plasticity Index of Soils (D4318)*, ASTM, West Conshohocken, PA, USA, 2010.
 - [33] ASTM, *Standard Test Methods for Laboratory Compaction Characteristics of Soil Using Standard Effort (D698)*, ASTM, West Conshohocken, PA, USA, 2012.
 - [34] ASTM, *Standard Test Method for Expansion Index of Soils (D4829)*, ASTM, West Conshohocken, PA, USA, 2019.

- [35] ASTM, *Standard Test Methods for Particle-Size Distribution (Gradation) of Soils Using Sieve Analysis (D6913)*, ASTM, West Conshohocken, PA, USA, 2009.
- [36] ASTM, *Standard Test Method for Particle-Size Analysis of Soils (D422)*, ASTM, West Conshohocken, PA, USA, 2007.
- [37] L. Xu, S. H. Liu, Y. Lu, Y. J. Song, and Q. Yang, "Physico-mechanical properties of expansive soil under freeze-thaw cycles," *Rock and Soil Mechanics*, vol. 37, no. 2, pp. 167–174, 2016.
- [38] A. R. Estabragh, B. Parsaei, and A. A. Javadi, "Laboratory investigation of the effect of cyclic wetting and drying on the behaviour of an expansive soil," *Soils and Foundations*, vol. 55, no. 2, pp. 304–314, 2015.
- [39] J. Lu, M. Zhang, X. Zhang, W. Pei, and J. Bi, "Experimental study on the freezing-thawing deformation of a silty clay," *Cold Regions Science and Technology*, vol. 151, no. 5, pp. 19–27, 2018.
- [40] K. Mu, L. W. Kong, X. W. Zhang, and S. Yin, "Experimental investigation on engineering behaviors of red clay under effect of wetting-drying cycles," *Rock and Soil Mechanics*, vol. 37, no. 8, pp. 2247–2253, 2016, in Chinese.
- [41] J. Qi, W. Ma, and C. Song, "Influence of freeze-thaw on engineering properties of a silty soil," *Cold Regions Science and Technology*, vol. 53, no. 3, pp. 397–404, 2008.
- [42] X. Y. Wu, Q. G. Liang, F. J. Niu, and C. Q. Li, "Study on hardened and softened classification in shear test," *Chinese Journal of Underground Space and Engineering*, vol. 13, no. 6, pp. 1457–1466, 2017, in Chinese.

Research Article

Experimental Study on Physical-Mechanical Properties of Expansive Soil Improved by Multiple Admixtures

Binhui Ma ^{1,2}, **Kai Cai**¹, **Xing Zeng**¹, **Zhuo Li**¹, **Zhiyong Hu**¹, **Qiunan Chen**^{1,2}, **Chengbin He**¹, **Bingchu Chen**¹, and **Xiaocheng Huang**^{1,2}

¹School of Civil Engineering, Hunan University of Science and Technology, Xiangtan 411201, China

²Hunan Provincial Key Laboratory of Geotechnical Engineering for Stability Control and Health Monitoring, Hunan University of Science and Technology, Xiangtan 411201, China

Correspondence should be addressed to Binhui Ma; mbh@hnust.edu.cn

Received 20 February 2021; Accepted 7 May 2021; Published 20 May 2021

Academic Editor: Rihong Cao

Copyright © 2021 Binhui Ma et al. This is an open access article distributed under the Creative Commons Attribution License, which permits unrestricted use, distribution, and reproduction in any medium, provided the original work is properly cited.

The treatment of expansive soil is always a difficult problem in engineering. Using coal gangue, fly ash, and other solid waste to treat expansive soil has gradually become a new way of energy saving and environmental protection. Most of the existing studies focus on using one or two kinds of admixtures to improve expansive soil, but there are few studies on improving expansive soil with multiple admixtures. In this paper, the expansion and shrinkage deformation and strength characteristics of expansive soil modified by coal gangue, fly ash, and lime are studied experimentally. Nine groups of different mixing schemes were designed through orthogonal tests, and the physical and mechanical properties of the improved expansive soil under different mixing ratios were tested. The sensitivity analysis of the test results was carried out to study the effect of each admixture on the improved expansive soil under different mixing ratios, and the optimal mix ratio under different conditions was obtained. The optimal mix ratio is 8% for coal gangue, 11% for fly ash, and 6% for lime. Further scanning electron microscopy (SEM) tests were carried out to analyze the microstructure of the improved expansive soil and explore the improvement mechanism of the multiadmixture. The results show that the optimal moisture content and the maximum dry density of the expansive soil with ash are decreased, and the properties of liquid plastic limit, free expansion rate, shear strength, and unconfined compressive strength of the expansive soil are improved obviously. Through the analysis of the comprehensive balance method, it is found that the content of lime has the greatest influence on the improvement effect of expansive soil, followed by that of coal gangue, and the least is that of fly ash. SEM structure analysis reveals that the particles of improved expansive soil are mainly aggregates, the soil structure is dense, particle agglomeration increases, and the overall structure is stronger. The research results can provide reference for the improvement of expansive soil with various admixtures and the resource utilization of coal gangue, fly ash, and other solid wastes.

1. Introduction

Coal gangue is the carbonaceous rock with high ash content and low calorific value associated with coal and is one of the largest industrial solid wastes in China [1]. In addition, it is easy to cause landslides, disintegration, and spontaneous combustion to produce toxic gases and other hazards, which seriously affect the agricultural ecological environment and people's healthy lives. Expansive soil, as a kind of diseased soil that affects the construction of farmland water conservancy facilities and other projects, has the characteristics

of water-absorbing expansion, water-loss shrinkage, water-bearing capacity reduction, and dry shrinkage crack [2–5]. Its properties are extremely unstable, which will lead to cracks, inclinations, and other hazards in road subgrade and construction. In terms of research on gangue and improved expansive soil, Liu et al. [6] studied the addition of gangue to cement, concrete, and other building materials and proposed that gangue can improve various properties of building materials, as well as the types, particle size, dosage, and grading of gangue. Wang and Wang [7] found that the physical and mechanical properties, corrosion resistance,

carbonation resistance, and reinforcement performance of gangue cement with less clinker, mainly coal gangue, were good through testing and analysis. Meng [8] established the relationship between the ratio of gangue and the parameters of shear strength and the relationship between the California Bearing Ratio (CBR) value and the compacting degree and the ratio of gangue through laboratory tests and analysis and calculation. Shen et al. [9] studied the composite improvement of strong expansive soil with lime, potassium chloride, polyvinyl alcohol, and polypropylene fiber and verified the effectiveness of the improved method by free expansion rate test and shear test. By analyzing gangue content and X-ray diffraction, Yang and Zhang [10] proved that the materials separated from coal gangue could be consolidated with expansive soil or undergo ion exchange reaction to improve the cohesion and shear strength of expansive soil. Zhang et al. [11, 12], respectively, studied the changes of various indexes of coal gangue powder and lime + coal gangue to improve expansive soil through laboratory tests of physical and mechanical properties and obtained that coal gangue powder and lime + coal gangue can effectively improve the physical properties of expansive soil and give the optimal mixing ratio of improved expansive soil. Wang [13] studied the expansive soil of the runway of Hefei Xinqiao Airport by combining laboratory experiment and field experiment. By adding lime to improve the expansive soil, good results are obtained, and the actual engineering requirements are satisfied. Qiu [14] studied the characteristics of lime improved expansive soil under dry wet cycle and carried out compaction test, free expansion rate test, crack development test, and consolidation fast shear test. According to the field construction and economy, it is suggested that the lime content should be 5%. Dai [15] used energy dispersive analysis of x-rays (EDAX) to analyze the composition of expansive soil and modified expansive soil with lime and concluded that the modification effect of lime modified expansive soil was better than that of fly ash modified expansive soil. Abbaspour et al. [16] modified the expansive soil with the Waste Tire Textile Fibers (WTTFs). The mechanical properties of sodium bentonite containing WTTF were evaluated by a set of standard compactions, direct shear, unconfined compressive strength (UCS), CBR, and expansive consolidation tests. Indiramma et al. [17] conducted an experimental investigation to study the individual and combined effects of admixtures viz, lime, and fly ash on the geotechnical characteristics of expansive soil. It is concluded that the combination of lime or fly ash and lime can be used as an effective stabilizing additive for expansive soil. Gireesh Kumar and Harika [18] used fly ash and other wastes as admixtures, mixed with expansive soil as stabilizer of expansive soil, for testing (to form a uniform and stable road base). The results show that more than 10% fly ash and black cotton soil are recommended to be used as the mixture, which can be used in the construction of paving stones and other foundation projects.

The above studies mostly improve the expansive soil subgrade from single admixture or double admixture, while the improvement of expansive soil with multiple admixtures remains to be further explored. In view of the existence and

harm of large amount of gangue waste, and the adverse effect of expansion and shrinkage of expansive soil on engineering construction, this paper analyzes and studies the feasibility and effect of the improvement of expansive soil in southern Hunan province with the addition of gangue, fly ash, and lime. With coal gangue, fly ash, and lime as test factors, the dosage of level, using the orthogonal design, 9 sets of test plan formulation, indoor routine test, and SEM test, and through the data analysis of expansive soil under different mixing ratio of various factors and the influence law of physical and mechanical properties and microstructure, determine its improvement effect, and the new improved expansive soil formula is concluded, which will provide a scientific basis for improved expansive soil engineering disease problem and engineering reference.

2. Experiments

2.1. Raw Material. Raw materials include expansive soil, coal gangue, fly ash, and lime. The expansive soil, coal gangue, and lime used in this test were all taken from southern Hunan, and the coal ash was taken from a coal-fired power plant in Hunan. The microstructure of each material obtained by the SEM test is shown in Figure 1.

The expanded soil was uniformly distributed with some little white calcareous nodules. The microstructure of the expanded soil was mainly flat aggregate and flake particles, and a large number of grains were deposited to form a grain depositing structure. The pores of the soil were of different shapes and nondirectional distribution and had the development trend of pores, providing a channel for water absorption and water loss for expansion and contraction deformation, the appearance of coal gangue is grayish black, the surface structure is hard, and it contains a large number of detritus tiny particles and irregular block structure with obtuse angle, and the surface is uneven. The fly ash is grey powdery, and its microstructure is mainly spherical particles with a small amount of slag particles and debris. Lime is a fine white powder solid with small crystal grain size and large pore size.

2.1.1. Expansive Soil. The natural moisture content of the soil sample was 15.2%. According to the test rules [19], the physical and mechanical indexes of expansive soil were tested, and its main components were measured by infrared spectroscopy, as shown in Table 1.

2.1.2. Coal Gangue. According to the requirements of the specification [20], the performance of coal gangue is studied, and its technical indexes and chemical composition are shown in Table 2. In order to fully stimulate the activity of coal gangue, the coal gangue was ground into powder and mixed into expansive soil according to different proportion.

2.1.3. Fly Ash. The physical performance indexes of fly ash are carried out according to the specification [21], and the test results are shown in Table 3. Oxides in fly ash are the

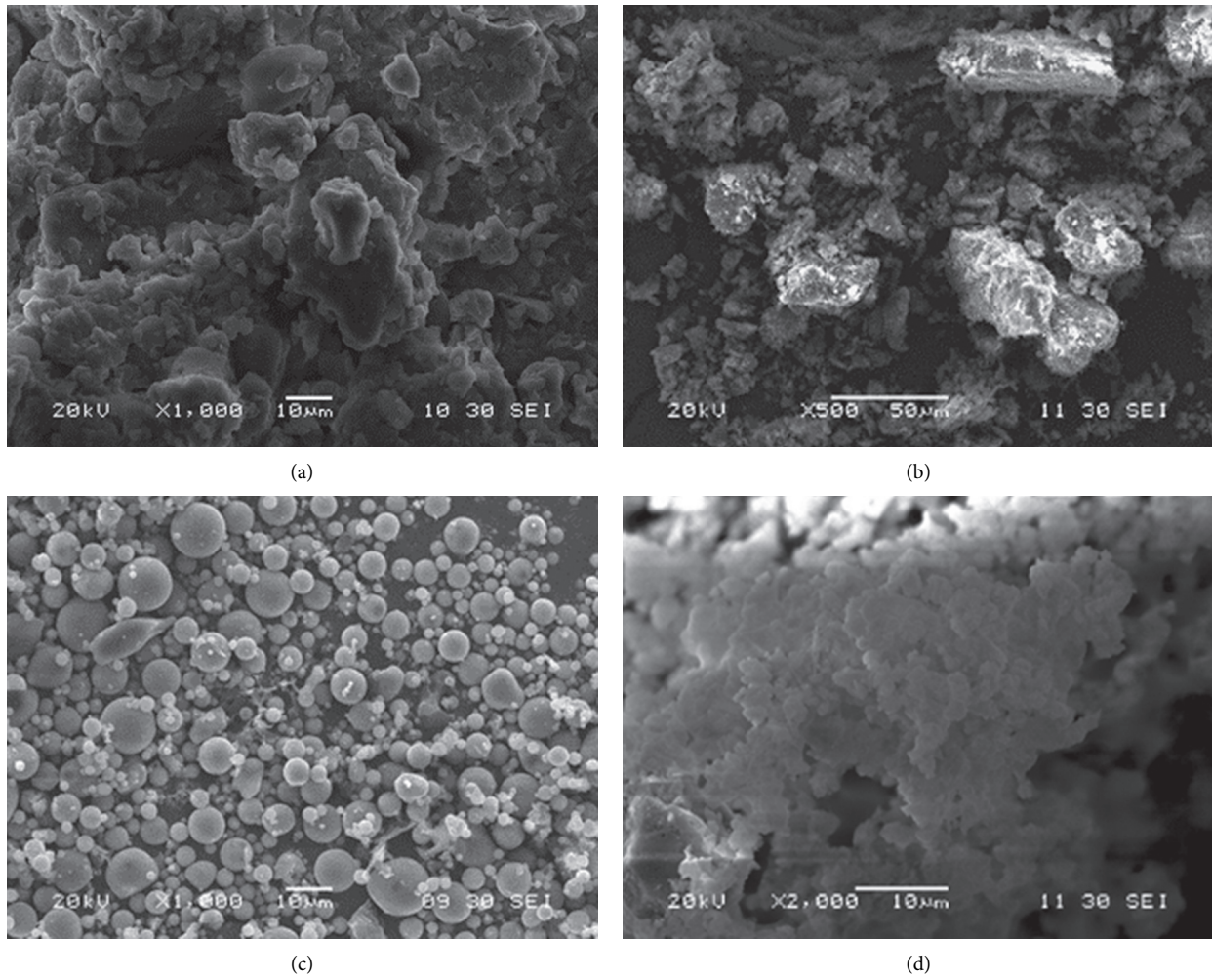


FIGURE 1: SEM appearance of materials. (a) Expansive soil. (b) Coal gangue. (c) Fly ash. (d) Lime.

TABLE 1: Physical index and chemical composition of expansive soil.

Physical index	Liquid limit (%)	Plastic limit (%)	Plasticity index (%)	Maximum dry density ($\text{g}\cdot\text{cm}^{-3}$)	Free swelling rate (%)	Optimum moisture content (%)
	51.50	23.56	27.94	1.80	53.1	19.0
Chemical composition	SiO_2 (%)	Al_2O_3 (%)	Fe_2O_3 (%)	CaO (%)	MgO (%)	K_2O (%)
	45.5	26.4	11.1	0.25	1.6	2.4

TABLE 2: Physical index and chemical composition of coal gangue.

Physical index	Rate of disintegration (%)	Ignition loss rate (%)	Free swelling rate (%)	Water absorption (%)	Crushing value (%)	Strong values (%)
	0.5	15.2	13.7	0.5	21.1	12
Chemical composition	SiO_2 (%)	Al_2O_3 (%)	Fe_2O_3 (%)	CaO (%)	MgO (%)	C (%)
	63.2	23.9	3.7	1.9	1.4	3.1

TABLE 3: Physical performance index of fly ash.

Physical index	Specific surface area ($\text{m}^2\cdot\text{g}^{-1}$)	Density ($\text{kg}\cdot\text{m}^{-3}$)	Packing density ($\text{kg}\cdot\text{m}^{-3}$)	Loss on ignition (%)	Fineness (45 μm triage) (%)	Water absorption (%)	Standard consistency of raw ash (%)
	0.43	1868	764	7.9	21	101	52.3
Chemical composition	SiO_2 (%)	Al_2O_3 (%)	Fe_2O_3 (%)	CaO (%)	K_2O (%)	Na_2O (%)	Other (%)
	40.02	23.41	7.92	5.16	1.41	0.88	21.2

main source and element of its activity, accounting for more than 70% and belonging to class F fly ash. CaO content does not exceed 10%, which also belongs to low calcium fly ash.

2.1.4. Lime. The hydrated lime [22] used in this test is slightly soluble in water and can react with CO_2 in the air to form calcium carbonate. Its microstructural crystallization has smaller grain size and larger pores. Its physical performance indexes are shown in Table 4.

2.2. Orthogonal Experiment. Orthogonal experiment is an efficient and economical design method to deal with multifactor experimental problems [23]. Based on the experimental data and considering 3 factors and 3 levels, $L_9(3^4)$ orthogonal table was selected to determine the mixture ratio design scheme of the three admixtures of improved expansive soil, as shown in Table 5, where Group 0 means the test of expansive soil without any admixtures. The Null column of the header of Table 5 is the error influence term.

2.3. Test Methods

2.3.1. Compaction Test. According to T0131-2007 method [19], dry soil method was used to prepare samples, and 5 mm sieve was used to make the soil properties consistent. A small amount of sand and gravel was removed from the soil. Five soil samples with different moisture content were prepared for each group, and water was added at 2% increment.

2.3.2. Liquid and Plastic Limits Test. The T0118-2007 method [19] was adopted to pass the different lime soil samples after compaction (one week after ash mixing, let them fully react) through 0.5 mm sieve. The experiment was carried out with a 100 g cone and a 30° cone Angle digital display combined soil liquid plastic limit measuring instrument. The coning depth of point A (liquid limit) was controlled to be 20 ± 0.2 mm, the coning depth of point B (between liquid plastic limit) was controlled to be 9–11 mm, and the coning depth of point C (plastic limit) was controlled to be about 3 mm.

2.3.3. Free Expansive Test. According to the T0124-1993 method [19], after one week of compaction, different lime soil samples were smashed with a wood hammer, screened over 0.5 mm, dried, and cooled to room temperature, and then a free expansion rate test was conducted. Readings (accurate to 0.1 ml) will be taken after the soil sample is settled in the measuring cylinder, and the volume change of the soil sample will be recorded every 3 h until the volume change of the soil sample is less than 0.2 ml, which means that the expansion is stable, and the measurement will stop. The difference between the two parallel measurements shall be less than 5%; otherwise, the test shall be repeated.

2.3.4. Direct Shear Test. According to the T0141-1993 method [19], the soil samples were sifted by 2 mm, and the soil samples of each group were prepared according to the

optimal moisture content. Plastic bags were used for one week to make the mixture fully react, and then compaction was conducted. Samples were taken with Vaseline coated ring cutter, and 5 specimens (one for later use) were taken from each group to conduct a direct shear test to determine the shear strength index of each mixture.

2.3.5. Unconfined Compressive Strength Test. According to the T0148-1993 method [19], the test soil sample was the same as the soil sample used in the direct shear test. After compaction of samples with different mixing ratios by compaction instrument, the specimens were made into cylinders with a diameter of 15.2 cm and a height of 12 cm, which were sealed with plastic bags and put into a curing box with constant temperature and humidity (22°C, 70% relative humidity) for seven days.

2.3.6. SEM Test. SEM is used to observe the morphology of the sample according to the secondary electronic signal imaging technology, and various effects are generated through the interaction between electron beam and the sample to obtain the microstructure and arrangement rule of the soil sample [24]. In the preparation of the test sample, the lime soil, which has been cured for a week after compaction according to the optimal moisture content, is mashed with a wooden hammer, dried naturally, passed a 0.5 mm sieve, and packed in a sealed bag. After the sample is made, the SEM test is used to observe the microstructure of the improved soil and analyze its improvement mechanism. In order to make the sample have good electrical conductivity, the sample holder was put into the steaming gold chamber, air was evacuated, and the conductive layer was steamed and plated for 5 minutes.

3. Results and Discussions

3.1. Basic Physical Performance Analysis

3.1.1. Maximum Dry Density and Optimal Moisture Content. From Table 6 and Figure 2, the best of the expansive soil moisture content was 19%, the best moisture content is in the range of 15.1%~18% with lime soil, expansive soil after the best moisture content is less than the element of adding in lime soil, due to the mixing lime soil through ion exchange, and the electric double layer thickness around the soil particles was reduced, so that more close contact between soil particles (which is called flocculation) results in the decrease of optimum moisture content of soil [25]. The maximum dry density of each ash admixture is lower than that of plain soil, mainly because the following [26]. First, the relative volume mass of the admixture is lower than that of plain expansive soil. Second, it has a certain cementing effect, and the new cementing substance reduces the compaction characteristic of the mixed lime soil, which leads to the decrease of dry density.

The optimum mean value and range of moisture content of each factor and level are calculated by formula and orthogonal design assistant. In order to more intuitively

TABLE 4: Physical properties of lime.

Density (kg·m ⁻³)	45 μm triage (%)	The moisture content (%)	Specific surface area (m ² ·kg ⁻¹)	Ignition loss rate (%)	Ca(OH) ₂ content (%)
1810	29.7	0.15	397	27.1	93.6

TABLE 5: L₉(3⁴) orthogonal test scheme.

Group number	Factors			Null column
	A (coal gangue) %	B (fly ash) %	C (lime) %	
0	0	0	0	-
1	6	7	2	1
2	6	9	4	2
3	6	11	6	3
4	8	7	4	3
5	8	9	6	1
6	8	11	2	2
7	10	7	6	2
8	10	9	2	3
9	10	11	4	1

TABLE 6: Optimum moisture content and maximum dry density.

Test number	0	1	2	3	4	5	6	7	8	9
Maximum dry density (%)	19.0	17.9	16.7	16.2	16.8	15.1	15.7	16.8	17.3	15.2
Maximum dry density (g/cm ³)	1.80	1.79	1.77	1.73	1.77	1.74	1.75	1.72	1.74	1.75

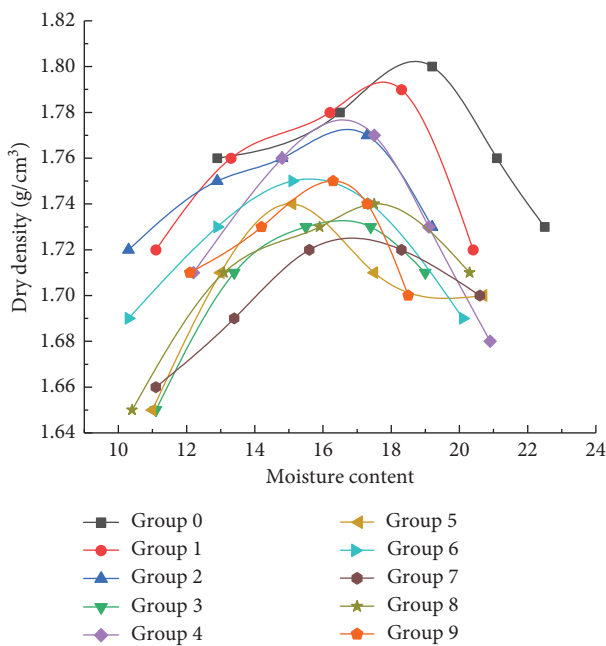


FIGURE 2: Curve of relationship between moisture content and dry density.

understand the influence of each admixture on the test results, the trend diagram of the relationship between each factor and the index results is drawn, as shown in Figure 3. The fly ash content is the main factor affecting the optimal moisture content of expansive soil, followed by the coal gangue powder content.

In order to analyze the importance of each factor to the test results, the Analysis of Variance (ANOVA) table was obtained according to the variance analysis of compaction test data by formula and orthogonal design assistant, as shown in Table 7.

It can be seen from the ANOVA table of optimal water content that the F ratio of the three factors is not greater than F_{0,1} critical value 9 (which can be obtained from tables in reference [27]), indicating that the effect of the three factors on the optimal water content of expansive soil is not significant. The F ratio of fly ash is 4.397, which is greater than F_{0,25} (2, 2) = 3, indicating that it has a certain influence on the test results, and the results are the same as the range analysis. The error estimate of the Null column shows that the error does not affect the test result, and the test result is reliable.

3.1.2. Analysis of Liquid Plastic Limit Index. It can be seen from Figure 4 that both the liquid limit and plastic index of the ash-doped soil are lower than those of the expansive soil, while the plastic limit of the expansive soil is higher than that of the ash-doped soil. The reason is that clay content and mineral hydrophilicity are the reflection of soil plasticity. The plasticity index of expansive soil decreases after ash addition, which indicates that clay content and hydrophilicity of soil particles decrease. As a result, the diffusion layer of soil particles becomes thinner, the binding water decreases, and the plasticity of soil decreases. Studies in reference [28] showed that the lower the plasticity index, the worse the expansibility of soil.

According to Figure 5, with the increase of the three factors, the plastic index of expansive soil decreases. Among

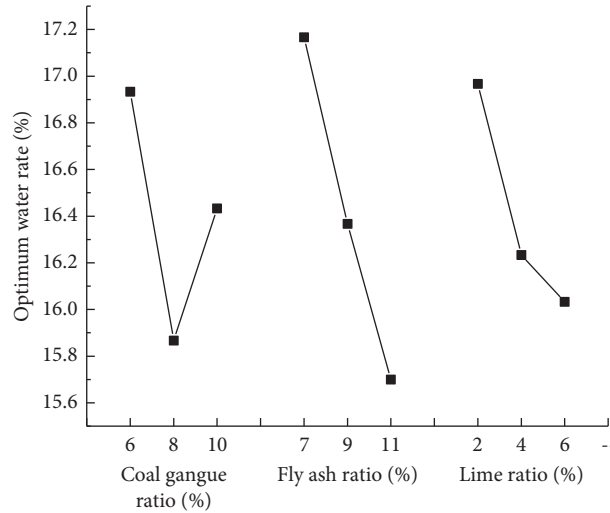


FIGURE 3: Trend chart of optimum moisture content.

TABLE 7: ANOVA table for optimum moisture content.

Factors	Square of deviance	Degree of freedom	Mean square	F ratio	F critical value	Significant
Coal gangue	1.709	2	0.8545	2.322	$F_{0.01} (2, 2) = 99$	
Fly ash	3.236	2	1.618	4.397	$F_{0.05} (2, 2) = 19$	O
Lime	1.449	2	0.7245	1.969	$F_{0.1} (2, 2) = 9$	
Error	0.736	2	0.368		$F_{0.25} (2, 2) = 3$	
Sum	7.13	8				

In ANOVA, if the mean square value of a factor is less than or equal to the error mean square, it will be treated as the error term, and F value will not be calculated, where “***” means very significant $P < 0.01$, “**” means significant $0.01 \leq P < 0.05$, “*” means relatively significant $0.05 \leq P < 0.1$, and “O” means that $0.1 \leq P < 0.25$ has a certain influence.

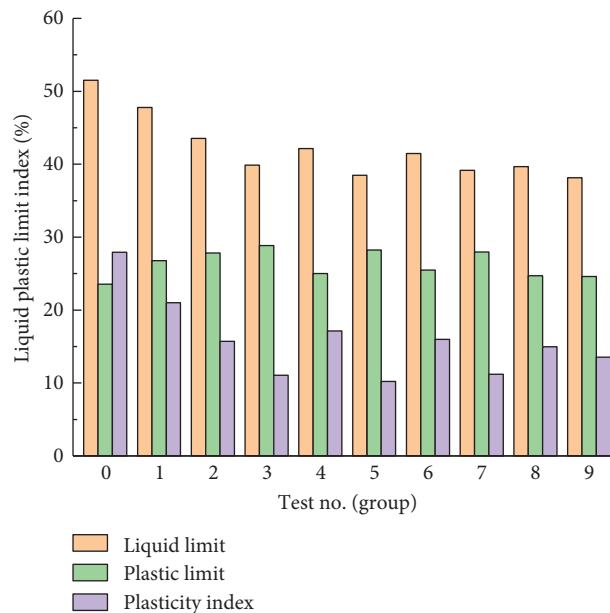


FIGURE 4: Results of liquid plastic limit indices.

them, there is an approximate linear relationship between the coal gangue content and the lime content, and the plastic index of expansive soil has the greatest influence on the plastic index of expansive soil. It can be judged that the

content of lime is the main factor affecting the plasticity index of expansive soil, followed by fly ash and coal gangue.

It can be seen from Table 8 that the F ratio of lime content and fly ash content both is greater than $F_{0.05} (2, 2) =$

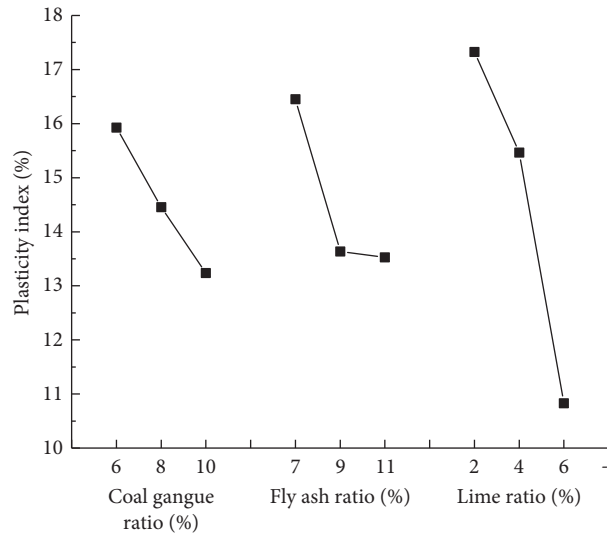


FIGURE 5: Trend chart of plasticity index.

TABLE 8: ANOVA table for plasticity index.

Factors	Square of deviance	Degree of freedom	Mean square	F ratio	F critical value	Significant
Coal gangue	10.887	2	5.4435	15.553	$F_{0.01}(2, 2) = 99$	*
Fly ash	16.511	2	8.2555	23.587	$F_{0.05}(2, 2) = 19$	**
Lime	67.221	2	33.6105	96.030	$F_{0.1}(2, 2) = 9$	**
Error	0.700	2	0.350		$F_{0.25}(2, 2) = 3$	
Sum	95.32	8				

In ANOVA, if the mean square value of a factor is less than or equal to the error mean square, it will be treated as the error term, and F value will not be calculated, where “***” means very significant $P < 0.01$, “**” means significant $0.01 \leq P < 0.05$, “*” means relatively significant $0.05 \leq P < 0.1$, and “O” means that $0.1 \leq P < 0.25$ has a certain influence.

9, indicating that these two factors have a significant influence on the plasticity index of expansive soil. Among them, the F ratio of lime is 96.030, which is very significant. The content factor of gangue powder is relatively significant, and its influence on the plasticity index of expansive soil is as follows: lime > fly ash > coal gangue.

3.1.3. Analysis of Free Expansion Rate. According to Figure 6, the free expansion rate decreases with the increase of fly ash and lime content. With the increase of the content of gangue powder, the free expansion first decreases and then increases. As a result of the excess content of gangue powder, some of the gangue powder has not yet fully reacted after the interaction and hardening effect, and it has certain expansibility, which leads to the increase of the free expansion and springback rate of soil particles. The main factor affecting the free expansion rate of expansive soil is the content of lime, and the coal gangue powder is the secondary factor. When the proportion of coal gangue powder A_2 is 8%, the proportion of fly ash B_3 is 11%, and the proportion of lime C_3 is 6%, and the improvement effect of free expansion rate of expansive soil is the best. The optimal scheme is $A_2B_3C_3$.

Table 9 shows that coal gangue powder, fly ash, and lime content have significant effects on the free expansion rate of expansive soil. The maximum F ratio of lime is 49.998 F, and the minimum F ratio of fly ash is 38.932. The primary and

secondary results of factors are the same as the results of range analysis. The error of the Null column is very small, which means that it does not affect the test result, and the test result is reliable.

3.2. Mechanical Property Analysis

3.2.1. Analysis of Shear Strength Index. It can be seen from the correlation coefficient R in Figure 7 and Table 10 that the linear correlation of data is highly significant. The shear strength index of the mixed soil has been greatly improved, among which the cohesion has been increased by 101.7 kPa to the maximum, the internal friction Angle has been increased by 18.1° to the maximum, and the shear strength has also been greatly improved, indicating that the improvement effect is good. Due to expansive soil mixed ash, Ion exchange, agglomeration, and gelation will occur [25], and silica and aluminum in expansive soil will react chemically with admixture to form some strong bonding materials like $CaSiO_3$ and $CaO \cdot Al_2O_3$ and so on, which makes structure of the expansive soil and interactions between soil particles enhanced, some fine grain become coarse particles, and interparticle friction increase. Thus, the interface slippage between particles can be prevented when shear action occurs, the internal friction angle increases, and the cohesion and strength increase.

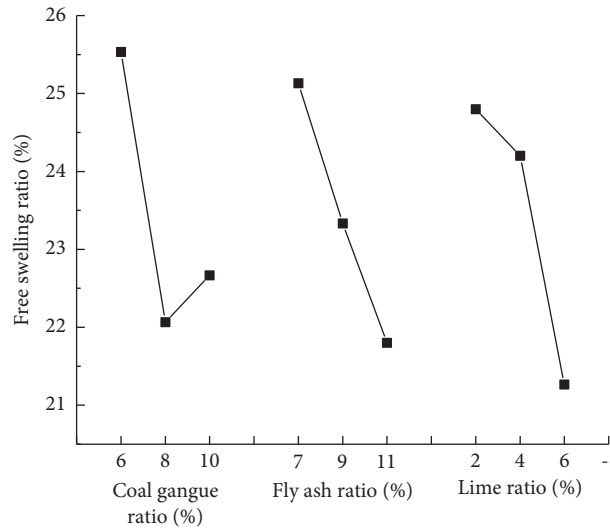


FIGURE 6: Trend diagram of free expansion rate.

TABLE 9: ANOVA table for free expansion rate.

Factors	Square of deviance	Degree of freedom	Mean square	F ratio	F critical value	Significant
Coal gangue	20.596	2	10.298	48.009	$F_{0.01}(2, 2) = 99$	**
Fly ash	16.702	2	8.351	38.932	$F_{0.05}(2, 2) = 19$	**
Lime	21.449	2	10.7245	49.998	$F_{0.1}(2, 2) = 9$	**
Error	0.429	2	0.2145		$F_{0.25}(2, 2) = 3$	
Sum	59.18	8				

In ANOVA, if the mean square value of a factor is less than or equal to the error mean square, it will be treated as the error term, and F value will not be calculated, where “***” means very significant $P < 0.01$, “**” means significant $0.01 \leq P < 0.05$, “*” means relatively significant $0.05 \leq P < 0.1$, and “O” means that $0.1 \leq P < 0.25$ has a certain influence.

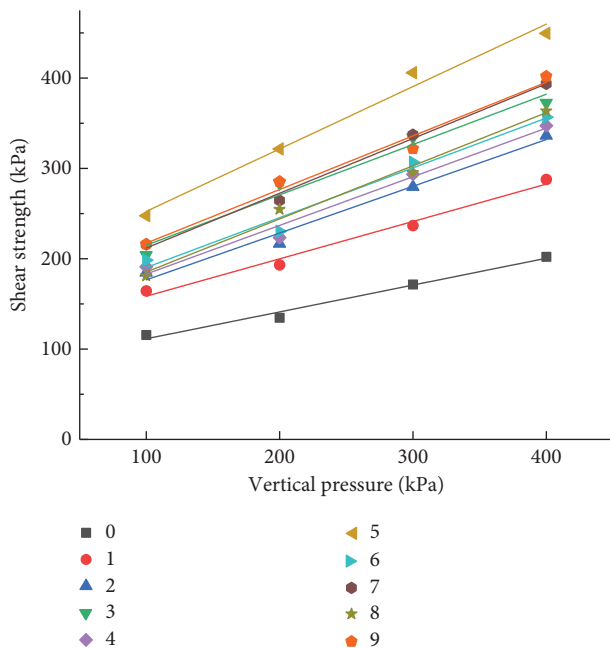


FIGURE 7: Relationship between shear strength and vertical pressure.

It can be seen from the trend in Figure 8 that the degree of influence of different factors is different, among which the primary and secondary factors affecting the shear strength of expansive soil are the largest lime, followed by coal gangue powder. When the proportion of gangue powder is 8%, the shear strength reaches the maximum. When the content of gangue powder continues to increase, the addition of excess gangue powder is equivalent to the addition of silt into expansive soil, which has no cohesive force, resulting in the decrease of soil strength. When the proportion of fly ash increases from 7% to 11%, and the proportion of lime increases from 2% to 6%, the shear strength of expansive soil increases gradually without a peak, indicating that the content of fly ash and lime still has room to rise. However, for this orthogonal experiment, the optimal scheme is $A_2B_3C_3$.

According to Table 11, the F ratio of three mixtures were less than $F_{0.1}$ which is equal to 9, which shows that three mixtures' influence on shear strength of expansive soil is not significant, and the dosage of lime has effects on shear strength, and lime, which is equal to 5.709, is greater than that of coal gangue powder, which is equal to 2.737, and F ratio of fly ash, which is equal to 0.971, is very small to be neglected. The effect of lime on the shear strength of

TABLE 10: Results of direct shear test.

Sample number	Fitting equation	Cohesive force c (kPa)	Internal friction angle φ ($^{\circ}$)	Shear strength τ (kPa) (the normal stress is 100 kPa)	Correlation coefficient r	Correlation index R^2
0	$\tau = 0.297\sigma + 81.75$	81.75	16.5 $^{\circ}$	115.5	0.9931	0.9794
1	$\tau = 0.4136\sigma + 117.2$	117.2	22.5 $^{\circ}$	164.5	0.9926	0.9779
2	$\tau = 0.5175\sigma + 124.95$	124.95	27.4 $^{\circ}$	184.7	0.9919	0.9759
3	$\tau = 0.5571\sigma + 159.3$	159.3	29.1 $^{\circ}$	204.0	0.9863	0.9593
4	$\tau = 0.5385\sigma + 129.25$	129.25	28.3 $^{\circ}$	191.2	0.9910	0.9732
5	$\tau = 0.6906\sigma + 183.45$	183.45	34.6 $^{\circ}$	247.5	0.9924	0.9774
6	$\tau = 0.5512\sigma + 135.25$	135.25	28.9 $^{\circ}$	198.3	0.9894	0.9684
7	$\tau = 0.6058\sigma + 151.35$	151.35	31.2 $^{\circ}$	215.8	0.9974	0.9923
8	$\tau = 0.5879\sigma + 126.55$	126.55	30.5 $^{\circ}$	180.9	0.9944	0.9832
9	$\tau = 0.5935\sigma + 157.95$	157.95	30.7 $^{\circ}$	216.1	0.9908	0.9725

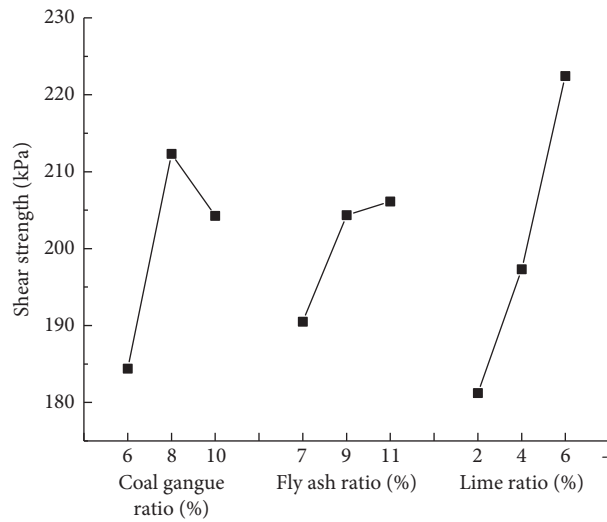


FIGURE 8: Trend chart of shear strength.

TABLE 11: ANOVA table for shear strength.

Factors	Square of deviance	Degree of freedom	Mean square	F ratio	F critical value	Significant
Coal gangue	1240.027	2	620.0135	2.737	$F_{0.01}(2, 2) = 99$	
Fly ash	439.807	2	219.9035	0.971	$F_{0.05}(2, 2) = 19$	
Lime	2586.660	2	1293.33	5.709	$F_{0.1}(2, 2) = 9$	O
Error	453.087	2	226.5435		$F_{0.25}(2, 2) = 3$	
Sum	4719.58	8				

In ANOVA, if the mean square value of a factor is less than or equal to the error mean square, it will be treated as the error term, and F value will not be calculated, where “***” means very significant $P < 0.01$, “**” means significant $0.01 \leq P < 0.05$, “*” means relatively significant $0.05 \leq P < 0.1$, and “O” means that $0.1 \leq P < 0.25$ has a certain influence.

expansive soil is greater than that of coal gangue powder and fly ash, showing poor results. The error of the Null column does not affect the test result, and the test result is reliable.

3.2.2. Analysis of Unconfined Compressive Strength Index.

Table 12 shows that the unconfined compressive strength of the expansive soil after ash addition is significantly increased, and the maximum increase is nearly double. The reason is that both the expansive soil and the material in the admixture have a hard coagulation reaction to form a kind of strong viscous cementing material, which improves the unconfined compressive strength of the expansive soil.

In Figure 9, average unconfined compressive strength and level of various factors trend diagram shows that when the proportion of coal gangue powder is 8%, the unconfined compressive strength, the largest 11% of fly ash and lime proportion was 6%, the unconfined compressive strength reached maximum, and mixing the unconfined compressive strength of lime soil with fly ash and lime proportion is approximate linear relationship, it showed that the dosage of fly ash is 11%, when dosage of lime is 6%, not necessarily belonging to the best content, but from the current test, the optimum scheme is $A_2B_3C_3$.

In Table 13, the dosage of lime and coal gangue powder content F were greater than $F_{0.01}(2,2) = 99$, suggesting that

TABLE 12: Results of unconfined compressive strength test.

Test number	0	1	2	3	4	5	6	7	8	9
Unconfined compressive strength/kPa	733.5	965.51	1060.85	1255.38	1180.44	1353.48	1232.24	1292.86	1150.68	1239.95

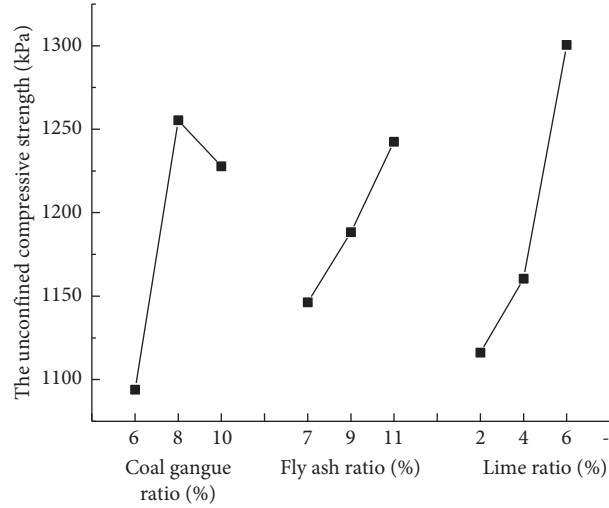


FIGURE 9: Trend chart of unconfined compressive strength.

TABLE 13: ANOVA table for unconfined compressive strength.

Factors	Square of deviance	Degree of freedom	Mean square	F ratio	F critical value	Significant
Coal gangue	44766.681	2	22383.341	270.513	$F_{0.01}(2, 2) = 99$	***
Fly ash	13970.503	2	6985.2515	84.420	$F_{0.05}(2, 2) = 19$	**
Lime	55619.083	2	27809.542	336.091	$F_{0.1}(2, 2) = 9$	***
Error	165.488	2	82.744		$F_{0.25}(2, 2) = 3$	
Sum	114521.75	8				

In ANOVA, if the mean square value of a factor is less than or equal to the error mean square, it will be treated as the error term, and F value will not be calculated, where “***” means very significant $P < 0.01$, “**” means significant $0.01 \leq P < 0.05$, “*” means relatively significant $0.05 \leq P < 0.1$, and “O” means that $0.1 \leq P < 0.25$ has a certain influence.

the dosage of lime and coal gangue powder content factors impact on the rate of free expansion of expansive soil effect is very significant, the dosage of fly ash F ratio is greater than $F_{0.05}(2, 2) = 19$, and its influence is significant, illustrating that different mixing ratio of admixture on the unconfined compressive strength of expansive soil has special effects, and various factors on the unconfined compressive strength of expansive soil influence the sequence of significance of lime powder, coal gangue, and fly ash.

3.3. Comprehensive Analysis. According to the range and variance analysis of each index, it is found that the size of the influencing factors and the optimal scheme of each index are different, so it is necessary to use the comprehensive balance method to comprehensively compare and analyze the results of the multi-index sample and get the size of the influencing factors and the optimal scheme.

Table 14 shows that, with different test indexes, the factors of influence degree and the optimal scheme are also different. Through comprehensive balance method, the influencing factors of modified expansive soil for primary

and secondary factors are concluded: $C > A > B$, one of the most optimum schemes for $A_2B_3C_3$; namely, coal gangue powder content is 8%, dosage of fly ash is 11%, and lime content is 6%.

According to the optimal solution for physical and mechanical properties of composite improved expansive soil basic indicators authentication contrast, as shown in Table 15, the measured results of the test index were improved obviously, which are better than the orthogonal experiment results. It shows that the mixture ratio scheme is reasonable and reliable and can be used as the reference for the optimal mixture ratio of the improved expansive soil subgrade engineering.

3.4. Improvement Mechanism Analysis. Scanning electron microscopy (SEM) is used to conduct scanning tests on 9 sets of different mixture-doped soils, and their microstructure result is shown in Figure 10.

It can be seen from Figures 10(a)–10(d) and 10(f) that the microstructures of expansive soil with different mixtures are basically the same. The surface and interior of the soil

TABLE 14: Multi-index analysis of test results.

Index	A (coal gangue)	B (fly ash)	C (lime)	D (null)	
The plastic index/%	k_1	15.927	16.453	17.327	14.930
	k_2	14.453	13.637	15.463	14.300
	k_3	13.237	13.527	10.827	14.387
	Range R	2.690	2.926	6.500	0.630
	Primary and secondary factors Optimal solution			C > B > A C ₃ B ₃ A ₃	
Free expansion rate/%	k_1	25.533	25.133	24.800	23.400
	k_2	22.067	23.333	24.200	23.700
	k_3	22.667	21.800	21.267	23.167
	Range R	3.466	3.333	3.533	0.533
	Primary and secondary factors Optimal solution			C > A > B C ₃ A ₂ B ₃	
Shear strength/kPa	k_1	184.400	190.500	181.233	209.367
	k_2	212.333	204.367	197.333	199.600
	k_3	204.267	206.133	222.433	192.033
	Range R	27.933	15.633	41.200	17.334
	Primary and secondary factors Optimal solution			C > A > B C ₃ A ₂ B ₃	
The unconfined compressive strength/kPa	k_1	1093.913	1146.270	1116.143	1186.313
	k_2	1255.387	1188.337	1160.413	1195.317
	k_3	1227.830	1242.523	1300.573	1195.500
	Range R	161.474	96.253	184.430	9.187
	Primary and secondary factors Optimal solution			C > A > B C ₃ A ₂ B ₃	

TABLE 15: Physical and mechanical indexes of improved expansive soil.

Test materials	Liquid limit (%)	Plastic limit (%)	Plastic index (%)	Maximum dry density (g·cm ⁻³)	Optimum moisture content (%)	Free expansion rate (%)	Shear strength (kPa)	Unconfined compressive strength (kPa)
Unimproved expansive soil	51.5	23.56	27.94	1.80	19.0	53.1	115.5	733.50
Expansive soil improved by lime	43.41	26.74	16.67	1.66	17.84	25.7	248.4	1259.23
Expansive soil improved by three mixtures	38.64	28.75	9.89	1.73	16.53	17.4	279.4	1468.72

have obvious boundary planes, which contain a large number of fly ash globular particles, and the flake and flat particles are reduced. The microagglomeration formed by white lime connects the globular particles and the aggregate soil particles, among which the diameter of the globular particles is between 2 μm and 8 μm, filling most of the pores and making the pore diameter smaller.

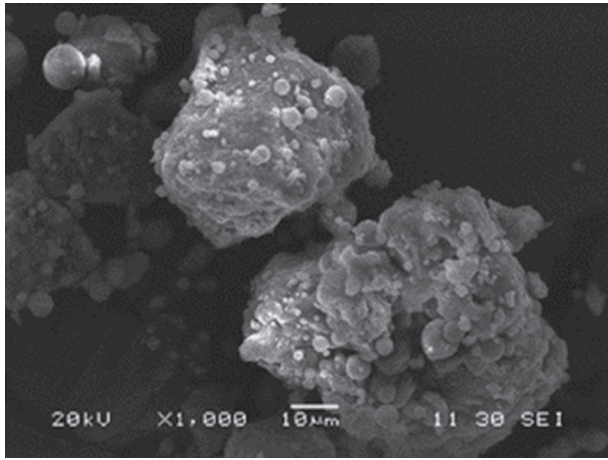
In Figures 10(e) and 10(i), there are many crystal grains of SiO₂, white Ca(OH)₂ and CaCO₃, including less sheet-shape grains, flat particles. The shape of the edge smooth structure of the unit is different, and its orientation is poorer, but connectivity is good, with small pores and different types. The pores are mixed with a few calcareous crystals and spherical particles, laminates and aggregates, and particles and microaggregates are filled in the structural skeleton pores.

In Figures 10(g) and 10(h), regarding the expansive soil in C, SiO₂ and silicon minerals such as calcium stone morphology of coal gangue, rhombohedron shaped, there are many small clay soil surface layers consisting of

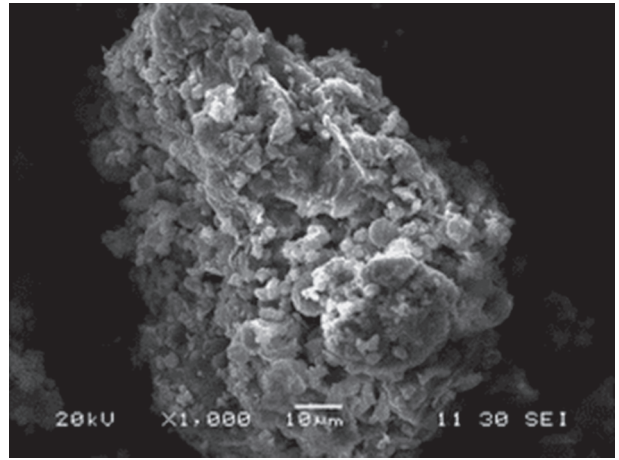
aggregate, larger aggregate inside, which is composed of single spherical particles, and the microconglomerate, internal to the grain structure, and the microstructure features with aggregate structure are given priority, also including granular pile structure.

From the above analysis, it can be seen that, with different mixing ratios, the aggregate formed by soil is also different, and the surface microstructure of the aggregate will also change. The skeleton structure of the improved soil microstructure is basically composed of aggregate and aggregate, aggregate and flake structure, and the pores in the soil structural skeleton are filled with particles and microaggregates [29]. Different proportions of coal gangue powder, fly ash, and lime admixtures are important factors to improve the microstructure of expansive soil.

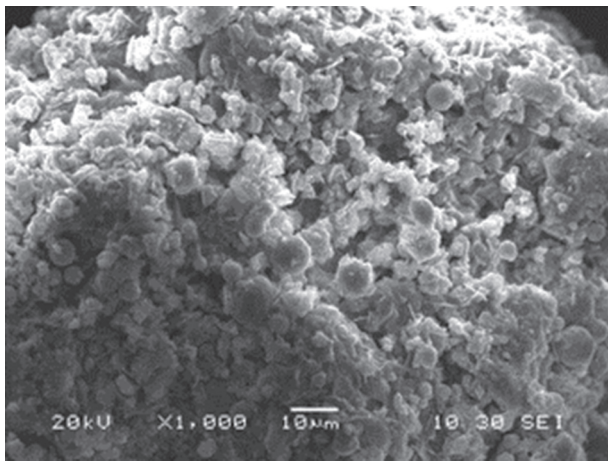
When coal gangue powder, fly ash, and lime are mixed into expansive soil, physical and chemical reactions will take place, and the improvement of expansive soil is mainly through four processes, namely, ion exchange, granulation,



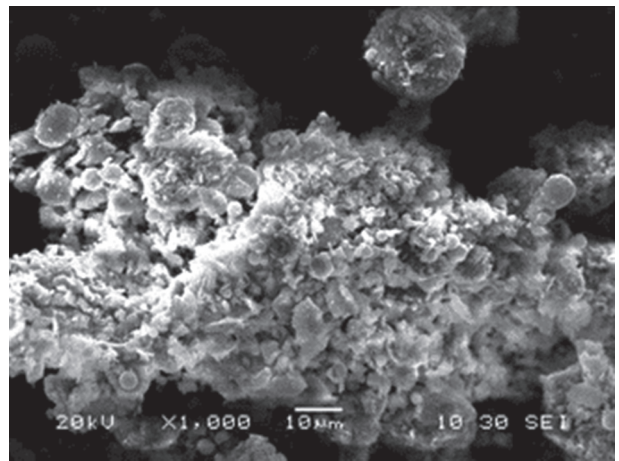
(a)



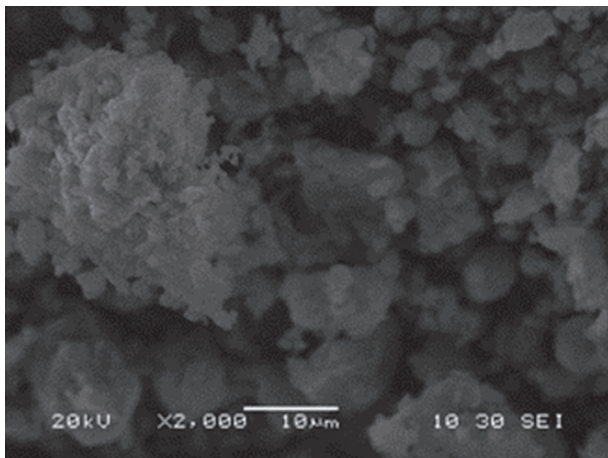
(b)



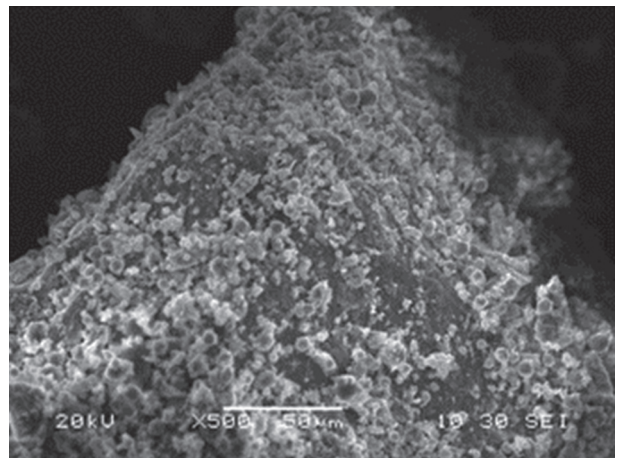
(c)



(d)



(e)



(f)

FIGURE 10: Continued.

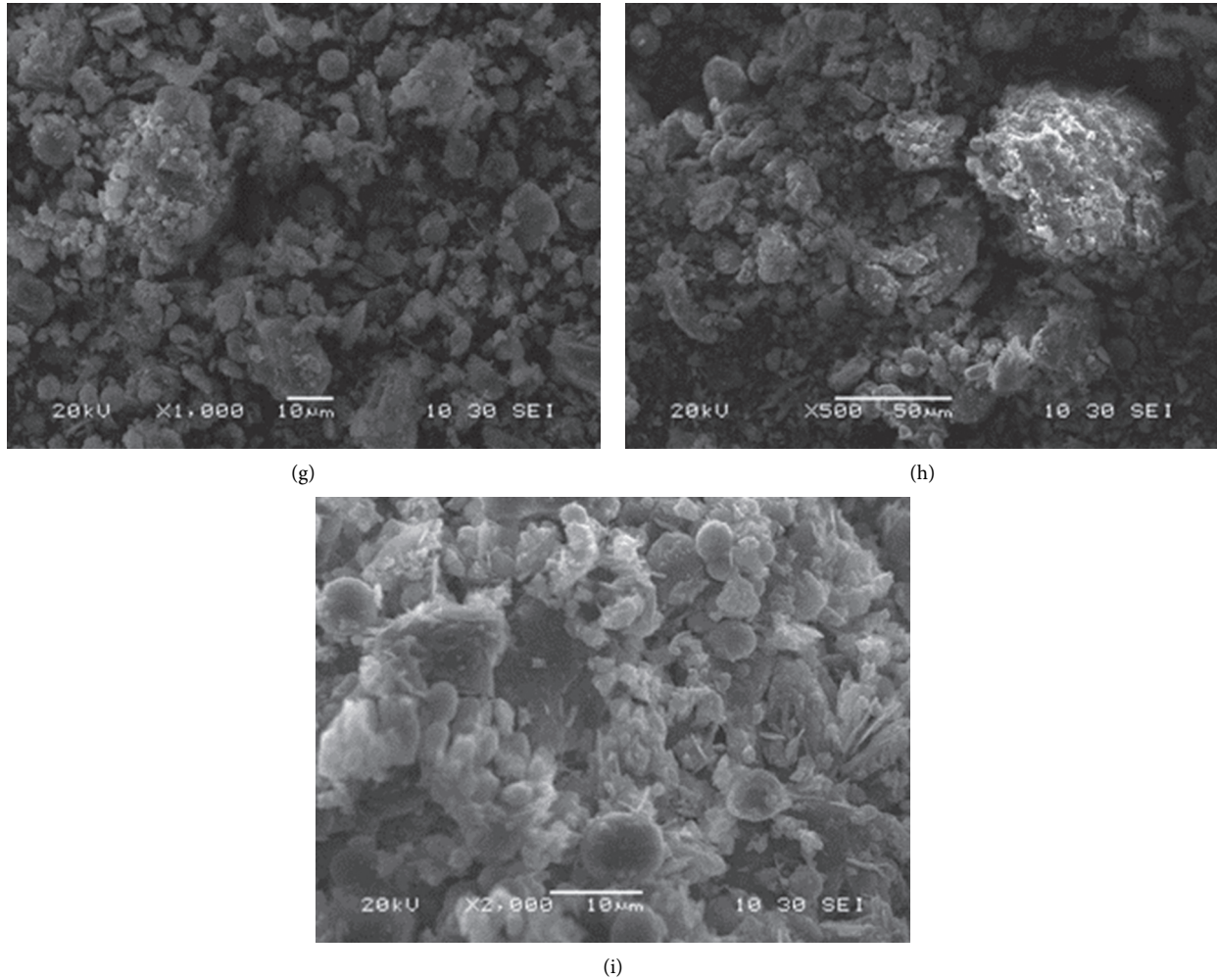


FIGURE 10: SEM of expansive soil with different mixtures. (a) The 1st group of soil sample. (b) The 2nd group of soil sample. (c) The 3rd group of soil sample. (d) The 4th group of soil sample. (e) The 5th group of soil sample. (f) The 6th group of soil sample. (g) The 7th group of soil sample. (h) The 8th group of soil sample. (i) The 9th group of soil sample.

carbonation, and gelation [30, 31]. Previous major ion exchange and aggregate effect, admixture of Ca^{2+} , Mg^{2+} exchange of clay particles on the surface of K^+ , Na^+ , and soil particles adsorption of water film thickness are reduced, which reduces soil plasticity, swelling, and dry density, and moisture content is also reduced, larger soil aggregate is deepened, forming the close link between them and leading to soil structure change, and clay content decreases. In addition, long time carbonic acid reaction occurs between CO_2 , $\text{Ca}(\text{OH})_2$ and $\text{Mg}(\text{OH})_2$ in soil, and CaCO_3 is generated, which results in soil cementation and soil reinforcement. In the late stage of the ion exchange reaction, the silica gel and aluminum gel in the expansive soil further are hardened with the admixture to produce CaSiO_3 and calcium aluminate, thus forming a stable protective film with strong adhesion and a network structure, which improved the strength of the soil and acted as a water-repellent effect, making the water of the expansive soil stable [32, 33]. The plasticity, dilatancy, and other properties of soil can be improved obviously by four kinds of action. Besides, when

there are more admixtures, the clay content of expansive soil is artificially reduced, which also improves the properties of expansive soil.

4. Conclusions

Based on the different amounts of coal gangue, fly ash, and lime admixture, 9 sets of mixing ratio schemes are designed and developed through orthogonal experiments. Routine laboratory tests and SEM in the experiment and the sensitivity analysis of the tested mechanical performance indicators were carried out. The effect and microstructure of the improvement of expansive soil under the conditions of different admixture ratios of multiple admixtures were studied, and the optimal admixture ratio scheme was determined. Conclusions are obtained as follows.

- (1) According to the orthogonal design, the physical and mechanical properties of the expansive soils were improved to different degrees by laboratory tests.

- (2) Based on range analysis and variance analysis, the main and secondary factors affecting the plasticity index of expansive soil are lime and fly ash. The sequences of influence on free expansion rate, shear strength, and unconfined compressive strength of expansive soil are lime, coal gangue, and fly ash. Through the comprehensive equilibrium method, the optimal mix ratio scheme of the improved expansive soil is $A_2B_3C_3$, which is 8% coal gangue, 11% fly ash, and 6% lime.
- (3) Through the selection test, the optimal scheme of the technical specifications of the improved expansive soil is the best value, the free expansion rate was reduced by 35.7%, the shear strength increases to 279.4 kPa, unconfined compressive strength increases to 1468.72 kPa, and the test results have been greatly improved, better than the lime improving expansive soil, and the reliability of the theory of mixture solution.
- (4) Through SEM structure analysis, it can be concluded that the microstructure of plain expansive soil is mainly flat aggregate and granular particles, and the bulk aggregate is the main expansive soil particles after ash mixing. The soil structure is dense, the agglomeration of particles increases, and the soil has better integration performance. The improvement mechanism of expansive soil was analyzed, and it was found that when coal gangue powder, fly ash, and lime were added into expansive soil, physical and chemical reactions would mainly take place. Ion exchange, granulation, carbonation, and gelation were used to reduce the swelling and shrinking property of expansive soil and improve the strength of soil.

Data Availability

The data used to support the findings of this study are available from the corresponding author upon request.

Conflicts of Interest

The authors declare that they have no conflicts of interest.

Acknowledgments

This work was fully supported by these grants from the National Natural Science Foundation of China (Award nos. 51778227, 51308208, and 41372303), the Provincial Natural Science Foundation of Hunan (Award nos. 2015JJ3069 and 18C0311), the Youth Talent Plan Program of Hunan (Award no. 2016RS3032), and the Postgraduate Scientific Research Innovation Project of Hunan Province (Award no. CX20200992).

References

- [1] H. Li, *Comprehensive Utilization of Coal Gangue*, Chemical Industry Press, Beijing, China, 2010.
- [2] L. ting, C. Tang, and D. Xu, "Research progress on engineering geological characteristics of expansive soil," *Journal of Engineering Geology*, vol. 26, no. 1, pp. 112–128, 2018.
- [3] Z. Yang, D. Hu, and Z. Wang, "Analysis on the evolution and disturbance law of expansion and shrinkage cracks in expansive soil," *Journal of Agricultural Engineering*, vol. 35, no. 17, pp. 169–177, 2019.
- [4] X. Wang, Z. Yao, F. Dang, and Z. Dong, "Microstructural evolution test of fissure expansive soil," *Journal of Agricultural Engineering*, vol. 32, no. 3, pp. 92–100, 2016.
- [5] G. Li, A. Li, J. Yuan, J. Wu, X. Cao, and S. Wu, "Cracking regularity and influencing factors of expansive soil on slope of river course in Jihuai River Project of Yanjiang River," *Journal of Agricultural Engineering*, vol. 34, no. 12, pp. 154–161, 2018.
- [6] N. Liu, K. Liu, and L. Rong, "Research on coal gangue and its application in building materials," *Concrete and Cement Products*, vol. 10, no. 9, pp. 74–76, 2012.
- [7] J. Wang and L. Wang, "Research on coal gangue clinker cement," *Cement*, vol. 3, no. 12, pp. 9–12, 2004.
- [8] F. Meng, *Study on the Shear Strength and CBR Variation Law of Coal Gangue Expansive Soil Subgrade*, Inner Mongolia Agricultural University, Hohhot, China, 2012.
- [9] T. Shen, S. Xing, S. Wang, M. Cheng, and W. Huang, "Screening of composite modifier for reducing the expansion rate of strong expansive soil and increasing the shear strength," *Chinese Journal of Agricultural Engineering*, vol. 33, no. 2, pp. 109–115, 2017.
- [10] X. Yang and Y. Zhang, "Analysis on the shear strength mechanism of improved expansive soil with coal gangue powder," *Coal Engineering*, vol. 46, no. 9, pp. 123–125, 2014.
- [11] Y. Zhang, X. Yin, and L. Tong, "Characteristics of coal gangue expansive soil and pore structure characterization under optimum mixing amount," *Journal of Agricultural Engineering*, vol. 34, no. 22, pp. 267–274, 2012.
- [12] Y. Zhang, X. Kang, and L. Guo, "Research on engineering characteristics of improved expansive soil with lime coal gangue," *Chinese Journal of Silicate*, vol. 34, no. 9, pp. 2720–2724, 2015.
- [13] M. W. Wang, K. Ge, and D. R. Zhu, "Experimental study of engineering behaviors on improved expansive soils in the Xinqiao Airport runway of Hefei," *Advanced Materials Research*, vol. 261–263, no. 261–263, pp. 1329–1335, 2011.
- [14] Q. Qiu, "Study on properties of lime improved expansive soil under dry wet cycle," *Subgrade Engineering*, vol. 1, pp. 79–83, 2021.
- [15] S. Dai, M. Song, and J. Huang, "Engineering properties of expansive soil," *Journal of Wuhan University of Technology (Material Science Edition)*, vol. 20, no. 2, pp. 109–110, 2005.
- [16] M. Abbaspour, S. S. Narani, E. Aflaki, F. M. Nejad, and S. M. M. Hosseini, "Strength and swelling properties of a waste tire textile fiber (WTF)-reinforced expansive soil," *Geosynthetics International*, vol. 27, no. 5, p. 1, 2020.
- [17] P. Indiramma, C. Sudharani, and S. Needhidasan, "Utilization of fly ash and lime to stabilize the expansive soil and to sustain pollution free environment - an experimental study," *Materials Today: Proceedings*, vol. 22, no. 3, pp. 694–700, 2020.

- [18] P. Gireesh Kumar and S. Harika, "Stabilization of expansive subgrade soil by using fly ash," *Materials Today: Proceedings*, vol. 22, no. 12, pp. 1–4, 2020.
- [19] JTJ E40-2007, *Highway Geotechnical Test Rules*, People's Communications Press, Beijing, China, 2007.
- [20] JTJ034-2000, *Technical Specification for Highway Pavement Base Construction*, People's Communications Press, Beijing, China, 2000.
- [21] GBT 1596-2017, *Fly Ash Used in Cement and Concrete*, People's Communications Press, Beijing, China, 2017.
- [22] S. Shan, *Experimental Study on Cement-Lime Improved Loess and its Engineering Application*, Chang'an University, Xi'an, China, 2017.
- [23] Y. Li and C. Hu, *Experimental Design and Data Processing*, Chemical Industry Press, Beijing, China, 2008.
- [24] Q. Liu, W. Xiang, and D. Cui, "Research on the mechanism of improving expansive soil with ionic soil stabilizer," *Chinese Journal of Geotechnical Engineering*, vol. 33, no. 4, pp. 648–654, 2011.
- [25] L. S. Chafusheng and Y. Du, "Improvement of expansive soil with lime and fly ash," *Journal of Southeast University (Natural Science Edition)*, vol. 37, no. 2, pp. 339–344, 2007.
- [26] F. G. Bell, "Lime stabilization of clay minerals and soils," *Engineering Geology*, vol. 42, no. 1/2, pp. 223–237, 1996.
- [27] Y. Li, W. He, and H. Wang, "Calculation of critical value of F test method," *Nonferrous Metals (Mineral Processing)*, vol. 4, pp. 39–41, 1992.
- [28] J. K. Mitchell, *Fundamentals of Soil Behavior*, Wiley&Sons, New York, NY, USA, 2nd edition, 1993.
- [29] L. Tan, M. Zhang, W. Shao, and H. Lili, "Microstructural characteristics and engineering properties of disastrous expansive soils," *Journal of Geotechnical Engineering*, vol. 2, pp. 48–57, 1994.
- [30] B.-H. Ma, Z.-Y. Hu, Z. Li et al., "Finite difference method for the one-dimensional non-linear consolidation of soft ground under uniform load," *Frontiers in Earth Science*, vol. 8, no. 8, pp. 1–9, 2020.
- [31] B. Ma, Z. Li, K. Cai et al., "An improved nonlinear settlement calculation method for soft clay considering structural characteristics," *Geofluids*, vol. 2021, no. 1, 7 pages, Article ID 8837889, 2021.
- [32] B. Ma, Z. Li, K. Cai et al., "Pile-soil stress ratio and settlement of composite foundation bidirectionally reinforced by piles and geosynthetics under embankment load," *Advances in Civil Engineering*, vol. 2021, no. 1, 10 pages, Article ID 5575878, 2021.
- [33] B. Ma, Z. Hu, Z. Li et al., "A three-section-settlement calculation method for composite foundation reinforced by geogrid-encased stone columns," *Advances in Civil Engineering*, vol. 2021, no. 2, 10 pages, Article ID 5576713, 2021.

Research Article

Research on the Failure and Fracture Evolution of Mylonite with a Prefabricated Circular Opening by Discrete Element Method

Kunmeng Li,¹ Yuanhui Li ,^{1,2} Shuai Xu,¹ Zhipeng Xiong,¹ and Long An¹

¹Key Laboratory of Ministry of Education on Safe Mining of Deep Metal Mines, Northeastern University, Shenyang 110819, China

²China-Canada Centre of Deep Mining Innovation, Key Laboratory of Ministry of Education on Safe Mining of Deep Metal Mines, Northeastern University, Shenyang 110819, Liaoning, China

Correspondence should be addressed to Yuanhui Li; 877260351@qq.com

Received 15 January 2021; Revised 2 April 2021; Accepted 22 April 2021; Published 12 May 2021

Academic Editor: Chunyang Zhang

Copyright © 2021 Kunmeng Li et al. This is an open access article distributed under the Creative Commons Attribution License, which permits unrestricted use, distribution, and reproduction in any medium, provided the original work is properly cited.

In this paper, the failure and fracture process of mylonite with a prefabricated circular opening under biaxial loading is studied by PFC^{2D} code. Firstly, the hoop stress change law of opening wall in the process of loading is theoretically analyzed and three fracture patterns of rocks are proposed. Secondly, the biaxial loading tests of mylonite for numerical simulation are carried out, and the failure and fracture are analyzed from three aspects of space-time evolution of microcracks, energy conversion process, and final damage patterns. As the load progresses, the microcracks start to initiate at the side wall of the opening and the growth velocity of microcracks develops from the slow to fast and then slows down again. The final damage pattern of mylonite with a prefabricated circular opening belongs to shear fracture. The fracture zones start with the side wall spalling and then gradually extend to the border of the rock, which widen from the opening boundary to the border of the rock and slightly twist in the middle. The final fault zone width is about 6 times wider than the average size of simulation particles. Finally, based on the uniaxial compressive strength of mylonite in the laboratory, it is inferred that the fracture pattern of mylonite with a prefabricated circular opening by theoretical analysis is indeed shear failure, which is consistent with the result of numerical simulation.

1. Introduction

In recent years, with the continuous depletion of shallow mineral resources and global environmental agitations against mining, deep mining is becoming the development trend in the future. With the increase in mining depth, engineering geological disasters will become more frequent [1, 2], such as roof falling, side wall slabbing, and rock blasting. In order to ensure the safe and efficient mining of deep orebodies, it is essential to study the failure and fracture evolution mechanism of the surrounding rock mass after the orebody is mined [3–7].

Although the on-site monitoring results of the rock mass responses with mining operations are more reliable [8–10], the field industrial test is time-consuming and labor-intensive, making it difficult to achieve. In contrast, laboratory

and numerical simulation tests for small-sized rocks are easy to control the loading and boundary condition and set up more monitors, and the failure evolution process and the final fracture pattern of actual excavated rock mass can be correctly speculated according to the laboratory and numerical simulation tests [11–18]. Therefore, laboratory and numerical simulation tests for small-sized rocks have become the mainstream to study the damage mechanism of rock mass around underground excavation [19, 20].

Throughout the experimental studies of rocks with prefabricated openings in the whole world, it is shown that under the uniaxial compression condition, the ultimate damage pattern of the rock with a circular opening mainly presents the tensile fractures at the top and bottom of the opening paralleling to the loading orientation, the compression fractures are produced on both sides of the opening,

and the far-field failures occurs around the opening [12, 21]. However, the final damage patterns cannot be characterized as the whole failure process of rocks, which includes the initiation, growth, and coalescence of microcracks. Compared with the physical experiment in the laboratory, numerical simulation can reproduce the failure evolution of rocks during the loading process, and it not only can be used to analyze the failure and fracture mechanism of rocks from different aspects but also the numerical simulation tests can be repeated to generate the reliable results [11, 21, 22]. If the numerical model can be accurately calibrated, the results will provide a guide for better forward prediction of the behaviors of engineering structures in rock mass.

At present, continuum model and discrete element method (DEM) are commonly adopted to simulate the damage and deformation behaviors of rocks [11, 23]. Compared with the continuum model, DEM does not involve the division of grids, so the mesh size sensitivity of grids does not need to be considered. DEM generates macroscopic response by the superimposition of mechanical behaviors among microscopic unit bodies, which saves the effort of presetting complex mathematical constitutive relationship into the model. The particle flow code PFC^{2D} based on the DEM can well simulate the local anisotropic behaviors of rocks during the loading process and can reproduce the space-time evolution of microcracks and the eventual fracture zones so which is therefore widely adopted to study the mechanical behaviors of various of rock mass [24] which utilized PFC^{2D} to predict the fracture zones of the Canadian underground laboratory. Potyondy and Autio [25] simulated the damage pattern of gneiss with an excavated circular opening during uniaxial compression process. Fakhimi et al. [11] conducted biaxial loading simulation tests of granite with a pre-existing circular opening, and the microcracks development results by numerical simulation and acoustic emission test were consistent. Fan et al. [26]

used the PFC program to establish numerical models containing one open flaw and two circular openings. Cao et al. [27] researched the mechanical behavior of an opening in a jointed rock-like specimen under uniaxial loading by experimental studies and particle mechanics approach. The above studies have confirmed that PFC^{2D} software can successfully simulate the mechanical behaviors of rocks with loading. However, previous studies have certain limitations as on the one hand they did not consider the differences in terms of rock type; on the other hand, they are relatively lack of the analysis of rock failure mechanism, therefore which cannot be accepted in predictions of the failure evolution mechanism of the other rocks.

The surrounding rock mass in the footwall at -850 depth in a Chinese gold mine mainly belongs to the mylonite, which is a kind of metamorphic rock, and the stability is relatively good. In this paper, the mylonite is taken as the research object, and the failure and fracture process of mylonite with a prefabricated circular opening is researched under the biaxial loading condition by PFC2D. The simulated results are analyzed from three aspects: space-time evolution of microcracks, energy conversion process, and the final fracture patterns.

2. Theoretical Analyses

In order to understand the failure and fracture mechanism of mylonite with a prefabricated circular opening under the biaxial loading condition, the elastic stress state of the rock is calculated by Equations (1) to (4) [28]. Figure 1 shows the geometric loading condition of the rock, and the boundary stresses in vertical and horizontal directions are, respectively, shown as P_0 and λP_0 , where λ is the lateral pressure coefficient. Based on the theory of elasticity, the radial, hoop, and tangential stresses [28] of the rock around the circular opening are calculated, respectively, as following formulas:

$$\sigma_r = \frac{1}{2} (1 + \lambda) P_0 \left(1 - \frac{R_0^2}{r^2} \right) - \frac{1}{2} (1 - \lambda) P_0 \left(1 - 4 \frac{R_0^2}{r^2} + 3 \frac{R_0^2}{r^4} \right) \cos 2 \theta, \quad (1)$$

$$\sigma_\theta = \frac{1}{2} (1 + \lambda) P_0 \left(1 + \frac{R_0^2}{r^2} \right) + \frac{1}{2} (1 - \lambda) P_0 \left(1 + 3 \frac{R_0^2}{r^4} \right) \cos 2 \theta, \quad (2)$$

$$\tau_{r\theta} = \frac{1}{2} (1 - \lambda) P_0 \left(1 + 2 \frac{R_0^2}{r^2} - 3 \frac{R_0^2}{r^4} \right) \cos 2 \theta, \quad (3)$$

where σ_r , σ_θ , and $\tau_{r\theta}$ are radial, hoop, and tangential stresses, respectively; R_0 is the radius of the circular opening; and r is the distance from the opening center to the point for obtaining the stress state. It can be calculated that when $r=0$, the stress state at the wall of the circular opening is

$$\begin{aligned} \sigma_r &= 0, \\ \sigma_\theta &= (1 + \lambda) P_0 + 2 (1 - \lambda) P_0 \cos 2 \theta, \\ \tau_{r\theta} &= 0. \end{aligned} \quad (4)$$

As shown in Figure 2, during the biaxial loading tests of rocks, the lateral pressure coefficient λ continuously

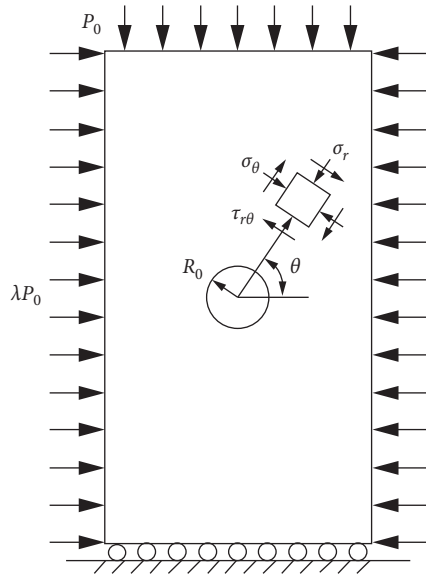
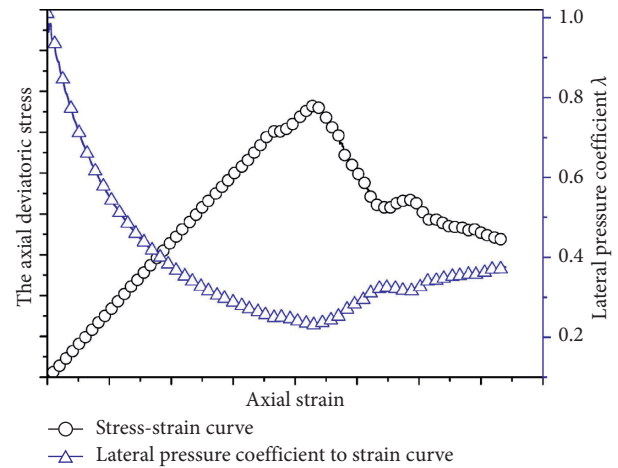


FIGURE 1: Geometric loading condition.

decreases with loading but which is always less than 1. Corresponding to different λ , the distribution of hoop stresses on the circular opening wall of the rock is shown in Figure 3 [29]. The straight length which surrounds and is perpendicular to the opening represents the magnitude of hoop stresses on the opening wall. When the straight line is located inside the opening, it represents tensile stress, while when it is located outside the opening, it indicates compressive stress. It is apparent from Figure 3 that the reduction of λ may result in the increase in compressive stresses on the two sides of the opening wall as well as the reduction of compressive stresses at the top and bottom of the opening wall. When $\lambda = 1/3$, the hoop compressive stresses at the top and bottom of the opening wall are reduced to 0, and the tensile stress begins to appear at the top and bottom of the opening wall along with continuous loading.

Based on the variation of hoop stresses on the opening wall during the biaxial loading process, it can be speculated that there are no more than three reasons that eventually lead to rock fractures. (1) When the tensile stresses at the top and bottom of the opening do not reach the peak strength while the compressive stresses on both sides of the opening have already reached the peak strength, only the shear fractures of rocks occur on both sides of the opening and the both sides of the opening spall and extend to the border with loading, as schematically shown in Figure 4(a). (2) When the compressive stresses on both sides of the opening do not reach the peak strength while the tensile stresses at the top and bottom of the opening have already reached their peak strength, the tensile fractures of rocks occur at the top and bottom of the opening and the top and bottom of the opening spall and extend to upper and lower ends with loading, as schematically shown in Figure 4(b). (3) When the compressive stresses on both sides of the opening and the tensile stresses at the top and bottom of the opening all reach the peak strength, the shear fractures of rocks occur on both

FIGURE 2: Conceptual axial deviatoric stresses with different λ .

sides of the opening and the tensile fractures of rocks occur at the top and bottom of the opening. Meanwhile, the both sides of the opening spall extend to the border and the top and bottom of the opening spall and extend to upper and lower ends, as schematically shown in Figure 4(c).

3. Numerical Simulation

When PFC^{2D} is applied to simulate the mechanical behaviors of rocks, the rock is modeled as a collection of circular particles for 3D or disks for 2D. The deformation of rocks is achieved by the positive and shear stiffness between particles, and the rock strength is controlled by additional contact bond keys and friction parameters. The formation of failures follows the Coulomb criterion, and the initiation of microcracks is consistent with the breaks of bond keys. The contact constitutive model between the particles is shown in Figure 5.

3.1. Determination of Microscopic Parameters. Before simulating the mechanical behaviors of specific types of rocks, PFC^{2D} needs to determine a set of particle microscopic parameters such as particle size distribution, contact stiffness, and strength between particles. The microscopic parameters of the numerical model are the basis for obtaining accurate simulation results. However, the mechanical behavior of rocks is commonly described by the elastic deformation constant, compressive strength, residual strength, and other macroscopic parameters. As the microscopic parameters of numerical simulation are nonlinear to the macroscopic response of laboratory tests, the microscopic parameters cannot be calculated directly by the macroscopic response.

In view of the blindness of “trial and error method” [11, 30] for determining the microscopic parameters of the PFC^{2D} numerical model, Li et al. [31] proposed a parameter determination method based on laboratory test response in the previous research. The geometry parameters of the numerical model are obtained by the basic characteristics of rocks. The contact constitutive parameters between particles

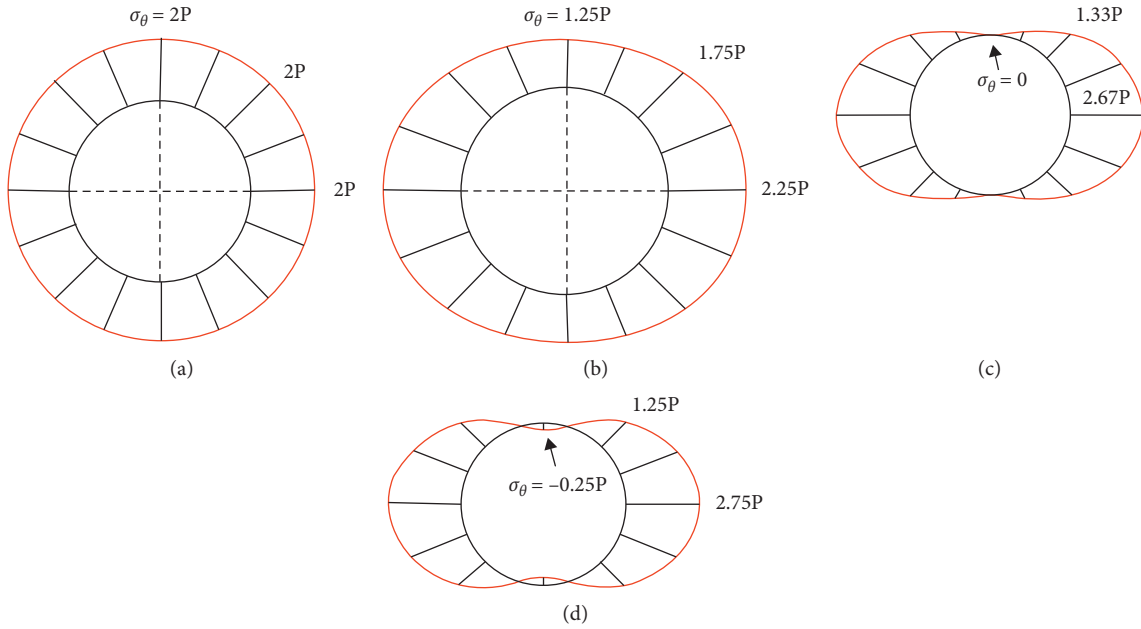


FIGURE 3: Hoop stresses distribution on the opening wall: (a) $\lambda = 1.00$, (b) $\lambda = 0.75$, (c) $\lambda = 0.33$, and (d) $\lambda = 0.25$.

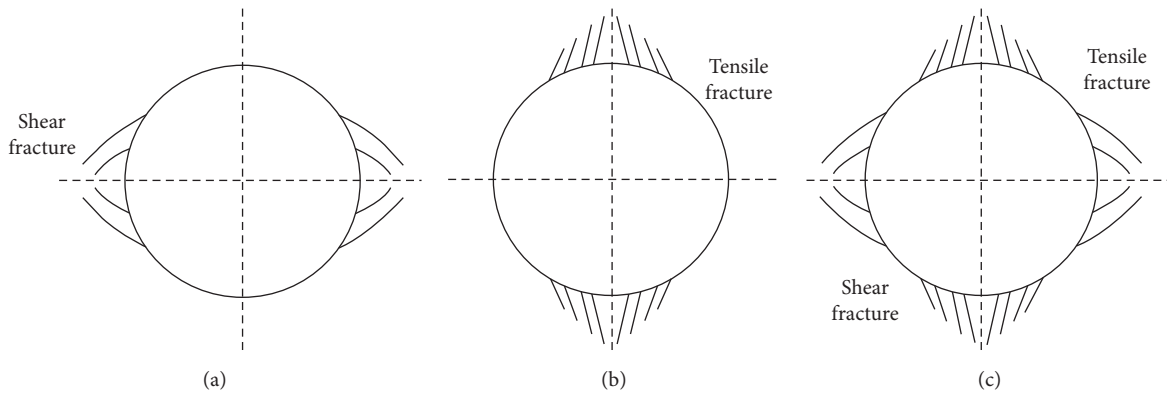


FIGURE 4: Final fracture patterns: (a) shear fractures, (b) tensile fractures, and (c) coexistence of shear and tensile fractures.

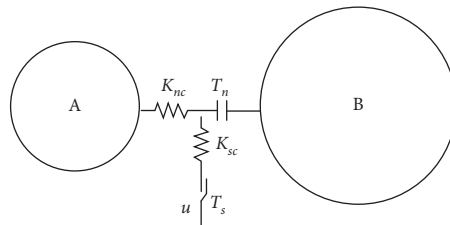


FIGURE 5: PFC^{2D} microscopic contact constitutive model.

are calculated by means of laboratorial test response, and the specific process can be summarized as the following steps. (1) The elastic modulus E , Poisson's ratio ν , peak strength $\bar{\sigma}_c$, initial failure strength $\bar{\sigma}_{ci}$, and post-peak residual strength $\bar{\sigma}_{ca}$ of mylonite are obtained by the uniaxial or conventional triaxial physical test and which are, respectively, $3.48e^{10}$ Pa, 0.26 , $5.21e^7$ Pa, $16.1e^6$ Pa, and $74.5e^6$ Pa. (2) On the basis of

ensuring that the boundary, loading, and termination conditions are consistent with the physical tests, numerical simulation experiments are carried out. (3) The correspondence between the numerical simulation microscopic parameters and the macroscopic response is established by continuously changing the constitutive parameters in an orderly manner. (4) The specific values of various contact

constitutive parameters are calculated according to the equal principle of macroresponse between numerical simulation and physical test. The detailed process can refer to the previous research [31]. As shown in Table 1, the determined microscopic parameters of mylonite located in the footwall of -850 depth in a Chinese gold mine can be described as the maximum and minimum radius ratio $R_{\max}/R_{\min} = 1.66$, where $R_{\min} = 0.2e^{-4}$ m, and the particle radius satisfies uniform distribution, particle collection porosity $n = 9\%$, the density per unit volume $\rho = 2630$ kg/m³, contact modulus between particles $E_c = 6e^{10}$ MPa, positive stiffness and tangential stiffness ratio $K_n/K_s = 4.5$, positive strength $T_n = 45e^6$ MPa, positive strength to tangential strength $T_n/T_s = 1/5$, the strength deviations T_{dn}/T_n and T_{ds}/T_s are 1:10, and friction coefficient $u = 0.5$. On the basis of the microscopic parameters, uniaxial and biaxial simulation experiments are carried out. As shown in Figure 6, the results show that the response of numerical simulation and laboratory test has a good consistency. Therefore, it is confirmed that the determined microscopic parameters are reliable and have strong applicability.

3.2. Numerical Model and Loading Condition. In order to simulate the failure evolution of rocks with the prefabricated circular opening, the rock sample is constructed in Figure 7(a), with height \times width = 100 mm \times 50 mm, and the diameter of the prefabricated circular opening is 10 mm and which is located in the center of sample. During the biaxial loading, a constant loading velocity $V_p = 1e^{-3}$ mm is designed and the confining stress is kept as 10 MPa. The specific loading condition is shown as in Figure 7(b).

3.3. Results and Analysis. The failure and fracture evolution mechanism of mylonite with a prefabricated circular opening is analyzed from three aspects: space-time evolution of microcracks, energy conversion process, and the final fracture patterns. PFC^{2D} software identifies failures by monitoring the quantity of microcracks and drawing the microcracks with loading. Figure 8 shows the relationship between the quantity change of microcracks and the stress-strain curve during the biaxial loading test. Figure 9 is the spatial evolution process of microcracks, where the solid yellow line indicates breaks of the positive bonds and the solid red line represents breaks of the tangential bonds.

The results show that at the initial loading period, rocks with prefabricated openings are in the elastic deformation stage without cracks generation. As the load progresses, when the axial stress reaches the initial crack generation strength (about 73% of the peak strength), microcracks occur and the rock begins to enter the plastic deformation phase. Because of the concentration of compressive stress, shear cracks are created on both sides of the opening, as shown the red tangential bonds breaking in Figure 9(a). Before reaching the peak strength, microcracks are generated in a moderate speed, and the quantity of microcracks increases rapidly after the peak strength is reached and before the residual strength stabilizes when individual microcracks link and mutually merge, resulting that the

rupture zones gradually generate and extend to the boundary of the rock, as shown in Figures 9(b) and 9(c). Meanwhile, the far-field cracks are formed and are far from the opening region. When the residual strength is stable, the fracture zones are basically shaped and the crack generation velocity slows down as well, as shown in Figure 9(d).

The rock loading process is often accompanied by the energy conversion. Figure 10 shows the evolution of different kinds of energies with loading. It can be seen that the whole loading process is mainly about the conversion of strain energy, border energy, and friction energy, and the variation trend of strain energy has a good correlation with axial stress-strain curve. The loading process can be divided into two stages from the perspective of energy conversion. Before the microcracks are generated, only border energy is converted into the strain energy, and the rock is in an elastic deformation stage. As the loading continues, a certain amount of border energy is further consumed and the crack is generated, and the coalescence of individual microcracks occurs and particles on the fracture regions begin to slip, causing that the friction energy increases. Meanwhile, the elastic strain energy at the rock damage zones is released. Therefore, the border energy mainly converts to the strain energy and friction energy. Before the peak strength is reached, the elastic strain energy of rock keeps increasing. However, as the elastic strain energy derived from border energy is not sufficient to offset its dissipation caused by extensive damage after the peak strength, the elastic strain energy starts to decrease. Before the residual intensity stabilizes, the strain energy decreases at a quite significant velocity, which is caused by the rapid generation of numerous microcracks at this stage, as shown the microcracks generation curve in Figure 8.

The failure evolution of mylonite with a circular opening extends from both sides of the opening to the boundary of the rock, as shown in Figure 9, and the final fracture pattern belongs to the shear failure. A central symmetric shear fracture zones are formed on the two sides of opening, whose direction is at an angle of 30° from the axial loading direction. Figure 11 shows the enlarged view to the left of fracture zones in Figure 12(a), and the arrows represent the particle displacement field. The solid blue lines indicate breaks of the positive bonds, and the solid red lines represent breaks of the tangential bonds. The displacement field of the ultimate fault zones can be divided into three regions of A, B, and C. In the region A and C, the particle moving follows the standard rigid body motion, which is greatly different from the transition region B. The region B is exactly the fault zone where particle displacement is almost zero and contains most of the microcracks. Meanwhile, the direction of microcracks is not exactly the same as that of the macroscopic fault zones. The fault width of region B keeps increasing from the opening to the border of rock, and the fault region slightly twists in the middle. The width of the fault zone is about six times wider than the average size of particles, i.e., the average diameter of particles is 0.532 mm and the average thickness of the fault is 3.2 mm.

When the confining stress is 10 MPa, the relationship among the maximum compressive stress $\sigma_{c\max}$, the

TABLE 1: The microscopic parameters of the PFC^{2D} numerical model.

Parameters	R_{\max}/R_{\min}	R_{\min} (m)	ρ (kg/m ³)	n (%)	E_c (Pa)	K_n/K_s	T_n (Pa)	T_n/T_s	T_{dn}/T_n (T_{ds}/T_s)	u
Value	1.66	$0.2e^{-4}$	2630	9	$6e^{10}$	4.5	$45e^6$	1/5	1:10	0.5

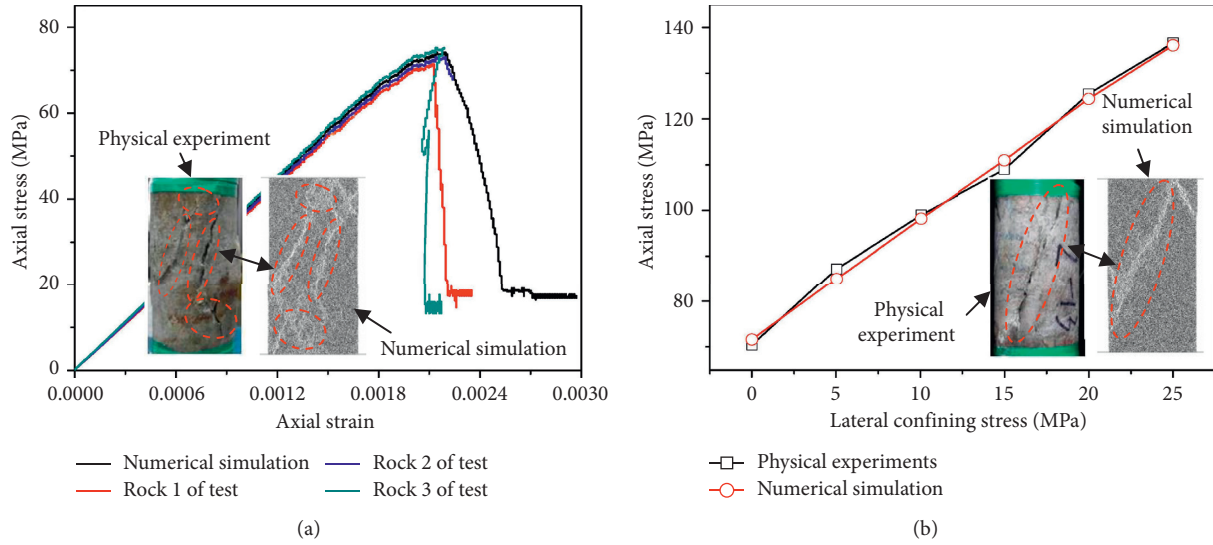


FIGURE 6: The compared results of physical experiments and numerical simulation: (a) uniaxial experiments and (b) biaxial experiments.

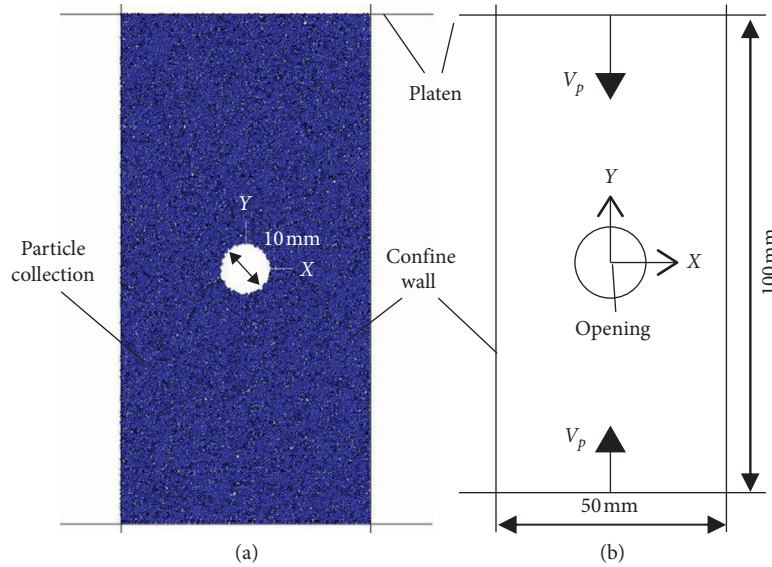


FIGURE 7: (a) The numerical model and (b) the loading condition.

maximum tensile stress σ_{tmax} , and the lateral pressure coefficient λ of mylonite and sandstone are listed in Table 2 (corresponding to Figures 3(a)–3(d)) as the load progresses. The average uniaxial compressive strength of mylonite located in the footwall at –850 depth in a Chinese gold mine is 71.5 MPa [31]. Therefore, when the axial stress reaches the compressive strength of the rock, there is still no tensile stress in the hoop stress on the opening wall, resulting that the final damage conforms to the first shear fracture pattern of theoretical analysis, as shown in Figure 4(a). The damage

pattern of mylonite by theoretical analysis is consistent with numerical simulation, as shown in Figure 9. In order to further verify the three fracture patterns in Figure 4, the damage pattern of sandstone is evaluated. The uniaxial compressive strength of sandstone studied by Fakhimi et al. [11] was about 43 MPa, and when the axial stress reaches the compressive strength of the rock, tensile failure still does not occur. Therefore, the ultimate damage pattern of sandstone is shear fracture, which compares well with the physical experiment, as shown in Figure 12(c) and Table 2.

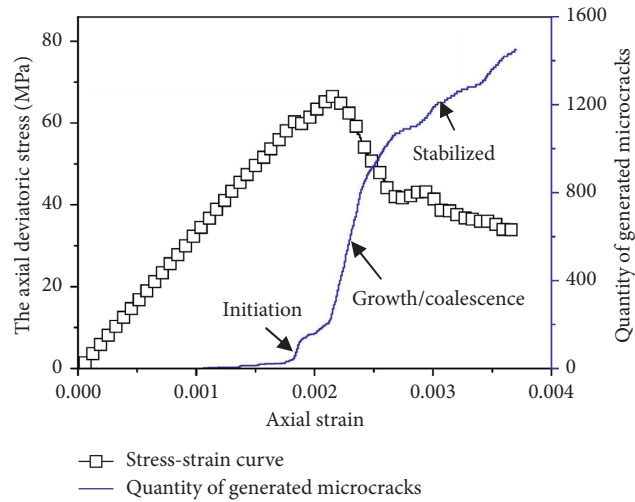


FIGURE 8: Relationship between the quantity of microcracks and axial stress-strain curve.

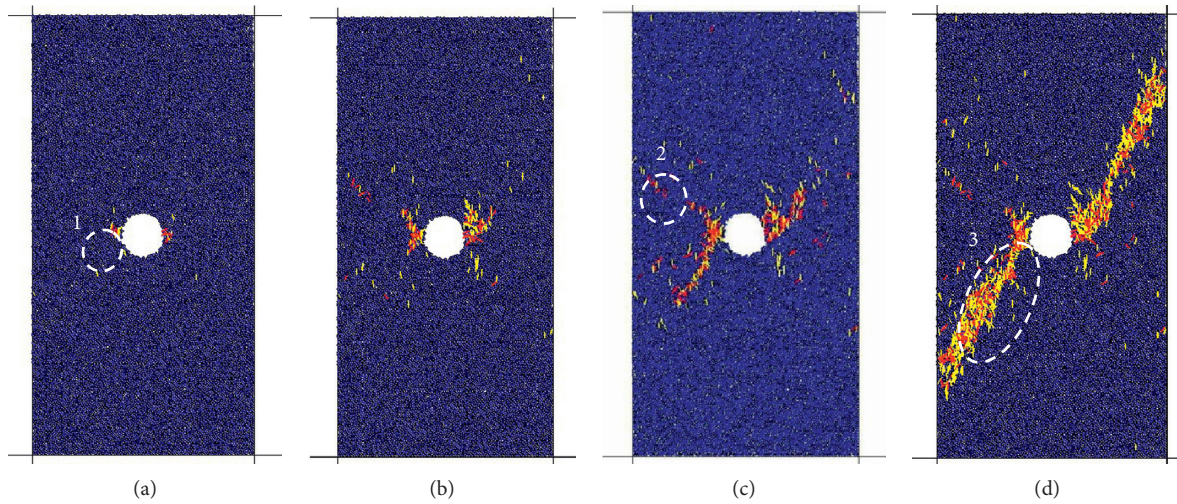


FIGURE 9: Space-time evolution process of microcracks during loading: (a) 85,000 step before peak, (b) 94,120 step at peak, (c) 100,000 step after peak, and (d) 109,120 step after peak. 1: notch fractures; 2: far-field fractures; 3: shear damage.

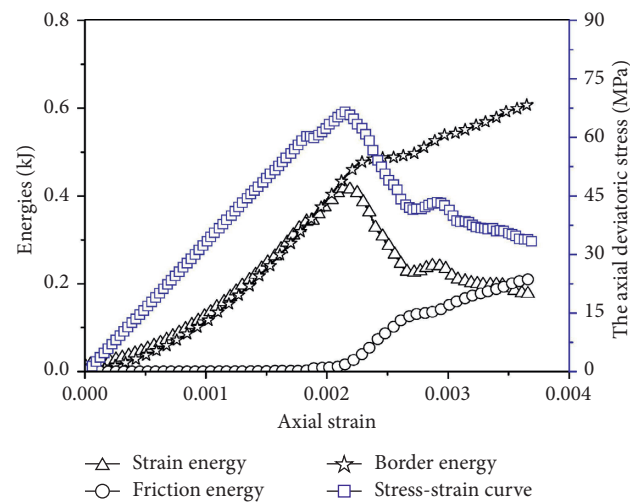


FIGURE 10: The changes of different energies.

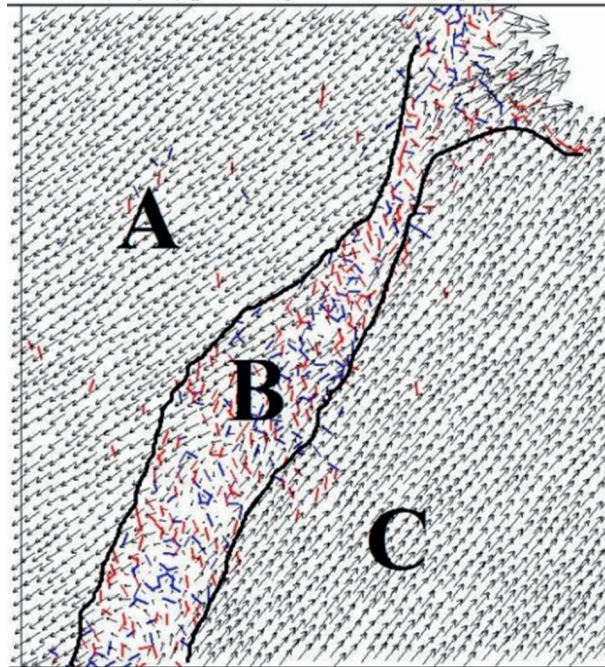


FIGURE 11: Microstructure of the fault zones after loading.

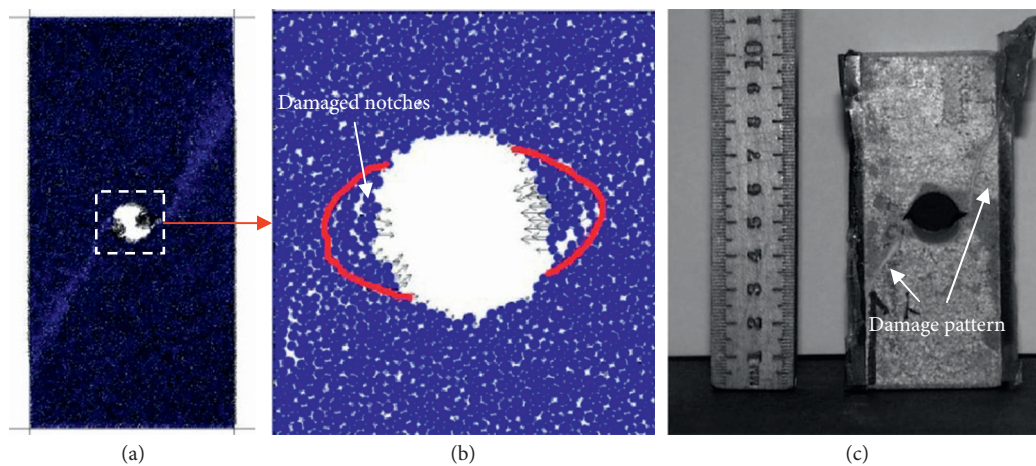


FIGURE 12: The fault zones and notch formation: (a) the displacement field, (b) the damaged notches near the opening, and (c) the sandstone fault pattern [11].

TABLE 2: Statistics of the maximum compressive stress and the maximum tensile stress with different λ .

Lithology	λ	1	0.75	0.33	0.25
Mylonite	σ_{cmax}/MPa	20	30	79.5	110
	σ_{tmax}/MPa	0	0	0	10
Sandstone	σ_{cmax}/MPa	7.5	22.5	60.075	82.5
	σ_{tmax}/MPa	0	0	0	7.5

4. Conclusion

In this paper, the failure and fracture mechanism of mylonite with a prefabricated circular opening is studied. From the perspective of theoretical analysis, three kinds of fracture patterns of the rock with a circular opening are proposed,

that is, shear fractures at the sides of the opening, tensile fractures at the top and bottom of the opening, and the coexistence of shear and tensile fractures. In the biaxial loading process of mylonite with a prefabricated circular opening, the microcracks initiate on the side wall of opening when the loading stress is of about 73% of the peak strength with a 10 MPa confining stress. The fracture zones mainly start to spall from the side wall and then gradually extend to the border of the rock. In terms of energy conversion, the process of rock fractures can be divided into two stages. Before the generation of microcracks, only the border energy is converted into the elastic strain energy of the rock, while after the microcracks begin to appear, the border energy is transformed into strain energy and friction energy. After the test load is completed, the fault zones widen and slightly

twist in the middle from the opening boundary to the border of the rock, and the fault zone width is about six times wider than the average size of simulation particles. According to the uniaxial compressive strength of mylonite in laboratory tests, when the loading stress reaches the peak compressive strength, there is no hoop tensile stress on the opening side wall, so the final fracture pattern of mylonite should be the shear failure pattern, which coincides with the numerical simulation.

Data Availability

The data used to support the findings of this study are included within the article.

Conflicts of Interest

The authors declare that they have no conflicts of interest.

Acknowledgments

This work was supported by the State Key Research Development Program of China (grant numbers 2018YFC0604601 and 2018YFC0604405), the National Natural Science Foundation of China (grant numbers 52004054 and 51874068), the Program for Innovative Talents in Liaoning University (grant number LR2016024), and the Fundamental Research Funds for the Central Universities (grant numbers N180701016, N2001001, and N182608003).




References

- [1] B. G. White, "Shear mechanism for mining-induced fractures applied to rock mechanics of coal mines," in *Proceedings of the 2002 21st International Conference on Ground Control in Mining*, pp. 328–334, Morgantown, WV, USA, August 2002.
- [2] R. T. Ewy and N. G. W. Cook, "Deformation and fracture around cylindrical openings in rock-I. Observations and analysis of deformations," *International Journal of Rock Mechanics and Mining Sciences & Geomechanics Abstracts*, vol. 27, no. 5, pp. 387–407, 1990.
- [3] F.-Q. Gong, Y. Luo, X.-B. Li, X.-F. Si, and M. Tao, "Experimental simulation investigation on rockburst induced by spalling failure in deep circular tunnels," *Tunnelling and Underground Space Technology*, vol. 81, pp. 413–427, 2018.
- [4] Y. Luo, F. Gong, D. Liu, S. Wang, and X. Si, "Experimental simulation analysis of the process and failure characteristics of spalling in D-shaped tunnels under true-triaxial loading conditions," *Tunnelling and Underground Space Technology*, vol. 90, pp. 42–61, 2019.
- [5] H. Wu, G. Zhao, and W. Liang, "Mechanical properties and fracture characteristics of pre-holed rocks subjected to uniaxial loading: a comparative analysis of five hole shapes," *Theoretical and Applied Fracture Mechanics*, vol. 105, Article ID 102433, 2020.
- [6] R.-H. Cao, C. Wang, R. Yao et al., "Effects of cyclic freeze-thaw treatments on the fracture characteristics of sandstone under different fracture modes: laboratory testing," *Theoretical and Applied Fracture Mechanics*, vol. 109, Article ID 102738, 2020.
- [7] Y. Zhao, L. Zhang, J. Liao, W. Wang, Q. Liu, and L. Tang, "Experimental study of fracture toughness and subcritical crack growth of three rocks under different environments," *International Journal of Geomechanics*, vol. 20, no. 8, 2020.
- [8] M. Cai, P. K. Kaiser, H. Morioka et al., "FLAC/PFC coupled numerical simulation of AE in large-scale underground excavations," *International Journal of Rock Mechanics and Mining Sciences*, vol. 44, no. 4, pp. 550–564, 2007.
- [9] C. Zhang, C. Pu, R. Cao, T. Jiang, and G. Huang, "The stability and roof-support optimization of roadways passing through unfavorable geological bodies using advanced detection and monitoring methods, among others, in the Sanmenxia Bauxite Mine in China's Henan Province," *Bulletin of Engineering Geology and the Environment*, vol. 78, no. 7, pp. 5087–5099, 2019.
- [10] Y. Zhao, L. Zhang, W. Wang, and G. Cheng, "Experimental study on shear behavior and a revised shear strength model for infilled rock joints," *International Journal of Geomechanics*, vol. 20, no. 9, 2020.
- [11] A. Fakhimi, F. Carvalho, T. Ishida, and J. F. Labuz, "Simulation of failure around a circular opening in rock," *International Journal of Rock Mechanics and Mining Sciences*, vol. 39, no. 4, pp. 507–515, 2002.
- [12] X.-D. Zhao, H.-X. Zhang, and W.-C. Zhu, "Fracture evolution around pre-existing cylindrical cavities in brittle rocks under uniaxial compression," *Transactions of Nonferrous Metals Society of China*, vol. 24, no. 3, pp. 806–815, 2014.
- [13] C. Y. Zhang, Y. X. Wang, H. Ruan, B. Ke, and H. Lin, "The strain characteristics and corresponding model of rock materials under uniaxial cyclic load/unload compression and their deformation and fatigue damage analysis," *Archive of Applied Mechanics*, vol. 1-16, 2021.
- [14] C. Y. Zhang, Y. X. Wang, and T. T. Jiang, "The propagation mechanism of an oblique straight crack in a rock sample and the effect of osmotic pressure under in-plane biaxial compression," *Arabian Journal of Geosciences*, vol. 13, no. 15, 2020.
- [15] Z.-M. He, D. Xiang, Y.-X. Liu, Q.-F. Gao, and H.-B. Bian, "Deformation behavior of coarse-grained soil as an embankment filler under cyclic loading," *Advances in Civil Engineering*, vol. 2020, no. 3, pp. 1–13, 2020.
- [16] R. H. Cao, R. B. Yao, J. J. Meng, Q. B. Lin, H. Lin, and S. Li, "Failure mechanism of non-persistent jointed rock-like specimens under uniaxial loading: laboratory testing," *International Journal of Rock Mechanics and Mining Sciences*, vol. 132, 2020.
- [17] L. Weng, X. Li, A. Taheri, Q. Wu, and X. Xie, "Fracture evolution around a cavity in brittle rock under uniaxial compression and coupled static-dynamic loads," *Rock Mechanics and Rock Engineering*, vol. 51, no. 2, pp. 531–545, 2018.
- [18] Y. L. Zhao, C. S. Zhang, Y. X. Wang, and H. Lin, "Shear-related roughness classification and strength model of natural rock joint based on fuzzy comprehensive evaluation," *International Journal of Rock Mechanics and Mining Sciences*, vol. 137, 2021.
- [19] R. H. Cao, R. B. Yao, T. Hu, C. S. Wang, K. H. Li, and J. J. Meng, "Failure and mechanical behavior of transversely isotropic rock under compression-shear tests: laboratory testing and numerical simulation," *Engineering Fracture Mechanics*, vol. 241, 2021.
- [20] Z.-M. He, Z.-F. Liu, X.-H. Liu, and H.-B. Bian, "Improved method for determining active earth pressure considering arching effect and actual slip surface," *Journal of Central South University*, vol. 27, no. 7, pp. 2032–2042, 2020.
- [21] S. Y. Wang, L. Sun, C. Yang, and C. A. Tang, "Numerical study on static and dynamic fracture evolution around rock

- cavities,” *Journal of Rock Mechanics and Geotechnical Engineering*, vol. 5, no. 4, pp. 262–276, 2012.
- [22] S.-R. Zhang, B. Sun, C. Wang, and L. Yan, “Influence of intermediate principal stress on failure mechanism of hard rock with a pre-existing circular opening,” *Journal of Central South University*, vol. 21, no. 4, pp. 1571–1582, 2014.
- [23] X. Fan, X. Jiang, Y. Liu, H. Lin, K. Li, and Z. He, “Local stress distribution and evolution surrounding flaw and opening within rock block under uniaxial compression,” *Theoretical and Applied Fracture Mechanics*, vol. 112, no. 2, Article ID 102914, 2021.
- [24] D. Potyondy and P. Cundall, *The PFC Model for Rock: Predicting Rock-Mass Damage at the Underground Research Laboratory*, Itasca Consulting Group, Minneapolis, USA, 2002.
- [25] D. Potyondy and J. Autio, “Bonded-particle simulations of the insitu failure test at olkiluoto,” in *Proceedings of the 38th US Rock Mechanics Symposium*, pp. 1553–1560, Washington D.C., USA, July 2001.
- [26] X. Fan, Z. Yang, and K. Li, “Effects of the lining structure on mechanical and fracturing behaviors of four-arc shaped tunnels in a jointed rock mass under uniaxial compression,” *Theoretical and Applied Fracture Mechanics*, vol. 112, no. 2, Article ID 102887, 2021.
- [27] R. H. Cao, P. Cao, H. Lin, G. W. Ma, X. Fan, and X. G. Xiong, “Mechanical behavior of an opening in a jointed rock-like specimen under uniaxial loading: experimental studies and particle mechanics approach,” *Archives of Civil and Mechanical Engineering*, vol. 18, no. 1, pp. 198–214, 2018.
- [28] G. Kirsch, “Die Theorie der Elastizität und die Bedürfnisse der Festigkeitslehre,” *Veit Vereines Deutscher Ingenieure*, vol. 42, no. 28, pp. 797–807, 1898.
- [29] W. C. Zhu, J. Liu, C. A. Tang, X. D. Zhao, and B. H. Brady, “Simulation of progressive fracturing processes around underground excavations under biaxial compression,” *Tunneling and Underground Space Technology*, vol. 20, no. 3, pp. 231–247, 2005.
- [30] C. Wang, D. D. Tannant, and P. A. Lilly, “Numerical analysis of the stability of heavily jointed rock slopes using PFC2D,” *International Journal of Rock Mechanics and Mining Sciences*, vol. 40, no. 3, pp. 415–424, 2003.
- [31] K. M. Li, Y. H. Li, S. Xu, and L. An, “Method to determine microcosmic parameters of PFC2D numerical calculation model,” *Journal of Northeastern University (Natural Science)*, vol. 37, no. 4, pp. 563–567, 2016.

Research Article

The Analysis of Anchoring Mechanism of Rock Slope in Two Layers Based on the Nonlinear Twin-Shear Strength Criterion

X. B. Gu ¹, Y. H. Wang,² X. J. Ji ¹ and Y. H. Zhu ³

¹School of Civil Engineering, Nanyang Institute of Technology, Nanyang, China

²School of Civil Engineering, Sichuan University of Science & Engineering, Zigong, China

³School of Civil Engineering, Neijiang Normal University, Neijiang, Sichuan, China

Correspondence should be addressed to X. J. Ji; jifeng988@163.com

Received 18 February 2021; Revised 11 March 2021; Accepted 28 March 2021; Published 3 May 2021

Academic Editor: Yunteng Wang

Copyright © 2021 X. B. Gu et al. This is an open access article distributed under the Creative Commons Attribution License, which permits unrestricted use, distribution, and reproduction in any medium, provided the original work is properly cited.

The nonlinear strength criterion is introduced into the paper firstly, and then the geometric anchoring characteristic model of rock slope separated from two layers according to rock type with the fracture surface of log-spiral curve considering nonlinear twin-shear criterion subjected to seismic loads is established. Finally, some correlated influential parameters are analyzed, and the conclusions are drawn, showing that the intermediate principal stress has great influence on the total anchoring force of bolt P , so when different criteria are selected, the influence of intermediate principal stress should not be omitted. The effects of thickness ratio h_1/h_2 on total anchoring force increase gradually with the increase of inclination angle ϕ . The total anchoring force P decreases gradually with the increase of inclination angle ϕ and surcharge load q . The total anchoring force increases gradually with the increase of horizontal seismic acceleration coefficients k_h and geometric coefficients m_i and GSI.

1. Introduction

The destabilization of slope is a complex and dangerous geological disaster phenomenon [1]; it brings about huge harms to the safety of life and property, so the investigation on the slope stability is always focused on [2–4]. Many supporting schemes are adopted in the process of slope governance, for example, antislip pile and retaining wall. Meanwhile, their many shortcomings are found in the application of civil engineering [5], such as high cost, difficult construction, and heavy work. To overcome the mentioned problems [6], the application of the anchoring bar on the slope solves the above problem, and anchoring bar plays a great role in the support of slope [7]. So, a great deal of theoretical and experimental investigations about the supporting theory of anchoring bar are performed. The mechanical mechanism of the load transfer of anchoring bar is studied by Lutz et al. [8–10]. The influential factors about the bearing capacity of anchoring bar are analyzed by Hyet and Badwen [11] using a great deal of experimental investigations. In China, the further investigation about the

anchoring technology in the geotechnical engineering is performed. The fracture modes of foundation pit with the support of anchoring bar are investigated by Jin-Qing and Zheng [12] using the limit equilibrium theory and finite difference method. Then, the optimum design of mechanical model is calculated by Li-De and Cong-Xin [13] by using the strength reduction method of finite element. The distribution law of loads along the anchoring bar and the mechanism of anchoring forces are studied by Gamse and Oberguggenberger [14] by using numerical simulation and theoretical investigation. Then, the consolidation actions of anchoring bar on the layer rock slope are simulated by Chen et al. [15] using the finite difference software FLAC3D. To investigate the anchoring mechanism of rock slope, lots of fracture criteria are utilized [16]; for example, Mohr–Coulomb criterion [17] and Hoek–Brown criterion [18] are often adopted; although the obvious effects are obtained in the actual engineering, the influences of intermediate principal stress in these criteria are often omitted [19, 20], and a large deal of engineering practices demonstrated that the influence of intermediate principal stress

should be valued [21], so the twin-shear strength criterion in the paper is introduced; and, to conform to the engineering practice, earthquake loads, different rock types, and fracture modes of rock slope are, respectively, considered in the paper, a new thought and method for the stability design of rock slope can be provided.

The paper is organized as follows. In Section 2, nonlinear twin-shear criteria and method of upper bound limit analysis are introduced at first. In Section 3, the mechanical model of rock slope with the anchoring bar is established, the kinematic method of limit analysis considering nonlinear twin-shear criteria is deduced, and the anchoring mechanism of rock slope is analyzed. In Section 4, results and discussions are performed. In Section 5, conclusions are drawn.

2. Method and Theory

2.1. The Relevant Fracture Criterion. The nonlinear united strength failure criterion can be expressed as [22]

$$F = \sigma_1 - \frac{1}{1+c} (c\sigma_2 + \sigma_3) - \sigma_c \left[\frac{m}{(1+c)\sigma_c} (c\sigma_2 + \sigma_3) + s \right]^{(1/2)} = 0, \quad \text{when } F \geq F', \quad (1)$$

$$F' = \frac{1}{1+b} (\sigma_1 + c\sigma_2) - \sigma_3 - \sigma_c \sqrt{\frac{m\sigma_3}{\sigma_c} + s} \leq 0, \quad \text{when } F < F', \quad (2)$$

where σ_c is the uniaxial compressive strength of intact rock, m is constant value, and b represents the intermediate principle stress coefficients; s is a constant value relevant to the rock mass and it can be determined in the two following equations:

$$\frac{m}{m_i} = \exp\left(\frac{\text{GSI} - 100}{28 - 14D}\right), \quad (3)$$

$$s = \exp\left(\frac{\text{GSI} - 100}{9 - 3D}\right), \quad (4)$$

where D is a disturbance coefficient, and its range is from 0.0 to 1.0. GSI is the geological strength index, and its range is from 0 to 80. The magnitude of m_i is obtained from compression tests on an intact rock. If no test data are available, Hoek parents the approximate values for five types of rocks as follows [23]:

- (1) When the value of $m_i \approx 7$, it is applied to calculate carbonate rock types, such as dolomite, limestone, and marble
- (2) When the value of $m_i \approx 10$, it is applied to calculate lithified argillaceous rock types, such as mudstone, siltstone shale, and slate
- (3) When the value of $m_i \approx 15$, it is applied to calculate arenaceous rock types, such as mudstone, siltstone shale, and slate

- (4) When the value of $m_i \approx 17$, it is applied to calculate fine-grained polymineralic igneous crystalline rock types, such as andesite, dolerite, and diabase
- (5) When the value of $m_i \approx 25$, it is applied to calculate coarse-grained polymineralic igneous and metamorphic rock types, such as amphibolite, gabbro, gneiss, granite, and quartz diorite

In equations (1) and (2), when $c = 0$, this demonstrates that the influences of the intermediate principal stress are omitted, so Hoek–Brown criterion can be expressed as follows:

$$F = \sigma_1 - \sigma_3 - \sigma_c \left[\frac{m\sigma_3}{\sigma_c} + s \right]^{(1/2)}. \quad (5)$$

For $c = 1$, this demonstrates that the influences of the intermediate principal stress are taken into consideration, and the nonlinear united strength criterion can be obtained as follows [24]:

$$F(\underline{\sigma}) = \sigma_1 - \frac{1}{2} (\sigma_1 + \sigma_2) - \sqrt{\frac{m\sigma_c}{2} \times (\sigma_2 + \sigma_3) + s\sigma_c^2} \leq 0, \quad \text{when } F > F',$$

$$F(\underline{\sigma}) = \frac{1}{2} (\sigma_1 + \sigma_2) - \sigma_3 - \sqrt{m\sigma_c\sigma_3 + s\sigma_c^2} \leq 0, \quad \text{when } F < F'. \quad (6)$$

2.2. Kinematic Method of Limit Analysis. The seismic stability analysis is performed within the framework of limit analysis theory [25]. To get the upper bound solution, the construction of velocity is required in the method. The implementation of the kinematic method of limit analysis depends on the following fundamental inequality [26]:

$$\Theta_{ex}(\underline{U}) \leq \Theta_{mr}(\underline{U}), \quad (7)$$

where \underline{U} is any virtual admissible velocity field. $\Theta_{ex}(\underline{U})$ is the work performed by external loading, and $\Theta_{mr}(\underline{U})$ is the maximum resisting work originating from the rock materials. The formula of maximum resisting work according to Saada's work [27] can be obtained as

$$\Theta_{mr}(\underline{U}) = \int_{\Omega} \psi[\underline{d}(\underline{x})] d\Omega + \int_{\Sigma} \psi\{\nu(\underline{x}); [\underline{U}(\underline{x})]\} d\Sigma, \quad (8)$$

where \underline{d} is the strain rate tensor associated with \underline{U} at any point of rock mass volume Ω . $[\underline{U}(\underline{x})]$ means the jump at a point \underline{x} through a possible velocity discontinuity surface Σ and Σ' following its normal $\nu(\underline{x})$, and the ψ -functions are the support functions defined by the duality from the strength condition $F(\underline{\sigma}) \leq 0$.

$$\psi[\underline{d}] = \sup_{\underline{\sigma}} \{ \underline{\sigma} : \underline{d} | F(\underline{\sigma}) \leq 0 \}, \quad (9)$$

$$\psi[\nu; [\underline{U}]] = \sup_{\underline{\sigma}} \{ [\underline{U}] \cdot \underline{\sigma} \cdot \nu | F(\underline{\sigma}) \leq 0 \}. \quad (10)$$

For nonlinear twin-shear rock masses, the corresponding 3D closed-form expressions of the foregoing ψ -functions are obtained as follows [28]:

$$\psi[\underline{d}] = -\frac{s\sigma_c}{m} \text{tr} \underline{d} + \frac{3}{4} m\sigma_c \frac{\chi(\underline{d})}{\text{tr} \underline{d}}, \quad \text{if } \text{tr} \underline{d} \geq 0, \quad (11)$$

$$\chi(\underline{d}) = [\max(0, d_1) + \max(0, d_2) + \max(0, d_3)]^2, \quad (12)$$

where d_1 , d_2 , and d_3 represent the eigenvalues of \underline{d} .

Similarly, it has been found that the ψ -functions relative to a velocity jump and defined by equation (7) take the following form:

$$\psi[\underline{\gamma}; [\underline{U}]] = -\frac{s\sigma_c}{m} [\underline{U}] \cdot \underline{\gamma} + \frac{3}{4} m\sigma_c \frac{\chi(\underline{\gamma}; [\underline{U}])}{[\underline{U}] \cdot \underline{\gamma}}, \quad \text{if } [\underline{U}] \cdot \underline{\gamma} > 0, \quad (13)$$

where

$$\chi(\underline{\gamma}; [\underline{U}]) = \frac{1}{4} (|[\underline{U}]| - [\underline{U}] \cdot \underline{\gamma})^2. \quad (14)$$

It should be noted that the conditions $\text{tr} \underline{d} > 0$ in equation (11) and $[\underline{U}] \cdot \underline{\gamma} > 0$ in equation (13) demonstrate the fact that $\psi[\underline{d}] < +\infty$ and $\psi[\underline{\gamma}; [\underline{U}]] < +\infty$, respectively. These conditions are necessary for the kinematic method of limit analysis expressed by equation (7) which results in nontrivial upper bound solutions.

3. The Establishment of Mechanical Model

3.1. The Analysis of Failure Mechanism. The failure mechanism, depicted in Figure 1 and considered in the investigation, is a direct transportation of those usually employed for homogeneous nonlinear twin-shear strengthen slope. In such model, two layers of rock mass are composed in the rock mass slope, there are, respectively, different compressive strengths and unit weight in two layers, and the earthquake loads are considered in two layers of rock mass; and the quasistatic method is adopted in the manuscript. Because horizontal wave has a great influence on the fracture of rock slope, only horizontal action of earthquake loads is considered. Its inclined angle along the fracture surface AC is ϕ . The failure routine is a straight line in the upper layers of rock slope, and it is assumed that the fracture surface is parallel with the rock slope surface, so quadrangle is parallel quadrangle. There exist uniform distribution external loads q in the roof of rock slope. There are lots of support bars in the rock slope surface. It is assumed that fracture surface of rock slope represents a log-spiral curve in lower layer of rock slope, a volume of rock mass is rotating about a point O with an angular velocity ω , the curve CE separating this volume from the structure that is kept motionless is a log-spiral arc and focus O, and it necessarily follows that the velocity jump at any point of line CE is inclined at angle ϕ with respect to the tangent at the same point. The inclination angle of anchoring bar is β with a horizontal direction. Five parameters are involved in such a mechanism: four angles θ_1 ,

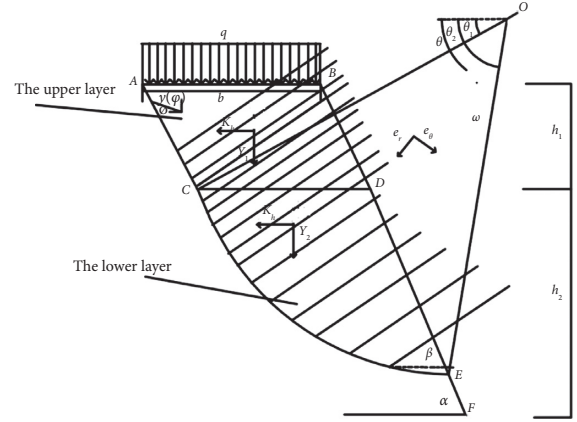


FIGURE 1: The anchoring mechanism of rock slope.

θ_2 , ϕ , and β and the distance $r_0 = R$ defining the radius of log-spiral curve for $\theta = \theta_1$; accordingly, this curve is defined in polar coordinates (o, r, θ) by equation $r = r_0 e^{(\theta - \theta_1) \tan \phi}$.

3.2. The Work Rate of External Forces and Maximum Resisting Work Rate

3.2.1. The Work of External Forces in the Upper Layer of Rock Slope

- (1) The work rate of gravitational force is

$$\Theta_{ug} = \gamma_1 b h_1 V \sin(\beta - \phi), \quad (15)$$

where Θ_{ug} is the work rate of gravitational force in the upper layer of rock slope; γ_1 is the unit weight of rock mass in the upper layer of rock slope.

- (2) The work rate of external load q is

$$\Theta_{uq} = q b V \sin(\beta - \phi), \quad (16)$$

where Θ_{uq} is the work rate of uniform distribution load q and b is the width of roof.

- (3) The work rate of seismic load is

$$\Theta_{uhs} = -k_h \gamma_1 b h_1 V \cos(\beta - \phi), \quad (17)$$

where Θ_{uhs} is the work rate of horizontal earthquake loads in the upper layer; k_h is the horizontal earthquake load coefficient.

- (4) The work rate of roof bolt is

$$\Theta_{up} = -\sum_{i=1}^n P_i V \cos(\beta - \phi) \cos \beta, \quad (18)$$

where Θ_{up} is the work rate of antisliding force about anchors in the upper layer; P_i is the antisliding force of the i th roof bolt.

- (5) The maximum resisting work rate is

$$\Theta_{mru} = \sigma_{Cu} \frac{h_1}{\sin \alpha} V \cos \phi \left[\frac{s}{m} + \frac{3}{4} m \left(\frac{1 - \sin \phi}{2 \sin \phi} \right)^2 \right], \quad (19)$$

where Θ_{mru} is the maximum resisting work rate in the upper layer; σ_{Cu} is the compressive strength of rock mass in the upper layer.

3.2.2. The Work Rate of External Forces in the Lower Layer of Rock Slope

(1) The work rate of gravitational force is

$$l_1 = \frac{1}{3} \frac{e^{3 \tan \varphi (\theta_1 - \theta_2)} (3 \tan \varphi \cos \theta_2 + \sin \theta_2) - (3 \tan \varphi \cos \theta_1 + \sin \theta_1)}{9 \tan^2 \varphi + 1}, \quad (20a)$$

$$l_2 = \frac{1}{6} \sin \theta_1 \left[\frac{2b}{r_0} \cos \theta_1 - \left(\frac{b}{r_0} \right)^2 \right], \quad (20b)$$

$$l_3 = -\frac{1}{3} \left(\frac{r_B}{r_0} \right)^3 \sin^3 (\theta_B + \alpha) \left[\frac{\cos \alpha}{2} \left(\frac{1}{\sin^2 (\theta_B + \alpha)} - \frac{1}{\sin^2 (\theta_2 + \alpha)} \right) + \sin \alpha \left(\frac{\cos (\theta_B + \alpha)}{\sin (\theta_B + \alpha)} \frac{\cos (\theta_2 + \alpha)}{\sin (\theta_2 + \alpha)} \right) \right]. \quad (20c)$$

(2) The work rate of seismic load is

$$\Theta_{lhs} = k_h \gamma_2 r_0^3 \omega (l_4 + l_5 + l_6), \quad (21)$$

$$\Theta_{ig} = \gamma_2 r_0^3 \omega (l_1 + l_2 + l_3), \quad (20)$$

where Θ_{ig} is the work of gravitational force; expressions of l_1 , l_2 , and l_3 can be, respectively, expressed as

where Θ_{lhs} is the work rate of seismic load. The expressions of l_4 , l_5 , and l_6 can be, respectively, expressed as

$$l_4 = \frac{1}{3} \frac{e^{\tan \varphi (\theta_1 - \theta_2)} (3 \tan \varphi \cos \theta_2 - \cos \theta_2) - (3 \tan \varphi \sin \theta_1 - \cos \theta_1)}{9 \tan^2 \varphi + 1}, \quad (21a)$$

$$l_5 = -\frac{1}{3} \left(\frac{b}{r_0} \right) \sin^3 \theta_1, \quad (21b)$$

$$l_6 = -\frac{1}{3} \left(\frac{r_B}{r_0} \right)^3 \sin^3 (\theta_B + \alpha) \left[-\frac{\sin \alpha}{2} \left(\frac{1}{\sin^2 (\theta_B + \alpha)} - \frac{1}{\sin^2 (\theta_2 + \alpha)} \right) + \cos \alpha \left(\frac{\cos (\theta_B + \alpha)}{\sin (\theta_B + \alpha)} \frac{\cos (\theta_2 + \alpha)}{\sin (\theta_2 + \alpha)} \right) \right], \quad (21c)$$

where different parameters are shown in formulas (20)–(21c). The expressions of r_B and θ_B can be, respectively, expressed as

$$r_B = r_0 \sqrt{1 - 2 \left(\frac{b}{r_0} \right) \cos \theta_1 + \left(\frac{b}{r_0} \right)^2}, \quad (21d)$$

$$\theta_B = \arctan \left(\frac{\sin \theta_1}{\cos \theta_1 - (b/r_0)} \right). \quad (21e)$$

(3) The work rate of roof bolt is

$$\Theta_{lp} = \sum_{i=1}^n P_i r_0 \omega e^{(\theta - \theta_1) \tan \phi} \sin (\theta - \beta), \quad (22)$$

where Θ_{lp} is the work rate of antisliding force of roof bolts; P_i is the antisliding force of the i th bolt. i is the number of roof bolts.

(4) The maximum resisting work rate is defined as follows.

The maximum resisting work results from the velocity jump along the log-spiral line CF , and the expression of resisting work derived from equations (10)–(12) can be depicted as follows:

$$\Theta_{mrl} = \frac{1}{2} \sigma_{CL} \omega r_0^2 \left(e^{2(\theta_1 - \theta_2) \tan \phi} - 1 \right) \left[\frac{s}{m} + \frac{3}{4} m \left(\frac{1 - \sin \phi}{2 \sin \phi} \right)^2 \right]. \quad (23)$$

3.2.3. The Expression of Anchoring Force. According to the fundamental inequality (7), the expression of anchoring force $\sum_{i=1}^n P_i$ can be shown as follows:

$$\sum_{i=1}^n P_i \leq \frac{\Theta_{mru} + \Theta_{mrl} - \Theta_{ug} - \Theta_{uq} + \Theta_{uhs} - \Theta_{lhs} - \Theta_{ig}}{r_0 \omega e^{(\theta - \theta_1) \tan \phi} \sin (\theta - \beta) - V \cos (\beta - \theta) \cos \beta}. \quad (24)$$

3.2.4. *The Critical Anchoring Force.* According to the investigation of Ling and Leshchinsky [29], the expression of the total anchoring force is defined as

$$F = \frac{\sum_{i=1}^n P_i}{0.5\gamma H^2}. \quad (25)$$

According to the principal of limit analysis theory, when $f = 1$, the critical total anchoring force can be expressed as

$$F \leq F_u = \min \frac{\Theta_{mru} + \Theta_{mrl} - \Theta_{ug} - \Theta_{uq} + \Theta_{uhs} - \Theta_{lhs} - \Theta_{lg}}{0.5(h_1 + h_2)^2 \left[r_0 \omega e^{(\theta - \theta_1) \tan \phi} \sin(\theta - \beta) - V \cos(\beta - \theta) \cos \beta \right]} \left(\frac{1}{\gamma_1} + \frac{1}{\gamma_2} \right). \quad (26)$$

4. Results and Discussion

4.1. *The Effects of Intermediate Principal Stress on the Total Anchoring Force.* To investigate the influence of intermediate principal stress on the total anchoring force, the following parameters are listed as follows: $r_0 = 12$ m, $m_i = 10$, $GSI = 10$, and $b = 5$ m; $\gamma_1 = 15$ (kN/m³), $\gamma_2 = 20$ (kN/m³), $h_1 = 8$ m, $h_2 = 9$ m, $q = 20$ kPa, $\omega = 0.2$, $V = 0.1$ mm/s, $\sigma_{cu} = 6$ MPa, $\sigma_{cl} = 10$ MPa, $\alpha = 20^\circ$, $kh = 0.18$, $\theta_1 = 200$, $\theta_2 = 500$, $\theta = 300$, $\theta_B = 35^\circ$, $\theta_B = 35^\circ$, and $\beta = 20^\circ$. It is shown in Figure 2 that the total anchoring force P increases as the velocity inclination angle increases whether Hoek–Brown criterion [30] or twin-shear strength criterion strengthens. However, it can be found in comparison that the magnitude for $c = 1$ (it means that the influence of intermediate principal stress is not considered) is higher than one of $c = 0$ (it means that the influence of intermediate principal stress is considered), and the conclusions are drawn, showing that the intermediate principal stress has a great influence on total anchoring force of bolt P , so when different criteria are selected, the influence of intermediate principal stress is not omitted.

4.2. *The Influence of Bolt Inclination Angle on the Total Anchoring Force.* The range on the inclination angle of bolt is 10° – 35° , so the inclination angle of anchor is, respectively, adopted for $\beta = 10^\circ$, 20° , and 30° and the comparison and analysis are carried out among three cases. The following parameters are determined: $r_0 = 12$ m, $m_i = 10$, $GSI = 10$, and $b = 5$ m; $\gamma_1 = 15$ (kN/m³), $\gamma_2 = 20$ (kN/m³), $h_1 = 8$ m, $h_2 = 9$ m, $q = 20$ kPa, $\omega = 0.2$, $V = 0.1$ mm/s, $\sigma_{cu} = 6$ MPa, $\sigma_{cl} = 10$ MPa, $\alpha = 20^\circ$, $kh = 0.18$, $\theta_1 = 20^\circ$, $\theta_2 = 50^\circ$, $\theta = 30^\circ$, and $\theta_B = 35^\circ$. The effects of anchoring inclination angle α on the total anchoring force are depicted in Figure 3. It can be found that the total anchoring force P decreases gradually with the increase of inclined angle ϕ ; and it can also be found that the total anchoring force P increases gradually as the anchoring inclination angle β increases. The influence of anchoring inclination angle β on the total anchoring force decreases gradually with the increase of velocity inclination angle ϕ . For example, for $\phi = 10^\circ$, the value of P increases approximately by 108% when the value of α increases from 10° to 30° ; then, for $\phi = 15^\circ$, it increases only by 59.8%.

4.3. *The Influence of Rock Layer Thickness on the Total Anchoring Force P .* The effects of thickness of rock layer on the total anchoring force are depicted in Figure 4. To explain the relation, the ratio of thickness between two rock layers is, respectively, selected as $1/3$, $1/2$, and $2/3$ in this paper, and the following parameters are listed: $r_0 = 12$ m, $m_i = 10$, $GSI = 10$, and $b = 5$ m; $\gamma_1 = 15$ (kN/m³) and $\gamma_2 = 20$ (kN/m³); $h_1 = 8$ m; $h_2 = 9$ m; $q = 20$ kPa, $\omega = 0.2$, $V = 0.1$ mm/s, $\sigma_{cu} = 6$ MPa, $\sigma_{cl} = 10$ MPa, $\alpha = 200$, $kh = 0.18$, $\theta_1 = 200$, $\theta_2 = 500$, $\theta = 300$, $\theta_B = 35^\circ$, and $\beta = 20^\circ$. It can be found in Figure 4 that the total anchoring force P increases gradually as the thickness ratio of rock layer (namely, different rock types) increases, but it can be also found that the effects of thickness ratio (h_1/h_2) on total anchoring force increase gradually with the increase of inclination angle ϕ ; to illustrate, for $\phi = 100$, when (h_1/h_2) increases from $1/2$ to $2/3$, the value of total anchoring force P increases approximately by 11.76%; then, for $\phi = 250$, when (h_1/h_2) increases from $1/2$ to $2/3$, the value of P increases by 27.12%. So, conclusions can be drawn, showing that the total anchoring force P increases gradually with the increase of thickness ratio, but the influence of the thickness ratio on the anchoring force P gradually increases with the increase of velocity inclination angle ϕ .

4.4. *The Influence of Surcharge Load q on the Anchoring Force P .* When the influence of surcharge load q is taken into account, to explain the relation, the value of surcharge load q is, respectively, adopted as 10 MPa, 15 MPa, and 20 MPa in this paper. The following parameters are listed: $r_0 = 12$ m, $m_i = 10$, $GSI = 10$, and $b = 5$ m; $\gamma_1 = 15$ (kN/m³) and $\gamma_2 = 20$ (kN/m³); $h_1 = 8$ m; $h_2 = 9$ m; $\omega = 0.2$, $V = 0.1$ mm/s, $\sigma_{cu} = 6$ MPa, $\sigma_{cl} = 10$ MPa, $\alpha = 200$, $kh = 0.18$, $\theta_1 = 200$, $\theta_2 = 500$, $\theta = 300$, $\theta_B = 35^\circ$, and $\beta = 20^\circ$; the effects of surcharge load q on the total anchoring force are depicted in Figure 5. It can be found that the total anchoring force P decreases gradually with the increase of inclination angle ϕ and surcharge load q . So, conclusions can be drawn, showing that the surcharge load q of rock slope has great influences on the total anchoring force P .

4.5. *The Influence of Horizontal Seismic Acceleration Coefficients on the Total Anchoring Force.* When the influences of horizontal seismic acceleration coefficients k_h on the

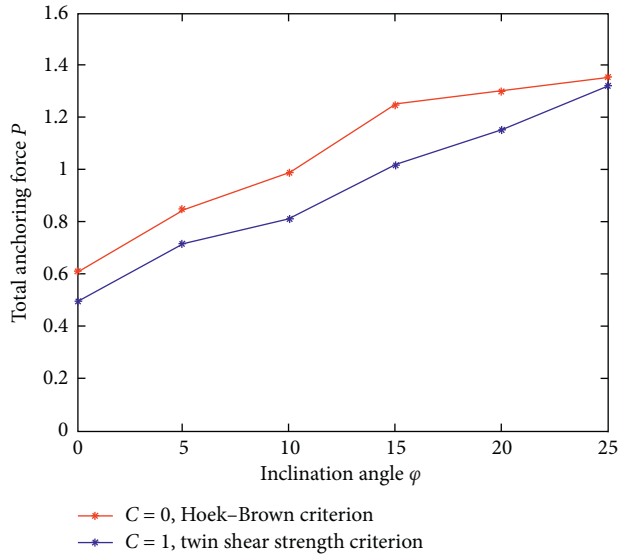


FIGURE 2: The relation between intermediate principal stress and anchoring force.

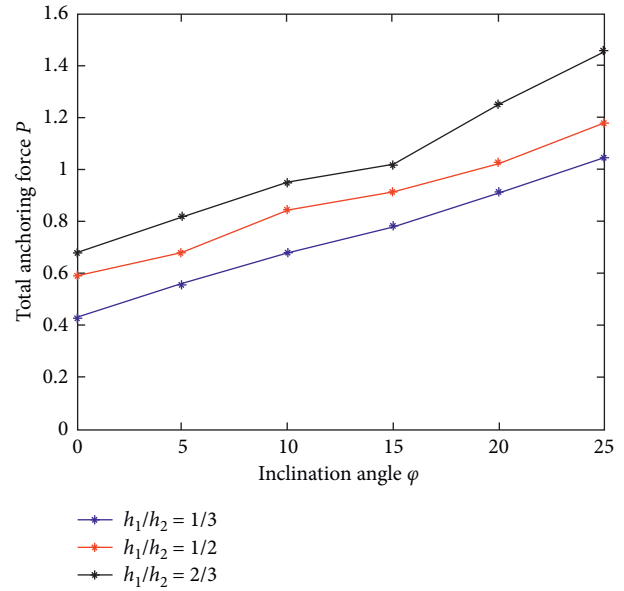


FIGURE 4: The relation between unit weight and anchoring force.

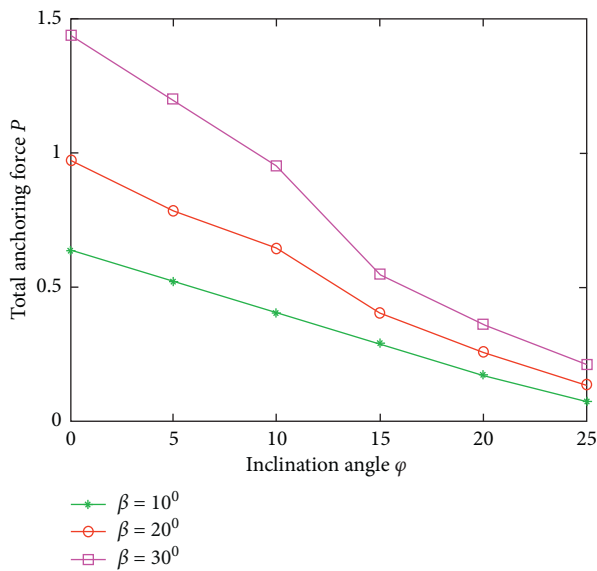


FIGURE 3: The relation between bolt inclination angle and anchoring force.

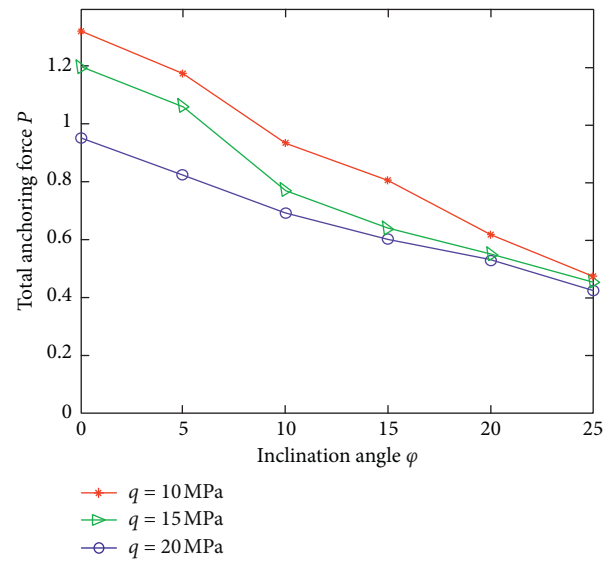


FIGURE 5: The relation between surcharge load and anchoring force.

anchoring force are considered, the following parameters are listed: $r_0 = 12$ m, $m_i = 10$, $GSI = 10$, and $b = 5$ m; $\gamma_1 = 15$ (kN/m³) and $\gamma_2 = 20$ (kN/m³); $h_1 = 8$ m; $h_2 = 9$ m; $q = 30$ kPa, $\omega = 0.2$, $V = 0.1$ mm/s, $\sigma_{cu} = 6$ MPa, $\sigma_{cl} = 10$ MPa, $\alpha = 200$, $\theta_1 = 200$, $\theta_2 = 500$, $\theta = 300$, and $\theta_B = 35^\circ$. The effects of k_h on the total anchoring force are plotted in Figure 6. It can be found in Figure 6 that the total anchoring force increases gradually with the increase of horizontal seismic acceleration coefficients; it demonstrates that the slope becomes more dangerous; for example, for $\phi = 100$, when the value of k_h increases from 0.08 to 0.24, the total anchoring force increases from 0.5206 to 1.0322.

4.6. The Influence of Geometric Coefficients GSI and m_i on the Total Anchoring Force. When the influences of geometric coefficients GSI and m_i on the anchoring force are, respectively, regarded, the following parameters are listed: $r_0 = 12$ m; $b = 5$ m; $\gamma_1 = 15$ (kN/m³) and $\gamma_2 = 20$ (kN/m³); $h_1 = 8$ m; $h_2 = 9$ m; $q = 30$ kPa, $\omega = 0.2$, $V = 0.1$ mm/s, $\sigma_{cu} = 6$ MPa, $\sigma_{cl} = 10$ MPa, $\alpha = 200$, $k_h = 0.18$, $\theta_1 = 200$, $\theta_2 = 500$, $\theta = 300$, and $\theta_B = 35^\circ$. The effects of GSI and m_i on the anchoring force are, respectively, shown in Table 1. It can be found in Table 1 that the total anchoring force decreases gradually with the increase of geometric coefficients m_i and GSI , and the geometric parameters have a great influence on the total anchoring force P .

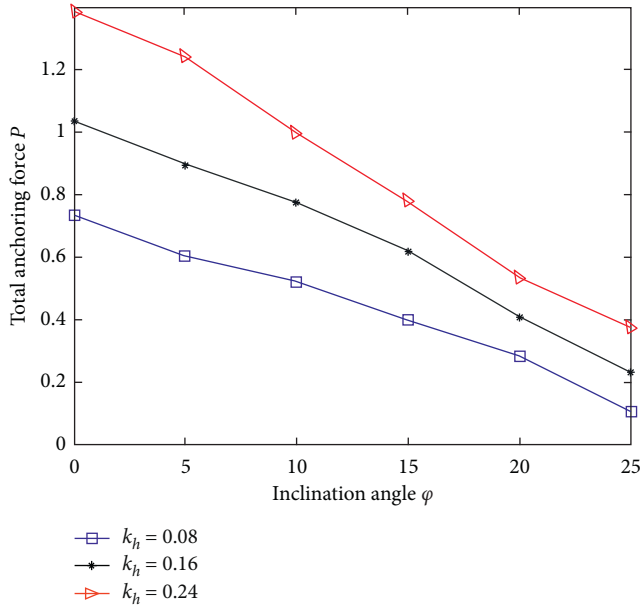


FIGURE 6: The relation between horizontal seismic acceleration coefficients and anchoring force.

TABLE 1: The relation between anchoring force P and geometric parameters GSI and m_i .

GSI	$m_i = 1$	$m_i = 10$	$m_i = 15$	$m_i = 17$	$m_i = 25$
10	1.4256	1.2826	1.0586	0.8264	0.6952
20	1.2754	1.1346	0.9421	0.7188	0.5684
30	1.1315	1.0023	0.8685	0.6021	0.5023
40	0.9524	0.8933	0.7876	0.5321	0.3956
50	0.7564	0.6992	0.6275	0.4897	0.3211
60	0.6025	0.5624	0.5033	0.4533	0.2836

5. Conclusions

The limit dynamic analysis method of upper bound solution based on nonlinear twin-shear criterion is adopted to analyze anchoring mechanism of two layers of failure slope in the investigation. The intermediate principal stress, the anchoring inclination angle β , thickness ratio (h_1/h_2) of rock layer, surcharge load q , seismic acceleration coefficients k_h , and geometric coefficients GSI and m_i have great influences on the total anchoring force. Finally, the following conclusions are drawn:

- (1) The intermediate principal stress has a great influence on the total anchoring force of bolt P , so when different criteria are selected, the influence of intermediate principal stress is not omitted. The total anchoring force P decreases gradually with the increase of inclination angle ϕ . The total anchoring force P increases gradually as the anchoring inclination angle β increases. The influence of anchoring inclination angle β on the total anchoring force decreases gradually with the increase of velocity inclination angle ϕ .

- (2) The total anchoring force P increases gradually as the thickness ratio of rock layer (namely, different rock types) increases. But the effects of thickness ratio (h_1/h_2) on total anchoring force increase gradually with the increase of inclination angle ϕ . The total anchoring force P decreases gradually with the increase of inclination angle ϕ and surcharge load q .
- (3) The total anchoring force increases gradually with the increase of horizontal seismic acceleration coefficients. The total anchoring force decreases gradually with the increase of geometric coefficients m_i and GSI, and the geometric parameters have a great influence on the total anchoring force P .

Data Availability

The data used to support the findings of this study are available from the corresponding author upon request.

Conflicts of Interest

The authors declare that they have no conflicts of interest.

Acknowledgments

This work was supported by the first batch of Natural Science Foundation of Sichuan Provincial Department of Education (no. 17ZA0270), the cross project in Nanyang Institute of Technology (230067), the opening projection of Sichuan Province University Key Laboratory of Bridge Non-Destruction Detecting and Engineering Computing (2017QYY01), the National Natural Science Foundation of China (41672357), the Start-Up Foundation (510126), and the Sichuan Science and Technology Program (no. 2020YJ0424).

References

- [1] X.-B. Gu and Q.-H. Wu, "Seismic stability analysis of waterfront rock slopes using the modified pseudo-dynamic method," *Geotechnical and Geological Engineering*, vol. 37, no. 3, pp. 1743–1753, 2019.
- [2] X.-P. Zhou, Y.-X. Zhang, Q.-L. Ha, and K.-S. Zhu, "Micro-mechanical modelling of the complete stress-strain relationship for crack weakened rock subjected to compressive loading," *Rock Mechanics and Rock Engineering*, vol. 41, no. 5, pp. 747–769, 2008.
- [3] X. P. Zhou, E. M. Xia, H. Q. Yang, and Q. H. Qian, "Different crack sizes analyzed for surrounding rock mass around underground caverns in Jinping I hydropower station," *Theoretical and Applied Fracture Mechanics*, vol. 57, no. 1, pp. 19–30, 2012.
- [4] X. P. Zhou, H. Cheng, and Y. F. Feng, "An experimental study of crack coalescence behaviour in rock-like materials containing multiple flaws under uniaxial compression," *Rock Mechanics and Rock Engineering*, vol. 47, no. 6, pp. 1961–1986, 2014.
- [5] X.-P. Zhou and J.-Z. Zhang, "Experimental study on the growth, coalescence and wrapping behaviors of 3d cross-embedded flaws under uniaxial compression," *Rock Mechanics and Rock Engineering*, vol. 51, no. 5, pp. 1379–1400, 2018.

- [6] X.-P. Yoshimine, "Analysis of the localization of deformation and the complete stress-strain relation for mesoscopic heterogeneous brittle rock under dynamic uniaxial tensile loading," *International Journal of Solids and Structures*, vol. 41, no. 5-6, pp. 1725-1738, 2004.
- [7] X. P. Yu and H. Q. Yang, "Micromechanical modeling of dynamic compressive responses of mesoscopic heterogeneous brittle rock," *Theoretical and Applied Fracture Mechanics*, vol. 48, no. 1, pp. 1-20, 2007.
- [8] L. Lutz and Gergeley, "Mechanics of bond and slip of deformed bars in concrete," *Journal of American Concrete Institute*, vol. 64, no. 11, pp. 711-721, 1967.
- [9] N. W. Hanson, "Influence of surface roughness of prestressing strand on bond performance," *PCI Journal*, vol. 14, no. 1, pp. 32-45, 1969.
- [10] Y. Goto, "Cracks formed in concrete around deformed tension bars," *Journal of American Concrete Institute*, vol. 58, no. 4, pp. 244-251, 1971.
- [11] A. Hyet and J. Bawden, "The effect of rock mass confinement on the band strength of fully grouted cable bolts," *International Journal of Rock Mechanics and Mining Sciences & Geomechanics Abstracts*, vol. 29, no. 5, pp. 503-524, 1992.
- [12] J. Jin-Qing and W. Zheng, "Study and application of flexible retaining method with prestressed anchor," *Chinese Journal of Geotechnical Engineering*, vol. 27, no. 11, pp. 1257-1261, 2005.
- [13] W. Li-de and C. Cong-xin, "Developing the numerical simulating methods of the 3-D bolt," *Rock and Soil Mechanics*, vol. 28, pp. 315-320, 2007.
- [14] S. Gamse and M. Oberguggenberger, "Assessment of long-term coordinate time series using hydrostatic-season-time model for rock-fill embankment dam," *Structural Control and Health Monitoring*, vol. 24, no. 1, p. e1859, 2017.
- [15] H. Chen, B. Jiang, N. Lu, and Z. Mao, "Multi-mode kernel principal component analysis-based incipient fault detection for pulse width modulated inverter of China Railway High-speed 5," *Advances in Mechanical Engineering*, vol. 9, no. 10, 2017.
- [16] M. M. Kou, Y. J. Lian, and Y. T. Wang, "Numerical investigations on crack propagation and crack branching in brittle solids under dynamic loading using bond-particle model," *Engineering Fracture Mechanics*, vol. 212, pp. 41-56, 2019.
- [17] S. Maghous, P. de Buhan, and A. Bekaert, "Failure design of jointed rock structures by means of a homogenization approach," *Mechanics of Cohesive-Frictional Materials*, vol. 3, no. 3, pp. 207-228, 1998.
- [18] A. Serrano and C. Olalla, "Ultimate bearing capacity of rock masses," *International Journal of Rock Mechanics and Mining Sciences & Geomechanics Abstracts*, vol. 31, no. 2, pp. 93-106, 1994.
- [19] X. P. Wong, Y. X. Zhang, and Q. L. Ha, "Real-time computerized tomography (CT) experiments on limestone damage evolution during unloading," *Theoretical and Applied Fracture Mechanics*, vol. 50, no. 1, pp. 49-56, 2008.
- [20] X. P. Zhou, J. Bi, and Q. H. Qian, "Numerical simulation of crack growth and coalescence in rock-like materials containing multiple pre-existing flaws," *Rock Mechanics And Rock Engineering*, vol. 48, no. 3, pp. 1097-1114, 2015.
- [21] X.-P. Zhou, Y.-D. Shou, and Q.-H. Qian, "Three-dimensional nonlinear strength criterion for rock-like materials based on the micromechanical method," *International Journal of Rock Mechanics and Mining Sciences*, vol. 72, pp. 54-60.
- [22] M.-H. Yu, Y.-W. Zan, and J. Zhao, "A unified strength criterion for rock material," *International Journal of Rock Mechanics and Mining Sciences*, vol. 39, no. 8, pp. 975-989.
- [23] J. Bi, X. P. Zhou, and Q. H. Qian, "The 3D numerical simulation for the propagation process of multiple pre-existing flaws in rock-like materials subjected to biaxial compressive loads," *Rock Mechanics and Rock Engineering*, vol. 49, no. 5, pp. 1611-1627, 2016.
- [24] X. B. Gu, Q. H. Wu, and Y. H. Zhu, "The experimental investigation on the propagation process of crack for brittle rock similar material," *Geotechnical and Geological Engineering*, vol. 37, no. 6, pp. 4714-4740, 2019.
- [25] W. F. Chen and X. L. Liu, *Limit Analysis in Soil Mechanics*, Elsevier, Amsterdam, The Netherlands, 1990.
- [26] X.-P. Zhou, X.-B. Gu, and Q.-H. Qian, "Seismic bearing capacity of shallow foundations resting on rock masses subjected to seismic loads," *KSCE Journal of Civil Engineering*, vol. 20, no. 1, pp. 216-228, 2016.
- [27] Z. Saada and S. Maghousb, "Gamier, D. Seismic bearing capacity of shallow foundations near rock slopes using the generalized Hoek-Brown criterion," *International Journal for Numerical and Analytical Methods in Geomechanics*, vol. 35, no. 6, pp. 211-218, 2011.
- [28] B. G. Rajesh and D. Choudhury, "Generalized seismic active thrust on retaining wall with submerged backfill using modified pseudo-dynamic method," *International Journal of Geomechanics*, vol. 17, no. 3, pp. 261-273, 2016.
- [29] H. I. Ling and D. Leshchinsky, "Effects of vertical acceleration on seismic design of geosynthetic-reinforced soil structures," *Géotechnique*, vol. 48, no. 3, pp. 347-373, 1998.
- [30] Z. Saada, S. Maghous, and D. Garnier, "Bearing capacity of shallow foundations on rocks obeying a modified Hoek-Brown failure criterion," *Computers and Geotechnics*, vol. 35, no. 2, pp. 144-154, 2008.

Research Article

Similar Physical Modeling of Roof Stress and Subsidence in Room and Pillar Mining of a Gently Inclined Medium-Thick Phosphate Rock

Xiaoshuang Li,^{1,2,3,4} Zhifang Liu,¹ and Shun Yang¹ 

¹School of Resources and Environmental Engineering, Jiangxi University of Science and Technology, Ganzhou, Jiangxi 341000, China

²School of Resources Engineering, Xi'an University of Architecture and Technology, Xi'an, Shanxi 710000, China

³Sinosteel Maanshan General Institute of Mining Research Co. Ltd., Maanshan, Anhui 243000, China

⁴State Key Laboratory of Safety and Health for Metal Mines, Maanshan, Anhui 243000, China

Correspondence should be addressed to Shun Yang; shunyang202016@163.com

Received 24 December 2020; Revised 24 February 2021; Accepted 3 April 2021; Published 26 April 2021

Academic Editor: Rihong Cao

Copyright © 2021 Xiaoshuang Li et al. This is an open access article distributed under the Creative Commons Attribution License, which permits unrestricted use, distribution, and reproduction in any medium, provided the original work is properly cited.

Gently inclined medium-thick orebodies are generally recognized as the most difficult type of orebody to mine, using current available strategies (i.e., the room and pillar method). In the present study, a similar physical model was used to investigate the roof stress and subsidence for mining gently inclined medium-thick phosphate rock from the Jinning Phosphate Mine, Yunnan Province, China. The stress field, displacement field, and roof failure evolution characteristics of the surrounding rock with stope structures of 3 m, 5 m, or 8 m ore pillars were considered. The results showed that, after mining stopped, obvious pressure relief areas formed above the three stope structures, and pressure-bearing areas formed at the front of the roof. With extending the mining in the working face, the stress relief boundary also gradually increased, and the top of the roof tended to sink with a maximum subsidence of -14.58 mm, -4.67 mm, and -3.48 mm. Due to the mining activity, the overlying strata bent and subsided from top to bottom, creating bending subsidence, fracture, and caving zones.

1. Introduction

Gently inclined medium-thick orebodies are generally defined as those characters with a thickness of 5–15 m and a dip angle of 5–50°. The effective method of mining them has an intense interest in a wide range of rock engineering processes [1–4]. The thickness and dip angle of an orebody limit the flexible use of trolleybuses, which is a major problem in the mine output due to result in excessive losses. The room and pillar mining method has been considered as an effective mining strategy for gently inclined medium-thick orebodies [5–7]. However, this method greatly disturbs the initial stress within the rock. Due to mining activity, the overlying rock mass of the stope undergoes continuous dynamic changes in its stress and displacement fields under spatio-temporal dimension.

Most previous research in terms of metal and coal mines has only focused on gently inclined medium-thick phosphate orebodies [8–11]. These investigations considered deformation and failure laws of the overlying rock mass affected by the stope parameters, room and pillar mining size, and the roof; for example, previous studies indicated that the careful selection of stope parameters plays an important role in ensuring a safe mining environment and in protecting surrounding buildings [12–16]. The load-bearing capacity of an ore pillar is positively related to its size [17, 18]. Zhao et al. [19] considered the influence of burial depth and used Platts' theory to derive a theoretical formula for the optimal ore pillar size, combining this with the characteristics of phosphate rock. Li and Chai [20] established a mechanical model based on the medium-thick plate theory for metal mine caving and filling isolation pillars for

selection of the pillar size. Wang et al. [21] used a numerical and similar physical model to analyze the stress and deformation of the roof and the failure rules for the overlying rock. Guan et al. [22] investigated a gently inclined medium-thick gold orebody by the numerical and physical models to assess the displacement and surface settlement rules for the overlying rock in a filling stope. Steel fiber-reinforced shotcrete is adopted by Zhang et al. [23] to improve the excavation rate and guarantee the safety of roadways when passing through unfavorable geological bodies.

However, phosphorite rock mines differ from metal and coal mines in terms of the orebody morphology, metallogenetic regularity, stratum structure, and tectonic stress. The lower the rock strength, the higher the swelling, and rheological characteristics make the roof structure around an ore pillar more likely to fail under the mining and water load. Thus, the objective of this study is to explore the deformation and failure laws for the rock surrounding the roof of a gently sloping medium-thick phosphate rock in room and pillar mining and to consequently identify an optimal stope structure within the No. 6 mining area of the Jinning Phosphate Mine in Yunnan Province, China. Similar physical experiments were adopted to investigate the rock mass stability of three stope structures consisting of 3 m, 5 m, and 8 m ore pillars. The findings of this study are of particular use for geotechnical engineering on providing guidelines for mining similar phosphate rocks to ensure the sustainable development of mining systems.

2. Engineering Background

The Jinning Phosphate Mine is located in Kunming City, Yunnan Province, China (see Figure 1). Figure 1 shows the location of the mine (see Figure 1(a)), the remote sensing image of the mine (see Figure 1(b)), and the current mine structure (see Figure 1(c)). It is a large sedimentary rock phosphate deposit located in the hinterland of the Yunnan Plateau. The elevation ranges from 2202.0 m to 2459.3 m above sea level. The single ore bed has a monoclinical structure that runs from north to south. The average thickness of the industrial layer is 10.45 m, with a phosphate ore percent of 26–30%. The orebody is classified as a gently inclined medium-thick phosphate orebody. After decades of pit mining, the western area of the No. 6 pit has been fully mined. The eastern area has a mining depth of 150–180 m, a 1000 m trend extension, and an inclination angle of 40–50°. If the phosphate rock had continued to be mined using an open pit, the mining operation would lose the economic and technical advantages. The transition from open pit to underground orebody mining would be the best strategy.

For underground mining, the roof rock and the mining pillars of a stope form a unified system, and the stability of the stope is determined by its structural parameters. Before the orebody is excavated, the stress in each stope is balance. After the initial orebody is excavated, the stress in the surrounding rock is redistributed.

This study was designed to investigate the stress and displacement laws of a gently inclined medium-thick phosphate rock and the rock surrounding a stope in room

and pillar mining after continuous excavations. It is well known that the experiment/test is the most reliable way to study mechanical problems [24–37]; therefore, in this paper, a similar physical model was adopted with a stope structure consisting of a size of 10 × 10 m room with 3 × 3 m, 5 × 5 m, and 8 × 8 m pillars, respectively. The stress distribution of the surrounding rock, the change in the subsidence displacement of the overlying rock mass, and the roof deformation and failure laws were explored. Based on the deformation and failure of the surrounding rock, optimal structural parameters for the stope were identified.

3. Experimental Model Design

Experimental study needs a good design plan [38–51], and the No. 6 mining area of the Jinning Phosphate Mine is divided into nine rock strata based on a geological investigation. The depth of the rock strata ranges from +2283 m to +2050 m. The main phosphate rock strata have a burial depth of +2150 m and a thickness of 13.30 m.

The model frame size is determined according to the prototype size and geometric similarity ratio. A plane stress model was selected for the simulation experiment with a model frame size of 3.00 × 0.30 × 2.00 m (length × width × height). In order to obtain similar experimental parameters, a preliminary uniaxial mechanical experiment was conducted, and the model similarity was determined based on similarity theory [52, 53]. The geometrical similarity ratio, time similarity ratio, strength similarity ratio, and bulk density similarity ratio are 1 : 240, 1 : 296.3, and 1 : 1.23, respectively. The initial conditions and boundary conditions of the model can be approximated as a homogeneous gravity field based on the field stress field data, which is similar to the prototype.

In the similar physical model, river sand, gypsum, and calcium carbonate were employed as the main aggregates. Cement, sawdust powder, mica, plastic, and motor oil were used as auxiliary materials. Borax and mica powder were used for the retarder and the sandwich material. Using an orthogonal experiment, 40 experimental proportioning schemes were designed and screened. Material proportioning schemes with similar mechanical properties to the prototype were selected. According to the geological conditions of the mining area, 9 types of rock formations were set up in this test and distinguished by different colors. The details are illustrated in Tables 1 and 2.

4. Experimental Excavation Plan

The similar physical model was used to investigate three stope structures, with a size of 4.1 × 4.1 cm mine room with 1.2 × 1.2 cm, 2 × 2 cm, and 3.3 × 3.3 cm pillars. Based on the geometrical similarity ratio (i.e., 1 : 240), the actual size of pillars was 10 × 10 m room with 3 × 3 m, 5 × 5 m, and 8 × 8 m pillars. Each stope structure was divided into nine mine rooms by using four excavation steps. An electric drill was adopted to excavate mine room once every 2 hours (total twice). The first step included mine room #1, the second step included mine rooms #2 and #3,

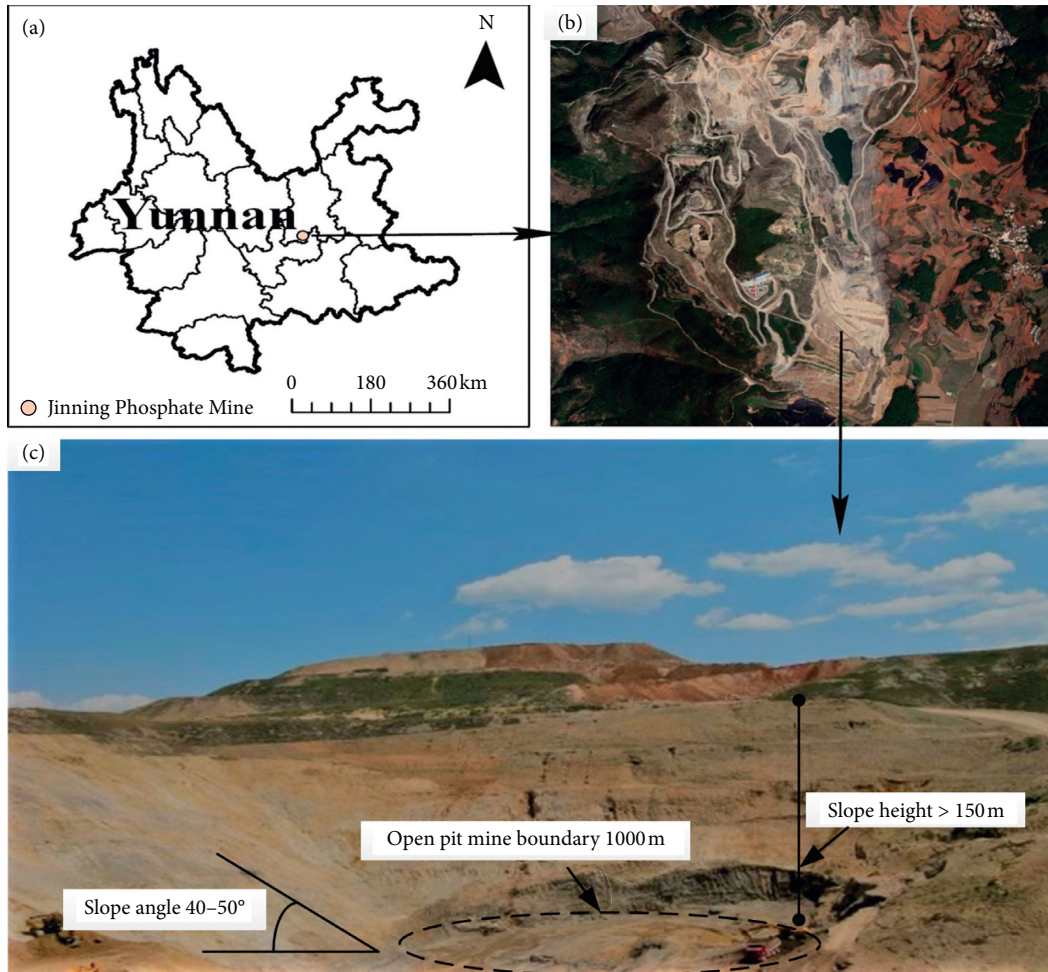


FIGURE 1: Geographical position and current mining operations at the Jinning Phosphate Mine in 2015: (a) location of the mine; (b) remote sensing image of the mine; (c) the current mine structure.

TABLE 1: Proportion of the materials in each rock stratum of the similar physical model.

Rock stratum	Material ratio (sand: calcium carbonate: gypsum)	Actual rock thickness (m)	Similar physical model thickness (cm)
Sandy soil	6 : 7 : 3	17.04	7.10
Medium- to coarse-grained dolomite	4 : 2 : 8	104.00	43.33
Bedded argillaceous dolomite	4 : 5 : 5	9.00	3.75
Quartz sandstone	3.8 : 5 : 5	17.80	7.42
Phosphate ore	3 : 2 : 8	13.30	5.54
Low-grade phosphorus ore	3.2 : 3 : 7	16.87	7.03
Boundary ore	3.8 : 4 : 6	5.06	2.11
Light grey primary dolomite	3.5 : 3 : 7	16.00	6.67
Deep grey medium-thick layered primary dolomite	3.5 : 3.5 : 6.5	33.50	13.96

the third step included mine rooms #4–6, and the fourth step included mine rooms #7–9. The details are illustrated in Figure 2.

Stress sensors were used to monitor changes in the stress within the phosphate rock roof. Changes in displacement were monitored by using electronic total stations, and a camera was used to record the deformations of the surrounding rock and pillars.

5. Arrangement of Stress and Displacement Observation Points

A WS3811-J12 static resistance strain collector and BX-1 series soil sensors were installed to monitor roof stress. Stress observation points were located at a longitudinal distance of 6.3 cm and 10.4 cm from the phosphate rock stratum, with a horizontal distance of 25 cm, 108.3 cm,

TABLE 2: Materials used in the rock strata of the similar physical model.

Rock stratum	Sand (kg)	Calcium carbonate (kg)	Gypsum (kg)	Water (kg)	Borax (kg)
Sandy soil	88.73	10.35	4.44	11.50	115.00
Medium- to coarse-grained dolomite	505.40	25.27	101.09	70.19	701.90
Bedded argillaceous dolomite	43.74	5.47	5.47	6.07	60.70
Gravel quartzite	85.64	11.27	11.27	12.02	120.20
Phosphate ore	60.58	4.04	16.16	8.97	89.70
Low-grade phosphorus ore	78.10	7.32	17.08	11.39	113.90
Boundary ore	24.35	2.56	3.85	3.42	34.20
Light grey primary dolomite	75.64	6.48	15.13	10.81	108.10
Deep grey medium-thick layered primary dolomite	158.31	15.83	29.40	22.62	226.20

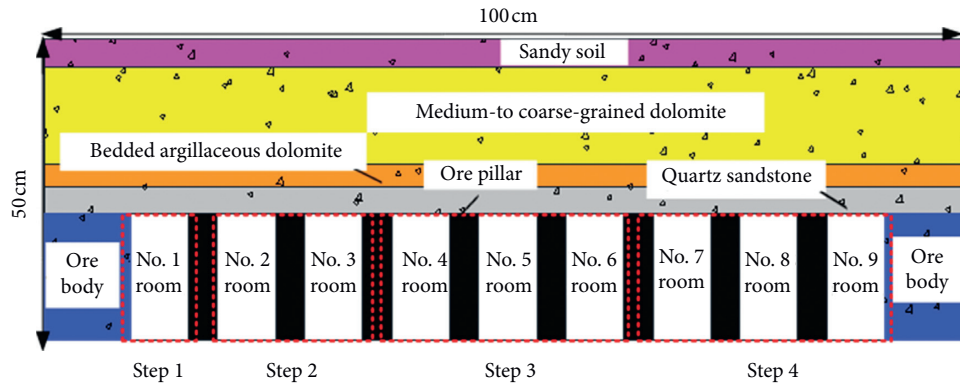


FIGURE 2: Mine room excavation plan.

and 201.6 cm from the model endpoint for pillar sizes of 1.2 cm, 3.3 cm, and 2 cm, respectively. The intervals for the stress points were 8.3 cm, 10.4 cm, and 12.5 cm for the three pillar sizes, respectively. The details are illustrated in Figure 3.

A Nikon DTM-502 total station was used to monitor rock layer displacement. The first horizontal displacement line was located 19.1 cm away from the endpoint of the model. The horizontal interval of the displacement points was 11.6 cm, and seven observation points were positioned on each measurement line at longitudinal distances of 6.25 cm, 10.4 cm, 14.5 cm, 22.9 cm, 31.2 cm, 43.7 cm, and 56.2 cm from the phosphate rock stratum (marked as 1–7 in the model). A total of 22 displacement observation lines and 154 displacement observation points were used in the model, as shown in Figure 4.

6. Test Results and Analysis

By monitoring the stress points, it was found that the initial stress of the three stope structures was the same, with the stress before excavation positively correlated with the buried depth. In particular, the stress at M1, M2, N1, N2, P1, and P2 was 12.00 kPa, while the stress at M3–M6, N3–N6, and P3–P6 was 12.40 kPa. Maps of the initial stress distribution were rendered using MATLAB software with cubic spline interpolation (see Figure 5). Because of the same initial stress of the stope structures, only the structure with 1.2 cm pillars is presented.

6.1. Stope Deformation and Failure Laws for Mine Rooms with 3 m Ore Pillars. Data from the stress measurement points and the displacement measurement lines for all three stope structures were processed in MATLAB with cubic spline interpolation. The stress nephogram and subsidence displacement nephogram of the surrounding rock for the stope structure with 1.2 cm pillars based on the M1–M6 stress measurement points and the L1–L5 displacement measurement lines are presented in Figures 6 and 7. Figure 6 shows the lower roof stress and overlying rock subsidence for the four-step excavation of the stope structure with 3 m ore pillars. Figure 6(a) and 6(b) represent the first step of excavation; Figures 6(c) and 6(d) represent the second step of excavation step; Figures 6(e) and 6(f) represent the third step of excavation; and Figures 6(g) and 6(h) represent the fourth step of excavation. Figure 7 shows the deformation and failure characteristics of the roof for the 3 m ore pillars. Figure 7(a) represents the deformation and failure characteristics of the roof of the first step of excavation; Figure 7(b) represents the deformation and failure characteristics of the roof of the second step of excavation; Figure 7(c) represents the deformation and failure characteristics of the roof of the fourth step of excavation. The displacement measurement points were labeled LB-1, LB-2, LB-3, LB-4, LB-5, LB-6, and LB-7 according to their vertical distance from the stope roof (6.25 cm, 10.4 cm, 14.5 cm, 22.9 cm, 31.2 cm, 43.7 cm, and 56.2 cm, respectively) (B represents the line number).

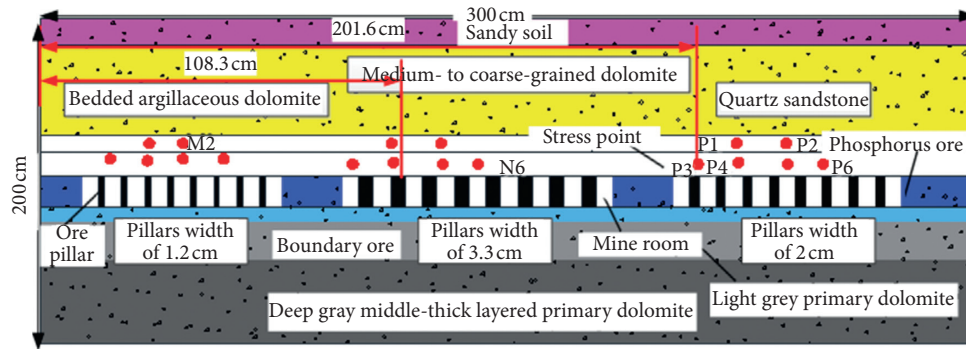


FIGURE 3: Stress point monitoring in the similar physical model. The mining site at the stress measurement points is a size of 10 × 10 m room with the width of 3 × 3 m, 5 × 5 m, and 8 × 8 m pillars. These points are labeled M1–M6, N1–N6, and P1–P6, respectively.

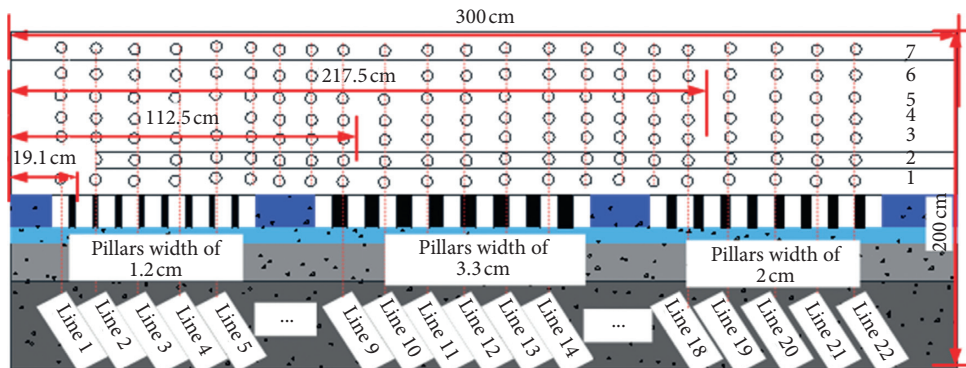


FIGURE 4: Displacement point monitoring. The measurement lines are marked as Line 1 to Line 22 in order from left to right. Each measurement line has seven measurement points. The measurement points are marked as LB-1, LB-2, LB-3, LB-4, LB-5, LB-6, and LB-7, with B denoting the line number, according to the distance from the stope roof (6.25 cm, 10.4 cm, 14.5 cm, 22.9 cm, 31.2 cm, 43.7 cm, and 56.2 cm, respectively).

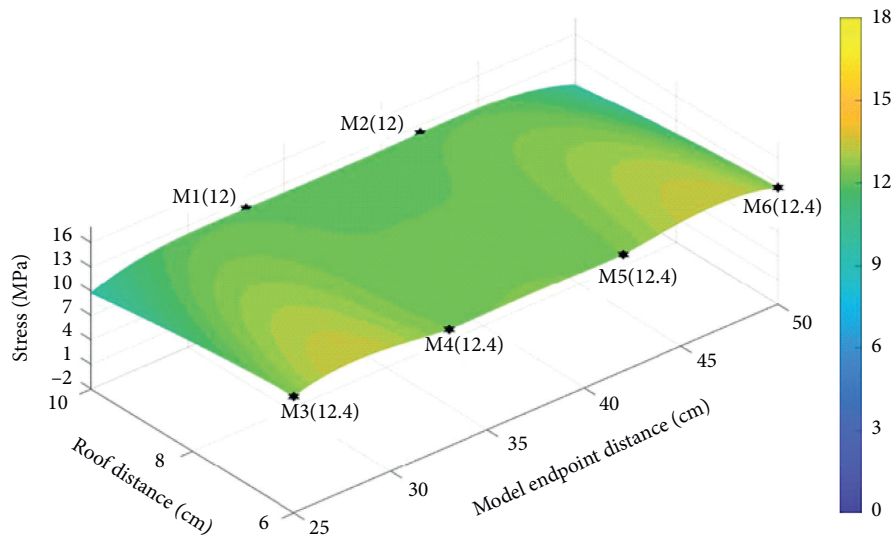


FIGURE 5: Initial stress distribution

After the first excavation step, mine room #1 formed a goaf. A pressure relief zone appeared above the roof of the stope, and the M3 stress fell from 12.40 kPa to 11.02 kPa. The stress of the overlying rock moved towards the front of the goaf under the influence of mining. The displacement measurement points L1-1 and L1-2 subsided slightly by

−0.5 mm (actual scale −12 cm) and −0.13 mm (actual scale −3 cm), respectively. There was a slightly loose area above the top plate, but the model was generally stable.

In the second excavation step, the range of the goaf was expanded into mine room #3. The stress relief area in the roof increased further, achieving the maximum stress relief

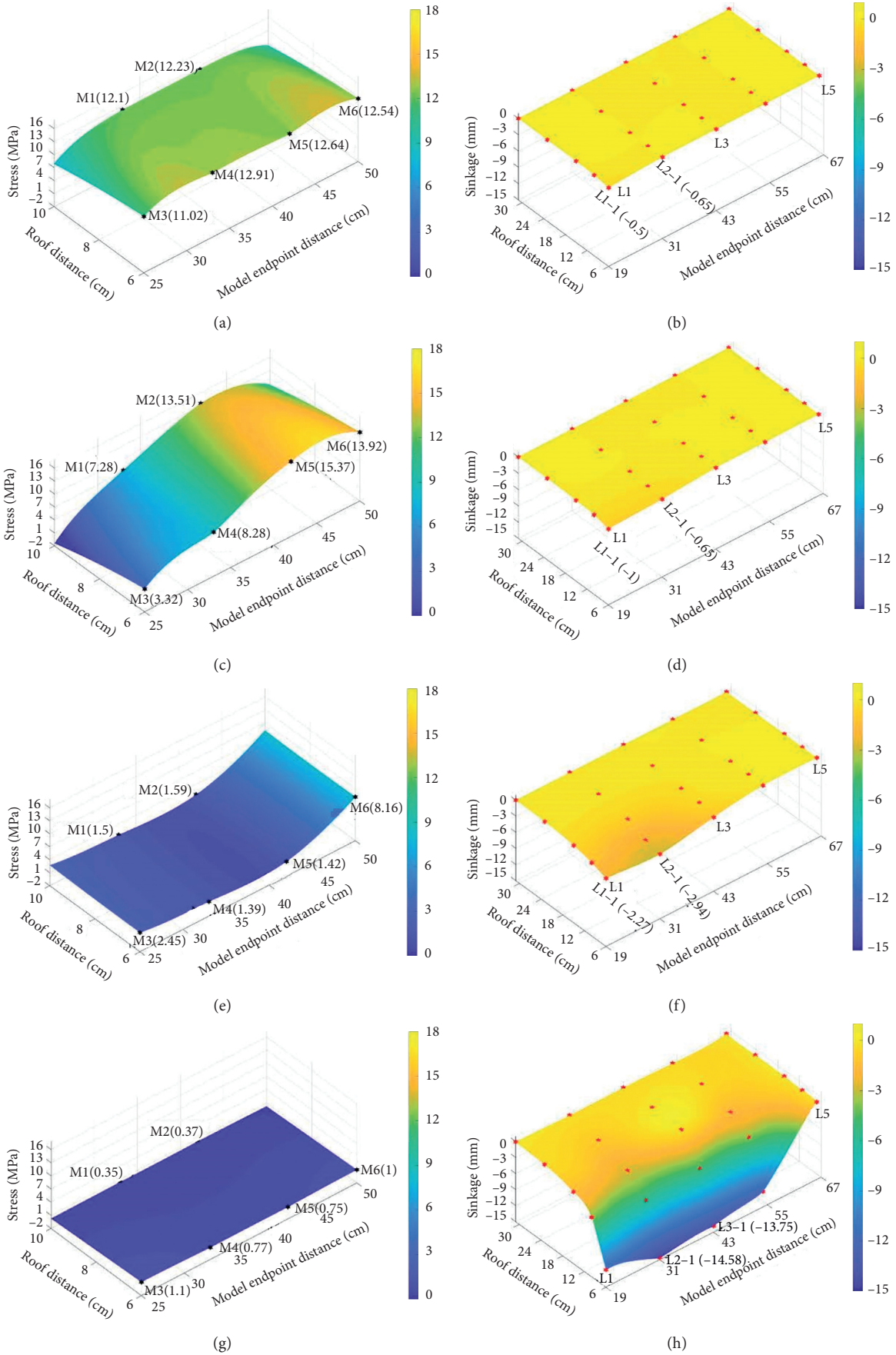


FIGURE 6: Lower roof stress and overlying rock subsidence for the four-step excavation of the stope structure with 3 m ore pillars: (a, b) first step; (c, d) second step; (e, f) third step; and (g, h) fourth step.

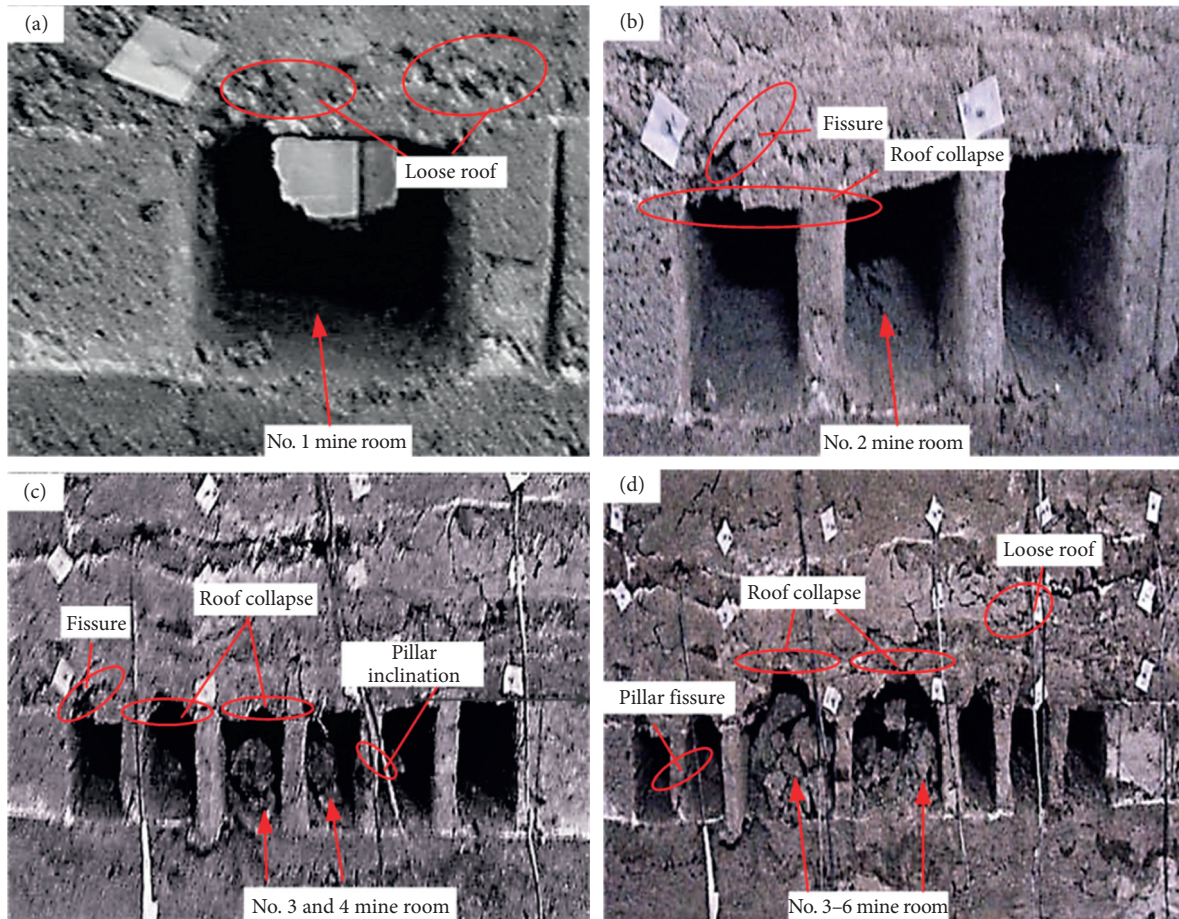


FIGURE 7: Deformation and failure characteristics of the roof for the 3 m ore pillars: (a) first step; (b) second step; (c) third step; (d) fourth step.

pressure observed at M3 (3.32 kPa). The area of increased pressure moved forward dynamically as the goaf experienced overburden stress. The impact range of the overburden rock subsidence increased from survey line L1 to L2. The maximum subsidence point was at L1-1 and L2-1 at a vertical distance of 15 m from the roof with a subsidence of -1.00 mm (actual size -29.0 cm) and -0.65 mm (actual size -15.6 cm), respectively. At the same time, a roof crack with 3.24 cm and loosening belts appeared in the upper left corner of mine room #1. Accompanied by a minor collapse, mine rooms #2 and #3 were slightly bent.

After the third excavation step, the goaf was expanded into mine room #6. The roof stress relief area continued to expand, and the stress at each measurement point decreased sharply. The maximum pressure relief position was observed at M5 (1.42 kPa), with 90% stress reduction. Due to the mining activity, the settlement area of the overlying rock layer expanded horizontally in the direction of the survey line L3 and vertically from 6.2 cm to 10.4 cm. The maximum subsidence point was at L2-1 with -2.94 mm displacement (actual -70.6 cm). It was observed that the points closer to the center of the stope experienced a greater subsidence. Affected by stress and the subsidence of the overlying rocks, the pillars #1–4 were pushed sideways, and the roof of the stope broke and collapsed.

After the fourth excavation step, the goaf was expanded into mine room #9, and the stress of the overburden rock in the stope moves forward. The area of maximum pressure relief was observed at M6, with a stress of 1 kPa. The stress of the overlying rock on the stope continually moved forward. The further away from the center of the goaf the survey lines L1, L4, and L5 were, the weaker the effect of the mining on rock mass. The maximum subsidence points were observed at L2-1 and L3-1 with -14.58 mm (actual -350.0 cm) and -13.75 mm (actual -330.0 cm), respectively. Pillar #1 had a macrobreak fracture, and the remaining pillars were inclined. The roof of mine rooms #3–6 in the middle of the goaf experienced a large area of collapse, and the entire physical model was unstable.

6.2. Stope Deformation and Failure Laws for the Mine Rooms with 5 m Ore Pillars. The stress measurement points N1–N6 and the displacement survey lines L18–L22 for the roof of the phosphate ore layer under the stope structure with 2 cm ore pillars were monitored, as illustrated in Figures 8 and 9. Figure 8 shows the lower roof stress and overlying rock subsidence for the four-step excavation of the stope structure with 5 m ore pillars. Figures 8(a) and 8(b) represent the

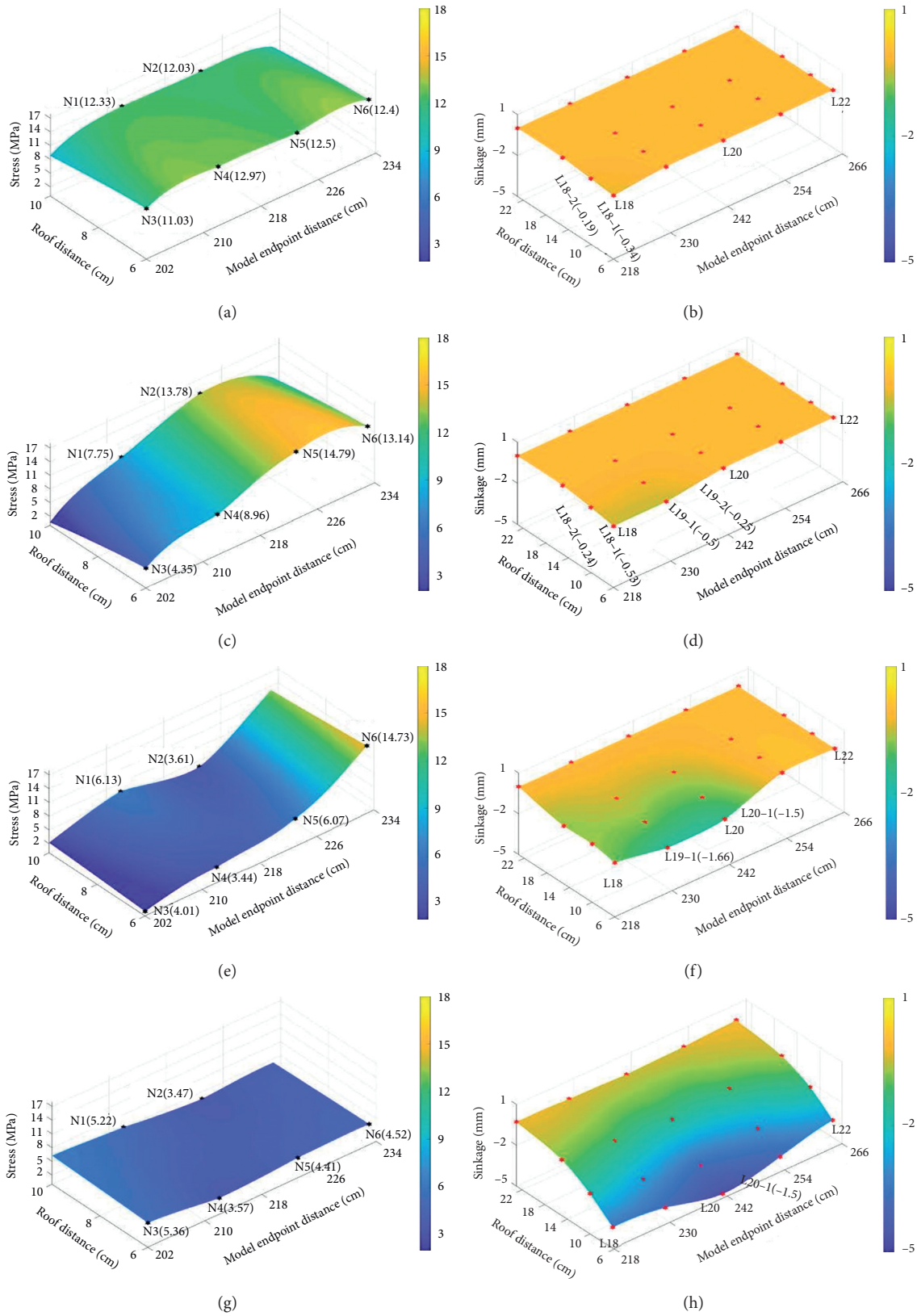


FIGURE 8: Lower roof stress and overlying rock subsidence in the four-step excavation of the stope structure with 5 m ore pillars: (a, b) first step; (c, d) second step; (e, f) third step; and (g, h) fourth step.

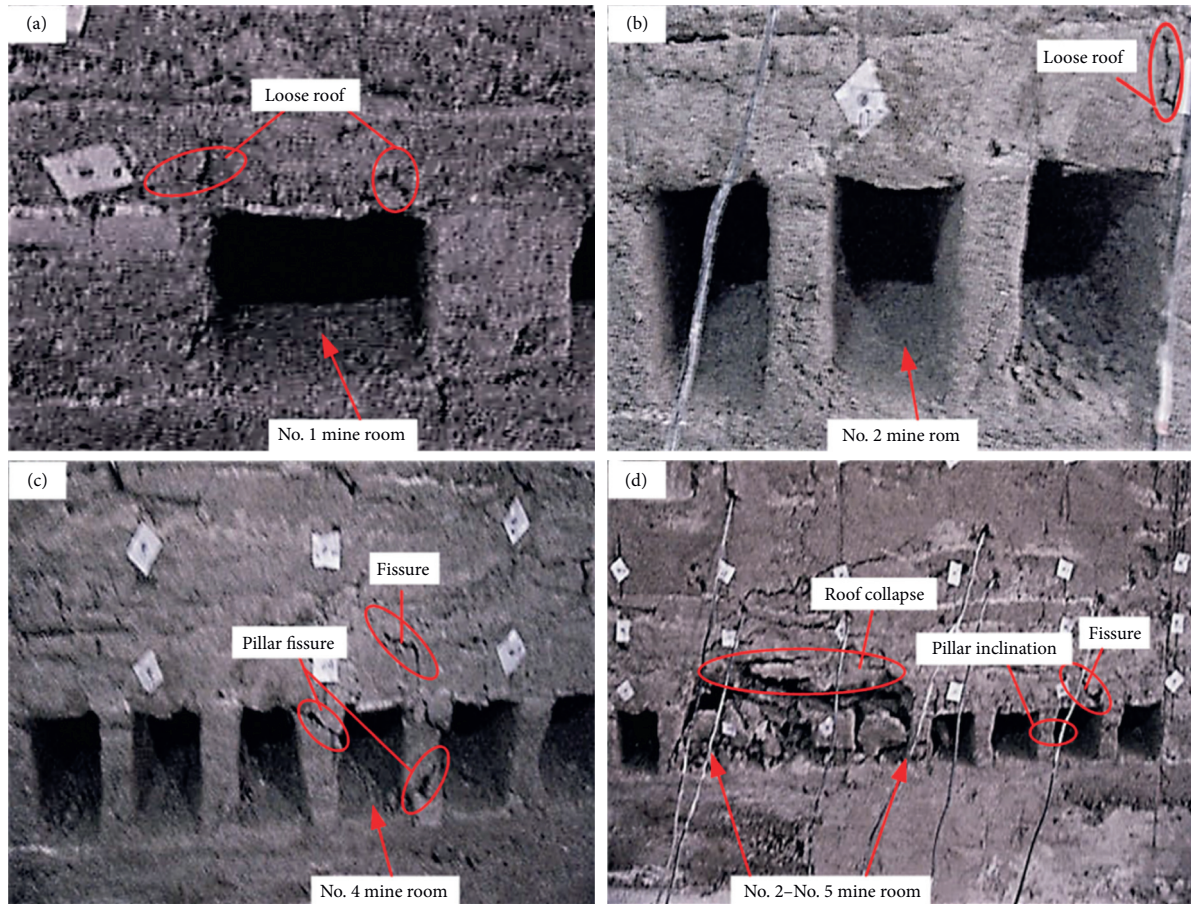


FIGURE 9: Deformation and failure characteristics of the roof for the 5 m ore pillars: (a) first step; (b) second step; (c) third step; (d) fourth step.

first step of excavation; Figures 8(c) and 8(d) represent the second step of excavation step; Figures 8(e) and 8(f) represent the third step of excavation; Figures 8(g) and 8(h) represent the fourth step of excavation. Figure 9 shows the deformation and failure characteristics of the roof for the 5 m ore pillars. Figure 9(a) represents the deformation and failure characteristics of the roof of the first step of excavation; Figure 9(b) represents the deformation and failure characteristics of the roof of the second step of excavation; Figure 9(c) represents the deformation and failure characteristics of the roof of the fourth step of excavation. The displacement measurement points were labeled LB-1, LB-2, LB-3, LB-4, and LB-5 according to their vertical distance from the stope roof (6.25 cm, 10.4 cm, 14.5 cm, and 22.9 cm, respectively), with B representing the line number.

After the first excavation step, the roof above the stope exhibited a stress relief area. The maximum stress relief was observed at N3, which fell from 12.40 kPa to 11.03 kPa. In contrast, the stress at the measurement points N1, N2, N3, N4, and N5 was 12.33 kPa, 12.03 kPa, 12.97 kPa, 12.50 kPa, and 12.40 kPa, respectively. The stress at measurement point N6 remained at 12.40 kPa. Overall, the increased degree of stress at each measurement point decreased with increasing distance from the goaf. Affected by mining, the subsidence of survey points L18-1 and L18-2 was -0.34 mm (actual

-8.2 cm) and -0.19 mm (actual -4.6 cm), respectively. Only a small loose band appeared at both corners of the top plate, and the model was generally stable.

In the second step of the excavation, the range of the goaf extended to mine room #3, and the stress relief area in the stope transferred dynamically to the front rock mass. The stress at measurement points N1, N3, and N4 exhibited a gradual decrease with an increase in the distance from the center of the goaf. At measurement point N3 above the goaf, the stress was 4.35 kPa and 60% lower than the initial value. The measurement points N2, N5, and N6 were in the area of increased stress, with a maximum stress of 14.79 kPa at N5. The maximum subsidence area in the overlying rock layer was observed at survey lines L18 and L19. The subsidence at L18-1 and L18-2 was measured as -0.53 mm (actual -12.6 cm) and -0.24 mm (actual -5.9 cm), respectively. Besides, the subsidence at L19-1 and L19-2 was obtained at -0.5 mm (actual -11.9 cm) and -0.25 mm (actual -6 cm), respectively. Mine room #3 exhibited obvious roof loosening and collapse in response to mining activity.

After the third step of the excavation, the goaf was expanded into mine room #6. The roof stress relief area again moved to the front rock body. The stress at N4 and N5 at the center of the goaf fell to 3.44 kPa and 6.07 kPa, respectively. Measurement point N2 quickly switched from an area of

increased stress in top plate to a pressure-relieving area, with the stress falling to 3.61 kPa, 70% lower than the initial value. The measurement point N6 was located in the zone of increased stress, and a stress of 14.73 kPa was recorded. The subsidence area of the overlying rock expanded from 6.2 cm to 14.5 cm along the horizontal direction of the orebody, but the extent of the subsidence at each measurement point decreased in sequence. The maximum subsidence at L19-1 and L19-2 was -1.66 mm (actual -39.90 cm) and -1.50 mm (actual -36.00 cm), respectively. Macrocracks appeared on the roof of mine rooms #4 and #5, and fractures appeared in the ore pillars.

After the fourth excavation step, the goaf was extended to mine room #9. The stress relief boundary range expanded to the measurement point N6, with the stress falling from 14.73 kPa to 4.52 kPa and 70% lower than the initial value. In the area behind the old goaf, the measurement point N3 experienced gradual compaction due to the subsidence of the overlying rock layer. The stress at N3 increased from 4.01 kPa to 5.36 kPa. The influence of overburden rock subsidence also increased, with the overburden rock subsidence area expanding from 6.2 cm to 22.9 cm away from the roof along the horizontal direction of the orebody. The maximum subsidence at L20-1 was -4.67 mm (actual -112.00 cm). A transfixion macrocrack appeared on the roof of mine room #2–5. The remaining mine pillars leaned, and the #2–5 mine room collapsed.

6.3. Stope Deformation and Failure Laws for the Mine Rooms with 8 m Ore Pillars. For the stope structure with 8 m ore pillars, the results from the stress measurement points P1–P6 and the measurement lines L9–L14 from the roof of the phosphate ore layer are presented in Figures 10 and 11. Figure 10 shows the lower roof stress and overlying rock subsidence for the four-step excavation of the stope structure with 8 m ore pillars. Figures 10(a) and 10(b) represent the first step of excavation; Figures 10(c) and 10(d) represent the second step of excavation step; Figures 10(e) and 10(f) represent the third step of excavation; and Figures 10(g) and 10(h) represent the fourth step of excavation. Figure 11 shows the deformation and failure characteristics of the roof for the 8 m ore pillars. Figure 11(a) represents the deformation and failure characteristics of the roof of the first step of excavation; Figure 11(b) represents the deformation and failure characteristics of the roof of the second step of excavation; Figure 11(c) represents the deformation and failure characteristics of the roof of the fourth step of excavation. The displacement measurement points were labeled LB-1, LB-2, and LB-3 for vertical distances of 6.25 cm, 10.4 cm, and 14.5 cm, respectively.

After the first excavation step, mine room #1 was the goaf. A stress relief area formed around measurement point P3, with the stress falling from 12.4 kPa to 12.3 kPa. The overpressure zone from the overburden stress in the stope dynamically shifted to the front rock mass, and the maximum stress at P4 increased to 12.84 kPa. The subsidence at L9-1 was -0.18 mm (actual -4.4 cm), while the remaining subsidence measurement points did not subside. The structure of the mine room was very stable.

In the second step of the excavation, the goaf area expanded to mine room #3. The stress relief area of the roof expanded, with the maximum stress at P3 falling from 12.30 kPa to 5.12 kPa, 63% lower than the initial value. The overburden stress in the stope formed a pressurization zone. The maximum stress at P5 increased from 12.44 kPa to 14.22 kPa and 14% lower than the initial value. At the same time, the subsidence range of the overlying rock expanded from the measuring points L9-1 to L10-1, with subsidence of -0.33 mm (actual -7.92 cm) and -0.28 mm (actual -6.72 cm), respectively. Though the roof plate in mine rooms #1 and #2 exhibited obvious bending, the overall structure of the model was stable.

After the third excavation step, the range of the goaf was expanded to mine room #6. The stress relief zone continually moved forward, and the stress at P5 fell from 14.22 kPa to 4.41 kPa and 68% lower than the initial value. The stress at P6 in the goaf pressurization area rose from 13.04 kPa to 17.36 kPa (33% lower than the initial value). Considering measurement points P1 and P4 in the center of the goaf as the axis of symmetry, the stress relief of the roof gradually exhibited a saddle-shaped distribution. The range of overburden rock subsidence expanded further, and the overburden rock subsidence area expanded from 6.2 cm to 10.4 cm from the roof along the horizontal direction of the orebody. The maximum subsidence at L10-1 was -1.44 mm (actual -34.6 cm). Bending and subsidence occurred in the roof of each mine room, and a clear crack appeared in the middle of the roof in mine rooms #3 and #4, accompanied by minor slippage of loose and broken rock.

After the fourth excavation step, the goaf was expanded to mine room #9. The stress at each measurement point fell within the stress relief area. The maximum stress at P6 reduced from 17.36 kPa to 3.88 kPa and 77% lower than the initial value. At this time, mine rooms #1 and #2 were located in the old goaf. The stress at measurement point P3 increased from 5.09 kPa to 7.38 kPa. That is because the roof gradually compacted after falling, supported by overburden gravity. The range of overburden subsidence extended horizontally to L14 and gradually increased to 14.5 cm along the horizontal direction of the orebody. The maximum subsidence at L11-1 was -3.48 mm (actual -83.6 cm). With an increase in the distance from the center of the goaf, the degree of subsidence decreased monotonously. The bending of the roof in each mine room increased, and some of the pillars were inclined. However, there was no collapse, and the model was basically stable.

7. Discussion

7.1. Stress and Displacement Deformation Laws for the Surrounding Rock in the Stope. The changes in the stress and displacement of the surrounding rock in the stope reflect the stability of the overlying strata. In the early stages of phosphate rock mining, the original stress equilibrium of the surrounding rock is disrupted. In the present study, the stress and displacement deformation failure of the surrounding rock for different ore pillar sizes exhibited some general rules as follows.

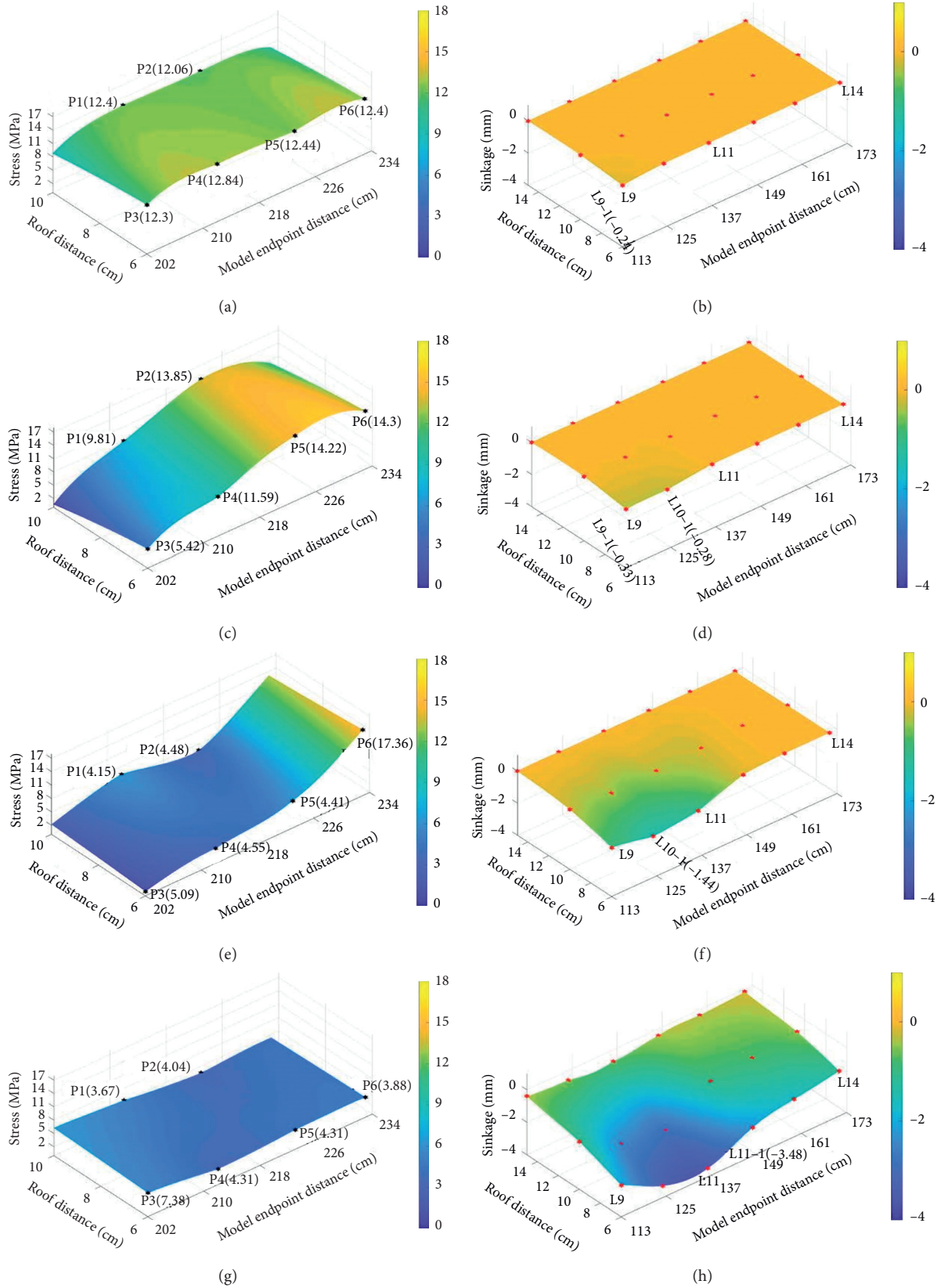


FIGURE 10: Lower roof stress and overlying rock subsidence in the four-step excavation of the stope structure with 8 m ore pillars: (a, b) first step; (c, d) second step; (e, f) third step; and (g, h) fourth step.

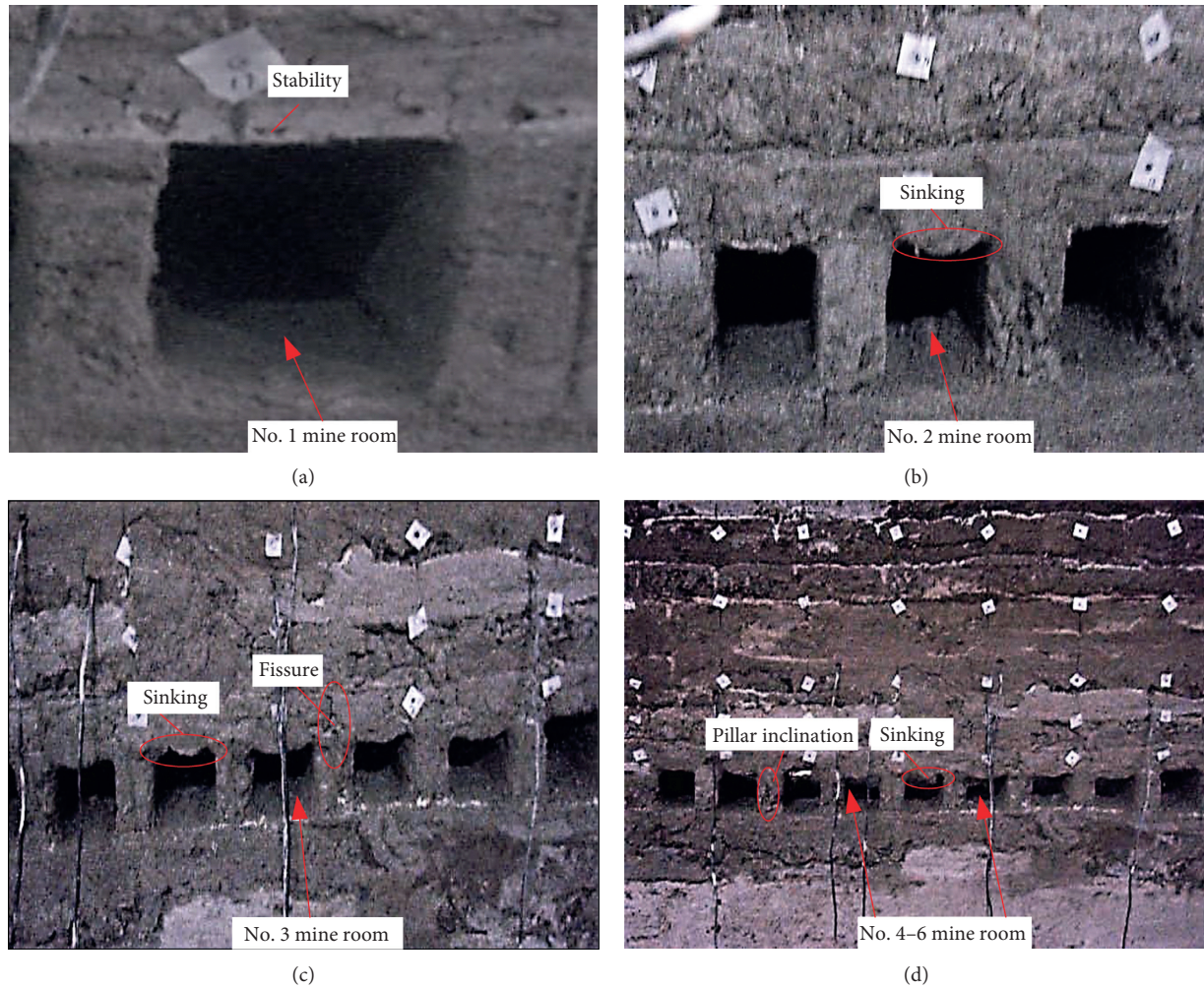


FIGURE 11: Deformation and failure characteristics of the roof for the 8 m ore pillars: (a) first step; (b) second step; (c) third step; (d) fourth step.

During the mining process, a pressure relief area first formed in the upper central area of the roof of the goaf. At the same time, the roof began to bend and subside, causing the stress of the overlying rock to move forward within the stope to create a pressurized area. As the working face continued to advance, the stress relief boundary also increased. When the stress of the overlying rock reached its yield state, microcracks began to appear in the overlying rock. In addition, the expansion of the stope space transferred the whole overlying rock layer weight on the pillars [52, 53]. When the gravity of the overlying rock reached a critical point at the ore pillar, the microcracks gradually generated to form a local fissure zone.

When the excavation of the phosphate orebody was complete, the surrounding rock in the roof of the goaf exhibited obvious deformation and failure characteristics. Three deformation zones could be identified based on the extent of deformation and failure in the overlying rock including bending, fracture, and caving zones, as shown in Figure 12.

The fracture zone had an obvious layered structure, and the inside of the rock mass exhibited both vertical layered fissures and separated layer fissures in the horizontal direction.

The rock mass in a caving zone is affected by mining disturbances, and the distribution is disordered. In addition, the caving zone has a loose internal structure, and it is also compressible. The caving and the fracture zone are collectively referred to as the water-conducting fissure zone. When vertical stress is applied to the upper region of the water-conducting fissure zone, a superimposed compressive effect occurs between the two zones, resulting in uneven settlement.

In the present study, as the excavation advanced, the stress and subsidence of the overlying rock layer increased dramatically. The variation in the subsidence was associated with the spatial distance along the orebody and from the stope. In other words, as the distance along the orebody and from the stope is greater, the influence of each moving line is weaker; the bearing capacity of the surrounding rock is

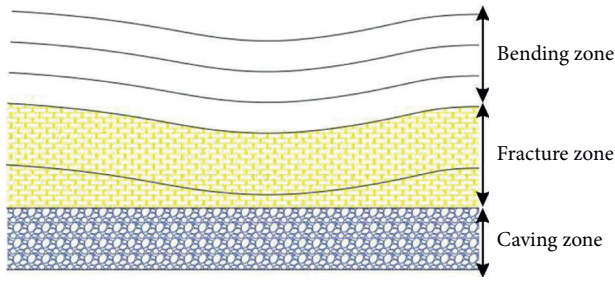


FIGURE 12: Overlying strata movement zones in a goaf.

stronger, the subsidence of the overlying rock is lower, and the deformation of the surrounding rock is less.

7.2. Determining the Optimal Stope Structure. The pillars are crucial to the overall stability of the stope in room and pillar mining. Once a pillar is unstable, the surrounding rock in the roof will fall, increasing the difficulty in mining the orebody and the dilution rate of the orebody. In addition, the sudden collapse of a stope can also cause casualties. The characteristics of stress deformation and failure in the roof and the subsidence of overlying rock depend on the pillar size. Generally, a larger pillar size produces a more stable stope structure. However, larger pillar sizes can lead to the waste of resources and increase mining costs. For this reason, the mining disturbance coefficient and subsidence coefficient [7, 54, 55] were used in the present study to quantitatively analyze the stope structures with 3 m, 5 m, and 8 m pillars, and finally, it was determined which structure maximized the return on mining activity while also ensuring mine safety.

The mining disturbance coefficient is defined as the ratio of the maximum variation in stress to the initial stress for each excavation in the stope structure. It reflects the degree of disturbance of the mining stress on the surrounding rock in the stope roof, as shown in (1). The subsidence coefficient is the ratio of the maximum subsidence of the overlying strata to the mining thickness of the phosphate rock under the full mining of the stope structure, which reflects the degree of influence the mining disturbance on the overlying rock, as shown in (2):

$$K_{\max} = \left| \frac{(\sigma_i - \sigma_1)_{\max}}{\sigma_0} \right| \in [0, +\infty), \quad (1)$$

where σ_i is the stress of each excavation step (MPa), σ_1 is the stress of the first excavation step (MPa), and σ_0 is the initial stress (MPa).

$$W = \frac{W_{\max}}{D}, \quad (2)$$

where W is the maximum subsidence of the overlying rock (m) and D is the thickness of the orebody mined (m). The thickness of the orebody in this study is 5.4 cm.

In Figure 13(a), it indicates that the disturbance coefficients increased for the first three excavation steps in all three kinds of stope structures. When mine rooms #4–6 were

excavated after the third step, an inflection point (the disturbance coefficient began to decrease) appeared in the stope structures with 3 m and 5 m pillars. These results are related to the continuous increase in the stope space and the superposition of mining stress as the roof span became larger. Due to the weight of the rock and tectonic stress, the roof bent and subsided, causing cracks to appear in the pillars supporting the overlying strata. Once the ultimate load of the pillars was reached, some of the mine rooms collapsed, and the collapsed broken rock mass was gradually compacted by the weight of the overlying strata, enabling pillars to support the overlying strata. Therefore, the stress disturbance coefficient of the fourth mining step decreased.

Figure 13(b) shows the overlying rock subsidence coefficient for the three stope structures. By comparing the subsidence coefficient for the overlying strata in the three stope structures, it can be concluded that, for the same excavation step, larger pillars produced a lower subsidence coefficient and increased the stability of the overlying strata. In particular, the structural stability of the stope with 3 m pillars was extremely poor while those with 5 m and 8 m pillars were relatively stable.

Overall, the disturbance and subsidence coefficients for the stope structure with 3 m pillars were larger than those of the other two stope structures. After the third excavation step, the mine rooms #2–4 collapsed over a wide area, and the entire model was unstable. Following the third step, the stope structure with 5 m pillars exhibited partial instability in the old stope area. However, if reinforcement is conducted in advance, the stope damage can be prevented. The stope structure with 8 m pillars was always stable. However, the grade of the phosphate rock in this mining area is 26–30%, and the price of phosphate rock is high. From an economic and safety perspective, a stope structure with 10 m mine rooms and 5 m pillars can be used to mine this orebody.

7.3. Analysis of the Excavation Characteristics and Stope Structure of Different Ore Types. The shape, metallogenic regularity, stratum structure, and tectonic stress of gently inclined medium-thick phosphate rock are different when compared to metal and coal mines. Thus, there are likely to be differences in the deformation laws for the surrounding rock in the roof and the selection of the optimal stope structure depending on the type of ore being mined. The deformation characteristics of the surrounding rock and the selection of the stope structure are discussed further in this section.

The deformation and failure of the overlying strata in stopes with different orebody characteristics under room and pillar mining have similarities, and differences are summarized in Table 3.

The incline of the orebody affects the characteristics of the overburden deformation. For example, in gently inclined coal seams, there is a tendency for obvious delamination above the excavation area, but no significant delamination is observed in inclined or steeply inclined coal seams. The extent of the deformation is weakened and more uniform, meaning that the damage to the overlying rock layer and the

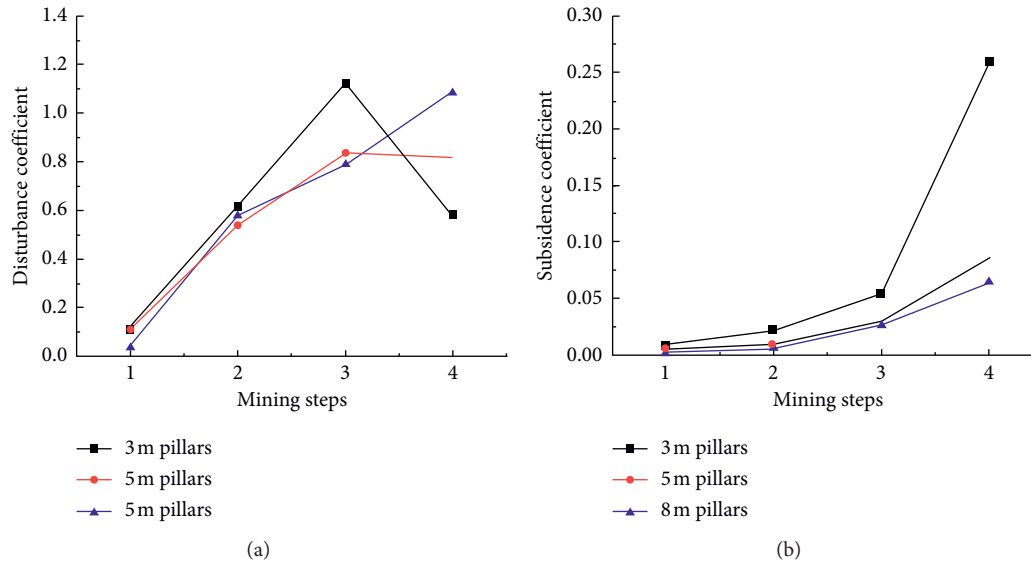


FIGURE 13: (a) Mining disturbance coefficient and (b) overlying rock subsidence coefficient for the three stope structures.

TABLE 3: Law of deformation and failure for stopes in various mine types.

Mine characteristics	Differences	Explanation
Gently inclined medium-thick phosphate rock (the present study)	The surrounding rock in the roof gradually evolves from stable to unstable and dynamic balance during the mining process In the present study, because of the unique characteristics of the ore, the overlying rock mass had obvious bending, fracture, and caving zones	The characteristics and range of the surrounding rock deformation are closely related to the rock mass quality, rock layer contact zone, and orebody burial depth
Slowly inclined medium-thick metal ore [56–59]	In the mining process, the surrounding rock in the roof exhibits a process of gradual caving, gradual caving, sudden caving, and then again gradual caving, sudden caving, and then surface collapses, which is repeatable and instantaneous	—
Shallow coal mine [60–63].	The coal seam is shallow; thus, the caving zone caused by deformation and damage to the overlying rock directly extends to the surface; there are no subsidence, fracture, or caving zones	—
Similarities		
For a certain room size, the larger the pillars, the less change in the stress and displacement of the overlying rock and the more stable the stope		
During mining, tensile stress forms in the roof of the stope, and the maximum tensile stress appears in the center area of the roof.		

degree of roof subsidence are lower. On the deformation of overlying rocks in gently inclined medium-thick phosphate orebodies, obvious delamination also occurs, but whether this deformation in inclined and steeply inclined phosphate orebodies follows similar rules of coal seams in shallow coal mine requires further investigation.

Stope structural parameters are important for assessing stope stability in room and pillar mining. Sherizadeh and Kulatilake [64] investigated nine stope plans for a Guihua copper deposit (thickness of 0.5–0.7 m) using the three-dimensional numerical simulation of stope stress, safety factors, vertical displacement, and the plastic zone. The results indicated that a mine room span of 10 m and a pillar size of 3 m were the optimal structure. However, this stope structure is not suitable for the gently inclined medium-

thick phosphate orebody in this study. Although the difference in mechanical properties has a little influence on the stress distribution in different geological conditions, the tensile strength and cohesion of the rock mass are different, and the plastic zone of the surrounding rock in the roof differs from the plastic zone under mining disturbance. Therefore, even with the same stope parameters, there can be significant differences in stope stability [65–68].

8. Conclusions

A large-scale similar physical model was conducted to investigate the roof stress, displacement, and overlying rock deformation laws of the No. 6 pit in the Jinning Phosphate Mine. Some valuable conclusions are as follows.

In the process of underground mining, the roof stress, displacement, and overlying rock deformation laws of gently inclined medium-thick phosphate rock were different from those of other mines (metal mines and coal mines). With the gradual advance in the working face, the stress relief boundary moved forward dynamically, and the value of stress relief, subsidence, and pressurization decreased from the center of the roof to the periphery. With three different stope structures, the 3 m stope of the pillar took the lead in bending and sinking. The lateral tilt of the pillar caused local cracks, and some mine rooms collapsed. Microcracks appeared in the roof of the 5 m mine pillar, while the 8 m pillar structure remains stable during the entire excavation process. Due to the influence of mining, the overlying strata of all three stope structures exhibited bending, fracture, and caving zones.

The best structure for combined mining of gently inclined medium-thick phosphate rock rooms and pillars are the combined mining of 10 m mine rooms and 5 m mine pillars and the roof of the mine needs to be reinforced in advance (without considering the action of complex external influence factors (earthquake, rain, and freeze-thaw)).

Through the above research, future research should explore more mining methods for underground mining of sloping medium-thick, gently inclined thin to medium-thick phosphorous deposits, especially the combined mining derived from the existing caving method, open field method, and filling method to further increase the recovery rate of underground mining and reduce the dilution rate.

Data Availability

The data used to support the findings of this study are included within the article.

Conflicts of Interest

The authors declare that there are no conflicts of interest regarding the publication of this paper.

Authors' Contributions

Xiaoshuang Li conceptualized the study and analyzed using software. Zhifang Liu performed formal analysis. Shun Yang wrote the original draft.

Acknowledgments

This work was supported by the National Natural Science Foundation of China (Grant nos. 41702327 and 41867033), Postdoctoral Science Foundation of China (Grant no. 2019M650144), State Key Laboratory of Safety and Health for Metal Mines (Grant no. zdsys2019-005), and Undergraduate Innovation Project (Grant no. zs-2019-s042). The authors wish to acknowledge these supports.

References

- [1] M. F. Ding, Z. Wang, D. W. Wang, S. H. Wang et al., "The optimization of mining method scheme for gentle dip and filmness ore body," *Gold Science and Technology*, vol. 22, pp. 56–59, 2014.
- [2] K. P. Zhou, J. B. Zhai, P. L. Hu et al., "Study on optimizing stope parameters and false-inclined layout in the gentle dip thin ore-body," *Journal of Guangxi University: Natural Sciences Education*, vol. 37, pp. 376–381, 2012.
- [3] W. Song, W. Xu, J. Du, and H. Wan, "Stability of workface using long-wall mining method in extremely thin and gently inclined iron mine," *Safety Science*, vol. 50, no. 4, pp. 624–628, 2012.
- [4] X. Li, Z. Wang, and J. Zhang, "Stability of roof structure and its control in steeply inclined coal seams," *International Journal of Mining Science and Technology*, vol. 27, no. 2, pp. 359–364, 2017.
- [5] Z.-F. Song, J.-H. Lei, X.-T. Wang, X.-M. Xu, and X.-P. Xin, "Study on roadway parameters of broken compound roof of gently inclined thick coal seam," *Energy Procedia*, vol. 16, pp. 334–340, 2012.
- [6] Q. R. Kang, J. X. Tang, H. Hu, and W.-Z. Zhang, "Stress distribution rule of roadway affected by overhead mining in gently inclined coal seams group," *Transactions of Nonferrous Metals Society of China*, vol. 21, no. Supplement 3, pp. 529–535, 2011.
- [7] A. Zingano and A. Weiss, "Subsidence over room and pillar retreat mining in a low coal seam," *International Journal of Mining Science and Technology*, vol. 29, no. 1, pp. 51–57, 2019.
- [8] X. B. Li, D. X. L. Peng, F. Feng, and X. S. Li, "Stability analysis of horizontal insulating pillar in deep mining from caving to filling method on the basis of refined plate theory," *Journal of China University of Mining and Technology*, vol. 48, no. 3, pp. 484–494, 2019.
- [9] J. N. Merwe and M. Mathey, "Probability of failure of South African coal pillars," *Journal of the South African Institute of Mining and Metallurgy*, vol. 113, no. 11, pp. 849–857, 2011.
- [10] D. Hu, P. Wu, K. X. Dong et al., "Study on stope structure parameters and stability for slightly inclined multi-layer ore bodies with room and pillar mining method," *China Mining Magazine*, vol. 23, pp. 5–8, 2014.
- [11] E. Ghasemi and K. Shahriar, "A new coal pillars design method in order to enhance safety of the retreat mining in room and pillar mines," *Safety Science*, vol. 50, no. 3, pp. 579–585, 2012.
- [12] L. Xiu, M. Qiao, and Z. J. Li, "Study on mining method of gently inclined medium thick orebody," *Nonferrous Metals: Mine Part*, vol. 3, pp. 1–3, 2011.
- [13] J. P. Ren, Y. P. Yang, L. Deng et al., "Mining status and development trend of inclined medium thick orebodies at home and abroad," *Modern Mining*, vol. 40, pp. 1–4, 2013.
- [14] Y. Li, K. Li, X. Feng, and M. Cai, "Development and evaluation of artificial expandable pillars for hard rock mining," *International Journal of Rock Mechanics and Mining Sciences*, vol. 110, pp. 68–75, 2018.
- [15] G. B. Yu, P. Yang, and Z. C. Chen, "Study on surrounding rock stability of pillar extraction in thin gently inclined ore body," *Journal of China Coal Society*, vol. 38, pp. 294–298, 2013.
- [16] K. Zhao and Z. G. Li, "Optimization and application of room and pillar mining scheme for gently inclined medium thick orebody," *Light Metals*, vol. 12, pp. 5–9, 2017.
- [17] E. Ghasemi, M. Ataei, K. Shahriar, F. Sereshki, S. E. Jalali, and A. Ramazanzadeh, "Assessment of roof fall risk during retreat mining in room and pillar coal mines," *International Journal of Rock Mechanics and Mining Sciences*, vol. 54, pp. 80–89, 2012.

- [18] W. B. Guo, Y. F. Zou, and Q. L. Hou, "Fractured zone height of longwall mining and its effects on the overburden aquifers," *International Journal of Mining Science and Technology*, vol. 22, no. 5, pp. 603–606, 2012.
- [19] G. Y. Zhao, L. Zhou, J. Y. Li, and P. Yu, "Reasonable pillar size design and nugget structural parameters optimization in room-and-pillar mining," *Journal of Central South University: Science and Technology*, vol. 45, no. 11, pp. 3943–3948, 2014.
- [20] X. Li and Y. Chai, "Determination of pillar width to improve mining safety in a deep burst-prone coal mine," *Safety Science*, vol. 113, pp. 244–256, 2019.
- [21] X. F. Wang, W. B. Luo, Z. D. Wu et al., "Mechanical evolution law of macroscopic deformation and failure of surrounding rocks in deep mining," *Modern Tunnelling Technology*, vol. 56, pp. 99–106, 2019.
- [22] S. A. Guan, S. Li, Y. Jin, and D. Liu, "Study on overlying strata movement law in backfill mining of gently inclined medium thick orebody," *Journal of Northeastern University. (Natural Science)*, vol. 40, no. 11, pp. 1630–1635, 2019.
- [23] C. Y. Zhang, C. Z. Pu, R. H. Cao, T. T. Jiang, and G. Huang, "The stability and roof-support optimization of roadways passing through unfavorable geological bodies using advanced detection and monitoring methods, among others," *Bulletin of Engineering Geology and the Environment*, vol. 78, no. 7, pp. 5087–5099, 2019.
- [24] C. Y. Zhang, P. Zou, Y. X. Wang, T. T. Jiang, and P. Cao, "An elasto-visco-plastic model based on stress functions for deformation and damage of water saturated rocks during the freezing-thawing process," *Construction and Building Materials*, vol. 250, 2020.
- [25] C. Y. Zhang, Y. X. Wang, and T. T. Jiang, "The propagation mechanism of an oblique straight crack in a rock sample and the effect of osmotic pressure under in-plane biaxial compression," *Arabian Journal of Geosciences*, vol. 13, no. 15, 2020.
- [26] R. H. Cao, R. B. Yao, J. J. Meng, Q. B. Lin, H. Lin, and S. Li, "Failure mechanism of non-persistent jointed rock-like specimens under uniaxial loading: Laboratory testing," *International Journal of Rock Mechanics and Mining Sciences*, vol. 132, 2020.
- [27] R. H. Cao, R. B. Yao, T. Hu, C. S. Wang, K. H. Li, and J. J. Meng, "Failure and mechanical behavior of transversely isotropic rock under compression-shear tests: laboratory testing and numerical simulation," *Engineering Fracture Mechanics*, vol. 241, 20 21.
- [28] R. H. Cao, C. S. Wang, R. B. Yao et al., "Effects of cyclic freeze-thaw treatments on the fracture characteristics of sandstone under different fracture modes: laboratory testing," *Theoretical and Applied Fracture Mechanics*, vol. 109, 2020.
- [29] Y. X. Wang, S. B. Shan, C. Zhang, and P. P. Guo, "Seismic response of tunnel lining structure in a thick expansive soil stratum," *Tunnelling and Underground Space Technology*, vol. 88, pp. 250–259, 2019.
- [30] Y. X. Wang, P. P. Guo, H. Lin et al., "Numerical analysis of fiber-reinforced soils based on the equivalent additional stress concept," *International Journal of Geomechanics*, vol. 19, no. 11, 2019.
- [31] Y. Chen, G. Wen, and J. Hu, "Analysis of deformation characteristics of fully grouted rock bolts under pull-and-shear loading," *Rock Mechanics and Rock Engineering*, vol. 53, no. 3, pp. 2981–2993, 2020.
- [32] Y. L. Zhao, L. Y. Zhang, J. Liao, W. J. Wang, Q. Liu, and L. Tang, "Experimental study of fracture toughness and subcritical crack growth of three rocks under different environments," *International Journal of Geomechanics*, vol. 20, no. 8, 2020.
- [33] Y. L. Zhao, L. Y. Zhang, W. J. Wang, Q. Liu, L. M. Tang, and G. Cheng, "Experimental study on shear behavior and a revised shear strength model for infilled rock joints," *International Journal of Geomechanics*, vol. 20, no. 9, 2020.
- [34] Y. L. Zhao, C. S. Zhang, Y. X. Wang, and H. Lin, "Shear-related roughness classification and strength model of natural rock joint based on fuzzy comprehensive evaluation," *International Journal of Rock Mechanics and Mining Sciences*, vol. 137, 2021 Available online.
- [35] Y. Zhao, C. L. Wang, and J. Bi, "Analysis of fractured rock permeability evolution under unloading conditions by the model of elastoplastic contact between rough surfaces," *Rock Mechanics and Rock Engineering*, vol. 53, no. 12, pp. 5795–5808, 2020.
- [36] H. Lin, H. Yang, Y. X. Wang, Y. L. Zhao, and R. H. Cao, "Determination of the stress field and crack initiation angle of an open flaw tip under uniaxial compression," *Theoretical and Applied Fracture Mechanics*, vol. 104, no. 12, 2019.
- [37] Y. Chen and H. Lin, "Consistency analysis of Hoek-Brown and equivalent Mohr-coulomb parameters in calculating slope safety factor," *Bulletin of Engineering Geology and the Environment*, vol. 78, no. 6, pp. 4349–4361, 2019.
- [38] S. J. Xie, H. Lin, Y. F. Chen, R. Yong, W. Xiong, and S. Du, "A damage constitutive model for shear behavior of joints based on determination of the yield point," *International Journal of Rock Mechanics and Mining Sciences*, vol. 128, 2020.
- [39] S. Xie, H. Lin, Y. Wang et al., "A statistical damage constitutive model considering whole joint shear deformation," *International Journal of Damage Mechanics*, vol. 29, no. 6, pp. 988–1008, 2020.
- [40] Y. Zheng, C. Chen, F. Meng, H. Zhang, K. Xia, and X. Chen, "Assessing the stability of rock slopes with respect to block-flexure toppling failure using a force-transfer model and genetic algorithm," *Rock Mechanics and Rock Engineering*, vol. 53, no. 8, pp. 3433–3445, 2020.
- [41] Y. Zheng, C. Chen, F. Meng, T. Liu, and K. Xia, "Assessing the stability of rock slopes with respect to flexural toppling failure using a limit equilibrium model and genetic algorithm," *Computers and Geotechnics*, vol. 124, 2020.
- [42] Y. Zheng, C. Chen, T. Liu, H. Zhang, and C. Sun, "Theoretical and numerical study on the block-flexure toppling failure of rock slopes," *Engineering Geology*, vol. 263, 2019.
- [43] Y. Zheng, C. Chen, T. Liu, D. Song, and F. Meng, "Stability analysis of anti-dip bedding rock slopes locally reinforced by rock bolts," *Engineering Geology*, vol. 251, pp. 228–240, 2019.
- [44] Y. Zheng, C. Chen, T. Liu, H. Zhang, K. Xia, and F. Liu, "Study on the mechanisms of flexural toppling failure in anti-inclined rock slopes using numerical and limit equilibrium models," *Engineering Geology*, vol. 237, pp. 116–128, 2018.
- [45] H. Lin, D. Lei, R. Yong, C. Jiang, and S. Du, "Analytical and numerical analysis for frost heaving stress distribution within rock joints under freezing and thawing cycles," *Environmental Earth Sciences*, vol. 79, p. 305, 2020.
- [46] H. Lin, X. Zhang, R. Cao, and Z. Wen, "Improved nonlinear Burgers shear creep model based on the time-dependent shear strength for rock," *Environmental Earth Sciences*, vol. 79, p. 149, 2020.
- [47] Z. M. He, D. Xiang, Y. X. Liu, Q. F. Gao, and H. B. Bian, "Deformation behavior of coarse-grained soil as an embankment filler under cyclic loading," *Advances in Civil Engineering*, vol. 2020, Article ID 4629105, , 2020.

- [48] Z.-M. He, Z.-F. Liu, X.-H. Liu, and H.-B. Bian, "Improved method for determining active earth pressure considering arching effect and actual slip surface," *Journal of Central South University*, vol. 27, no. 7, pp. 2032–2042, 2020.
- [49] R. Jiang, F. Dai, Y. Liu, and A. Li, "Fast marching method for microseismic source location in cavern-containing rockmass: performance analysis and engineering application," *Engineering*, vol. 4, 2021.
- [50] X. Fan, X. D. Jiang, Y. X. Liu, H. Lin, K. H. Li, and Z. M. He, "Local stress distribution and evolution surrounding flaw and opening within rock block under uniaxial compression," *Theoretical and Applied Fracture Mechanics*, vol. 112, 2021.
- [51] C. Y. Zhang, Y. X. Wang, H. Ruan, B. Ke, and H. Lin, "The strain characteristics and corresponding model of rock materials under uniaxial cyclic load/unload compression and their deformation and fatigue damage analysis," *Archive of Applied Mechanics*, pp. 1–6, 2021.
- [52] F. F. Liu, B. Q. Liu, C. Zhai, Z. Li, F. Li, and C. Zhou, "Research of real-time effects of horizontal protecting stratum mining based on similar simulation experiment," *Procedia Engineering*, vol. 26, pp. 431–440, 2011.
- [53] Q. Y. Tian, J. T. Zhang, and Y. L. Zhang, "Similar simulation experiment of expressway tunnel in karst area," *Construction and Building Materials*, vol. 176, pp. 1–13, 2018.
- [54] M. Tzalamarias, I. Tzalamarias, A. Benardos, and V. Marinos, "Room and pillar design and construction for underground coal mining in Greece," *Geotechnical and Geological Engineering*, vol. 37, no. 6, pp. 1729–1742, 2019.
- [55] J. J. Song, C. J. Han, P. Li et al., "Quantitative prediction of mining subsidence and its impact on the environment," *International Journal of Mining Science and Technology*, vol. 22, no. 2, pp. 69–73, 2012.
- [56] M. L. Zhong, H. J. Ma, and Y. Lin, "Study on mining methods and stope structure parameters for gently inclined complex orebody," *Industrial Minerals & Processing*, vol. 46, pp. 53–56, 2017.
- [57] G. H. Yao, A. X. Wu, and Y. M. Wang, "Stability analysis of stope retention pillars in broken rock conditions," *Journal of University Science and Technology Beijing*, vol. 33, pp. 400–405, 2011.
- [58] M. S. Kulkova and A. V. Zemtsovskiy, "Optimizing parameters of stopes and pillars for the zhdanov deposit mining," *Eurasian Mining*, vol. 5, pp. 13–15, 2019.
- [59] J. X. Fu, J. H. Du, and Y. Y. Tan, "The falling process and mechanism of concealed gob roof during the caving mining of the gently inclined heavy ore," *Journal of Mining Safety Engineering*, vol. 34, pp. 891–898, 2017.
- [60] B. B. Gao, X. L. Wang, M. L. Zhu et al., "Dynamic development characteristics of "two zones" of overburden in fully mechanized caving face of high gas thick seam with composite roof," *Chinese Journal of Rock Mechanics and Engineering*, vol. 31, pp. 3444–3452, 2018.
- [61] F. Zhang and B. Lehane, "A numerical study to assist assessment of the stability of shallow coal mine goafs," *Geotechnical and Geological Engineering*, vol. 37, no. 4, pp. 2837–2846, 2019.
- [62] F. G. Bell, T. R. Stacey, and D. D. Genske, "Mining subsidence and its effect on the environment: some differing examples," *Environmental Geology*, vol. 40, no. 1-2, pp. 135–152, 2000.
- [63] Y. H. Guo and K. P. Hou, "Stope structural parameters optimization of gently inclined and extremely thin orebody with room and pillar mining method," *Electronic Journal of Geotechnical Engineering*, vol. 19, pp. 3707–3719, 2014.
- [64] T. Sherizadeh and P. H. S. W. Kulatilake, "Assessment of roof stability in a room and pillar coal mine in the U.S. using three-dimensional distinct element method," *Tunnelling and Underground Space Technology*, vol. 59, pp. 24–37, 2016.
- [65] X. Liu, Z. X. Liu, A. H. Liu et al., "Chaotic optimization of structural parameters in gold mining field," *Journal of Mining and Safety Engineering*, vol. 27, pp. 548–552, 2010.
- [66] Y. L. Shang, "Similar simulation test research on overburden activity law of "two hard" working face in Sihe No. 2," *Coal*, vol. 26, pp. 12–14 + 58, 2017.
- [67] H. Xiao, *Study on Similar Simulation Test of Layered Rock Slope Excavation Process*, Kunming University of Science and Technology, Kunming, China, 2014.
- [68] J. P. Zheng and Y. J. Feng, "Strata behavior law of fully mechanized top coal caving face based on similar simulation test," *Metal Mines*, vol. 2, pp. 44–46, 2013.

Research Article

Numerical Study on Failure Mechanisms of Shaft Wall Consisting of Steel Plate and Concrete under the Effects of Explosion

Yanjun Qi,^{1,2} Linming Dou,² Zhaoxing Dong ¹ and Bo Meng¹

¹School of Mechanics and Civil Engineering, China University of Mining and Technology, Xuzhou 221116, China

²State Key Laboratory of Coal Resources and Safe Mining, China University of Mining and Technology, Xuzhou 221116, China

Correspondence should be addressed to Zhaoxing Dong; dongzx1966@163.com

Received 17 March 2021; Revised 6 April 2021; Accepted 12 April 2021; Published 24 April 2021

Academic Editor: Rihong Cao

Copyright © 2021 Yanjun Qi et al. This is an open access article distributed under the Creative Commons Attribution License, which permits unrestricted use, distribution, and reproduction in any medium, provided the original work is properly cited.

To enhance the antidynamic and static load resistance of reinforced concrete structures, the measure of covering steel plates on the inner surface of concrete structures arises, which has been rapidly developed and applied in civil engineering and other fields and has achieved a good performance. A new shaft wall structure consisting of steel plate reinforced concrete has been widely used in shaft of deep mining. In order to investigate the stability and obtain the optimum structure parameters of the new shaft structure, the numerical software of LS-DYNA was used to analyze the influences of different factors, including the explosive payload, steel plate thickness, concrete strength grade, and the included joint angle between two plates, on the stability of steel plate reinforced concrete structures. After the verification of the accuracy of numerical simulation results, 23 simulation schemes were proposed and numerically calculated. For all the tests, the principal tensile stress and particle vibration velocity were, respectively, chosen as the failure criteria to evaluate the impacts of those four factors. The results indicate that a quadratic function can be well used to describe the relationships between each factor and both the principal tensile stress and particle vibration velocity. Based on the results, the optimum structure parameters were finally determined, which are suggested as 250 kg, 15 mm, C85, and 40° for the explosive payload, steel plate thickness, concrete strength grade, and joint angle, respectively. The research results can provide a certain theoretical basis and design guidance for solving the problem of water leakage of single-layer shaft wall structures.

1. Introduction

With the depth increase of coal mine in China, great breakthrough has been made in the deep freezing technology. Meanwhile, the new shaft wall structure, which consists of the concrete body and steel joint plates, is bound to replace the past unreasonable single wall structure which is a superthick and simple structure. The key technology to ensure the integrity and water resistance is how to avoid the failure in concrete and along the interface between the concrete and steel plate under an applied explosive load [1, 2]. The main methods used to study the issue include model test and numerical simulation. Because of the accuracy and reliability of the numerical simulation, with big difficulty and high cost of

the model test, numerical simulation has been the most practical and efficient method.

Based on the study on the bend and failure modes of both the beam and plate structure under an applied explosive load, a simplified resistance model and an equivalent system of degree of freedom (DOF) of the beam and plate were proposed [3–6]. The reliability of the numerical simulation was proved by comparing the numerical simulation results using the finite element method (FEM) software and the real explosion tests of the dynamic response of concrete under an applied explosive load [7, 8]. The dynamic response of the concrete wall under explosion effects was obtained [9], and similar studies have been conducted by other reports [10, 11]. The deformation rules of concrete walls under an explosive load were gained from the numerical simulation

using the software of ANSYS/LS-DYNA [12, 13], and the dynamic response characteristics and failure patterns of the reinforced concrete slab subjected to an applied explosive load were investigated using both the experimental tests and FEM simulations [14–16]. All those reports used numerical simulations as an important means to analyze the mechanical properties of concrete under explosion. In addition, the reliability and accuracy of numerical simulations have also been verified.

Many works, including both the theoretical calculation and numerical simulation, have been conducted to study the mechanical and stability characteristics of steel plate reinforced concrete (SPRC) structure under an applied explosive load. The break characteristics of SPRC structures under an explosive load were investigated by analyzing the changes of the deformation and stress theoretically [17, 18]. The study results determined that the existence of steel plate decreases the crack in the concrete dramatically. By using a theoretical calculation model, a proper rock-concrete-steel plate example was built [19], and based on the example, the reinforcement mechanisms of steel plate and propagation mechanisms of waves in different media have been studied. A new calculation method of SPRC obtained from physical scaled model tests, which has been used in the engineering design, was proposed [20–22]. The numerical simulation that used ANSYS/LS-DYNA was performed to study the stability of tunnel lining structures under an applied explosive load, and the composite materials greatly improved the antiexplosion performances of the concrete [23]. Based on layered civil air defense works, a design scheme of layered civil air defense works used Split Hopkinson Pressure Bar (SHPB) and physical model tests were proposed [24–26]. In order to study the influence of explosive loads on the collapse of reinforced concrete slab, the software ANSYS/LS-DYNA was used to study the damage failure of the concrete and propose a new collapse calculation formula [27–29].

The focus of this study is to determine the break rules and optimum structural forms of SPRC sidewalls under an applied explosive load by using the FEM numerical simulations. The influence of different factors, including the explosive payload, thickness of steel plate, concrete strength, and joint angle of plate, was systematically studied. Based on the simulation results, the optimum design parameters of the sidewall were obtained.

2. Basic Theory of Stress Wave Propagation

The range of stress waves is a typical plastic zone, and the rock medium will be damaged and elastically deformed; thus, both continuous and residual deformation of the rock transfer disturbance should be considered. After the shock wave enters the middle zone of blasting, its properties and waveforms have changed greatly. The relationship between the maximum radial component and the maximum tangential component of the particle velocity on the wave front and the maximum radial pressure and the maximum tangential pressure on the wave front is as follows:

$$\sigma_{r \max} = \rho_0 C_1 V_{r \max}, \quad (1)$$

$$\sigma_{\theta \max} = \rho_0 C_1 V_{\theta \max}, \quad (2)$$

where ρ_0 is the rock density, C_1 is the P-wave velocity in the rock, $V_{r \max}$ and $V_{\theta \max}$ are the maximum radial component and the maximum tangential component of the particle velocity on the wave front, and $\sigma_{r \max}$ and $\sigma_{\theta \max}$ are the maximum radial pressure and the maximum tangential pressure on the wave front.

Displacement of the particles corresponding to the time of t under applied positive pressures is as follows:

$$d = \int_0^x V(t)dt. \quad (3)$$

The impulse density can be calculated as

$$I_p = \rho_0 C_1 \int_0^x V(t)dt = \rho_0 C_1 d. \quad (4)$$

The energy flux density is

$$W_p = \rho_0 C_1 \int_0^x V(t)dt, \quad (5)$$

$$W_p = \frac{1}{\rho_0 C_1} \int_0^x \sigma^2(t)dt = \rho_0 C_1 d. \quad (6)$$

Total energy of waves can be obtained:

$$W_t = W_p S. \quad (7)$$

Because there is a cohesive force at the interface between the concrete and rock and there is no sliding at the interface, thus the displacement, particle velocity, and stress at the interface are continuous. The reflection stress and transmission stress of the normal incidence can be calculated.

$$\begin{cases} \sigma_r = \sigma_i \frac{\rho_1 C_2 - \rho_0 C_1}{\rho_1 C_2 + \rho_0 C_1}, \\ \sigma_t = \frac{2\sigma_i \rho_1 C_2}{\rho_1 C_2 + \rho_0 C_1}, \end{cases} \quad (8)$$

where ρ_2 is the density of concrete.

3. Engineering Situation

3.1. Geological Conditions. An auxiliary shaft of a coal mine, whose design production capacity is 12 MT/a, was analyzed as the engineering background in this paper. The geological lithology of the mine, which has large inclined bedding and cross bedding, is mainly brown-red coarse-medium-grained sandstone, followed by fine-grained sandstone. The rock is argillaceous and cementation, mainly composed of feldspar and quartz, with subangular particles and medium sorting, presenting unconformity contact with the underlying stability group (J2A). The softening coefficient of all kinds of rocks in this area is less than 0.75, which is easy to be softened, and the core can be crushed by hand. The strength of the rock is equivalent to the weathered rock, and the

weathering resistance of the rock is very weak. Under normal circumstances, the core will be broken after exposure for 2-3 days.

3.2. Structure and Size of Shaft Wall. The net diameter of the auxiliary shaft is 10.0 m, the depth of the shaft is 755 m, and the whole shaft is constructed by using the freezing method. The single-layer shaft wall of the frozen bedrock section is sunk by using the drilling and blasting method, which saves investment and speeds up the sinking speed, and overcomes the shortcomings of thick, high cost, and slow construction of the double-layer composite borehole wall.

The study object in the numerical simulation model is the depth range from -320 m to -580 m of the shaft wall. To improve the sealing performance of jointing parts of the borehole wall, the steel plate was applied as the joint to prevent seepage, which constitutes SPRC structures with concrete of the shaft wall. The SPRC structure is shown in Figure 1.

4. Model Building and Parameters Determination of the Numerical Simulation

4.1. Model Building. The shape, size, and boundary of the model are all displayed in Figure 2. According to the site condition, the shaft radius was set at 5 m and the concrete wall thickness was set at 0.95 m. In order to reduce the influence of boundary effects and ensure the accuracy of the simulation results, the outer diameter and height of the model were set at 30 m and 25 m, respectively. In order to reduce the computational time, the 1/4 cylinder model of the overall model was established, and the radial boundary of the 1/4 model was set as the symmetric boundary condition. Since the upper, lower, and outer parts of the selected part could be regarded as semi-infinite spaces, those boundaries were set as nonreflective boundaries. In addition, only the total charge mass was taken into account in this paper, and the influence of the blast hole layout was neglected. Therefore, concentrated charge and primary detonation were used in the model. In order to study the secondary influence of explosion on the constructed steel sheet concrete composite structures, two (upper and lower) SPRC structures were established when building the model.

The model was built and meshed using the software of ANSYS and the material parameters are defined in LS-DYNA. The established numerical simulation model of the vertical shaft wall is shown in Figure 2.

4.2. Determination of the Material Parameters. Dynamic analysis software LS-DYNA was used for numerical simulation analysis in this study. The built model includes the explosive unit, concrete unit, surrounding rock medium unit, and steel unit, all of which are solid elements under dynamic loads, and the SOLID164 solid unit was selected.

In LS-DYNA, the material of MAT_HIGH_EXPLOSIVE_BURN was used to simulate high explosive materials and the state equation of EOS_JWL was applied to control the explosion process. In the initialization stage, the ignition

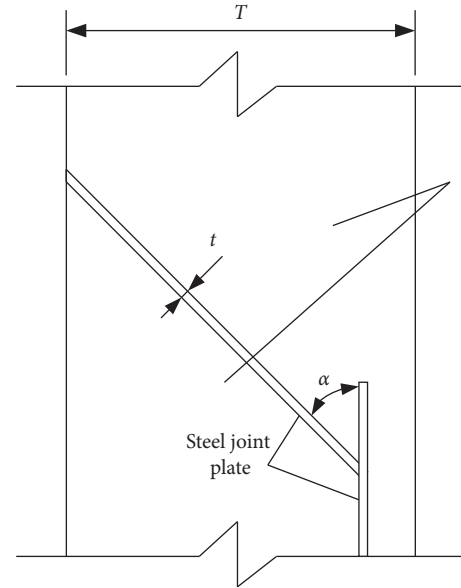


FIGURE 1: Layout Schematic of the SPRC structure in shaft wall.

time t_1 at the centroid (i.e., the position of the integration point) of each unit is calculated, which is equal to the distance L between the centroid of the unit and the detonation point divided by the detonation velocity D of the explosive. At time t , the combustion reaction rate F of the unit is as follows:

$$F = \max(F_1, F_2), \quad (9)$$

$$F_1 = \begin{cases} \frac{2(t-t_1)D}{3(V_e/A_{e\max})}, & t > t_1, \\ 0, & t \leq t_1, \end{cases} \quad (10)$$

$$F = \frac{1-V}{1-V_{cj}}, \quad (11)$$

where V_e is the unit volume, $A_{e\max}$ is the maximum unit area, V is the relative unit volume, and V_{cj} is the Chapman Jouguet pressure.

The form of the EOS_JWL state equation is as follows:

$$P = A \left(1 - \frac{\omega}{R_1 V} \right) e^{-R_1 V} + B \left(1 - \frac{\omega}{R_2 V} \right) e^{-R_2 V} + \frac{\omega E_0}{V}, \quad (12)$$

where A , B , R_1 , R_2 , and ω are state coefficients characterizing explosive properties and E_0 is the initial internal energy density.

According to the water-gel explosive used in the field, the parameters of the simulated explosive and state equation of JWL are shown in Table 1, where ρ is the density, D is the detonation velocity, E_0 is the initial internal energy of detonation, and P_{cj} is the detonation pressure. Other parameters are constantly used in the state equation.

The elastoplastic material of MAT_PLASTIC_KINEMATIC in LS-DYNA was applied to simulate the rock and concrete in this paper. The material model is a typical

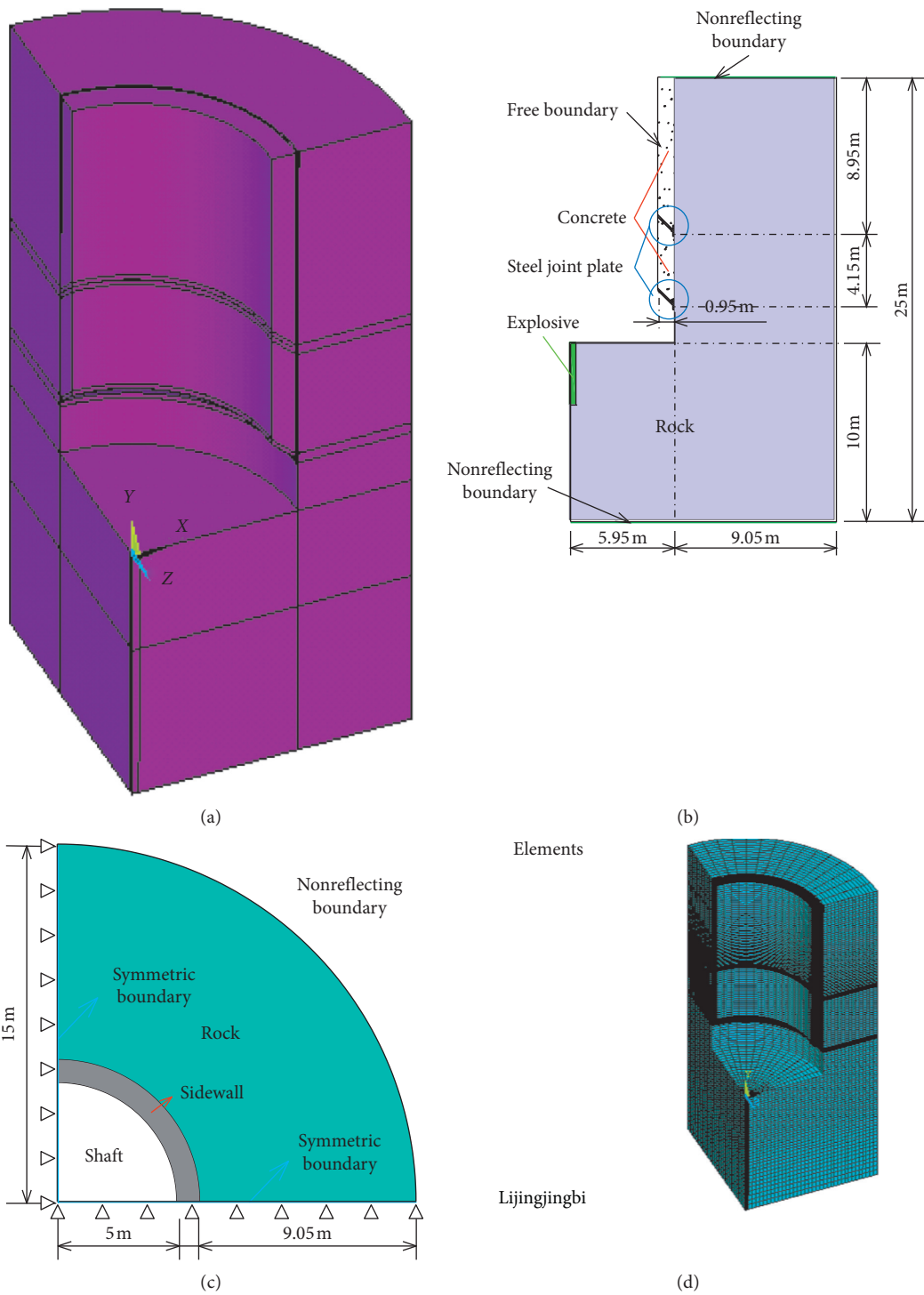


FIGURE 2: Numerical simulation model of the vertical shaft wall. (a) Schematic diagram of the model. (b) Front view of the model. (c) Top view of the model. (d) Meshing of the model.

TABLE 1: Parameters used in the explosive materials and state equation.

ρ (g/cm ³)	D (m/s)	P_{cj} (GPa)	A /(GPa)	B /(GPa)	R_1	R_2	ω	E_0 /J/m ³
1.02	4000	5.3	374	7.33	4.15	0.95	0.30	7×10^9

kind of isotropic and follow-up hardening mixture, which is related to the strain rate and takes the failure into account. The same material model was applied to simulate the rock and concrete, with the parameters shown in Table 2.

Generally, under the action of stress waves, the steel plate is considered to produce elastic deformation only, without plastic deformation or failure; thus, the elastic *MAT_JOHNSON_COOK material mode was selected. The parameters of the steel and state equation of GRUNEISEN are shown in Table 3.

4.3. Determination of the Simulation Experimental Scheme. In order to maximize economic benefits, new mines are often required to be built and put into production as soon as possible. Therefore, in the process of shaft excavation, the construction party often increases the explosive charge quantity in pursuit of progress. The larger amount of primary explosives will induce serious influences on the wellbore structures. Therefore, in order to clarify the specific impacts of the change of the explosive quantity on the steel plate concrete composite structures in shaft lining, this paper will study the dynamic response of the steel plate concrete composite structure under different explosive quantities based on the actual explosive quantity, from which, whether the current explosive quantity is reasonable is judged and the appropriate explosive quantity is obtained.

The increase of the steel plate thickness has little effect on the propagation of stress waves, while the tensile stress at the steel plate concrete interface will decrease significantly. The particle vibration velocity will only change the component size in each direction and has little effect on the actual particle vibration velocity. Therefore, this paper mainly studies the influence of the change of the steel plate thickness on the structural stress and determines the reasonable steel plate thickness.

The wave impedance of two adjacent media determines both the direction and value of the reflection and transmission of stress waves, and the change of the concrete strength grade will not affect the propagation of stress waves. When the stress wave causes the same stress in the steel plate and concrete, damage may occur when the strength grade of the concrete is too low. However, if the strength of the concrete is too high, it will not only increase the particle velocity but also make the strength surplus too large and cause waste. Therefore, it is necessary to study this factor and determine the reasonable strength grade of the concrete.

Considering the convenience of assembly and lifting, the included angle between the vertical and inclined steel plates is designed to be 45° in engineering fields. The changing included angles will vary the propagation path of the stress wave to some extent, resulting in differences between the reflection and transmission of stress waves and differences between the stress value and particle vibration velocity responses. Therefore, it is necessary to study the influences of the included angle between the steel plate and concrete and finally determine the appropriate angle.

Combined with the engineering practice, the influences of four factors including the explosive payload, thickness of

TABLE 2: Parameters of related rock and concrete.

Item	$\rho/(\text{g}/\text{cm}^3)$	$E/(\text{GPa})$	μ	Yield stress (MPa)
Rock	2.12	10	0.22	35
Concrete	2.50	35	0.19	—

TABLE 3: Parameters of the related steel plate.

Item	$\rho/(\text{g}/\text{cm}^3)$	$E/(\text{GPa})$	μ	C	S_1	S_2	V_0
Steel	7.8	210	0.27	0.45	1.49	0.0	1.0

steel plate, concrete strength, and included angle between steel plates on the failure and security of SPRC structures were studied in this paper. The initial scheme of this shaft is as follows: quantity of the primary explosive is 215 kg, thickness of steel plate is 8 mm, strength grade of concrete is C65, and the included angle between the vertical and inclined steel plates is 45°, with the scheme number of “215-8-65-45,” based on which, 24 schemes were designed, as shown in Table 4.

4.4. Verification of the Numerical Simulation Results. In order to verify the accuracy of the numerical simulation results, the peak pressure values at different positions of the cylindrical charge with an explosive quantity of 215 kg were calculated and then compared with the numerical simulation results. According to the observation data of the impact pressure in rock with the distance, the relationship between the shock pressure and distance follows an attenuation law [30]:

$$\sigma_{\max} = \frac{P_r}{\bar{r}^\alpha}, \quad (13)$$

where $\alpha = 2^+(\mu/1 - \mu)$; this expression is positive in the shock wave propagation region and negative in the stress wave propagation region. P_r is the pressure at the interface between the rock and explosive, \bar{r} is the relative distance, $\bar{r} = R/R_0$, R_0 is the radius of the explosive, R is the distance from the measure point to the explosive, and μ is Poisson's ratio.

The charge mode is a coupled cylindrical charge, according to the explosion force on the interface between the shock waves and stress waves, that is, the pressure at the interface between the rock and explosive, shown as the empirical formula [31]:

$$P_r = \frac{2\rho_m C_p}{\rho_m C_p + \rho_e D_e} * P_e, \quad (14)$$

where ρ_e and ρ_m are the density of the explosive and rock, respectively, C_p is the longitudinal wave velocity in the rock, D_e is the detonation velocity of the explosive, $\rho_m C_p$ and $\rho_e D_e$ are defined as the wave impedance of the rock and explosive, and P_e is the detonation pressure of the explosive.

The explosion wave pressure at the interface of the blast hole at different positions calculated by equation (2) and obtained from the numerical simulations is tabulated in Table 5. The maximum error between the theoretical and

TABLE 4: Numerical simulation schemes.

Item	Scheme					
EP	100-8-65-45	150-8-65-45	200-8-65-45	215-8-65-45	250-8-65-45	300-8-65-45
TSP	215-6-65-45	215-10-65-45	215-12-65-45	215-15-65-45	215-20-65-45	215-25-65-45
CS	215-8-C25-45	215-8-35-45	215-8-45-45	215-8-55-45	215-8-75-45	215-8-85-45
JA	215-8-65-30	215-8-65-40	215-8-65-45	215-8-65-50	215-8-65-60	

TABLE 5: Comparison of the theoretical calculation and numerical simulation results.

Position (m)	Value (MPa)		Relative error (%)
	Theoretical result	Simulation result	
0	720	610	15
0.5	207	212	2
1.0	62.9	58.4	7
3.0	9.5	9.2	3
5.0	4.0	3.95	1

numerical results is 15%, and the calculated and numerical results show good consistency. Therefore, the simulation results can be considered accurate and reliable.

4.5. Failure Criteria. Due to the fact that the dynamic tensile strength of the rock and concrete materials is far less than its dynamic compressive strength, the material in the SPRC structure is prone to brittle failure when subjected to a tensile stress. Thus, the first strength theory (the maximum tensile stress theory) is taken as one of the criteria to judge whether the concrete is damaged. In blasting engineering, the maximum vibration velocity (V_{\max}) of the structures should be less than some constants at a specific principal vibration frequency (PVF), as listed in Tables 6 and 7.

5. Analysis of the Numerical Simulation Results

As shown in Section 3.1, two steel joint layers were built in the simulation models, denoting the first layer and second layer from the bottom to top. Due to the numerous experimental groups, in order to reduce the workload, it is necessary to determine positions with the maximum stress and vibration velocity for analysis. In this study, scheme 215-8-65-45 is taken as an example, by comparing the stress and vibration velocity in three different points (Figure 3) of the two layers to determine which one possesses the larger stress and vibration velocity.

When the explosive explodes, it first produces a shock wave with a very strong peak pressure, then attenuates to a stress wave, and finally becomes an elastic wave until it disappears. The stress wave propagation law of the stress waves in the infinite rock mass is relatively clear, which radiates from the blasting center to the surrounding. However, when the stress wave propagates in an irregular structure, it will be affected by the shape and nature of the medium, and it is difficult to accurately describe its real propagation process. Figure 4 presents a typical spread process of stress waves in the steel plate and concrete

TABLE 6: Vibration velocity requirement for a roadway.

PVF (Hz)	$f \leq 10$ Hz	$10 \text{ Hz} \leq f \leq 50$ Hz	$f > 50$ Hz
V_{\max} (cm/s)	15~18	18~25	20~30

TABLE 7: Vibration velocity requirement for the newly poured concrete.

PVF (Hz)	$f \leq 10$ Hz			$10 \text{ Hz} \leq f \leq 50$ Hz			$f > 50$ Hz		
Age (day)	<3	3~7	7~28	<3	3~7	7~28	<3	3~7	7~28
V_{\max} (cm/s)	1~2	3~4	7~8	2~2.5	4~5	8~10	2.5~3	5~7	10~12

structures. The stress wave reaches the steel plate concrete composite structure at about 2000 us, and the peak value of stress waves increases significantly at the composite structure, which is due to the fact that the wave impedance of the concrete is less than that of the steel plate. With the change of time, the stress wave continues to propagate upwards the second layer of the composite structure, but the peak value of the stress wave becomes smaller. Finally, it decays to the elastic wave until it disappears.

Then, the stress and vibration velocity values of 3 measure points (edge of the inclined steel plate, central section of the inclined plate, and the central section of the vertical plate) were, respectively, selected from the board and compared to finally determine the most dangerous point for research.

The tensile stress curves of those three points in the two steel platelayers are shown in Figure 5. The maximum principal tensile stress of the first steel plate appears at the central position of the inclined plate (number as point B). From the stress history curve, it can be seen that the time when the stress value response begins to appear is the same as the time when the stress wave arrives, and the form of the main tensile stress curves and stress wave curves at the same position is basically the same. In Figure 5(a), the stress at point B and the central position of the vertical plate (point C) are nearly equivalent. The reason can be explained as follows: the attenuation of the peak stress wave at point C is smaller, and the induced principal tensile stress is larger than that at point B. Although the stress wave has been attenuated when propagating to the center of the steel plate, the stress waves propagated through other paths also reach this position. The stress superimposition effect results in the principal tensile stress at point B slightly larger than that of point C.

Comparing Figures 5(a) and 5(b), it is obvious that the time when the stress appears in the upper steel plate is 1000 us later than that of the lower steel plate, which follows the wave propagation rule. The maximum tensile stress at the

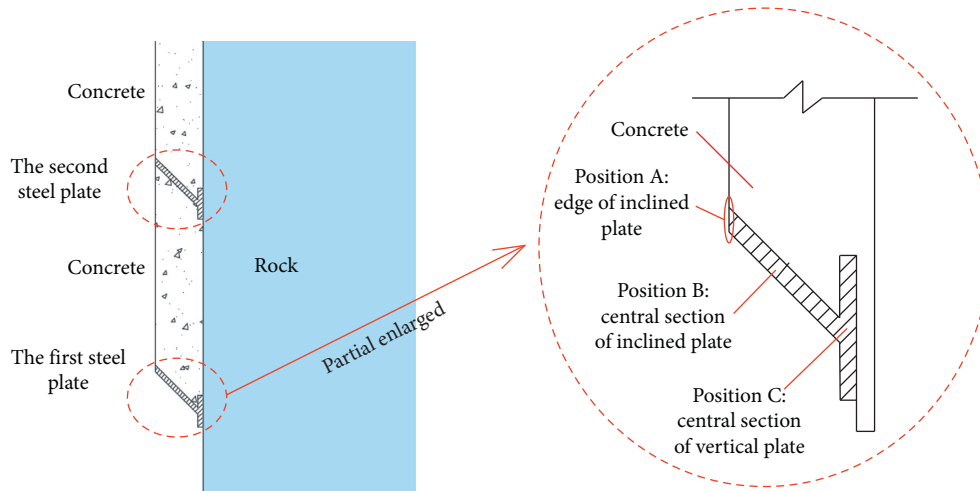


FIGURE 3: Partial enlargement of the joint plate.

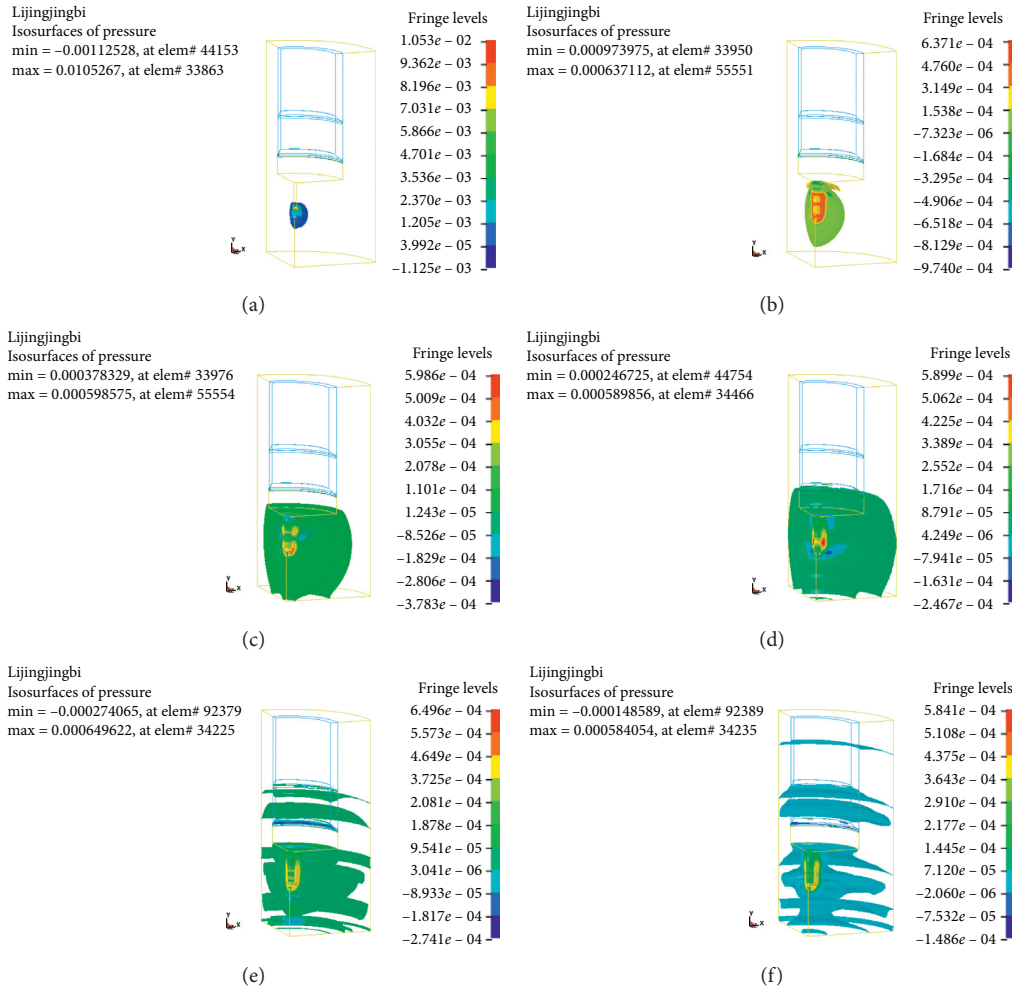


FIGURE 4: Spread process of stress waves. (a) $t = 300 \mu s$, (b) $t = 1100 \mu s$, (c) $t = 1700 \mu s$, (d) $t = 2000 \mu s$, (e) $t = 3000 \mu s$, and (f) $t = 5700 \mu s$.

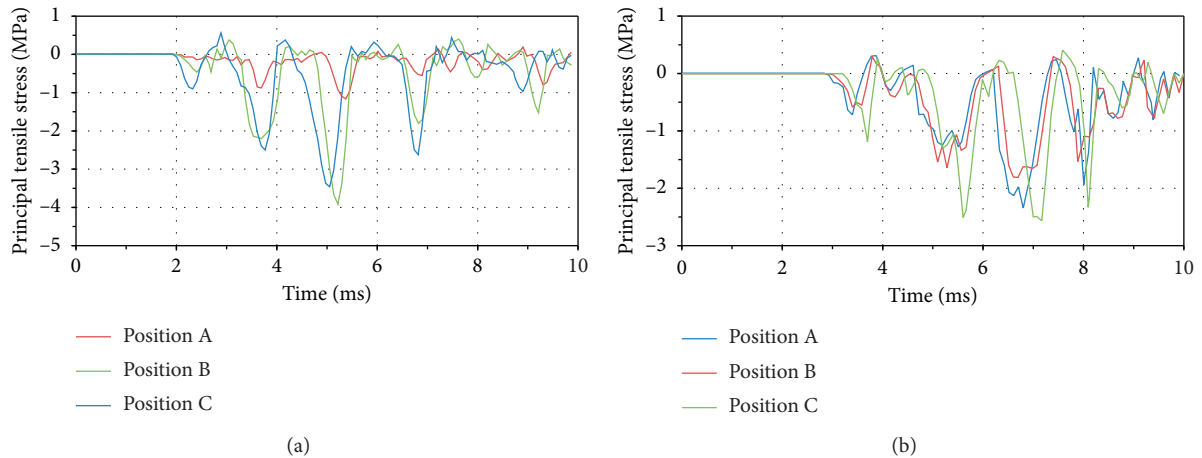


FIGURE 5: Principal tensile stress at different positions of the lower and upper steel plates. (a) Principal tensile stress curves at different positions of the lower plate. (b) Principal tensile stress curves at different positions of the upper plate.

upper steel plate is slightly smaller than that at the lower steel plate because the stress wave decays with the increase of the propagation distance and through different media, while the difference is not significant. In addition, for the upper steel plate, the maximum stress happens at point C, because of the superposition influence on the stress wave propagation caused by the irregularity of the whole wellbore structure, leading to different dynamic responses of those two steel joint plates. From the analysis above, point B at the lower (the central section of the inclined plate) is chosen as the study object to investigate the influences of different factors.

5.1. Influence of the Explosive Payload

5.1.1. Influence on the Principal Tensile Stress. With various explosive payloads, the principal tensile stress nephogram at the interface of the steel and concrete is shown in Figure 6(a). The principal tensile stress nephogram of the composite structure is basically the same at the same time with various primary explosive quantities. The stress response of the composite structure begins to appear at 2300 μ s, and the stress value of the composite structure reaches the maximum at 5200 μ s.

The time history curves of the principal stress at point B with different explosive payloads are shown in Figure 6(b). The shape of the principal tensile stress curves and the time when the maximum stress appears are approximately the same with different explosive payloads, indicating that different explosive payloads have little effect on both the propagation speed and reflection law of the stress waves. For the amount of explosives of 100, 150, 200, 215, 250, and 300 kg, the corresponding maximum tensile stress values are 2.7, 3.2, 3.7, 4.0, 4.1, and 4.4 MPa, respectively. With the increase in the explosive payload, the maximum tensile stress increases significantly but the growth rate decreases gradually. Therefore, increasing the explosive payload has a great impact on the stability of the SPRC structures. It is suggested that the short footage tunneling and small explosive payload should be used in the construction process to protect the SPRC structures from damage.

The fitting curve of the relationship between the maximum tensile stress at the center of the steel plate and the explosive payload is shown in Figure 6(c). The growth speed of the maximum tensile stress first increases quickly and then slows down. Particularly, the value of the maximum tensile stress with the explosive payload of 215 kg and 250 kg is close. In order to make the blasting effect better, the explosive payload can also be appropriately increased to 250 kg.

The dynamic strength of the concrete materials is significantly different with different strain rates. When the strain rate reaches $10^2/s$, the dynamic tensile strength of the concrete materials could reach about 10 times larger than the static tensile strength [32]. With a continuous increase of the strain rate, the dynamic tensile strength of the concrete will increase greatly. The strain rate of the concrete can reach $10^4/s$ when subjected to stress waves, and the induced dynamic strength of the concrete will be very large. In this study, a concentrated charge with a radius of 0.13 m was used, and the scope of the stress wave was 120~150 times larger than the charging radius [33]. Obviously, the concrete in the model is in the scope of stress waves. However, the current study on the tensile strength of the concrete was under static conditions with standard maintenance and low strain rates. Few reports focus on the dynamic tensile strength of the concrete with short setting time and high strain rates; thus, it is not accurate to determine whether the structure is damaged only from the aspect of the dynamic tensile strength.

5.1.2. Influence on the Vibration Velocity. Because the maximum value of the first principal stress is greater than the absolute value of the third principal stress under the same factor, the maximum particle velocity in the positive direction should be greater than the maximum particle velocity in the negative direction. Thus, the maximum vibration velocity of the structure particle was selected as the study object in this section, and the positive vibration velocity of the particle at point B was analyzed. The time

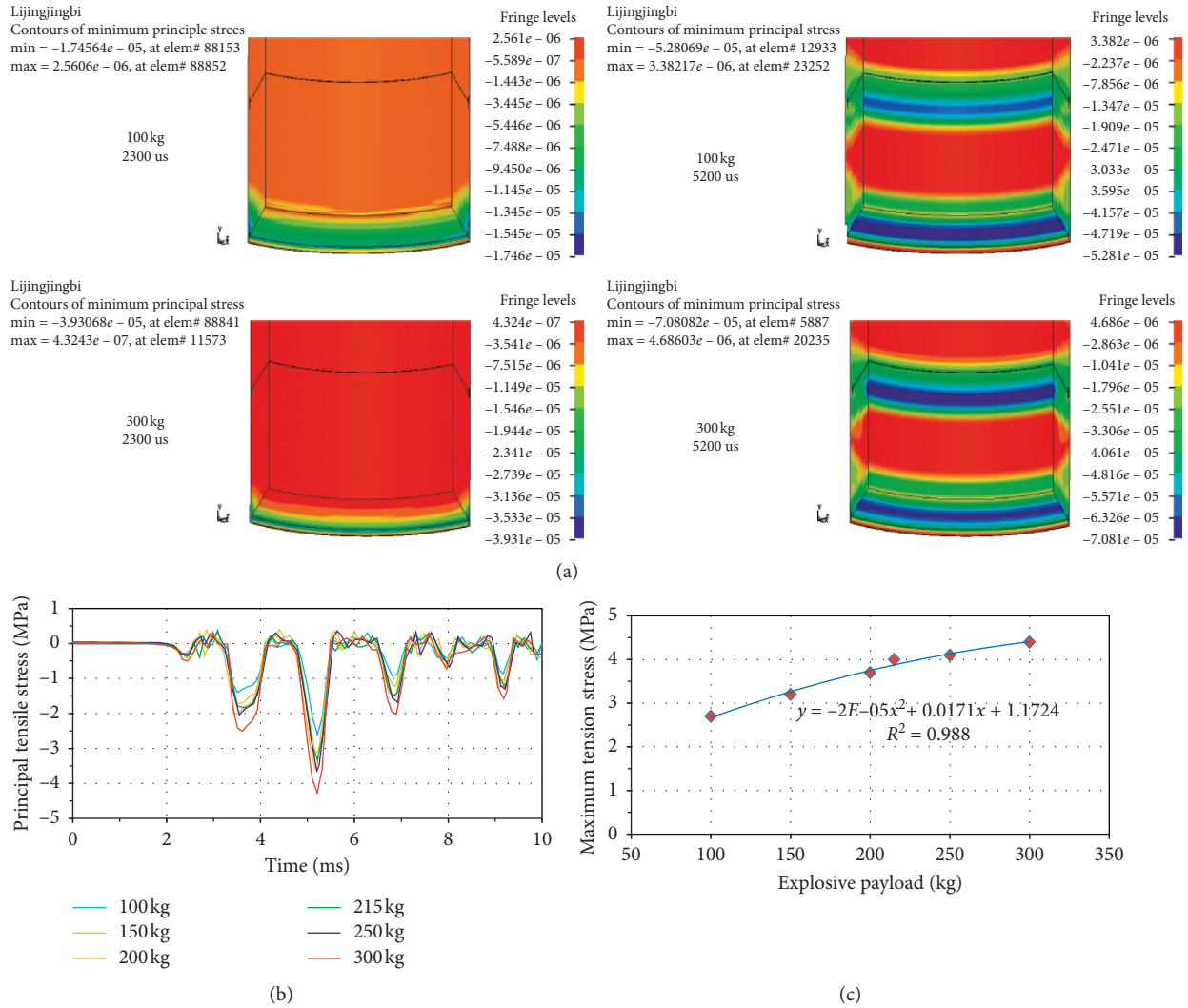


FIGURE 6: The relationships between principal tensile stress and explosive payloads. (a) Nephogram of the principal tensile stress at the center of the steel plate. (b) Principal tensile stress history curves with different explosive payloads. (c) Maximum tension stress with different explosive payloads in the steel center.

history curves of the particle vibration velocity at point B with different explosive payloads are shown in Figure 7(a).

From Figure 7(a), the vibration velocity increases with the increase in the explosive payload. Due to the fact that there is little influence of explosive payloads on the stress wave propagation, the shape of the vibration velocity curves and the corresponding time when the extreme values appear are generally consistent. The maximum particle vibration velocity at point B with six different groups of explosive payloads is 1.8 cm/s, 2.4 cm/s, 2.7 cm/s, 3.0 cm/s, 3.1 cm/s, and 3.4 cm/s, respectively, and the fitting curves of the relationships between the maximum particle vibration velocity and the detonating charge are plotted in Figure 7(b).

By means of the postprocessing software of LS-Prepost, the main vibration frequency was obtained after the transformation of the particle vibration curves by FFT (fast Fourier transform), and the calculated main frequency of the structure is 633 Hz. In the engineering field, the concrete setting time is about 3~7 days when the blasting

construction is applied. Table 7 in Section 3.5 shows that the safety vibration velocity of the concrete in this study is 5~7 cm/s. According to the numerical simulation results, when the explosive payload is 250 kg, the maximum particle vibration velocity is 3.1 cm/s, which is still smaller than the safety vibration velocity of the particles. Hence, a visible increase of the explosive payload would not result in particle vibration velocities of the SPRC structures exceeding the security scope. Thus, taking the economy and reducing the stress value and particle vibration velocity into account, it is suggested that the explosive dosage should be increased to 250 kg.

5.2. Influence of the Thickness of Steel Plates

5.2.1. Influence on the Principal Tensile Stress. The nephogram and the time history curves of the principal tensile stress at point B as well as the fitting curves of the relations between the third principal stress and thickness of the steel

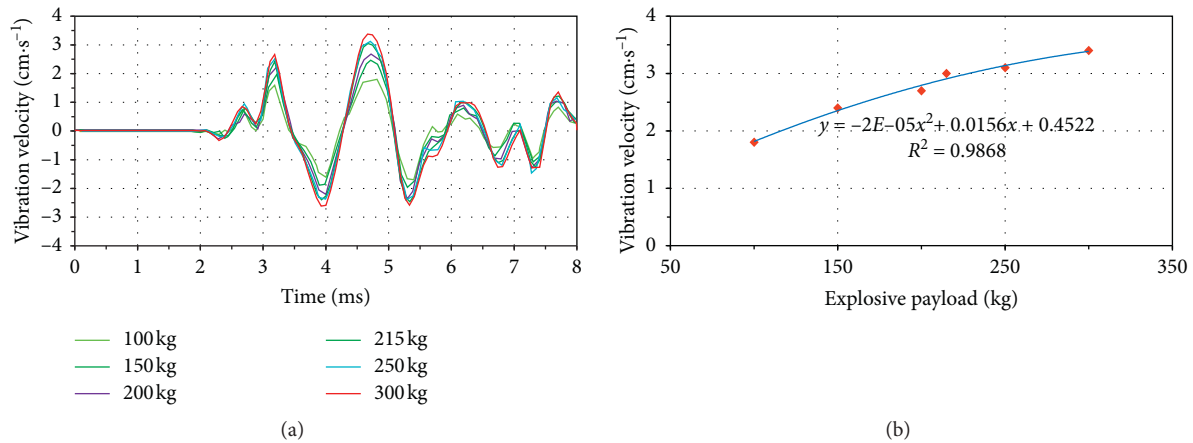


FIGURE 7: Vibration velocity of steel central position with different explosive payloads. (a) Velocity history curves of particle under different explosive payloads. (b) Positive velocity fitting curve under different explosive payloads.

plates are shown in Figure 8. With various thicknesses of steel plates, the principal tensile stress nephogram of the composite structure is basically the same at the same (Figure 8(a)). From Figure 8(b), the shape of the main tension curves is basically unchanged with various steel plate thickness, and the time when the peak tensile stress appears is generally the same, indicating that the thickness of steel plates has little influence on the propagation path of stress waves in the SPRC structures. The maximum tensile stress at the central position of the vertical plate with various thicknesses is 4.2, 4.0, 3.7, 3.6, 3.4, and 3.1 MPa, respectively. The maximum tensile stress decreases significantly with increasing plate thickness. Therefore, it is suggested that the thickness of the steel plates should be increased in the structural design to protect the composite structures of both steel plate and concrete from damage.

From the fitted curve in Figure 8(c), the increasing thickness of the steel plate leads to a reduction of the tensile stress of both the steel plate and concrete, and the reduction rate gradually diminishes. In practical engineering, the principal stress of the steel plate with a thickness of 8 mm is 4.0 MPa. Given that the significant increase in the thickness of the steel plate does not lead to a corresponding decrease in the tensile stress and adopting a thicker steel plate can significantly increase both the cost and difficulties of the structure assembled welding, the appropriate thickness of the steel plate can be selected as 15 mm or 20 mm, from the perspectives of the principal tensile stress of SPRC structures.

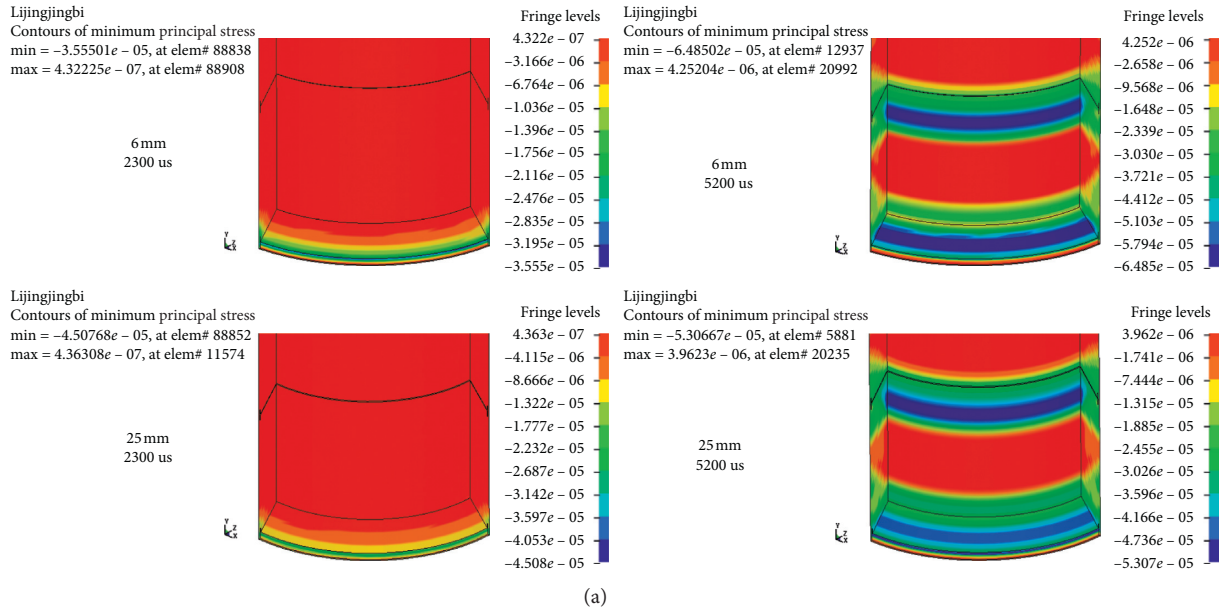
5.2.2. Influence on the Vibration Velocity. The effects of variations in the steel plate thickness on the vibration velocity of the structural particles are shown in Figure 9. As the steel plate thickness increases, the peak value of the positive vibration velocity at point B is nearly unchanged, while the peak value of the negative vibration velocity decreases significantly, and the time when the maximum particle vibration velocity appears is approximately the same. Therefore, from the particle velocity, the influence of the steel plate thickness cannot be considered during the structural design.

From Figure 9(b), the positive particle vibration velocity varies in the range of 2.8 cm/s to 3.1 cm/s with the increase of the steel plate thickness, while the safe particle vibration velocity is 5 cm/s~7 cm/s. In the engineering field, the maximum particle velocity induced by the steel plate thickness of 8 mm is 3.0 cm/s, which was far smaller than the safe velocity. The steel plate thickness is 10 mm, 12 mm, and 15 mm for the minimum vibration velocity of 2.8 cm/s. Considering the factors of economy, stress reduction, and particle vibration velocity, the thickness of 15 mm is recommended.

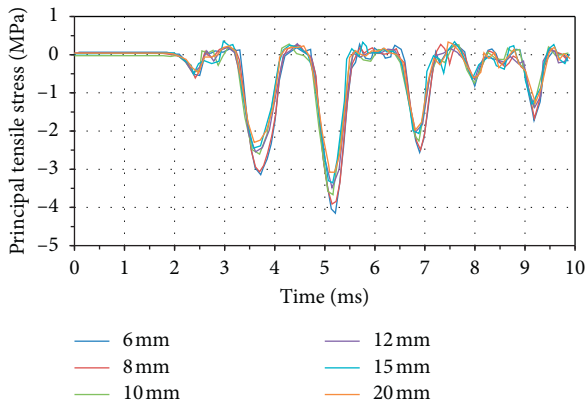
5.3. Influence of the Concrete Strength

5.3.1. Influence on the Principal Tensile Stress. The nephogram and time history curves of the principal tensile stress at point B with different concrete strength grades are shown in Figure 10. It can be seen that, with various concrete strengths, the principal tensile stress nephogram of the composite structure is basically the same, as shown in Figure 10(a). The change of the concrete strength grade does not have an obvious influence on variation trends of the principal tensile stress curves, and the time when the peak tensile stress appears on the steel-concrete interfaces is basically the same, indicating that the change of the concrete strength grade has little influence on the propagation speed of the stress waves (Figure 10(b)).

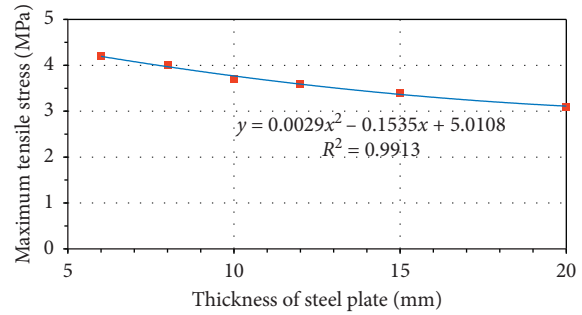
Corresponding to different concrete grades (C35, C45, C55, C65, C75, and C85), the maximum tensile stress value is 3.6 MPa, 3.7 MPa, 3.9 MPa, 4.0 MPa, 3.9 MPa, and 4.0 MPa, respectively. The maximum tensile stress increases generally with the increasing concrete strength grades. However, when the concrete strength grade is greater than C55, the maximum tensile stress remains almost constant values. Note, the increase in strength grades can significantly improve the dynamic tensile/compressive ability of the concrete. Thus, a high concrete grade of C75 or C85 is recommended considering the strength of the SPRC structures.



(a)

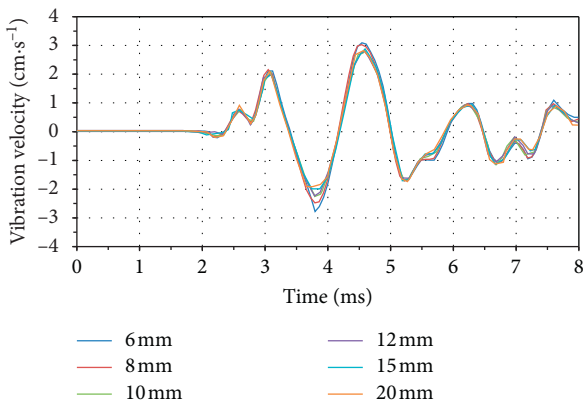


(b)

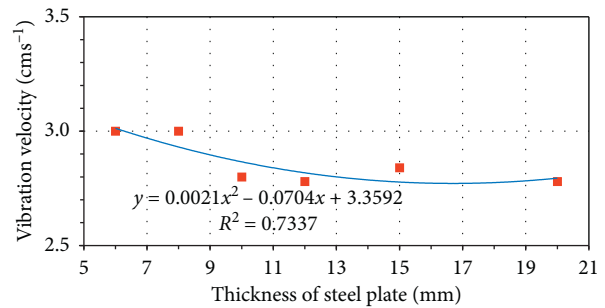


(c)

FIGURE 8: Tensile stress curve corresponding to different steel plate thickness. (a) Nephogram of the principal tensile stress at the center of the steel plate. (b) Principal tensile stress curves with different steel plate thickness. (c) Maximum tension stress corresponding to different steel plate thickness.



(a)



(b)

FIGURE 9: Vibration velocity curves corresponding to different steel plate thickness. (a) Vibration velocity curves with different steel plate thickness. (b) Vibration velocity fitting curve under different steel plate thickness.

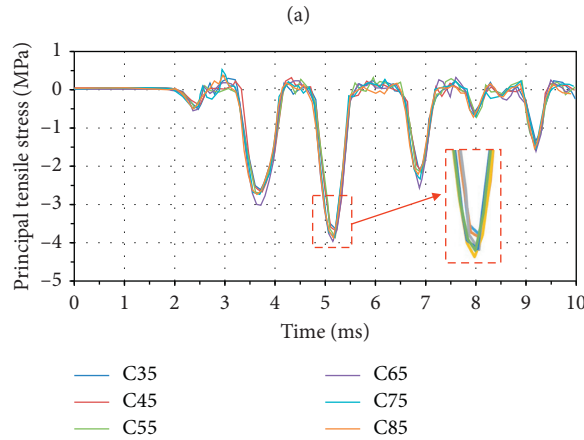
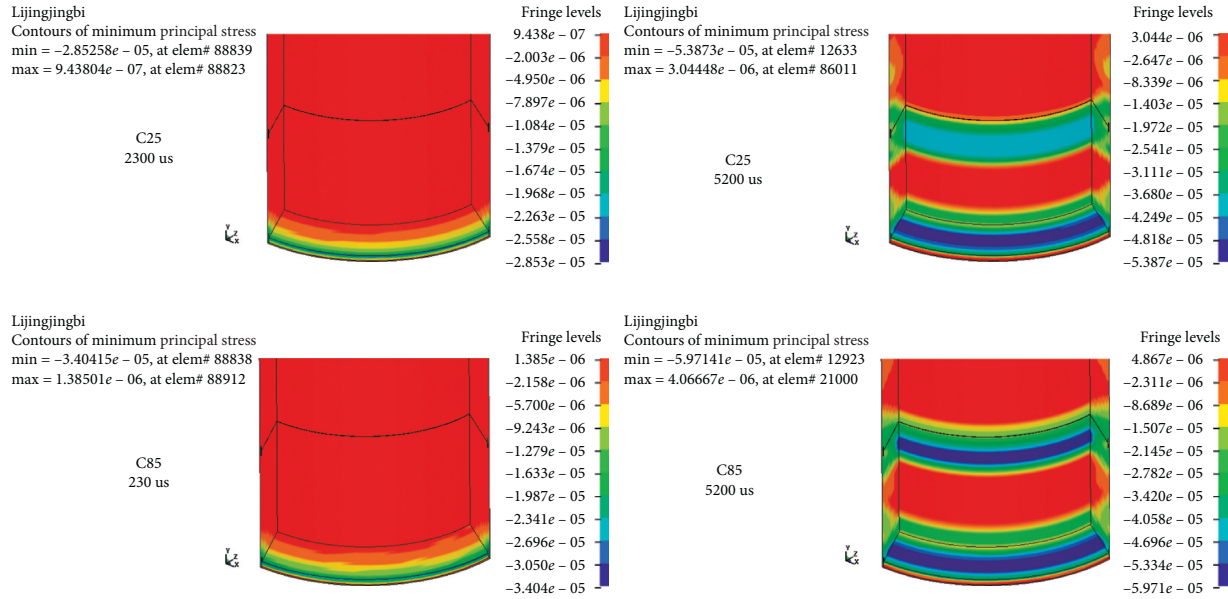


FIGURE 10: Principal tensile stress of the steel central position with various concrete strengths. (a) Nephogram of the principal tensile stress at the center of the steel plate. (b) Principal tensile stress curves with different concrete grades.

5.3.2. *Influence on the Vibration Velocity.* The influence of the concrete strength grade on the vibration velocity curves of the structural particles is shown in Figure 11. The maximum vibration velocity of particles at position B under six different concrete strength grades is 2.82 cm/s, 2.79 cm/s, 2.75 cm/s, 3.0 cm/s, 2.74 cm/s, and 2.7 cm/s, respectively. With an increase in the concrete strength grade, the peak value of the particle vibration velocity first increases and then decreases. Because the change of concrete strength grades has little influence on the propagation of stress waves, the form of vibration velocity curves is similar and the extreme values appear at the same time. According to the blasting vibration criterion, the safe particle vibration velocity of the structure is 5~7 cm/s. The maximum particle velocity caused by C65 concrete used in actual engineering is 3.0 cm/s, and the minimum vibration velocity is 2.7 cm/s for the concrete strength grade C55, C75, and C85. Considering the factors such as economy, reduction of stress value, and particle velocity, the strength grade of concrete is suggested to be C85.

5.4. *Influence of the Intersection Joint Angle*

5.4.1. *Influence on the Principal Tensile Stress.* The nephogram and time history curves of the principal tensile stress in the SPRC structures with various joint angles are shown in Figure 12. For the case of different angles between steel plates, the nephogram of the principal tensile stress varies greatly at the same time. The stress response of the composite structure begins to appear at 2300 us, while the stress value of the composite structure does not reach the maximum values at 5200 us (Figure 12(a)). It is obvious that the time when the peak stress appears is different with increasing joint angles. It is different from other factors which just affect the peak value but do not affect the corresponding time. Taking the joint angle of 45° as the division, when the joint angle is greater than 45°, the time when the principal tensile stress reaches the maximum value is the shortest, indicating that the position with the maximum stress appears before position B. The actual calculation results present that the

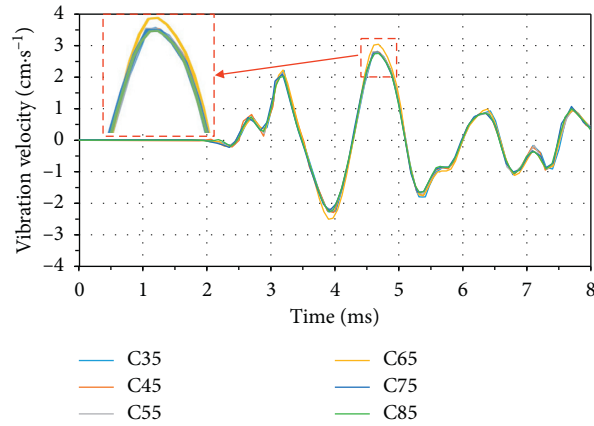
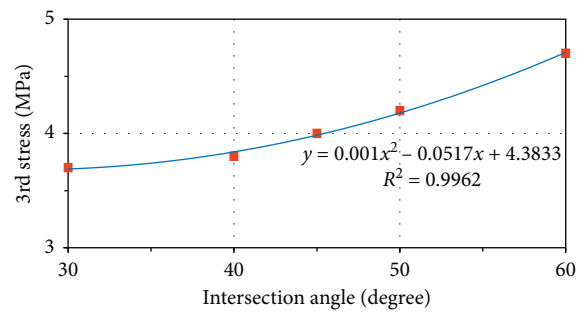
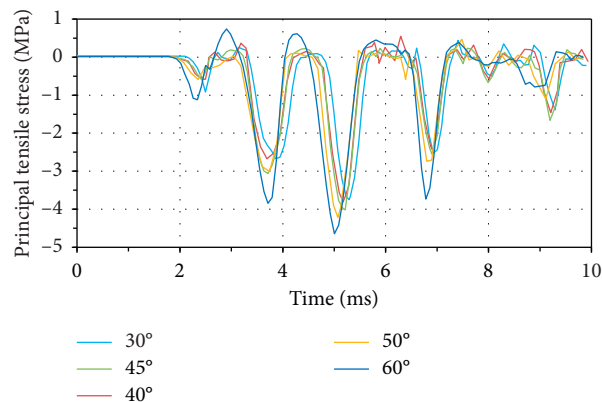
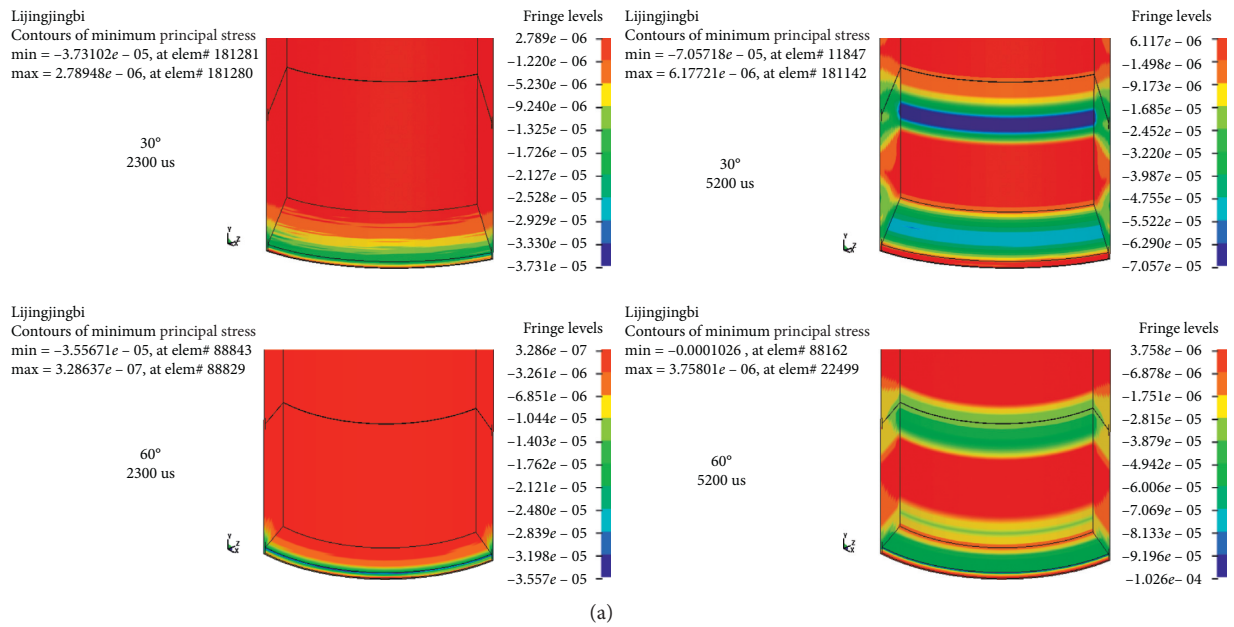


FIGURE 11: Velocity history curves under different concrete strength in the steel center.



(b)

(c)

FIGURE 12: Relationships between the tensile stress in SPRC structures and joint angles. (a) Nephogram of the principal tensile stress at the center of the steel plate. (b) Tensile stress curves with different joint angles between two steel plates. (c) Fitting curves between the maximum tensile stress and joint angles.

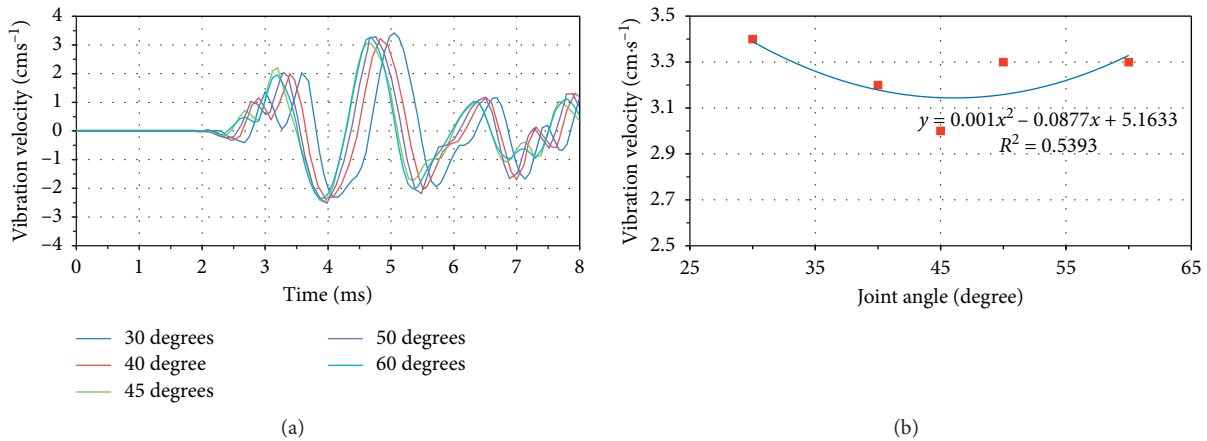


FIGURE 13: Relationships between vibration velocity and joint angles. (a) Velocity history curves with different joint angles of plates. (b) Fitting curves of vibration velocity with different joint angles.

maximum value appears at position C, and the opposite law is true when the joint angle is less than 45°. The maximum tensile stress is 3.7 MPa, 3.8 MPa, 4.0 MPa, 4.2 MPa, and 4.7 MPa, respectively, corresponding to the five groups of joint angles. The maximum tensile stress increases with the increasing joint angle between the vertical and inclined steel plates. Therefore, the change of joint angles has a great impact on the stress responses of the SPRC structures. It is suggested that the joint angle should be reduced in the structural design to protect the SPRC structures from damage (Figure 12(b)).

From Figure 12(b), the increase in joint angles results in the increase of the maximum tensile stress in the SPRC structures, and the growth rate gradually accelerates. In the engineering field, the principal tensile stress is 4.0 MPa when the angle equals 45°. Considering that the reduction of the joint angle can reduce the value of the principal tensile stress, the joint angle should be a smaller value. However, when the joint angle is reduced significantly, the tensile stress value does not significantly decrease. Moreover, too small joint angles will greatly increase the steel consumption, which will not only significantly increase the cost but also cause difficulties in the structure assembly. Therefore, considering the stress state of the structure, the appropriate joint angle is recommended to be 40°.

5.4.2. Influence on the Vibration Velocity. From the above studies, an obvious correspondence between the particle vibration velocity and principal stress value can be obtained; that is, the greater the principal tensile stress, the greater the negative vibration velocity of particles. Therefore, in this section, the positive vibration velocity of the particle at point B is mainly taken as a reference and compared with the safe vibration velocity.

The influence of the changes in the joint angle on the particle vibration velocity of the SPRC structures is shown in Figure 13. No matter how the joint angle varies, the peak value of the positive vibration velocity of the upper particle on the SPRC structures will increase, while the change range is small. When the joint angle is 60° and 45°, the time

when the particle vibration velocity reaches the maximum values is basically the same, but when the angle is 30°, the time to reach the maximum is later, which indicates that the maximum compressive stress is located between position A and position B. Therefore, from the perspective of the particle velocity, the influence of the angle between steel plates should be considered during the structural design.

From Figure 13(b), the maximum particle vibration velocity caused by the joint angle of 45° used in actual engineering is 3.0 cm/s, which is the minimum value of the particle vibration velocity. The maximum particle vibration velocity caused by the steel plate angle of 40° is 3.2 cm/s, which is also within the range of the safe vibration velocity. Therefore, considering economic factors, and influences of joint angles on both stress and particle velocity, it is suggested that the joint angle should be 40°.

6. Conclusions

In this study, numerical simulations were applied to investigate the influences of the explosive payload, thickness of steel plate, concrete strength grade, and the joint angle between the inclined and vertical plates on the SPRC structures. The maximum tensile stress and vibration velocity were selected as the failure criteria. From those above studies, some conclusions can be drawn as follows:

- (1) The stress analysis was carried out on the same position of the upper and lower steel joint plate structures, the maximum stress was determined at the center section of the inclined steel plates of the lower steel plate structures (position B), and this point was taken as the study object of different influence factors.
- (2) The change of explosive payloads has little effect on the shape of the stress waves, but the maximum principal tensile stress and particle vibration velocity could be varied significantly. It is found that both the tensile stress and particle vibration velocity increase with the increasing explosive payload. It is suggested that the explosive payload should be less than 250 kg.

- (3) The change of the thickness of steel plates has little effect on the shape of the stress waves. With an increase in the thickness of steel plates, the tensile stress is significantly reduced, but the particle vibration velocity is almost unchanged. It is suggested that the thickness of the steel plate should be 15 mm.
- (4) The change of concrete strength grades has little effect on the form of stress waves. With the increase in the concrete strength grades, the tensile stress and particle velocity increase and decrease, respectively. It is suggested that the strength grade of the concrete should be C85.
- (5) Different from the above three factors, the change of joint angles has a great influence on the shape of stress waves and changes the propagation path of the stress waves. It is found that the principal tensile stress increases significantly with the increase of the joint angle, but the particle vibration velocity always increases with no matter decreasing or increasing joint angles. The joint angle is recommended to be 40°.

Data Availability

All data during this study are available from the corresponding author upon request.

Conflicts of Interest

The authors declare that they have no known conflicts of interest or personal relationships that could have appeared to influence the work reported in this paper.

Acknowledgments

The financial support from the National Natural Science Foundation of China (51874292 and 51934007); National Key Basic Research and Development Program of China (no. 2016YFC0801403), and Key Basic Research and Development Program of Jiangsu Province (no. BE2015040) is gratefully acknowledged.

References

- [1] H. Dong, Y. Zhao, W. Cao, X. Chen, and J. Zhang, "Interfacial bond-slip behaviour between reinforced high-strength concrete and built-in steel plate with studs," *Engineering Structures*, vol. 226, no. 3, p. 111317, 2021.
- [2] Q. Yin, R. Liu, H. Jing, H. Su, L. Yu, and L. He, "Experimental study of nonlinear flow behaviors through fractured rock samples after high-temperature exposure," *Rock Mechanics and Rock Engineering*, vol. 52, no. 9, pp. 2963–2983, 2019.
- [3] T. Krauthammer, "Shallow-buried RC box-type structures," *Journal of Structural Engineering*, vol. 110, no. 3, pp. 637–651, 1984.
- [4] T. Krauthammer, N. Bazeos, and T. J. Holmquist, "Modified SDOF analysis of RC box-type structures," *Journal of Structural Engineering*, vol. 112, no. 4, pp. 726–744, 1986.
- [5] T. Krauthammer, A. Assadi-Lamouki, and H. M. Shanaa, "Analysis of impulsively loaded reinforced concrete structural elements-I. theory," *Computers & Structures*, vol. 48, no. 5, pp. 851–860, 1993.
- [6] C.-J. Huang, X.-A. Wu, S.-J. Chen, and X.-B. Song, "Behaviors of steel-plate and concrete in steel-concrete-steel panels subjected to biaxial tension-compression," *Structures*, vol. 30, no. 5, pp. 217–228, 2021.
- [7] K. B. Morrill, L. J. Malvar, J. E. Crawford, and J. M. Ferritto, "Blast resistant design and retrofit of reinforced concrete columns and walls," in *Proceedings of the 2004 Structures Congress-Building on the Past: Securing the Future*, Nashville, TN, USA, 2004.
- [8] J. W. Zhang, F. Z. Li, and S. J. Liu, "Influence of different fibers on cracking resistance of shaft wall mass concrete," *Key Engineering Materials*, vol. 852, pp. 150–159, 2020.
- [9] P. T. Nash, C. V. G. Vallabhan, and T. C. Knight, "Spall damage to concrete walls from close-in cased and uncased explosions in air," *ACI Structural Journal*, vol. 92, no. 6, pp. 680–688, 1995.
- [10] S. T. Dennis, J. T. Baylot, and S. C. Woodson, "Response of 1/4-scale concrete masonry unit (CMU) walls to blast," *Journal of Engineering Mechanics*, vol. 128, no. 2, pp. 134–142, 2002.
- [11] J. T. Baylot, B. Bullock, T. R. Slawson, and S. C. Woodson, "Blast response of lightly attached concrete masonry unit walls," *Journal of Structural Engineering*, vol. 131, no. 8, pp. 1186–1193, 2005.
- [12] C. D. Eamon, J. T. Baylot, J. L. O'Daniel, and L. James, "Modeling concrete masonry walls subjected to explosive loads," *Journal of Engineering Mechanics*, vol. 130, no. 9, pp. 1098–1106, 2004.
- [13] M. Labibzadeh and R. Hamidi, "A design formula for lateral load resistance of concrete filled double-steel-plate walls with small height-to-length ratio," *KSCE Journal of Civil Engineering*, vol. 23, no. 4, pp. 3493–3508, 2019.
- [14] A. C. Jacinto, R. D. Ambrosini, and R. F. Danesi, "Experimental and computational analysis of plates under air blast loading," *International Journal of Impact Engineering*, vol. 25, no. 10, pp. 927–947, 2001.
- [15] M. Z. Zineddin, "Behavior of structural concrete slabs under localized impact," Doctoral dissertation, The Pennsylvania State University, University Park, PA, USA, 2002.
- [16] S. Guo and D. V. Griffiths, "Failure mechanisms in two-layer undrained slopes," *Canadian Geotechnical Journal*, vol. 57, no. 5, pp. 1617–1621, 2020.
- [17] J. Liu, Q. Fang, Z. Gong, and J. Fan, "Analysis of dynamic responses and failure modes of R/C beams under blast loading," *Explosion And Shock Waves*, vol. 1, pp. 25–30, 2003.
- [18] J. Liu, Q. Fang, Y. Zhang, and X. Zhao, "Analysis of local effects on steel-backed concrete composite structures under blast loading," *Acta Armamentarii*, vol. 6, pp. 773–776, 2004.
- [19] X. Li, Y. Zheng, and G. Xu, "Local response analysis of layered structure for rock-concrete-steel panel subject to blast loading," *Journal of Logistical Engineering University*, vol. 4, pp. 21–24, 2007.
- [20] G. Lu and R. Lin, "Calculating method for deformation of structures of reinforced concrete-steel plate against explosion action," *Journal of Tongji University*, vol. 5, pp. 510–512, 2000.
- [21] S. Yan, B. X. Qi, H. Yan, and L. Yang, "Numerical simulation on failure modes of light steel columns under high temperature and explosion," *Applied Mechanics and Materials*, vol. 204–208, pp. 3351–3356, 2012.
- [22] A. A. Sharba, "The efficiency of steel slag and recycled concrete aggregate on the strength properties of concrete," *KSCE Journal of Civil Engineering*, vol. 23, no. 5, pp. 4846–4851, 2019.

- [23] M. Zhang, "Study on the anti-blasting numerical simulation of urban shallow tunnel lining structure," Doctoral dissertation, Xi'an University of Science and Technology, Xi'an, China, 2009.
- [24] K. Zhao, "The attenuation and dispersion effects on explosive wave of layered protective engineering," Doctoral dissertation, University of Science and Technology of China, Hefei, China, 2007.
- [25] Z. W. Xie, X. Y. Wu, and Q. Wan, "Relation between actual mass and simulation mass of far-field underwater explosion," *Applied Mechanics & Materials*, vol. 127, pp. 350–354, 2012.
- [26] J. Zhou, P. Li, and N. Guo, "Seismic performance assessment of a precast concrete-encased CFST composite wall with twin steel tube connections," *Engineering Structures*, vol. 207, p. 110240, 2020.
- [27] J. F. Hajjar, "Composite steel and concrete structural systems for seismic engineering," *Journal of Constructional Steel Research*, vol. 58, no. 5–8, pp. 703–723, 2002.
- [28] X. Zhang, X. Yang, Z. Chen, and G. Deng, "Explosion spalling of reinforced concrete slabs with contact detonations," *Journal of Tsinghua University (Science and Technology)*, vol. 6, pp. 765–768, 2006.
- [29] S. K. Hashemi and M. A. Bradford, "Numerical simulation of free-air explosion using LS-DYNA," *Applied Mechanics and Materials*, vol. 553, pp. 780–785, 2014.
- [30] P. Shao, Z. Dong, and Y. Zhang, "Comment on the research of rock blast models," *Rock and Soil Mechanics*, vol. 3, pp. 91–96, 1999.
- [31] J. Zhang, "Study on the attenuation law of explosion stress wave in rock of cylinder charge," Doctoral dissertation, North University of China, Taiyuan, China, 2005.
- [32] J. R. Klepaczko and A. Brara, "An experimental method for dynamic tensile testing of concrete by spalling," *International Journal of Impact Engineering*, vol. 25, no. 4, pp. 387–409, 2001.
- [33] Z. Wang, Y. Ni, J. Cao, and W. Zhang, "Recent advance of dynamic mechanical behavior of concrete under impact loading," *Explosion and Shock Wave*, vol. 6, pp. 519–527, 2005.

Research Article

A Three-Section-Settlement Calculation Method for Composite Foundation Reinforced by Geogrid-Encased Stone Columns

Binhui Ma ^{1,2}, **Zhiyong Hu**¹, **Zhuo Li**¹, **Kai Cai**¹, **Minghua Zhao**³, **Chengbin He**¹, **Qiunan Chen**^{1,2}, **Bingchu Chen**¹, and **Xiaocheng Huang**^{1,2}

¹School of Civil Engineering, Hunan University of Science and Technology, Xiangtan 411201, China

²Hunan Provincial Key Laboratory of Geotechnical Engineering for Stability Control and Health Monitoring, Hunan University of Science and Technology, Xiangtan 411201, China

³School of Civil Engineering, Hunan University, Changsha 410082, China

Correspondence should be addressed to Binhui Ma; mbh@hnust.edu.cn

Received 20 February 2021; Revised 18 March 2021; Accepted 2 April 2021; Published 23 April 2021

Academic Editor: Rihong Cao

Copyright © 2021 Binhui Ma et al. This is an open access article distributed under the Creative Commons Attribution License, which permits unrestricted use, distribution, and reproduction in any medium, provided the original work is properly cited.

The analysis of the bearing characteristics and deformation mechanism of composite foundation reinforced with geogrid-encased stone columns is presented in order to obtain its settlement calculation method. The settlement of composite foundation is divided into three sections which are the reinforced section, unreinforced section, and underlying stratum. Based on Hooke's law of space problem and the thoughts of the layer-wise summation method, the relative slip displacement between pile and soil of reinforced section without plastic zone is analyzed. The settlement of reinforced section is calculated by the layered iteration method based on the pile element model. The compatibility of vertical and radial deformations of unreinforced section is analyzed based on the pile-soil element model. The settlement of underlying stratum is still calculated by the layer-wise summation method. Finally, two engineering examples are analyzed and the results show that the settlement calculated by the presented method is close to the measured one. The method overcomes the defect that the calculated results by the other existing methods are more dangerous and it is more feasible and can be applied in engineering practice.

1. Introduction

Stone column has been widely used in soft clay improving engineering as a common reinforcement [1]. The bearing capacity of stone column mainly depends on the lateral restraint provided by the surrounding soil [2]. When the lateral restraint force is insufficient, the top part of the stone column body is prone to swelling, resulting in the reduction of its bearing capacity and the increase of settlement, which fails to achieve the expected effect of reinforcement [3]. In engineering practice, the treatment method of covering the geogrid encasement into stone column in the depth range of 2~3 times of pile diameter is adopted to make use of the hoop effect of the geogrid encasement on the pile body to increase its lateral restraint force and limit the swelling deformation of the pile body, so as to improve the bearing capacity and reduce the settlement. This new type can be

called composite foundation by geogrid-encased stone columns. Because of the effect of the geogrid encasement, the bearing capacity and deformation characteristics of the stone column have changed, so it is not appropriate to simply apply the existing settlement calculation method of the composite foundation to analyze the settlement of the composite foundation reinforced by geogrid-encased stone columns. Therefore, how to combine the characteristics of geogrid-encased stone columns and deeply discuss the settlement calculation method of that has an important theoretical significance for engineering design.

At present, the research methods of geogrid-encased stone columns are mostly laboratory tests, numerical simulation and field tests, etc. The research mainly focuses on the analysis of bearing capacity and stability. The bearing capacity of geogrid-encased stone columns is early analyzed by Zhou and Zhang [4] with the limit equilibrium theory.

Chen et al. [5–7], respectively, derived the bearing capacity calculation formula of the top-reinforced stone column based on the expansion theory of circular hole, the slider balance method, and the upper limit analysis method. Based on the progress of limit equilibrium theory and considering the failure mode of geogrid-reinforced crushed stone pile, Zhao et al. [8,9] deduced the calculation formula of ultimate bearing capacity of single reinforced crushed stone pile. However, the research on settlement calculation of composite foundation reinforced by geogrid-encased stone columns is relatively few. Cao and Yang [10] divided geogrid-encased stone column into reinforced section, unreinforced plastic section, and unreinforced elastic section according to the relative slip between column and surrounding soil, established corresponding settlement analysis model according to the deformation characteristics of different sections, and obtained the settlement calculation method of geogrid-encased stone column composite foundation under flexible foundation. Wu and Chen [11] also divided the reinforcement into three sections and derived settlement formulas for each section based on elastic mechanics and pile-soil coordinated deformation. According to the observation and conclusion of numerical simulation results, Tan et al. [12] established the analytical solution of the ultimate bearing capacity of geogrid-encased stone column in soft clay. Esameldin and Zalihe [13] studied the bearing capacity of geogrid-encased stone column in different soft soils through laboratory experiments.

Although these research studies on the bearing deformation mechanism of the geogrid-encased stone column are fine, they are still with some limitations and shortcomings. For example, the friction of geogrid-encased stone column caused by relative slip of column and soil is too complicated to be considered. The lateral deformation of column decreases rapidly with depth, and there is not necessarily a plastic zone, so the assumption that there are three sections is not necessarily valid. In addition, from the calculation results, the theoretical value is less than the measured value, and the calculation is biased to the danger. Therefore, on the basis of previous research, the composite foundation reinforced by geogrid-encased stone column is divided into three sections, which are the reinforced section, unreinforced section, and underlying stratum. Based on Hooke's law of space problem and the thoughts of the layer-wise summation method, the deformation of stone column is calculated based on the pile element by the layer-iteration method, considering the relative slip of pile and soil without plastic zone. The pile-soil unit model is introduced for analysis according to the coordination of the vertical and radial deformations of pile and soil in the unreinforced section. The settlement of the underlying stratum is calculated by the layer-wise summation method, and then the settlement calculation method of the composite foundation is proposed.

2. Deformation Mechanism Analysis

Generally speaking, the settlement of composite foundation reinforced by geogrid-encased stone columns consists of

cushion, reinforcement area, and underlying layer [1] (Figure 1).

Because the thickness of the cushion is generally smaller and the compaction degree is higher, the settlement deformation is basically completed in the construction stage, so it can be ignored. Therefore, the settlement S of geogrid-encased stone column composite foundation can be regarded as the sum of the compression amount S_1 in the reinforcement area and the compression amount S_2 in the underlying strata, namely,

$$S = S_1 + S_2. \quad (1)$$

According to the existing research results [9–11], the reinforcement area can be divided into reinforced section and unreinforced section according to whether the pile is wrapped by geogrid encasement, so S_1 can be expressed as

$$S_1 = S_{11} + S_{12}. \quad (2)$$

In the formula, S_{11} and S_{12} are the compression amount of the stiffened segment and the nonstiffened segment, respectively. Thus, equation (1) can be rewritten as

$$S = S_{11} + S_{12} + S_2. \quad (3)$$

Formula (3) is the settlement calculation method of composite foundation reinforced by geogrid-encased stone column that is commonly used at present, in which the compression deformation of the underlying strata S_2 is solved by the traditional layered summation method. It can be seen from this that the key to the settlement calculation of composite foundation lies in the determination of compression deformation S_{11} and S_{12} in the reinforcement area.

2.1. Reinforced Section. As the pile body is wrapped by the grille sleeve, the integrity and deformation stiffness of the reinforced section are greatly improved, and a relatively clear pile-soil contact surface is formed by means of the grille. The deformation mechanism is similar to that of a flexible pile or semirigid pile. However, the pile body is composed of loose materials and has no cohesive force. Under the action of load, the stress concentration of the pile body produces ineligibility swelling deformation. When the composite foundation bears a large load, there is a relative displacement or displacement trend at the pile-soil interface of the reinforced section, which leads to the existence of pile lateral friction at the pile-soil interface. In this paper, the pile element is used and the layered iterative method is used to calculate.

2.2. Unreinforced Section. Without the lateral restraint of geogrid, the stiffness of unreinforced section of stone column decreases obviously. There are vertical and radial deformations existing in the unreinforced section under the vertical load, especially the radial deformation is extremely obvious because of the sudden change of the stiffness of stone column at the junction of the reinforced and unreinforced section, which is also the reason for the bulging failure of the geogrid-encased stone columns [14]. Without

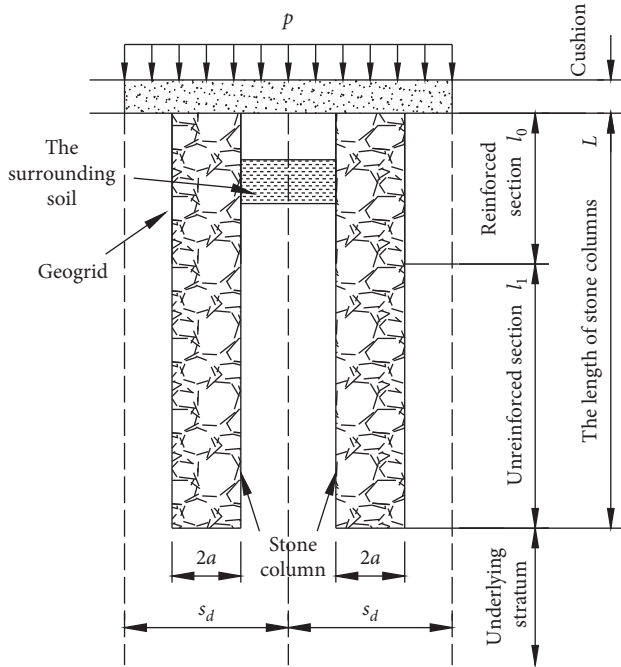


FIGURE 1: Composition of composite foundation reinforced by geogrid-encased stone columns.

geogrid encasement, stone columns are embedded into the surrounding soil, which makes the boundary between columns and soil very fuzzy, and the relative displacement small to be neglected. In addition, due to stress diffusion, the additional stress of the pile decreases sharply with depth, and its lateral deformation decreases correspondingly. Therefore, the bulging deformation of the whole unreinforced section is not uniform. However, considering the continuous and coordinated deformation characteristics of the pile-soil, the unreinforced section is analyzed by pile-soil element to simplify the calculation.

Therefore, the settlement analysis method of composite foundation reinforced by geogrid-encased stone column established in this paper must fully reflect the deformation mechanics mechanism of the reinforced section and the unreinforced section. Therefore, the settlement deformation of reinforced segment and unreinforced segment will be analyzed, respectively, on this basis.

3. Compression Deformation Analysis

3.1. The Basic Assumptions. In this paper, the research is mainly limited to the reinforced stone column formed by the two-way high-strength geogrid at the depth of 2~3 times of the pile diameter below the top of the stone column, and to simplify the calculation, the following basic assumptions are made:

- The geogrid encasement has sufficient strength and stiffness and will not be plastic deformation or tension due to pile deformation
- The mesh hole of the geogrid encasement is smaller than the particle size of gravel, and the gravel particles are not allowed to bulge out from the sleeve

- Under normal working conditions, the pile body and the soil around the pile can be linear elastomer
- Only the influence of additional stress on the compression deformation of pile body and soil around pile is considered, not the influence of dead weight
- Effect of pile-group is not considered in the composite foundation
- The microelement body of the selected segment is very small, and the volume change of the pile and soil element body can be ignored

The pile body and the unit body composed of soil around the pile within its influence range were taken as research objects for analysis, as shown in Figure 2 where a is the radius of pile body and b is the radius of pile and soil unit body, which can be obtained from the distance of pile body and the way of pile layout:

$$d_e = c_g s_d = 2b, \quad (4)$$

where d_e is the diameter of the element body; s_d is the center distance between piles; and c_g is the influence coefficient of pile layout (for plum-shaped or equilateral triangular pile, $c_g = 1.05$; for square pile, $c_g = 1.13$). Under the above conditions, the compression deformation analysis method of reinforced section and unreinforced section of composite foundation is discussed.

3.2. Compression Deformation Analysis of Reinforced Section.

In view of the characteristics and deformation characteristics of stone column, this paper adopts the iterative method of subcascade generation for compression deformation analysis. Now, the reinforced section is divided into M microsegment units, the length of the reinforced section is l_0 , and then the thickness of the i microsegment unit ΔH_i is

$$\Delta H_i = \frac{l_0}{M} \quad (5)$$

The microsegment unit of pile body i -th of the stiffened section was taken for analysis, as shown in Figure 3. According to the basic assumption, the pile deformation is uniform and the volume remains the same before and after deformation. At the same time, it can be obtained by ignoring the high-order trace:

$$a \Delta h_i = 2 \Delta H_i \Delta r_i, \quad (6)$$

where Δh_i and Δr_i are the vertical and radial deformations of the i -th pile microsegment element, respectively.

Based on the coordinated and continuous deformation of pile and soil, it can be known that the swelling amount of pile body should be equal to the shrinkage amount of soil around the pile; that is, the mean circumjacent stress $\bar{\sigma}_{\theta pi}$ of the microsegment element body is equal to the mean radial stress $\bar{\sigma}_{r pi}$.

According to Hookie's law in spatial problems, it can be concluded that

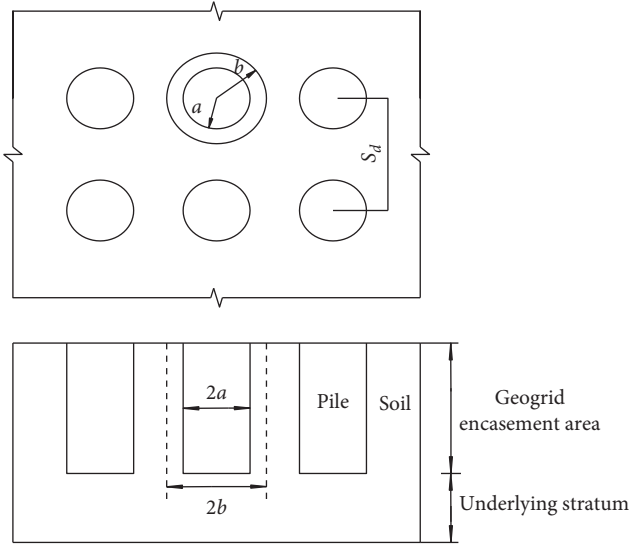
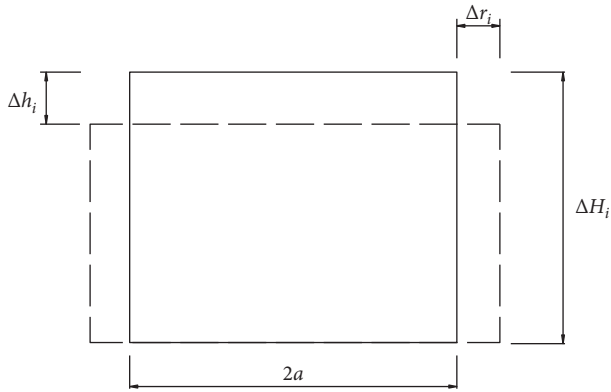


FIGURE 2: The unit of pile and soil.

FIGURE 3: Deformation of the i -th microelement of pile.

$$\varepsilon_{zpi} = \frac{\Delta h_i}{\Delta H_i} = \frac{1}{E_p} [\bar{\sigma}_{zpi} - \mu_p (\bar{\sigma}_{rpi} + \bar{\sigma}_{\theta pi})] = \frac{1}{E_p} (\bar{\sigma}_{zpi} - 2\mu_p \bar{\sigma}_{rpi}), \quad (7)$$

$$\varepsilon_{rpi} = \frac{\Delta r_i}{a} = \frac{1}{E_p} [\bar{\sigma}_{rpi} - \mu_p (\bar{\sigma}_{zpi} + \bar{\sigma}_{\theta pi})] = \frac{1}{E_p} [(1 - \mu_p) \bar{\sigma}_{rpi} - \mu_p \bar{\sigma}_{zpi}], \quad (8)$$

where ε_{rpi} and ε_{zpi} are the radial and vertical strains of the i -th microsegment element of pile body, respectively; E_p is the compression modulus of pile body; μ_p is Poisson's ratio of the pile; and $\bar{\sigma}_{zpi}$ is the average vertical additional stress of the i -th pile microsegment element, and the average value of the additional stress at the bottom and top of the element can be taken as

$$\bar{\sigma}_{zpi} = \frac{(\sigma_{zpi} + \sigma_{zp(i-1)})}{2}. \quad (9)$$

From equations (7) and (8), the vertical and radial deformation of the i -th pile element microsegment element can be obtained as

$$\Delta h_i = \frac{\Delta H_i}{E_p} (\bar{\sigma}_{zpi} - 2\mu_p \bar{\sigma}_{rpi}), \quad (10)$$

$$\Delta r_i = \frac{a}{E_p} [(1 - \mu_p) \bar{\sigma}_{rpi} - \mu_p \bar{\sigma}_{zpi}]. \quad (11)$$

Substituting equation (9) into equations (10) and (11), the additional stress σ_{zpi} on the bottom of the pile microsegment unit is

$$\sigma_{zpi} = A_i \Delta h_i + B_i \Delta r_i - \sigma_{zp(i-1)}, \quad (12)$$

where A_i and B_i are calculating parameters, $A_i = (2E_p/\Delta H_i)(1 + (2\mu_p^2/1 - \mu_p - 2\mu_p^2))$, $B_i = 4E_p\mu_p/(1 - \mu_p - 2\mu_p^2)a$.

Take the i -th pile microsegment unit for force analysis, as shown in Figure 4, and from the vertical static balance of the pile, we can get

$$\begin{aligned} \pi(a + \Delta r_{(i-1)})^2 \sigma_{zp(i-1)} + 2\pi(a + \Delta r_i)(\Delta H_i - \Delta h_i)\tau_i \\ = \pi(a + \Delta r_i)^2 \sigma_{zpi}. \end{aligned} \quad (13)$$

In the formula, τ_i is the average frictional force on the pile side of the i -th pile microsection unit. From equation (6), we can see that Δr_i is a function of Δh_i , and we can make $\Delta r_i = f_1(\Delta h_i)$; substituting Δr_i for equation (12), we can see that σ_{zpi} is a function of Δh_i , so that $\sigma_{zpi} = f_2(\Delta h_i)$; equation (13) can obtain another functional relationship between σ_{zpi} and Δh_i , and $\sigma_{zpi} = f_3(\Delta h_i)$.

Simultaneously, equations (12) and (13) can be used to obtain a univariate quadratic equation about Δh_i ; that is,

$$F_{1i}\Delta h_i^2 + F_{2i}\Delta h_i + F_{3i} = 0, \quad (14)$$

where F_{1i} , F_{2i} , and F_{3i} are the calculation parameters of the i -th pile microsegment unit, $F_{1i} = (a\tau_i/\Delta H_i) + (a^2\sigma_{zpi}/4\Delta H_i^2)$, $F_{2i} = a\tau_i + (a^2\sigma_{zpi}/\Delta H_i) - a^2A_i - (a^3B_i/2\Delta H_i)$, $F_{3i} = 2a^2\sigma_{zpi} - 2a\tau_i\Delta H_i$.

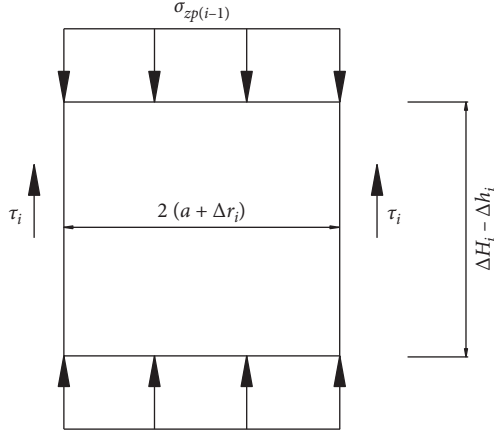
Δh_i can be obtained from equation (14):

$$\Delta h_i = \frac{-F_{2i} + \sqrt{F_{2i}^2 - 4F_{1i}F_{3i}}}{2F_{1i}}, \quad (15)$$

$$\tau_i = c_a + k_0 p_{szi} \tan \varphi_a,$$

where c_a is the cohesion between piles and soil; φ_a is the friction angle at the pile-soil interface; p_{szi} is the vertical additional stress of soil around the pile at the depth z_i in the middle of the microsegment element of the i -th pile; and k_0 is the static earth pressure coefficient of soil around the pile. Because the soil around the pile has a certain shear strength, it is impossible to transfer excessive shear stress, so the pile lateral friction resistance is related to the soil's shear strength and is τ finite value. It can be considered that the pile lateral friction resistance does not exceed the soil's shear strength τ , and the pile lateral friction resistance of the whole reinforced section is

$$\tau_z = c_a + k_0 p_{sz} \tan \varphi_a \leq \tau. \quad (16)$$

FIGURE 4: Stress analysis of the i -th microelement of pile.

3.3. *Compression Deformation Analysis of Unreinforced Section.* Similar to the above method, the unreinforced segment is divided into N pile-soil microsegment units, and then the thickness of the j -th pile-soil microsegment unit ΔH_j is

$$\Delta H_j = \frac{l_1}{N}. \quad (17)$$

From the above analysis, it can be seen that the impact of vertical deformation and radial deformation should be taken into account in calculating the compression deformation of nonstiffened segment as well as that of stiffened segment, but the relative slip of pile and soil should be ignored in nonstiffened segment and analyzed according to the pile-soil element.

Therefore, the compression deformation of nonstiffened segment can be analyzed by using the compression deformation method of stiffened segment. The j -th pile and soil element was taken for force analysis, as shown in Figure 5.

Considering the symmetry of pile-soil microsegment element and the stress coordination at the boundary of pile-soil element, the vertical stress at the boundary of pile-soil microsegment element $\tau_j = 0$, and then the vertical static equilibrium of pile-soil microsegment element can be obtained as follows:

$$\begin{aligned} & \pi(a + \Delta r_{(j-1)})^2 \sigma_{zp(j-1)} + \pi \left[b^2 - (a + \Delta r_{(j-1)})^2 \right] \sigma_{zs(j-1)} \\ & = \pi(a + \Delta r_j)^2 \sigma_{zpj} + \pi \left[b^2 - (a + \Delta r_j)^2 \right] \sigma_{zsj}, \end{aligned} \quad (18)$$

where $\Delta r_{(j-1)}$ and Δr_j are, respectively, the radial deformations of the $(j-1)$ th and j -th micropile soil elements; $\sigma_{zp(j-1)}$ and σ_{zpj} are the $(j-1)$ th and j -th micropile soil element vertical stress at the bottom of the element pile; $\sigma_{zs(j-1)}$ and σ_{zsj} are the vertical stress at the bottom of the $(j-1)$ th and j -th microelement soil element, and $\sigma_{zs(j-1)} = \sigma_{zp(j-1)}/n_{(j-1)}$, $\sigma_{zsj} = \sigma_{zpj}/n_j$, where $n_{(j-1)}$ and n_j are the pile-soil stress ratios at the bottom of the $(j-1)$ th and j -th pile-soil units, respectively.

According to the reinforced section of compression deformation calculation, it is a cubic equation of one variable Δh_j as follows:

$$\lambda_{3j} \cdot \Delta h_j^3 + \lambda_{2j} \cdot \Delta h_j^2 + \lambda_{1j} \Delta h_j = \lambda_j, \quad (19)$$

where λ_j , λ_{1j} , λ_{2j} , and λ_{3j} are parameters, $\lambda_j = [n_j(a + \Delta r_{(j-1)})^2 + b^2] \sigma_{zp(j-1)} + n_j [b^2 - (a + \Delta r_{(j-1)})^2] \sigma_{zs(j-1)}$, $\lambda_{1j} = [b^2 + (n_j - 1)a^2] (F_{1j} + (F_{2j}a/2\Delta Z_j)) - ((n_j - 1)a^2 \sigma_{zp(j-1)}/\Delta Z_j)$, $\lambda_{2j} = ((n_j - 1)a^2/\Delta Z_j) (F_{1j} + (\lambda_{2j}a/2\Delta Z_j) - (\sigma_{zp(j-1)}/4\Delta Z_j))$, $\lambda_{3j} = ((n_j - 1)a^2/4\Delta Z_j^2) (F_{1j} + (F_{2j}a/2\Delta Z_j))$.

An analytical solution can be obtained from formula (19); that is,

$$\begin{aligned} \lambda_j &= [n_j(a + \Delta r_{(j-1)})^2 + b^2] \sigma_{zp(j-1)} + n_j [b^2 - (a + \Delta r_{(j-1)})^2] \sigma_{zs(j-1)}, \\ \lambda_{1j} &= [b^2 + (n_j - 1)a^2] \left(F_{1j} + \frac{F_{2j}a}{2\Delta Z_j} \right) - \frac{(n_j - 1)a^2 \sigma_{zp(j-1)}}{\Delta Z_j}, \\ \lambda_{2j} &= \frac{(n_j - 1)a^2}{\Delta Z_j} \left(F_{1j} + \frac{\lambda_{2j}a}{2\Delta Z_j} - \frac{\sigma_{zp(j-1)}}{4\Delta Z_j} \right), \\ \lambda_{3j} &= \frac{(n_j - 1)a^2}{4\Delta Z_j^2} \left(F_{1j} + \frac{F_{2j}a}{2\Delta Z_j} \right), \\ \Delta h_j &= \sqrt[3]{-\frac{q_j}{2} + \sqrt{\left(\frac{q_j}{2}\right)^2 + \left(\frac{p_j}{3}\right)^3}} + \sqrt[3]{-\frac{q_j}{2} - \sqrt{\left(\frac{q_j}{2}\right)^2 + \left(\frac{p_j}{3}\right)^3}} - \frac{\lambda_{2j}}{3\lambda_{3j}}, \end{aligned} \quad (20)$$

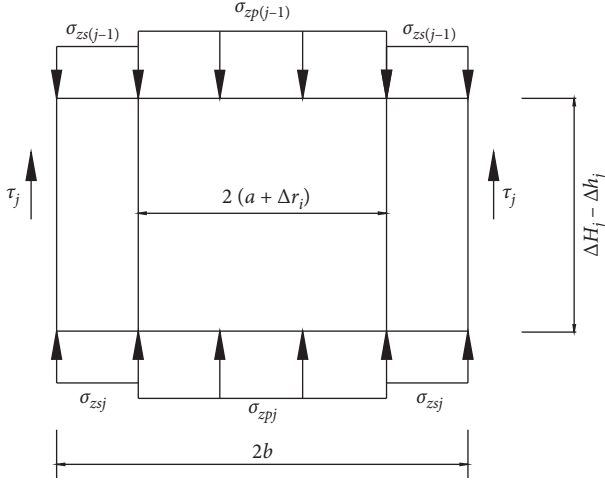


FIGURE 5: Stress analysis of the j -th pile-soil microelement in the unreinforced section.

where q_j and p_j are parameters, $q_j = (\lambda_{2j}(2\lambda_{2j}^2 - 9\lambda_{1j}\lambda_{3j}) - 27\lambda_j\lambda_{3j}^2)/(27\lambda_{3j}^3)$, $p_j = (3\lambda_{1j}\lambda_{3j} - \lambda_{2j}^2)/(3\lambda_{2j}^2)$.

3.4. Calculation of Compressive Deformation in Reinforced Section. From the above analysis, it is known that the compression deformation amount S_{11} of the reinforced section in the reinforced area is $S_{11} = \sum_{i=1}^M \Delta h_i$, and the compression deformation amount S_{12} of the unreinforced section in the reinforced area is $S_{12} = \sum_{j=1}^N \Delta h_j$. The calculation formula of the compression deformation amount of the entire reinforced area is S_1 :

$$S_1 = S_{11} + S_{12} = \sum_{i=1}^M \Delta h_i + \sum_{j=1}^N \Delta h_j. \quad (21)$$

3.5. Determination of Related Calculating Parameters. The abovementioned analysis method for the settlement of the reinforced stone column reinforcement zone has been established. From equations (15) and (20), it can be known that the compression deformation S_1 in the reinforced section is related to the following parameters:

$$S_1 = F(a, b, \Delta H_i, \Delta H_j, \Delta r_i, \Delta r_j, \sigma_{zpi}, \sigma_{zsi}, \sigma_{zpj}, \sigma_{zsj}, n_j), \quad (22)$$

where a , b , ΔH_i , and ΔH_j are geometric parameters for composite foundation, which can be determined by the engineering condition and the calculation precision; Δr_i , σ_{zpi} , σ_{zsi} , Δr_j , σ_{zpj} , σ_{zsj} , and n_j are stress-strain parameters, which need to be calculated and determined. The determination process of parameters is as follows.

Step 1. Determining Δr_i and Δr_j . In the reinforced section, Δr_i is the radial deformation of the top of the $(i+1)$ -th pile microsegment unit (that is the bottom of the i -th pile microsegment unit). Since the compression deformation analysis of the pile is recursive from top to bottom, the i -th

element is calculated from the $(i-1)$ -th element, and Δr_i can be obtained by analogy from the radial initial deformation Δr_0 . Since the first microsegment element of the pile body is close to the bottom of the foundation or cushion, which has a greater constraint on the pile, $\Delta r_0 = 0$ is assumed in order to simplify the calculation. $\Delta r_{(j-1)}$ can also be obtained by using the same method in the unreinforced section, where the first microelement of the pile body is the radial deformation of the interface between the reinforced section and the unreinforced section. The radial deformation of the top surface of the first pile-soil element is equal to the one of the bottom surfaces of the adjacent pile-soil element in the unreinforced section, that is, $\Delta r_j|_{j=0} = \Delta r_i|_{i=M}$.

Step 2. Determining σ_{zp} and σ_{zs} . In the reinforced section, $\sigma_{zp(i-1)}$ is the vertical additional stress of the top surface of the i -th pile-soil unit, and $\sigma_{zs(i-1)}$ is the vertical additional stress of the surrounding soil. Likewise, $\Delta r_{(i-1)}$, $\sigma_{zp(i-1)}$ and $\sigma_{zs(i-1)}$ can be determined by the initial condition, that is, σ_{zp0} and σ_{zs0} of the first pile-soil unit, which are calculated as follows:

$$\sigma_{zs0} = p_s = \frac{P}{[1 + m(n-1)]}, \quad (23)$$

$$\sigma_{zp0} = p_p = np_s, \quad (24)$$

where p_p and p_s are the vertical additional stresses on the top of the pile and surrounding soil; p is the vertical pressure on the top of the composite foundation; m is the area replacement rate; and n is the stress ratio of the pile and soil, which can be calculated by the following formula (14) when there is no measured value:

$$n = \frac{E_p}{2k_p E_s \ln(b/a)} + \frac{k_s}{k_p}, \quad (25)$$

where E_p is the compression modulus of the pile, E_s is the compression modulus of the soil, k_p is the coefficient of lateral pressure of pile, and k_s is the coefficient of lateral pressure of the soil around the pile.

In the unreinforced section, considering the continuity of stress, the vertical additional stress of the pile and soil at the top of the unreinforced section is equal to the one at the bottom of the reinforced section, that is,

$$\sigma_{zpj}|_{j=0} = \sigma_{zpi}|_{i=M}, \quad (26)$$

$$\sigma_{zsj}|_{j=0} = \sigma_{zsi}|_{i=M}.$$

Step 3. Determining the pile-soil stress ratio n_j of the element. Considering that the stone column is divided into many units and the thickness is small, the pile-soil stress ratio varies little in a pile-soil unit. To simplify the calculation, it can be assumed that the pile-soil stress ratio of the unit remains unchanged, that is,

$$n_j = \frac{\sigma_{zpj}}{\sigma_{zsj}} \approx \frac{\sigma_{zp(j-1)}}{\sigma_{zs(j-1)}} \approx \frac{\sigma_{zp0}}{\sigma_{zs0}}. \quad (27)$$

4. Engineering Case Analysis

In order to verify the rationality and feasibility of the above calculation method for the composite foundation of the reinforced stone column composite foundation, an engineering example is cited for analysis.

4.1. Case 1. When the length of the reinforced section of the reinforced stone column is zero, the settlement calculation method of the composite foundation of the reinforced stone column can be transformed into the settlement calculation method of the ordinary stone column composite foundation. In order to verify the versatility and rationality of the above calculation method for the settlement of the reinforced stone column composite foundation, an example of common stone column composite foundation engineering is first introduced for analysis.

Taking a water conservancy project in [15] as an example, a sluice is planned to be built on silt and silty sand foundation, the surface layer is 2.0~4.5 m which is silt, and the bearing capacity of the foundation is 100 kPa; below the silt is livery-grey silt sand with a foundation bearing capacity of 80 kPa. The groundwater is 2 m below the ground. The foundation of the lock chamber is reinforced with vibrating stone piles. The literature [15] used the finite element method to analyze the foundation strengthened by crushed stone piles. The simulated pile diameter was 1 m, the pile length was 11 m, and the total calculated depth of the foundation was 12 m. For other specific parameters, see the literature. When the upper load is 150 kPa, the settlement of the composite foundation is 4.76 cm. The above data are used to calculate the settlement of the project using the method in this paper. The length of the reinforced section of the composite foundation is set to zero, the unreinforced section is equally divided into 50 units, and the calculated $S_{12} = 3.97$ cm; the lower layer is calculated using the layered sum method to calculate $S_2 = 0.87$ cm; the total settlement of the project is $S = 4.84$ cm, which is close to the calculation results of the finite element method, which shows that the method in this paper is reasonable and can be degraded to one of the ordinary composite foundations reinforced by stone columns.

4.2. Case 2. This project is a ramp of a highway interchange in Sichuan, which uses geogrid encasement, stone column, and sand cushion to reinforce the roadbed [16]. The parameters of the composite foundation are as follows: the thickness of cushion is $h = 10$ cm, the compression modulus of cushion is $E_c = 20$ MPa, the diameter of stone column is $d = 0.6$ m, the length of pile is $L = 6$ m, the arrangement of piles is like a plum blossom, pile spacing is $S_d = 2$ m, internal friction angle of stone is $\varphi_p = 38^\circ$, and Poisson's ratio is $\mu_p = 0.35$, the length of geogrid encasement is $l_0 = 2$ m, and the compression modulus of reinforced section is $E_p = 100$ MPa and $E_p = 20$ MPa in the unreinforced section. The distribution of pile and soil layers is shown in Figure 6, and the calculating parameters are shown in Table 1. A uniformly distributed load $p = 120$ kPa is applied to the

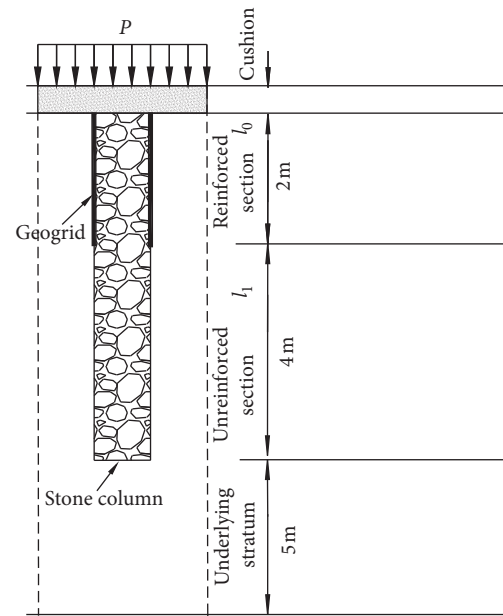


FIGURE 6: Distribution of pile and surrounding soil.

treated subgrade surface. The measured pile-soil stress ratio is $n = 3.12$, and the subgrade settlement is $S = 11$ cm.

The settlement calculation of the subgrade project is carried out by using the above data in Table 1 and the method in this paper. The specific process is as follows:

- Calculating the replacement rate of the composite foundation area $m = 8.2\%$ and the pile-soil stress ratio $n = 3.12$. From formulas (23) and (24), the load on the pile-soil top surface is $\sigma_{zp0} = 350.84$ kPa and $\sigma_{zs0} = 112.45$ kPa.
- Calculating S_{11} : the reinforced section is divided into 10 element bodies, and the element body is analyzed and calculated one by one from top to bottom. Finally, the compression deformation of the reinforced section is $S_{11} = 2.547$ cm.
- Calculating S_{12} : the unreinforced section is divided into 20 element bodies, and the element body is analyzed and calculated one by one from top to bottom. The final compression deformation of the unreinforced section is $S_{12} = 8.251$ cm.
- The compression deformation of the underlying stratum: using the layer-wise summation method to obtain the settlement $S_2 = 1.072$ cm.
- According to formula (3), it can be known that the total deformation of composite foundation $S = 11.87$ cm.

In order to facilitate comparative analysis, other methods are used to calculate the settlement in Case 2, and the results are shown in Table 2. It can be seen from Table 2 that the calculated results of this method and other methods are close to the measured values. The calculated results of this method are larger than those of other methods. Considering that theoretical derivation is generally the final settlement of

TABLE 1: Calculating parameter.

Section	Soil type	φ (°)	E_s (MPa)	ρ_s (g/cm ³)	μ_s	c (kPa)
Reinforced section	Filled soil	31	6	1.70	0.4	14.9
Unreinforced section	Weak soil	5.8	2.74	1.75	0.45	11
Underlying stratum	Pebble soil	26	50	1.60	0.4	8

TABLE 2: Calculation results of different methods.

Method	Calculated value (cm)	Measured values (cm)	Relative error (%)
Method from the literature [10]	10.8	11.0	-1.82
Finite element method [16]	10.9	11.0	-0.91
Proposed method	11.87	11.0	+7.90

foundation, while the measured value is the settlement at a certain time, and the value is generally less than the final settlement, the method in this paper is more in line with the actual situation and avoids the defect that the analysis results of other methods are too dangerous. Therefore, the method used in this paper to calculate the settlement of composite foundation is in good agreement with the actual situation. However, it is undeniable that there still exists certain calculation error of the method in this paper, the main reason is the research object is limited to by high tensile bidirectional geogrid on top of the stone column within the following 2~3 times the depth of the pile diameter fan sleeve formed by confining hoop reinforcement stone column composite foundation, and the formula is derived using the continuous homogeneous medium assumption and the basic principle of mechanics of elasticity. We assume unit cell of constant stress ratio of pile-soil and add composite foundation reinforced by geogrid-encased stone column settlement and the actual engineering by the combination of many factors, such as stone column itself has large discreteness, and when the upper load is bigger, grille sleeve reinforced section will appear larger nonlinear deformation. The stress of pile and soil will increase with load-increasing.

5. Conclusions

Based on the analysis of bearing and deformation mechanism of composite foundation reinforced by geogrid-encased stone columns, the settlement calculation method of this type of composite foundation is discussed. Theoretical analysis shows that the geogrid encasement effectively limits the radial deformation of the upper half of the stone column, making the half of the stone column body flexible or semirigid. The load transfer capacity of the stone column is stronger, and the deformation is more. Therefore, considering the relative slip of the pile and soil in the reinforced section and the coordinated characteristics of vertical and radial deformation of the pile and soil in the unreinforced section, the composite foundation reinforced by geogrid-encased stone column is divided into the reinforced section, unreinforced section, and underlying stratum.

The settlement calculation model was established in the three sections of the horizontal layer, which accorded with

the bearing and deformation characteristics of composite foundation reinforced by the geogrid-encased stone column. The analysis of engineering examples shows that the proposed method for calculating the settlement of the composite foundation of the geogrid-encased stone column composite foundation has good engineering accuracy and overcomes the shortcomings of the analysis results of the existing analysis methods, which are biased to danger, and it has good rationality and feasibility.

In addition, the settlement calculation method of geogrid-encased stone column composite foundation proposed in this paper is mainly aimed at the reinforced gravel formed by the sleeve hoop within the depth range of 2~3 times of the pile diameter below the top of the stone column using a two-way high-strength geogrid reinforcement, and the theoretical derivation uses the assumption of continuous homogeneous medium and the basic principles of elastic mechanics and the calculation assumption that the pile-soil stress ratio of the unit body is constant. In practice, the settlement of composite foundation reinforced by geogrid-encased stone column is affected by many factors such as the stiffness of stone column [17], the failure model of stone column [18], and the consolidation state of soil [19]. In addition, the method proposed in this paper still cannot consider the plastic state of pile and soil and needs to be further improved.

Nomenclature

List of symbols

- S : Settlement of geogrid-encased stone column composite foundation
- S_1 : Amount of compression in reinforcement area
- S_2 : The amount of compression in the underlying strata
- S_{11} : Amount of compression in stiffened section
- S_{12} : Amount of compression in nonstiffened segment
- a : The radius of pile body
- b : Pile and soil element body radius
- d_e : The diameter of the element body
- S_d : The center distance between piles
- c_g : The influence coefficient of pile layout
- l_0 : The length of the reinforced section
- ΔH_i : The thickness of the i -th microsegment element
- Δh_i : The vertical deformation of the i -th pile microsegment element

Δr_i :	The radial deformation of the microsegment element of the i th pile body
$\bar{\sigma}_{\theta pi}$:	Mean circumferential stress
$\bar{\sigma}_{r pi}$:	Mean radial stress
$\varepsilon_{r pi}$:	Radial strain of the i -th pile microsegment element
$\varepsilon_{z pi}$:	The vertical strain of the i -th pile microsegment element
E_p :	The compression modulus of pile body
E_s :	The compression modulus of the soil
μ_p :	Poisson's ratio of the pile
$\bar{\sigma}_{z pi}$:	The average vertical additional stress of the i -th pile microsegment element
τ_i :	The average frictional force on the pile side of the i -th pile microsegment unit
F_{1i} :	The calculation parameters of the i -th pile microsegment unit
F_{2i} :	The calculation parameters of the i -th pile microsegment unit
F_{3i} :	The calculation parameters of the i -th pile microsegment unit
c_a :	The cohesion between piles and soil
φ_a :	The friction angle at the pile-soil interface
$p_{sz i}$:	The vertical additional stress of soil around the pile at the depth z_i in the middle of the microsegment element of the i -th pile
k_0 :	The static earth pressure coefficient of soil around the pile
τ :	The soil's shear strength
ΔH_j :	The thickness of the j -th pile-soil microsegment unit ΔH_j
$\Delta r_{(j-1)}$:	The radial deformations of the $(j-1)$ th micropile soil elements
Δr_j :	The radial deformations of the j -th micropile soil elements
$\sigma_{zp(j-1)}$:	The $(j-1)$ th micropile soil element vertical stress at the bottom of the element pile
σ_{zpj} :	The j -th micropile soil element vertical stress at the bottom of the element pile
$\sigma_{zs(j-1)}$:	The vertical stress at the bottom of the j -th microelement soil element
σ_{zsj} :	The vertical stress at the bottom of the j -th microelement soil element
$n_{(j-1)}$:	The pile-soil stress ratios at the bottom of the $(j-1)$ th pile-soil units
n_j :	The pile-soil stress ratios at the bottom of the j -th pile-soil units
λ_j :	The calculation parameter
λ_{1j} :	The calculation parameter
λ_{3j} :	The calculation parameter
q_j :	The calculation parameter
p_j :	The calculation parameter
k_p :	The coefficient of lateral pressure of pile
k_s :	The coefficient of lateral pressure of the soil around the pile.

Data Availability

The data used to support the findings of this study are available from the corresponding author upon request.

Conflicts of Interest

The authors declare that they have no conflicts of interest.

Acknowledgments

The work described in this paper was fully supported by these grants from the National Natural Science Foundation of China (award nos. 51778227, 51308208, and 41372303), the Provincial Natural Science Foundation of Hunan (award nos. 2015JJ3069 and 18C0311), the Youth Talent Plan Program of Hunan (award no. 2016RS3032), and the Postgraduate Scientific Research Innovation Project of Hunan Province (award no. CX20200992).

References

- [1] B. Wang, F. Zhang, and B. Wang, "Development of stone column compound foundation and its application in hydraulic projects," *Advances in Science and Technology of Water Resources*, vol. 21, no. 4, pp. 56–58, 2001.
- [2] F. Zhang, B. Wang, B. Wang et al., "Application of large grain-size stone columns to strengthening saturated super-soft ground," *Journal of Hohai University (Natural Sciences)*, vol. 34, no. 4, pp. 430–434, 2006.
- [3] X. Gong, *Composite Foundation Theory and Engineering Application*, China Building Industry Press, Beijing, China, 2007.
- [4] Z. Zhou and Q. Zhang, "Analysis on the bearing capacity of geogrid reinforced stone-column," *Chinese Journal of Geotechnical Engineering*, vol. 19, no. 1, pp. 18–21, 1997.
- [5] C. Chen and Q. Li, "Calculation of bearing capacity of geosynthetic-encased stone column based on cavity expansion theory," *Journal of Hunan University (Natural Science)*, vol. 38, no. 10, pp. 7–12, 2011.
- [6] C. Chen and M. Wu, "Computational method for bearing capacity of upper geosynthetic-encased stone columns based on block limit equilibrium method," *Chinese Journal of Geotechnical Engineering*, vol. 35, no. 7, pp. 1253–1260, 2013.
- [7] C. Wang, C. Chen, and Y. Zhao, "Upper-bound limit analysis of ultimate bearing capacity of upper geosynthetic-encased stone column," *Rock and Soil Mechanics*, vol. 36, no. 6, pp. 1801–1805, 2015.
- [8] M. Zhao, Q. Chen, L. Zhang et al., "Calculation of bearing capacity of geosynthetic-encased stone columns," *Journal of Highway and Transportation Research and Development*, vol. 28, no. 8, pp. 7–12, 2011.
- [9] M. Zhao, Z. Zhang, M. Liu et al., "Calculation of ultimate bearing capacity of composite foundation with geosynthetic encased stone columns," *Hydrogeology & Engineering Geology*, vol. 41, no. 1, pp. 67–73, 2014.
- [10] W. Cao and Z. Yang, "Method for analyzing settlement of reinforced-pile composite ground under flexible foundation," *Chinese Journal of Geotechnical Engineering*, vol. 34, no. 11, pp. 1997–2004, 2012.
- [11] M. Wu and C. Chen, "Settlement computation of composite foundation of upper geosynthetic-encased stone column," *China Science Paper*, vol. 8, no. 11, pp. 1095–1099, 2013.
- [12] X. Tan, L. J. Feng, and H. U. Zheng, "Failure modes and ultimate bearing capacity of the isolated stone column in soft soil," *Bulletin of Engineering Geology and the Environment*, no. 1, 2021.

- [13] F. R. Esameldin and N. Zalihe, "Behavior of geotextile encased single stone column in soft soils," *Arabian Journal for Science and Engineering*, vol. 45, no. 5, pp. 3877–3890, 2020.
- [14] M. J. Gao, *Experimental Study on Load-Bearing Characteristics of Tubular Grilled-Reinforced Stone Columns*, Hohai University, Nanjing, China, 2008.
- [15] W. Yu, F. Su, and X. Tang, "Finite element analysis on soft soil foundation reinforcement with stone column," *Journal of Water Resources and Architectural Engineering*, vol. 11, no. 5, pp. 114–117, 2013.
- [16] B. Huang, *Mechanism of GSPS Soft Base Reinforcement System and its Application in Chengdu Bypass Expressway*, Southwest Jiaotong University, Chengdu, China, 2002.
- [17] R. Cao, R. Yao, J. Meng, Q. Lin, H. Lin, and S. Li, "Failure mechanism of non-persistent jointed rock-like specimens under uniaxial loading: laboratory testing," *International Journal of Rock Mechanics and Mining Sciences*, vol. 132, Article ID 104341, 2020.
- [18] R. Cao, R. Yao, and T. Hu, "Failure and mechanical behavior of transversely isotropic rock under compression-shear tests: laboratory testing and numerical simulation," *Engineering Fracture Mechanics*, vol. 241, Article ID 107389, 2021.
- [19] R. Cao, C. Wang, R. Yao et al., "Effects of cyclic freeze-thaw treatments on the fracture characteristics of sandstone under different fracture modes: laboratory testing," *Theoretical and Applied Fracture Mechanics*, vol. 109, Article ID 102738, 2020.

Research Article

Unloading Mechanics and Energy Characteristics of Sandstone under Different Intermediate Principal Stress Conditions

Yingjie Zhang , Jiangteng Li , Gang Ma, and Shuangfei Liu

School of Resources and Safety Engineering, Central South University, Changsha 410083, China

Correspondence should be addressed to Jiangteng Li; ljtcusu@csu.edu.cn

Received 23 February 2021; Revised 26 March 2021; Accepted 12 April 2021; Published 22 April 2021

Academic Editor: Yunteng Wang

Copyright © 2021 Yingjie Zhang et al. This is an open access article distributed under the Creative Commons Attribution License, which permits unrestricted use, distribution, and reproduction in any medium, provided the original work is properly cited.

The TRW-3000 true triaxial rock testing machine was used to conduct loading and unloading tests of sandstone under different σ_2 , and the true triaxial lateral unloading mechanics and energy characteristics of sandstone under different σ_2 were studied. The experimental results show the following: (1) compared with the results of the loading test, the peak strength of the sandstone under the unloading σ_3 path is reduced, the unloading direction has obvious expansion and deformation, and the amount of expansion increases significantly with the increase of σ_2 ; sudden brittle failure occurs at the end of unloading. E gradually decreases with the increase of H , and it performs well to use the cubic polynomial to fit the curve of $E-H$. (2) The Mogi-Coulomb strength criterion can accurately describe the true triaxial strength characteristics of sandstone under loading and unloading conditions. Compared with the results of the loading test, the values of c and φ obtained based on this criterion under the unloading σ_3 path are reduced. (3) Under the condition of unloading σ_3 , U , U^e , and U^d , when the specimen is broken, are all linearly positively correlated with σ_2 . U^d increases nonlinearly with the increase of H , and as σ_2 increases, the slope of the U^d-H curve becomes larger, and the specimen consumes more energy under the same unloading amount. Most of the energy absorbed by the specimen under the unloading σ_3 path is converted into U^e , but as σ_2 increases, U^d/U increases, and the energy consumed when the specimen is broken is greater.

1. Introduction

The stress redistribution induced by the excavation of underground engineering and slope engineering results in obvious unloading deformation of the excavation face [1], which will cause serious engineering problems such as landslides, mine roof fall, slabs, and goaf collapses. If the surrounding rock is in a high-stress environment, the sudden release of the internally accumulated energy in the excavation process may also cause a large-scale rock burst [2]. The mechanical behaviors of rocks under unloading are different from those of rocks under loading [3]. Therefore, it is important to study the mechanical and energy properties of rocks under the unloading condition. The rock mass in actual excavation projects is mostly anisotropic and presents three-dimensional unequal characteristics [4]. Scientists and

engineers assumed that the intermediate principal stress has an important effect on the mechanics and failure characteristics of rock mass under true triaxial loading [5–7]. Therefore, it is important to investigate the lateral unloading mechanics and energy characteristics of rocks subjected to different intermediate principal stresses, which is helpful to understand the unloading failure mechanism of rock masses under real geostress states.

In recent years, a substantial number of laboratory tests were conducted to reveal the macromechanical and failure behaviors of rock masses under different loads, e.g., uniaxial compression, conventional triaxial compression [8], and true triaxial compression [9, 10]. Mogi [11] first employed precise testing methods to study the influence of the combined stress system, particularly of the intermediate principal stress, on rock failure. Ma et al. [12] studied the

unloading failure and deformation feature of siltstone under different intermediate principal stress coefficients b and discussed the strength feature of the rock mass based on the Mogi–Coulomb strength criterion. At the same time, many scholars have investigated rock failure from the perspective of energy [13]. Xie et al. [14–16] proposed the overall rock failure criterion based on energy dissipation according to the characteristics of energy dissipation and release in the process of rock deformation and failure. Actually, rock masses are discontinuous media containing initial defects, such as grain boundaries, microcracks, and pores; initiation and propagation of microcracks significantly affect the failure of rock materials [17]. In order to investigate the influence of initiation and propagation of microcracks on the failure of rock materials, micromechanical methods [18–20] were employed to understand the failure of rock materials and establish the corresponding strength criteria and constitutive relations. Zhou et al. [21] proposed a nonlinear three-dimensional strength criterion for rock-like materials based on the micromechanical methods, in which the effects of the intermediate principal stress on the failure of rock-like materials are taken into account. Zhou et al. [22] used the real-time CT technique to obtain the computerized tomography (CT) images and CT values for the process of unloading, microcracking, and dilation up to the failure of limestone specimens under different unloading levels and established a damage model based on the CT value and a new failure criterion. Besides, due to the dispersion of rock materials and the expensive and time-consuming laboratory equipment, the rapid development of computers has given scholars new methods to study the properties of rock materials [23]. Different numerical simulation methods such as the finite element method (FEM) [24, 25], discrete element method (DEM) [26–29], smoothed-particle hydrodynamics (SPH) [30], and peridynamics (PD) [31, 32] were proposed to investigate the mechanical behaviors and failure characteristics of rock specimens under different compressive loading conditions. Zhang et al. [33] employed a 3D particle-based discrete element methodology to investigate the mechanical and failure characteristics of fissured marble specimens in true triaxial compression with a new loading stress path.

In this paper, the true triaxial loading and unloading test was carried out with sandstone as the object, in which the effects of the intermediate principal stress on unloading failure and energy dissipation of the rock material are considered. It is of great value for theoretical research and engineering practice.

2. Materials and Methods

2.1. Materials and Equipment Used in the Tests. The experiment process used the TRW-3000 rock mechanics test system of Central South University, as is shown in Figure 1. To ensure the homogeneity of the specimens, the specimens were taken from the same sandstone rock block with good homogeneity. The specimen size is $100\text{ mm} \times 100\text{ mm} \times 100\text{ mm}$, the unevenness is less than 0.05 mm , and the nonperpendicularity is less than 0.25° .



FIGURE 1: TRW-3000 rock mechanics test system.

2.2. Experimental Scheme and Procedure. To explore the influence of σ_2 on the true triaxial unloading mechanics and energy characteristics of sandstone, a true triaxial loading and unloading test was carried out. The test was divided into two parts as follows:

Part I: true triaxial loading:

Step 1: all directional stresses were loaded to the initial stress level at a rate of $0.05\text{ MPa}\cdot\text{s}^{-1}$.

Step 2: the stress was kept stable in all directions. After 30 s, when σ_2 and σ_3 remained unchanged, σ_1 was loaded until specimens were destroyed.

Part II: true triaxial lateral unloading:

Step 1: all directional stresses were loaded to the initial stress level at a rate of $0.05\text{ MPa}\cdot\text{s}^{-1}$.

Step 2: the stress was kept stable in all directions. After 30 s, when σ_2 and σ_3 remained unchanged, σ_1 was loaded to a predetermined value (90% of the peak strength σ_1^{max} obtained by the true triaxial loading test under the same initial stress condition).

Step 3: σ_1 and σ_2 were kept stable, and σ_3 was unloaded until specimens were destroyed. The initial stress level is shown in Table 1. The test stress path diagram is shown in Figure 2.

3. Results and Discussion of the Mechanical Characteristics

3.1. Stress-Strain Curve. The rock material is typically inhomogeneous, containing initial defects, such as grain boundaries, microcracks, and pores. Due to the dependence of the load path, the mechanical behaviors of rocks under unloading are different from those under loading. The rock material contains a number of randomly oriented preexisting microcracks. The preexisting microcracks will be closed under loading, but they will be open under unloading, so the deformation of the rock material under unloading is more than under loading. The frictional sliding on preexisting cracks will occur under loading, but the frictionless sliding on preexisting cracks may occur under unloading. The strength of the rock material under unloading is less than under loading. In the micromechanical approach, the

TABLE 1: Initial stress level.

Type	Initial stress (MPa)			Unloading point (MPa)	Unloading rate of σ_3 (MPa·s ⁻¹)
	σ_1^0	σ_2^0	σ_3^0		
Loading test	20	5, 11, 17, 20	5	–	–
Lateral unloading test	20	5, 11, 17, 20	5	$\sigma_1 = 0.9\sigma_1^{\max}$	0.05

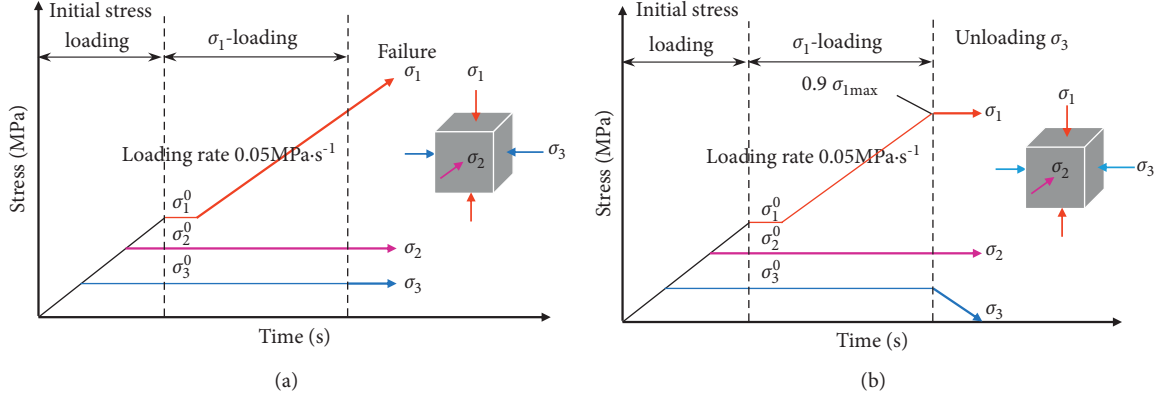


FIGURE 2: Stress path schematic diagram of the (a) true triaxial loading test and (b) true triaxial lateral unloading test.

nucleation, growth, and coalescence of microcracks dominate the failure and macroscopic properties of the rock under loading and unloading paths [3].

In this paper, the starting point of the σ_1 -loading stage is used as the reference point for data processing. Figure 3 shows the loading and unloading stress-strain curves of sandstone under different σ_2 when $\sigma_3^0 = 5$ MPa and $\sigma_1^0 = 20$ MPa. According to the loading curves, the deformation trend of the specimens under different σ_2 is the same. The early stage is approximately elastic deformation, and the later stage shows obvious plastic deformation until the final failure. As for the unloading σ_3 curve, the bearing capacity of the specimens is reduced, and obvious lateral expansion occurs when σ_1 is maintained at $0.9\sigma_1^{\max}$. Among them, the direction of σ_3 is the main expansion direction, and the minimum principal strain ε_3 increases. As σ_2 increases, the expansion in the unloading direction increases, and the peak strength increases. Sudden brittle failure occurs at the end of unloading σ_3 .

3.2. Deformation Modulus and Unloading Ratio. To study the change law of sandstone mechanical parameters under the true triaxial unloading σ_3 condition, the concept of H is introduced to analyze the relationship between mechanical parameters and unloading degree. Considering the initial stress σ_3^0 of the specimen and the unloading amount, H is defined as [9]

$$H = \frac{\sigma_3^0 - \sigma_3^i}{\sigma_3^0}, \quad (1)$$

where σ_3^i is the real-time stress value in the σ_3 direction during unloading σ_3 and H reflects the overall unloading degree of σ_3 . The initial confining pressure and the magnitude of the unloaded stress in the unloading direction have

an obvious impact on the rock deformation, failure, and strength parameters' degradation during the unloading process [34]. Quantitative research on the change law of mechanical parameters during rock unloading by H has strong theoretical and practical significance [35].

Define the true triaxial unloading deformation modulus as

$$E_0 = \frac{\sigma_1 - \sigma_1^0}{\varepsilon_1 - \varepsilon_1^0}. \quad (2)$$

Figure 4 depicts the E_0 - H curves of sandstone under different σ_2 during true triaxial unloading. The curves are fitted with the cubic polynomial, and the fitting coefficients R^2 are all up to 0.99, a good fitting effect. The curves show that E_0 gradually decreases with the increase of H during unloading σ_3 . At the initial stage of unloading, the curves are relatively gentle, as H increases, the curves gradually become steeper, and the rate of decrease of E_0 increases. The reason is that the decline of σ_3 is small, and the development of the specimen deformation is slow in the initial stage of unloading, but as H increases, the decline of σ_3 increases, the restraint of the specimen becomes weaker, the bearing capacity of the specimen decreases, and the deformation accelerates. At the same time, the curves under different σ_2 also show certain differences: the curves are generally gentle when σ_2 is small, but the curves become steeper as σ_2 increases, and when the initial stress level is high, a small unloading ratio can cause a significant deformation of the specimen, indicating that when the initial stress level is higher, more energy is stored in the specimen. Under the unloading condition, the energy stored in the specimen is released suddenly, and the failure deformation of the specimen is more significant.

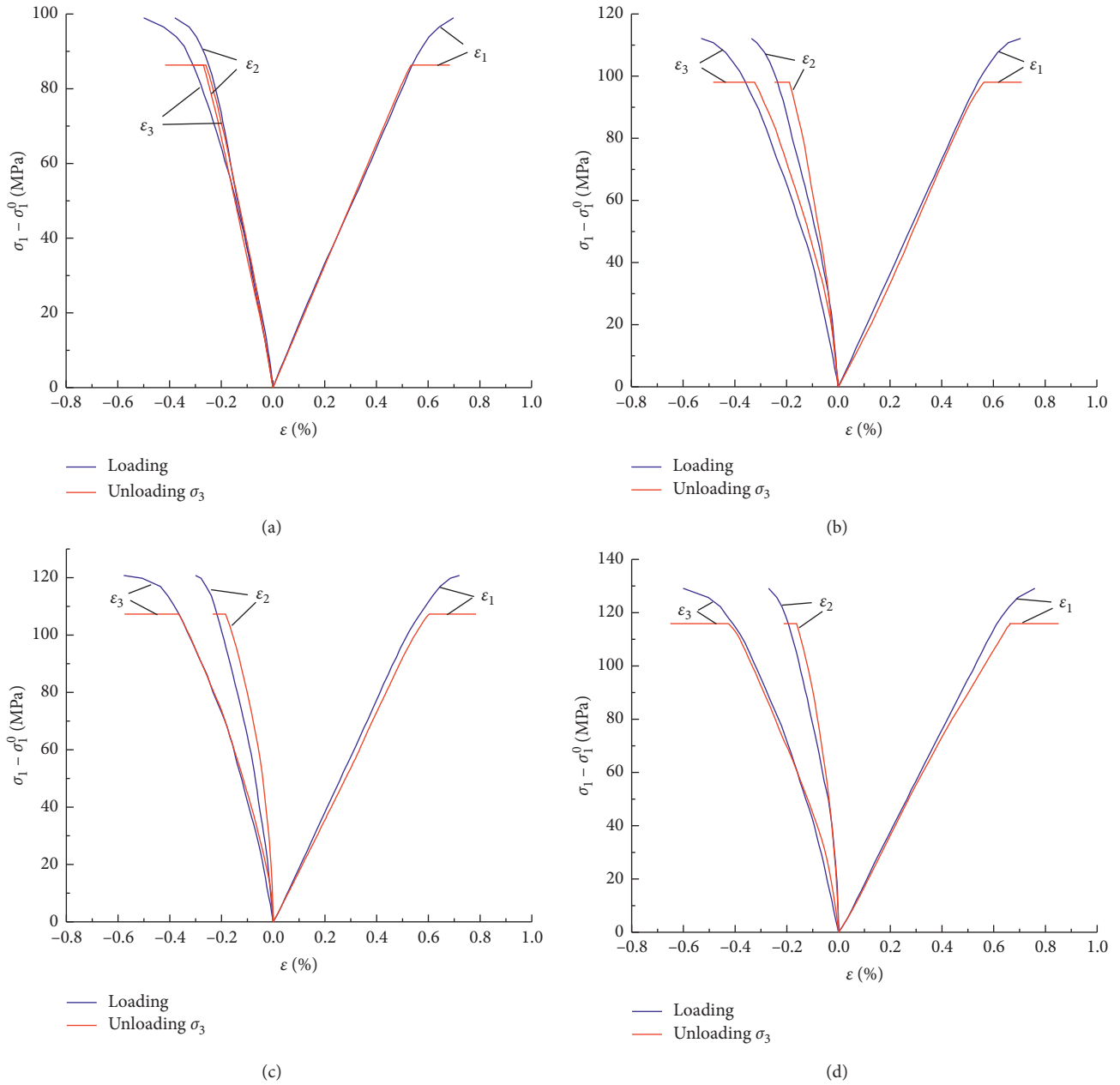


FIGURE 3: Loading and unloading stress-strain curves under different σ_2 . (a) $\sigma_2 = 5$ MPa. (b) $\sigma_2 = 11$ MPa. (c) $\sigma_2 = 17$ MPa. (d) $\sigma_2 = 20$ MPa.

3.3. Strength Characteristics. The Mohr–Coulomb criterion is the most commonly used shear failure criterion in practice, but it only considers the influence of σ_1 and σ_3 on rock failure and underestimates rock strength by ignoring the effect of σ_2 . To solve this defect, scholars have proposed many rock strength criteria based on the three-dimensional force [36–38].

Among them, through the analysis of numerous true triaxial test data, Mogi found that the yield or failure of the rock is affected by σ_2 and proposed the Mogi yield criterion based on the octahedral shear stress τ_{oct} and the effective intermediate principal stress $\sigma_{m,2}$ [36], which essence is still the shear failure criterion:

$$\tau_{\text{oct}} = f(\sigma_{m,2}),$$

$$\tau_{\text{oct}} = \frac{1}{3} \sqrt{(\sigma_1 - \sigma_2)^2 + (\sigma_2 - \sigma_3)^2 + (\sigma_1 - \sigma_3)^2}, \quad (3)$$

$$\sigma_{m,2} = \frac{\sigma_1 + \sigma_3}{2}.$$

As the distortional strain energy is proportional to the octahedral shear stress, this criterion is equivalent to asserting that failure will occur when the distortional strain energy reaches some critical value that increases monotonically with σ_2 [39]. The function in the Mogi yield

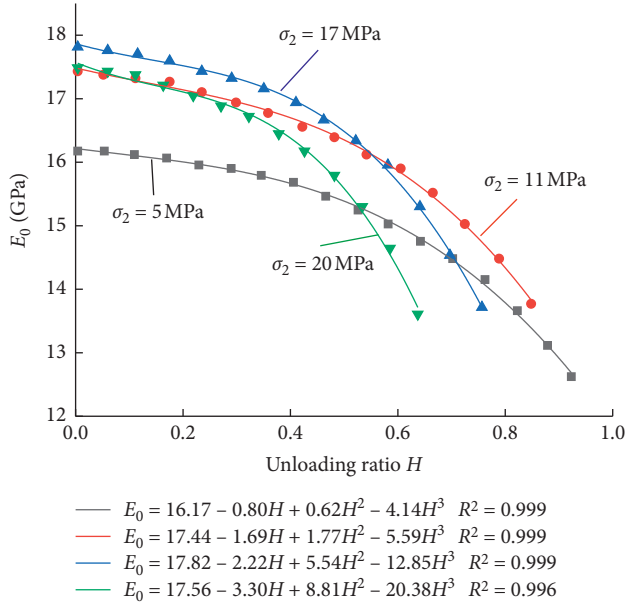


FIGURE 4: The deformation modulus and unloading ratio curves of the sandstone under different σ_2 during true triaxial unloading.

criterion is often regarded as a nonlinear power function. The parameters obtained based on formula (3) cannot well connect with the strength parameters c and φ of the Mohr–Coulomb criterion. To solve this problem, Al-Ajmi and Zimmerman [39, 40] put forward the view that the f function is linear and used numerous test data to verify it. They found that the linear fitting effect of τ_{oct} and $\sigma_{m,2}$ was good, and then they combined it with the Mohr–Coulomb criterion and renamed it the Mogi–Coulomb criterion:

$$\tau_{oct} = a + b\sigma_{m,2} \quad (4)$$

where a and b are fitting parameters, and the intensity parameter expression based on the Mohr–Coulomb criterion is

$$a = \frac{2\sqrt{2}}{3} c \cdot \cos \varphi, \quad (5)$$

$$b = \frac{2\sqrt{2}}{3} \sin \varphi.$$

Figure 5 is the fitting curve of sandstone strength based on the Mogi–Coulomb criterion under true triaxial loading and lateral unloading conditions, which is in good agreement with the experimental data, and the fitting coefficients R^2 are all higher than 0.99, a good fitting effect, indicating that the criterion can well describe the strength relationship of sandstone. The strength parameters a and b can be approximated from a set of triaxial loading and unloading tests, and then the strength parameters c and φ of sandstone can be calculated based on this strength criterion. As is shown in Table 2, compared with the values under the loading path, the c and φ values of sandstone under the unloading σ_3 path are all reduced. The cohesive force c decreases by 24.36%, and the internal friction angle φ decreases by 16.13%, that is,

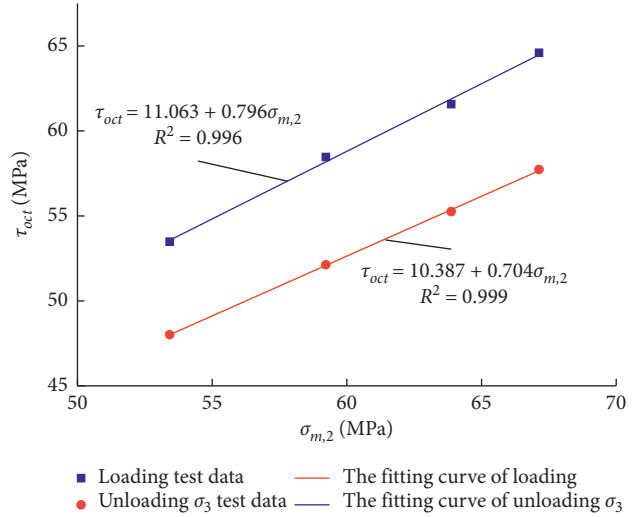


FIGURE 5: Specimen strength fitting curves based on the Mogi–Coulomb criterion.

TABLE 2: Fitting parameters of sandstone under different stress paths.

Loading method	Mogi–Coulomb criterion				
	a	b	c (MPa)	φ (°)	R^2
True triaxial loading	11.063	0.796	21.90	57.60	0.996
True triaxial lateral unloading	10.387	0.704	16.56	48.31	0.999

the specimen is softened during unloading σ_3 , and the strength is lower than that under the loading path.

4. Results and Discussion of the Energy Characteristics

4.1. Energy Calculation Principle. The rock produces deformation during loading, and the heat exchange between the rock and outside during this process is ignored; that is to say, the specimen can be considered as a closed system. According to the first law of thermodynamics,

$$U = U^d + U^e, \quad (6)$$

where U is the total work done by the external force during the test, that is, the total energy input; U^d is the dissipated energy, which is used to form internal damage and plastic deformation of the specimen, and its change satisfies the second law of thermodynamics, that is, the internal state change conforms to the increasing trend of entropy; and U^e is the releasable elastic energy, which is used to generate elastic deformation of the specimen.

This paper takes the starting point of the σ_1 -loading stage as the base point of data processing and regards the energy input and dissipation in the initial stress loading stage as changes in the internal energy of the specimen, so it is ignored. The energy of each part of the specimen under the complex stress states can be expressed as equation (7) [14–16].

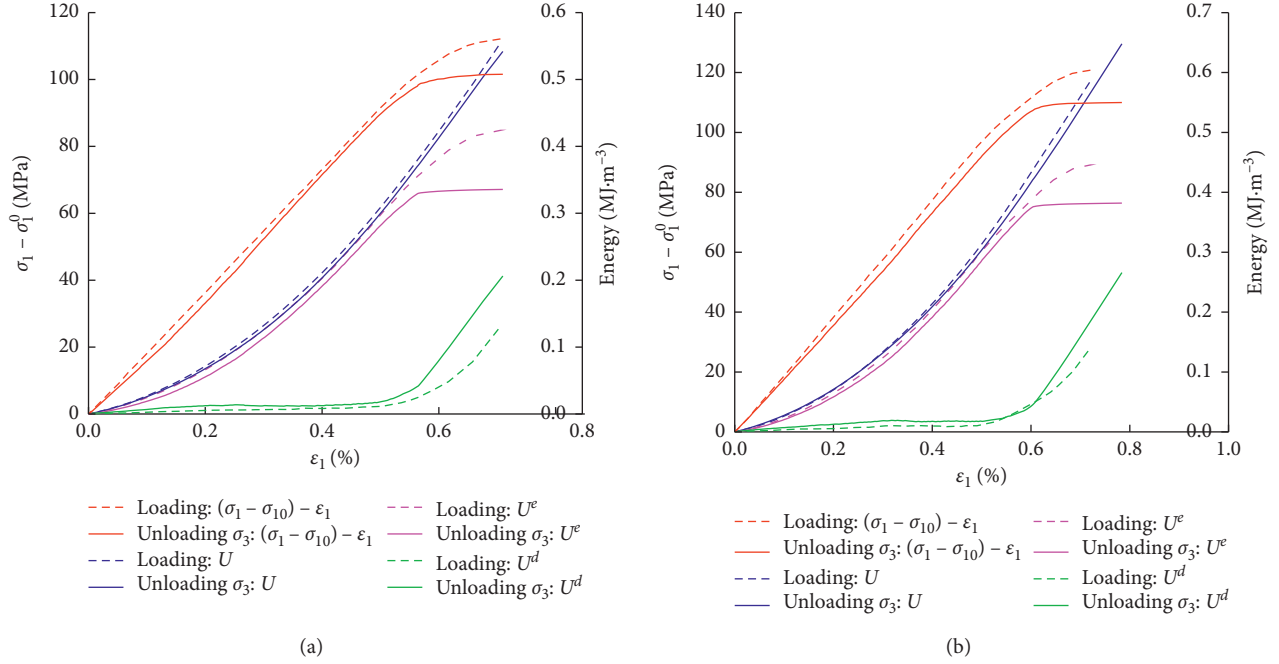


FIGURE 6: Energy-strain curves. (a) $\sigma_3 = 5$ MPa and $\sigma_2 = 11$ MPa. (b) $\sigma_3 = 5$ MPa and $\sigma_2 = 17$ MPa.

In equation (7), σ_1 , σ_2 , and σ_3 are the maximum, middle, and minimum principal stresses, respectively, ε_1 , ε_2 , and ε_3 are the strains in the directions of the principal stresses, μ is Poisson's ratio, E is the unloading elastic modulus, which is replaced by the elastic modulus in the calculation, and U_0 and U_0^e are the total energy input and the releasable elastic energy in the initial stress loading stage.

$$U = \int_0^{\varepsilon_1} \sigma_1 d\varepsilon_1 + \int_0^{\varepsilon_2} \sigma_2 d\varepsilon_2 + \int_0^{\varepsilon_3} \sigma_3 d\varepsilon_3 - U_0,$$

$$U^e = \frac{1}{2E} [\sigma_1^2 + \sigma_2^2 + \sigma_3^2 - 2\mu(\sigma_1\sigma_2 + \sigma_2\sigma_3 + \sigma_3\sigma_1)] - U_0^e. \quad (7)$$

4.2. Energy-Strain Curve. Figure 6 depicts the energy-strain curve of the specimen under loading and unloading σ_3 conditions, which shows that the initial forces of the two stress paths are the same, so the early changes of the energy-strain curve under the two paths are similar. That is to say, the energy is mainly stored as U^e , and the part converted into U^d is very small. However, because the forces of the two stress paths change in the later stage, there are obvious differences in the later stage of the energy-strain curves: according to the loading curve, one part of the energy is stored as U^e , and the other part of the energy is converted into U^d . As for the unloading curve, U^d increases significantly, while U^e remains stable with minor changes, indicating that the energy input in the later stage is used for internal damage and plastic deformation of the specimen, and the excess U^d is transformed into the kinetic energy of the falling rock.

4.3. Energy Analysis of Lateral Unloading. Table 3 depicts the energy value of each characteristic point of the specimen under the unloading σ_3 condition. As is shown in Table 3, when σ_2 increases from 5 MPa to 20 MPa, all types of energy at the specimen failure point increase, among which the maximum increment is U^d : from $0.18 \text{ MJ} \cdot \text{m}^{-3}$ to $0.32 \text{ MJ} \cdot \text{m}^{-3}$, an increase of 77.8%. Meanwhile, the increment of U and U^d increases with the increase of σ_2 , but the increment of U^e remains unchanged. Figure 7 shows the fitted curves of energy- σ_2 at the unloading failure point under the unloading σ_3 condition when $\sigma_3^0 = 5$ MPa and $\sigma_1^0 = 20$ MPa, which depict that U , U^d , and U^e are linearly related to σ_2 , and the linear fitting coefficients R^2 are all above 0.9, a good fitting effect.

Figure 8 depicts the U^d - H curve under the unloading σ_3 condition, which shows that U^d increases slowly with the increase of H in the initial unloading stage, but as H increases, U^d increases rapidly until the final specimen failure. The influence of σ_2 on the change of U^d during the unloading process is mainly manifested as follows: with the increase of σ_2 , the slope of the curve becomes larger, and the growth rate of U^d increases; the specimen deformation consumes more energy under the same unloading amount.

The total energy absorbed by the specimen during the loading process is used to store as U^e and convert it into U^d for the initiation and propagation of cracks inside the specimen. Therefore, even if the energy input during the loading process is the same, different energy distributions will cause the specimen failure mode to change. Figure 9 is the energy distribution diagram of the specimen under the unloading σ_3 condition when $\sigma_3^0 = 5$ MPa and $\sigma_1^0 = 20$ MPa, which shows that U^e/U is generally above 0.5, while U^d/U increases with the increase of σ_2 , indicating that most of the

TABLE 3: The energy of unloading and failure points under different σ_2 .

Initial stress (MPa)	Unloading point energy (MJ·m ⁻³)			Unloading failure point energy (MJ·m ⁻³)			Unloading σ_3 energy increase (MJ·m ⁻³)			
	$\sigma_1^0, \sigma_2^0, \sigma_3^0$	U	U^e	U^d	U	U^e	U^d	ΔU	ΔU^e	ΔU^d
20, 5, 5		0.32	0.30	0.02	0.49	0.31	0.18	0.17	0.01	0.16
20, 11, 5		0.37	0.33	0.04	0.55	0.34	0.21	0.18	0.01	0.17
20, 17, 5		0.43	0.38	0.05	0.65	0.38	0.27	0.22	0.00	0.22
20, 20, 5		0.49	0.42	0.07	0.75	0.43	0.32	0.26	0.01	0.25

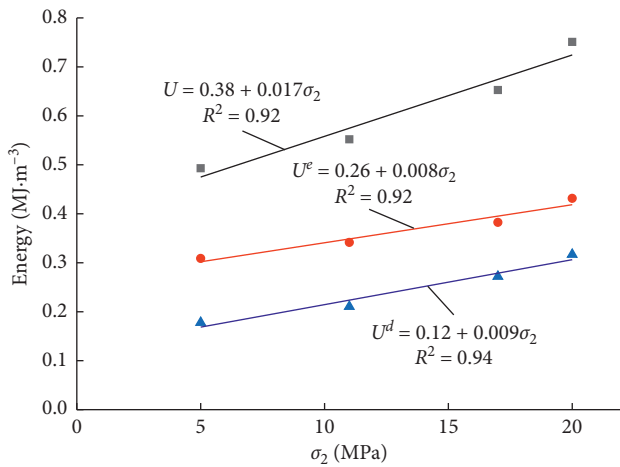


FIGURE 7: The fitting curves of energy- σ_2 at the failure point under the unloading σ_3 condition.

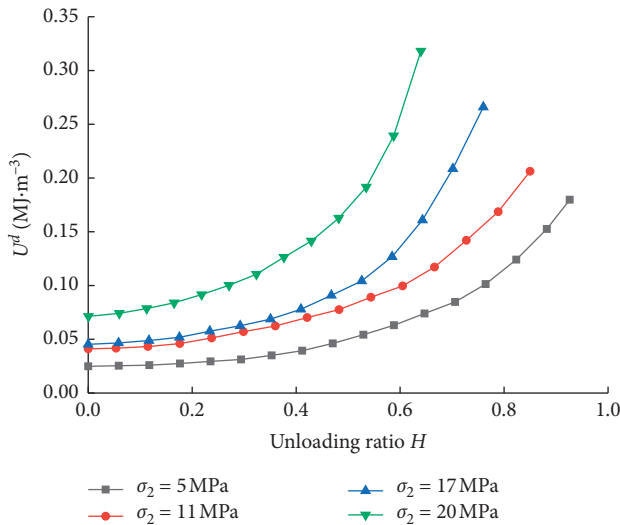


FIGURE 8: Dissipated energy-unloading ratio curves.

total energy absorbed by the specimen under the unloading σ_3 path is converted into U^e and stored inside the specimen, but as σ_2 increases, the proportion of U^d increases, and specimen destruction consumes relatively more energy.

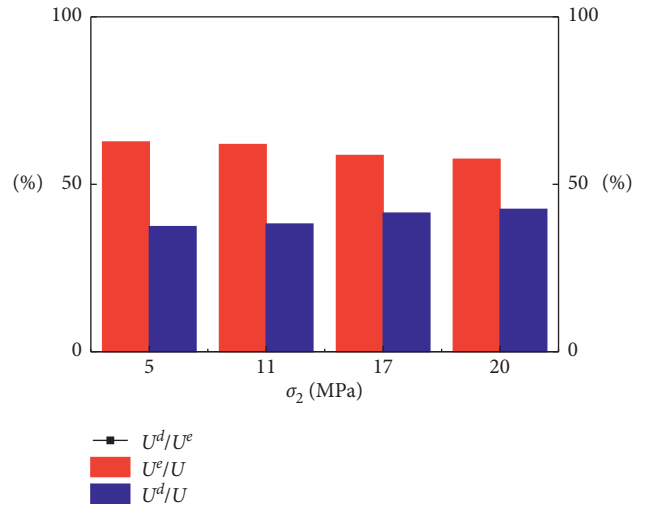


FIGURE 9: Failure point energy distribution under the unloading σ_3 condition.

5. Conclusion

- (1) Compared with the results of the loading test, the peak strength of the sandstone under the unloading σ_3 path is reduced, and sudden brittle failure occurs at the end of unloading. During the unloading σ_3 process, the unloading direction of the specimen expands significantly, E gradually decreases with the increase of H , and the relationship between E and H can be fitted with a cubic polynomial, a good fitting effect.
- (2) It is accurate to describe the true triaxial strength characteristics of specimens under different stress paths by using Mogi-Coulomb criterion. Compared with the values under the loading path, the c and φ values of the sandstone under the unloading σ_3 path are reduced, of which the cohesive force c decreases by 24.36%, and the internal friction angle φ decreases by 16.13%.
- (3) U , U^d , and U^e are all positively linearly correlated with σ_2 when the specimen is damaged under the unloading σ_3 condition. U^d increases nonlinearly with H , and with the increase of σ_2 , the slope of the U^d - H curve becomes larger, and the specimen consumes more energy under the same unloading amount. Most of the total energy absorbed by the specimen under the unloading σ_3 path is converted into U^e and stored inside the specimen, but as σ_2 increases, the U^d/U curve rises, the proportion of U^d increases, and the energy consumed when the specimen is broken is greater.

Abbreviations

- σ_1 : Maximum principal stress
- C : Cohesive force
- σ_2 : Intermediate principal stress
- Φ : Internal friction angle

σ_3 : Minimum principal stress
 U : Total energy
 H : Unloading ratio
 U^e : Elastic energy
 E : Deformation modulus
 U^d : Dissipation energy.

Data Availability

The data used to support the findings of this study are included within the article.

Conflicts of Interest

The authors declare that there are no conflicts of interest regarding the publication of this paper.

Acknowledgments

This paper obtained funding from projects (no. 51979293) supported by the National Natural Science Foundation of China. The authors wish to acknowledge the support.

References

- [1] J. Yu, G. Liu, Y. Cai et al., "Time-dependent deformation mechanism for swelling soft-rock tunnels in coal mines and its mathematical deduction," *International Journal of Geomechanics*, vol. 20, no. 3, pp. 04019186.1–04019186.10, 2020.
- [2] A.-Z. Hua and M.-Q. You, "Rock failure due to energy release during unloading and application to underground rock burst control," *Tunnelling and Underground Space Technology*, vol. 16, no. 3, pp. 241–246, 2001.
- [3] X. P. Zhou, "Localization of deformation and stress-strain relation for mesoscopic heterogeneous brittle rock materials under unloading," *Theoretical and Applied Fracture Mechanics*, vol. 44, no. 1, pp. 27–43, 2005.
- [4] R. Cao, R. Yao, J. Meng, Q. Lin, H. Lin, and S. Li, "Failure mechanism of non-persistent jointed rock-like specimens under uniaxial loading: laboratory testing," *International Journal of Rock Mechanics and Mining Sciences*, vol. 132, p. 104341, 2020.
- [5] X.-T. Feng, Y. Gao, X. Zhang, Z. Wang, Y. Zhang, and Q. Han, "Evolution of the mechanical and strength parameters of hard rocks in the true triaxial cyclic loading and unloading tests," *International Journal of Rock Mechanics and Mining Sciences*, vol. 131, p. 104349, 2020.
- [6] R. P. Tiwari and K. S. Rao, "Post failure behavior of a rock mass under the influence of triaxial and true triaxial confinement," *Engineering Geology*, vol. 84, no. 3-4, pp. 112–129, 2006.
- [7] B. Haimson and J. W. Rudnicki, "The effect of the intermediate principal stress on fault formation and fault angle in siltstone," *Journal of Structural Geology*, vol. 32, no. 11, pp. 1701–1711, 2010.
- [8] Y. Wang, D. Liu, J. Han, C. Li, and H. Liu, "Effect of fatigue loading-confining stress unloading rate on marble mechanical behaviors: an insight into fracture evolution analyses," *Journal of Rock Mechanics and Geotechnical Engineering*, vol. 12, no. 6, pp. 1249–1262, 2020.
- [9] X. Si and F. Gong, "Strength-weakening effect and shear-tension failure mode transformation mechanism of rockburst for fine-grained granite under triaxial unloading compression," *International Journal of Rock Mechanics and Mining Sciences*, vol. 131, p. 104347, 2020.
- [10] X. Li, F. Feng, D. Li, K. Du, P. G. Ranjith, and J. Rostami, "Failure characteristics of granite influenced by sample height-to-width ratios and intermediate principal stress under true-triaxial unloading conditions," *Rock Mechanics and Rock Engineering*, vol. 51, no. 5, pp. 1321–1345, 2018.
- [11] K. Mogi, "Effect of the intermediate principal stress on rock failure," *Journal of Geophysical Research*, vol. 72, no. 20, pp. 5117–5131, 1967.
- [12] Y. P. Ma, J. T. Li, and S. F. Liu, "Experimental study on lateral unloading mechanical properties of siltstone considering intermediate principal stress," *Journal of Central South University (Science and Technology)*, vol. 50, no. 11, pp. 2792–2800, 2019.
- [13] R. Cao, C. Ping, H. Lin, and X. Fan, "Experimental and numerical study of the failure process and energy mechanisms of rock-like materials containing cross un-persistent joints under uniaxial compression," *PLoS One*, vol. 12, no. 12, p. e0188646, 2017.
- [14] H. P. Xie, R. D. Peng, J. U. Yang, and H. Zhou, "Energy analysis of rock failure," *Chinese Journal of Rock Mechanics and Engineering*, vol. 24, no. 15, pp. 2603–2608, 2005.
- [15] H. P. Xie, Y. Ju, L. Y. Li, and R. D. Peng, "Energy mechanism of deformation and failure of rock masses," *Chinese Journal of Rock Mechanics and Engineering*, vol. 27, no. 9, pp. 1729–1740, 2008.
- [16] H. P. Xie, J. U. Yang, and L. Y. Li, "Criteria for strength and structural failure of rocks based on energy dissipation and energy release principle," *Chinese Journal of Rock Mechanics and Engineering*, vol. 24, no. 17, pp. 3003–3010, 2005.
- [17] X. P. Zhou and H. Q. Yang, "Dynamic damage localization in crack-weakened rock mass: strain energy density factor approach," *Theoretical & Applied Fracture Mechanics*, vol. 97, pp. 289–302, 2018.
- [18] X. P. Zhou, "Triaxial compressive behavior of rock with mesoscopic heterogeneous behavior: strain energy density factor approach," *Theoretical and Applied Fracture Mechanics*, vol. 45, no. 1, pp. 46–63, 2006.
- [19] X.-P. Zhou, Y.-X. Zhang, Q.-L. Ha, and K.-S. Zhu, "Micro-mechanical modelling of the complete stress-strain relationship for crack weakened rock subjected to compressive loading," *Rock Mechanics and Rock Engineering*, vol. 41, no. 5, pp. 747–769, 2008.
- [20] X. P. Zhou and H. Q. Yang, "Micromechanical modeling of dynamic compressive responses of mesoscopic heterogeneous brittle rock," *Theoretical and Applied Fracture Mechanics*, vol. 48, no. 1, pp. 1–20, 2007.
- [21] X.-P. Zhou, Y.-D. Shou, Q.-H. Qian, and M.-H. Yu, "Three-dimensional nonlinear strength criterion for rock-like materials based on the micromechanical method," *International Journal of Rock Mechanics and Mining Sciences*, vol. 72, pp. 54–60, 2014.
- [22] X. P. Zhou, Y. X. Zhang, and Q. L. Ha, "Real-time computerized tomography (CT) experiments on limestone damage evolution during unloading," *Theoretical and Applied Fracture Mechanics*, vol. 50, no. 1, pp. 49–56, 2008.
- [23] M. Kou, X. Liu, S. Tang, and Y. Wang, "3-D X-ray computed tomography on failure characteristics of rock-like materials under coupled hydro-mechanical loading," *Theoretical and Applied Fracture Mechanics*, vol. 104, p. 102396, 2019.

- [24] C. A. Tang, "Numerical simulation of progressive rock failure and associated seismicity," *International Journal of Rock Mechanics and Mining Sciences*, vol. 34, no. 2, pp. 249–261, 1997.
- [25] C. A. Tang and S. Q. Kou, "Crack propagation and coalescence in brittle materials under compression," *Engineering Fracture Mechanics*, vol. 61, no. 3-4, pp. 311–324, 1998.
- [26] J. Yu, W. Yao, K. Duan, X. Liu, and Y. Zhu, "Experimental study and discrete element method modeling of compression and permeability behaviors of weakly anisotropic sandstones," *International Journal of Rock Mechanics and Mining Sciences*, vol. 134, p. 104437, 2020.
- [27] P. A. Cundall and O. Strack, "A discrete numerical model for granular assemblies," *Géotechnique*, vol. 30, no. 3, pp. 331–336, 2008.
- [28] D. O. Potyondy and P. A. Cundall, "A bonded-particle model for rock," *International Journal of Rock Mechanics and Mining Sciences*, vol. 41, no. 8, pp. 1329–1364, 2004.
- [29] M. M. Kou, Y. J. Lian, and Y. T. Wang, "Numerical investigations on crack propagation and crack branching in brittle solids under dynamic loading using bond-particle model," *Engineering Fracture Mechanics*, vol. 212, pp. 41–56, 2019.
- [30] G. W. Ma, X. J. Wang, and F. Ren, "Numerical simulation of compressive failure of heterogeneous rock-like materials using SPH method," *International Journal of Rock Mechanics and Mining Sciences*, vol. 48, no. 3, pp. 353–363, 2011.
- [31] Y. Wang, X. Zhou, and X. Xu, "Numerical simulation of propagation and coalescence of flaws in rock materials under compressive loads using the extended non-ordinary state-based peridynamics," *Engineering Fracture Mechanics*, vol. 163, pp. 248–273, 2016.
- [32] Y.-T. Wang, X.-P. Zhou, and M.-M. Kou, "Three-dimensional numerical study on the failure characteristics of intermittent fissures under compressive-shear loads," *Acta Geotechnica*, vol. 14, no. 4, pp. 1161–1193, 2019.
- [33] Y. Zhang, S. Liu, M. Kou, and Z. Wang, "Mechanical and failure characteristics of fissured marble specimens under true triaxial compression: insights from 3-D numerical simulations," *Computers and Geotechnics*, vol. 127, no. 7, p. 103785, 2020.
- [34] F. Xiao, D. Jiang, F. Wu et al., "Effects of prior cyclic loading damage on failure characteristics of sandstone under true-triaxial unloading conditions," *International Journal of Rock Mechanics and Mining Sciences*, vol. 132, p. 104379, 2020.
- [35] D. Y. Li, Z. Sun, X. B. Li, and T. Xie, "Mechanical response and failure characteristics of granite under different stress paths in triaxial loading and unloading conditions," *Chinese Journal of Rock Mechanics and Engineering*, vol. 35, no. 2, pp. 3449–3457, 2016.
- [36] K. Mogi, "Fracture and flow of rocks under high triaxial compression," *Journal of Geophysical Research*, vol. 76, no. 5, pp. 1255–1269, 1971.
- [37] D. C. Drucker and W. Prager, "Soil mechanics and plastic analysis or limit design," *Quarterly of Applied Mathematics*, vol. 10, no. 2, pp. 157–165, 1952.
- [38] L. Zhang and H. Zhu, "Three-dimensional Hoek-Brown strength criterion for rocks," *Journal of Geotechnical and Geoenvironmental Engineering*, vol. 133, no. 9, pp. 1128–1135, 2007.
- [39] A. M. Al-Ajmi and R. W. Zimmerman, "Relation between the Mogi and the coulomb failure criteria," *International Journal of Rock Mechanics and Mining Sciences*, vol. 42, no. 3, pp. 431–439, 2005.
- [40] A. M. Al-Ajmi and R. W. Zimmerman, "Stability analysis of vertical boreholes using the Mogi-Coulomb failure criterion," *International Journal of Rock Mechanics and Mining Sciences*, vol. 43, no. 8, pp. 1200–1211, 2006.

Research Article

Research on Bearing Characteristics of Open-Ended Pipe Piles under Static Load

Haibao Feng ^{1,2}, Xingke Dai ³, Shuiyue Chen ³ and Jianwei Chen ³

¹State Key Laboratory of Hydraulic Engineering Simulation and Safety, Tianjin University, Tianjin 300072, China

²The Second Engineering Co., Ltd., of CCCC First Harbor Engineering Co., Ltd., Qingdao 266071, China

³Institute of Civil Engineering, Qingdao University of Technology, Qingdao 266033, China

Correspondence should be addressed to Haibao Feng; xxhfb@cccchj.com

Received 24 January 2021; Revised 21 March 2021; Accepted 2 April 2021; Published 14 April 2021

Academic Editor: Yunteng Wang

Copyright © 2021 Haibao Feng et al. This is an open access article distributed under the Creative Commons Attribution License, which permits unrestricted use, distribution, and reproduction in any medium, provided the original work is properly cited.

The accurate estimate of the ultimate bearing capacity of a single pile in the vertical direction is an important issue in the design of the pile foundation. This paper presents a static test on a single-pile model. The test was performed through a large-scale model casing test equipment that is independently developed. Various factors that affect the different test soil samples have been taken into account. In addition, the test has measured the pile's internal stress and displacement through the sensors that were installed on the pile. What is more, a series of studies on the settling character of the single pile, pile lateral friction, changing nature of tip resistance, and its development with settling have been carried out. Finally, this paper analyzes the bearing capacity behavior and load transfer mechanism in the compressive static load test on the single pile in the vertical direction. The test results show that, under the same static load, the lateral friction of a pile in the sand is bigger than that in the silty clay, and with the increasing load at the pile tip, the increment speed of tip resistance in the silty clay is much faster than that in the sand, while pile's bearing capacity in the sand is much bigger than that in the silty clay.

1. Introduction

The rapid urbanization has led to huge demands on the infrastructure constructions in city area. Meanwhile, the pile foundation is one of the most common forms of the infrastructure foundations in the constructional engineering. The design concept of the pile foundation with settling control has increasingly been accepted by the academia and engineering community [1]. The most urgent problems in optimizing the settling control for the pile foundation design include the following: how to figure out the load transfer mechanism at the pile-soil interface during the static load process; what is the development nature of tip resistance with pile settling; how to seasonably calculate the pile foundation settling. These issues provide a theoretical foundation for the accurate estimate of the ultimate bearing capacity of a pile. Many scholars explore the working mechanism of a single pile by bringing forward empirical methods [2, 3], elastic theory method [4], load transmitting

method [5–7], and numerical method [8, 9]. These methods study the mechanical property of the static load from a macroscopic perspective; therefore, they have limited application range. Some scholars have used the Mohr-Coulomb criterion to study the fracture state of rock under the ultimate load-bearing state through the comparative analysis of model tests and numerical simulations and have made good progress [10–15]. In addition, according to the principle of layerwise summation method, Hong and Yang in 2008 extended the elastic theory based on Mindlin displacement solution and successfully established a method similar to the single-pile load distribution and settlement calculation under soil hierarchical solution [16]. In 2010, Wang et al. studied the rule of distribution for the lateral and tip resistances under different loads [17], as well as the changing nature of lateral friction with the settling of pile tip and of a pile in sand layer and silty clay with the relative displacement of such sand or silty clay. In the same year, Zhou et al. conducted an indoor single-pile static model test

through their independently designed visible box model [18], and by taking into account the influencing factors on different pile diameters and soil compactness, their team studied the settlement mode of the single pile, changing nature of lateral, tip resistances, and their development with settling. Their results further revealed the micro- and macromechanisms in the static load process. In 2011, Diao et al. explored the static load test on pile under different loads through on-site test and finite element modeling [19]. In 2012, Hong applied the elastic theory based on Mindlin displacement solution to the establishment of a theoretical simulation method by conducting the single-pile static load test based on pile-loading and anchor-pile methods [20]. They also made a contrastive analysis between the two methods. In 2016, Gao et al. conducted and analyzed the PHC pile static test in Qingdao [21], and their study indicates that PHC pile has a great bearing potential in the complex geology of Jiaozhouwan reclamation area. In 2017, Huang and Zhang combined three socketed piles that were taken from a construction project in Qingdao to perform an on-site static load test and have studied the settling nature [22]. In 2020, Huo et al. conducted field tests based on the rock-socketed pile foundation of an engineering quartz sandstone formation and obtained the lateral resistance and end resistance through the conversion of uniaxial compressive strength theory [23]. However, the mechanical property of soil comes from the reaction of all elements in the soil. To the best of the authors' knowledge, only a few studies focus on the mechanical property of soil in the static load process.

Through the indoor test on the large-scale open pile model, this paper studies the settlement mode, bearing capacity, and lateral friction during the static load process of a single pile, as well as the working nature of tip friction, which have revealed the internal mechanism of pile-soil interaction in static load process.

2. The Indoor Model Test on Single Pile's Static Load

2.1. The Equipment and Soil Sample Used for Indoor Model Test. This test adopts the large-scale model casing equipment that is independently developed by the Qingdao University of Technology, with its internal dimension of 3000 mm × 3000 mm × 2000 mm ($L \times W \times H$), as shown in Figure 1. The dimension of its steel plate installed on its facade is 900 mm × 900 mm × 6 mm ($L \times W$ Thickness), as a discharge opening for the convenience of disassembly. Tempered glass is installed at intervals in the middle of the facade as the viewing windows. The equipment is soldered together with steel plate, and its welding lines are sealed with high-strength solid sealant for waterproof. Its drainage adopts stainless steel tubes equipped with ball valves, which are installed at its four corners for the drainage consolidation of soil sample. All of the steel used for the equipment is painted with peacock blue antirust paint, with servo-load

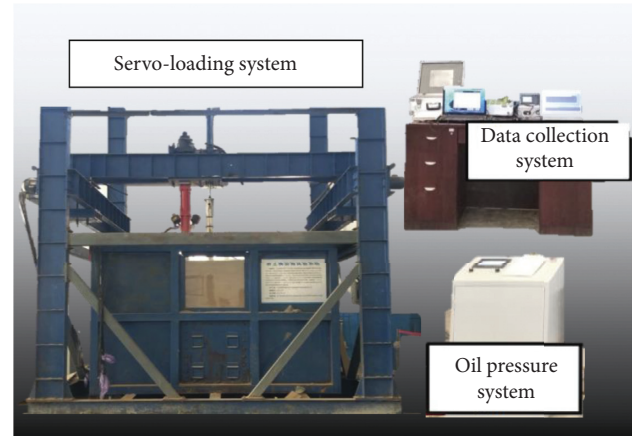


FIGURE 1: The large-scale model casing test equipment.

system used for loading in static load process, as shown in Figure 1.

The pile model used for the test consists of two aluminum alloy tubes with concentric circles, and their inner and outer tubes are connected to the pile shoe, with Poisson's ratio 0.3 and elasticity modulus 72 GPa. The pile model P1 is of 1000 mm long, 140 mm in diameter, and 13 mm in thickness, while the pile model P2 is of 1000 mm long, 160 mm in diameter, and 13 mm in thickness. Except for the diameter, the pile model P1 and P2 are made in the same structure, as shown in Figure 2. The cross-sectional dimensions of P1's outer tube are 140 mm × 134 mm (outer × inner diameter) and 3 mm in thickness, while the cross-sectional dimensions of its inner tube are 120 mm × 114 mm (outer × inner diameter) and 3 mm in thickness. The cross-sectional dimension of P2's outer tube is 160 mm × 154 mm (outer × inner diameter) and 3 mm in thickness, while the cross-sectional dimension of its inner tube is 140 mm × 134 mm (outer × inner diameter) and 3 mm in thickness.

On the outer wall of the outer tube, a groove is opened for fiber bragg grating (FBG) microsensor to be stuck in and sealed with epoxy resin glue, while the sensor of inner tube is also installed onto its outer wall and placed into the enclosed annular space to protect it from environmental disturbance (see Figure 3 for both tubes). Both the inner and outer tubes for FBG microsensor installment are in a symmetrical layout on both sides. Starting from the pile tip, the height of outer tube should be, respectively, 20 mm, 200 mm, 380 mm, 560 mm, 740 mm, and 920 mm, and on each side of the outer tube, six sensors should be installed, totaling 12. The height of inner tube should be, respectively, 20 mm, 110 mm, 200 mm, 290 mm, 380 mm, 560 mm, and 740 mm, and on each side of the inner tube, seven sensors should be installed, totaling 14 sensors. FBG microsensor measures the axial force of pile shaft through detecting the pile strain change in order to get the shaft friction. The stress obtained by the sensor at the bottom of outer tube is approximately equal to tip resistance, and the displacement

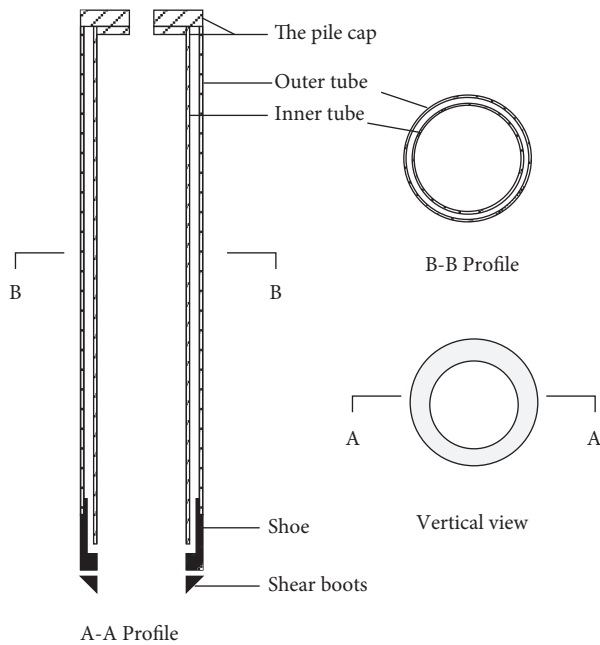


FIGURE 2: The structure of double-walled pile.

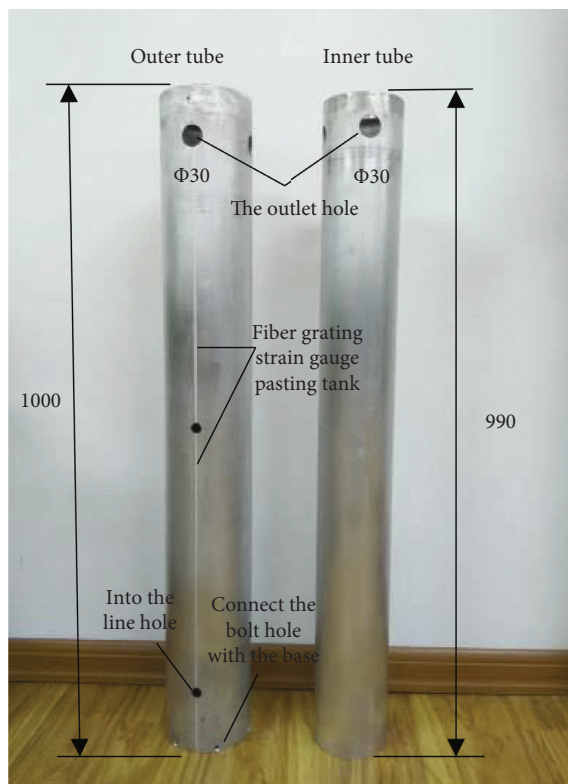


FIGURE 3: The inner and outer tubes of double-walled open-ended pile.

and accumulated settlement at the pile tip are measured through the displacement sensor of the servo-loading system.

Two soil samples are used for this test: one is the sea sand, and the other is the silty clay taken in a Qingdao area.

The sea sand used is dried out to reduce the influence from other factors, and the relative density of the sand is $G_s = 2.65$; maximum void ratio is $e_{max} = 0.52$; minimum void ratio is $e_{min} = 0.30$; relative compactness is $D_r = 0.73$; median size is $d_{50} = 0.72$ mm; particle size range (mm) is 0–15; internal friction angle is $\phi = 42.8^\circ$; dry density is $\rho_d = 1.95$ kg/mm³. The grain composition obtained through sieving method is shown in Figure 4.

As for the silty clay, its optimum moisture content is $w = 23\%$; maximum dry density is $\rho_d = 1.69$ kg/mm³; liquid limit is $w_l = 31.6\%$; plastic limit is $w_p = 13.8\%$; plastic index is $I_p = 17.9\%$; internal friction angle is $\phi = 30^\circ$; cohesive force is $c = 27$ kPa; compressibility coefficient is $\partial_{v1-2} = 0.32$ MPa; compression modulus is $E_{S1-2} = 5.5$ MPa; Poisson's ratio is 0.3. Soil is filled into the foundation by layer and then compacted manually or mechanically. After the preparation is finished, slowly add water into the soil until complete saturation and then wait for 20 d to ensure that the moisture in the soil is evenly distributed.

2.2. Soil Preparation. According to inner dimensions of casing model 3000 mm × 3000 mm × 2000 mm (length × width × height), the height of soil sample is 1800 mm, and the sample is filled into the casing model in nine times, and large scraper is used to fill in the soil at 200 mm each time, and each layer of the soil sample is tamped down both manually (two times) and mechanically (one time). Each layer of soil is given at least 12 h for its self-compactness relying on gravity, so as to ensure the homogeneity of test sample. In each layer of soil, eight cutting rings are placed each at 300 mm from the edge to the four faces of the casing model. After the test, take out all cutting rings from each layer to measure the soil compactness and work out the average compactness.

2.3. Test Procedures

2.3.1. Test Preparation.

- ① Fill the soil sample into the casing model with layers at a height of 200 mm for each layer, manually (two times) and mechanically (one time), until the soil at each layer is tamped to the required height.
- ② Place an open-ended pile into the casing model after determining its sinking position in the casing model, using a leveling rod to adjust the perpendicularity of the pile, so as to ensure its perpendicularity during pile sinking.
- ③ Use a hydrocylinder to slowly press the pile to reach the required height. After sinking the pile into the required position, give the sand sample at least 15 d and the saturated foundation soil at least 28 d before starting the test.

2.3.2. Loading and Measurement. The servo-loading system and the casing model counterforce device are adopted as the loading devices for this test. The pile is applied with net load

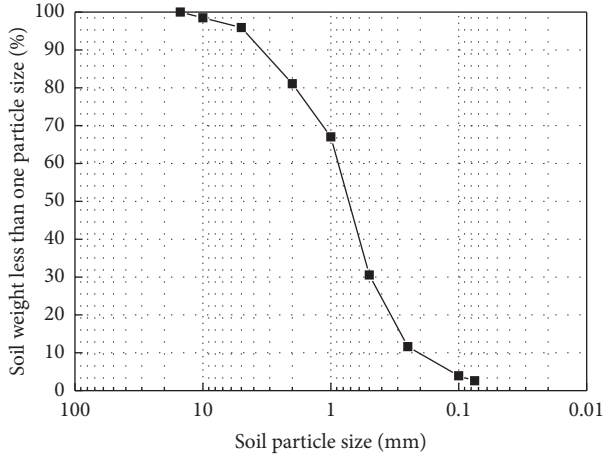


FIGURE 4: The grain composition of sand sample.

by the grading of servo-loading system to reach the ultimate load. The loading in the test is in accordance with the slow maintenance loading method as specified in The Technical Code for Building Pile Foundation (JGJ94-94) [24].

During the static test, net load is applied by the servo-loading system through the loading device to reach the ultimate load. In the sand, the load of pile model in the first level is 8 kN; in the second level, it is 16 kN; in the third level, it is 24 kN; in the fourth level, it is 32 kN; in the fifth level, it is 40 kN or damaged. In silty clay, the load of pile model in the first level is 1 kN; in the second level, it is 2 kN; in the third level, it is 3 kN; in the fourth level, it is 4 kN; in the fifth level, it is 5 kN; in the sixth level, it is 6 kN; in the seventh level, it is 7 kN; in the eighth level, it is 8 kN; in the ninth level, it is 9 kN or damaged. Loading should be stopped if, at a certain level, the settling volume of the pile model under the load effect is five times as much as the settling volume of the previous level, or there is no obvious increase in the load of pile foundation.

2.3.3. The Measurement on Stress and Deformation. Before loading at each level, record the data collected by each pile sensor and measure the displacement at the pile tip. Load for 30 min to repeat the aforementioned operation, and then measure the displacement at the pile tip after each 15 min of loading. The specific test plan is shown in Table 1.

3. Test Data Analysis

3.1. The Axial Force of Pile Shaft. According to the data collected from the sensors, we can obtain the axial force of pile shaft through the following formula:

$$N_i = \frac{R_i}{S_{ir}} \times 10^{-3} EA = \varepsilon_i EA, \quad (1)$$

in which N_i is the axial force (kN) of i section; R_i is the data (nm) collected by the sensor of i section; S_{ir} is the sensitivity coefficient (Pm/ μE) of the sensor of i section; E is the elasticity modulus (kPa) of pile model; A is the pile sectional area (m^2); ε_i is the strain measured by the sensor of i section.

3.2. Lateral Friction. According to the axial force of each section, pile lateral friction can be obtained through the following formula:

$$F_i = N_i - N_{i+1}. \quad (2)$$

According to the lateral friction of soil layer, the unit side friction of such layer can be worked out through the following formula:

$$f_i = \frac{F_i}{Ul_i}, \quad (3)$$

in which F_i is the lateral friction (kN); N_i is the axial force (kN) of i section; N_{i+1} is the axial force (kN) of $i+1$ section; f_i is the unit side friction (kPa) of i layer; U is the perimeter (m) of pile section; l_i is the distance (m) from i layer section to $i+1$ layer section.

3.3. Tip Resistance. According to the data collected by the sensor at the bottom of pile lateral side, the tip resistance can be worked out through the following formula:

$$F_d = \varepsilon EA, \quad (4)$$

where F_d is the tip resistance; ε is the stress measured by the sensor of the section; E is the elasticity modulus (kPa) of pile model; A is the pile sectional area (m^2).

4. Test Results Analysis

4.1. Pile Working Principle. At the start of the static test, the increasing load will first compress the upper part of the pile, with part of the load passing down and the other part becoming lateral friction. With increasing load, the compressed upper part of the pile will have a relative displacement, while the lateral side will receive an upward side friction. When all of the lateral frictions have reached the limit and the load is still increasing, the pile tip will bear more load; the tip settlement will also grow and even reach or surpass the allowable deformation, and the pile will be damaged.

4.2. Pile Test Results. The purposes of this indoor large-scale static test on open-ended pile include the following: (1) studying the basic mode of single-pile settlement in the sand and silty clay; (2) investigating the single-pile bearing capacity, tip resistance, operating characteristic of lateral friction, and development of pile tip displacement under the application of static load.

Figure 5 shows the curves of single pile's tip displacement in different soils for various loading conditions. It can be seen from the figure that the double-walled open-ended pile in the test has an increasing vertical displacement at the pile tip with the application of load at the pile tip increased at the same time. When the vertical displacements are the same at pile tip, the settling volume of P1 is bigger than that of P2, and the settling volume of each pile in silty clay is bigger than that in sand. In the test, the ultimate bearing capacity of P1 in silty clay is about 6 kN and that of P2 is about 8 kN, while

TABLE 1: Single-pile static test.

No.	Type	Shape	Outer diameter (mm)	Inner diameter (mm)	Length (mm)	The thickness of inner and outer walls (mm)	Test sample
1	Single pile	Double-walled open-ended	140	114	1000	3	Sand
2	Single pile	Double-walled open-ended	140	114	1000	3	Silty clay
3	Single pile	Double-walled open-ended	160	134	1000	3	Silty clay

that of P1 in sand is about 30 kN. From the aforementioned, we can see that the bearing capacity of double-walled open-ended pile in the sand is far bigger than that in the silty clay.

Figure 6 is the curves of single pile's lateral friction in different soils along with load change. As can be seen from the figure, the double-walled open-ended pile in the test has seen its lateral friction increased with the application of load at its tip increased at the same time. Applying the same load, the increment speed of lateral friction in the sand is much faster than that in the silty clay. Applying the same load at the pile tip, the lateral friction of pile in the sand is far bigger than that in the silty clay. During the process of static load application, whether in the sand or the clay, the lateral friction of the pile body increases rapidly at the early stage. With the application of the load, the rate of increase of lateral friction of the pile body gradually slows down or even decreases. The main reason is that, at the initial stage of static load application, the pile body mainly resists the deformation and settlement of the pile body through the side friction of the pile body. As the static load increases, the side friction resistance of the pile body is quickly transmitted from top to bottom until the side friction resistance is fully exerted. The static load causes a certain settlement of the pile, the relative displacement between the pile and the soil, and a thin layer of shear band at the pile-soil interface. In the sandy soil, the pile-soil interface shrinks continuously with the static load, which causes the normal stress at the interface to gradually decrease, and the shear stress decreases, which results in softening under reduced pressure. The main mechanism of the stress is that, at the initial stage of static load, the long axis and short axis of the soil particles are arranged in disorder and cross. With the increase of the static load, the settlement of the soil is increasing, the long axis direction of the soil particles is consistent with the shear direction, the soil particles are arranged more orderly, and the space area occupied by the particles is reduced. In addition, with the continuous shearing, the soil particles near the pile-soil interface appear to be very obviously broken. Large soil particles break into small soil particles. The newly broken small particles enter the gap between the large particles, and the soil near the contact surface is further compacted. Therefore, the friction between the pile and the soil is reduced, and the side friction resistance decreases. Due to continuous shear in the clay, a layer of water will gradually form between the pile and the soil, which will play a certain role in lubrication and reduce the interface friction coefficient. Therefore, the side friction resistance of the pile-soil interface will also decrease.

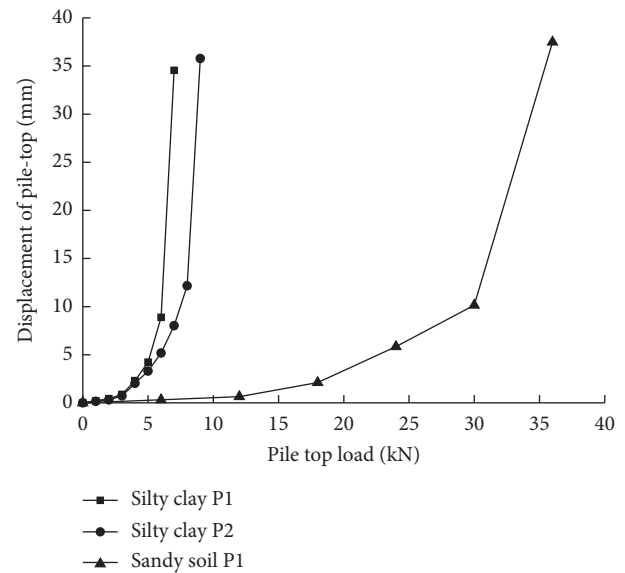


FIGURE 5: The tip displacement of pile in different soils along with load change.

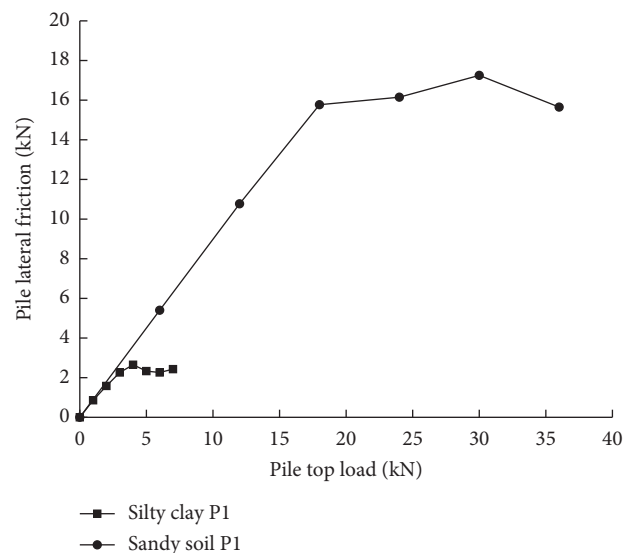


FIGURE 6: The lateral friction of pile in different soils along with load change.

Figure 7 illustrates the curves of lateral friction of single pile in different diameters along with load change. From that, we can see that the double-walled open-ended pile in

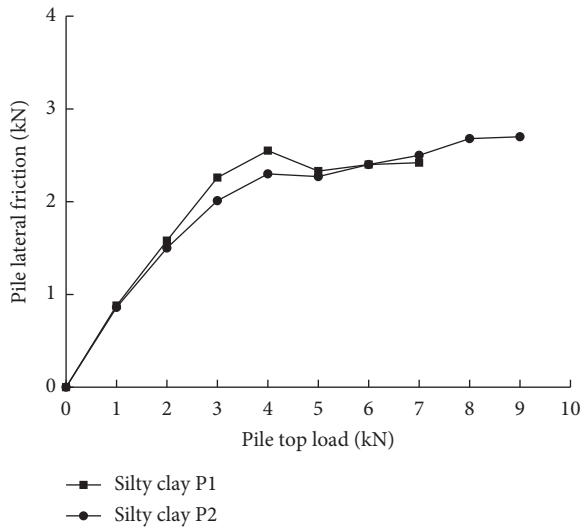


FIGURE 7: The lateral friction of pile with different diameters in soil samples along with load change.

the test has seen its lateral friction increased with the application of load at the tip increased at the same time. Applying the same load, the lateral friction of P1 is bigger than that of P2, or under the same load, the smaller the diameter of a pile, the larger the proportion of lateral friction.

Figure 8 shows the curves of tip resistance of single pile in different soils for different loading conditions. The curves show that the double-walled open-ended pile in the test has seen its tip resistance increased with the application of load at the tip increased at the same time. The increment speed of tip resistance in the silty clay is far faster than that in the sand. Applying the same load at pile tip, the tip resistance of pile in the silty clay is far bigger than that in the sand. The main reason is that the friction coefficient between the sand particles and the pile is larger than that in the clay, and the unit side friction resistance of the pile-soil interface in the sand can be exerted to a greater level than the clay. Under the same test conditions, the pile top load in sand needs to overcome the larger side friction resistance to be transmitted to the pile end, which results in a smaller increase in pile-end resistance in sand than in clay. Whether in sand or clay, the resistance at the end of the pile increases slowly at the beginning of the static load. With the application of the static load, the speed of the resistance at the end of the pile increases continuously until the increasing speed reaches stability. The main reason is that, with the load increases, the side friction resistance of the pile-soil interface gradually increases at the initial stage of static load, resulting in a relatively slow increase in pile-end resistance.

With the increase of the load, the side friction resistance of the pile body gradually reaches the maximum level. At this

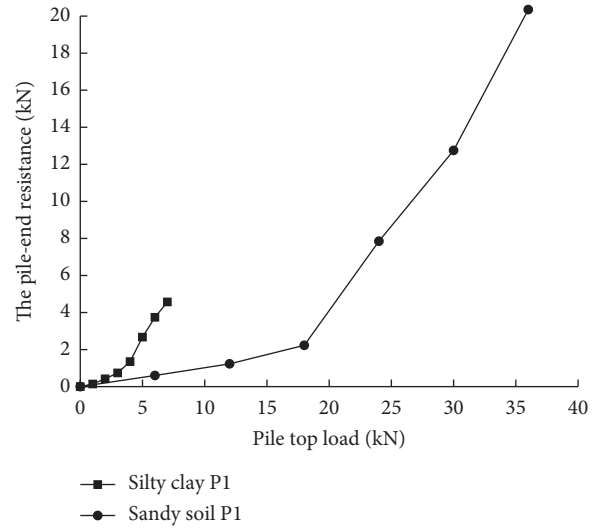


FIGURE 8: The tip resistance of pile in different soil samples along with load change.

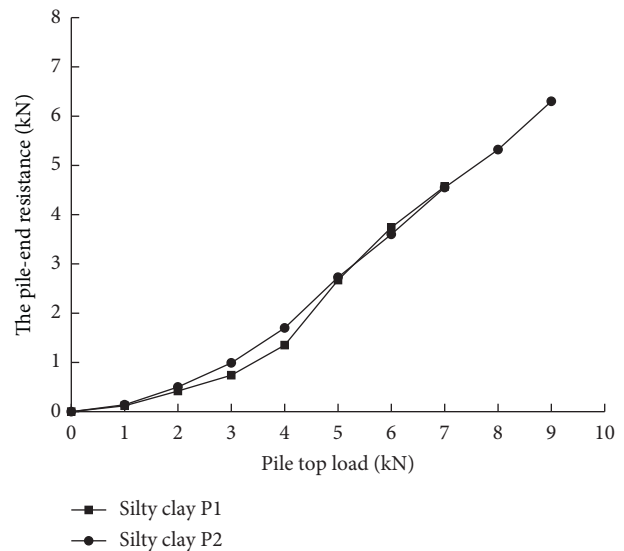


FIGURE 9: The tip resistance of piles with different diameters in various soil samples along with load change.

time, the load increases again, and the side friction resistance no longer increases, resulting in a larger increase in the pile-end resistance.

The relationship between the tip resistance of the single pile and the pile load is revealed in the curved shown in Figure 9. From the figure, we can see that the double-walled open-ended pile in the test has its tip resistance increased slowly along with increase of load application at the pile tip. With further increase of load application at pile tip, the tip resistance starts to increase quickly. Under the same load,

the tip resistance of P2 is bigger than that of P1, or under the same load, the bigger the diameter of a pile, the larger the proportion of tip resistance.

5. Conclusions

In this paper, we have studied the settlement mode of a single pile in the static load process, its bearing capacity and lateral friction, and the working properties of its tip resistance. Based on the results, the main conclusions can be drawn as follows.

- (1) With increase of tip load, the vertical displacement of pile tip is increasing. Applying the same load at pile tip, the bigger the pile diameter, the smaller the settling volume. Under the same load, the settling volume of a pile in the sand is less than that in the silty clay.
- (2) The bearing capacity of a pile in the sand is far bigger than that in the silty clay.
- (3) Applying the same load at pile tip, the less the diameter of a pile, the larger the proportion of its lateral resistance, and the bigger the diameter of a pile, the larger the proportion of its tip resistance. With the increase of load application at pile tip, the tip resistance experiences slow to quick increase.
- (4) Applying the same load at pile tip, the tip resistance of a pile in the sand is smaller than that in the silty clay. From that, we can see that, under the same load at pile tip, the lateral friction of a pile in the sand is bigger than that in the silty clay.

Data Availability

Some or all data that support the findings of this study are available from the corresponding author upon reasonable request.

Conflicts of Interest

The authors declare no conflicts of interest.

Acknowledgments

This research was funded by the National Natural Science Foundation of China (41772318).

References

- [1] W. S. Gao, G. X. Mei, T. H. Zhou et al., "Innovation and development of foundation technology," *China Civil Engineering Journal*, vol. 53, no. 6, pp. 97–121, 2020.
- [2] K. V. Terzaghi and R. B. Peck, *Theoretical Soil Mechanics*, John Wiley and Sons, New York, NY, USA, 1948.
- [3] G. G. Meyerhof, "Compaction of sands and bearing capacity of piles," *Journal of the Soil Mechanics and Foundations Division*, vol. 85, no. 6, pp. 1–29, 1959.
- [4] H. G. Poulos and N. S. Matters, "Settlement methods for pile groups and pile rafts," *Aust. Géotechnique*, vol. 47, no. 4, pp. 791–816, 1997.
- [5] H. B. Seed and L. C. Reese, "The action of soft clay along friction piles," *Transactions Proceedings*, pp. 731–754, 1957.
- [6] P. Wu, W. M. Gong, and S. T. Liang, "Study on load transfer law of overlength piles considering depth effect," *Rock and Soil Mechanics*, vol. 28, no. 12, pp. 1265–1268, 2007.
- [7] S. M. He and G. S. Lu, "Study on load transfer characteristic of rock-socketed pole," *Rock and Soil Mechanics*, vol. 28, no. 12, pp. 2598–2602, 2007.
- [8] C. S. Desai, "Numerical design-analysis for piles in sands," *Journal of the Geotechnical Engineering Division*, vol. 100, no. 6, pp. 613–635, 1974.
- [9] H. G. Poulos and E. H. Davis, *Pile Foundation Analysis and Design*, John Wiley and Sons, New York, NY, USA, 1980.
- [10] Y. Wang, X. Zhou, and X. Xu, "Numerical simulation of propagation and coalescence of flaws in rock materials under compressive loads using the extended non-ordinary state-based peridynamics," *Engineering Fracture Mechanics*, vol. 163, pp. 248–273, 2016.
- [11] Y. Wang, X. Zhou, and Y. Shou, "The modeling of crack propagation and coalescence in rocks under uniaxial compression using the novel conjugated bond-based peridynamics," *International Journal of Mechanical Sciences*, vol. 128–129, pp. 614–643, 2017.
- [12] Y. Wang, X. Zhou, Y. Wang, and Y. Shou, "A 3-D conjugated bond-pair-based peridynamic formulation for initiation and propagation of cracks in brittle solids," *International Journal of Solids and Structures*, vol. 134, pp. 89–115, 2018.
- [13] Y.-T. Wang, X.-P. Zhou, and M.-M. Kou, "Three-dimensional numerical study on the failure characteristics of intermittent fissures under compressive-shear loads," *Acta Geotechnica*, vol. 14, no. 4, pp. 1161–1193, 2019.
- [14] M. M. Kou, Y. J. Lian, and Y. T. Wang, "Numerical investigations on crack propagation and crack branching in brittle solids under dynamic loading using bond-particle model," *Engineering Fracture Mechanics*, vol. 212, pp. 41–56, 2019.
- [15] M.-M. Kou, X.-R. Liu, Z.-Q. Wang, and S.-D. Tang, "Laboratory investigations on failure, energy and permeability evolution of fissured rock-like materials under seepage pressures," *Engineering Fracture Mechanics*, vol. 247, Article ID 107694, 2021.
- [16] X. Hong and M. Yang, "A new calculation method for single pile load and settlement in layered soils," *Chinese Journal of Underground Space and Engineering*, vol. 3, pp. 431–435, 2008.
- [17] Y. G. Wang, Z. R. Mei, and J. C. Zhang, "Experimental researches on bearing characteristics of a single pile," *Chinese Journal of Geotechnical Engineering*, vol. 32, no. 1, pp. 7–11, 2010.
- [18] J. Zhou, J. J. Guo, Z. Zhang, and M. C. Jia, "Model test of single pile static load in sands and numerical simulation using particle flow code," *Rock and Soil Mechanics*, vol. 31, no. 6, pp. 1763–1768, 2010.
- [19] Y. Diao, G. Zheng, J. Xu, H. M. Ouyang, and Y. Xu, "Comparative analysis of static uplift pile load tests under different loading conditions," *Chinese Journal of Geotechnical Engineering*, vol. 33, no. S2, pp. 464–470, 2011.
- [20] X. Hong, "Theoretical simulation and factors for static loading tests on a single pile," *Chinese Journal of Geotechnical Engineering*, vol. 34, no. 1, pp. 176–183, 2012.
- [21] Q. Gao, M. Y. Zhang, and X. Y. Bai, "Analysis of static load test of PHC piles in Jiaozhou Bay reclamation area," *Engineering Construction*, vol. 48, no. 1, pp. 58–78, 2016.
- [22] K. Huang and M. Y. Zhang, "Analysis of static load test of rock-socketed driven piles in a certain area of Qingdao," *Engineering Construction*, vol. 49, no. 3, pp. 62–66, 2017.

- [23] S. L. Huo, H. Y. Deng, Q. Y. Yu, and M. X. Zhu, "Field test study on vertical bearing behavior of rock-socketed piles," *Building Structure*, vol. 50, no. S2, pp. 690–695, 2020.
- [24] Technical Code for Building Pile Foundation (JGJ94—2008), Construction Science and Technology, 2012(Z1):38-39, JGJ94-94.

Research Article

Chloride Ion Corrosion Pattern and Mathematical Model for C60 High-Strength Concrete after Freeze-Thawing Cycles

Yan Li,¹ Bing Li ,¹ Lian-ying Zhang ,¹ Chao Ma ,¹ Jiong Zhu ,¹ Ming Li ,²
and Hai Pu ²

¹School of Civil Engineering, Xuzhou Institute of Technology, Xuzhou 221008, Jiangsu, China

²State Key Laboratory of Geomechanics and Deep Underground Engineering, China University of Mining & Technology, Xuzhou 221008, Jiangsu, China

Correspondence should be addressed to Bing Li; libing_libing_2007@163.com

Received 20 February 2021; Revised 22 March 2021; Accepted 27 March 2021; Published 8 April 2021

Academic Editor: Chunyang Zhang

Copyright © 2021 Yan Li et al. This is an open access article distributed under the Creative Commons Attribution License, which permits unrestricted use, distribution, and reproduction in any medium, provided the original work is properly cited.

In this study, the porosities of C60 high-strength concrete after 0, 30, 60, and 90 freeze-thaw cycles determined via the water retention method are 1.30%, 3.65%, 5.14%, and 7.34%, respectively. Furthermore, a mathematical model of porosity varying with the number of freeze-thaw cycles is established. Using an artificial environment simulation experimental system and the natural diffusion method, the chloride diffusion law of C60 high-strength concrete after 0, 30, 60, and 90 freeze-thaw cycles is obtained. The corresponding diffusion coefficients are calculated based on the experimental results and Fick's law, where 0.3431×10^{-12} , 0.5288×10^{-12} , and 0.6712×10^{-12} , and 0.8930×10^{-12} m²/s are obtained, respectively, and a mathematical model of diffusion coefficient with freeze-thawing is established. Transport control equations comprising solution flow and solute migration control equations are established for chloride ions in concrete after freeze-thawing cycles. The equations consider the effects of freeze-thawing, solution pressure, solution concentration, solution density, convection, mechanical dispersion, and chemisorption on chloride ion transport in concrete. Using COMSOL numerical software, the transport control equations for chloride ions are solved using a real concrete numerical model, and the chloride ion corrosion process in concrete after freeze-thaw cycles is simulated. The simulation results are consistent with the experimental values.

1. Introduction

With the continuous increase in energy demand, mineral resources extraction has gradually shifted to deeper strata, and the development depth of vertical shafts has increased consequently, along with the increase in the cross-sectional size of the shaft [1–12]. For the development of deep and thick unstable aquifer mines, the artificial ground freezing method is widely used [13–15]. When constructing using the freezing method, the freezing shaft lining is crucial, and its main function is to block groundwater and withstand the temporary load to ensure the safety and smooth operation of shaft sinking construction [16–19]. The structural forms of freezing shaft lining primarily include single-layer reinforced concrete, double-layer reinforced concrete, and reinforced concrete composite shaft lining. Currently, concrete materials are essential in the construction of all

freezing shaft lining. With the increase in mining depth, high-strength and high-performance concrete materials such as C60 and C70 have been used for freezing shaft lining, and many scholars have conducted relevant studies [20–24].

As the freezing shaft lining is generally cast on site, pouring concrete will produce a large amount of heat of hydration, and the heat of hydration will contribute to part of the freezing lining temperature. After the heat of hydration dissipates, the freezing lining will refreeze, and the temperature will decrease; therefore, the freezing shaft lining will be in a freeze-thaw environment with a changing temperature field, posing a significant challenge to the strength and stability of the freezing lining. Hence, many scholars have investigated the effect of temperature on the rupture of vertical shaft lining [20–32]. Reinforced concrete structures for freezing shaft lining not only are affected by temperature and stress fields but also are susceptible to the

corrosive effects of the subsurface environment. For example, sulfate has a certain corrosive and destructive effect on concrete materials, and the intrusion of chloride ions accelerates the rusting of reinforcing steel bars, thereby affecting the stability of the structure; this is closely associated with the durability problem of concrete structures and materials [33–37].

By understanding the corrosion law of chloride ions in C60 high-strength concrete after freeze-thawing, we aim to establish control equations for chloride ion transport in concrete considering freeze-thawing, solution pressure, solution concentration, solution density, convection, mechanical dispersion, and chemisorption and verify them by numerical calculations to provide some theoretical basis for the design, construction, and safe use evaluation of freezing shaft lining.

2. Porosity of Concrete after Freeze-Thawing Cycles

2.1. Materials and Mix Proportions. They are cement: 42.5 grade ordinary silicate cement supplied by Xuzhou Zhonglian Cement Plant, the composition of which is shown in Table 1; fine aggregate: river sand with a fineness modulus of 2.8, good gradation, apparent density of 2679 kg/m³, and silt content of 2.49%; and coarse aggregate: stone, particle size of 5–20 mm, apparent density of 2719 kg/m³, and silt content of 0.54%. The mix proportions of concrete were 453 kg/m³ cement, 740 kg/m³ sand, 1112 kg/m³ stone, and 145 kg/m³ water; the water-cement ratio was 0.32. The compressive strength of the sample was 57.0 MPa after 28 d of standard curing.

2.2. Test Procedure. The test procedure, as shown in Figure 1, is as follows.

Three cylindrical concrete samples of diameter d 100 mm and height h 50 mm (standard curing for 28 d) were used. Their actual height was measured, and then they were subjected to 0, 30, 60, and 90 freeze-thaw cycles (based on the GBT50082-2009 standard, China, shown in Figure 1(a)) and porosity tests (shown in Figures 1(a)–1(d)).

The porosity test was performed using the water saturation method. The freeze-thaw treated samples were first dried at 40°C for 48 h (shown in Figure 1(b)) and then weighed using an electronic balance, placed in a water tank with a 16 mm diameter PVC pipe underneath, and filled with room-temperature water such that the water surface was 4–5 mm above the bottom of the sample (shown in Figure 1(c)). The samples were removed at 5, 10, 30, 60, 120, 720, and 1440 min, respectively, and then weighed (shown in Figure 1(d)) and placed back immediately until all intervals were completed. Finally, the samples were completely submerged, and their water-saturated mass was measured after another 48 h.

2.3. Porosity. Porosity ϕ is calculated using the following equation:

$$\phi = \frac{V_{ws}}{V_{cs}}, \quad (1)$$

where ϕ is the porosity, V_{ws} is the volume of water in the sample when saturated, and V_{cs} is the actual volume of the sample.

V_{ws} and V_{cs} are calculated using the two following equations, respectively:

$$V_{ws} = \frac{m_{ws}}{\rho_w}, \quad (2)$$

$$V_{cs} = \frac{1}{4} \pi d^2 h_c. \quad (3)$$

In equation (2), m_{ws} is the mass of water in the sample when saturated, and ρ_w is the density of water; in equation (3), the diameter of the sample $d = 100$ mm, and h_c is the actual height of the sample.

m_{ws} is calculated using the following equation:

$$w = \frac{m_1 - m_0}{m_0}, \quad (4)$$

where m_1 is the mass of the concrete sample when saturated and m_0 is the initial mass of the concrete sample after drying.

The porosity of concrete after 0, 30, 60, and 90 freeze-thaw cycles was calculated to be 1.30%, 3.65%, 5.14%, and 7.34%, respectively, and a model of porosity ϕ_n varying with the number of freeze-thaw cycles n was obtained, as shown in the following equation:

$$\phi_n = \phi_0 \eta e^{(\theta n)}, \quad (5)$$

where ϕ_n is the porosity of concrete after freeze-thawing; ϕ_0 is the initial porosity of concrete before freeze-thawing; η and θ are the material parameters, set at 1.61459 and 0.0143, respectively; n is the number of freeze-thaw cycles. The experimental values were compared with the calculated values, as shown in Figure 2.

3. Corrosion Pattern of Chloride Ions in Concrete after Freeze-Thawing Cycles

3.1. Test Methodology. The sample measured 100 mm × 100 mm × 400 mm; the materials and mix proportions are shown in Section 2.1, and the test procedure is shown in Figure 3. In the test, four groups (three samples in each group) were formed and treated with 0, 30, 60, and 90 freeze-thaw cycles, respectively (based on GBT50082-2009, shown in Figure 3(a)); subsequently, a 100 mm × 400 mm rectangular surface of each sample was used as the corrosive surface, and the other surfaces were sealed with epoxy resin (shown in Figure 3(b)). The sealed samples were placed into an artificial marine climate simulation laboratory for salt spray corrosion test (shown in Figure 3(c)), and the humidity in the environmental chamber was controlled at 75%–80%. The salt spray corrosion settings were as follows: salt spray “on” for 12 h/d (hour/day) + salt spray “off” for 12 h/d and NaCl mass concentration of 5% in the salt spray solution. When the corrosion time reached 30, 110, 190, and 270 d, the samples were removed, concrete powder was obtained by drilling to depths of 5, 10, 15, 20, 25, 30, 35, and 40 mm, respectively (shown in Figure 3(d)), and the chloride ion concentration values were measured using a DY-2501A chloride ion

TABLE 1: Composition of cement.

Materials	SiO ₂ (%)	Al ₂ O ₃ (%)	Fe ₂ O ₃ (%)	CaO (%)	MgO	Na ₂ O (%)	K ₂ O (%)	SO ₃ (%)
Cement	21.6	4.13	4.57	64.47	1.06%	0.11	0.56	1.74
Fly ash	55.6	25.8	6.90	8.70	1.80%	0.30	0.10	0.60

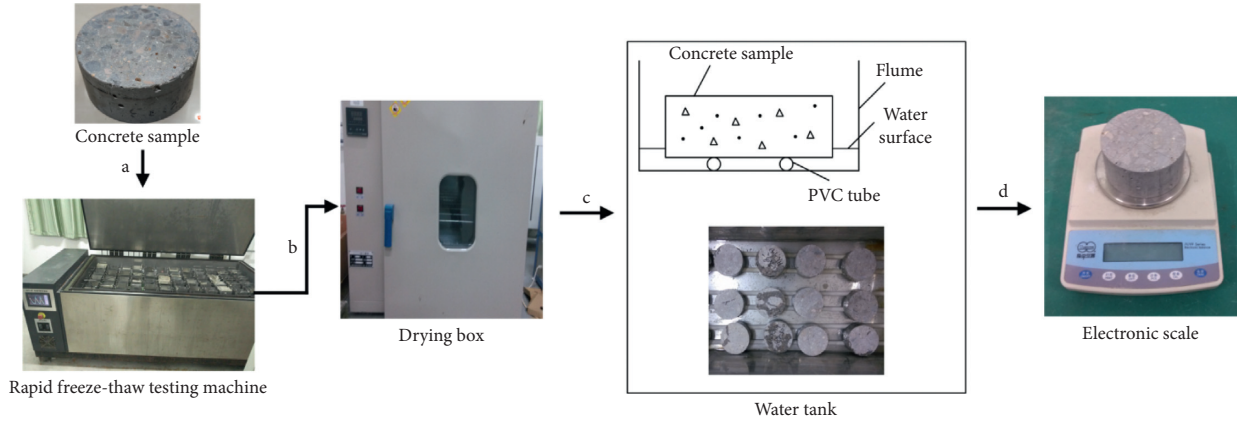


FIGURE 1: Schematic diagram of test procedure to determine water absorption performance.

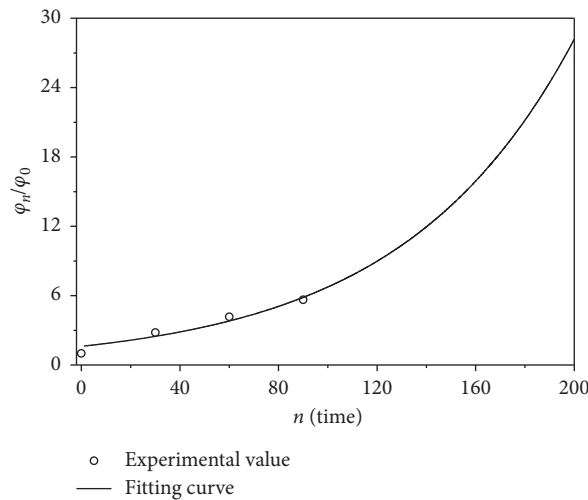


FIGURE 2: Porosity ratio (ϕ_n/ϕ_0) varying with number of freeze-thaw cycles (n).

concentration rapid tester (shown in Figure 3(e)). After each drilling of powder, the borehole was sealed with a sealant. Subsequently, the samples were placed back into the artificial marine climate simulation laboratory and continued to be corroded until the next testing time point (shown in Figure 3(f)), that is, until the end of 270 d of corrosion.

3.2. Chlorine Ion Concentration. Figures 4(a)–4(d) present the variation patterns of chloride ion concentration value c with depth l after 30, 110, 190, and 270 d of chloride ion corrosion, respectively, the analysis of which shows that c of the samples decreased with increasing l . In this experiment, the salt spray cycle corrosion mechanism was used, and the driving force for chloride ion intrusion into concrete was primarily provided by capillary action and concentration

gradient. The chloride ion concentration gradient in the surface layer of concrete was relatively large, whereas the chloride ion concentration gradient in the deep layer was relatively small; hence, more chloride ions were accumulated in the surface layer of concrete. As the corrosion time progressed, the total chloride ion corrosion and corrosion depth increased. As the number of freeze-thaw cycles increased, the porosity of the concrete increased, the water and air permeability of the samples increased, chloride ions were more easily accessible and stored, and the corrosion concentration of chloride ions increased (at the same depth).

3.3. Chloride Ion Diffusion Coefficient. Fick’s second law was used to describe the corrosion pattern of chloride ions in concrete, as shown in the following equation:

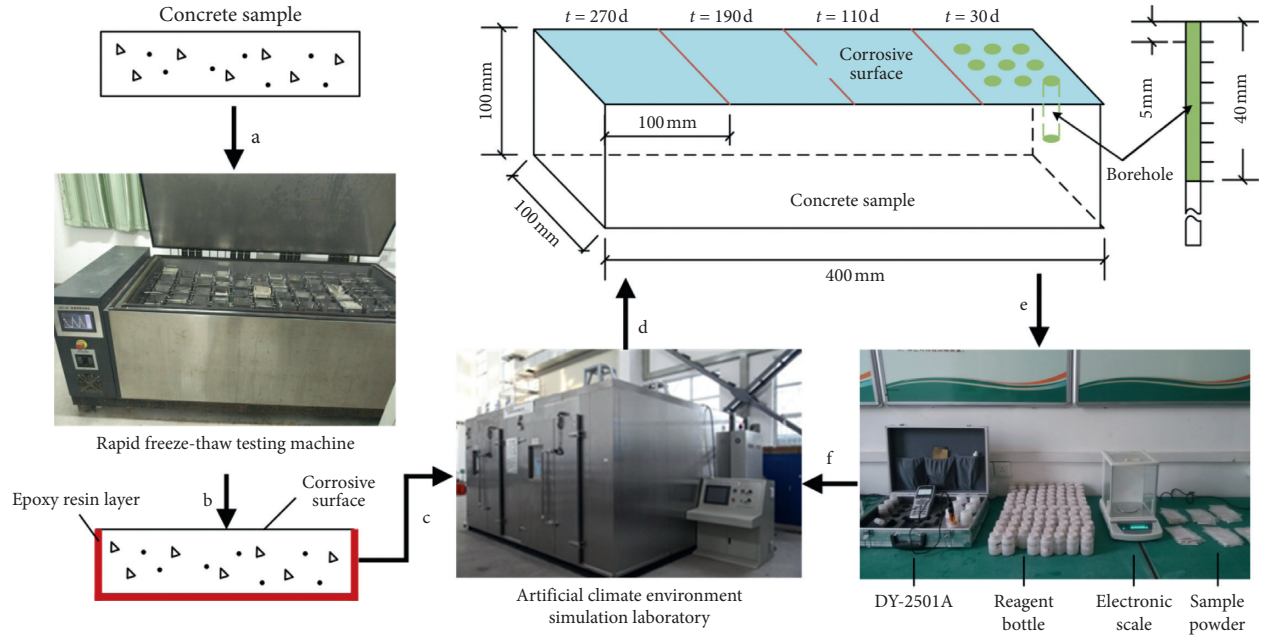


FIGURE 3: Flow chart of concrete chloride ion corrosion test.

$$C(l, t) = C_0 + (C_s - C_0) \left(1 - \operatorname{erf} \frac{l}{2\sqrt{Dt}} \right). \quad (6)$$

C_0 is the initial chloride ion mass concentration at any section of concrete, C_s is the chloride ion mass concentration at the concrete surface at any moment t , D is the chloride ion diffusion coefficient, t is the time, l is the distance from the concrete surface, and erf is the error function.

The inverse solution of equation (6) yields the equation for the chloride ion diffusion coefficient as follows:

$$D = \frac{1}{t} \left\{ \frac{l}{2 \operatorname{erf}^{-1} [1 - (C(l, t) - C_0) / (C_s - C_0)]} \right\}^2. \quad (7)$$

The mass concentration of chloride ions on the concrete surface C_s is calculated as follows:

$$c_s = \frac{\phi \rho_{cw} \omega}{\rho_s + \phi \rho_{cw} \omega} \times \frac{35.5}{58.5} \times 100\%, \quad (8)$$

where ϕ is the porosity of concrete; ρ_w is the density of sodium chloride solution, that is, 1034 kg/m^3 ; ρ_s is the density of concrete, that is, 2400 kg/m^3 ; ω is the mass concentration of sodium chloride in the solution, that is, 5%.

Based on equations (7) and (8), the chloride ion diffusion coefficient D at $l = 5 \text{ mm}$ was calculated using MATLAB, and the results are shown in Table 2.

A mathematical model correlating the chloride ion diffusion coefficient D_n with the number of freeze-thaw cycles n was developed, as shown in the following equation:

$$D_n = D_0 \zeta e^{(\psi n)}, \quad (9)$$

where D_n is the diffusion coefficient of concrete after freeze-thawing; D_0 is the diffusion coefficient of concrete before freeze-thawing; ζ and ψ are the material parameters, which were set to 1.02151 and 0.00916, respectively; n is the number

of freeze-thaw cycles. The experimental and calculated values were compared, as shown in Figure 5.

4. Control Equations for Chloride Ion Transport in Concrete after Freeze-Thawing Cycles

4.1. Basic Hypotheses. To derive the control equations for chloride ion transport in freeze-thaw corroded concrete, the following hypotheses are proposed: the liquid in concrete is an ideal liquid; the effect of temperature on liquid flow is not considered; and only a single solute (chloride ion) is considered. The transport of chloride ions in concrete can be classified into two main processes: solution flow and solute migration, in which the effects of freeze-thawing on both primarily affect the porosity and diffusion coefficient.

4.2. Control Equation for Solution Flow

4.2.1. Mass Continuity Equation.

$$\frac{\partial(\rho\phi)}{\partial t} + \nabla \cdot (\rho \vec{v}) = 0, \quad (10)$$

where ρ is the density of the solution, ϕ is the porosity, t is the time, $\vec{v} = (v_x, v_y, v_z)^T$, and $\nabla = ((\partial/\partial x), (\partial/\partial y), (\partial/\partial z))$.

4.2.2. Porosity. Introducing the parameter ξ , pore deformation due to pore pressure changes can be characterized.

$$\xi = \frac{1}{U_w} \frac{dU_w}{dP}, \quad (11)$$

where U_w denotes the pore volume.

The volume of each component phase of the porous medium is expressed as follows:

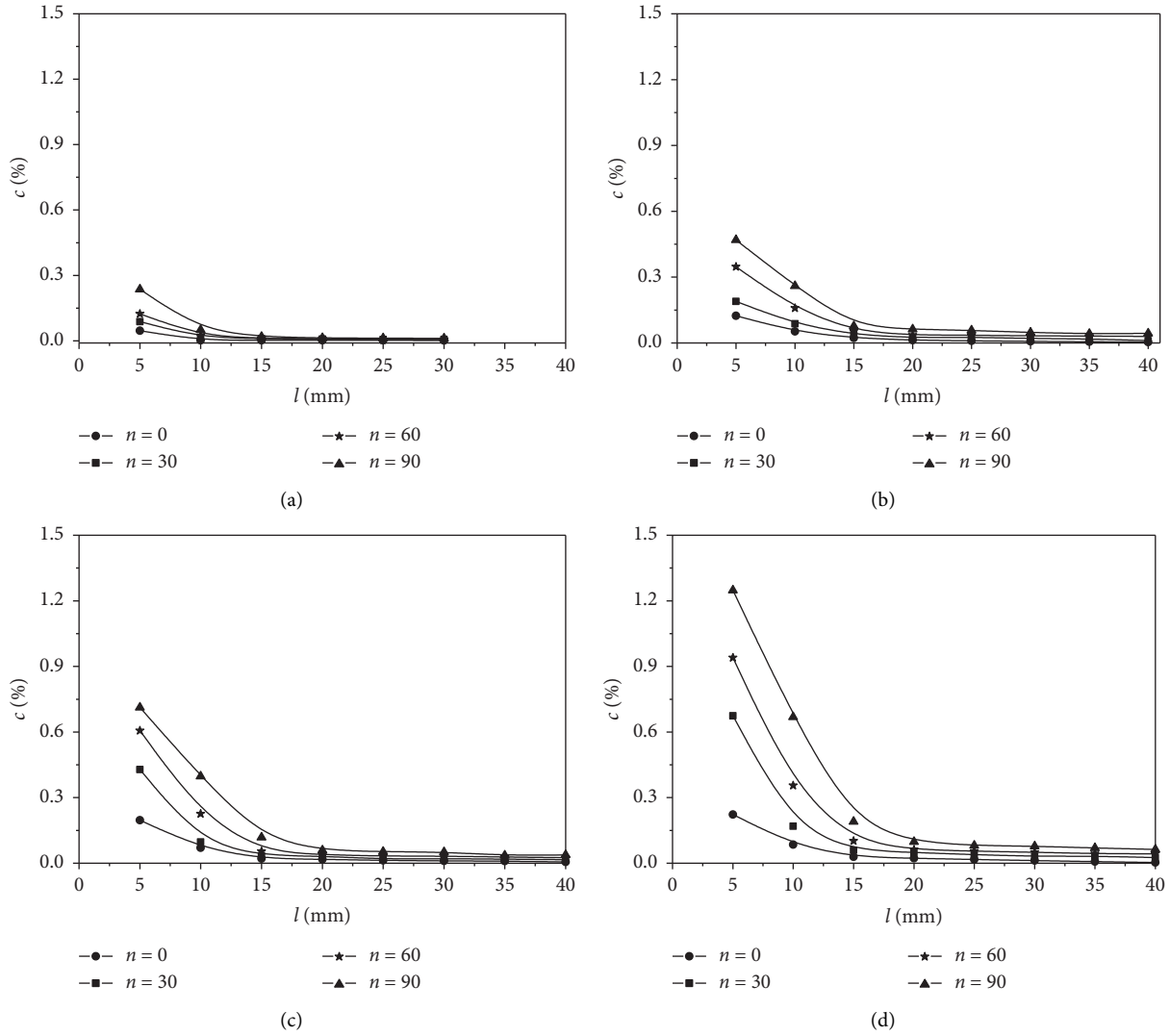


FIGURE 4: Variation pattern of concrete chloride ion concentration (c) with depth (l) after freeze-thawing. (a) $t = 30$ d. (b) $t = 110$ d. (c) $t = 190$ d. (d) $t = 270$ d.

TABLE 2: Chloride ion diffusion coefficient D .

Number of freeze-thaw cycles n /cycle	Chloride ion diffusion coefficient $D/(\times 10^{-12} \text{ m}^2/\text{s})$				Mean value ($\times 10^{-12} \text{ m}^2/\text{s}$)
	$t = 30$ d	$t = 110$ d	$t = 190$ d	$t = 270$ d	
0	0.8230	0.3162	0.2247	0.1683	0.3831
30	1.0160	0.3812	0.3545	0.3636	0.5288
40	1.1580	0.5320	0.4680	0.5267	0.6712
90	1.5610	0.6552	0.5455	0.8102	0.8930

$$U = \frac{1}{\phi} U_w = U_w + U_s, \quad (12)$$

where U is the total volume of the porous medium, U_s is the volume of the solid skeleton of the porous medium, and ϕ is the porosity of the porous medium. Based on the above hypothesis that the solid particles do not undergo deformation, U_s is a constant; that is, $dU_s = 0$.

Subsequently, equation (12) was used to obtain a model of porosity varying with pore pressure as follows:

$$\phi = \frac{f(P)}{1 + f(P)}, \quad (13)$$

where $f(P) = (\phi_{n0}/1 + \phi_{n0})e^{\xi(P-P_0)}$ and ϕ_{n0} is as shown in equation (5).

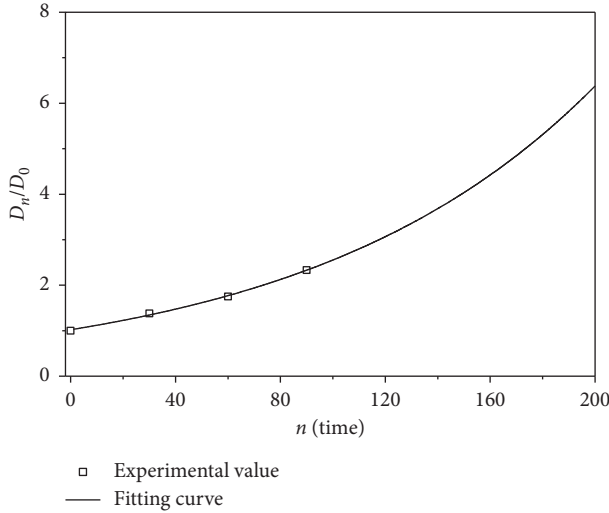


FIGURE 5: Variation curve of diffusion coefficient ratio $D_n/(D)$ 0 with respect to number of freeze-thaw cycles (n).

4.2.3. Solution Flow Rate. It is assumed that the solution flow in the porous medium conforms to Darcy's law and that the effect of gravity is not considered.

$$\vec{v} = -\frac{k}{\mu}\nabla P, \quad (14)$$

where k is the permeability of the solution and μ is the dynamic viscosity of the solution.

The relationship between permeability and porosity is described using the Kotyakhov [38] model, as shown in the following equation:

$$k = \frac{d^2 \phi^3}{72(1-\phi)^2}, \quad (15)$$

where d is the effective diameter of the porous medium particles. Based on equation (15), the following can be derived:

$$\frac{k}{k_0} = \left(\frac{\phi}{\phi_0}\right)^3 \left(\frac{1-\phi_n}{1-\phi}\right)^2, \quad (16)$$

where k_0 is the initial permeability of the solution. Because $1-\phi_n \approx 1$ and $1-\phi \approx 1$, equation (16) can be simplified as follows:

$$\frac{k}{k_0} = \left(\frac{\phi}{\phi_0}\right)^3. \quad (17)$$

Therefore, based on equations (13) and (17), the solution velocity can be expressed as

$$\vec{v} = -\frac{1}{\mu} \frac{k_0}{\phi_n^3} \left[\frac{f(P)}{1-f(P)} \right]^3 \nabla P. \quad (18)$$

4.2.4. Solution Density. As chloride ions are transported through concrete, the pore pressure and solution concentration change, resulting in changes in the solution density.

Hence, the density of solution ρ is a function of the pore pressure P and concentration c ; that is,

$$\rho = \rho(P, c). \quad (19)$$

Taking the derivative of both sides of equation (19) yields

$$d\rho = \frac{\partial \rho}{\partial P} dP + \frac{\partial \rho}{\partial c} dc. \quad (20)$$

To effectively characterize the density as a function of pore pressure and solution concentration, two parameters β_P and β_c were introduced, which are the pressure compression coefficient and concentration compression coefficient, respectively.

$$\beta_P = \frac{1}{\rho} \frac{d\rho}{dP}, \quad (21)$$

$$\beta_c = \frac{1}{\rho} \frac{d\rho}{dc}.$$

Parameters β_P and β_c represent the ratio of the change in density due to a unit change in pressure to the initial density and the ratio of the change in density due to a unit change in concentration to the initial density, respectively.

Substituting equation (21) into equation (20) yields

$$d\rho = \rho(\beta_P dP + \beta_c dc). \quad (22)$$

Integrating both sides of equation (22) yields

$$\rho = \rho_0 e^{[\beta_P(P-P_0) + \beta_c(c-c_0)]}, \quad (23)$$

where ρ_0 denotes the initial density, P_0 denotes the initial pore pressure, and C_0 denotes the initial concentration.

4.2.5. Control Equation for Solution Flow. Using equations (10), (13), (18), and (23), the flow control equation for chloride ion solution in concrete porous medium was obtained as follows:

$$\left[\rho\phi\beta_P + \frac{\rho\xi\phi}{1+f(P)} \right] \frac{\partial P}{\partial t} + \rho\phi\beta_c \frac{\partial c}{\partial t} + \nabla \cdot \left(-\rho \frac{k}{u} \nabla P \right) = 0. \quad (24)$$

4.3. Control Equation for Solute Migration. Chloride migration in concrete is governed by convection, molecular diffusion, mechanical dispersion, precipitation dissolution, complexation, and chemisorption. However, only the effects of convection, mechanical dispersion, and chemisorption on chloride migration were considered in this study.

4.3.1. Convective Effects. The convective migration of chloride ions is described by convective flux, as shown in the following equation:

$$\vec{J}_v = \vec{u}c, \quad (25)$$

where $\vec{J}_v = (J_{vx}, J_{vy}, J_{vz})^T$ is the convective flow vector; $\vec{u} = (v_x, v_y, v_z)^T$ is the solution flow velocity vector.

4.3.2. *Mechanical Dispersion.* The mechanical dispersion migration flux of chloride ions is expressed by Fick's first law, as shown in the following equation:

$$\vec{J}_d = -\phi[D_d]\nabla c, \quad (26)$$

where $\vec{J}_d = (J_{dx}, J_{dy}, J_{dz})^T$ is the dispersion flux vector; $D_d = (D_{dx}, D_{dy}, D_{dz})^T$ represents the mechanical dispersion coefficients in the x-, y-, and z-directions, respectively. If we assume that the porous medium is isotropic, then $D_d = D_{dx} = D_{dy} = D_{dz}$ and $J_d = J_{dx} = J_{dy} = J_{dz}$; therefore, $\vec{J}_d = -\phi D_d \nabla c$.

4.3.3. *Chemisorption.* The Langmuir adsorption theory was used to describe the chemisorption of chloride ions in concrete transport, as shown in the following equation:

$$(1 - \phi)\rho_s c_k = (1 - \phi)\rho_s K_L \frac{C_{\max} c}{1 + K_L c}, \quad (27)$$

where ρ_s is the dry density of the skeleton material, c_k is the isothermal adsorption concentration, K_L is the Langmuir isothermal nonlinear adsorption partition coefficient, and C_{\max} is the maximum adsorption capacity.

4.3.4. *Control Equation for Solute Migration.*

$$\frac{\partial(\phi c)}{\partial t} - \nabla \cdot (\phi[D] \cdot \nabla c) + \nabla \cdot (\vec{v}c) = 0. \quad (28)$$

Equation (28) is the chloride ion convection-diffusion equation, where $[D]$ denotes the chloride ion diffusion coefficient tensor. It is assumed that the diffusion coefficient is uniform everywhere in the concrete; therefore, the diffusion coefficient can be expressed as shown in equation (9). Considering adsorption, the mass of chloride ions in the representative elementary volume is expressed as $\phi c - (1 - \phi)\rho_s K_L (C_{\max} c / (1 + K_L c))$, and the convection-diffusion equation for chloride ions in concrete considering adsorption can be obtained by replacing ϕc in equation (28) with the above equation; that is,

$$\begin{aligned} & \left[c + \rho_s K_L \frac{C_{\max} c}{1 + K_L c} \right] \frac{\partial \phi}{\partial t} + \left[\phi + (\phi - 1)\rho_s K_L \frac{C_{\max}}{(1 + K_L c)^2} \right] \frac{\partial c}{\partial t} \\ & - \nabla \cdot (\phi D \cdot \nabla c) + \nabla \cdot (\vec{v}c) = 0. \end{aligned} \quad (29)$$

Substituting equation (13) into equation (29) yields the convection-diffusion equation for chloride ions expressed in terms of pressure P and concentration c , as in the following equation:

$$\begin{aligned} & \left[\xi \left(c + \rho_s K_L \frac{C_{\max} c}{1 + K_L c} \right) \frac{\phi}{1 + f(P)} \right] \frac{\partial P}{\partial t} \\ & + \left[\phi + (\phi - 1)\rho_s K_L \frac{C_{\max}}{(1 + K_L c)^2} \right] \frac{\partial c}{\partial t} \\ & - \nabla \cdot (\phi D \cdot \nabla c) + \nabla \cdot (\vec{v}c) = 0. \end{aligned} \quad (30)$$

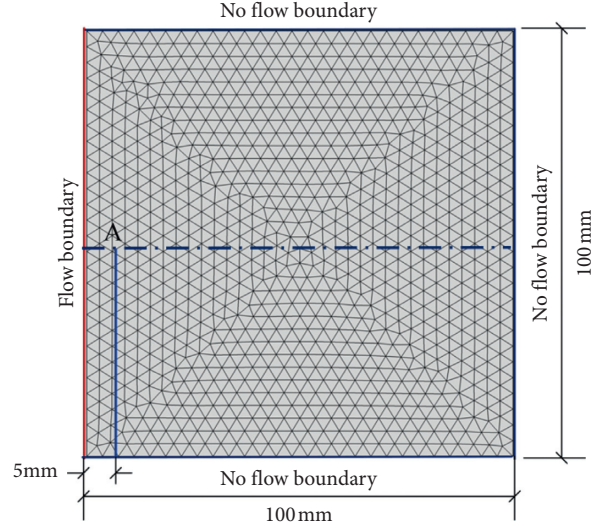


FIGURE 6: Numerical calculation model.

4.4. *Control Equations for Chloride Ion Transport in Concrete.*

The control equations for chloride ion transport in concrete considering the freeze-thaw action comprise two parts, that is, the solution flow control equation and the solute migration control equation, as shown in 31a and 31b, respectively, which contain the effects of convection, diffusion, and chemisorption, reflecting the coupling between the seepage and solute migration fields, where ϕ and D are shown in equations (13) and (9), respectively.

$$\left[\rho \phi \beta_p + \frac{\rho \xi \phi}{1 + f(P)} \right] \frac{\partial P}{\partial t} + \rho \phi \beta_c \frac{\partial c}{\partial t} + \nabla \cdot \left(-\rho \frac{k}{u} \nabla P \right) = 0, \quad (31a)$$

$$\begin{aligned} & \left[\xi \left(c + \rho_s K_L \frac{C_{\max} c}{1 + K_L c} \right) \frac{\phi}{1 + f(P)} \right] \frac{\partial P}{\partial t} \\ & + \left[\phi + (\phi - 1)\rho_s K_L \frac{C_{\max}}{(1 + K_L c)^2} \right] \frac{\partial c}{\partial t} \\ & - \nabla \cdot (\phi D \nabla c) + \nabla \cdot (\vec{v}c) = 0. \end{aligned} \quad (31b)$$

The initial and boundary conditions are solved as follows.

The solution flow and solute migration can be described using the Dirichlet and Neumann boundary conditions as follows:

$$p = \tilde{p}(t), \quad \vec{n} \cdot \frac{k}{\mu} \nabla p = \tilde{Q}(t), \quad (32)$$

$$c = \tilde{c}(t), \quad \vec{n} \cdot D \nabla c = F(t),$$

where $\tilde{p}(t)$ and $\tilde{Q}(t)$ are the fluid pressure and fluid flow velocity on the solution domain boundary $\partial\Omega$; $\tilde{c}(t)$ and $F(t)$ are the chloride ion concentration and chloride ion diffusion flux on the solution domain boundary $\partial\Omega$, respectively. The initial conditions for fluid flow and chloride ion diffusion can be expressed as

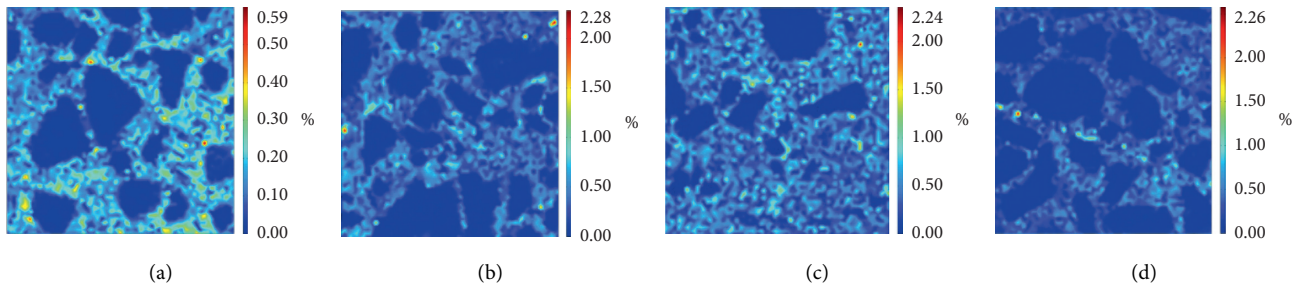


FIGURE 7: Cloud plots of initial porosity distribution of concrete after freeze-thawing. (a) $(n) = 0$. (b) $(n) = 3$. (c) $(n) = 60$. (d) $(n) = 90$.

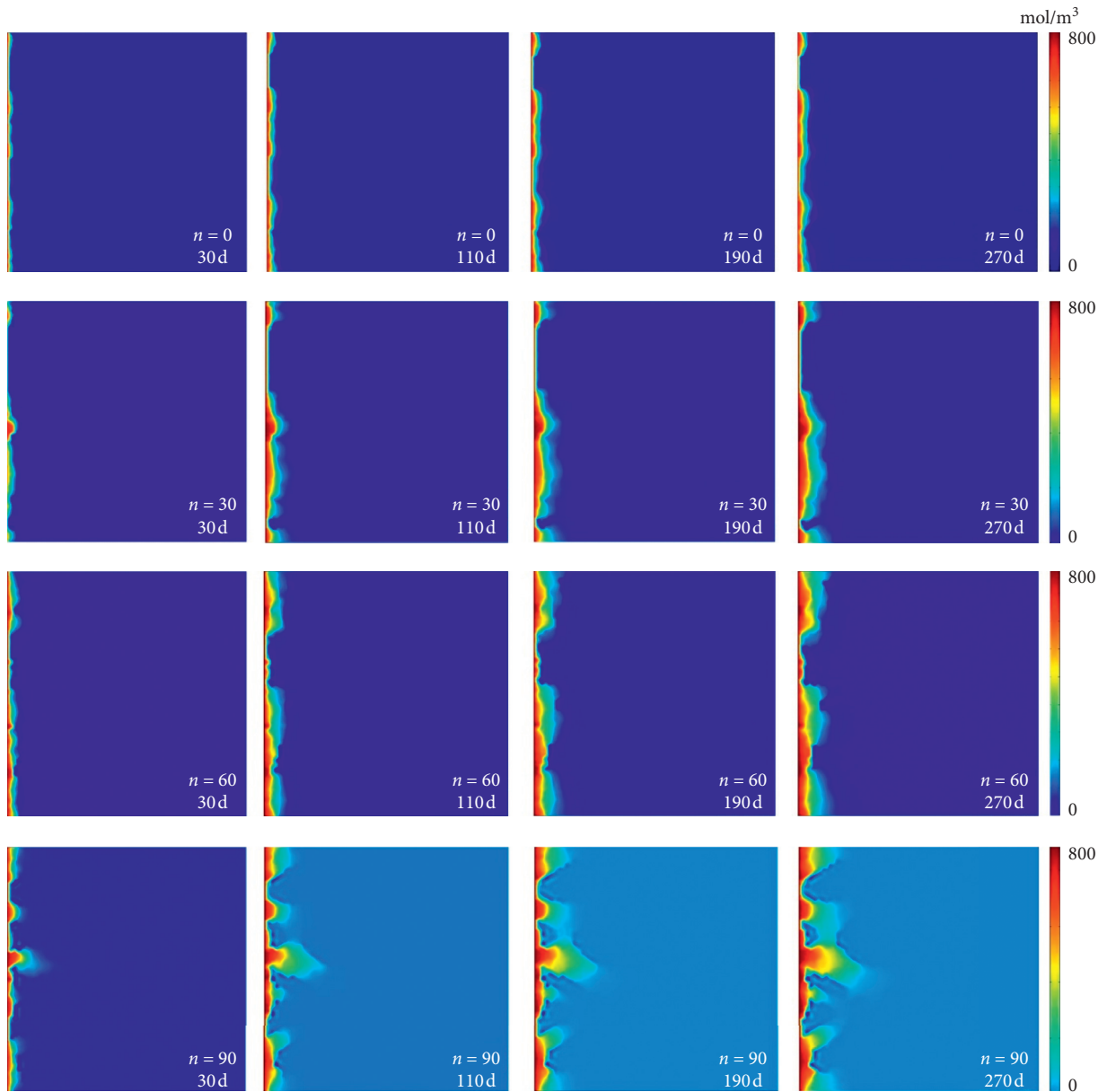


FIGURE 8: Cloud plots of chloride ion corrosion concentration distribution of concrete after freeze-thawing.

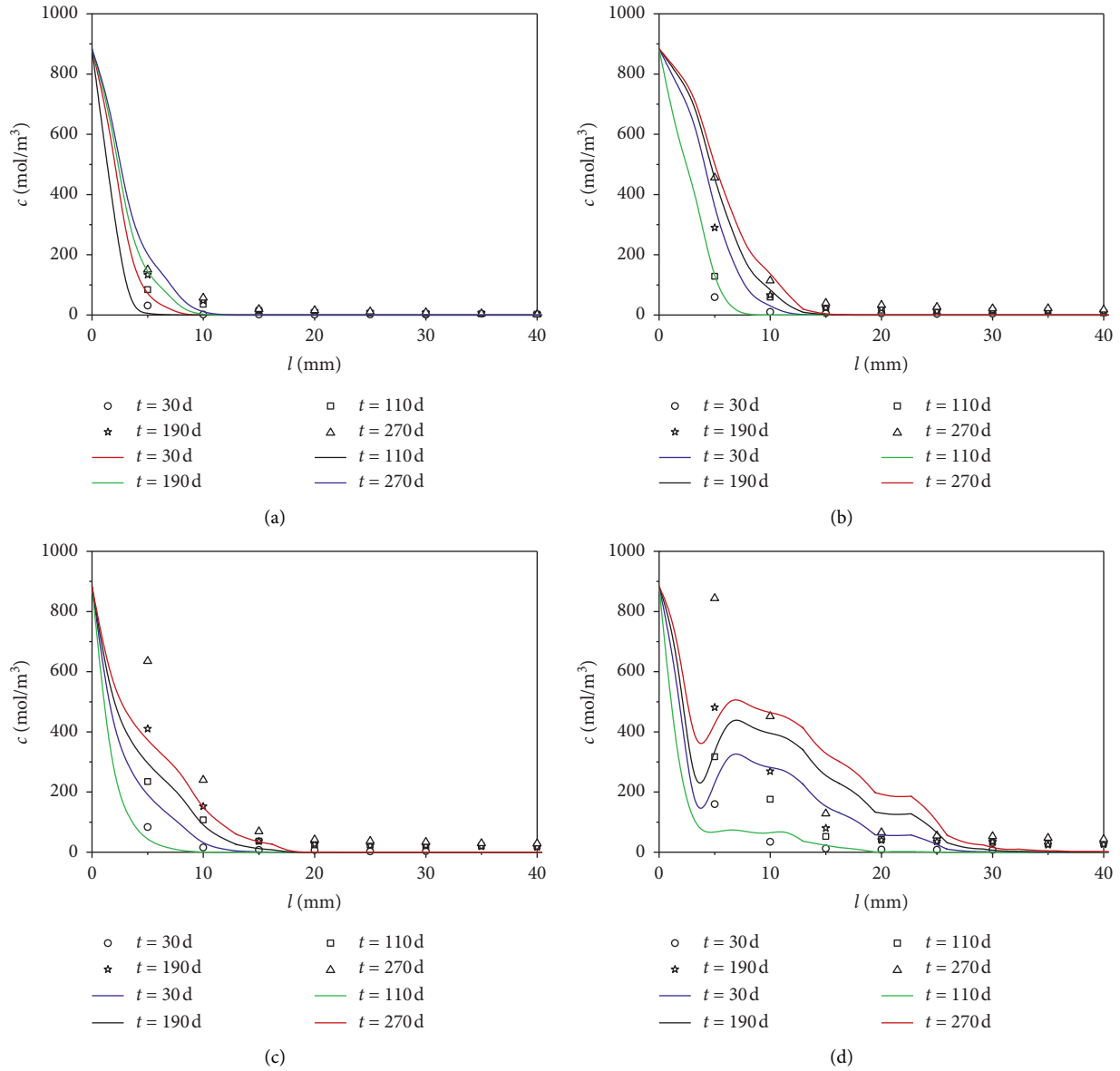


FIGURE 9: Numerically calculated curves of chloride ion concentration c with depth l compared with experimental values. (a) $n = 0$. (b) $n = 30$. (c) $n = 60$. (d) $n = 90$.

$$P(0) = P_0, c(0) = c_0, \tag{33}$$

where P_0 and c_0 are the initial fluid pressure and chloride ion concentration distribution over the solution domain Ω , respectively.

5. Model Calculation and Validation

5.1. Calculation Scheme

5.1.1. *Numerical Model.* Equations (31a) and (31b) were solved using COMSOL numerical calculation software to simulate the chloride ion corrosion in concrete after freeze-thawing. The numerical model measured 100 mm × 100 mm, the left boundary was set as the chloride ion corrosion boundary, and the other boundaries were no-flow

boundaries. Point A is a point on the midline at a distance 5 mm from the left boundary, as shown in Figure 6. To study the effect of freeze-thaw concrete chloride ion corrosion, numerical simulation scenarios involving 0, 30, 60, and 90 freeze-thaw cycles and 5% chloride salt concentration were investigated. Because of the complex coupled model and boundary conditions, the solution was complex; therefore, the model parameters were partially simplified in the calculation; for example, the porosity ϕ , solution density ρ_w , chloride ion diffusion coefficient D , and other parameters were set as constants in the calculation.

5.1.2. *Initial Pore Size Distribution.* As shown in Figure 7, the processed numerical plots can accurately reflect the pore-fissure distribution in concrete, with smaller porosity

corresponding to coarse aggregates and larger porosity corresponding to cracks. When the numbers of freeze-thaw cycles were 0, 30, and 60, no cracks were observed in the concrete; therefore, the pores were relatively dispersed, and large pores dominated the mortar, as shown in Figures 7(a)–7(c); when the number of freeze-thaw cycles was 90, wider diagonal cracks appeared in the concrete, and the distribution of cracks can be observed well, as shown in Figure 7(d).

5.2. Calculation Results and Analysis

5.2.1. Concentration Distribution. Figure 8 shows the cloud plots of the chloride ion concentration distribution after 30, 110, 190, and 270 d of chloride ion corrosion of concrete at a corrosive surface concentration of 854 mol/m^3 (5% NaCl solution) when the numbers of freeze-thaw cycles n were 0, 30, 60, and 90, respectively. As shown, the chloride ions eroded nonuniformly from the surface to the interior; with the increase in the number of freeze-thaw cycles, chloride ion corrosion accelerated significantly, primarily due to the increased porosity of the concrete. Meanwhile, the chloride ion diffusion and permeation of the concrete after 90 freeze-thaw cycles were significantly faster than those of the concrete after 60 freeze-thaw cycles, primarily due to the increased porosity of the concrete and the generation of microcracks.

5.2.2. Chloride Ion Diffusion. Figure 9 shows the numerical simulation curves of chloride ion corrosion concentration c in concrete with depth l (horizontal model midline) after different numbers of freeze-thaw cycles compared with the experimental values, where the scatter points represent the experimental values, and the curves represent the simulated value. As shown, the simulated value of chloride ion concentration with depth was not a smooth decreasing curve owing to the introduction of the real concrete numerical model. Furthermore, the results reflected the effect of the coarse aggregates, as shown in Figure 9(d). The simulated curves deviated slightly from the experimental values, particularly in the smaller numbers of freeze-thaw cycles, as shown in Figures 9(a) and 9(b).

6. Conclusion

The porosities of C60 high-strength concrete after 0, 30, 60, and 90 freeze-thaw cycles determined using the water retention method were 1.30%, 3.65%, 5.14%, and 7.34%, respectively, and a mathematical model of porosity varying with the number of freeze-thaw cycles was developed.

The chloride ion diffusion patterns of C60 high-strength concrete after 0, 30, 60, and 90 freeze-thaw cycles were obtained using an artificial environment simulation experimental system and the natural diffusion method, and the corresponding diffusion coefficients were calculated to be 0.3431×10^{-12} , 0.5288×10^{-12} , 0.6712×10^{-12} , and $0.8930 \times 10^{-12} \text{ m}^2/\text{s}$, respectively. Furthermore, a mathematical model of diffusion coefficients varying with the number of freeze-thaw cycles was developed.

Transport control equations for chloride ions in concrete after freeze-thawing comprising a solution flow control equation and a solute migration control equation were developed, in which the effects of freeze-thawing, solution pressure, solution concentration, solution density, convective action, mechanical dispersion, and chemisorption on the transport of chloride ions in concrete were considered.

The chloride ion transport control equation was solved using a real concrete numerical calculation model in COMSOL numerical software to simulate the chloride ion corrosion process after different numbers of freeze-thaw cycles, and the simulated values of chloride ion concentration agreed well with the experimental values.

Data Availability

Some or all data, models, or code generated or used during the study are available from the corresponding author upon request.

Conflicts of Interest

The authors declare that there are no conflicts of interest regarding the publication of this paper.

Acknowledgments

The authors gratefully acknowledge the financial support for this study provided by the and 51974296), research project of “333 project” in Jiangsu Province of China (BRA2019236), Natural Science Research Project of Higher Education of Jiangsu (General Programs 16KJB560017, 17KJA560004, and 18KJB560019), Research Program of Xuzhou Institute of Technology (XKY2018131), Xuzhou Key Research and Development Program (KC18090 and KC20176), and Science and Technology Project of Xuzhou City (KC18241).

References

- [1] W.-H. Yang, G.-X. Cui, G.-Q. Zhou, Y. Li, X.-D. Chen, and H.-L. Lv, “Fracture mechanism of shaft lining under special strata condition and the technique preventing the shaft from fracturing (Part One),” *Journal of China University of Mining and Technology*, vol. 25, no. 4, pp. 1–5, 1996.
- [2] L.-F. Dai and J. Tan, “Development and application of the special mine shaft sinking technology to coal mines in China,” *Coal Engineering (China)*, vol. 45, no. 12, pp. 9–12, 2013.
- [3] Q. Yu, J. Ma, H. Shimada, and T. Sasaoka, “Influence of coal extraction operation on shaft lining stability in eastern Chinese coal mines,” *Geotechnical and Geological Engineering*, vol. 32, no. 4, pp. 821–827, 2014.
- [4] Y. Chen, H. Lin, X. Ding, and S. Xie, “Scale effect of shear mechanical properties of non-penetrating horizontal rock-like joints,” *Environmental Earth Sciences*, vol. 80, p. 192, 2021.
- [5] C.-Y. Zhang, C.-Z. Pu, R.-H. Cao, T.-T. Jiang, and G. Huang, “The stability and roof-support optimization of roadways passing through unfavorable geological bodies using advanced detection and monitoring methods, among others,” *Bulletin of Engineering Geology and the Environment*, vol. 78, no. 7, pp. 5087–5099, 2019.
- [6] C.-Y. Zhang, Y.-X. Wang, H. Ruan, B. Ke, and H. Lin, “The strain characteristics and corresponding model of rock

- materials under uniaxial cyclic load/unload compression and their deformation and fatigue damage analysis,” *Archive of Applied Mechanics*, 2021.
- [7] C.-Y. Zhang, Y.-X. Wang, and T.-T. Jiang, “The propagation mechanism of an oblique straight crack in A rock sample and the effect of osmotic pressure under in-plane biaxial compression,” *Arabian Journal of Geosciences*, vol. 13, no. 15, p. 736, 2020.
 - [8] Z.-M. He, D. Xiang, Y.-X. Liu, Q.-F. Gao, and H.-B. Bian, “Deformation behavior of coarse-grained soil as an embankment filler under cyclic loading,” *Advances in Civil Engineering*, vol. 2020, Article ID 4629105, 13 pages, 2020.
 - [9] Z.-M. He, Z.-F. Li, X.-H. Liu, and H.-B. Bian, “Improved method for determining active earth pressure considering arching effect and actual slip surface,” *Journal of Central South University*, vol. 27, no. 7, pp. 2032–2042, 2020.
 - [10] R.-H. Cao, H. Lin, Q. Lin, and J. Meng, “Failure mechanism of non-persistent jointed rock-like specimens under uniaxial loading: laboratory testing,” *International Journal of Rock Mechanics and Mining Sciences*, vol. 132, Article ID 104341, 2020.
 - [11] R.-H. Cao, R.-B. Yao, T. Hu, C.-S. Wang, K.-H. Li, and J.-J. Meng, “Failure and mechanical behavior of transversely isotropic rock under compression-shear tests: laboratory testing and numerical simulation,” *Engineering Fracture Mechanics*, vol. 241, Article ID 107389, 2021.
 - [12] R.-H. Cao, C.-S. Wang, R.-B. Yao et al., “Effects of Cyclic Freeze-thaw Treatments on the Fracture Characteristics of Sandstone under Different Fracture Modes: Laboratory Testing,” *Theoretical and Applied Fracture Mechanics*, vol. 109, Article ID 102738, 2020.
 - [13] X.-S. Chen, “Time-space design theory for deep ice wall of short cylinder,” *Chinese Journal of Geotechnical Engineering*, vol. 20, no. 5, pp. 13–16, 1998.
 - [14] R.-J. Chen, G.-D. Cheng, S.-X. Li, X.-M. Guo, and L.-N. Zhu, “Development and prospect of research on application of artificial ground freezing,” *Chinese Journal of Geotechnical Engineering*, vol. 22, no. 1, pp. 40–44, 2000.
 - [15] T. Wang, F.-T. Yue, Y.-D. Jiang, and T.-Q. Zheng, “Research and practice on forced thaw Technology applied to frozen wall of mine shaft,” *Journal of China Coal Society*, vol. 35, no. 6, pp. 918–922, 2010.
 - [16] Z.-S. Yao, H. Cheng, and J.-J. Yang, “The experimental study on high strength reinforced concrete shaft lining in deep alluvium,” *Journal of China Coal Society*, vol. 29, no. 4, pp. 167–171, 2004.
 - [17] Z.-S. Yao, “An experimental study on steel fiber reinforced high strength concrete shaft lining in deep alluvium,” *Chinese Journal of Rock Mechanics and Engineering*, vol. 24, no. 7, pp. 1253–1258, 2005.
 - [18] Z.-S. Yao, H. Cheng, and C.-X. Rong, “Experimental study on composite shaft lining of inner steel plate cylinder and high strength reinforced concrete in deep frozen shaft,” *Chinese Journal of Rock Mechanics and Engineering*, vol. 27, no. 1, pp. 154–160, 2008.
 - [19] Z.-S. Yao, H. Cheng, and C.-X. Rong, “Shaft structural design and optimization of deep freezing bedrock shaft in west area,” *Journal of China Coal Society*, vol. 35, no. 5, pp. 760–764, 2010.
 - [20] B. Li, H. Yin, X. Mao et al., “Macroscopic and microscopic fracture features of concrete used in coal mine under chlorine salt erosion,” *International Journal of Mining Science and Technology*, vol. 26, no. 3, pp. 455–459, 2016.
 - [21] C. Zhang, W.-H. Yang, J.-H. Liu, Z.-C. Wei, and H.-P. Li, “Construction Technology and monitoring analysis on concrete strain of a new single-layer shaft lining in deep aqueous bed rock during freeze sinking,” *Journal of China Coal Society*, vol. 37, no. 2, pp. 192–199, 2012.
 - [22] Y.-F. Gao, K.-M. Liu, H. Xie, K.-P. Gao, B.-H. Chen, and F.-Y. Zhang, “Steel tube concrete support applied to dynamic pressure roadway in kilometers deep mine,” *Coal Science and Technology*, vol. 43, no. 8, pp. 7–11, 2015.
 - [23] B. Li, L.-Y. Zhang, Y. Li, H.-G. Yin, and R.-X. Liu, “Stepwise loading-unloading creep testing of fly ash concrete and its constitutive model,” *Thermal Science*, vol. 23, no. 3 Part A, pp. 1539–1545, 2019.
 - [24] W. Lu, B. Jiang, Q. Wang, H.-B. Sun, Y. B. Huang, and P. Zhang, “Mechanical characteristics and parameter influencing mechanism of square steel confined concrete arch components in deep soft rock roadway,” *Journal of Mining & Safety Engineering*, vol. 37, no. 3, pp. 473–480, 2020.
 - [25] J.-L. Liu, L.-W. Chen, and J.-L. Wang, “Design method for shaft wall strength of coal mine considering influence of temperature stress,” *Chinese Journal of Rock Mechanics and Engineering*, vol. 30, no. 8, pp. 1577–1563, 2011.
 - [26] J.-L. Liu, L.-W. Chen, and J.-L. Wang, “Characteristic analysis of temperature stresses of shaft wall,” *Rock and Soil Mechanics*, vol. 32, no. 8, pp. 2389–2390, 2011.
 - [27] L.-W. Jing and H.-L. Li, “The affection caused by variance of temperature to the strength of shaft wall in shafts constructed by freezing method,” *Journal of China Coal Society*, vol. 25, no. 1, pp. 40–44, 2000.
 - [28] L.-W. Jing and H. Zhang, “Fracture analysis and prevention measures of fraction initiation in the melting stage of frozen shaft wall,” *Engineering Mechanics*, vol. 20, no. 1, pp. 122–126, 2003.
 - [29] L.-W. Jing, Q.-C. Gao, H.-D. Xu, and R.-S. Yang, “Thermal stress analysis of shaft in melting stage of frozen wall,” *Rock and Soil Mechanics*, vol. 25, no. 9, pp. 1357–1362, 2004.
 - [30] L.-W. Jing, Q.-C. Gao, F. Liu, and X.-C. Niu, “Rupture Mechanism and Rupture Forecast of The Shaft Wall in Mine,” *Engineering Mechanics*, vol. 23, no. 3, pp. 156–161, 2006.
 - [31] Y.-S. Wang, Z.-J. Yang, Y.-F. Yang, and C.-G. Zhang, “Mechanics model and ultimate horizontal bear capacity of outer shaft lining during freezing sinking,” *Journal of Mining and Safety Engineering*, vol. 26, no. 3, pp. 359–366, 2009.
 - [32] Y.-S. Wang, J.-P. Cheng, L.-B. Xue, Y.-L. Ren, Z.-J. Yang, and J.-H. Li, “In-situ measurements and analysis of frost-heave pressure inside and outside the ice wall during freeze sinking,” *Journal of China University of Mining and Technology*, vol. 38, no. 3, pp. 303–308, 2009.
 - [33] Y. Yi, D.-J. Zhu, S.-C. Guo, Z.-H. Zhang, and C.-J. Shi, “A review on the deterioration and approaches to enhance the durability of concrete in the marine environment,” *Cement and Concrete Composites*, vol. 113, Article ID 103695, 2020.
 - [34] S. Yin, J. Liu, S.-Y. Zhou, and G.-P. Li, “Experimental investigation on the freeze-thaw durability of concrete under compressive load and with joints,” *Construction and Building Materials*, vol. 229, Article ID 116893, 2019.
 - [35] M. Shafikhani and S. E. Chidiac, “Quantification of concrete chloride diffusion coefficient—a critical review,” *Cement and Concrete Composites*, vol. 99, pp. 225–250, 2019.
 - [36] S. Yin, L. Jing, M. Yin, and B. Wang, “Mechanical properties of textile reinforced concrete under chloride wet-dry and freeze-thaw cycle environments,” *Cement and Concrete Composites*, vol. 96, pp. 118–127, 2019.
 - [37] R.-X. Liu, H.-G. Yin, L.-Y. Zhang, B. Li, and X.-B. Mao, “Model for the patterns of salt-spray-induced chloride corrosion in concretes under coupling action of cyclic loading and salt spray corrosion,” *Processes*, vol. 7, no. 84, 2019.
 - [38] G. V. Chilingar, “Relationship between porosity, permeability, and grain-size distribution of sands and sandstones,” *Developments in Sedimentology*, vol. 1, pp. 71–75, 1964.

Research Article

Experimental Research on Bending Bearing Capability of Grouted Double Mortise-Tenon Joint for Prefabricated Metro Station Structure

Xiuren Yang ^{1,2}, Fang Lin ^{1,2} and Meiqun Huang^{1,2}

¹Beijing Urban Construction Design and Development Group Co., Ltd, Beijing 100037, China

²National Engineering Laboratory for Green & Safe Construction Technology in Urban Rail Transit, Beijing 100037, China

Correspondence should be addressed to Fang Lin; felyo@foxmail.com

Received 20 December 2020; Revised 24 February 2021; Accepted 5 March 2021; Published 17 March 2021

Academic Editor: Yunteng Wang

Copyright © 2021 Xiuren Yang et al. This is an open access article distributed under the Creative Commons Attribution License, which permits unrestricted use, distribution, and reproduction in any medium, provided the original work is properly cited.

The grouted mortise-tenon joint, invented as the connection between the large prefabricated elements, is the most important component in the prefabricated underground structures. This paper conducts analysis of load-carrying capacity performance and failure mode with 1 : 1 prototype test in key working direction of different double mortise-tenon joint types for the prefabricated metro station. The resistance moment is developed and used to analyze the bending bearing characteristic curve, and the corresponding test results of each stage of the characteristic curve are described in detail. In addition, the bending bearing performance of different types of double-tenon joints under different load conditions is compared. The test results clarify the ultimate failure mode of double-tenon joint and the variable bearing capacity characteristics of the joint with the increase in axial load and explain the bearing performance of each stage. It is also found the auxiliary pretightening device is helpful to delay the appearance of cracks and improve the bearing capacity, especially when it is set on the tension side. The research results have important application value for the joint design of prefabricated metro station structures.

1. Introduction

Since the rapid development of urban rail transit in China in 2000, it has maintained a high-speed growth trend. All cities are facing tremendous pressure in terms of construction period, environmental impact, labor shortage, project quality, etc. The traditional open-cut metro station structure is generally constructed by cast-in-place construction technology, which has many construction links, slow construction speed, serious construction dust and noise pollution, a large number of on-site workers and high labor intensity, difficult project quality control, and frequent leakage, and it is greatly affected by the climate conditions.

Prefabricated building structure has significant advantages such as high efficiency, high quality, and green and environmental protection and is widely used in the field of aboveground construction, especially in developed countries such as Europe, America, and Japan, while the application of

underground structures is mainly concentrated in shield tunnel engineering. In order to solve the problem of winter construction in the former Soviet Union, the prefabricated technology was studied and applied in the open-cut metro station and shield-driven tunnel structure engineering. Due to the limitations of early technology, the large-scale metro station mostly adopts the prefabricated rectangular frame structure with relatively complex system, and the joints are mainly connected by cast-in-place concrete, so the prefabrication advantage is not obvious [1–10].

The prefabricated station of Changchun Metro Line 2 is a two-story single arch long-span structure with open excavation. The prefabricated station structure is 20.5 m wide and 17.45 m high. It is built by assembling seven 2 m-wide prefabricated components without any concrete wet spraying (see Figure 1), which belongs to the fully prefabrication type. Compared with the aboveground structure, shield tunnel, or foreign prefabricated structure with cast-in-

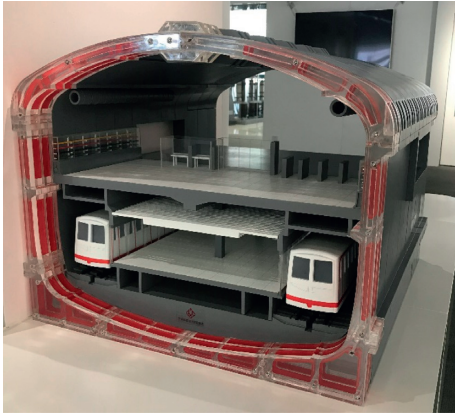


FIGURE 1: Model of prefabricated metro station.

place joint, this prefabricated metro structure has great differences in the use of environmental characteristics, stress characteristics, waterproof requirements, construction technology, and other aspects.

The grouted double mortise-tenon joint is used in most of the connections between prefabricated components for prefabricated stations (see Figure 2). The mechanical behavior of the joint is the key factor affecting the overall mechanical behavior of the prefabricated structure [11–14]. There is no precedent of grouted double mortise-tenon joint used in large underground structure [15–17]. Therefore, in order to study the mechanical behavior of the grouted double mortise-tenon joint under eccentric compression, a set of self-developed joint comprehensive test system was applied to carry out the bearing performance and destructive test of the prototype joint specimen (the key bearing direction is 1 : 1, and the width of noncritical direction is 1/2). The bending bearing capacity and failure mode of grouted double-tenon joints with the same type and structure are studied in depth.

2. Test Scheme

In this study, ten groups of loading tests were carried out for the double-tenon joint under different axial force and bending moment combinations, including three types of joints: without auxiliary pretightening device, auxiliary pretightening device on tension side, and auxiliary pretightening device on compression side. The specific test conditions are shown in Table 1 [18]. The types and structures of the three test joints are shown in Figure 3. The auxiliary pretightening device (blue-dotted line in Figure 4; specific dimensions are shown in Figure 3) refers to a boss structure on the outside of the joint to install two steel bars which can exert pretension. The test loading mode and loading sequence are shown in Figure 4. In the joint test, the straight joint specimen is applied axial load and bending moment independently. The axial load forms the joint axial force, and the bending moment is formed by applying the transverse concentrated force. This loading mode can combine different axial loads and bending moment values arbitrarily. In the loading sequence, multistage stable axial

load is set and loaded from large to small. Under the condition of maintaining a certain axial load, transverse concentrated load is applied step by step from small to large to form bending moment loading from small to large. In order to describe the test phenomenon conveniently, the side with opening tendency is defined as tension side, and the side with compression tendency is defined as compression side. The tenon on tension side is defined as tenon A, and the tenon on compression side is defined as tenon B.

The stable axial load is set at 1250 kN, 1000 kN, and 500 kN, and the bending moment increases gradually from 0 kN·m until the specimen is destroyed. During the test, the development law of crack on the joint surface, joint angle, surface concrete stress, and reinforcement stress change law were observed, and the basic mechanical behavior of joint was analyzed; different types of joints were compared and analyzed.

3. Analysis of Test Results

In the test, the crack development is the most direct performance of the joint bending load. Therefore, this paper will start from the crack development law to analyze the bending bearing characteristics.

3.1. Crack Development and Change Law of Joint.

Through observation, the double-tenon joint specimens go through the following stages: crack appearance → crack development → crack transfixion of tenon on tension side → crack transfixion between mortises A and B → structural crack transfixion → structural instability.

From the test results of various working conditions, the load acting value of structural crack transfixion is basically consistent with that of structural instability, which indicates that the bearing allowance from structural crack transfixion to structural instability is limited. The crack development in various types of double-tenon joints is analyzed as follows.

3.1.1. Crack Development of the Joint without Auxiliary Pretightening Device.

Taking 1000 kN axial load condition as an example (see Figure 5), the crack development patterns under various bending moments are shown in Table 2.

The crack development law of joint specimen without auxiliary pretightening device under different axial load conditions is summarized in Figure 6.

- (a) Under the condition of small axial load (500 kN), microcrack I first appears at the shoulder position (point A_a) of tenon A, which develops along the root of tenon A to the shoulder of tenon B. At the same time, another crack II with the same starting position (point A_a) appears, which develops along point A_b and point A_c of tenon A, forming a through-crack of tenon A.
- (b) Under the condition of large axial load (1000 kN and 1250 kN), the first crack also appears at the shoulder position A_a of the tension side. The crack grows along the A_b direction and develops along the

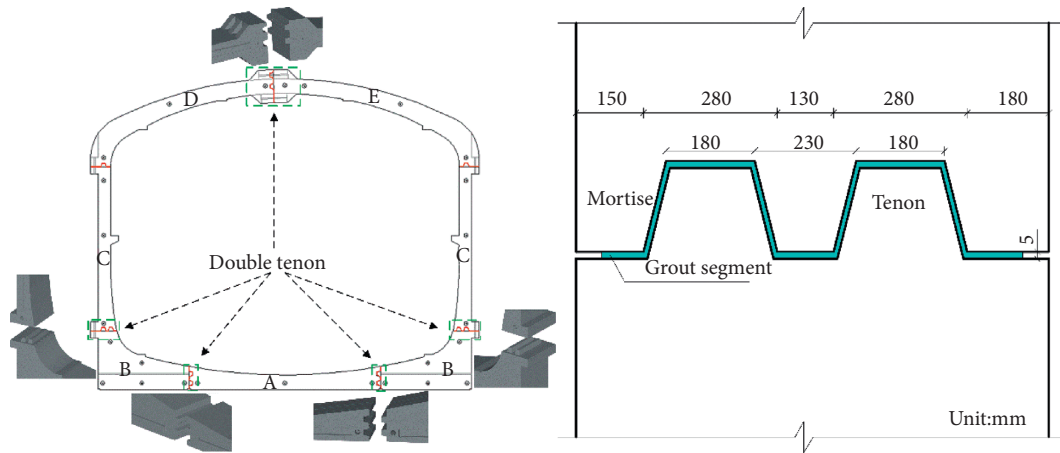


FIGURE 2: Arrangement and detail of double mortise-tenon joint.

TABLE 1: Test cases.

Test cases	Stable axial load Three types	500 kN, 1000 kN, 1250 kN Without auxiliary pretightening device, auxiliary pretightening device on tension side, auxiliary pretightening device on compression side
Test collection content		Concrete surface stress, reinforcement stress, record the whole process of joint and component crack development, joint deformation, joint rotation

direction of crack III. At the final failure, a main through crack (crack III) appears at the tenon.

- (c) The final failure of the joints without auxiliary pretightening device is cracking along the outer side of the tenon reinforcement protective layer, forming the main through crack III. The through-crack penetrates from tenon A to tenon B along the outer side of the protective layer. When the joint is finally damaged, cracks appear at the mortise position and connect with the tenon crack, and the outer side of the reinforcement protective layer on tensile side of the tenon shoulder (B_a) is also cracked.

3.1.2. *Crack Development of the Joint with Auxiliary Pretightening Device on Tension Side.* For the specimen with auxiliary pretightening device on tension side, the crack development under different axial load conditions is summarized in Figure 7.

- (a) Under the condition of small axial load (500 kN), the first crack I appears at point A_a and then appears crack II. At the same time, the crack III starts from the joint of grouting section and nongrouting section at the upper boss of A_a near the shoulder of tension side, and it grows along the reinforced and concrete joint of tenon A.
- (b) When the axial load is large (1000 kN and 1250 kN), the first crack I also appears at point A_a , and no crack II appears. When the crack I drives out of B_a (the second arrow), crack III begins to develop.
- (c) The small crack appears in the joint between the boss and the tenon when the crack III develops in the B_a

area. The small crack is short in length and develops slowly. A main through-crack appears at the tenon position at the final failure (crack III), which runs from the tenon of the tension side layer and along the outer side of the protective to the tenon of the compression side (from A to B). Cracks appear at the mortise position, which are connected with the tenon crack, and run to the shoulder (position B_a , between mortise A and mortise B) at the outer side of the reinforcement protective layer on tension side.

3.1.3. *Crack Development of the Joint with Auxiliary Pretightening Device on Compression Side.* For the specimen with auxiliary pretightening device on compression side, the summary of crack development is shown in Figure 8.

- (a) Under the condition of small axial load (500 kN), the first crack I starts from the position of tenon foot on tension side (the intersection of A_a and A_b) and develops along the reinforcement protective layer close to the joint surface (A_b , A_c , and A_d).
- (b) Under the condition of large axial load (1000 kN and 1250 kN), the first crack II develops along the direction of B_a from the intersection point of A_a and A_b . With the increase in bending moment, the development path of the first crack I appears under the condition of small axial load. Finally, when the crack passes through, crack III extends to the boundary between grouting section and nongrouting section on A_a .
- (c) The joint of boss and tenon develops two cracks parallel to the steel bar from the boundary of

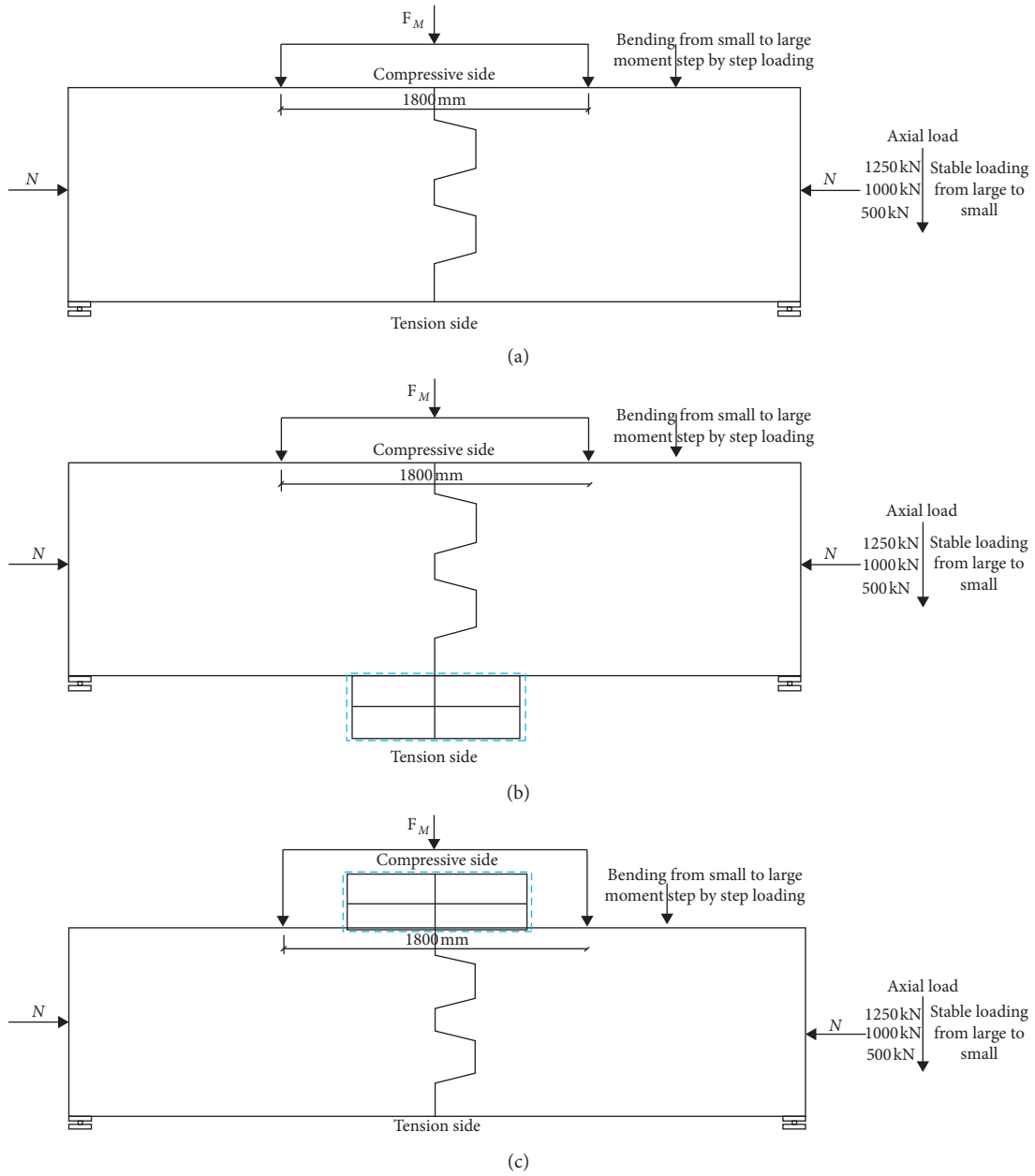


FIGURE 4: Layout for loading mode and sequence of specimens: (a) without auxiliary pretightening device; (b) auxiliary pretightening device on tension side; (c) auxiliary pretightening device on compression side.

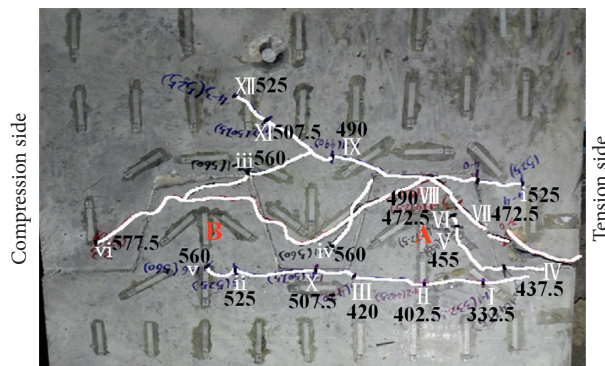


FIGURE 5: Crack development of double mortise-tenon joint without auxiliary pretightening device (axial load 1000 kN).

TABLE 2: Crack development under increasing bending moment.

Bending moment	Crack development
332.5 kN·m	Crack I appears
420 kN·m	Crack extends from II to III
455 kN·m	Crack extends from IV to V
490 kN·m	Crack extends from VII to VIII, crack IX appears
525 kN·m	Cracks XII (i and ii) appear, cracks IX (i) XI, and XII transfixion, cracks VII and VIII transfixion, tenon A transfixion
577.5 kN·m	Cracks VII and VIII connect the whole tenons and crack vi appears, crack iii and VII and VIII and vi connect, structural crack transfixion
402.5 kN·m	Crack extends from I to II
437.5 kN·m	Crack IV appears
472.5 kN·m	Crack extends from V to VI, crack VII appears
507.5 kN·m	Crack extends from III to X, crack extends IX to XI
560 kN·m	Through cracks i, IX, XI, and XII derive from cracks iii and iv, crack extends from ii to v, tiny cracks appear near the cracks IV, V, and VI, cracks between the two tenons A and B are connected

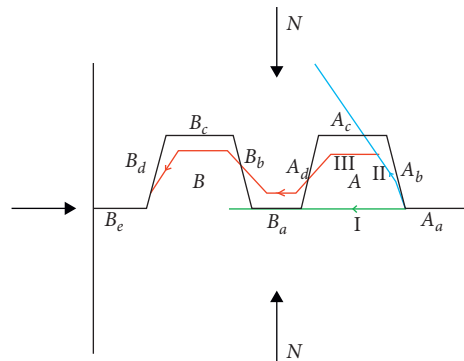


FIGURE 6: Crack development of double mortise-tenon joint without auxiliary pretightening device.

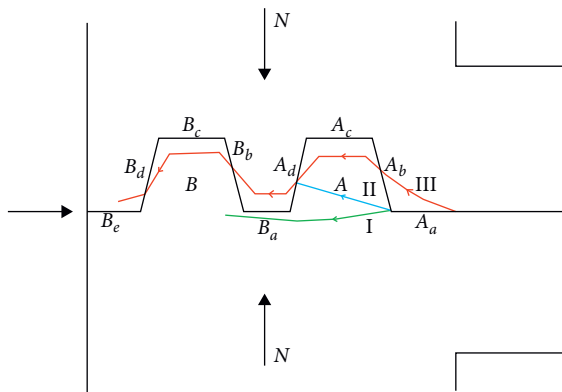


FIGURE 7: Crack development of double mortise-tenon joint with auxiliary pretightening device in tension side.

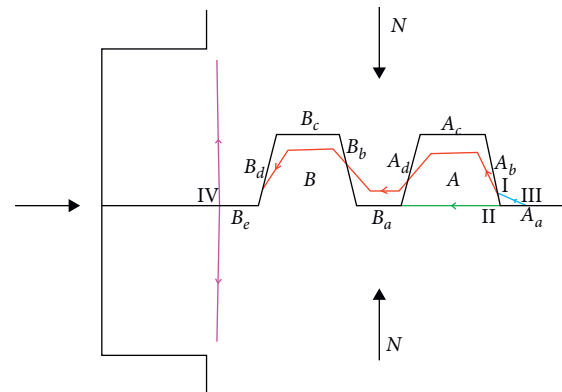


FIGURE 8: Crack development of double mortise-tenon joint with auxiliary pretightening device in compression side.

stage III (453 kN m ~ 539 kN m) is obviously smaller than the first two stages, and it is the joint softening stage, which accounts for a larger proportion than stage II; at the end of bearing stage IV (539 kN m ~ 578 kN·m), the slope tends to be horizontal, and the slight increase in bending moment leads to sharp increase in rotation angle, which accounts for a small proportion. In addition, it can be seen that the

resistance moment M_R almost coincides with the inflection point b (under the action of axial load, the moment M_R is formed by the effective contact surface of the joint to resist the action of bending moment). When the joint is loaded beyond the resistance moment, the slope of the curve decreases obviously, and the bearing capacity obviously weakens. It also reflects that the bending resistance of the

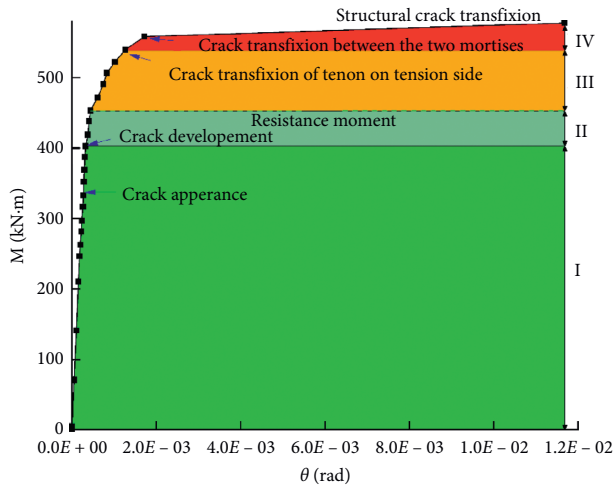


FIGURE 9: Relationship of crack development and bearing characteristic curve for double mortise-tenon joint.

tenon is not obvious due to the different properties of the two tenons (one pulls and one presses), and the ultimate failure state is the tenon pull-out.

From the perspective of crack development (combined with Figure 5), some concrete exceeds the limit state of tensile stress at the position of the foot of tenon A, and then, cracks appear for the first time at the end of stage I, so the linear stage ends. From stage II, the cracks begin to develop, but in the whole stage II, due to the effect of resistance moment, the development is relatively slow, and there are only small cracks in the inner part of tenon A. When the load exceeds the resistance moment, it enters stage III, the bending resistance of the tenon is weak, and the crack development increases. At the end of this stage, the cracks of tenon A are connected. Then, the curve goes into stage IV, and tenon A on tension side loses bearing capacity due to crack transfixion. At this time, the property of the tenon B on compression side changes from compression to tension, and bending performance of the tenon B becomes weak. Soon, cracks go through the mortise A and mortise B, and then, the structural cracks go through and the joint loses the bearing capacity. The end of the bearing stage is relatively short.

3.3. Analysis of Test Results Corresponding to Curve Characteristics. The following results are combined with the concrete and reinforcement stress performance and the curve of the bending bearing characteristics of each bearing stage.

3.3.1. Performance of Concrete Surface Stress. It is found that the changes in concrete surface stress between the two tenons and the two tenon regions themselves are the most obvious, and the stress concentration phenomenon exists. The stress curve of tenon A on tension side changes most intensely, while the mechanical performance of tenon B on compression side is completely opposite to that of the tenon A, and the change is obvious only after the cracks of tenon A pass through.

Also taking an axial load of 1000 kN without auxiliary pretightening device condition as an example, the performance of concrete surface stress is explained in the following content. The layout of concrete strain gauges is shown in Figure 10, which shows the crack development when the joint is damaged. The measuring points outside the joint contour of the compression side and the tension side indicate the strain gauges attached to these two sides, i.e., the 500 mm wide surface shown in Figure 3. The development curve of concrete stress at representative measuring points is drawn in Figure 11, four stages of bearing are added, and the crack development stage is identified by dotted lines at the significant inflection points of the curve. Figure 11(a) represents the curve of measuring points at the position of the tenon on tension side, Figure 11(b) represents the curve of measuring points at the position of the tenon on compression side, and Figure 11(c) represents the curve of measuring points at the mortise between tenons A and B and the curve of measuring point on both sides of compression side and tension side. From these figures, we can see the following rules:

- From Figure 11(a): the first inflection point of tenon A appears around the resistance moment, and then, there is an obvious inflection point at the time of tenon penetration on tension side; the next inflection point occurs at the crack connection time between the two mortises at the end of the bearing period. The tensile stress state of #73 and #74 is obvious after the resistance moment, especially at #74 which is closer to the tension side changes dramatically around the time of tenon penetration on tension side.
- From Figure 11(b): the properties of the tenon on compression side are completely different from those on tension side. The changes in the measuring points #65 and #67 in the first three stages and the measuring point #66 in the first two stages are not obvious, and the later stage mainly shows the state of compressive stress.

When the load exceeds the resistance moment, the three measuring points have obvious inflection points at the time when the cracks of the two mortises pass through, and then, the compressive stress increases.

With the increase in the compressive stress, the increase in #64 on the wall of the mortise on compression side increases continuously, and when the load exceeds the resistance moment, it reaches the limit state of compressive stress at the moment when the cracks between the two mortises pass through.

- Figure 11(c): the compressive stress of the measuring point #58 located on compression side increases with loading, and the compressive stress becomes larger when the load exceeds the resistance moment. In stage IV, when the crack between the two mortises is connected, it increases rapidly to the limit state of compressive stress.

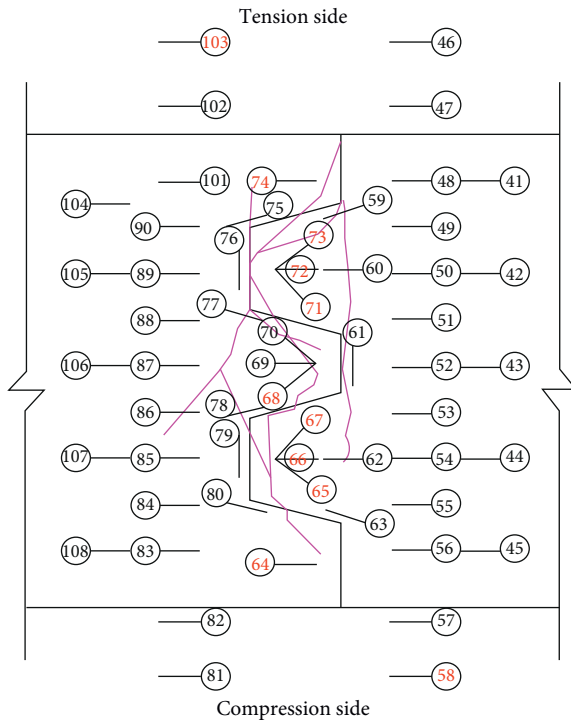


FIGURE 10: Strain gauge arrangement of concrete surface for an axial load of 1000 kN.

The tensile stress of the measuring point #103 on tension side increases with loading and reaches the limit state of tensile stress in the middle of stage II.

The measuring point #68 between the two mortises has little change in the first two stages. When the load exceeds the resistance moment, the compressive stress caused by the axial load decreases. At the later stage of stage III, tenon A reaches the minimum compressive stress state when the crack comes through the tenon A, and then, the compressive stress increases; the inflexion point of increasing compressive stress appears when the cracks between the two mortises pass through. At this time, the crack passes through the strain gauge of #68.

3.3.2. Stress Performance of Reinforcement at Representative Measuring Points. From the performance of reinforcement stress, it can also be observed that the closer to the tenon, the larger the stress of the measuring point, and the stress change in tenon and mortise is more severe than that in other places; there is a certain degree of stress concentration. Also taking an axial load of 1000 kN without auxiliary pretightening device as an example, the stress change curve of the joint reinforcement is extracted in Figure 12. Figure (a) is the tenon area on tension side, and Figure (b) is the tenon area on compression side. From the figures, we can see the following rules:

- (a) For the measuring point on the tenon A of the tension side, the reinforcement stress increases slowly with loading in the first two stages. The increasing speed is obvious when the load exceeds the

resistance moment. At stage IV, the reinforcement stress increases obviously and reaches the peak value when the cracks between the two mortises pass through, which provides the main driving force for the joint's tensile strength.

- (b) For the measuring points on the tenon B of the compression side, except the measuring points #13 and #15 on the tenon are in the state of tensile stress at stage II when the load is close to the resistance moment; the rest of the measuring points change little in the first two stages and are in the state of compressive stress; when the load exceeds the resistance moment, the tensile stress increases slowly. The inflexion point appears when the cracks between the two mortises are connected, and then, the tensile stress increases rapidly, but the change degree is less than that of the tenon on tension side.
- (c) From the performance of reinforcement stress, the reinforcement stress changes little in the first two bearing stages, the bending resistance of the joint mainly depends on the resistance moment, and then, the tenon begins to play the bending role. Except for the measuring points on the tenon of the tension side, the overall reinforcement stress is not large. Due to the opposite effect of tension and compression of the two tenons, the bending effect of the tenons is not strong.

According to the inflexion point of stress on the tension and compression sides at the time the cracks between the two mortises pass through, combined with the performance of the crack and concrete stress, the failure mode of the joint is the tenon pull-out.

3.4. Analysis of Joint Bearing Capacity at Different Stages. The $M-\theta$ bending moment-rotation curves of different types of double-tenon joint under different working conditions are extracted. It is found that the bearing characteristic curve of double-tenon joint can be divided into four stages, which can be simplified into four polylines diagram, as shown in Figure 13. The bearing capacity space of different stages of double-tenon joint bearing characteristic curve and the relationship between each stage and crack development are also counted in Figure 13:

- (a) The $M-\theta$ curve of double-tenon joint can be simplified as a three inflexion points four polylines diagram. The load-bearing capacity is obviously divided into four stages. The proportion of each bearing stage in the whole bearing period is counted on the left side of the figure. Stage I is a linear segment, which accounts for the largest proportion, mainly depending on the resistance moment. Stage II is a quasilinear segment, the slope of stage II is slightly smaller than that of stage I, and its proportion is very small. The resistance moment of the section is also the main part in stage II. Stage III enters the nonlinear stage with joint softening. The slope of stage III is obviously lower than that of the

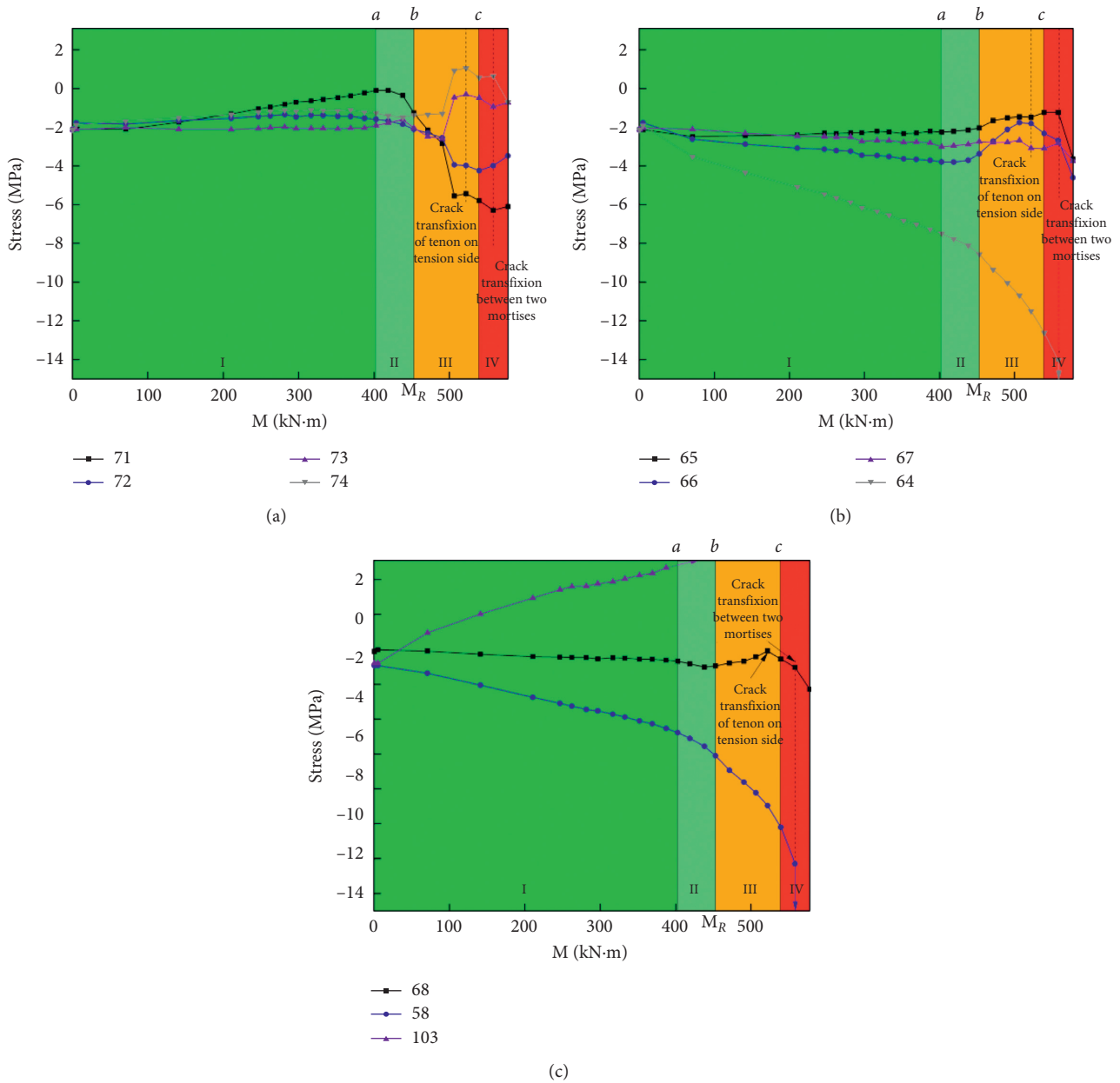


FIGURE 11: Change curve in stress with bending moment.

first two stages, and the proportion of this stage is almost twice as that of stage II, which mainly depends on the bending of tenon A on the tension side. The slope of stage IV decreases sharply, and the joint deformation intensifies and continues to weaken. Depending on the residual bending resistance of tenon A on tension side and the weak bending resistance of the region between mortise A and mortise B which can also be regarded as the tenon on the mortise side (B_a position in Figure 6), the joint carries out the final stage of loading.

(b) For the double-tenon joint, the resistance moment almost coincides with the boundary of stage II and stage III. When the load exceeds the resistance

moment, the bearing capacity decreases. Depending on the bending resistance of tenon A on tension side and the engagement of three tenons (tenon A on tension side, tenon B on compression side, and the tenon between mortise A and mortise B on the mortise side), the joint has experienced a nonlinear stage III longer than stage II. In the later stage III, the crack of tenon A on tension side passes through, and the curve goes into stage IV with the bearing capacity decreasing rapidly. At this moment, the cracks between the two mortises are connected, and then, the bearing limit is quickly reached.

(c) According to statistics, the first two stages of all types of double-tenon joints (including those with

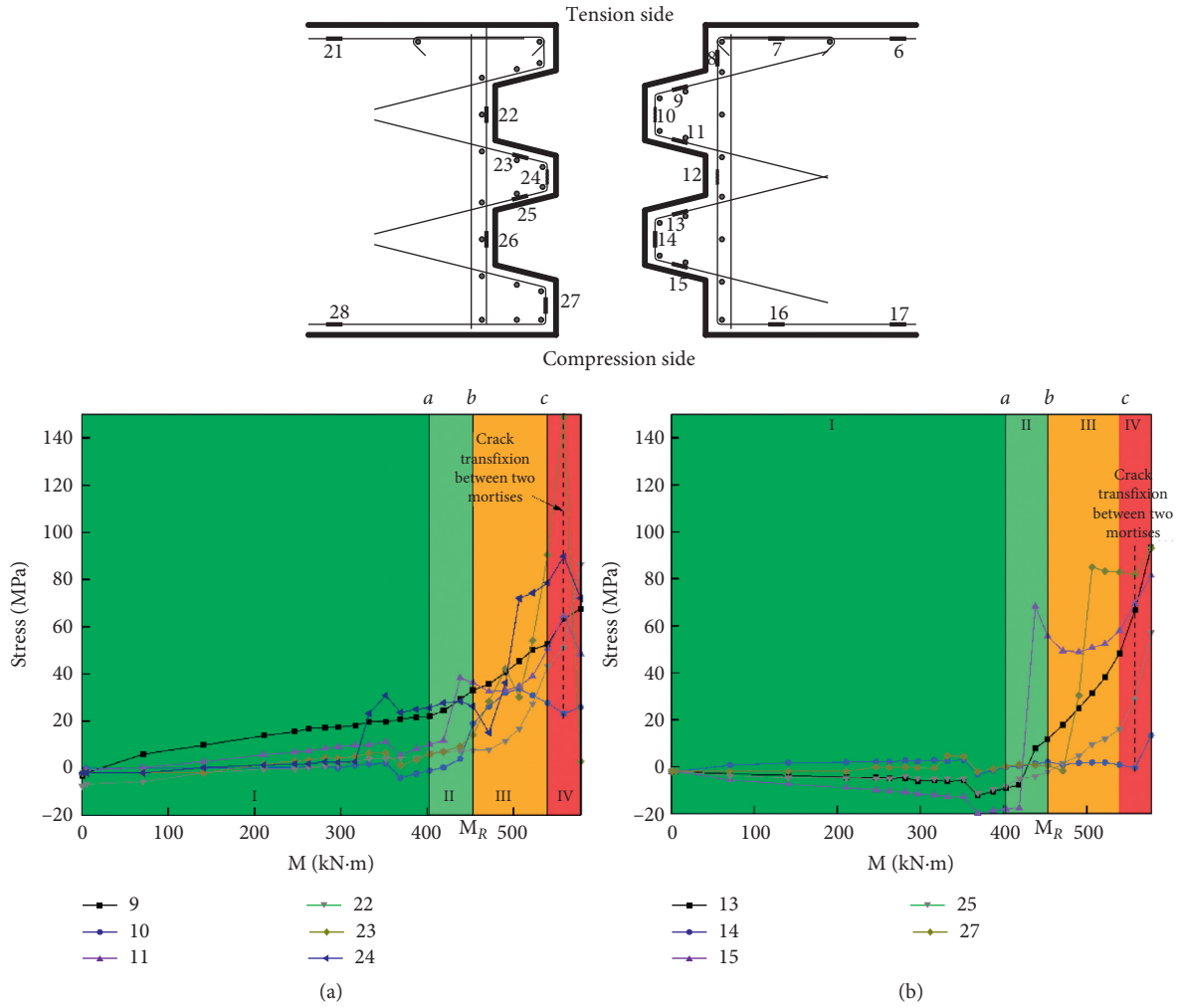


FIGURE 12: Change curve in reinforcement with bending moment (without auxiliary pretightening device).

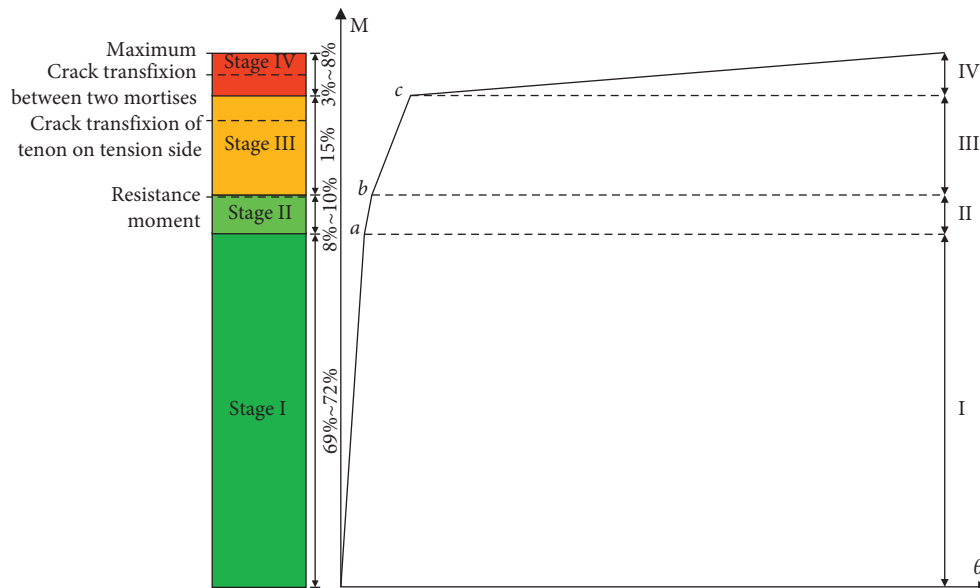


FIGURE 13: Bearing stage of bearing characteristic curve for grouted mortise-tenon joint.

auxiliary pretightening tension devices) account for 77% ~ 82%, and the first two stages mainly depend on section resistance moment, and the joint deformation is small, so it is recommended to consider the first two stages as the design and use stage.

4. Bearing Capacity Analysis of Different Types of Double-Tenon Joint

In order to judge the difference in bearing characteristics of different types of double-tenon joints more vividly, Figure 14 analyzes the stress change in reinforcement at the same position of different types of joints. Figure (a) shows the position of measuring point #9 of the tenon on tension side (see Figure 12 reinforcement stress arrangement), and Figure (b) shows stress change in pretightening steel bar. From the figure, the following is observed:

- (a) It can be seen from the stress change in measuring point #9 on the tenon A of the tension side that the curve of the joint without auxiliary pretightening device is close to the joint with auxiliary pretightening device on tension side, and the tensile stress increases with the increase in bending moment. When the load exceeds the resistance moment, the curve increases faster, and the auxiliary pretightening device increases the bearing capacity, and the curve is longer than joint without auxiliary pretightening device. However, the curve of the joint with auxiliary pretightening device on compression side does not start to play a tensile role until the inflection point c. The reason is that after the auxiliary pretightening device is compressed on the compression surface, the section resistance length actually increases, and the actual resistance moment is greater than the other two types. Therefore, at the end of the bearing period, tensile stress of the reinforcement at measuring point #9 which is close to the tensile side increases, because at the end of the bearing period, the increase and the slope of the curve are very large.
 - (b) From the comparison of the stress of the pretightening steel bar on tension side and the compression side, the pretightening steel bar on tension side is fully developed and reaches the yield strength after the cracks of the two tenons are connected. When the auxiliary pretightening device is located on the compression side, the tensile performance of the pretightening steel bar is not fully exerted, and it shows the compressive stress state in the later stage.
- (b) The bending moment of the joint with auxiliary pretightening device is significantly larger than the joint without auxiliary pretightening device in typical stage. For example, compared with the joint without auxiliary pretightening device, under the action of an axial load of 500 kN, the bending moment of crack appearance is increased by 6.67%, the bending moment of crack transfixion of tenon A on tension side is increased by 40.91%, the bending moment of crack transfixion between mortise A and mortise B is increased by 39.13%, and the ultimate bearing moment is increased by 37.5%. Under the action of an axial load of 1000 kN, the bending moment increases by 10.53% when cracks appear, the bending moment increases by 13.33% when the crack passes through tenon A on tension side, the through bending moment of cracks between mortise A and mortise B increases, and the ultimate bearing moment increases by 39.39%. Under the action of an axial load of 1250 kN, the bending moment increases by 4.84% when cracks appear, the bending moment increases by 25% when the crack passes through tenon A on tension side, the bending moment of crack transfixion between mortise A and mortise B increases by 21.05%, and the ultimate bearing moment increases by 20.51%. It can be seen that the setting of auxiliary pretightening device plays a more obvious role in delaying the appearance of cracks and improving the ultimate bearing capacity under the action of small axial load.
 - (c) Compared with the auxiliary pretightening device on tension side, the bending moment of the auxiliary pretightening device on compression side is smaller, which is 6.8% less at 1250 kN and 6.9% at 1000 kN, and the amplitude reaches 32% under small axial load (500 kN). The bending moments of the auxiliary pretightening device on compression side are 15% and 14% larger at the beginning of the crack under the condition of large axial load (1000 kN and 1250 kN).
 - (d) When the load exceeds the resistance moment, the joint cracks develop, and then, the cracks of tenon A on tension side pass through. At this time, there is no crack in the region of mortise B on compression side and the tenon between tenon A and tenon B. It can be seen that when the load is greater than the resistance moment, the tenon A on tension side first plays an occlusive role, which mainly bears the tensile force, and failure mode of tenon A belongs to the tensile failure during which the crack penetrates to failure. However, when the cracks of tenon A on tension side are penetrated, the tenon B on compression side starts occlusion. Although the main bearing pressure is compression stress, the tenon A on tension side loses the main bearing capacity after the crack is penetrated, and the crack propagation tension is transmitted. Finally, the tenon B on compression side does not reach the

Next, the bending moment of typical crack development stages of various types of double-tenon joints under different axial loads is shown in Figure 15, and the resistance moment of various types of double-tenon joints is also counted in the figure. From the figure, the following could be inferred:

- (a) The bending moment of double-tenon joint increases with the increase in axial load.

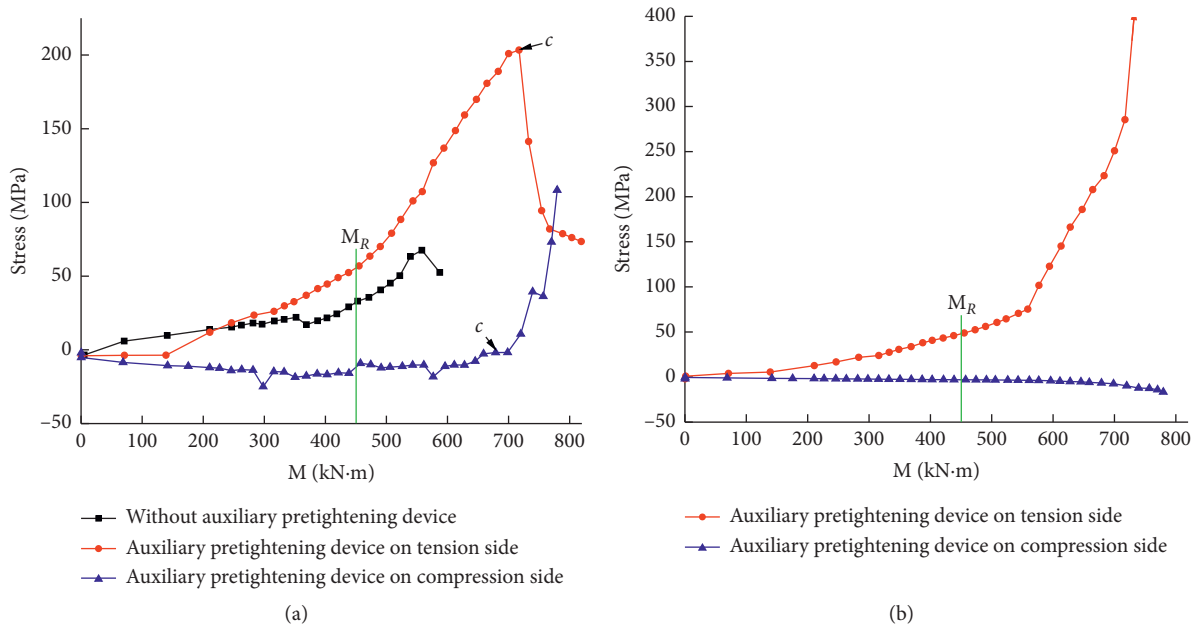


FIGURE 14: Comparison of rebar stress for different types of double mortise-tenon joints.

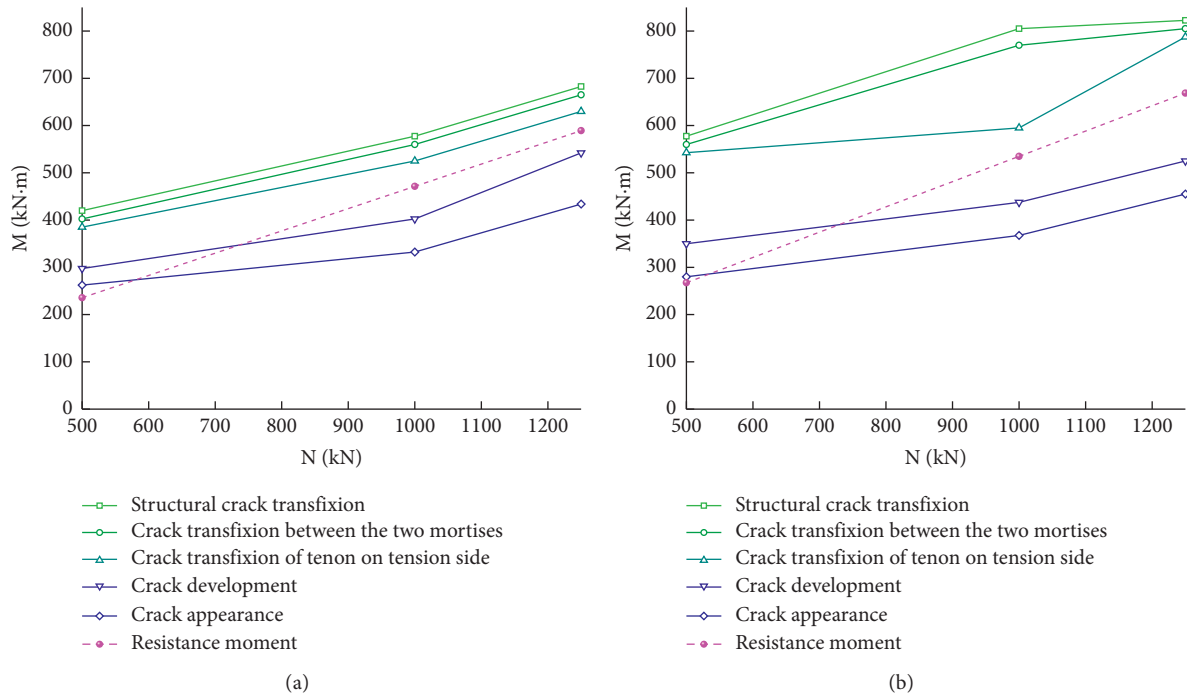


FIGURE 15: Continued.

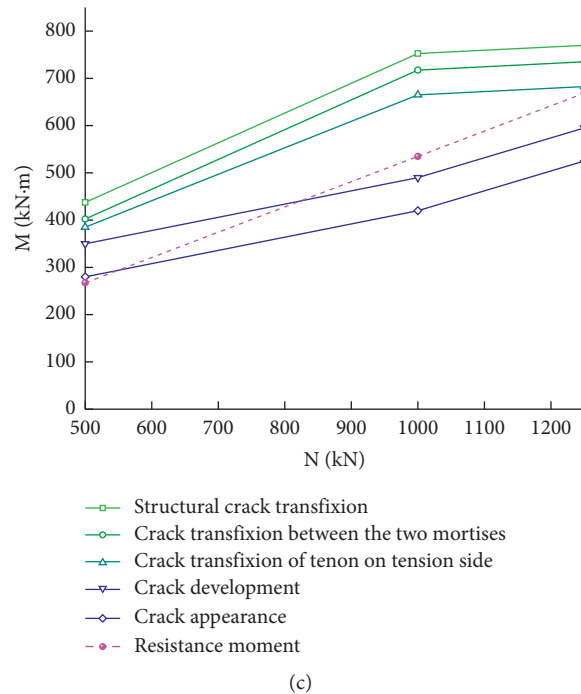


FIGURE 15: Key bending moments of different double mortise-tenon joints under various loads: (a) without auxiliary pretightening device; (b) auxiliary pretightening device on tension side; (c) auxiliary pretightening device on compression side.

compressive stress limit, which is affected by the crack development caused by the tensile force from the tenon A on tension side to the mortise between tenon A and tenon B. The failure mode of tenon B also belongs to the tensile failure. It can be seen from the figure that the above phenomenon occurs when the axial load is greater than or equal to 800 kN.

When the axial load is less than or equal to 800 kN, especially under the condition of 500 kN, the crack will appear only after the load exceeds the resistance moment. The reason is that the contribution of the axial load component under the action of large axial load makes the distinction of the pulling and pressing properties of the two tenons more obvious, while under the action of small axial load, the two tenons play the occlusive role of the key teeth with only little help of resistance moment. The influence of the different properties of the tenons with one pulling and one pressing is not obvious under the action of the small axial force. That is to say, under the condition of small axial load, when the load exceeds the resistance moment, the tenon can play some bending functions to resist the force, but under the condition of large axial load, when the load exceeds the resistance moment, the bending effect of the joint with one pulling tenon and one pressing tenon is weakened. The tenon A on tension side plays the main role, and the bending effect of tenon A on tension side is greater than that of tenon B on compression side. The ultimate failure mode is that the two tenons are pulled out successively.

5. Conclusion

In this paper, the 1:1 prototype load-bearing performance and destructive test of the double-tenon joint with a different stiffness in various types and working conditions are carried out. Through the analysis of the results and the in-depth study on its failure mode and bearing performance, the following conclusions are obtained:

- When the load exceeds the resistance moment, the tenon on tension side plays a main bearing role. Finally, the failure mode is that the two tenons are damaged one after another. The main crack develops along the tenon outline on tensile side and penetrates into the tenon on compression side.
- The load-bearing characteristic curve of double-tenon joint can be simplified as three inflection points and four polylines diagram. The bearing capacity is divided into four stages: stage I is linear, the bearing capacity mainly depends on the section resistance moment; stage II is quasilinear, and the bearing capacity is also dominated by section resistance moment; stage III is nonlinear, which mainly depends on the bending resistance of the tenon on tension side; stage IV is nonlinear, the joint has been weakened, and the tenon remains the residual bending resistance.
- For the same type of double-tenon joint, under the same loading mode, the bending moment of each key stage increases with the increase in axial load.

The greater the axial load is, the stronger the bending resistance of the joint is.

- (d) Under the same axial load condition, the bending moment of the critical stage of the joint with auxiliary pretightening device (pretightening steel bar + boss) is significantly larger than the joint without auxiliary pretightening device. The auxiliary pretightening device is helpful to delay the occurrence of cracks and improve the bearing capacity, especially when the axial load is small.
- (e) It is more effective to place the pretightening steel bar on tension side than on compression side.

Data Availability

The data used to support the findings of this study are available from the corresponding author upon request.

Conflicts of Interest

The authors declare that there are no conflicts of interest.

Authors' Contributions

Xiuren Yang supervised the project and developed the concept and methodologies with Meiqun Huang. Fang Lin performed the experimental and theoretical studies.

Acknowledgments

This research was funded by the National Key S&T Special Projects (Grant no. 2017YFB1201104).

References

- [1] L. Rozsa, "Precast concrete segment lining of the Budapest Metro," *Tunnels & Tunnelling International*, vol. 11, no. 10, 1979.
- [2] K. Beilassov, Q. H. Qian, and C. Z. Qi, *The Essence of the Construction of Russian Underground Railway*, China Railway Press, Beijing, China, 2012.
- [3] J. H. Liu and X. Y. Hou, "The History of Shield Tunneling," China Railway Press, Beijing, China, 1991.
- [4] H. Backmann and A. Steinle, *Precast Concrete Structures*, Ernst & Sohn, Berlin Germany, 2011.
- [5] J. Bi, X. P. Zhou, and Q. H. Qian, "The 3D numerical simulation for the propagation process of multiple pre-existing flaws in rock-like materials subjected to biaxial compressive loads," *Rock Mechanics and Rock Engineering*, vol. 49, no. 5, pp. 1611–1627, 2016.
- [6] Y.-H. Huang, S.-Q. Yang, P. G. Ranjith, and J. Zhao, "Strength failure behavior and crack evolution mechanism of granite containing pre-existing non-coplanar holes: experimental study and particle flow modeling," *Computers and Geotechnics*, vol. 88, pp. 182–198, 2017.
- [7] J. Bi, P. Liu, and F. Gan, "Effects of the cooling treatment on the dynamic behavior of ordinary concrete exposed to high temperatures," *Construction and Building Materials*, vol. 248, Article ID 118688, 2020.
- [8] Q. H. Qian and X. P. Zhou, "Failure behaviors and rock deformation during excavation of underground cavern group for Jinping I hydropower station," *Rock Mechanics and Rock Engineering*, vol. 51, no. 8, pp. 2639–2651, 2018.
- [9] Q. H. Qian, X. P. Zhou, H. Q. Yang, Y. X. Zhang, and X. H. Li, "Zonal disintegration of surrounding rock mass around the diversion tunnels in Jinping II Hydropower Station, Southwestern China," *Theoretical and Applied Fracture Mechanics*, vol. 51, no. 2, pp. 129–138, 2009.
- [10] T. Liu, J. Lu, D. Wang, and H. Liu, "Experimental investigation of the mechanical behaviour of wall–beam–strut joints for prefabricated underground construction," *International Journal of Concrete Structures and Materials*, vol. 15, no. 1, pp. 1–19, 2021.
- [11] X. R. Yang, M. Q. Huang, and F. Lin, "Research strategies on new prefabricated technology for underground metro stations," *Urban Rail Transit*, vol. 5, pp. 145–154, 2019.
- [12] X. R. Yang and F. Lin, "Prefabrication technology for underground metro station structure," *Tunnelling and Underground Space Technology*, vol. 108, Article ID 103717, 2021.
- [13] X. R. Yang, Z. H. Shi, and Z. F. Lin, "Influence of geometrical parameters on performance of grouted mortise and tenon joints for application in prefabricated underground structures," *Advances in Civil Engineering*, vol. 2019, Article ID 3747982, 2019.
- [14] X. R. Yang, Z. H. Shi, and Z. F. Lin, "Research on shear capacity and checking method of MT·G-joint for application in prefabricated underground structures," *Advances in Materials Science and Engineering*, vol. 2019, Article ID 4065301, 2019.
- [15] S. Teachavorasinskun and T. Chub-Uppakarn, "Influence of segmental joints on tunnel lining," *Tunneling and Underground Space Technology*, vol. 25, no. 4, pp. 490–494, 2010.
- [16] D. A. Steinhardt and K. Manley, "Adoption of prefabricated housing—the role of country context," *Sustainable Cities and Society*, vol. 22, pp. 126–135, 2016.
- [17] B. Tvede-Jensen, M. Faurschou, and T. Kasper, "A modelling approach for joint rotations of segmental concrete tunnel linings," *Tunnelling and Underground Space Technology*, vol. 67, pp. 61–67, 2017.
- [18] X. R. Yang, M. Q. Huang, and F. Lin, "Experimental method of grouted mortise-tenon joint for prefabricated metro station structure," *Urban Rail Transit*, vol. 32, no. 5, pp. 83–90, 2019.